Title
Structural Response and Cost Characterization of Bridge Construction using Seismic Performance Enhancement Strategies

Author
Aviram Traubita, Ady

Publication Date
2009

Peer reviewed|Thesis/dissertation

Structural Response and Cost Characterization of Bridge Construction using Seismic Performance Enhancement Strategies

by

Ady Aviram Traubita

A dissertation submitted in partial satisfaction of the

requirements for the degree of

Doctor of Philosophy

in

Engineering - Civil and Environmental Engineering

in the

Graduate Division

of the

University of California, Berkeley

Committee in charge:

Professor Bozidar Stojadinovic, Chair
Professor Khalid Mosalam
Professor Douglas Dreger

Fall 2009

Structural Response and Cost Characterization of Bridge Construction using Seismic Performance Enhancement Strategies

by

Ady Aviram Traubita

ABSTRACT

Structural Response and Cost Characterization of Bridge Construction using Seismic Performance Enhancement Strategies

by

Ady Aviram Traubita

Doctor of Philosophy in Engineering – Civil and Environmental Engineering

University of California, Berkeley

Professor Bozidar Stojadinovic, Chair

The improved seismic performance and cost-effectiveness of two innovative performance-enhancement technologies in typical reinforced concrete bridge construction in California were assessed in an analytical and experimental study. The technologies considered were lead rubber bearing isolators located underneath the superstructure and fiber-reinforced concrete for the construction of bridge piers.

A typical five-span, single column-bent reinforced concrete overpass bridge was redesigned using the two strategies and modeled in OpenSees finite element program. Two alternative designs of the isolated bridge were considered; one with columns designed to remain elastic and the other such that minor yielding occurs in the columns (maximum displacement ductility demand of 2). The analytical model of the fiber-reinforced concrete bridge columns was calibrated using the results from two bidirectional cyclic tests on approximately ¼-scale circular cantilever column specimens constructed using concrete with a 1.5% volume fraction of high-strength hooked steel fibers, relaxed transverse reinforcement, and two different longitudinal reinforcement details for the plastic hinge zone.

Pushover and nonlinear time history analyses using 140 ground motions were carried out for the different bridge systems. The PEER performance-based earthquake engineering methodology was used to compute the post-earthquake repair cost and repair time of the bridges. Fragility curves displaying the probability of exceeding a specific repair cost and repair time thresholds were developed. The total cost of the bridges included the cost of new construction and post-earthquake repair cost required for a 75 year design life of the structures. The intensity-dependent repair time model for the different bridges was computed in terms of crew working days representing repair efforts. A financial analysis was performed that accounted for a wide range of discount rates and confidence intervals in the estimation of the mean annual post-earthquake repair cost.

Despite slightly higher initial construction costs, considerable economic benefits and structural improvements were obtained from the use of the two performance-enhancement

techniques considered, in comparison to the fixed-base conventionally reinforced concrete bridge, especially seismic isolation. The isolation of the bridge superstructure resulted in a significant reduction in both column and abutment displacement and force demands. The repair time of the isolated bridges was also significantly reduced, leading to continuous operation of the highway systems and reduced indirect economic losses. The experimental and analytical results also demonstrated that the use of fiber-reinforced concrete to build bridge columns leads to improved damage-tolerance, shear strength, and energy dissipation under cyclic loading compared to conventional reinforced concrete columns. These improvements result in better seismic performance and lower total 75-year cost of the fiber-reinforced column bridges.

ACKNOWLEDGMENTS

My years studying at the University of California, Berkeley have been blessed with enriching and challenging academics and research projects, exciting experiences and travels, as well as many lifelong friendships. I would like to take this opportunity to express my deep appreciation to all the people that have, in some manner, contributed to my doctoral studies.

First and foremost I would like to express my sincere gratitude to my research advisor and academic mentor, Professor Bozidar Stojadinovic, for his guidance and firm support throughout my time at Berkeley. With his encouraging words and exemplary attitude, he had convinced me to transfer to the Ph.D. program and pursue my research interests. His confidence in my capabilities and criteria had allowed me to have sufficient freedom in defining the scope and direction of the research projects I was involved in, or at least to believe so. I could not have wished for a better, smarter, and more inspiring advisor.

I would like to thank Professor Kevin R. Mackie from the University of Central Florida and Professor Gustavo Parra-Montesinos from the University of Michigan for their important contributions in the development of this dissertation. Professor Mackie and I have collaborated on several research projects and papers, and he has been a truly encouraging figure throughout my years in Berkeley. Both had presented valuable insights during the elaboration of this project, as well as critical suggestions and reviews regarding this dissertation. I would also like to take this opportunity to thank my friend and fellow Ph.D. student, Vesna Terzic, for her generous advice and support, as well as for the contributing information obtained from her research which allowed for the interesting comparison and assessment of our experimental results.

Special thanks are also due to the laboratory staff at Davis Hall for their hard work and friendly manner during the experimental program of my project. I am especially grateful to Dr. Lev Stepanov, Jeff Higginbotham, and Philip Wong for their assistance.

To my parents, Dr. Kalman and Ela Aviram, and to my brother, Shahar Aviram, I am forever thankful for their unconditional love and support in all my endeavors. This dissertation is dedicated to them. To my dad, who has been my biggest fan and at the same time my biggest inspiration, I deeply thank for teaching me the true meaning of hard work and perseverance. To my mom and best friend, I thank for her love and compassion, and especially for always helping me put things in perspective and carry on. To my dear brother, I deeply thank, for helping me develop a competitive spirit from childhood, and for his forgiveness and constant encouragement throughout the ups and downs of our relationship. I love you all with all my heart.

I would also like to thank my boyfriend, Fernando Siu, for being the love and joy of my life, for helping me become a better person, and for emotionally supporting me throughout the different phases of my doctoral studies at Berkeley. In addition, I would like to acknowledge his valuable insight and contribution to many aspects of the financial analysis presented in this dissertation. For these and many other reasons I will forever be grateful.

To all my friends in Berkeley and the Bay Area, I am thankful for their support and companionship, and for all the happy memories we created together. Lizzie Blaisdell, Rosie Sejung Chae, Dana Cohen, Jeffery Hunt, Dimitris Konstantinidis, Cagla Meral, Andreas Schellenberg, and Clair Song, you have become my family here and have made this experience the best part of my life, so far. To my dear friends in Costa Rica, Vivian Grunspan and Gabriel Odio, I thank you for being my true loving friends for over a decade and a half. I greatly appreciate your constant encouragement and the faith you have had in me throughout the years.

The work presented in this dissertation was supported in parts by an NSF EERC program grant EEC-9701568 as PEER Projects 209, 213 and 244, by the PEER Center Transportation Systems Research Program, by Caltrans project EQ042-59A0506, and by the LASPAU-OAS (Organization of American States) fellowship under award 20040536. Any opinions, findings, conclusions, or recommendations expressed in this material are those of the authors and do not necessarily reflect those of the sponsors.

TABLE OF CONTENT

LIST OF FIGURES

LIST OF TABLES

LIST OF SYMBOLS

The main symbols and acronyms used in this report are as follows:

A, A_{RCR}, A_{RT} : Mean annual repair cost, repair cost ratio, and repair time, respectively
A_g : Column gross cross-sectional area
ALR : Axial load ratio
BC : Base column tested by Terzic *et al.* (2008)
B_i : Equivalent isolator dimension (square)
BI, BI1, BI2 : Bridge isolation, isolated bridge 1, isolated bridge 2
c.o.v. : Coefficient of variation
C_s : Seismic coefficient
CWD : Crew working days
d_b : Rebar diameter
D_c, D_{col} : Column diameter
D_i, D_L, D_{max} : Isolator diameter, lead plug diameter, isolator maximum displacement
DFRC : Ductile fiber-reinforced concrete
DM, dm : Damage measure, damage measure threshold
DS, ds : Damage state, damage state threshold
DV, dv : Decision variable, decision variable threshold
$E_{c,FRC}$: Fiber-reinforced concrete modulus of elasticity
EDP, edp : Engineering demand parameter, engineering demand parameter threshold
f, f_{res} : Peak and residual flexural strength in fiber-reinforced concrete beam
f'_c, $f'_{c,FRC}$: Regular and fiber-reinforced concrete compressive strength, respectively
FRC : Fiber-reinforced concrete
f_y, f_u : Yield and failure strength of steel reinforcement
g : Gravity acceleration. In financial model: capital annual growth rate
H, H_{col}, H_{tot} : Height, total column height
H_{eff} : Effective height of column between inflection points
H_i : Total isolator height
h_{Lp} : Height from the column base to the bottom of the plastic hinge zone
HPFRC : High-performance fiber-reinforced concrete
i : Discount or interest rate
I_{eff}, I_g : Effective and gross moment of inertia of column
IM, im : Seismic intensity measure, intensity measure threshold
J_{eff}, J_g : Effective and gross torsional inertia of column bent cap
K_d, K_e : Isolator post-yield characteristic and idealized elastic stiffness
K_{lat} : Lateral stiffness
K_v : Column or bearing axial stiffness
K_θ, K_T : Bearing rotational and torsional stiffnesses, respectively
L_d : Development length
L_f : Length of fiber
LLRCAT : Local linearization repair cost and time methodology
L_p : Plastic hinge length
LPR : Labor production rate

LRB	:	Lead rubber bearing isolator
m	:	Tributary mass
M, M_w	:	Earthquake magnitude
$M_{p,col}$	:	Column plastic moment
NC	:	Cost of new construction
NPV	:	Net present value
P, P	:	Probability, total applied force on beam or axial force in column
PBEE	:	Performance-based earthquake engineering
PE	:	Probability of exceedance
PEER	:	Pacific Earthquake Engineering Research Center
PG	:	Performance group
PGV	:	Peak ground velocity
P_{max}, P_n, P_{res}	:	Column peak axial force, nominal axial capacity, residual axial capacity
Q, q	:	Repair quantity, repair quantity threshold
Q_d	:	Isolator characteristic strength
R	:	Distance to fault
RC	:	Reinforced concrete
RT, rt	:	Repair time, repair time threshold
RCR, rcr	:	Repair cost ratio, repair cost ratio threshold
s	:	Spiral spacing
S1, S2	:	Fiber-reinforced concrete column specimens 1 and 2, respectively
S_a, S_d	:	Pseudo-spectral acceleration and spectral displacement, respectively
SSC	:	Shear-short column tested by Terzic *et al.* (2008)
t	:	Time
T	:	Natural period
THA	:	Time history analysis
t_i, t_r	:	Isolator height (rubber and steel sheets), total rubber thickness
v	:	Column shear stress
V, V_x, V_y	:	Total, X-, and Y-components of column shear
V_b, V_c, V_{col}	:	Bridge base shear, column shear
V_f	:	Fiber volume fraction
V_{max}	:	Maximum shear obtained at each cycle or throughout loading history
V_s	:	Shear resistance provided by transverse steel reinforcement
u, u_{flex}, u_{max}	:	Total, flexural, and peak lateral deformations of column, respectively
u_b	:	Peak bond stress
UC, uc	:	Unit repair cost, unit repair cost threshold
β	:	Damping coefficient or st. deviation parameter in lognormal distrbution
δ	:	Beam deflection
δ_x, δ_y	:	Column top displacement in X- and Y- directions
$\delta_{y,L}$, $\delta_{y,T}$	:	Longitudinal and transverse yield displacements, respectively
Δ, Δ_x, Δ_y	:	Total, X-, and Y-components of column drift ratio
ε, ε_y	:	Strain, yield strain
ε_{50}	:	Strain at 50% stress decay in fiber-reinforced concrete
$\varepsilon_{failure}$	:	Longitudinal strain at failure in fiber-reinforced concrete
$\varepsilon_{oc,FRC}$	:	Longitudinal strain at peak stress in fiber-reinforced concrete
$\varepsilon_{ot,FRC}$	:	Transverse strain at peak long. Stress in fiber-reinforced concrete

$\varepsilon_{s,long}$	:	Maximum strain recorded for longitudinal rebar at a height of 24”
ε_u	:	Failure strain of steel reinforcement
ϕ, ϕ_y	:	Curvature, yield curvature
ϕ_{bottom}	:	Curvature at the bottom section of the column
ϕ_f	:	Diameter of fiber
ϕ_{Top}	:	Curvature recorded at a height of 24” above the foundation
γ	:	Shear deformation
λ	:	Hazard curve or median parameter of lognormal distribution
μ	:	Mean of repair item labor production rate in PERT-beta distribution
μ, μ_d, μ_{nom}	:	Nominal displacement ductility demand
$\mu_{d,L}$, $\mu_{d,T}$	:	Longitudinal and transverse displacement ductility, respectively
ν	:	Vertical deformation
θ	:	Rotation
ρ_l	:	Longitudinal reinforcement ratio
ρ_s	:	Transverse reinforcement ratio
σ	:	Stress, In financial analysis: St. dev. of LPR in PERT-beta distribution
σ_i, σ_{max}	:	Isolator pressure, isolator maximum pressure
$\sigma_{res,FRC}$	:	Residual stress in fiber-reinforced concrete stress-strain curve
τ_y	:	Isolator yield strength in shear
ζ_{eq}	:	Equivalent viscous damping coefficient

1 Introduction

1.1 BRIDGE PERFORMANCE ENHANCEMENT

Numerous structures, including cast-in-lace and precast reinforced concrete infrastructure systems, suffered significant damage or collapse during historical and recent earthquakes around the world (1964 Alaska, USA; 1964 Niigata, Japan; 1971 San Fernando, USA; 1976 Guatemala; 1989 Loma Prieta, USA; 1994 Northridge, USA; 1995 Kobe, Japan; 1999 Kocaeli, Turkey; 1999 Chi-Chi, Taiwan; 2001 Gujarat, India; 2005 Kashmir, Pakistan; etc.), primarily due to deficient structural design. To guarantee post-earthquake serviceability and reduce the elevated repair costs of highway bridge systems, research efforts in recent years have been directed to the development and implementation of innovative designs and materials for new and existing structures to enhance their seismic performance. Since bridge columns provide both the gravity and lateral load-resisting capacity of bridge structural systems, they can be considered as the most seismically vulnerable components of the structure. During moderate and large earthquake events certain regions of bridge column bents may experience large and repeated cycles in the inelastic range of response. The extent of damage in these plastic hinge regions depends on ground motion characteristics as well as column details.

Damage in bridge columns directly affects the overall performance of a bridge during a seismic event and the feasibility of restoring it to its original condition. The seismic performance enhancement methods developed in recent years focus on limiting the load and displacement demand in the column bents as well as improving their damage-tolerance characteristics. Appendix A presents a review of the literature related studies regarding the analytical modeling and experimental testing of the lateral and axial load-carrying capacity of bridge columns in seismic regions. Four principal strategies for bridge seismic performance enhancement are examined in this study. They are: 1) use of fiber-reinforced concrete to build critical structural elements such as bridge piers; 2) use of base isolation devices to control and reduce the demand on bridge piers; 3) use of bridge pier post-tensioning to minimize or eliminate permanent deformation of the bridge pier; and 4) use of column jacketing to increase ductility capacity of existing reinforced concrete bridge piers. Preliminaries on each strategy are presented below.

1.1.1 Fiber-Reinforced Concrete (FRC)

Fiber reinforced concrete is a cementitious material enhanced by addition of metallic and/or non-metallic fibers. The mechanical characteristics of FRC depend on the choice and amount of fibers and design of the concrete mix; however, in general, FRC exhibits significantly larger tensile strength, higher shear resistance, more deformation capacity and better compression

response than conventional reinforced concrete. Given that the seismic response of a bridge during an earthquake and its ability to carry gravity loads after an earthquake is, to a large extent, controlled by the flexural, shear and axial strength of its columns, the enhanced properties of FRC may significantly improve bridge seismic performance compared to bridges made using conventional reinforced concrete. Furthermore, use of FRC to reduce rebar congestion may significantly simplify and accelerate bridge construction.

To date, two types of FRC have been used in studies aimed to demonstrate its advantages over conventional reinforced concrete in seismic applications. They are: Ductile FRC (DFRC) (Lee *et al.* 2007); and High Performance FRC (Naaman 1987; Vasconez *et al.* 1998; Chao *et al.* 2007; Naaman *et al.* 2007). Several structural applications of DFRC for seismic design and retrofit, such as unbonded post-tensioned concrete bridge piers with DFRC, were experimentally investigated (Yoon *et al.* 2002; Billington and Yoon 2004). In this research small-scale columns were segmentally precast with DRFC material integrated into the plastic hinge zone with a height-to-width ratio of 1 and no confinement reinforcement. Continuous longitudinal reinforcing bars were not provided between the joints segments, besides the vertical unbonded post-tensioning tendons. The cantilever element was subjected to high shear and flexure demand, displaying high energy dissipation and damage tolerance to large cyclic displacements. However, overall, very few reversed-cyclic loading experiments have been conducted on DFRC materials to date. Furthermore, significant differences were observed in the uniaxial tensile response of DFRC materials with different specimen geometries and scale. The widespread use of these mixtures is therefore pending further research (Kesner *et al.* 2003).

Saiidi *et al.* (2009) experimentally tested the cyclic behavior of three circular concrete column specimens with a special plastic hinge zone constructed using either conventional or super-elastic shape memory alloy longitudinal reinforcement, and either plain concrete or DFRC. The column outside the plastic hinge zone was detailed with conventional reinforcement and plain concrete. The columns were cycled up to a drift level of 14%; however strength degradation occurred at different lower cycles for the three column specimens. Improved damage tolerance and significant reductions in the maximum and residual displacements were observed for the column with DFRC material and special steel reinforcement in the plastic hinge zone, compared to the conventionally-reinforced plain concrete column specimen.

Numerous tests have been carried out on structural members using high-performance fiber-reinforced concrete (HPFRC) built with steel macrofibers which exhibits strain-hardening tensile behavior with multiple cracking (Canbolat *et al.* 2005; Wight *et al.* 2007; Harajili *et al.* 1995; Cheng and Parra-Montesinos 2007; Naaman *et al.* 2007; Henager 1977; Ramey 1984; Filiatrault *et al.* 1995; Vasconez *et al.* 1998; Parra-Montesinos *et al.* 2007; Parra-Montesinos and Chompreda 2006; Parra-Montesinos and Chompreda 2007; Harajli and Rteil 2004). The enhanced structural properties of these HPFRC members indicate that this material has great potential for use in flexural elements subjected to large drift demands during ground motions, such as bridge piers with either flexural-dominated behavior or with strong flexure-shear interaction. The compressive behavior of 13 full-scale bridge columns constructed using plain and steel fiber-reinforced concrete was determined experimentally by Aoude *et al.* (2009). Self-consolidating concrete and varying transverse reinforcement and hooked-end steel fiber ratios were used in the construction of the different square column specimens. The use of fibers in the concrete mix was proven to result in improved load-carrying capacity and post-peak response, as well as significant delays in cover spalling. The results also demonstrated that steel fibers can partially substitute confinement reinforcement in bridge columns, thus improving bridge

constructability. Longitudinal bar buckling could not be prevented in fiber-reinforced column specimens with large transverse reinforcement spacing due to the detachment of load-carrying concrete from the longitudinal rebar.

Appendix A presents an extended literature review on the behavior of FRC composites and the testing of large-scale structural members constructed with FRC used for seismic applications. To the best of author's knowledge, no full-scale cyclic testing of bridge piers or even columns in typical frame systems using HPFRC materials and typical longitudinal reinforcement details have been carried out to date.

1.1.2 Bridge Isolation

Seismic base isolation technology is one of several seismic response modification technologies developed and adopted in structural engineering practice over the last three decades. The response of a structural system to horizontal components of earthquake ground motion is modified by inserting a soft structural layer at the base of the structure. This soft structural layer is designed to develop large deformations without damage such that the structure above it is effectively isolated from the ground. This is achieved using engineered base isolation devices, a range of devices based on the ability of rubber to deform or on sliding or rolling along machined surfaces. The horizontal forces transmitted through the isolation layer are proportional to its stiffness and deformation, and thus can be efficiently limited to acceptable levels.

The significant damage to infrastructure after large earthquakes in the US, Japan, and other countries have led to the rapid growth of the seismic isolation technology and development of specific guidelines for the design, construction and testing of elastomeric, sliding, and other isolation devices, as well as the analysis of isolated bridge structures (AASHTO 1999; Buckle *et al.* 2006; CHBDC 2000; JRA 2002). The effectiveness of isolation devices underneath the superstructure of a bridge system in uncoupling the substructure from the horizontal components of ground motion excitation and therefore reducing its force and displacement demand has been thoroughly assessed through numerous experimental and analytical research studies.

Seismically isolated bridge structures in the US incorporate primarily lead-plug rubber, friction-pendulum, or so-called Eradiquake bearings as isolation devices. The elastomeric lead-plug rubber bearing device is the most commonly used system in bridge applications worldwide due to its relatively simple design, low fabrication costs, and low maintenance requirements. The use of sliding and friction pendulum bearings for the seismic protection of simple bridge structures was experimentally and analytically examined by Mosqueda *et al.* (2004). The system response of analytical bridge models with seismic isolation using high-damping rubber bearings was examined for varying ground motion intensity (Grant *et al.* 2004). It was found that while at design levels of earthquake intensity the high-damping rubber bearings are highly effective, at higher levels of ground motion intensity significant inelastic displacement demands are expected in the bridge piers.

In an analytical study (Warn and Whittaker 2004) the AASHTO specifications were found to underestimate the median maximum horizontal displacements determined from bidirectional nonlinear response-history analyses. The two main factors contributing to the increase in maximum isolator displacement are the additional displacement demand from a second (orthogonal) component, and the coupled response of seismic isolators. The sensitivity of the seismic response of bridge systems due to variations in the mechanical properties defined for

individual bilinear seismic isolators in bridge models was determined in a following analytical study (Warn and Whittaker 2006). Nonlinear response history analyses using a suite of bidirectional horizontal ground motion excitations were carried out for a simplified bridge model and property modification factors were proposed to assist engineers in preliminary design procedures of bridge isolation.

Cost-benefit analysis and fragility curves for bridges are a key input for performing seismic risk assessment. Empirical fragility curves developed using bridge damage data from past earthquakes and analytical fragility curves based on dynamic analysis results and estimated damage states and repair costs have been developed for different regions in the world. Seismic fragility curve theory for typical highway bridges was proposed following a comparison of analytical and empirical fragilities obtained from the 1995 Kobe, Japan earthquake damage indices (Mander and Baszos 1999). Fragility curves have also been developed for the central and southeastern United States (Mid-America) using a suite of synthetic ground motion records and nonlinear analytical models for commonly used bridge types found in that region, i.e. multi-span simply supported steel girder bridges (DesRoches *et al.* 2006).

The effect of seismic isolation on fragility curves of highway bridges in Japan was assessed through an analytical study (Karim and Yamazaki 2007). In this study, 30 isolated bridge models designed according to the seismic design code of highway bridges in Japan and consisting of a wide range of pier heights, weights, and structural over-strength ratios were considered. The fragility curve for each bridge was developed using a simplified procedure and 250 strong motion records. It was observed that the damage probability for the isolated system for a given over-strength ratio is lower and higher than that of the non-isolated bridge for short and long piers, respectively. Additional research studies have led to fragility curves for seismically isolated bridges in low to moderate seismic hazard regions (Shinozuka 1998; Koh *et al.* 2000; Choi *et al.* 2004). Directivity effects in near-fault ground motions and the use of expansion joints in isolated bridge systems have been studied as well (Dicleli 2008).

1.1.3 Post-Tensioning

Post-tensioning of bridge columns in the context of improving their seismic performance refers to the use of a lightly stressed post-tensioning cable placed along the column axis at the centrorid of its cross-section. The cable force is utilized to apply a re-centering moment such that its permanent deformation after an earthquake is minimized or eliminated.

The use of post-tensioning techniques in bridge piers and bent caps to minimize residual displacements and improve post-earthquake functionality of a bridge has been comprehensively investigated. Ito *et al.* (1997) studied the behavior of columns with different amounts of vertical mild reinforcing steel and unbonded post-tensioning under cyclic loading. Mander and Cheng (1997) investigated the use of unbonded post-tensioning in a bridge pier system to restrain lateral displacements during seismic loading. Sritharan *et al.* (1999) investigated the use of bonded prestressing in bridge pier cap beams to reduce required joint reinforcement without compromising joint performance. The use of unbonded post-tensioned concrete bridge piers with ductile fiber reinforced cement based materials for the plastic hinge zone was experimentally investigated using small-scale columns (Yoon *et al.* 2002). The effectiveness of self-centering bridge piers in seismic performance of bridge structures was experimentally and analytically

demonstrated in terms of expected post-earthquake downtime and repair cost by Lee *et al.* (2007).

1.1.4 Concrete Confinement and Retrofit Techniques

Several externally applied measures have been proposed and tested for the seismic strengthening and retrofit of existing bridge and building columns. One of the most effective techniques to increase both the shear strength and the deformation capacity of bridge columns is jacketing. Jackets made using steel or carbon-fiber composites provide the confining pressure to improve the compressive behavior of concrete, increase the shear strength of the column, and provide lateral support to postpone buckling of column longitudinal reinforcement.

Chai *et al.* (1991) investigated the effect of steel jacketing for restoring the flexural strength and the ductility of damaged columns. They found that this technique was effective for specimens that suffered complete bond failure of reinforcement spliced in the plastic hinge region. In an experimental study by Laplace *et al.* (2005) the effectiveness of steel and carbon fiber jackets in increasing the flexural capacity and ductility of retrofitted columns was demonstrated.

Aboutaha *et al.* (1999) examined the effect of two confinement steel types and different repair methods on the compressive strength and ductility of bridge piers. The results of rectangular specimens showed that the retrofitted columns reached their design strength and displayed good shear strength retention and ductility.

Circular bridge piers models confined by fiber reinforced polymer composites around the perimeter of the element have been tested to investigate their confining and strengthening effects (Saadatmanesh *et al.* 1996). This research was extended to investigate the flexural behavior of four earthquake-damaged reinforced concrete columns repaired with prefabricated fiber-reinforced plastic wraps, showing an enhanced flexural strength and displacement ductility compared to the original column.

Harajli and Rteil (2004) tested rectangular concrete columns designed for gravity loads for building structures and evaluated the effectiveness of carbon fiber-reinforced polymers sheets or steel fiber reinforced concrete in confining and improving the seismic performance of the reinforced concrete members. These techniques were found effective in confining the concrete core and preventing the longitudinal bars form buckling under cyclic loading.

An experimental study was conducted to evaluate the seismic performance of shear-dominated bridge piers reinforced using fiber-reinforced polymer wraps in the critical end regions of the column after being subjected to moderate earthquakes (Chung *et al.* 2008). The specimens, designed according to the Korean bridge design specifications, exhibited enhanced flexural ductility even for a flexural-shear failure mode.

In an experimental investigation the performance of earthquake-damaged reinforced concrete columns repaired by different techniques according to the damage level and details of the original columns was compared (Lehman *et al.* 2001). The repair techniques included cover concrete patching with epoxy injection, headed reinforcement, and mechanical couplers. The comparison of the severely damaged columns showed the repair columns had the same or greater stiffness than the original specimens. The corresponding repaired strength of these columns was within 10% of the original strength. However, only the column repaired using mechanical couplers presented deformation capacity exceeding that of the original columns, while the

remaining techniques resulted in inferior deformability. The experimental results demonstrated the effectiveness of the three repair techniques for both moderately and severely damaged ductile reinforced concrete bridge columns.

1.2 QUANTIFICAITON OF BRIDGE POST-EARTHQUAKE PERFORMANCE

The Pacific Earthquake Engineering Research (PEER) Center performance-based earthquake engineering (PBEE) framework (Cornell and Krawinkler 2000) provides a methodology for quantifying seismic performance of structures. The PEER PBEE framework utilizes the total probability theorem to disaggregate the notion of performance into quantifiable intermediate probabilistic models of seismic hazard intensity, demand, damage and loss, as shown in Figure 1-1.

$$\lambda(DV > dv) = \int_{im}\int_{dm}\int_{edp} G(dv|dm)dG(dm|edp)dG(edp|im)|d\lambda(im)|$$

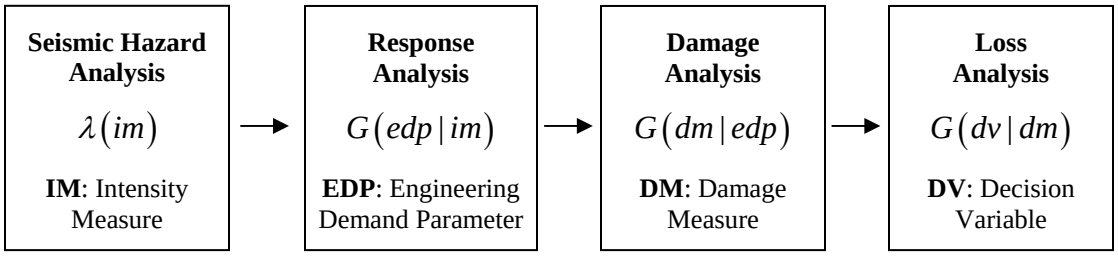

Figure 1-1 PEER Center PBEE methodology for quantifying seismic performance

The resulting triple integral is a mathematical representation of the PEER PBEE decision-making framework. It utilizes several intermediate continuous variables, each associated with its own epistemic and aleatory uncertainties. Measures that relate to decision-making are termed decision variables (DVs). The decision variables are conditioned on damage measures (DMs) related to bridge components repair quantities (Q). These local or global DMs are subsequently conditioned on levels of demand or response of the structure, quantified in terms of engineering demand parameters (EDPs). Finally, the EDPs are conditioned on earthquake intensity measures (IMs) which could correspond to different seismic hazard levels. The underlying assumption is that the intermediately variables are not correlated. Each of the three conditional probability relations between the fundamental variables in the PEER PBEE framework can be expressed as fragility.

The computation of the triple integral representing in the PEER PBEE framework can be carried out using a closed-form solution, numerical integration, summation, and simulation methods. Mackie and Stojadinovic (2006a) found that the different methods used to evaluate the PEER framework triple integral converge to the same solution as the number of discrete damage state increases.

Mackie *et al.* (2007, 2008) computed fragility curves based on a general closed-form solution of the PEER framework total probability integral for the repair costs of a typical ordinary standard reinforced concrete bridge designed according to AASHTO Standard Specifications for Highway Bridges (1996) and Caltrans Seismic Design Criteria (SDC) (2004).

These curves relate the repair cost of the bridge as a percentage of the total construction cost to an intensity measure of a single earthquake event such as the PGV (peak ground velocity). The fragility curves were obtained considering different possible repair methods for the bridge and cost computation procedures, thus resulting in different discontinuous piece-wise shapes. This local linearization repair cost and time methodology (LLRCAT) is applied in the present study to compare the repair costs of the different bridge types analyzed to assess their cost-effectiveness.

Kumar *et al.* (2009) developed a probabilistic approach to compute the life-cycle cost of corroding reinforced concrete bridges in earthquake-prone regions. Cumulative seismic damage is obtained from a low-cycle fatigue analysis. The proposed methodology accounts for uncertainties in ground motion parameters, distance to source, seismic demands of the bridge, and corrosion initiation times. The statistics of the accumulated damage and the cost of repairs throughout the bridge life-cycle are obtained in this methodology using Monte-Carlo simulation. The effects of design parameters on the life-cycle cost of an example reinforced concrete bridge were also studied. Based on this life-cycle cost analysis, conducting maintenance and inspections may only be economically justified for critical bridges in the transportation network.

The performance and vulnerability of highway bridges is a critical component in transportation network studies, assessed using large-scale simulation (HAZUS 1999; Werner *et al.* 2000) to study the economic impact and functionality of damaged transportation systems due to different seismic hazard scenarios. These simulations account for direct and indirect economic losses to the region due to seismically damaged or interrupted links of the transportation network. Direct losses include damage to bridge components and time delays in the network flow, while indirect losses result from the interruption of services, business and individuals due to the seismic impact. The required input data for such network simulations are bridge-level assessments of earthquake-induced damage, repair costs of different components of the bridge system, and loss of traffic function. Fragility curves representing the conditional probability of exceeding a limit-state performance goal given a specific intensity of the ground shaking at a bridge site are also required in these simulations.

1.3 RESEARCH OBJECTIVES

The primary objective of this study is to illustrate the use of PEER PBEE methodology to evaluate the effectiveness of different methods to improve the seismic performance of typical reinforced concrete bridge structures in California. Two methods for enhancing performance of new bridges are investigated: use of fiber reinforced concrete for bridge columns, and the use of lead-rubber bearing isolation devices to seismically isolate the bridge superstructure. These two performance enhancement methods are use to redesign the PEER PBEE testbed bridge. Then, the seismic performance of the new bridges is compared to the performance of the original, conventional reinforced concrete, PEER testbed bridge in the same seismic hazard environment. This is done by computing the repair cost and effort fragilities for the three bridge systems.

The second objective of this study is to extend the PEER PBEE methodology toward computing the life-cycle cost of a bridge in a seismic hazard environment. The information obtained from computing the repair cost and time fragilities is combined with estimates of the cost to build the conventional and the enhanced-performance bridges in different financial environments characterized by discount and capital growth rates. While the cost to maintain the bridges is not considered in this study, the accomplished extension of the PEER PBEE

methodology is the essential step toward the goal of a complete probabilistic characterization of the expected costs over a lifetime of a bridge in a highly seismic environment.

The third objective of the study is to conduct first-of-a-kind large-scale tests of HRFRC bridge column specimens under bi-direcitonal loading. Such tests provide the missing information about flexure-dominated HPFRC column response up to very high deformation demand levels and enable development of design equations for HPFRC bridge columns.

1.4 ORGANIZATION OF THE DISSERTATION

The evaluation of performance enhancement methods performed in this study is described in the following six chapters.

Chapter 2 describes the test setup, protocol and instrumentation scheme of an experimental study of two HPFRC bridge column specimens subjected to bidirectional quasi-static cyclic loading history. The construction procedure and results of the material testing used for the construction of the specimens are included in the corresponding appendix.

The experimentally observed behavior of the FRC specimens and a comparison to similar reinforced concrete specimens are presented in Chapter 3. A description and calibration of a finite element fiber-section based model used to simulate the nonlinear hysteretic behavior of HPFRC bridge columns is presented as well. Finally, design equations for HPFRC column moment and shear strength are proposed.

Chapter 4 presents the design details of the original reinforced concrete PEER testbed bridge and the enhanced-performance HPFRC bridge and the isolated bridge. The design of the HPFRC bridge columns is based on findings presented in Chapter 3. Seismic isolation of the PEER testbed bridge is placed at the top of the column bent caps to isolate the bridge deck. Two different designs, one that keeps the columns elastic and another where slight yielding of the bridge columns is allowed are presented in this Chapter. The finite element models of the bridges are also described in Chapter 4.

The nonlinear static and dynamic analysis results of the different bridge systems (isolated, conventionally reinforced, and fiber reinforced concrete bridges) are presented in Chapter 5. The comparison of the seismic performance of the different bridge systems is described in terms of the force and displacement demand vs. capacity, as well as other engineering demand parameters that describe the seismic on major structural components.

The construction costs and the post-earthquake repair costs and time effort at different seismic hazard levels obtained using the PEER PBEE framework of the different bridge structures analyzed in this study are presented in Chapter 6. The annual and total life-cycle cost-effectiveness of the different bridge types is presented as well.

Chapter 7 presents a summary of research findings and conclusions, as well as a list of topics for future research. Preliminary recommendations for the modeling, analysis and construction of bridge piers using HPFRC materials and base isolation devices are offered, based on the experimental, analytical and economic results obtained in this study.

2 HPFRC Column Tests

The present chapter provides a detailed description of the configuration and material properties of two fiber-reinforced concrete column specimens subjected to a bidirectional quasi-static loading history. The instrumentation scheme used for the measurement of internal strains, as well as global and relative external displacement of the column specimens, is presented as well. This experimental study was carried out to assess the cyclic behavior of fiber-reinforced concrete columns, in comparison to similar conventionally-reinforced concrete columns tested by Terzic *et al.* (2008). The description of the construction process, experimental setup, as well as the internal and external instrumentation scheme of the fiber-reinforced concrete specimens tested is presented in Appendix B.

2.1 TEST SPECIMENS

The cyclic bidirectional lateral displacement tests of two high-performance fiber-reinforced concrete (FRC) columns were carried out on March 30th and April 10th, 2009 in the structural laboratory of the Civil and Environmental Engineering Department of the University of California at Berkeley, located on the 2nd floor of Davis Hall. The circular column specimens, representing a ¼-scale cantilever bridge column, were constructed with high-performance FRC material with a 1.5% fiber volume fraction. This FRC was made by adding a single type of a commercially available hooked steel fiber to conventional ready-mix concrete in the truck on site. Placing was done using a bucket and conventional vibration (see Appendix B for detailed description of the construction process). The columns were detailed with relaxed transverse reinforcement and modified longitudinal reinforcement for the plastic hinge zone compared to the Caltrans Seismic Design Criteria (SDC) (2004) for regular concrete bridge columns.

The column specimens represent the bottom half of a typical bridge column with fixed-fixed boundary conditions deforming in double curvature. The length of the cantilever column corresponds to the distance from the column base or foundation to the assumed inflection point at mid-height. The columns were subjected to cyclic a bidirectional lateral displacement history and their behavior was compared to the experimental results of geometrically identical conventional concrete column specimens designed in accordance with Caltrans SDC by Terzic *et al.* (2008) (see Chapter 3 for experimental results). The influence of the pile response or soil-structure interaction was not considered in either study. A massive anchor block was constructed for both studies, simulating rigid boundary conditions at the column base.

Table 2-1 presents the principal geometric and reinforcement characteristics of the four column specimens compared in this study. The first two specimens, denoted as Specimen 1 (S1) and Specimen 2 (S2), were built with fiber-reinforced concrete, while the last two are the

reference bridge columns built with regular concrete and tested by Terzic *et al.* (2008). They are designated as the base column (BC) and shear-short column (SSC) specimens.

Table 2-1 Summary of geometric and reinforcement details of column specimens

Parameter	S1: FRC	S2: FRC	BC: Regular	SSC: Regular
D_{col} – Col. diameter	16”	16”	16”	16”
H_{col} – Total col. height	64”	64”	64”	40”
Aspect ratio	4	4	4	2.5
Long. reinf.	12#4+8#4 dowels	12#4+8#4 dowels	12#4	12#4
ρ_l – Long. reinf. ratio	2% (base), 1.2% (rest)	2% (base), 1.2% (rest)	1.2%	1.2%
Debonding sleeves	Dowels, L=10”	Main rebar, L=4”	-	-
Transv. reinf.	W3.5*@2.5”	W3.5@2.5”	W3.5@1.25”	W3.5@2.75”
ρ_s – Transv. Reinf. Ratio	0.75%	0.75%	1.5%	0.68%
f'_c- Conc. compressive strength	6.86 ksi	6.86 ksi	5.09 ksi	6.34 ksi

*W3.5: Diameter=0.21 in.

The construction details of column specimens S1 and S2 are presented in Figure 2-1 and Figure 2-2, respectively. The details of the column foundations are presented in Figure 2-3. The construction process and experimental test setup of the FRC column specimens is presented in Appendix B.

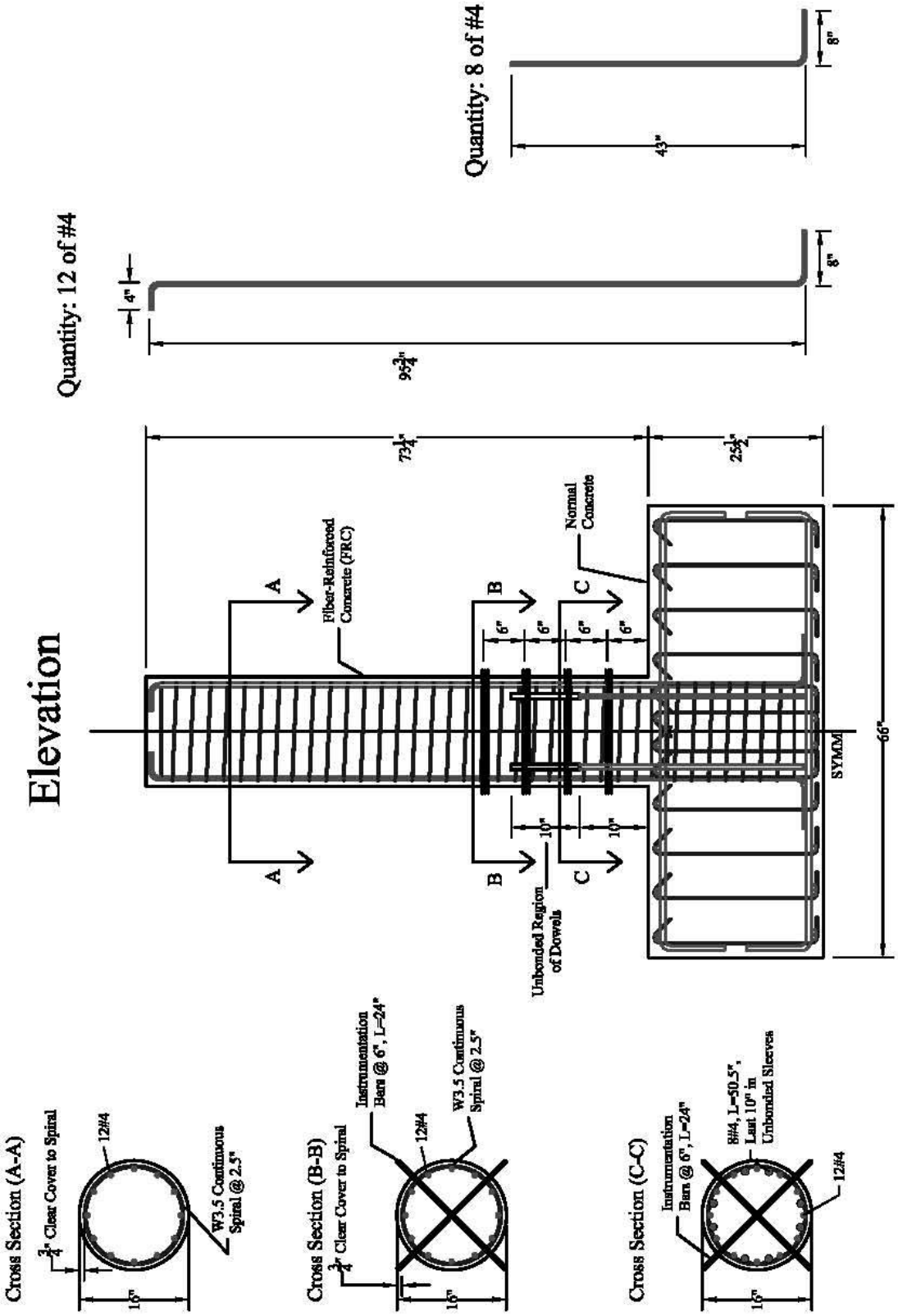

Figure 2-1 Construction details for S1 column specimen

Figure 2-2 Construction details for S2 column specimen

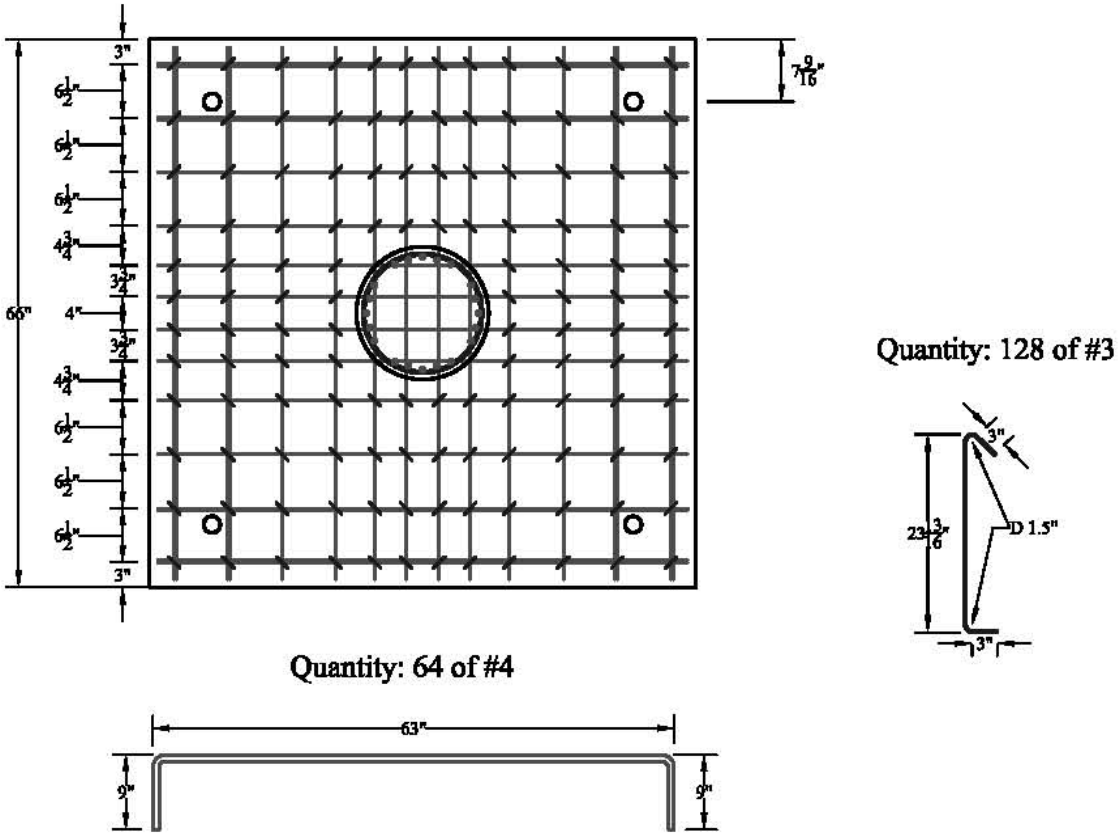

Figure 2-3 Construction details of anchor block of S1 and S2 column specimens

In the conventionally reinforced concrete columns BC and SSC the longitudinal reinforcement consisted of 12#4 bars and normal concrete in both column and foundations. In the FRC specimens normal concrete was used for the construction of the foundation block, while the column was built with FRC material. The cold joint at the interface between the column foundation block and the FRC column will therefore be susceptible to localization of wide base cracks and large concentrated rotations. Dowel reinforcement was consequently specified at the column base of the FRC specimens to move the inelastic deformations slightly above the foundation level. This design was intended to optimize the advantages obtained with the strain hardening properties and damage tolerance of the FRC material, thus allowing for a wider spreading of the plastic hinge zone, as well as improved displacement capacity and cyclic behavior of the column.

The spiral reinforcement of the FRC columns was half of that specified for the BC specimen. The relaxation in the transverse reinforcement in the FRC columns was done to increase the shear demand on the FRC material and evaluate its contribution to the column shear resistance at large drift levels and its effectiveness in providing concrete confinement. The use of a material with substantially greater ductility capacity both in tension and compression compared to normal concrete is expected to offset the unfavorable effects of reducing concrete confinement and rebar support with the relaxation of the transverse reinforcement ratio in the plastic hinge zone.

The experimental results obtained from the bidirectional cyclic tests of the two FRC column specimens were evaluated in terms of the hysteretic behavior of the columns,

longitudinal and transverse reinforcement strain profile, peak curvature and rotation profiles, degradation of stiffness and strength, progression of damage at increasing drift levels, and the degradation of shear resisting mechanisms during the application of lateral loading. The development of damage in the columns was quantified based on crack type (e.g., flexural and diagonal), crack width at various drift levels, observations of any concrete spalling or crushing, as well as rebar buckling and fracture. The residual gravity load carrying capacity of the FRC columns was evaluated analytically based on the ultimate stress obtained from material testing. These results were compared to the available data from the BC and SSC specimens tested by Terzic *et al.* (2008).

2.2 MATERIALS

The basic properties of plain concrete, fiber-reinforced concrete, longitudinal steel reinforcement, and spiral steel reinforcement used for the construction of the two FRC column specimens, obtained through cylinders, beams and coupon testing, are presented in this section. The material testing results are used in the calibration of the uniaxial stress-strain relationship of steel and concrete fibers used in the analytical model of the columns in OpenSees.

2.2.1 Longitudinal Reinforcement

The longitudinal reinforcement bars of the column specimens were specified as ASTM A706 #4/13M bars. The continuous longitudinal rebar used for the columns corresponded to one batch, while the longitudinal dowels used to reinforce the column base at the cold joint region between plain and fiber-reinforced concrete corresponded to a second batch. The reinforcing bars were cut into 24” segments and tested using the standard tension load test method specified in ASTM A370. The deformation measurements were performed at the center of each rebar segment. Three coupons were tested for the continuous longitudinal bars, as well as dowels, to obtain an average stress-strain relationship of the steel rebar corresponding to each batch. The fracture strain of the steel rebar was not determined experimentally since the coupons were unloaded after attaining the ultimate point of the stress-strain curve. The use of typical fracture strain values specified in Caltrans SDC (2004) was used instead in the analytical models of the FRC cantilever columns. The measured response of the test coupons is presented in Figure 2-4.

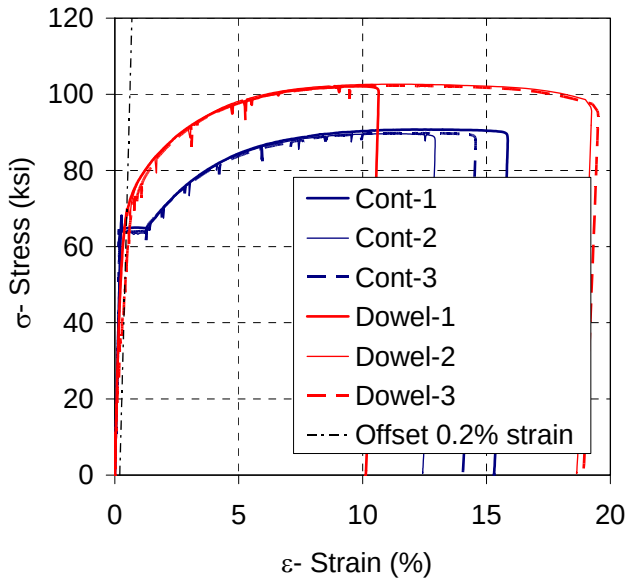

Figure 2-4 Stress-strain relationship for continuous longitudinal rebar and dowels used for the construction of the FRC columns

The average modulus of elasticity for the continuous rebar and dowels was approximately 27,600 and 24,500 ksi, respectively. The yield strength of the continuous rebar had an average value of 65.0 ksi (448 MPa). This steel presented a clear yield plateau extending from approximately 0.25% strain to 1.33% strain. The average ultimate strength of this steel was determined at 90.1 ksi (621 MPa). Due to a higher content of carbon in the steel alloy used to produce the longitudinal dowels rebar, the stress-strain curve of this steel did not present a clear yield point and plateau. A 0.2% strain offset of the initial slope is used to determine the yield strength of this steel. The resulting average yield strength of the three dowels coupons was approximately 70.0 ksi (483 MPa). The average ultimate strength of the steel rebar used for the column dowels was approximately 102.2 ksi (705 MPa). As mentioned above, the fracture strain was not determined in these coupon testing.

2.2.2 Spiral Reinforcement

A single batch of steel wire W3.5 fabricated according to ASTM A82 standards was used as the spiral reinforcement of the two column specimens and for the corresponding material testing. Three coupons were tested to obtain the stress-strain behavior of the spiral. Figure 2-5 shows the measured stress-strain response of the cold-rolled spiral reinforcement obtained from the coupon testing. The yield strength corresponded to an approximate yield strain of and was determined to be 92.5 ksi (638 MPa). The ultimate strength of the steel was 102.5 ksi (709 MPa). The elongation at fracture in a 2” length measured for the spiral coupons was approximately 7.5%, on average.

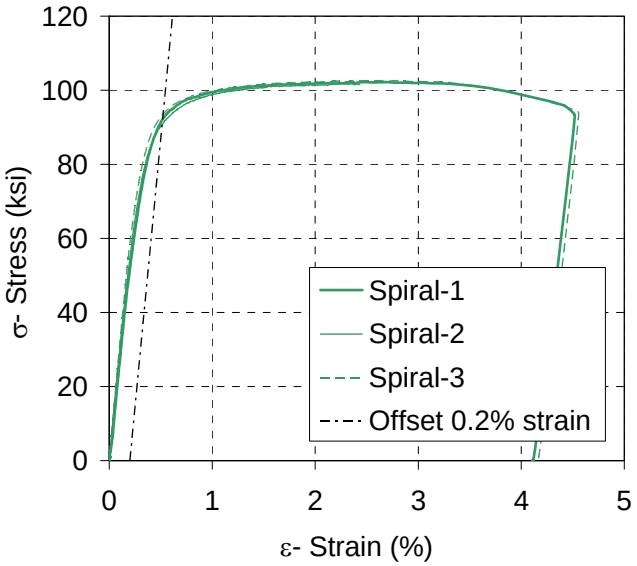

Figure 2-5 Stress-strain relationship for spiral reinforcement

2.2.3 Plain and Fiber-Reinforced Concrete

The concrete mix used for the construction of the foundation as well as the fiber-reinforced concrete columns was designed to resemble the prototype column mix used in Terzic *et al.* (2008), with 28-day target strength of 5.0 ksi. This mix design, with a proportion of 0.45: 1: 2.3: 1.86 (corresponding to water: cement: sand: course aggregate), was adjusted from Terzic *et al.* (2008) to appropriately incorporate the steel macro-fibers with acceptable workability conditions. A similar mix was successfully used in numerous experimental tests carried out in the University of Michigan and University of Minnesota on the performance of slab-column connections and other flexural members (Cheng and Parra-Montesinos 2007; Canbolat *et al.* 2005; Kim and Parra-Montesinos 2003; Naaman *et al.* 2007; Parra-Montesinos and Wight 2000; Parra-Montesinos *et al.* 2006 and 2007; Parra-Montesinos and Chompreda 2006 and 2007).

The foundations were cast on February 9th, 2009 in a single pour from a single plain concrete batch using the adjusted concrete mix (without fibers). This special mix was also used on the same day for the construction of the two fiber-reinforced concrete columns, cast in a single pour from a second concrete batch to which the fibers were added. Despite having a 28-day target strength of 5.0 ksi, at this water-to-cement ratio the reference curves applied to the concrete material supplied by Redy Mix and Concrete Pumping, Ltd. show a potential of 5.0 ksi at 14 days and 5.7 ksi at 28 days. The superplasticizer used for the mix was Glenium 3000NS by BASF manufacturer. Steel fibers type Dramix RC-80/30-BP were used for the fiber-reinforced concrete mix at a 1.5% volume-fraction. Table 2-2 provides the details of the mix for a 1.0 CY of concrete volume.

Table 2-2 Plain concrete mix design data

Item	Value
Max. size Aggregate (in)	3/8
28-Day Strength (ksi)	5.0
Slump (in)	6
W/C Ratio (-)	0.45
Coarse Aggregate Weight (lb)	1324
Top Sand Weight (lb)	1212
Blend Sand Weight (lb)	426
Total Fine Aggregate Weight (lb)	1638
Cement (lb)	712
Super-plasticizer (oz)	21
Water (lb)	320
Fibers (lb)	194

Before each casting, a slump test (ASTM C143) was performed on the concrete mix to verify the desired slump. The anchor block concrete had a slump of 5.0 inches, while the column concrete had a slump of 5.5 inches following the addition of the superplasticizer. A total of 12 plain concrete and 12 fiber-reinforced concrete 6×12" cylinders were cast with the anchor blocks and columns, respectively, to assess the development of concrete compressive strength using the ASTM C39 test method. In the case of the fiber-reinforced concrete cylinders, the complete stress-strain relationship was also determined using the same test method, but at a later date. A total of 9 6×6×24" beams were tested using the ASTMC1609 method to assess the flexural performance of fiber-reinforced concrete beams under third-point loading. The concrete strength test program used in this experimental study is summarized in Table 2-3.

Table 2-3 Concrete strength test program

Date	ASTM C39-Plain concrete cylinders (f'_c)	ASTM C39-FRC cylinders (f'_c)	ASTM C39-FRC cylinders (σ-ε)	ASTM C1609-FRC beams (P-δ)
14 days	3	2	-	-
28 days	3	2	-	3
49 days: Specimen 2 test	3	-	4*	3
60 days: Specimen 1 test	3	-	4*	3

*Tested at 167 days

The cylinders were kept in the same location as the test specimens to have the same curing conditions. The cylinder and the column forms were removed 11 days after the casting of the specimens, therefore the first cylinder testing was carried out on day 11 instead of day 14. Since the compressive strength test results of the FRC cylinders carried out on days 11 and 28 were consistent (the strength of each pair of cylinders was within 10% of each other), the remaining 2 cylinders were used to obtain the stress-strain relationship of specimens 1 and 2. Due to technical problems, the eight FRC cylinders were tested on July 27th, corresponding to 167 days after the casting of the FRC specimens. Figure 2-6 illustrates the development of concrete strength with time for both regular and FRC.

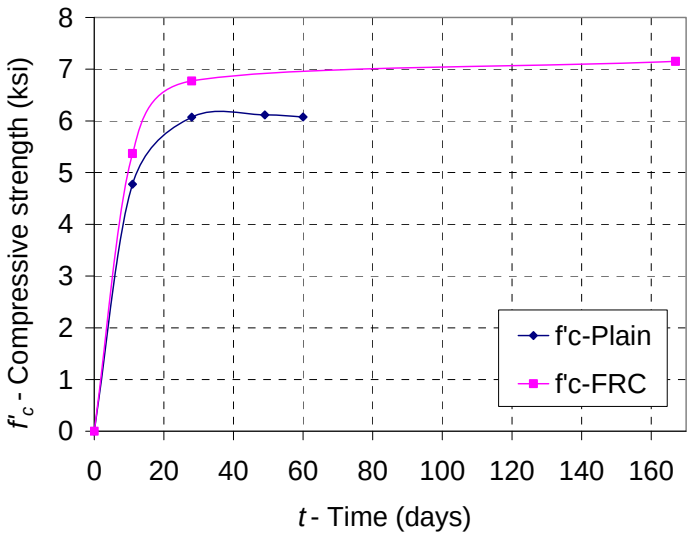

Figure 2-6 Development of concrete strength with time

The stress-strain relations of the eight FRC cylinders tested on day 167 using standard compression tests as per ASTM C39 displaying longitudinal and transverse strains are presented in Figure 2-7 and Figure 2-8, respectively. The longitudinal results are considered reliable only up to a strain value of 0.020. The main FRC cylinder test results and their corresponding variance are summarized in Table 2-4.

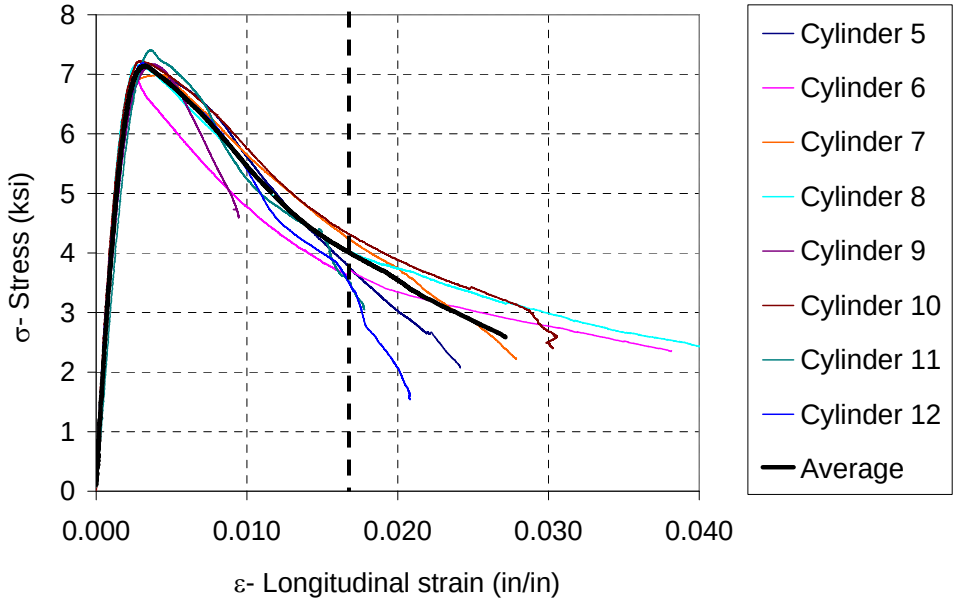

Figure 2-7 Longitudinal stress-strain relations of FRC cylinders

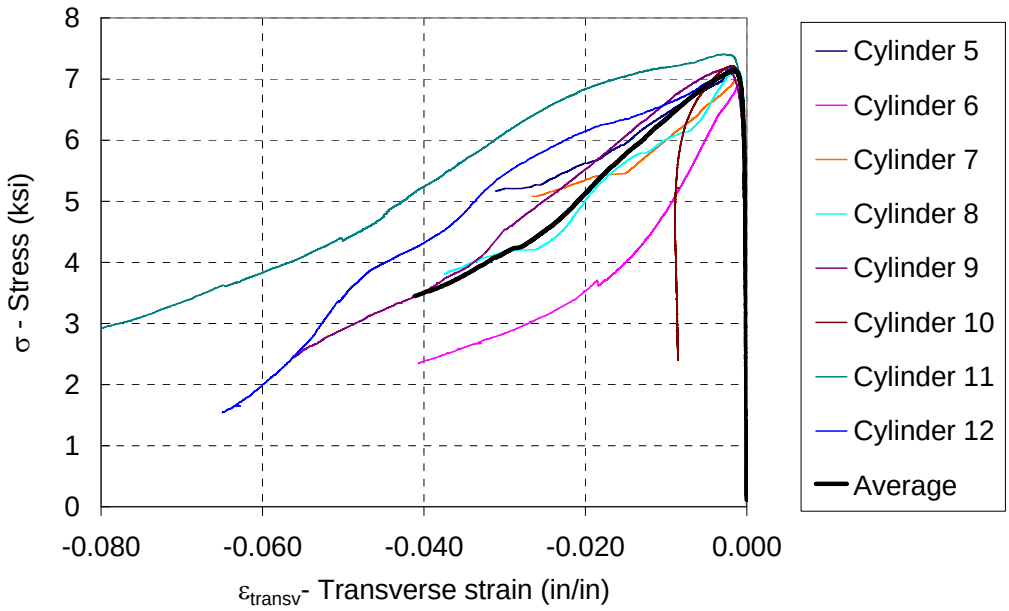

Figure 2-8 Longitudinal stress- transverse strain relations of FRC cylinders

Table 2-4 Summary of FRC cylinder test results

Parameter	Mean	St.dev.	c.o.v.
$f'_{c,FRC}$ – Compressive strength (ksi)	7.15	0.14	0.02
$\varepsilon_{oc,FRC}$ - Longitudinal strain at peak stress (in/in)	0.0033	6e-4	0.19
$\varepsilon_{ot,FRC}$ - Transverse strain at peak long. stress (in/in)	0.0018	7e-4	0.41
$E_{c,FRC}$ - FRC modulus of elasticity (ksi)	4560	722	0.16
$\sigma_{res,FRC}$ - Residual stress (ksi)	2.24	0.32	0.14
$\varepsilon_{failure}$ – Longitudinal strain at failure (in/in)	0.023	0.016	0.68
ε_{50}- Strain at 50% stress decay (in/in)	0.015	8e-3	0.57

Most of the FRC stress-strain results in Table 2-4 presented relatively low coefficient of variations and can therefore be considered consistent and acceptable for the present study. The exceptions for these are the transverse strain at peak longitudinal stress $\varepsilon_{ot,FRC}$, the longitudinal strain at failure $\varepsilon_{failure}$ corresponding to the last data point recorded experimentally, and the strain at 50% stress decay ε_{50}, which presented high variability among the eight cylinders tested and therefore cannot be considered reliable.

Figure 2-9 displays the average longitudinal stress-strain results of the eight FRC cylinders tested at 167 days and the scaled curves at 49 and 60 days obtained from linear interpolation of the average stress values based on the development of concrete strength presented in Figure 2-6. The average curve was obtained by taking the mean stress value of all eight cylinders at each strain level. The strain values at 49 and 60 days were not modified compared to the mean test results at 167 days. The resulting mean curve presented a concrete strength $f'_{c,FRC}$ of 7.15 ksi, a modulus of elasticity $E_{c,FRC}$ of 4425 ksi, a strain at peak stress $\varepsilon_{oc,FRC}$ of 0.0032 in/in, a residual stress $\sigma_{res,FRC}$ of 2.58 ksi, and a failure strain $\varepsilon_{failure}$ of 0.027 in/in. The stress values obtained above for the mean test results can be scaled down by the ratio of peak

strength values at 49 or 60 days vs. 167 days to estimate the main FRC material properties at the time of the respective cyclic test.

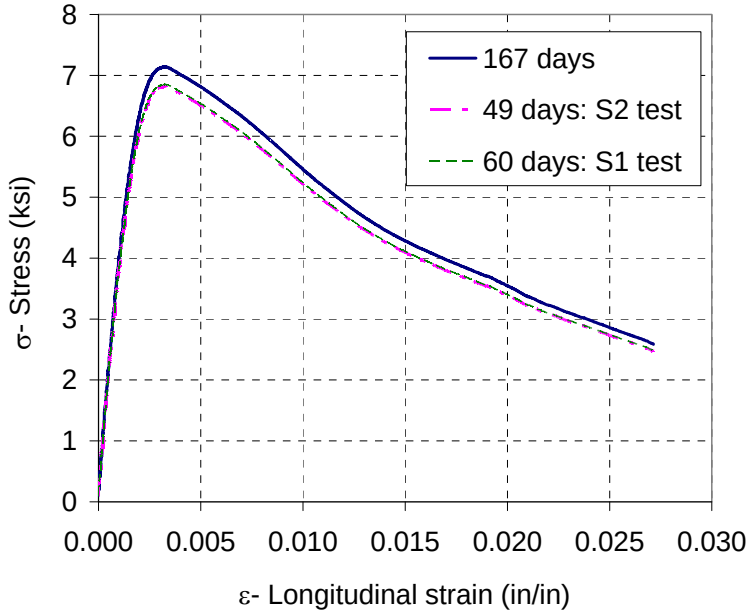

Figure 2-9 Longitudinal stress-strain relations of FRC at 49, 60, and 167 days

Table 2-5 summarizes the average compressive strength test results for plain and fiber-reinforced concrete representing the anchor blocks and column material behavior, respectively, as well as their corresponding standard deviations. The stress results for the FRC material at 49 and 60 days were obtained from linear interpolation of the stress-strain results at 167 days.

Table 2-5 Average concrete compressive strength results and standard deviations

Parameter	11 days	28 days	49 days	60 days
f'_c – Regular concrete compressive strength (ksi)	4.78	6.07	6.11	6.08
$f'_{c,FRC}$ - FRC compressive strength (ksi)	5.37	6.77	6.83*	6.86*
$\sigma_{f'c}$ - Standard deviation, plain concrete (ksi)	0.17	0.13	0.02	0.23
$\sigma_{f'c,FRC}$ - Standard deviation, FRC (ksi)	0.04	0.18	0.13*	0.13*

*Obtained indirectly from linear interpolation

Tensile strength tests were not carried out for neither plain nor fiber-reinforced concrete. The modulus of elasticity for the FRC material $E_{c,FRC}$ was also determined through the ASTM C1609 beam tests. The ASTM C1609 test setup used in this study and a representative flexural failure of a fiber-reinforced concrete beam specimen tested on day 49 are shown in Figure 2-10.

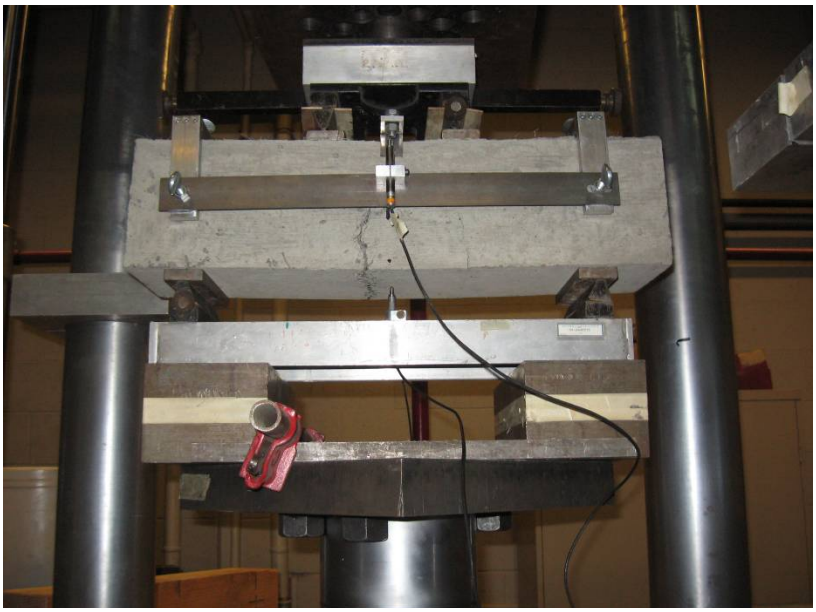

Figure 2-10 Flexural failure in FRC beam tested according to ASTM C1609

Since the fracture occurred inside the middle third of the spans for all beam specimens tested, the results of the flexural performance test using the ASTM C1609 method are valid. The force-deflection relationships of all beam tests are presented in Figure 2-11. Relatively large variability was obtained for the FRC beam results since the ASTM C1609 is susceptible to large variabilities and the test beams were casted following the construction of the two FRC column specimens, by which time the workability conditions of the mix had slightly deteriorated. The results beyond the maximum deflection δ_{max} specified as 0.12" by the ASTM C1609 standard are not considered highly reliable.

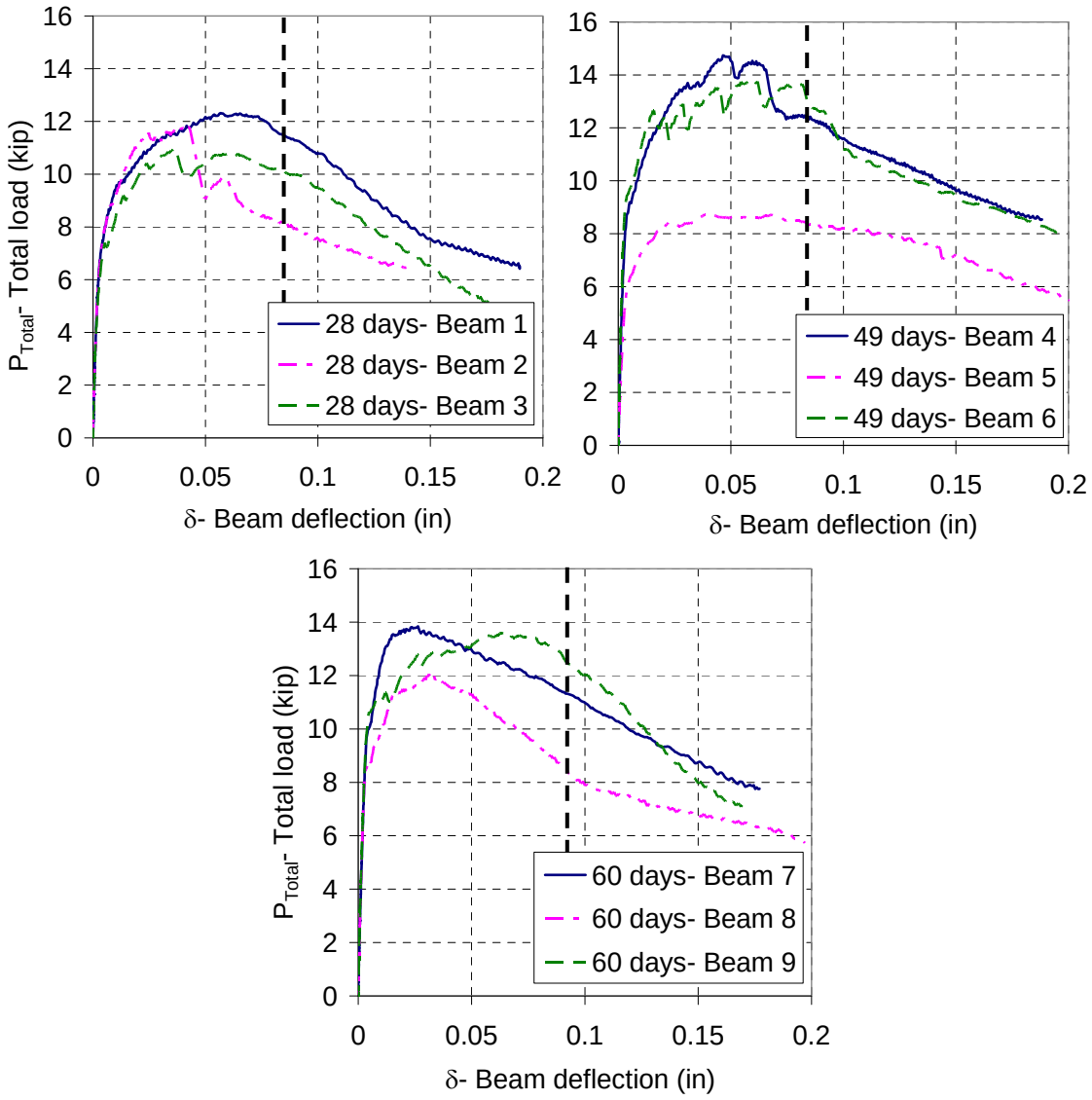

Figure 2-11 ASTM C-1609 test results: Flexural Performance of FRC beams

The peak and residual flexural strength of the fiber-reinforced concrete material was determined for each beam according to the ASTM C1609 procedure as $f=PL/bd^2$ at the peak load and residual load at net deflection of $L/150$, respectively, where L is the span length of the beam equal to 18", and $b=d=6$" are the average cross-sectional dimensions of the beams. The elastic modulus of the FRC beams was derived according to the corresponding procedure of ASTM C1609. The average peak and residual strength, as well as the elastic modulus results for each three-beam set are presented in Table 2-6. The standard deviation obtained for these estimates are presented as well.

Table 2-6 Average peak and residual flexural strength of FRC beams

Test day	f- Peak flexural strength, ksi (st.dev., ksi)	f_{res}- Residual flexural strength, ksi (st.dev., ksi)	$E_{c\text{-}FRC}$- Elastic modulus, ksi (st.dev., ksi)
28 days	0.97 (0.06)	0.68 (0.10)	5710 (2292.5)
49 days	1.03 (0.27)	0.81 (0.13)	3863 (1659.0)
60 days	1.10 (0.08)	0.78 (0.13)	9290 (2903.5)

2.3 LOADING HISTORY

The circular load pattern used for the bidirectional quasi-static cyclic test of the FRC column specimens was defined similarly to the load history used by Terzic *et al.* (2008) for the BC and SSC cyclic tests. This was done in order to compare, under the same displacement history, the cyclic behavior of FRC columns and that of geometrically identical conventionally reinforced concrete columns. The load history by Terzic *et al.* (2008) was selected following an extensive literature review and by monitoring the peak column displacement ductilities in all transverse directions resulting from a series of nonlinear time history analysis on two bridge models using 40 ground motions. Special care was taken when developing the loading pattern as to exclusively induce lateral displacement and no torsion in the column.

The circular loading pattern used on all four columns tested is defined by two circular cycles at each displacement level or full cycle, one clock-wise and the other counter-clock-wise, as seen in Figure 2-12. The displacement time history in the X- and Y- axes of the column for each cycle, normalized with respect to the target displacement level, is shown in Figure 2-12.

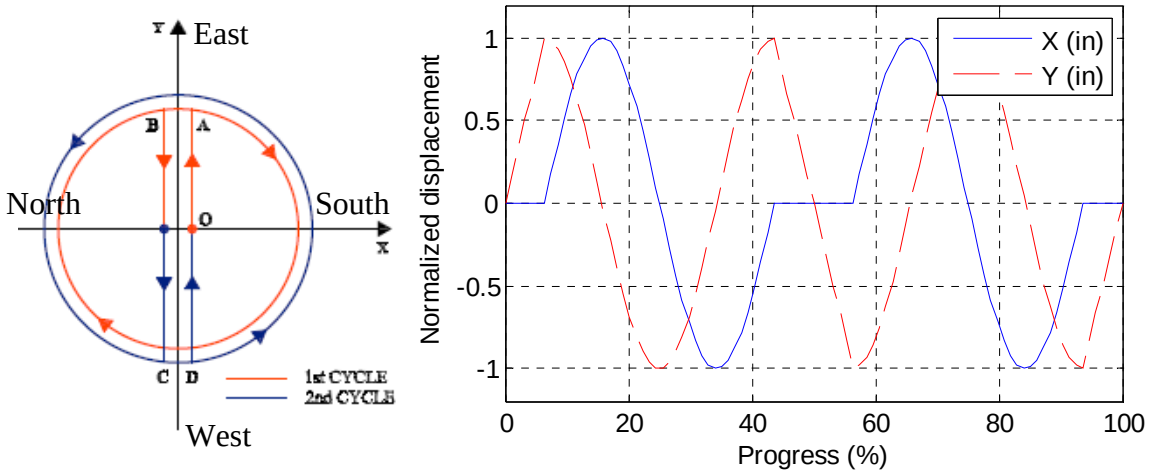

Figure 2-12 Loading history of a full cycle in the quasi-static test: (a) Loading pattern (Terzic *et al.* 2008); (b) Normalized displacement time history

The target displacement ductility demand of each complete cycle in the displacement history is presented in Table 2-7. The ductility demand is computed with respect to the BC column yield point, estimated at 0.55". The maximum ductility level attained during the tests of the reference columns BC and SSC was 4.5. Since the FRC columns were expected to develop higher ductility capacity than the RC columns, the imposed displacement history imposed on the

FRC columns was extended beyond that of the BC and SSC specimens. The maximum ductility level attained during the test of the S2 column was 6.25. Following this ductility level the column was cycled at a ductility level of 2 to observe its residual behavior. In the case of S1 column specimen, the maximum ductility level attained without substantial loss of gravity load carrying capacity and apparent shear-related damage was 12.5.

Table 2-7 Ductility level used at each cycle of the displacement history, defined with respect to the BC column yield displacement

Cycle	Ductility level	Displacement, in (Drift, %)	Cycle	Ductility level	Displacement, in (Drift, %)
1	0.08	0.04 (0.07)	10	3	1.65 (2.58)
2	0.2	0.11 (0.17)	11	1	0.55 (0.86)
3	0.4	0.22 (0.34)	12	4.5	2.48 (3.87)
4	1	0.55 (0.86)	13	1.5	0.83 (1.29)
5	0.33	0.18 (0.28)	14	6.25	3.44 (5.37)
6	1.5	0.83 (1.29)	15	2	1.10 (1.72)
7	0.5	0.28 (0.43)	16	8	4.40 (6.88)
8	2	1.10 (1.72)	17	2	1.10 (1.72)
9	0.67	0.37 (0.58)	18	12.5	6.88 (10.74)

The pre-yield displacement levels were defined by Terzic *et al.* (2008) to include one displacement level prior to cracking, two levels between cracking and yielding, and one level approximately corresponding to the first yield of the longitudinal reinforcement, equal to the nominal ductility level of 1. For the S1 and S2 FRC columns, the use of different reinforcement details and materials results in a different stiffness and behavior than the BC and SSC specimens. Therefore, the elastic displacement levels defined above correspond to different column damage states for the FRC column specimens.

For the post-yield displacement levels the magnitude of the subsequent cycles was determined by multiplying the current level by a scale factor ranging approximately from 1.25 to 1.5. This monotonic increase in the displacement demand level was carried out to monitor the accumulation of damage throughout the loading history. Since two circular cycles were imposed at each ductility level or full cycle, the degradation characteristics of the column were captured more effectively than through a single circular cycle. In the post-yield displacement history, each main cycle or displacement level was followed by a small displacement level equal to one-third of the primary cycle (last drift applied up to that point) to evaluate the column stiffness degradation throughout the time history.

In the cyclic tests of the BC and SSC specimens the last primary displacement level was followed by a series of small cycles. The magnitude of the small cycles decreased gradually until the residual lateral forces and displacement in the column were significantly reduced at the end of the test. The re-centered columns were then tested using a typical axial compression test to determine their residual gravity load-carrying capacity. In the case of S1 and S2 specimens, since the residual gravity load was not tested experimentally, these post-yield re-centering cycles were not required.

The loading rate of the FRC column cyclic tests at each ductility level was selected as to simulate static loading and obtain similar displacement rates among the different cycles, not exceeding 1.0 in/sec. The loading rates used for each cycle are presented in Table 2-8.

Table 2-8 Loading rates used in the bidirectional cyclic test of the FRC columns

Cycle	Ductility level	Loading rate (in/sec)	Cycle	Ductility level	Loading rate (in/sec)
1	0.08	0.10	10	3	0.50
2	0.2	0.18	11	1	0.45
3	0.4	0.25	12	4.5	0.45
4	1	0.45	13	1.5	0.50
5	0.33	0.24	14	6.25	0.60
6	1.5	0.45	15	2	0.48
7	0.5	0.25	16	8	0.75
8	2	0.50	17	2	0.50
9	0.67	0.49	18	12.5	1.05

The gravity load applied on the column, equal to 100.5 kip, corresponds to approximately 10% of the axial capacity (i.e., $0.1f'_cA_g$) of the benchmark BC column specimen tested by Terzic *et al.* (2008). This load is typically used to represent the average dead and live loads carried by column bents of overpass bridges in California. This axial load of approximately 100.5 kip was maintained during the entire lateral load history applied to the column top (or until the column axial load capacity lost). The lateral and gravity load test setup used for the cyclic bidirectional test of the FRC bridge columns is presented in Appendix B.

2.4 INSTRUMENTATION SCHEME

The following section presents the internal and external instrumentation scheme of the FRC column specimens, measuring strain deformations, and relative and absolute displacements along the column height.

2.4.1 Strain Gage Instrumentation

Strain gage installation on longitudinal rebar and spiral reinforcement is carried out in an experimental test to trace the strain history at various locations in a column specimen and to correlate internal strains to observed damage such as bar buckling and fracture. In quasi-static cyclic testing peak strains are achieved at the end of each increasing cycle, thus fully utilizing the life of strain gages installed on longitudinal rebar. In bidirectional cyclic testing peak strains in longitudinal rebar are obtained at multiple instances of each cycle, thus the strain history recorded by strain gages at their ultimate limit may be incomplete. Also, strain gages placed on longitudinal reinforcement in the plastic hinge zone of a column are subjected to higher strain demands than other locations; therefore, at high ductility levels and repeated excitations, the

utility of strain gages and ability to trace strain profiles along the height of the column is also limited.

The longitudinal and transverse reinforcement of the FRC columns were instrumented using a total of 33 and 29 strain gages for specimens S1 and S2, respectively, according to the scheme presented in Figure 2-13 and Figure 2-14. Strain gages were attached to four out of twelve continuous longitudinal reinforcing bars at four levels along the height of the column. The bars were gaged prior to construction and one bar was placed on each side of the column (East, North, West, and South). For S1 specimen, in each instrumented longitudinal continuous bar, the gages were placed in the following distances from the column-footing interface: 2" (Elevation 1-S), 10" (Elevation 2-S), 18" (Elevation 3-S), and 24" (Elevation 4-S). In terms of the diameter d_b of a #4 bar used for the longitudinal reinforcement, these distances are equivalent to: $4d_b$, $20d_b$, $36d_b$, and $48d_b$. In the S2 specimen, Elevation 2-S is defined at 8" above the foundation, equivalent to $16d_b$. The first level of strain gages was close to the foundation zone (Elevation 1-S), the following two levels (Elevation 2-S and 3-S) were in the plastic hinge region, while the top level of strain gages was above the plastic hinge zone (Elevation 4-S). The continuous longitudinal rebar with attached strain gages coincided with the XY axes of application of the lateral load, and were denoted according to their corresponding North-South-East-West orientation.

Strain gages were also attached to four out of eight longitudinal dowels at one and two levels along the height of the column, for S1 and S2 specimens, respectively. For S1 specimen, the gages were placed at 2" ($4d_b$) and 10" ($20d_b$) above the foundations, while for S2 specimen the gages were installed only at 2" ($4d_b$) above the foundation. The denomination of the instrumented bars was also done according to their approximate North-South-East-West orientation, as seen in Figure 2-13 and Figure 2-14.

The spiral reinforcement was also instrumented using a total of 9 strain gages for both S1 and S2 specimens. Strain gages were placed at three points along the perimeter of the column at three elevations coinciding with the first three strain gage levels of the continuous longitudinal rebar (Elevations 1-S, 2-S, and 3-S). The spacing varied slightly from specimen to specimen and from side to side on the same specimen due to variations of the actual spiral layout. However, the average height of the strain gages from the top of the footing was maintained. The strain gage type used to instrument the longitudinal rebar was YFLA-5-5L by TML (Texas Measurements, Inc.), while YFLA-2-5L gages by TML were used for the spiral.

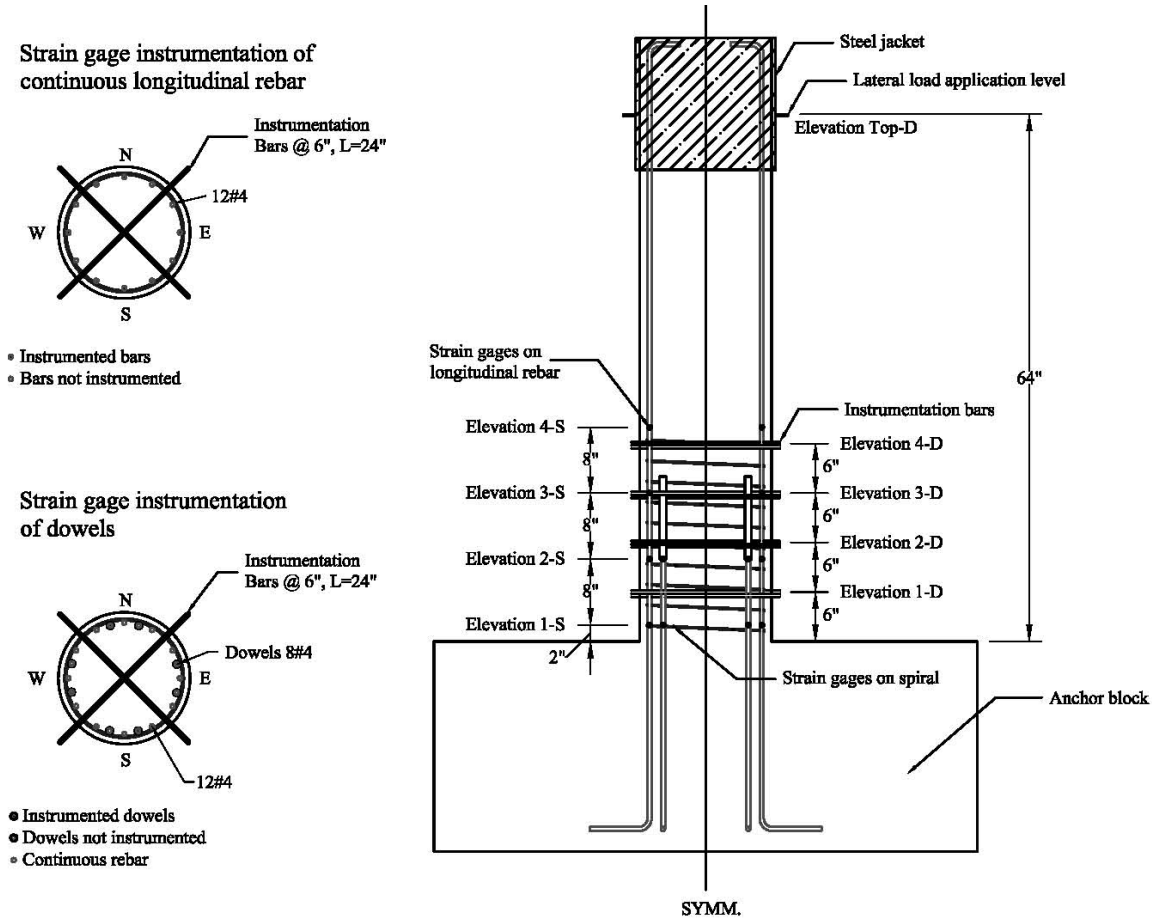

Figure 2-13 Strain gage instrumentation scheme of S1 specimen

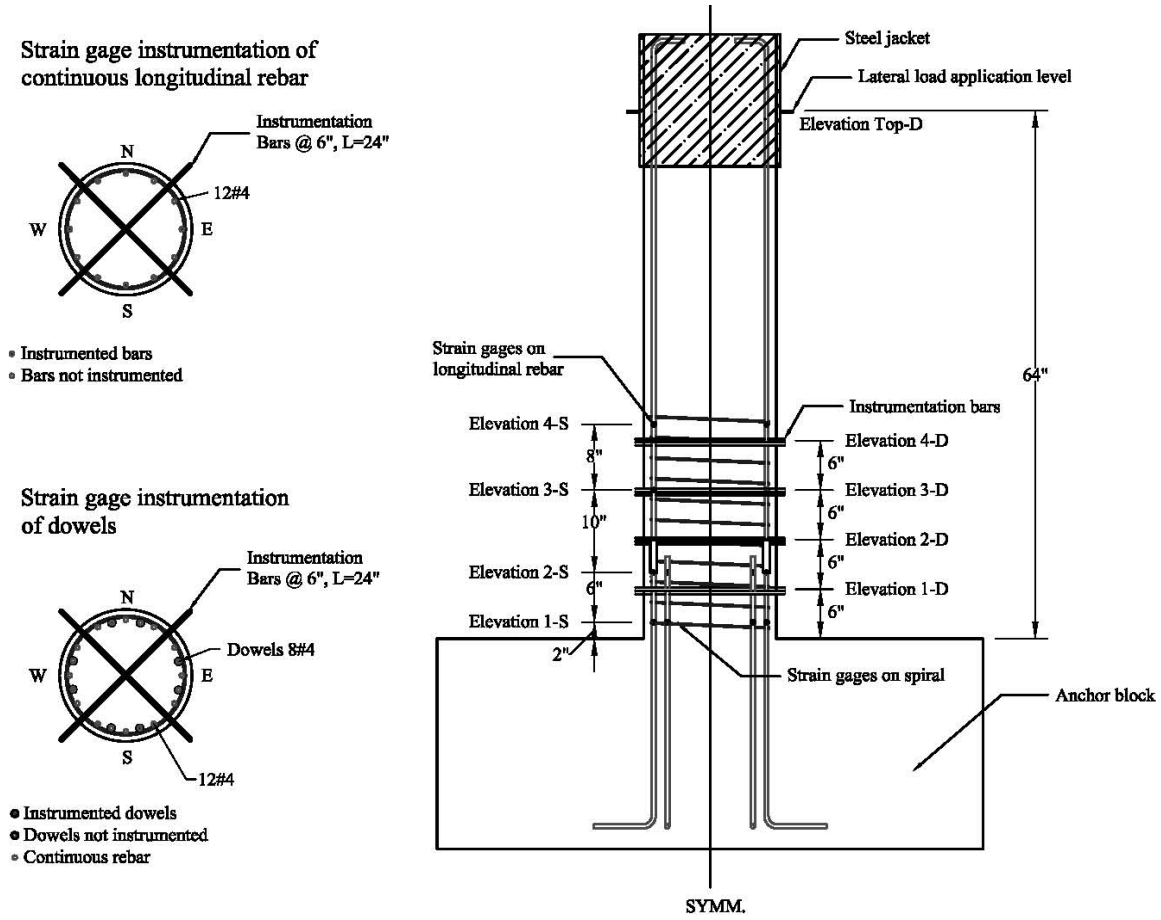

Figure 2-14 Strain gage instrumentation scheme for S2 specimen

2.4.2 External Instrumentation: Absolute Displacements

Global or absolute displacements of the FRC column specimens were measured using linear displacement potentiometers according to the instrumentation scheme in Figure 2-15 and Figure 2-16. Multiple wire potentiometers were placed on two stiff instrumentation frames located on the North and East sides of the specimen (see Figure 2-17). Two displacement potentiometers monitored the movement of the Northeastern corner of the column at five levels along its height: 6, 12, 18, 24, and 64" above the top of the anchor block. The first four elevations correspond to the instrumentation rods used for relative displacement and curvature measurements and the last elevation represents the column top and application point of the lateral load. These displacement measurements were denoted as CE-1 through CE-T to the East and CN-1 through CN-T to the North. These measurements were used to obtain the deflected shape of the column and verify the relative displacements and rotations of the specimens.

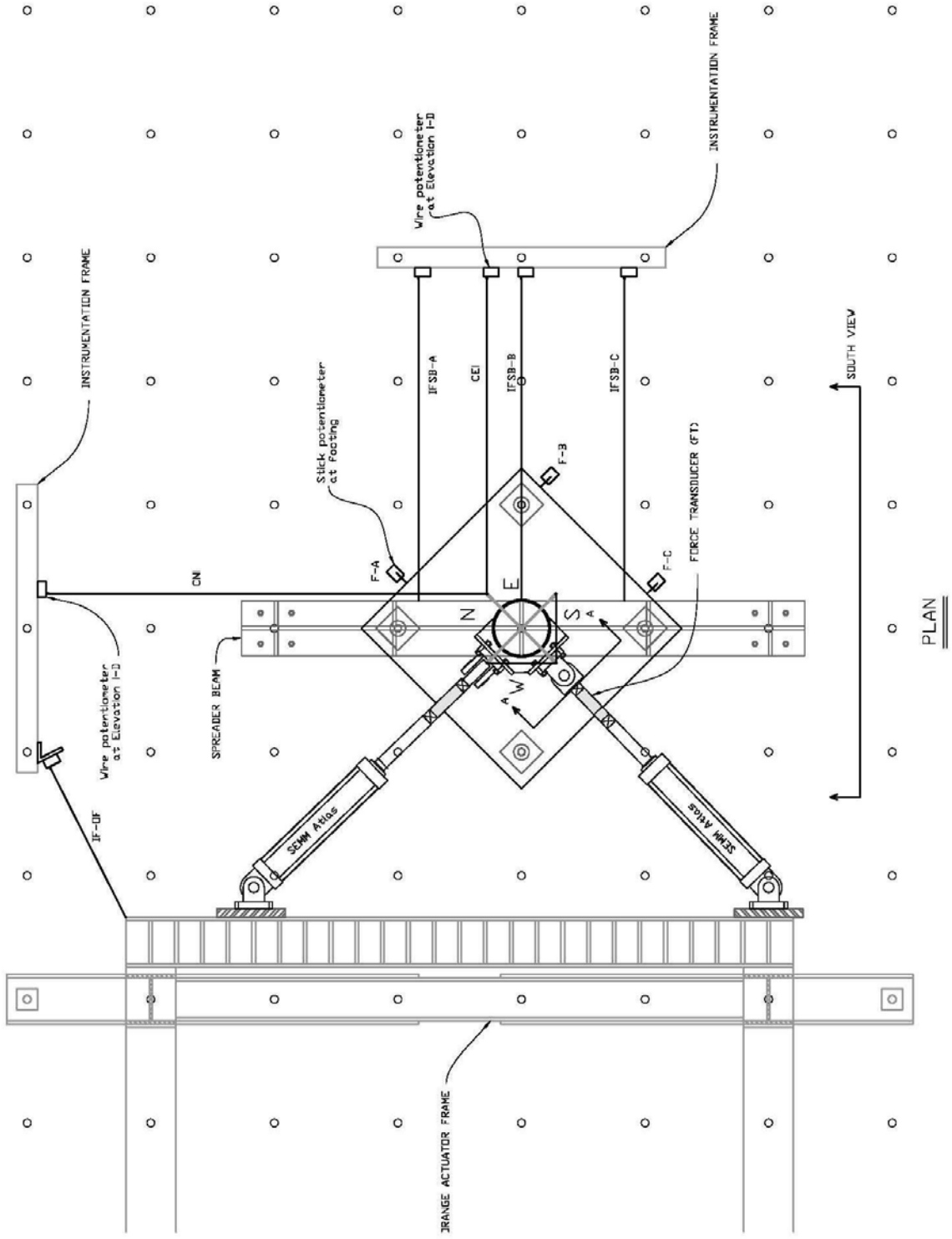

Figure 2-15 Plan view of external instrumentation scheme: absolute displacements

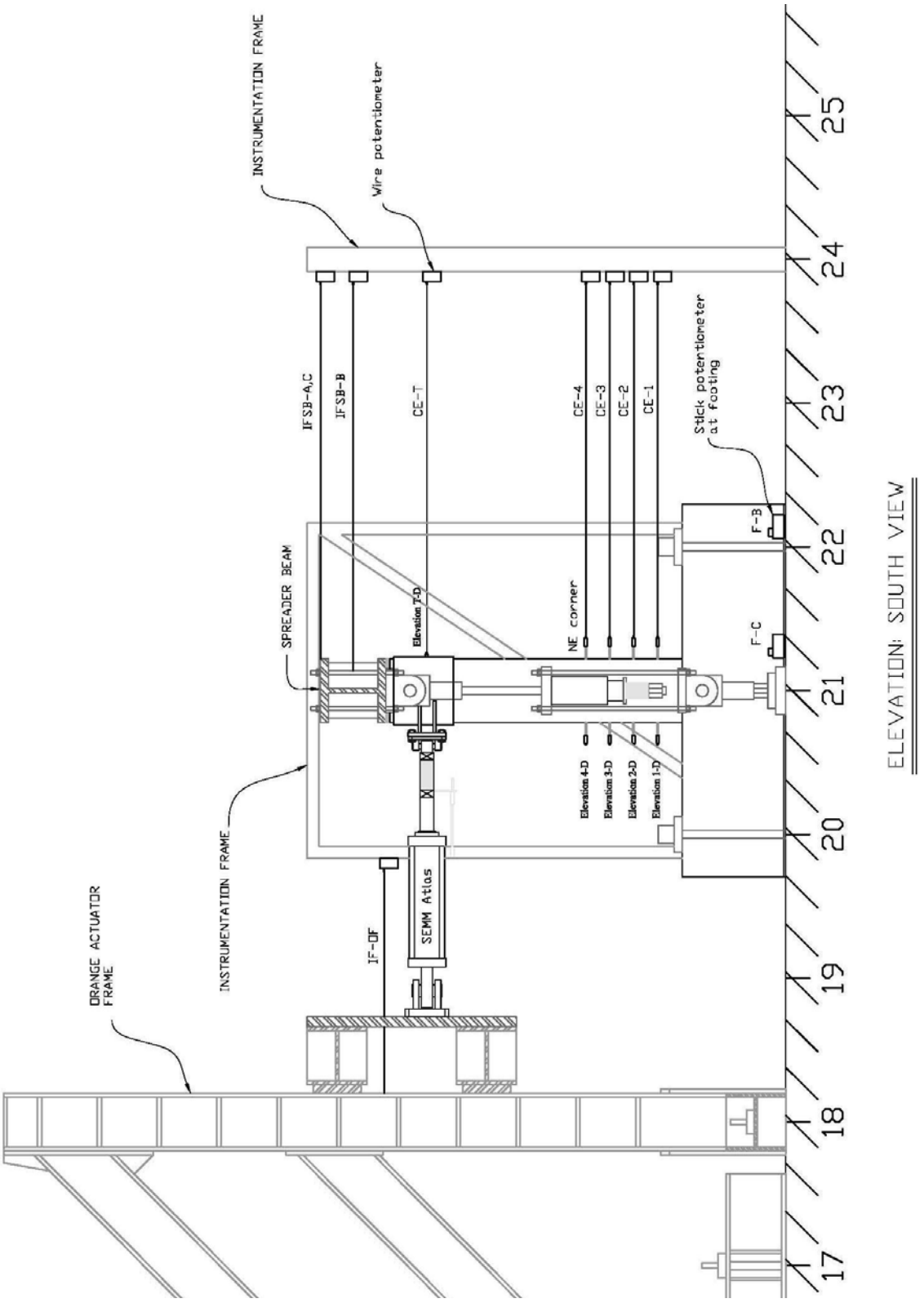

Figure 2-16 South view of external instrumentation scheme: absolute displacements

Figure 2-17 Instrumentation frames: (a) East side; (b) North side

Additional wire potentiometers were placed at three points along the length and height of the spreader beam to monitor the torsion of the column top in the global Z-axis and torsion of the spreader beam in the global X-axis (denoted as IFSB-A, IFSB-B, and IFSB-C). A single displacement potentiometer was used to monitor the movement of the actuator frame (IF-OF). The instruments were connected to the target points of the column by uncoated seven-strand fishing wires with 40 lb capacity. All instruments were attached to two instrumentation frames located on the eastern and northern sides of the specimens.

The displacements of any target point at any level of the column were measured in two spatial directions and mathematically transformed to displacements in global horizontal XY system. The vertical displacements of the column were not monitored directly; however, the load cells attached to the post-tensioned rods in the axial load setup were used to monitor the tilt of the spreader beam and column top.

Load cells were used to monitor the force and displacements of the two actuators connected to the column top and the two post-tensioned rods of the gravity load setup at each end of the spreader beam.

The displacement of the anchor block was also monitored by three additional displacement potentiometers in the event of slip of the specimen relative to the strong floor of the lab during the lateral bidirectional cyclic test (denoted as F-A, F-B, and F-C). These stick potentiometers were connected to thick steel plates, hydrostoned to the strong floor.

2.4.3 External Instrumentation: Relative Displacements

Stick displacement potentiometers of ±½" stroke in the vertical direction and ±1" stroke in the horizontal direction were used to measure the relative displacements between different sections of the column along its height. The instruments measured the displacements between the instrumentation rods crossing the section placed during construction, as seen in Figure 2-18 and Figure 2-19. The 3/8" diameter rods were located at the following elevations from the top of the footing: 6, 12, 18, and 24 in, along the Northwest-Southeast and Northeast-Southwest directions (see Figure 2-15). No rods were placed below the footing surface. The measurements of relative displacements taken on the South and West faces of the columns were used to estimate the peak curvatures, rotations, and shear deformations, as well as the average axial deformations along the height of the column. The locations and names of all the stick potentiometers used are shown in Figure 2-18.

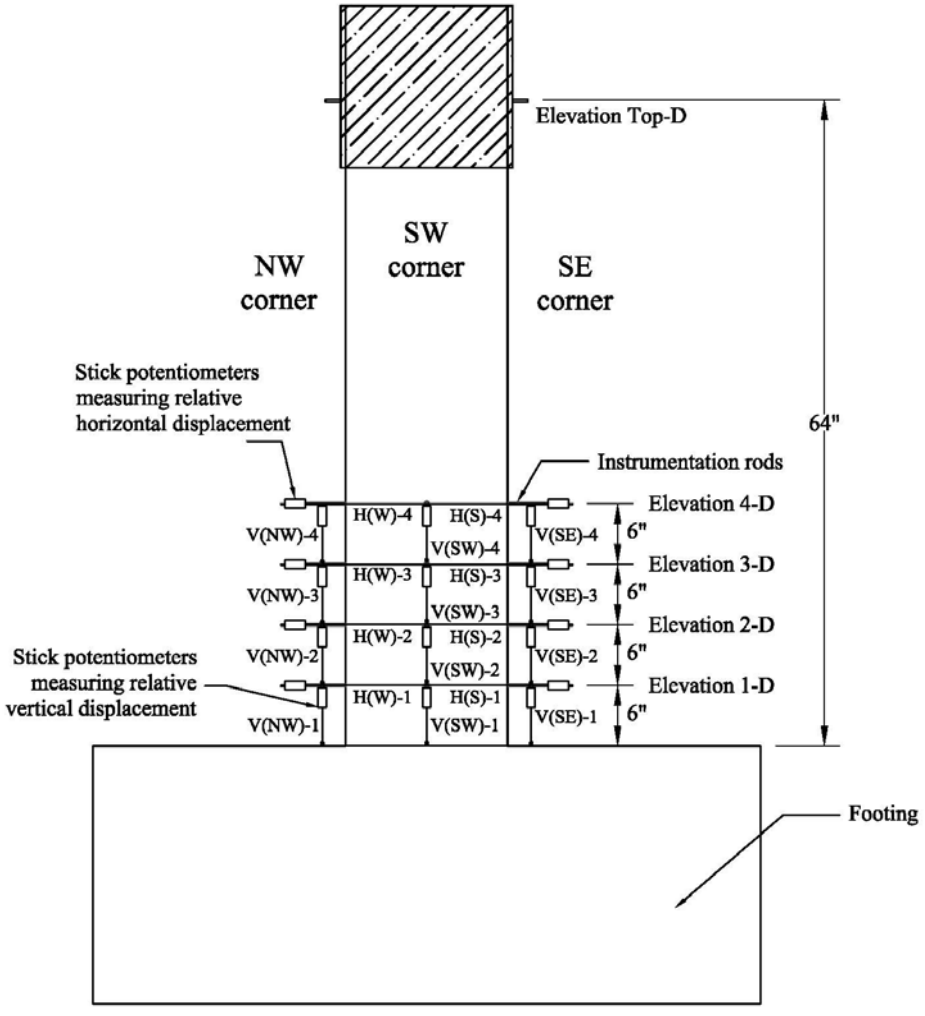

Section A-A
Elevation

Figure 2-18 External instrumentation scheme: relative displacements

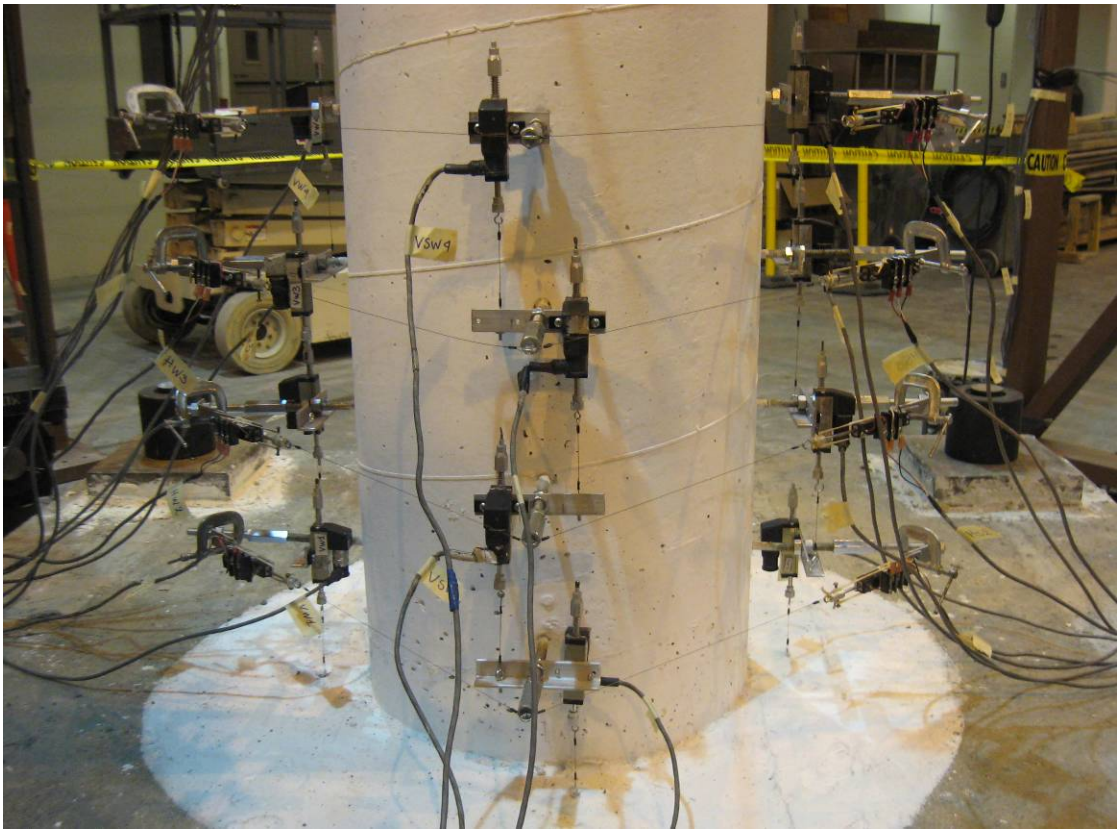

Figure 2-19 Relative displacement instrumentation

3 HPFRC Column Test Results

The present chapter describes the results obtained from the bidirectional quasi-static cyclic test of the two FRC column specimens. For each specimen, major response estimates and damage occurring during the primary cycles of the test are described and compared to that of the BC column tested by Terzic *et al.* (2008). The global response of the columns is presented in terms of their hysteretic behavior, as well as the degradation of their stiffness and strength occurring with increasingly larger cycles. Local response measures such as rotation and curvature profiles, and lateral displacements are discussed in the present chapter. Additional response measures such as longitudinal and transverse reinforcement strain profiles, as well as vertical and shear deformation profiles, are presented in Appendix C. The observed damage progression of the specimens throughout the cyclic tests and correlation to damage indices and recorded response are also presented in Appendix C.

3.1 GLOBAL RESPONSE MEASURES

3.1.1 Lateral Displacements

The actual displacement orbits of S1 and S2 column tops are presented in Figure 3-1. The displacement of the column top was determined through the external displacement measurements obtained from displacement potentiometers connected to the Northeastern face of the column at an elevation of 64”. The displacement of the footing, monitored during the entire cyclic test, was negligible. The main cycles in the S1 test correspond to displacement ductility levels of 1, 1.5, 2, 3, 4.5, 6.25, 8, and 12.5 (drift ratios of 0.86, 1.29, 1.72, 2.58, 3.87, 5.37, 6.88, and 10.74%). These ductility levels are computed with respect to the yield point of the BC column, and are therefore nominal ductility demand values. The maximum major cycle in the S2 test corresponds to a displacement ductility level of 6.25. The twist of the column, indirectly controlled during the cyclic test, was negligible due to special precautions of the test setup configuration and therefore, the actual displacement pattern closely follows the specified input pattern.

The lateral displacement profile of columns S1 and S2, obtained from the external displacement measurements described in Chapter 2, is presented in Figure 3-3. The deformed shape of both FRC column specimens display a concentration of lateral deformation at the bottom portion of the column extending from the base up to a height of approximately 18” and 12” for S1 and S2 columns, respectively (dowel reinforcement extended from the column base up to a height of 20” and 10” for specimens S1 and S2, respectively). As will be seen from the rotation and curvature profiles of the column, the center of rotation of S1 column was lower than

that of S2 specimen. The FRC columns presented a characteristic cantilever behavior with primary flexural deformations and negligible shear distortion, even for the high cyclic displacement levels (see Appendix C). The lateral displacement of the conventionally reinforced BC column presented in Figure 3-3 was closer to S2 column behavior with high rotations near the column base.

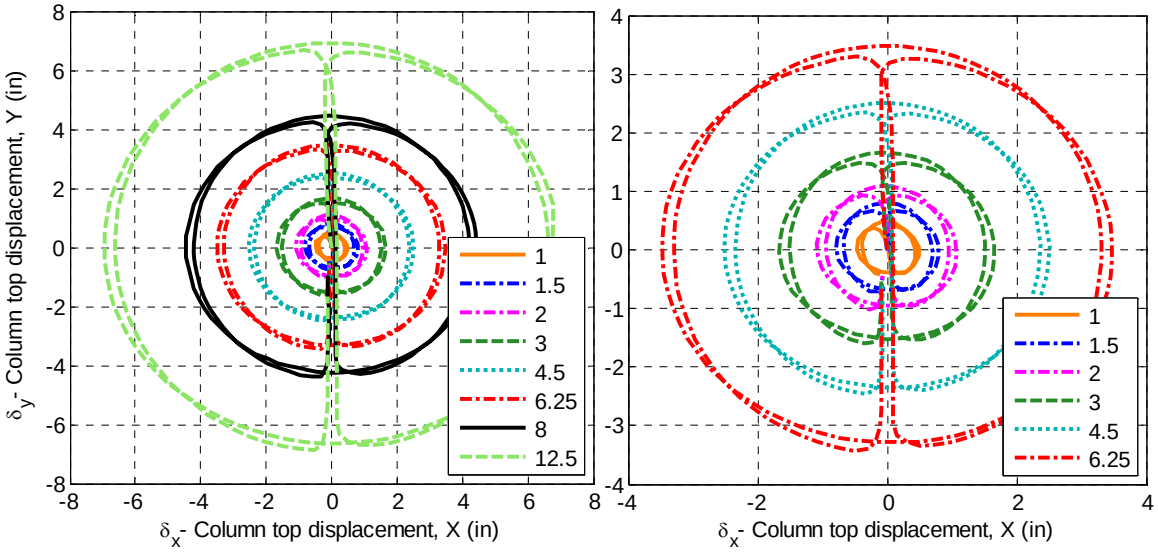

(a) S1 column (b) S2 column

Figure 3-1 Actual displacement pattern of FRC columns

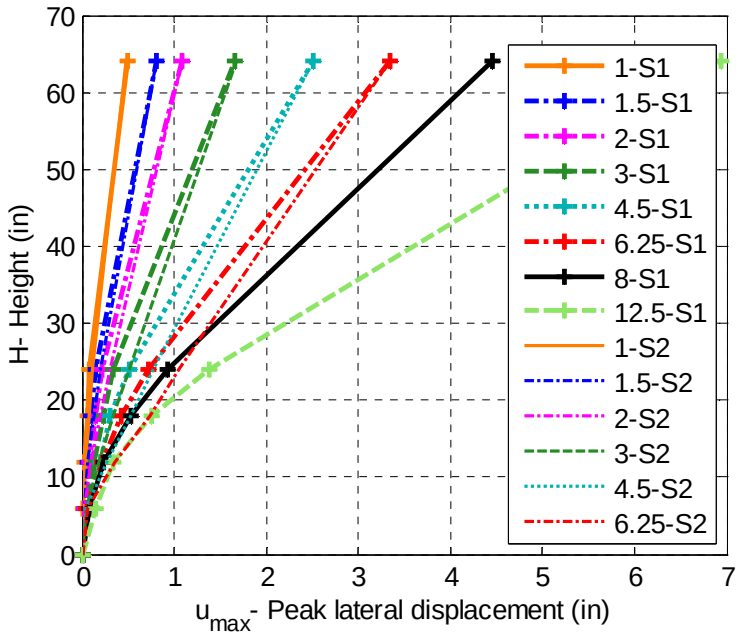

Figure 3-2 Measured peak displacement profile of S1 and S2 columns

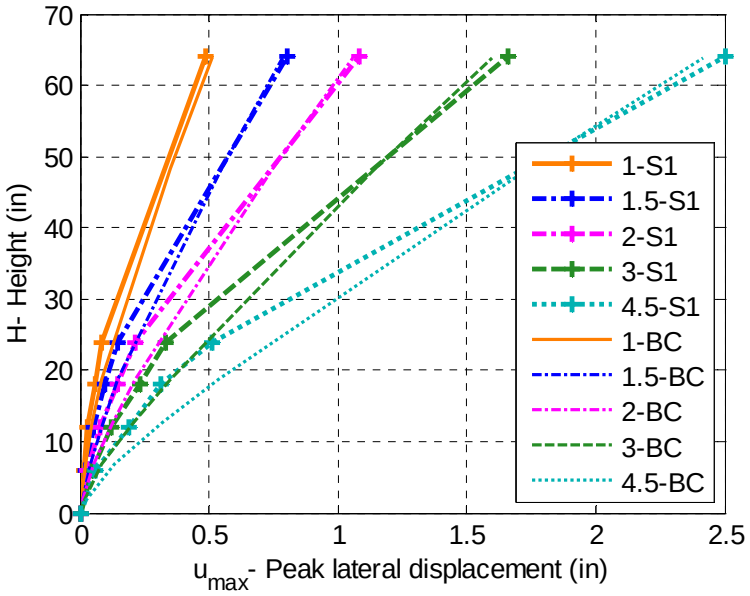

Figure 3-3 Measured peak displacement profile of S1 and BC columns up to a ductility level of 4.5

3.1.2 Hysteretic Behavior

The force-displacement results of the main cycles for specimens S1 and S2 are presented in Figure 3-4 through Figure 3-9. The total shear force on the column base is decomposed into two horizontal orthogonal directions X and Y, defined according to the loading pattern (see Figure 3-1). P-Delta effects produced by the gravity load applied through an unrestrained spreader beam at the displaced column center were considered in the computation of the net shear force applied on the column, according to the axial load setup and the rotation of the column top.

The shear force in the Y direction is slightly higher than in the X-direction due to the specific definition of the loading pattern. At the initial stages of a new cycle with increasingly higher demand level, less damage had occurred in the Y-direction before the X-direction is engaged.

A comparison of the S1 and S2 hysteretic behavior in the X- and Y-directions is presented in Figure 3-4 and Figure 3-5, respectively. The hysteresis loops of S1 and S2 columns, compared in Figure 3-6, were similar up to a ductility level of 6.25 (drift ratio of 5.37%). Both S1 and S2 columns presented stable hysteretic behavior at all the main cycles. The degradation of strength of S1 and S2 is initiated during the second cycle corresponding to a ductility level 6.25. For S1 column, which sustained higher displacement cycles compared to column S2, the stiffness and strength degradation becomes more evident at higher demand cycles corresponding to ductility levels of 8 and 12.5 (drift ratios of 6.88 and 10.74%), as shown in Figure 3-4. The hysteretic behavior for the S2 column at these displacement levels was not obtained experimentally because the quasi-static test was interrupted following the cycle corresponding to a ductility level of 6.25 due to the loss of gravity load carrying capacity of the column.

Both FRC columns presented elastic behavior up to a ductility level of 1.5, computed with respect to the BC column yield point. No additional flexibility of the test setup was captured through the instrumentation scheme described in Chapter 2. The shear force at a ductility level of

1 was considerably lower than the maximum capacity of both FRC column specimens for the X- and Y-directions of loading. The S2 specimen presented a symmetrical response in both X- and Y-directions. The shear force in the X-direction was symmetrical for S1 specimen. However, the shear force in the Y-direction of the S1 column was slightly lower than the S2 column in the negative Y-direction, possibly due to typical deviations in the distribution of the longitudinal reinforcement around the perimeter of the column during the construction process.

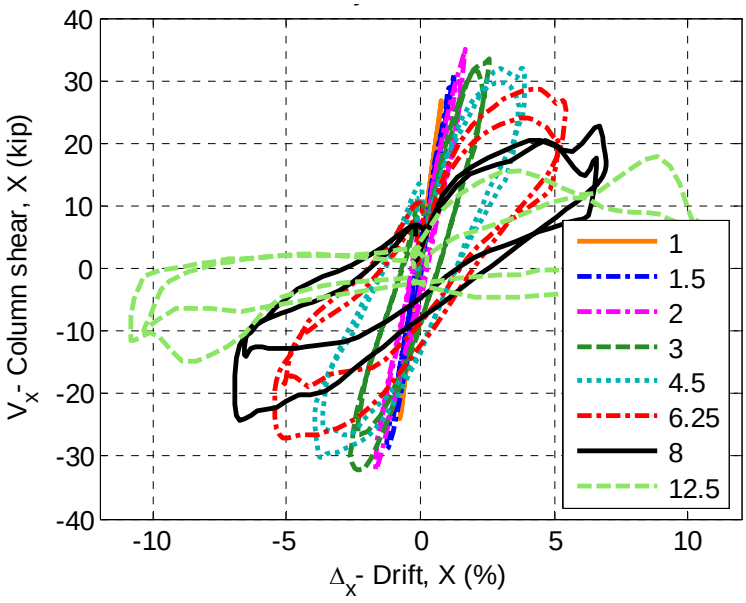

(a) X-axis

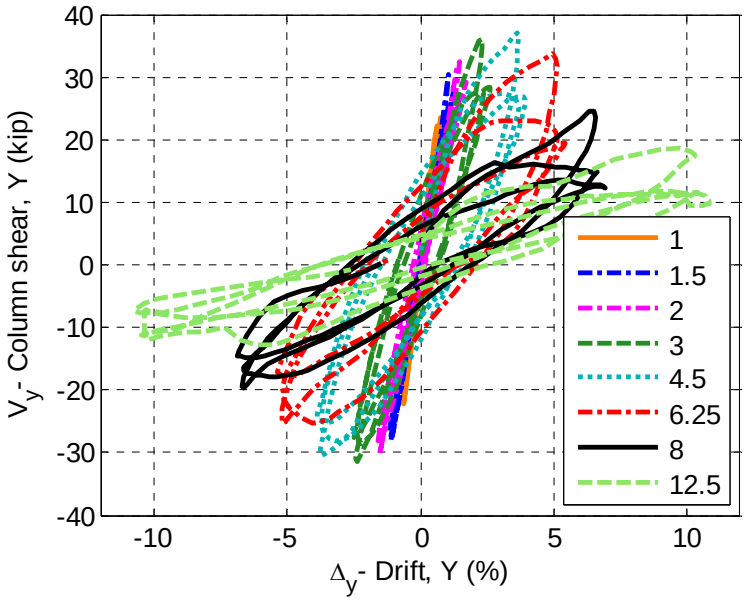

(b) Y-axis

Figure 3-4 S1 column hysteresis- shear force vs. drift

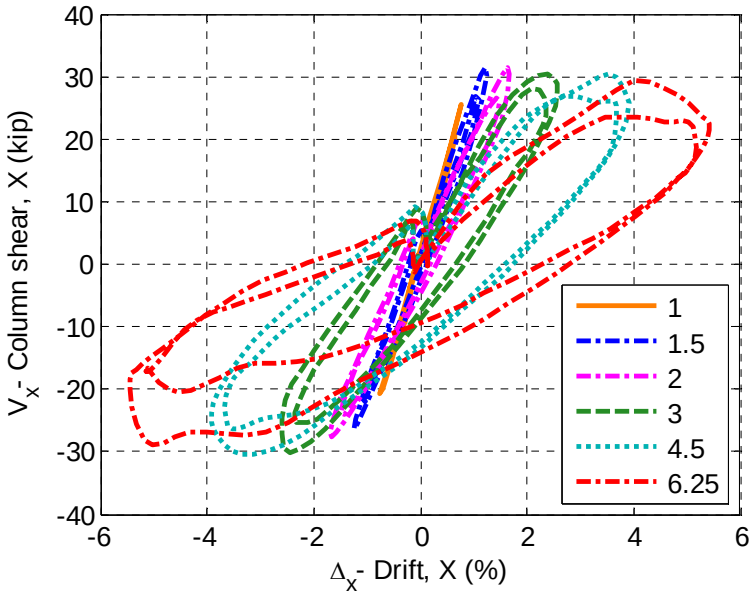

(a) X-axis

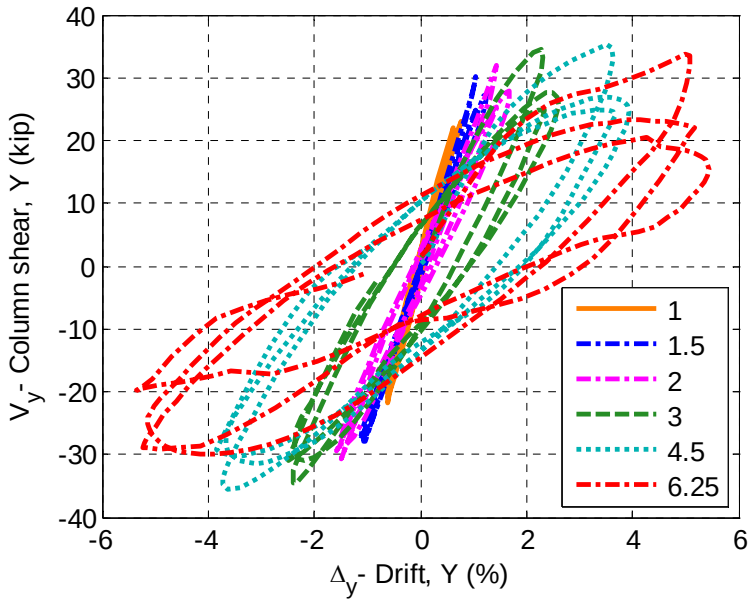

(b) Y-axis

Figure 3-5 S2 column hysteresis- shear force vs. drift

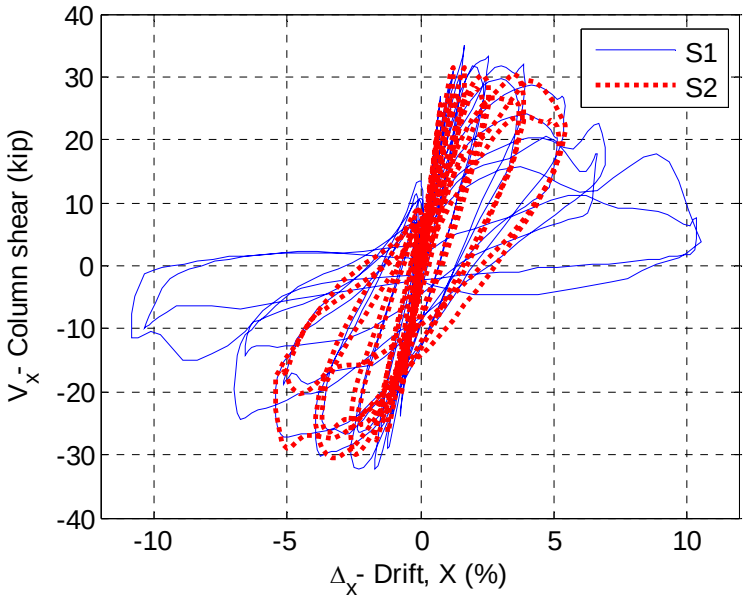

(a) X-axis

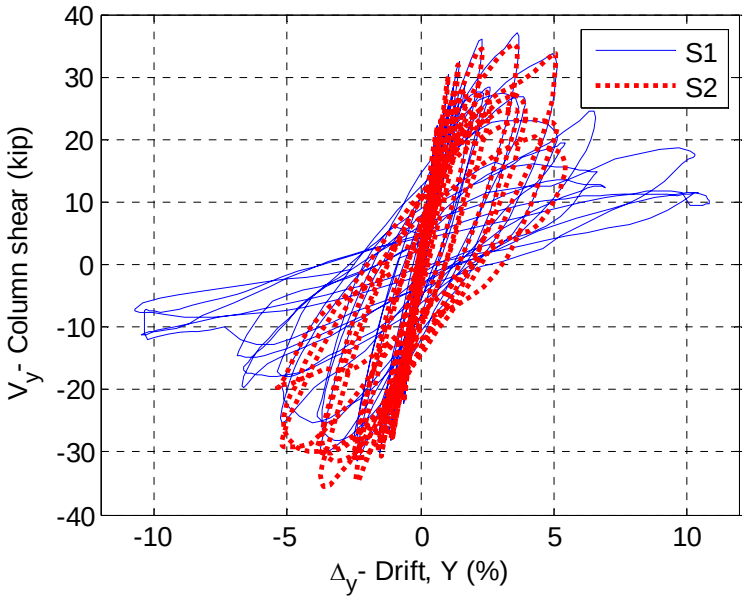

(b) Y-axis

Figure 3-6 Comparison of S1 and S2 column hysteresis

The total shear force on the columns was obtained as the magnitude of the resultant of the X- and Y- shear force components measured at each time step of the cyclic loading. The corresponding total drift at each time step was computed as the amplitude of displacement of the column top divided by the total height of 64". The resulting force-drift relation of S1 and S2 columns is presented in Figure 3-7. Since all four columns considered in this study were circular columns with circular symmetry, the comparison of their hysteretic behavior in terms of total shear force and total drift demand is more relevant.

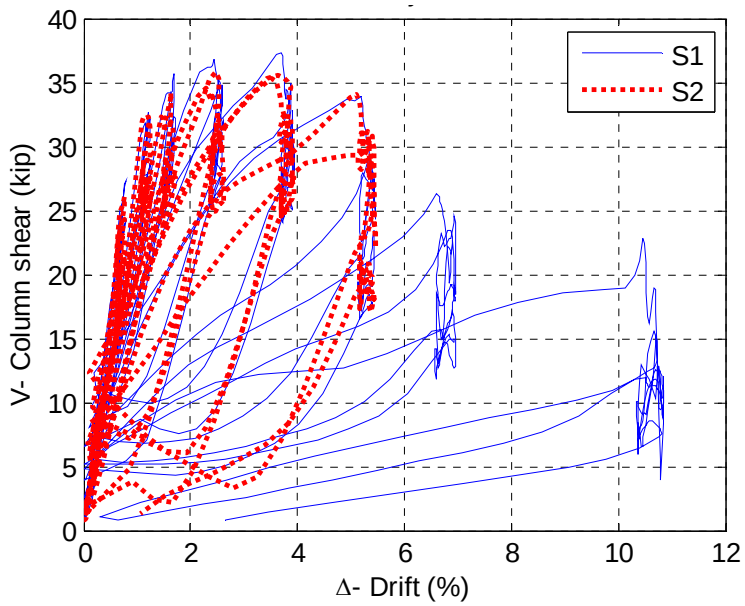

Figure 3-7 Comparison of S1 and S2 columns total shear vs. total drift hysteresis

The total shear stress was estimated for all four columns as the total shear force divided by the effective area in shear, defined by Caltrans SDC (2004) as 0.8 times the gross area of the column. The hysteretic behavior of BC and SSC columns was obtained from the experimental results of Terzic *et al.* (2008). The total shear stress obtained for S1, S2, BC, and SSC columns is presented in Figure 3-8.

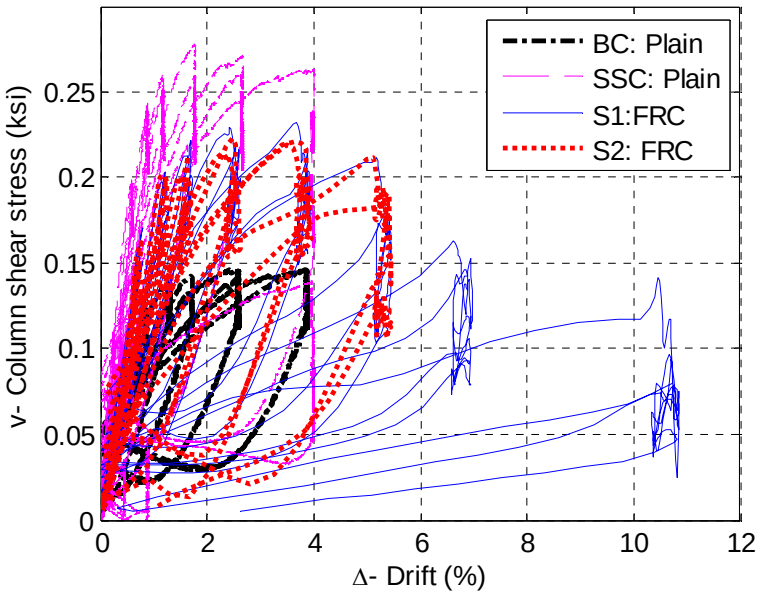

Figure 3-8 Comparison of S1, S2, BC, and SSC columns total shear stress vs. total drift hysteresis

Figure 3-8 demonstrates that the shear force of both FRC columns was approximately 60% higher than that of the geometrically identical BC specimen under the same displacement

demand. The shear force of the FRC columns was only slightly lower (in the order of 20%) than the SSC specimen, which has a reduced height (24" shorter than the FRC and BC columns) and therefore results in higher shear forces for a similar flexural capacity. For the FRC columns, the strength was governed by flexure and no shear related damage was observed at any drift demand level.

The total shear ratio was obtained for all four columns by dividing the total shear force in the column by the assumed shear strength provided by the transverse steel reinforcement at yielding, estimated according to Caltrans SDC (2004). The shear ratio of the S1, S2, BC, and SSC columns is presented in Figure 3-9. Clearly, since the transverse reinforcement ratio in S1, S2, BC, and SSC column specimens was different, the latter interpretation of the column shear demand in the normalized form is more adequate. Figure 3-9 displays an increased shear demand of the S1 and S2 specimens compared to the BC specimen due to the addition of macro fibers to the concrete mix and the 50% reduction in steel transverse reinforcement, which increased the demand on the concrete material. The shear ratio of the FRC columns was approximately 3 times higher than the BC specimen and only 30% lower than the SSC specimen. Additionally, the degradation of the shear force in the S1 and S2 FRC columns, governed by their flexural capacity, was only pronounced at the higher ductility demand level of 6.25, while in the BC and SSC plain concrete specimens notable stiffness and strength degradation was initiated at a lower ductility demand level of 4.5. No shear-related damage was observed throughout the cyclic loading history of the FRC columns and the degradation of shear force was solely governed by degradation in their flexural capacity, similar to the plain concrete specimens.

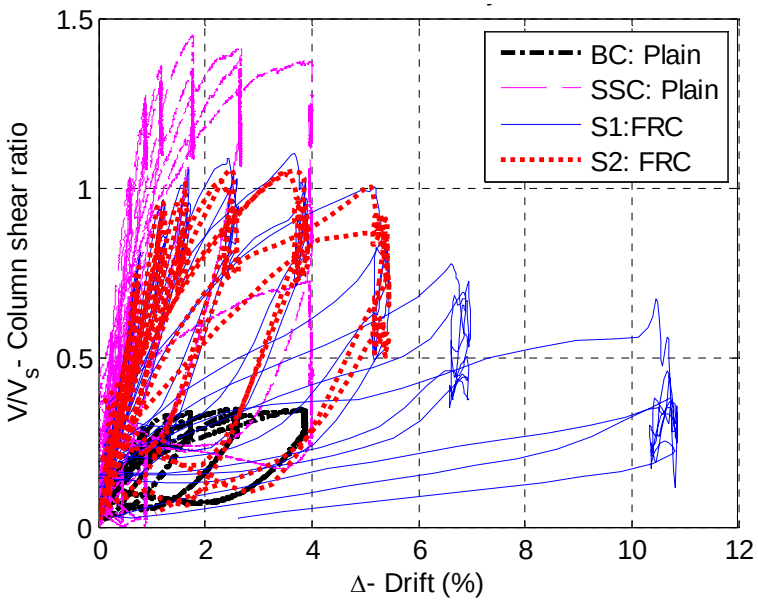

Figure 3-9 Comparison of S1, S2, BC, and SSC columns total shear ratio vs. total drift hysteresis

Figure 3-10 compares the total hysteretic behaviors of S1 and BC specimens at the main cycles of displacement, where the total shear force of each specimen is normalized with respect to its maximum shear force. Both columns displayed stable hysteretic loops and a response dominated by flexure. Sliding or significant shear distortions are not evident since no pinching (gap-like response) is visible in the hysteretic loops. The unloading and reloading of the columns

at a specific level of the cyclic test developed with a slope corresponding to the column residual stiffness at that level. The increase in the shear force with increasingly larger cycles was more pronounced in the S1 column than in the BC specimen due to the ductile behavior and strain hardening properties of the FRC material provided by the addition of steel macrofibers. Notable degradation of the shear force was initiated in both columns following the second circular cycle corresponding to a displacement ductility of 4.5 with respect to the BC column. The distorted shape of the hysteretic loop of the BC column at the re-centering phase of the load pattern (from peak drift applied to the column top to zero drift) is an artifact of data processing performed by Terzic *et al.* (2008) which does not correspond to the actual column unloading response.

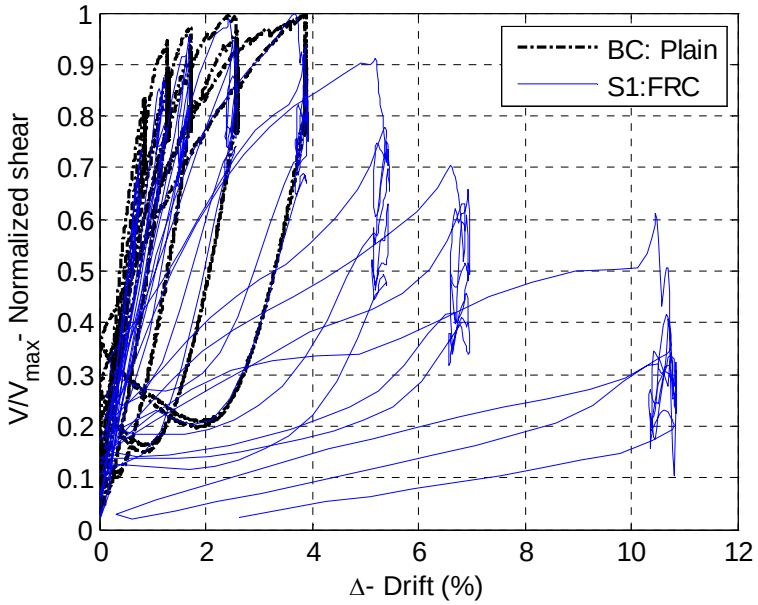

Figure 3-10 Comparison of S1 and BC normalized total shear vs. drift hysteresis

3.1.3 Stiffness and Strength Degradation

The degradation of the lateral stiffness and shear force of the FRC and BC columns is presented in Figure 3-11 and Figure 3-12, respectively. The stiffness degradation of the columns was determined for the main displacement ductility demand levels using the lateral stiffness of intermediate cycles equal to one-third of the amplitude of the primary cycles in the loading history. The lateral stiffness for these intermediate cycles was determined as the slope of the linear fit relating column shear and lateral displacement of the column top in the hysteretic loops. The degradation in the shear force of the columns as a function of the displacement ductility demand was determined using the maximum absolute shear force values recorded at each main cycle of the test.

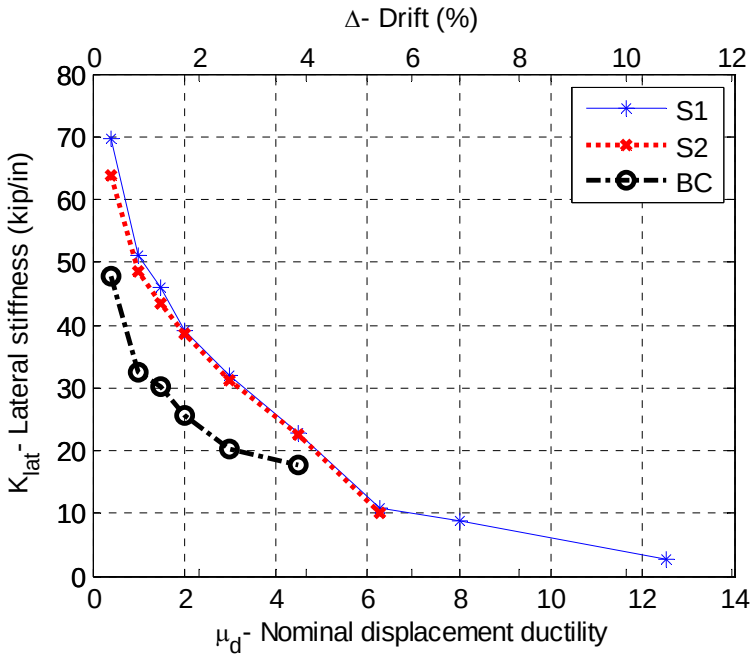

Figure 3-11 Degradation in lateral stiffness of FRC and BC columns

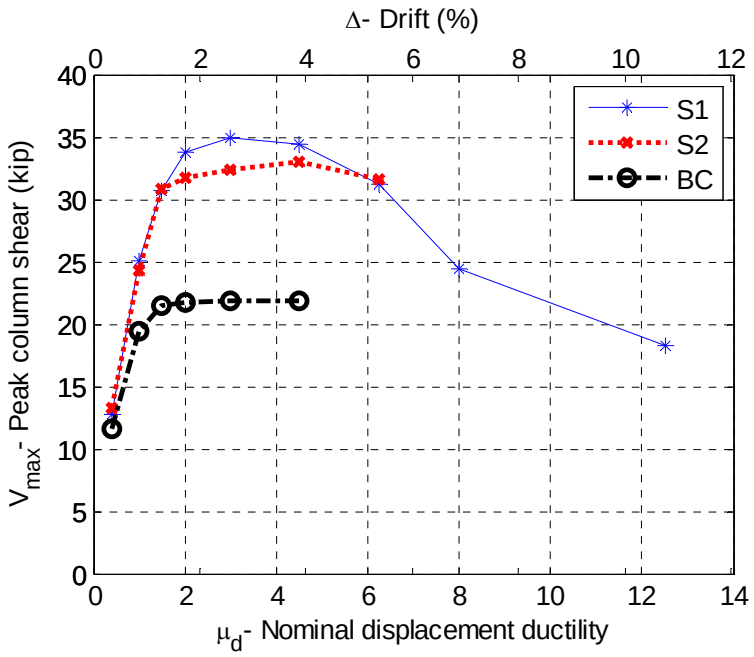

Figure 3-12 Envelope response for FRC and BC columns

The lateral stiffness of the FRC columns at the different ductility level were comparable due to very similar hysteretic behavior up to a ductility level of 6.25, where the S2 test was interrupted due to loss of gravity load carrying capacity of the column. The lateral stiffness of the FRC columns was higher than that of the BC column for all ductility levels considered and the degradation of stiffness for all columns was similar up to a ductility level of 3. However, the degradation of the lateral stiffness of the BC column was less pronounced than that of the FRC

columns for ductility levels higher than 3, displaying an asymptotic behavior and stabilized response at lower ductility levels than the FRC columns. The residual lateral stiffness of the BC columns extrapolated for ductility levels beyond the ultimate level tested of 4.5 is higher than the S1 column stiffness obtained for high ductility demand levels. The stiffness degradation of the BC columns was less prominent than the FRC columns primarily due to higher confining reinforcement ratio and smaller transverse reinforcement spacing which maintained the integrity of the concrete core and prevented bar buckling at later stages of the loading history. Despite these differences, the FRC and BC columns present relatively comparable stiffness degradation tendencies.

As discussed in section 3.1.2, the shear force demand of the FRC columns was up to 60% higher than the geometrically identical BC column. Nonlinear behavior was observed for the BC column for ductility levels greater than 1, while for both FRC specimens the column remained in the elastic range of response up to a ductility level of 1.5. The shear demand for the three columns remained generally constant between ductility level of 1 and 4.5 for the BC column and between 1.5 and 6.25 for the FRC columns. S1 column presented higher shear demand values than S2 column for ductility levels between 1.5 and 6.25; however, both presented similar peak shear values recorded at a ductility level of 6.25, after which significant degradation of strength was recorded for S1 column. Since BC column was not cycled beyond a ductility level of 4.5, the degradation of shear strength of the column was not captured. The shape of the peak shear values in terms of the displacement ductility demand on the column can be used to represent the lateral pushover response of the FRC column specimens.

3.2 LOCAL RESPONSE MEASURES

3.2.1 Rotation and Curvature Profiles

Biaxial curvature and rotation measurements along the column height were obtained from the instrumentation of relative vertical deformations on the face of the column at four sections extending from the column base to a height of 2 ft corresponding to Elevation D-4 (see external instrumentation scheme in Chapter 2). The measurement of vertical deformations on all four sides of the column (Northwest, Northeast, Southwest, and Southeast) obtained from displacement potentiometers is described in Appendix C. The biaxial rotations are approximated over the different regions of the column as described in Eq. 3-1:

$$\left[\theta_{NW-SE}\right]_i = \left[\theta_{NW-SE}\right]_{i-1} + \frac{(v_{NW} - v_{SE})_i}{\left(S_{H,NW-SE}\right)_i}, \qquad i=1,\ldots,4 \text{ and } \theta_1=0$$

$$\left[\theta_{NE-SW}\right]_i = \left[\theta_{NE-SW}\right]_{i-1} + \frac{(v_{NE} - v_{SW})_i}{\left(S_{H,NE-SW}\right)_i}, \qquad i=1,\ldots,4 \text{ and } \theta_1=0 \qquad \text{[Eq. 3-1]}$$

$$\left[\theta_{\max}\right]_i = \max\left\{\left[\theta_{NW-SE}\right]_i; \left[\theta_{NE-SW}\right]_i\right\}, \qquad i=1,\ldots,4$$

In the above equation v_i represents the vertical deformation (in inches) measured for a particular segment at one of the four instrumented sides of the column (NW, NE, SW, SE). S_{Hi}

represents the horizontal distance between the displacement potentiometers placed on opposite sides of the specimen (either NW and SE or NE and SW) at Elevation D-*i*. The rotation at a section *i* (in either NW-SE or NE-SW directions) was determined as the sum of the rotations at the section below (*i*-1) plus the rotation contribution of the region in between. The peak rotation at a region *i* was obtained as the maximum rotation calculated in the two directions considered (NW-SE and NE-SW) at the corresponding region. The peak rotation profiles of the FRC specimens are presented in Figure 3-13.

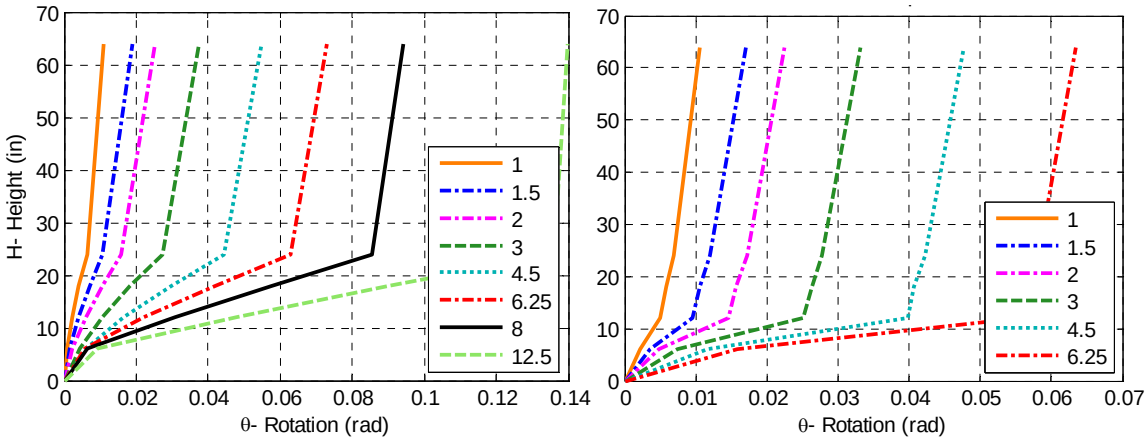

(a) S1 column (b) S2 columns

Figure 3-13 Peak rotation profile of FRC columns

The average curvature over a region (*i*,*i*+1) (in either the NW-SE or NE-SW directions) was calculated as the rotation over the corresponding region divided by the region height h_i, as seen in Eq. 3-2. The peak curvature at a region (*i*,*i*+1) was obtained as the maximum curvature calculated in the two directions considered (NW-SE and NE-SW) at the corresponding region. Constant curvature was specified for each region at the bottom portion of the column near the plastic hinge location up to a height of 2 ft where vertical deformation measurements were obtained, while a linear variation of curvature was assumed for the top portion of the column which remained essentially elastic.

$$[\phi_{NE-SW}]_{i,i+1} = \frac{[\theta_{NE-SW}]_{i+1} - [\theta_{NE-SW}]_i}{h_i}, \qquad i=1,\ldots,4$$

$$[\phi_{NW-SE}]_{i,i+1} = \frac{[\theta_{NW-SE}]_{i+1} - [\theta_{NW-SE}]_i}{h_i}, \qquad i=1,\ldots,4 \qquad \text{[Eq. 3-2]}$$

$$[\phi_{max}]_{i,i+1} = \max\{[\phi_{NW-SE}]_{i,i+1}; [\phi_{NE-SW}]_{i,i+1}\}, \qquad i=1,\ldots,4$$

The curvature at Elevation D-4 corresponding to the top portion of the column was estimated by scaling the yield curvature obtained from a moment-curvature analysis of the top column cross section by the ratio of strain measurements to the yield strain of the longitudinal reinforcing steel presented in Appendix A (i.e., $\phi_{Top}=\phi_{y,Top}(\varepsilon_{s,long}/\varepsilon_{sy,long})$). The curvatures for the top segment of S1 and S2 columns corresponding to region (4,Top) are presented in Table 3-1 and Table 3-2, respectively, where the yield strain of the longitudinal steel $\varepsilon_{sy,long}$ was 2.36e-3

and the yield curvature of the column top section $\phi_{y,Top}$ was determined as 0.576e-3. Note that the maximum strains recorded for the S1 column at ductility levels of 6.25 and higher were lower than the previous cycle (ductility level of 4.5) due to the degradation of the flexural strength occurring during damage progression in the plastic hinge zone. The rotations at the top segment of the column presented in Figure 3-13 were obtained for each ductility level by integrating the corresponding linear curvature variation over the column top portion and adding it to the rotation of the region below, i.e., $\theta_{Top}=\theta_4+\phi_{4,Top}(H_{Tot}-24")/2$.

Table 3-1 Estimated curvatures for the top portion of S1 column

Parameter	Ductility level							
	1	**1.5**	**2**	**3**	**4.5**	**6.25**	**8**	**12.5**
$\varepsilon_{s,long}$-Maximum strain recorded for longitudinal rebar at H=24" ($\times 10^{-3}$)	0.96	1.70	1.87	2.10	2.15	2.09	1.75	0.81
ϕ_{Top}- Curvature at Elevation D-4 (H=24") corresponding to column top segment ($\times 10^{-3}$)	0.23	0.41	0.46	0.51	0.52	0.51	0.43	0.20

Table 3-2 Estimated curvatures for the top portion of S2 column

Parameter	Ductility level					
	1	**1.5**	**2**	**3**	**4.5**	**6.25**
$\varepsilon_{s,long}$-Maximum strain recorded for longitudinal rebar at H=24" ($\times 10^{-3}$)	0.74	1.37	1.54	1.68	3.63	4.70
ϕ_{Top}- Curvature at Elevation D-4 (H=24") corresponding to column top segment ($\times 10^{-3}$)	0.18	0.33	0.38	0.41	0.89	1.15

The curvatures over the first bottom region of the column extending up to a height of 6" above the footing and calculated according to Eq. 3-2 included the effect of slip. Constant curvature was assumed for all four regions at the column base, each extending 6". The peak curvature profiles of the FRC specimens resulting from the approximations discussed above are presented in Figure 3-14.

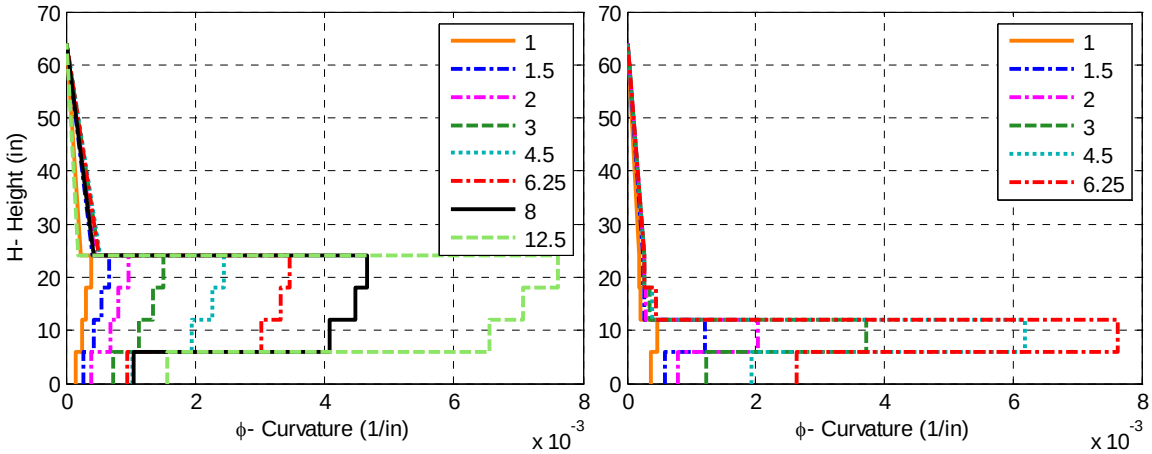

(a) S1 column (b) S2 columns

Figure 3-14 Peak curvature profile of FRC columns

From these figures the maximum length of the plastic hinge zone can be estimated as 18" and 6" for S1 and S2 columns, respectively, starting at an estimated height of 6" above the footing surface. However, since the exact variation of curvature between the different regions along the height of the column is unknown, the actual length and location of the plastic hinge zone cannot be solely based solely on the peak curvature profiles. Additional experimental data, such as measurements of strain profiles and observed damage of the column, can be used to better evaluate the plastic hinge region. Concentration of damage and plastic curvatures was located at the third and fourth regions for column S1 and at the second region for column S2 at the initial stages of inelastic loading of the columns. As observed from the peak curvature profile in Figure 3-14 and damage progression in Appendix C, the damage propagated down towards the column base with increasingly larger cycles. Higher plastic curvatures were obtained at the column base for specimen S2 in comparison to S1 column due to the formation of a primary crack at a height of 10" where a week zone had formed at the discontinuity level of the longitudinal dowels.

The peak rotation and curvature profiles of S1 and BC column specimens obtained up to a ductility level of 4.5 are compared in Figure 3-15 and Figure 3-16. As expected from the different deformed shapes of S1 and BC columns presented in Figure 3-3, their corresponding rotation and curvature profiles presented significant disparities. Concentration of plastic curvatures was located at the base of the BC specimen and the damage propagated upwards as the column was cycled at increasingly higher ductility levels. Conversely, the plastic hinge zone of the S1 column was located approximately 6" above the foundations with its center at an approximate height of 14". Furthermore, in the S1 column the observed damage progression displayed a propagation of inelastic behavior down towards the base of the column. The peak rotation profile in Figure 3-15 displays higher rotations at lower elevations and lower rotations at higher elevations for the BC column, in comparison to S1 specimen. Figure 3-16 displays an increasing variation of curvatures towards the base of the BC column with plastic curvatures in the plastic hinge zone measuring up to a maximum height of 18". In the FRC specimens inelastic action is offset from the column base upwards due to the addition of longitudinal dowels which prevent the formation of a major base crack at the cold joint interface between normal and fiber-reinforced concrete. The spreading of damage and the corresponding length of the plastic hinge

zone of S1 column was higher than the BC column, representing a more favorable response capable of higher energy dissipation through inelastic excursions.

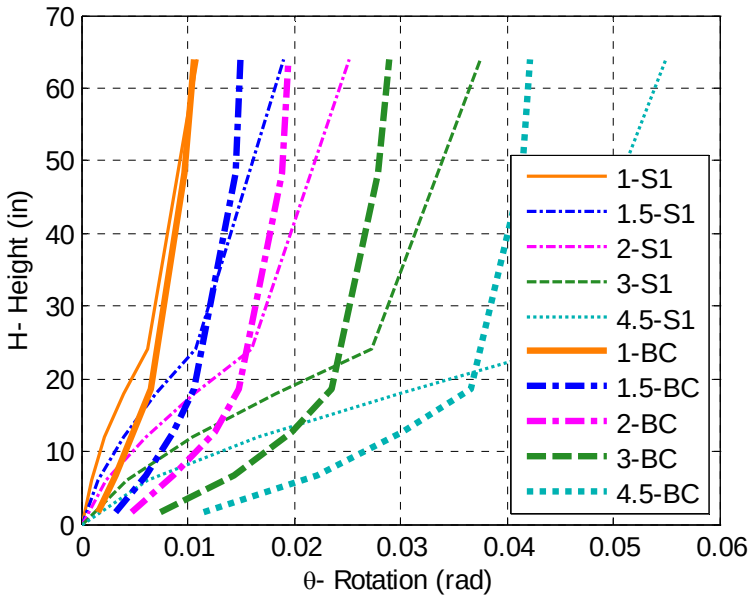

Figure 3-15 Comparison of peak rotation profiles of S1 and BC specimens up to a ductility level of 4.5

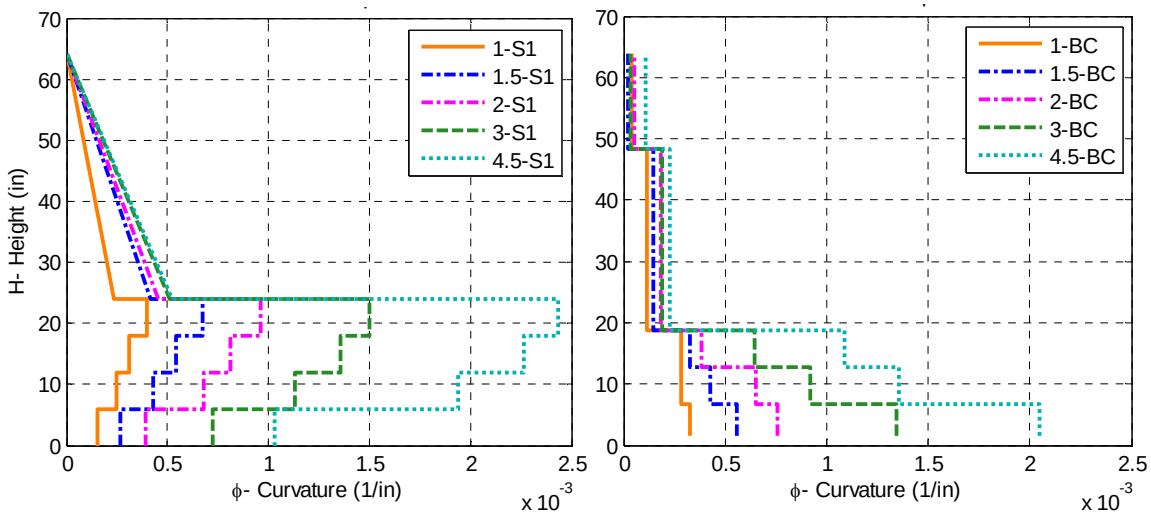

Figure 3-16 Comparison of peak curvature profiles of S1 and BC specimens up to a ductility level of 4.5

3.2.2 Lateral Flexural Deformations

The integration of curvatures along the height of the columns yields the rotations and horizontal displacements at different heights. The relative horizontal relative displacements due to flexure at each level i (u_i) can be computed from the distribution of rotations over the height of the column (Figure 3-13), as defined in Eq. 3-3:

$$u_i = u_{i-1} + \frac{\left([\theta_{\max}]_i + [\theta_{\max}]_{i-1}\right)}{2} h_{i-1}, \qquad i=2,...,4 \text{ and } u_1=0 \qquad \text{[Eq. 3-3]}$$

The moment-area method is an equivalent method that can be similarly used to determine the lateral displacements of the column based on the peak curvature profiles of the FRC columns presented in Figure 3-14. The resulting lateral flexural deformations of columns S1 and S2 are presented in Figure 3-17. The flexural deformation profile of S1 and BC columns obtained up to a ductility level of 4.5 are presented in Figure 3-18. As observed in both figures, due to higher rotations near the column base for the S2 and BC columns, the resulting lateral flexural deformations of these specimens is larger at lower levels than the S1 column.

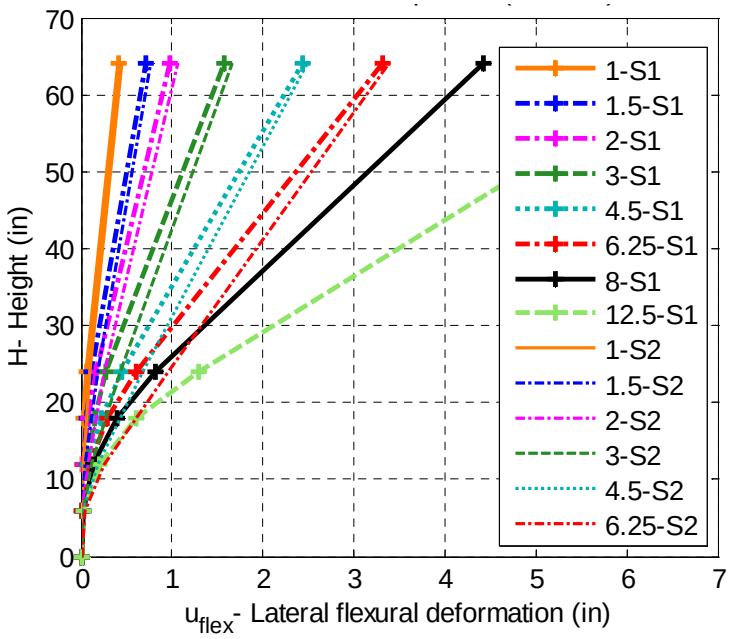

Figure 3-17 Lateral flexural deformations of FRC columns

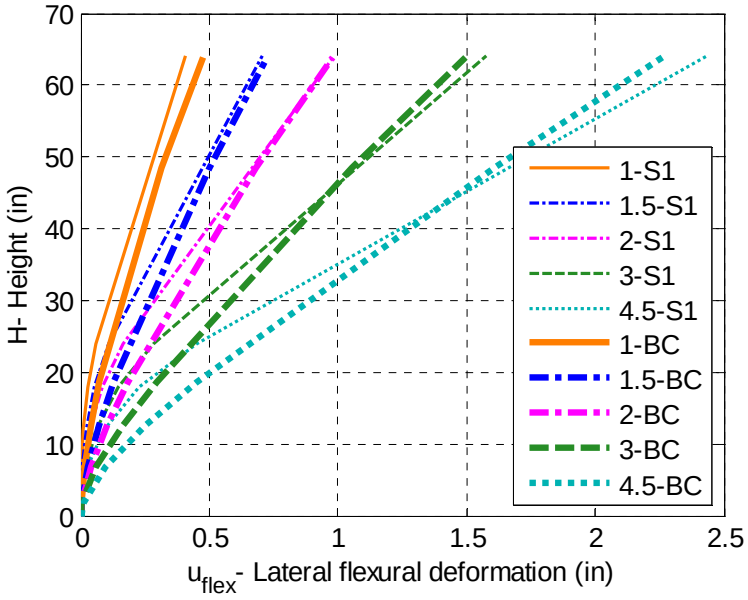

Figure 3-18 Comparison of lateral flexural deformation profiles of S1 and BC specimens up to a ductility level of 4.5

Figure 3-19 and Figure 3-20 compare two different measures of lateral deformation profiles for columns S1 and S2, respectively. The first measure represents the measured relative deformation of the column obtained directly from external (absolute) displacement measurements using linear displacement potentiometers (see external instrumentation scheme in Chapter 2).

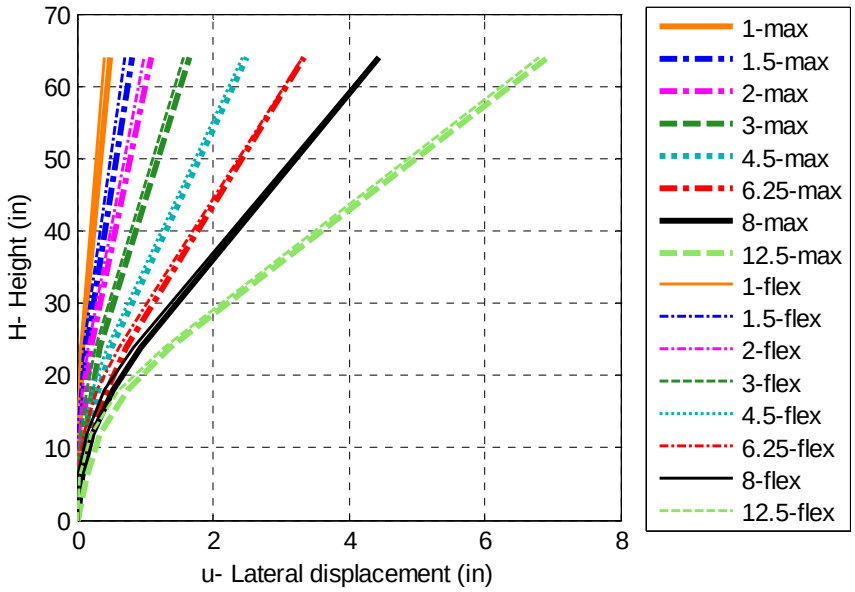

Figure 3-19 Comparison of maximum measured and calculated flexural lateral deformation profiles of S1 column

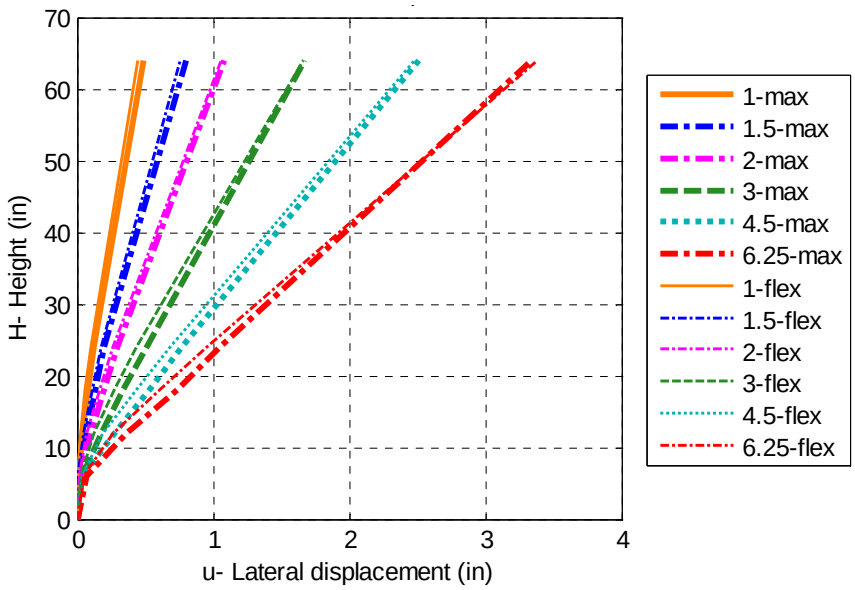

Figure 3-20 Comparison of maximum measured and calculated flexural lateral deformation profiles of S2 column

The lateral displacement profiles in Figure 3-19 and Figure 3-20 represent the total deformations due to flexure, shear, slip, and twist of the column. The second is the lateral flexural deformation profile obtained by integrating the curvature or rotation profiles along the height of the column, which includes the slip deformation at the column base. The figures display a good match between the two measures, indicating that shear contribution to the total deformation was negligible. The estimated shear deformation profiles of the FRC columns and BC specimen are presented in Appendix C.

3.2.3 Calibrated Plastic Hinge Model

A simplified plastic hinge model was determined for the FRC columns through an idealized curvature profile as a function of the nominal ductility capacity of the specimens. The idealized model consisted of three segments of the column: the top section above the plastic hinge zone with a linear variation of curvatures limited by the yield curvature, the plastic hinge zone with a single constant curvature, and the bottom portion with a single constant curvature value. The curvature profile at each segment was obtained through linear interpolation in terms of the nominal ductility capacity of the column, based on the measured curvature results presented in Figure 3-14 for both FRC columns. The idealized curvature profiles of the FRC columns obtained iteratively are presented in Figure 3-21.

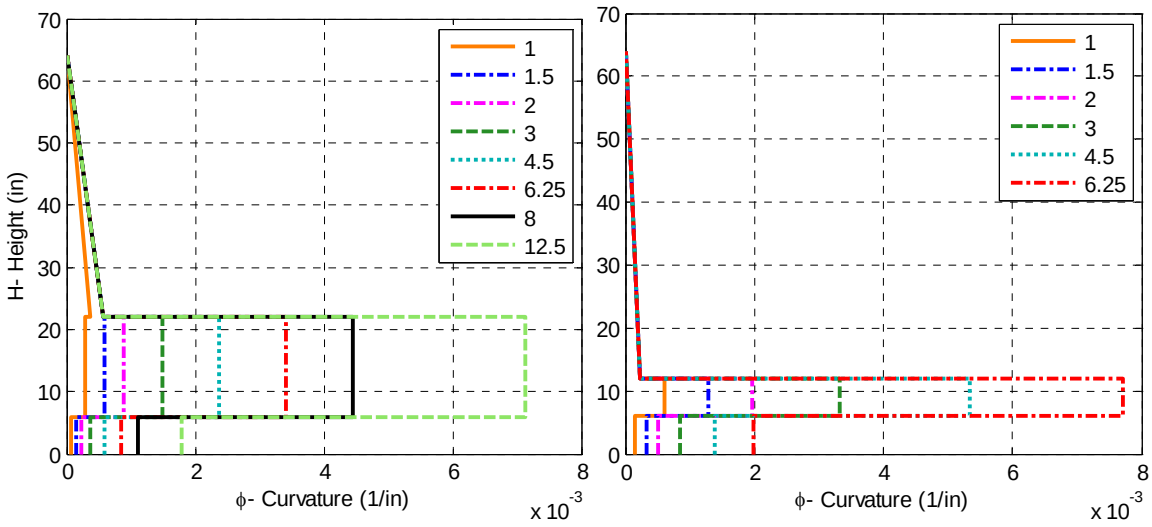

Figure 3-21 Idealized curvature profiles of FRC columns based on calibrated plastic hinge model

The integration of the curvatures along the column height resulting in an estimate of the flexural deformations at the column top was used as the calibrated plastic hinge model of the FRC columns. The final expression of the flexural deformations of S1 and S2 columns as a function of the curvature profile and nominal ductility capacity are presented in Eq. 3-4 and Eq. 3-5, respectively.

S1 column:

$$u(\mu) = \phi_{y,Top} \cdot \min\left(1, \frac{\mu}{H_{Tot}} \cdot \left(H_{Tot} - L_p - h_{Lp}\right)\right) \frac{\left(H_{Tot} - L_p - h_{Lp}\right)^2}{3} + \ldots$$
$$\phi_{y,Bottom}\left(\mu - 0.5\right) L_p \left(H_{Tot} - L_p/2 - h_{Lp}\right) + \ldots \qquad \text{[Eq. 3-4]}$$
$$\frac{\phi_{y,Bottom}}{4}\left(\mu - 0.5\right) h_{Lp}\left(H_{Tot} - h_{Lp}/2\right)$$

S2 column:

$$u(\mu) = \phi_{y,Top} \frac{1}{2H_{Tot}} \cdot \frac{\left(H_{Tot} - L_p - h_{Lp}\right)^3}{3} + \ldots$$
$$\phi_{y,Bottom}\left(2.35\mu - 1.3\right) L_p \left(H_{Tot} - L_p/2 - h_{Lp}\right) + \ldots \qquad \text{[Eq. 3-5]}$$
$$\frac{\phi_{y,Bottom}}{4}\left(2.35\mu - 1.3\right) h_{Lp}\left(H_{Tot} - h_{Lp}/2\right)$$

In the equations above the yield curvature at the top section of the column $\phi_{y,Top}$ was determined through a moment-curvature analysis of the cross section with a value of 0.576e-3, while at the bottom section of the column the yield curvature $\phi_{y,bottom}$ determined similarly was 0.594e-3. The plastic hinge length L_p of S1 and S2 columns determined iteratively was 16" and 6", respectively. The bottom height of the plastic hinge zone h_{Lp} was also determined iteratively with a value of 6" for both FRC columns and the total height of the FRC columns H_{Tot} was 64".

The resulting flexural deformations of the FRC specimens, calculated based on the calibrated plastic hinge model presented above, was compared to the corresponding measured

lateral displacements of the column top in Table 3-3 and Table 3-4 for S1 and S2 columns, respectively. Since the error obtained between the calculated and applied displacement presented in the tables was within 10% for both FRC columns, the calibrated plastic hinge model can be considered adequate for the estimation of curvature, rotation, and lateral displacement profiles of similar FRC columns.

Table 3-3 Calibration results for lateral displacement of S1 column top

Lateral displacement	Ductility level							
	1	**1.5**	**2**	**3**	**4.5**	**6.25**	**8**	**12.5**
Applied (in)	0.49	0.80	1.08	1.66	2.50	3.34	4.45	6.93
Calculated (in)	0.49	0.86	1.13	1.66	2.46	3.38	4.31	6.69
Error (%)	-0.1	7.6	4.5	0.2	-1.9	1.2	-3.1	-3.5

Table 3-4 Calibration results for lateral displacement of S2 column top

Lateral displacement	Ductility level					
	1	**1.5**	**2**	**3**	**4.5**	**6.25**
Applied (in)	0.49	0.80	1.09	1.67	2.51	3.49
Calculated (in)	0.47	0.75	1.04	1.62	2.48	3.48
Error (%)	-3.7	-5.9	-4.1	-3.2	-1.3	-0.1

Based on the calibrated plastic hinge model presented in Eq. 3-4 and Eq. 3-5, the converted ductility level, μ^* of the FRC columns at the different cycles of the quasi-static test can be estimated as (μ-0.5) and (2.35μ-1.3) for S1 and S2 columns, respectively, where μ is the nominal displacement ductility level of the BC column. For ductility levels corresponding to the elastic range of response, the curvature profile can be estimated using a linear variation and the converted displacement ductility level estimated for S1 and S2 columns. The nominal and converted displacement ductility results of the FRC columns are summarized in Table 3-5.

Table 3-5 Nominal and actual estimated displacement ductility demand of FRC columns during the main cycles of the quasi-static test

Cycle	**BC column: Nominal ductility, μ_{nom}**	**S1 column: Converted ductility, μ^***	**S2 column: Converted ductility, μ^***
4	1	0.5	1.1
6	1.5	1	2.2
8	2	1.5	3.4
10	3	2.5	5.8
12	4.5	4	9.3
14	6.25	5.75	13.4
16	8	7.5	-
18	12.5	12	-

From the table above it can be concluded that S1 column presented enhanced behavior with respect to the conventionally reinforced BC column since the ductility demand on the FRC

column was offset by 0.5 and nonlinear response was stable throughout the test. The S2 column, on the other hand, did not result in improved response with respect to the BC column since the ductility demand on the FRC column was considerably higher for increasingly larger cycles due to the formation of a major crack at a height of 10" above the footing resulting in concentration of damage and rotation instead of spreading of the plastic hinge zone.

The spread of yielding with increasing displacement ductility demands can be determined from the strain profiles of the continuous longitudinal steel in the FRC column specimens presented in Appendix C. The yielding regions in the FRC column, described in terms of minimum and maximum heights above the foundation level where strain values exceeding yield strain were recorded for the specimens, are presented in Table 3-6 for different nominal displacement ductility demand.

Table 3-6 Spread of yielding region in FRC columns with increasing displacement ductility demands

μ_{nom}- Ductility	S1 column	S2 column
1	-	-
1.5	2-18"	2-18"
2	2-18"	0-18"
3	2-22"	0-18"
4.5	0-24"	0-22"
6.25	0-26"	0-26"
8	0-26"	-
12.5	0-26"	-

Despite having similar size and pattern for the spreading of the yield region in both FRC columns, the strain profiles for longitudinal steel in Appendix C and the curvature profiles presented in Figure 3-14 indicate that concentration of strain and damage was more localized in the S2 specimen, in comparison to the BC and FRC columns. In the S2 column, a primary crack was observed at a height of 10" above the foundations and spreading of damage and the plastic hinge zone was limited. Conversely, the S1 specimen presented a significantly extensive plastic hinge region measuring up to 18" in length and propagation of yielding occurred from the center of the plastic hinge zone, estimated at a height of 14", upwards as well as towards the base of the column. Nonetheless, a clear pattern for the spreading of yielding with increasing ductility demand cannot be established from the recorded data.

3.2.4 Energy Dissipation in HPFRC Specimens

The equivalent hysteretic damping coefficient, ζ_{eq} computed as the ratio between the area in the force-displacement hysteretic loops and the area under the idealized elastic system of each column is used to characterize the energy dissipation characteristics of the BC and HPFRC specimens. This equivalent viscous damping coefficient was computed separately with respect to the X- and Y-components of the hysteretic loops for all three specimens as a function of the nominal displacement ductility demand on the column top, as shown in Figure 3-22 and Figure 3-23 in the linear and logarithmic scale, respectively.

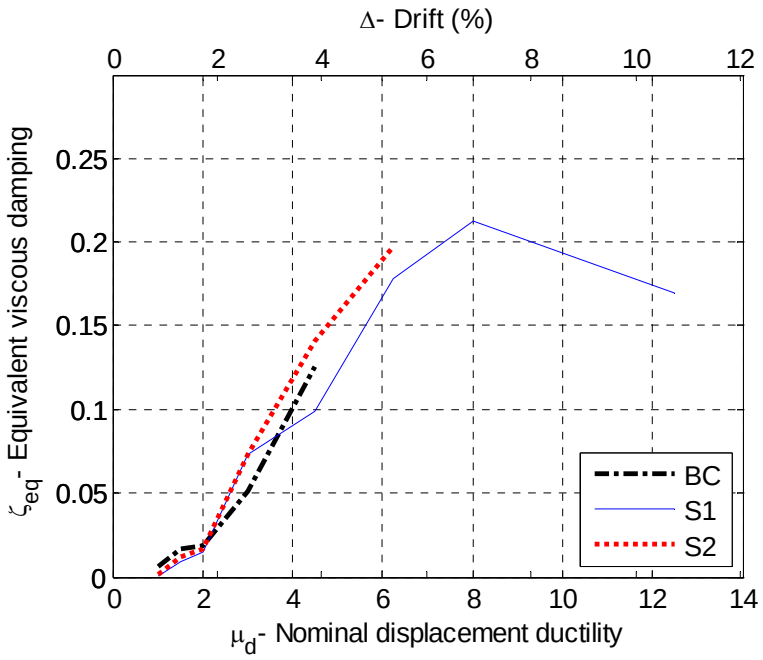

(a) X-axis

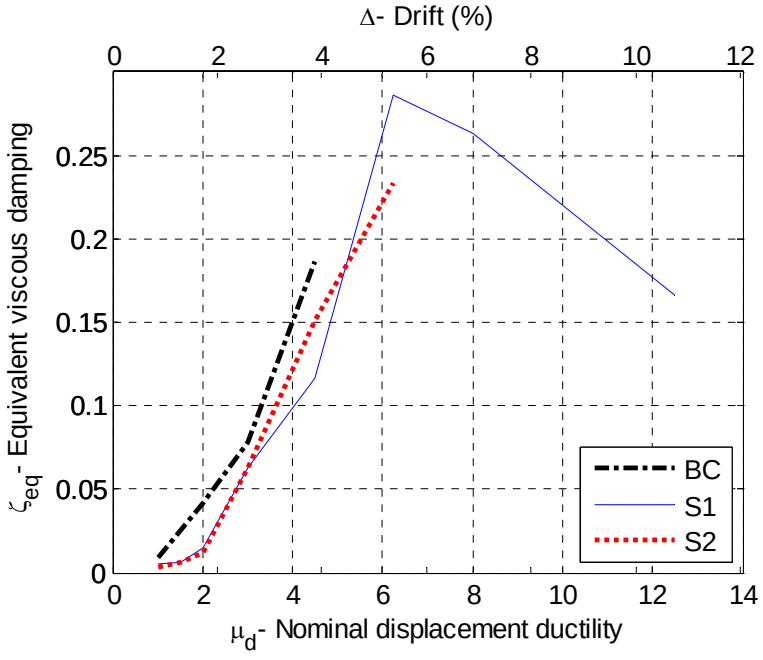

(b) Y-axis

Figure 3-22 Equivalent viscous damping ratio for the BC and HPFRC specimens

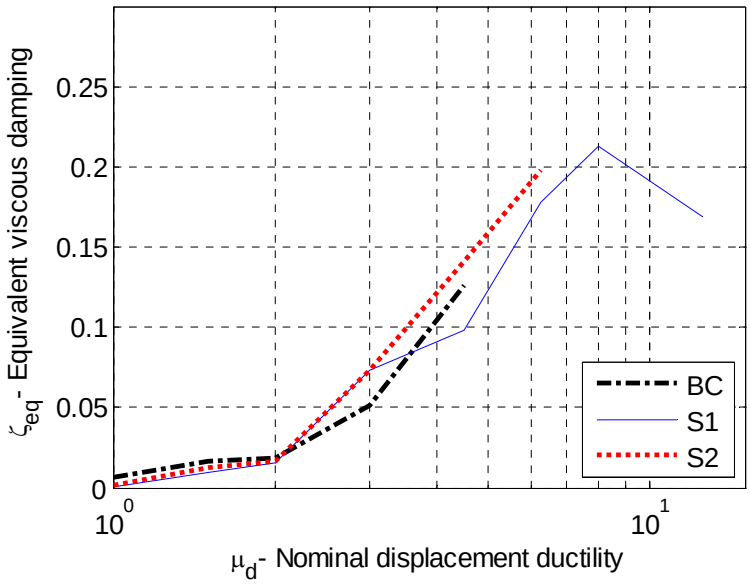

(a) X-axis

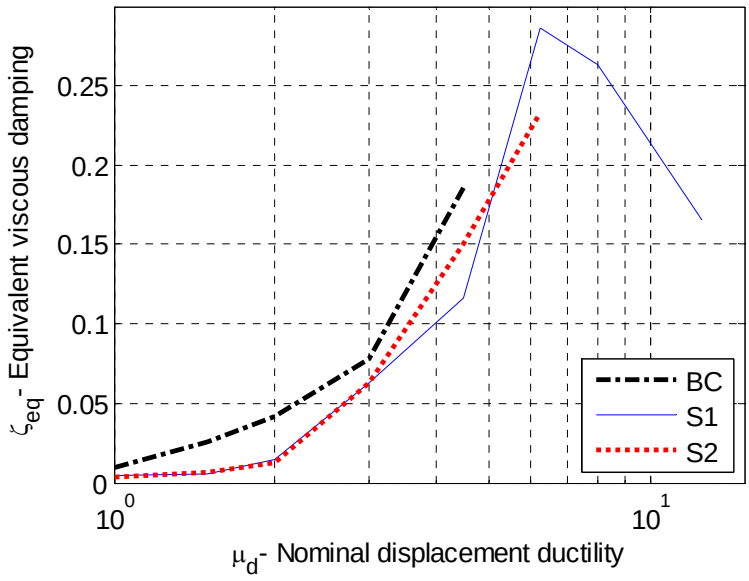

(b) Y-axis

Figure 3-23 Semi-logarithmic plot of equivalent viscous damping ratio for the BC and HPFRC specimens as a function of nominal displacement ductility

The response of the HPFRC specimens up to a nominal ductility level of 2 was characterized by a constant damping coefficient of approximately 1-2%, while in the BC specimen the damping ratio presented an increasing tendency starting at a ductility level of 1. This analysis demonstrates that the elastic limit in the HPFRC specimen was considerably offset beyond the BC column response, which developed nonlinear behavior at earlier states of the cyclic loading. The response of both HPFRC specimens was similar up to a nominal ductility level of 3, after which the S1 column continued developing multiple cracking and significant spread of the plastic hinge zone, while the S2 column developed a primary crack at the cut-off level of the dowels resulting in high concentration of rotation and damage at that region.

All specimens presented overall a similar increasing tendency in the damping coefficient, reflecting similar high energy dissipation characteristics through stable inelastic deformations of the plastic hinge zone throughout the cyclic loading test. The peak damping coefficients attained by the BC, S1, and S2 specimens in the X-direction were 13, 20, and 21%, respectively, while in the Y-direction even higher damping values were computed as 18, 23, and 29%, respectively. The difference in the damping coefficient values in the X- and Y-components is due to the specific definition of the load pattern (see Chapter 2), which results in and larger hysteretic loops in the Y-direction since at the initial stages of each new cycle with increasingly higher demand level, less damage had occurred in the Y-direction before the X-direction is engaged.

In the S1 column, a steep increase in the damping coefficient is evident between nominal ductility levels of 4.5 and 6.25, at which the extensive spreading of the plastic hinge zone allowed efficient and high energy dissipation capabilities. A drop in the equivalent viscous damping ratio occurs in the S1 column at nominal ductility levels of 6.25 and 8, for the Y- and X- components, respectively, after the specimen have reached its ultimate capacity. The measured increase and drop in the dissipated energy is consistent with the observed shape and width of the force-displacement hysteretic loops and the accumulation of damage in the specimens. E.g., the degradation in flexural strength of the S1 column during the second cycle at nominal ductility level of 6.25 due to bar buckling, concrete crushing, as well as spiral and longitudinal rebar fracture, is reflected in the shape of the X- and Y-components of the hysteretic loops.

The measured equivalent hysteretic damping coefficient of S1 column can be computed through a parabolic regression for the increasing portion of the curves in Figure 3-22 and Figure 3-23, using the least sum of square of the error (see Figure 3-24). Eq. 3-6 and Eq. 3-7 presents the resulting fit for the equivalent hysteretic damping coefficient in the X- and Y-direction of S1 column, respectively.

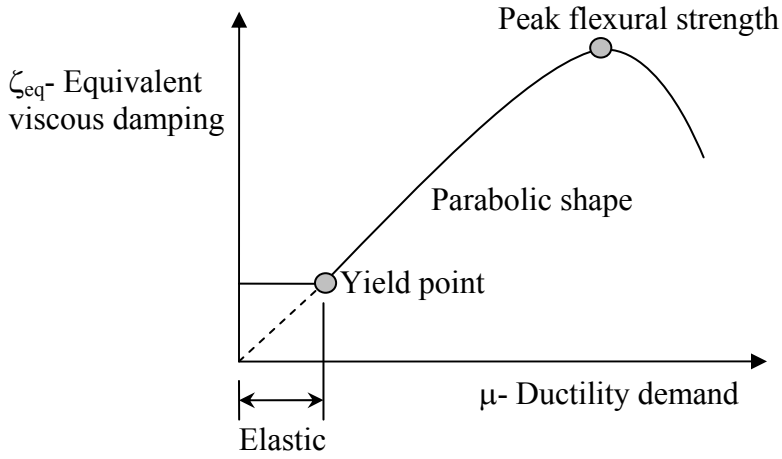

Figure 3-24 General relation between equivalent viscous damping and lateral displacement ductility demand in flexural-dominated cantilever columns

$$\xi_{eq,X} = \begin{cases} 0.02 & \text{if } \mu < 2 \\ -0.003\mu^2 + 0.057\mu - 0.07 & \text{otherwise} \end{cases} \qquad \text{[Eq. 3-6]}$$

$$\xi_{eq,Y} = \begin{cases} 0.02 & \text{if } \mu < 2 \\ -0.005\mu^2 + 0.087\mu - 0.12 & \text{otherwise} \end{cases} \quad \text{[Eq. 3-7]}$$

This model is representative of the cyclic behavior of S1 specimen governed primarily by flexural strength. It computes the peak damping coefficient attained at each cycle and excludes the degradation caused by repeated cyclic loading at the same displacement level.

3.2.5 Peak Bond Stress in FRC

Observing the strain profiles of the dowel reinforcement presented in Appendix C, the majority of the dowels in both S1 and S2 FRC column specimens presented strain values exceeding the yield strain of 2.86×10^{-3} estimated through coupon testing (see Chapter 2). The strain measurements in Appendix C show that a minimum development length L_d of 6" and 7.5" for columns S1 and S2, respectively, was sufficient to develop the yield capacity of the dowel reinforcement. In specimen S1, the top segment of the dowels was debonded from the adjacent FRC material through plastic sleeves with a length of 10"; however, the bottom section of the dowels was not debonded and presented strain profiles with strains exceeding the yield value at a height of 2.5" above the foundations. In specimen S2 strain values exceeding yield strain were computed at a height of 4" above the foundation level.

The bond stress in the FRC material was determined assuming an average uniform bond stress, u_b along the development length, L_d of the corrugated dowel reinforcement. From equilibrium of forces in the dowel, the uniform bond stress u_b acting on the surface of the bar $p_b L_d$ is equal to the resulting stress f_s over the cross-sectional area of the bar A_s, i.e., $F_b = f_s A_s = u_b p_b L_d$. In these equations $p_b = \pi d_b = 1.57$" is the perimeter of a #4 bar, the corresponding bar area is $A_s = \pi d_b^2/4 = 0.2$ in^2, and the stress in the bar, f_s is limited for simplicity by the yield stress $F_y = 70$ ksi computed for the dowel reinforcement from coupon testing (see Chapter 2). Solving for the bond stress, the resulting expression takes for form: $u_b = F_y d_b / 4L_d$. Substituting $L_d = 15 d_b = 7.5$" for S1 column and $L_d = 12 d_b = 6$" for S2, the peak bond stress that was developed in the FRC specimens is computed as $u_b = 1.46$ ksi, or in terms of the unconfined FRC compressive strength $f'_{c,FRC} = 6.86$ ksi obtained from cylinder testing as:

$$u_{b,\max} = 18\sqrt{f'_{c,FRC}} \quad \text{(psi)} \quad \text{[Eq. 3-8]}$$

This equation is based on the assumption of a linear variation of bar stress along the development length with zero stress at the edge of the bar. It is only applicable for the computation of the peak bond stress that can be developed in the FRC material used in this experimental study up to yield strain in the longitudinal bar. The degradation of bond stress with slip and crack propagation beyond the yield strain of the rebar that occur during cyclic loading was not computed due to lack of data. The equation above for peak bond stress in FRC material proves to provide relatively high bond strength values in comparison to plain concrete, where uniform bond stress of $12\sqrt{f'_c}$ and $6\sqrt{f'_c}$ is typically estimated for corrugated rebar with slip values smaller and larger than slip at rebar yield strain, respectively (Eligehausen *et al.* 1983). The high bond strength estimated for the FRC material was obtained for short anchorage lengths which have limiting concrete damage. This estimation did not discern between different

confining pressures in the FRC columns with varying transverse reinforcement ratios. Since these results were obtained based on solely two HPFRC column tests, further research is needed to verify these bond stress values and the conditions required for their development.

3.3 ANALYTICAL MODEL OF HPFRC CANTILEVER COLUMN

A finite element model of a cantilever column was analyzed using OpenSystem for Earthquake Engineering Simulation (OpenSees) by Mckenna *et al.* (2000) to simulate the cyclic response of the FRC columns tested experimentally. The geometric configuration and reinforcement details of the FRC column models were presented in Chapter 2. The cantilever column was modeled in OpenSees using fiber cross-sections (*Fiber* section in OpenSees) and force-based formulated beam-column elements with distributed plasticity (*nonlinearBeamColumn* in OpenSees). The fiber section of each element is represented by an assemblage of longitudinally-oriented steel and concrete fibers with specified uniaxial material stress-strain response. The distributed plasticity element is discretized using Gauss-Lobatto integration scheme with integration points at the ends and along the length of the element. The number of integration points used for each element is specified by the user. The fiber cross-sections are assigned to the different integration points of the corresponding element. A flexibility-based formulation of each element imposes a moment and axial force distribution along its length in equilibrium with the external loads imposed at the end nodes of the member. The curvatures and axial deformations at each integration point are estimated iteratively to satisfy the moment and axial load conditions at the section. The column response is finally obtained through weighted integration of the section deformations along each element length and subsequent summation of the resulting deformations over all the segments of the column.

Three elements were used along the column height, as seen in Figure 3-25, to distinguish between the different longitudinal reinforcement details in the column base, unbounded region and column top section. The number of integration points in each was established iteratively to obtain convergence and stable numerical response of the cantilever model under cyclic loading. Five integration points were used for the top segment of the column while only two integration points were used for the bottom two segments in the region of the plastic hinge zone. To model the FRC cross-section the fiber section was divided into three parts: concrete cover, concrete core and reinforcing steel rebar. A total of 24 and 96 fibers were defined for unconfined cover and confined core, respectively (see Figure 3-25). The number of reinforcing steel fibers varied along the column height due to the additional dowels than at the column base and the unbounded region at the end of the dowels (see Figure 3-25).

The dowels presented higher yield strength than the continuous longitudinal reinforcement, as shown in Chapter 2. The number of steel fibers at the bottom two sections representing the continuous longitudinal rebar and dowels was determined iteratively to better estimate the stiffness and nonlinear behavior of the column in the plastic hinge zone. The constitutive models used to represent the reinforcing steel, confined, and unconfined concrete material behavior were obtained based on the experimental material test results presented in Chapter 2 and through the calibration of the analytical model to match the experimental hysteretic behavior of the columns.

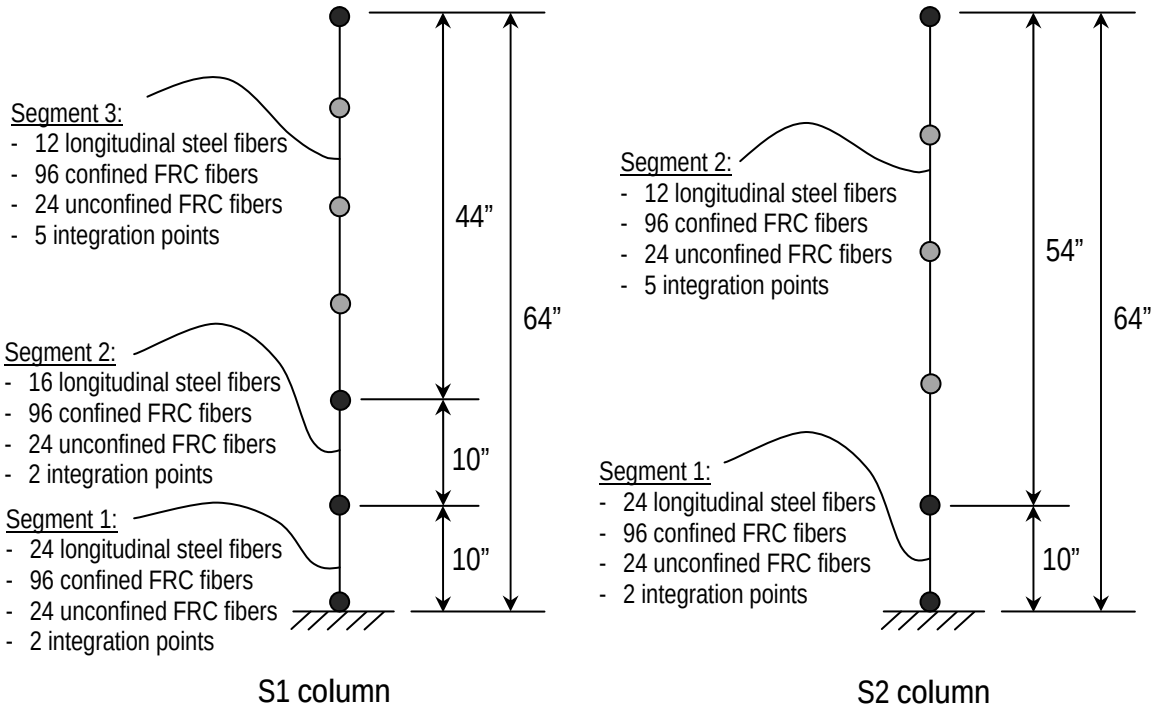

Figure 3-25 General scheme of OpenSees model of FRC cantilever columns

Due to the force-based formulation of the column element, its stiffness is determined according to the development of nonlinear behavior and crack propagation during each step of the cyclic loading history. The geometric transformation was used in the OpenSees model to account for P-Delta effect. The column foundation was modeled as a fixed boundary condition.

The cyclic loading on the FRC column was modeled in OpenSees by applying a bi-directional quasi-static incremental lateral displacement protocol up to peak displacement specified for each cycle. The circular displacement pattern was repeated for different ductility demand levels according to the specified loading history presented in Chapter 2. An axial load of 100.5 kip equal to 10% of the nominal axial load capacity of the BC column was maintained during the lateral loading of the FRC columns.

3.3.1 Uniaxial FRC Material Behavior

Predicting equations for basic mechanical properties of steel FRC have been developed by Thomas and Ramaswamy (2007) based on a large set of experimental data from unreinforced cube and cylinder FRC specimens. Additional predicting equations found in literature were also presented in this study. The various strength properties studies were cube and cylinder compressive strength, split tensile strength, modulus of rupture and postcracking performance, modulus of elasticity, Poisson's ratio, and strain corresponding to peak compressive stress. The main variables used for the models predicting the mechanical properties of FRC were based on main plain concrete strength properties and fiber reinforcement geometry (i.e., volume fraction V_f and aspect ratio L_f/ϕ_f).

Table 3-7 summarizes the prediction models for cylinder compressive strength ($f'_{c,FRC}$), modulus of elasticity ($E_{c,FRC}$) and strain at peak compressive strength ($\varepsilon_{oc,FRC}$) presented in Thomas and Ramaswamy (2007). The remaining mechanical properties are not relevant to the present study since limited material testing was performed on the FRC material used for the construction of the column specimens and a simplified uniaxial material behavior was used for the analytical model of the columns.

Table 3-7 Prediction models for main FRC mechanical properties

Property	Investigator	Prediction model
$f'_{c,FRC}$	Thomas and Ramaswamy (2007)	$f'_{c,FRC} = 0.84 f'_c + 0.046 f'_c RI + 1.02 RI$ (MPa)
	Song and Hwant (2004)	$f'_{c,FRC} = f'_c + 15.12 V_f - 4.17 V_f^2$ (MPa)
	Padmarajaiah (1999)	$f'_{c,FRC} = f'_c + 2.274 RI$ (MPa)
$E_{c,FRC}$	Thomas and Ramaswamy (2007)	$E_{c,FRC} = 4.58 f'^{0.5}_c + 0.42 f'_c RI + 0.39 RI$ (GPa)
	Gao *et al.* (1997)	$E_{c,FRC} = E_c [1 + 0.173 RI]$ (GPa)
	Padmarajaiah (1999)	$E_{c,FRC} = E_c + 2440.2 RI$ (GPa)
$\varepsilon_{oc,FRC}$	Thomas and Ramaswamy (2007)	$\varepsilon_{oc,FRC} = \left(493.4 f'^{0.4}_c + 3.58 f'_c RI + 485.0 RI\right) \times 10^{-6}$
	Taerwe (1992)	$\varepsilon_{oc,FRC} = \varepsilon_{oc} + 0.0115 \times 10^{-3} f'_c$
	Padmarajaiah (1999)	$\varepsilon_{oc,FRC} = \varepsilon_{oc} + 1.15 \times 10^{-6} RI$

In the equations above V_f is the fiber volume fraction equal to 1.5%, $L_f / \phi_f = 30/0.38 = 79$ is the aspect ratio, and RI is the fiber reinforcement index obtained as $V_f L_f / \phi_f$ and equal to 1.18. The plain concrete strength f'_c at the time of the two quasi-static tests was measured through standard cylinder compression tests as discussed in Chapter 2 and was approximately 6.1 ksi. The predicted mechanical properties for the FRC material used in the bidirectional cyclic column tests are compared to the average experimental results obtained through FRC cylinder test (see Chapter 2), as summarized in Table 3-8.

Table 3-8 Predicted and actual FRC mechanical properties

Property	Prediction results		Experimental results
	Investigator	Value	
$f'_{c,FRC}$	Thomas and Ramaswamy (2007)	5.63 ksi	6.86
	Song and Hwant (2004)	6.13 ksi	
	Padmarajaiah (1999)	6.49 ksi	
$E_{c,FRC}$	Thomas and Ramaswamy (2007)	4678.3 ksi	4245.5
	Gao *et al.* (1997)	5326.5 ksi	
	Padmarajaiah (1999)	4839.9 ksi	
$\varepsilon_{oc,FRC}$	Thomas and Ramaswamy (2007)	2.91e-3	3.3e-3
	Taerwe (1992)	3.50e-3	
	Padmarajaiah (1999)	4.38e-3	

The material properties of the FRC predicted using the proposed models from literature and the test data results obtained from the present study presented good correlation, as seen in the table above. The predicted concrete compressive strength and the elastic modulus were slightly under- and overestimated, respectively, in comparison to the experimental material test results. The actual concrete cover and core material behavior of the FRC column was defined using the uniaxial material model designated in OpenSees as *Concrete02* which uses the Kent-Scott-Park stress-strain behavior in compression and a bi-linear relationship in tension with linear tension softening. The constitutive model and parameters of *Concrete02* in OpenSees are presented in Figure 3-26.

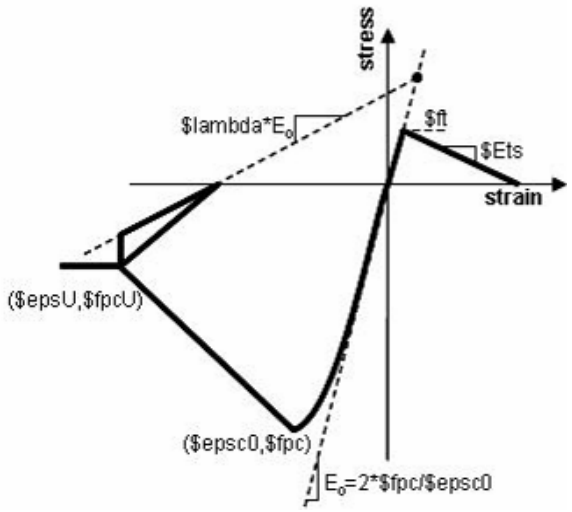

Figure 3-26 Constitutive model *Concrete02* in OpenSees used for FRC (Source: Mckenna *et al.* 2000)

The parameters used for the constitutive concrete models were defined based on the experimental results obtained from cylinder testing and the calibration of the hysteretic loops of S1 and S2 FRC column specimens to match the experimental results in section 3.1.2. The parameter definition of *Concrete02* constitutive models for the confined and unconfined FRC materials was carried out according to Figure 3-26.

For the FRC cover the compressive strength f_{pc} was taken as the mean compressive strength of the FRC concrete cylinders $f'_{c,FRC}$ equal to 6.86 ksi, the elastic modulus E_o was defined equal to $E_{c,FRC}$=4245.5 ksi, and the strain at peak compressive strength $epsc_0$ was calculated as $2f_{pc}/E_o$=0.0032, equal to the mean FRC material results. The residual strength f_{pcU} was defined iteratively as $0.1f_{pc}$=0.69 ksi at a strain value eps_U of 0.0325. The corresponding degrading slope of the unconfined FRC material was similar to the experimental material test results. A lower residual strength was defined for the analytical constitutive model of the FRC unconfined concrete than the material test results since the damage observed at high ductility levels included the crushing of the concrete cover following the buckling and fracture of the longitudinal rebar. The tensile strength of concrete f_t was defined with a value of 0.7 ksi, based on tensile tests carried out at the University of Michigan on FRC cylinders cast using a similar mix with the same fiber type at 1.5% volume fraction and 3/8" limiting coarse aggregate size (Chao *et al.* 2007). The tension softening stiffness E_{ts} was defined equal to E_o. However, the

tensile behavior defined for the analytical constitutive model of both confined and unconfined concrete did not affect significantly the hysteretic response of the FRC columns.

For the FRC core the compressive strength f_{pc} was defined with a value of 7.95 ksi, equal to the compressive strength of confined concrete f'_{cc} by Mander (1988) using the unconfined FRC material properties presented above. The elastic modulus E_o was defined similar to the unconfined FRC material as $E_{c,FRC}$=4245.5 ksi, thus the corresponding strain at peak compressive stress $epsc_0$= $2f_{pc}/E_o$ was equal to 0.0037. The residual strength f_{pcU} was defined as $0.36f_{cp}$=2.86 ksi at a strain value of 0.027, similar to the mean FRC material test results. The tensile behavior of the FRC confined concrete was defined similar to the unconfined concrete, with a tensile strength f_t of 0.7 ksi and a tension softening stiffness $E_{ts}=E_0$.

The resulting stress-strain relationships of confined and unconfined FRC material used in the OpenSees fiber model are presented in Figure 3-27. The same material properties were used in OpenSees for both FRC column models. A total of 96 fibers were used to model the confined concrete core (12 tangential wedges and 8 radial divisions), while only 24 fibers were defined for the cover (12 wedges and 2 radial divisions). The FRC material displayed a significantly more ductile behavior in comparison to plain concrete specimens, as seen from the experimental stress-strain relation for unconfined concrete in Figure 3-27. The OpenSees fiber model with uniaxial material behaviors defined for steel and concrete used in this study is adequate for flexure-dominated failure, as displayed by the FRC cantilever column specimens. For a shear-dominated failure of concrete columns, which was not observed for the experimental specimens tested in this study, a different modeling approach must be used.

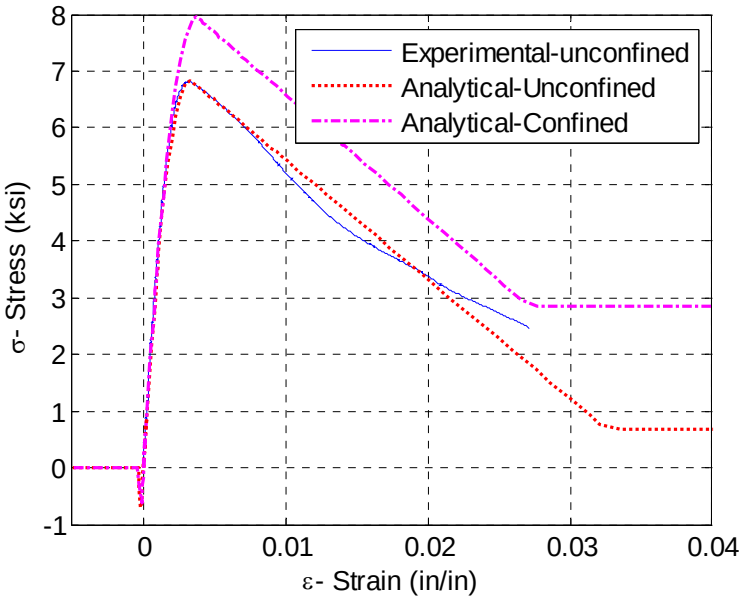

Figure 3-27 FRC stress-strain relationship used in OpenSees fiber model of FRC cantilever columns

3.3.2 Uniaxial Behavior of Steel Reinforcement

The longitudinal steel constitutive model and parameters were defined according to the coupon test results presented in Chapter 2 and the calibration of the hysteretic loops of the FRC columns

with the experimental results presented in section 3.1.2. The steel fibers in the OpenSees fiber model of the FRC cantilever columns utilized the *Hysteretic* uniaxial material model defined with a tri-linear hysteretic behavior, pinching of force and deformation, damage due to ductility and energy, and degraded unloading stiffness based on ductility. The main parameters used to define the *Hysteretic* constitutive model are shown in Figure 3-28.

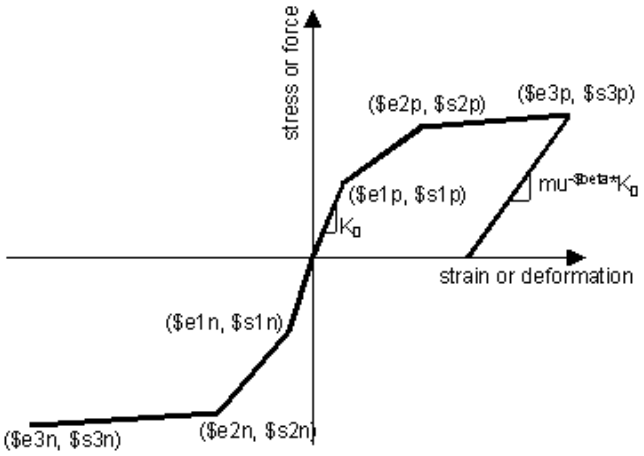

Figure 3-28 Constitutive model *Hysteretic* in OpenSees used for longitudinal steel (Mckenna *et al.* 2000)

The calibrated *Hysteretic* material was defined with the first point on the stress-strain envelope (ε_1,σ_1) corresponding to a modified yield point (ε_y,f_y) of the longitudinal steel coupons results. The yield stress f_y was equal to 65 ksi, similar to the material test results; however, the corresponding strain was obtained iteratively as $f_y/0.5E_s$, where E_s is the elastic modulus of steel equal to 29,000 ksi. A reduced initial stiffness value was used for the steel material since the FRC columns yielded at a nominal ductility level of 1.5 with respect to the conventionally reinforced concrete column BC yield point. The second point (ε_2,σ_2) was defined at an intermediate point on the on the experimental stress-strain curve (0.04,1.25f_y=81.25 ksi) obtained from steel coupons. Using these values the initial post-yield strain-hardening slope ratio of the steel is 0.016. The third point of the stress-strain curve (ε_3,σ_3) defined for the *Hysteretic* constitutive model corresponded to the failure point of the longitudinal steel at (ε_u=0.12,f_u=90.1 ksi). This ultimate strain of 0.12 was specified for both tensile and compressive behavior of the steel reinforcement according to the recommendations of Caltrans SDC (2004), since the corresponding experimental data was not available.

The pinching factors during reloading for strain ($pinch_X$) and stress ($pinch_Y$) were defined iteratively with values of 0.3 and 1.0, respectively. The damage due to ductility and energy using factors $damage_1$ and $damage_2$ was not included in the calibrated *Hysteretic* constitutive model. Instead, a degraded unloading stiffness equal to $\mu^{-\beta}$ was used in the material model based on ductility level of the steel fiber μ. The parameter β was determined iteratively as 0.65. The degrading hysteretic behavior under cyclic loading defined using the parameters above were found to be successful in simulating the stiffness and strength degradation of the column due to rebar elongation and buckling, spiral and longitudinal rebar fracture, and concrete crushing.

The monotonic stress-strain relationship used for the steel fiber in the OpenSees FRC cantilever columns is compared to the experimental coupon results in Figure 3-29. The hysteretic

stress-strain relation for the longitudinal steel reinforcement obtained from the OpenSees model of S1 column is presented in Figure 3-30. Additional constitutive models available in OpenSees such as *Steel02* with Giuffre-Manegotto-Pinto and Bauschinger effects, *Pinching4* with pinched load-deformation response and degradation under cyclic loading, and *ReinforcingSteel* with fatigue, buckling, and isotropic hardening behavior, were also used in the fiber model of the column specimens with less successful results.

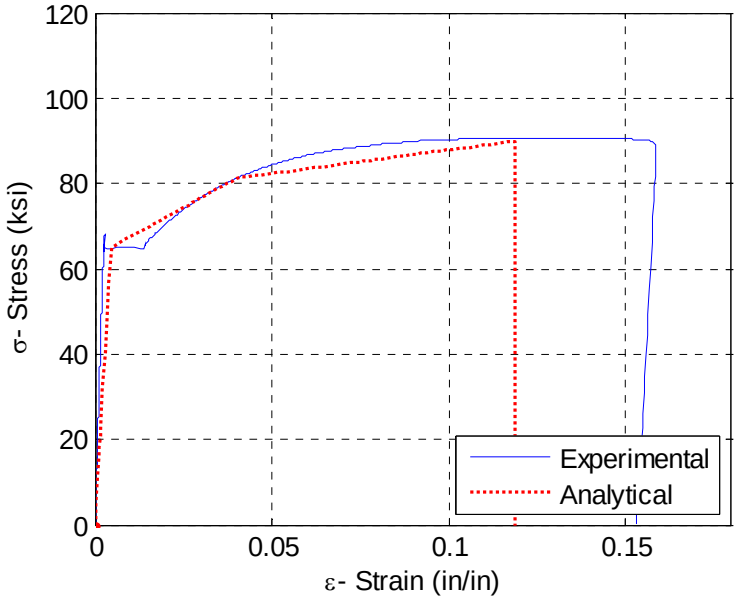

Figure 3-29 Monotonic stress-strain relationship for longitudinal steel reinforcement used in OpenSees fiber model of FRC cantilever columns

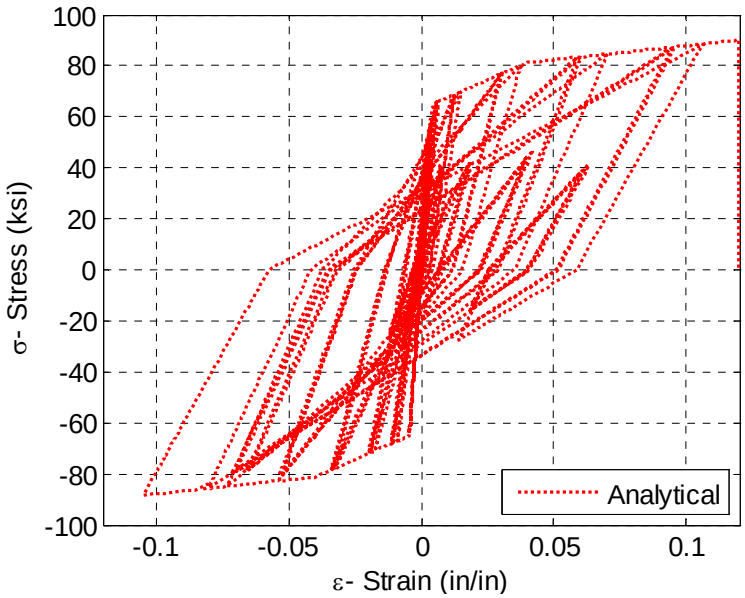

Figure 3-30 Hysteretic stress-strain behavior recorded for longitudinal steel in OpenSees model of S1 column for the complete cyclic loading history

In both S1 and S2 specimens several dowels developed nonlinear behavior at high ductility demands. Therefore, for simplicity, the stress-strain relationship for continuous longitudinal steel was used for all fibers representing the longitudinal reinforcement. The transverse reinforcement yield strength used to calculate the shear capacity of the FRC columns and verify that their behavior is controlled by flexure was defined with a value of 92.5 ksi, according to coupon test results presented in Chapter 2.

3.3.3 Comparison of Experimental and Analytical Hysteresis

The analytical and experimental hysteretic loops for S1 and S2 FRC columns are presented in Figure 3-31 through Figure 3-34. Using the calibrated constitutive models for longitudinal steel reinforcement, unconfined and confined FRC material described in the previous sections, the peak strength and general slope of the main hysteretic loops of the columns in both orthogonal directions were successfully matched. The total shear vs. total drift loops for S1 and S2 specimens are also presented in Figure 3-32 and Figure 3-34, respectively. At the last cycle of S1 column corresponding to a nominal ductility level of 12.5, major damage had occurred in the specimen including fracture of all longitudinal rebar, spiral fracture, and crushing of the concrete cover around the entire perimeter. The actual recorded behavior at this high ductility demand levels could not be matched successfully using the relatively simple constitutive models used in the OpenSees fiber model of the column, and therefore the analytical results are only presented up to a nominal ductility level of 8. Despite the lack of symmetry in the recorded shear response in the Y-direction of S1 column, possibly produced due to typical deviations in the distribution of the longitudinal steel, the analytical model was able to match well the resulting hysteretic behavior of the column.

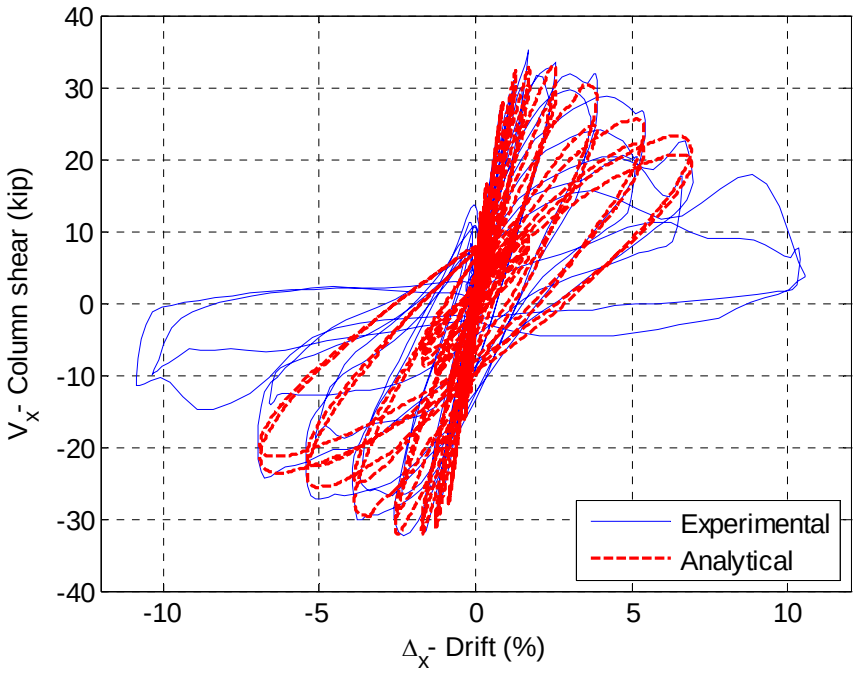

(a) X-axis

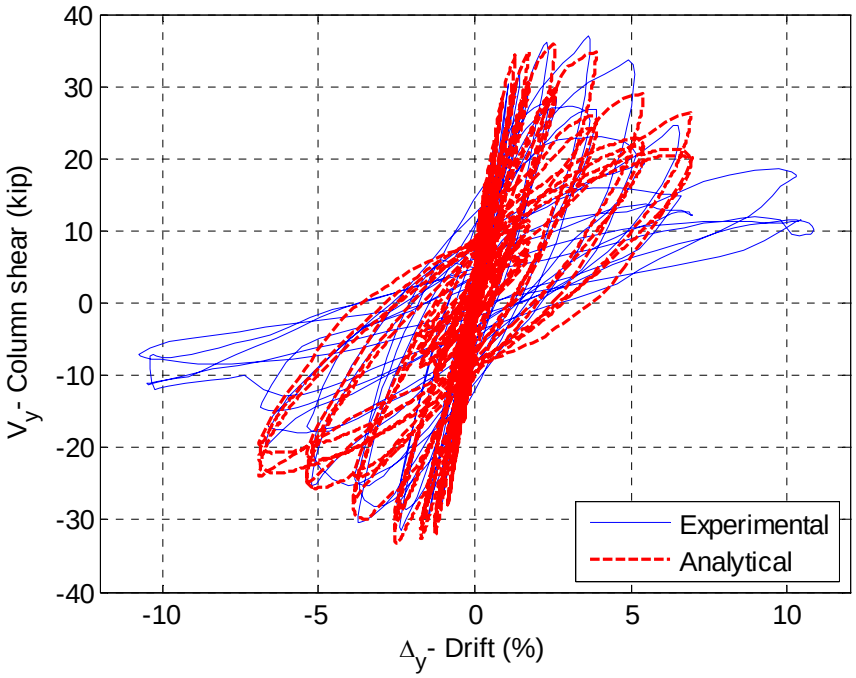

(b) Y-axis

Figure 3-31 Experimental vs. analytical hysteresis of S1 column at the main cycles of the quasi-static cyclic test

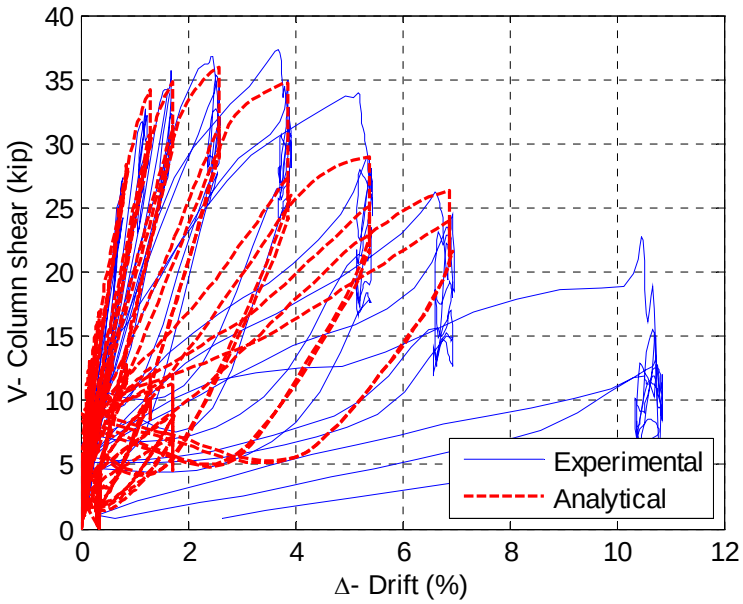

Figure 3-32 Experimental vs. analytical total shear vs. total drift hysteresis of S1 column at the main cycles of the quasi-static cyclic test

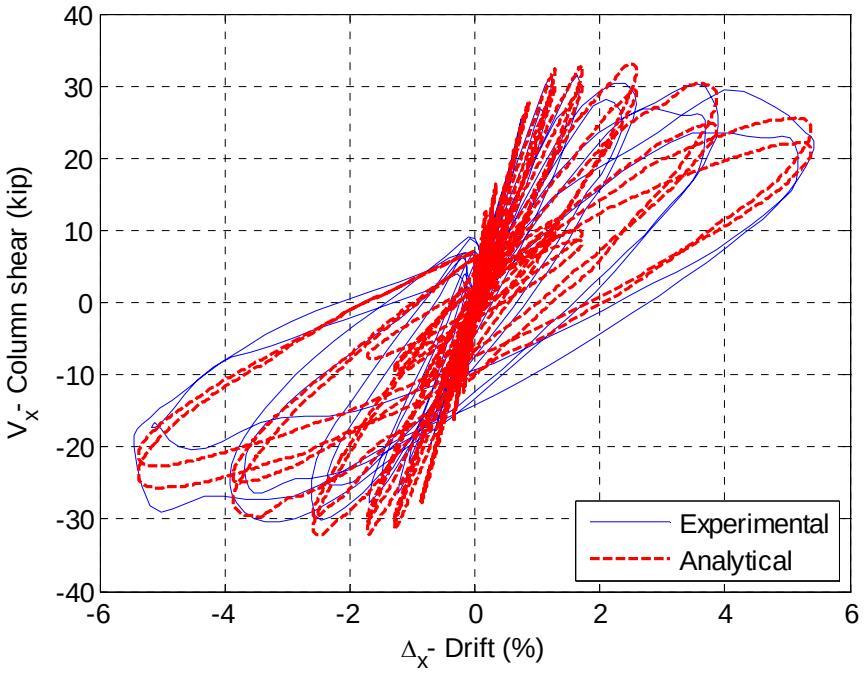

(a) X-axis

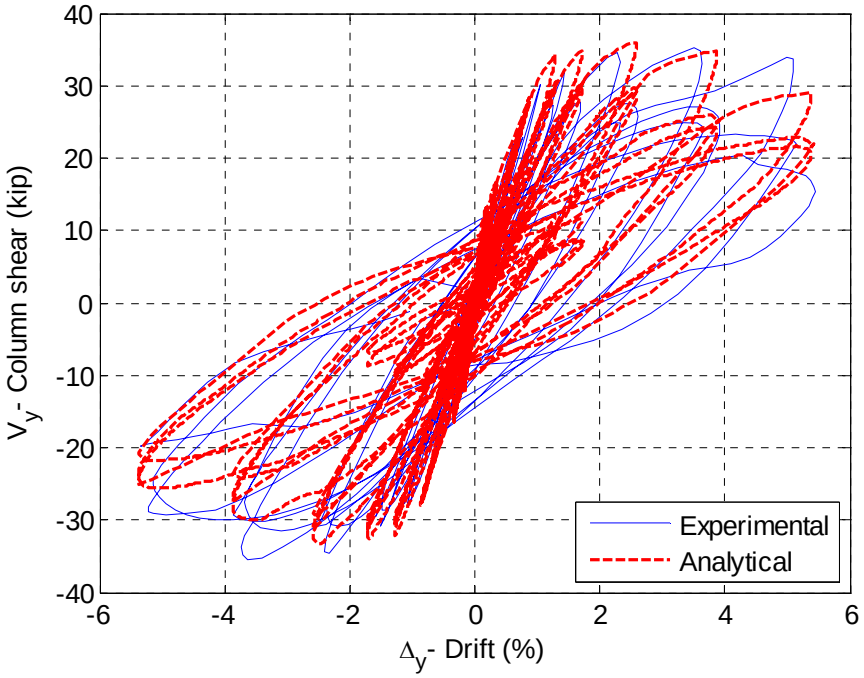

(b) Y-axis

Figure 3-33 Experimental vs. analytical hysteresis of S2 column at the main cycles of the quasi-static cyclic test

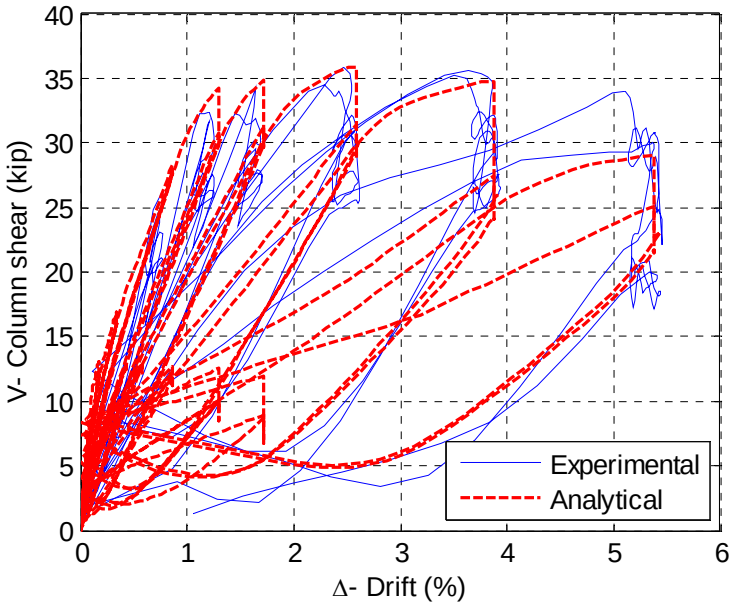

Figure 3-34 Experimental vs. analytical total shear vs. total drift hysteresis of S2 column at the main cycles of the quasi-static cyclic test

3.3.4 Residual Gravity Load Carrying Capacity

The residual gravity load carrying capacity of the FRC columns was determined analytically by performing a pushunder analysis of the calibrated OpenSees model of the FRC columns following a bilateral loading history to different target lateral displacement ductility levels. The calibration of the OpenSees models discussed in the previous sections was done according to cylinder compression tests results and steel coupon test results presented in Chapter 2. Figure 3-35 presents the pushunder curves of the OpenSees model of S1 column obtained following bilateral cyclic loading histories to different ductility levels. The axial forces in the pushunder curves were normalized with respect to the axial capacity P_n of S1 column. The curve corresponding to a ductility level of 0 represents the initial normalized axial force-deformation relation of S1 column prior to any cyclic loading. The maximum axial capacity P_n of S1 column obtained analytically was 1751 kip, while the axial capacity P_n of BC column tested experimentally by Terzic *et al.* (2008) was 1459 kip.

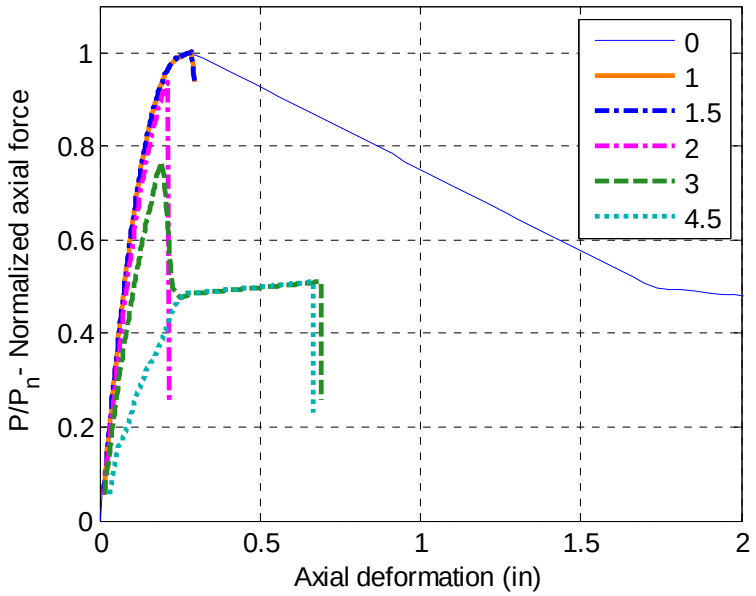

Figure 3-35 Analytical pushunder curves of S1 column following bilateral cyclic loading to different target ductility levels

The pushunder curves present deterioration in the axial capacity of S1 columns starting at a ductility level of 1.5, which coincides with the initiation of inelastic response of the column determined through observation of external damage, recorded hysteretic response, and measured local deformations and internal strains. Following cycles at a nominal ductility level of 4.5, the residual capacity of S1 column obtained from the analytical pushunder analysis of the OpenSees fiber model was equal to approximately 50% of its maximum axial capacity P_n. The residual axial capacity of S1 column cycled to higher target displacement ductility levels of 6.25 and 8 was also equal to approximately $0.5P_n$, since further strength degradation was not captured using the available features of the constitutive material models in OpenSees. Following cycles to a target nominal ductility level of 12.5, both the analytical and experimental specimens of S1 column presented zero residual gravity load carrying capacity.

The degradation of the axial capacity of S1 column with increased nominal lateral displacement ductility level is presented in Figure 3-36. The normalized residual axial capacities of test specimens of the BC column cycled to different ductility levels are also presented. The residual capacity of each column following cyclic histories to different target ductilities is normalized with respect to the axial strength of the corresponding column.

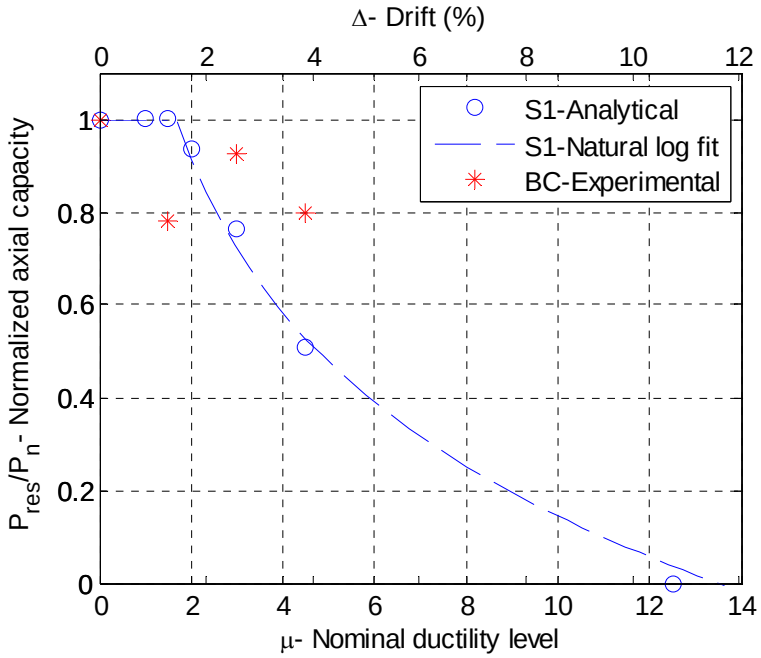

Figure 3-36 Normalized residual axial capacity of S1 column vs. nominal ductility level obtained from pushuner analysis of calibrated OpenSees model

A natural log fit was used for the analytical residual axial capacity data of S1 column as a function of the nominal displacement ductility level (obtained with respect to the yield point of BC column) with an upper bound equal to the normalized maximum axial capacity of the column, as seen in Eq. 3-9. Terzic *et al.* (2008) did not present a specific relation for the degradation of axial strength based on their experimental results. Nonetheless, observing the general tendency of the experimental data points, the degradation of axial capacity of the BC column appears to be less pronounced than the FRC S1 column, probably due to higher confining steel reinforcement ratio and smaller spiral spacing.

$$\frac{P_{res}}{P_{\max}}(\mu) = \min\begin{cases} -0.48\ln(\mu) + 1.25 \\ 1 \end{cases} \qquad \text{[Eq. 3-9]}$$

Higher residual axial capacities were obtained experimentally for the BC column specimens for target ductility levels of 3 and 4.5, in comparison to the analytical results of S1 column. However, following cycles to a target ductility of 1.5, the residual axial capacity of the BC was significantly lower than the S1 column results and BC columns specimens cycled to higher ductilities. Additional values of the residual capacity of the BC column are not available since no other specimens were tested experimentally. Overall, the degradation of the residual axial capacity of both S1 and BC column specimens presented a similar pattern, although the BC column presented higher normalized residual capacity values primarily due to the fact that the transverse reinforcement ratio and spacing of the BC column specimens was significantly higher than the S1 column.

4 Bridge Design and Modeling

The following section presents the design scheme, basic assumptions and the final dimensions and material properties used for the three-dimensional nonlinear models of the conventionally-reinforced concrete (RC), fiber-reinforced concrete (FRC) and seismically isolated (BI) bridges implemented in OpenSees structural analysis program. The basic dynamic properties of the three bridge systems analyzed are presented as well.

4.1 CONVENTIONALLY-REINFORCED CONCRETE BRIDGE

4.1.1 Introduction

A series of design, seismic evaluation, and cost estimating studies were performed (Ketchum *et al.* 2004) to provide an improved understanding of the influence of design ground motion level on construction costs of routine concrete bridges typically used in California highway construction. These studies, denominated as the "Testbed bridge design for PEER Lifeline project", addressed the most commonly used bridge and foundation types. The levels of ground motion considered in these studies corresponded to earthquake magnitudes (M_w) of 6.5, 7.25, and 8. The Caltrans soil profile type D corresponding to stiff soil, as defined according to Caltrans SDC (2004), was assumed for the bridge foundation.

A total of 11 testbed bridge types were considered in the testbed bridge studies (types 1 through 11). Type 1 bridge consisted of a simple 2-box girder superstructure cross section and short column bents. For bridge type 1 a total of 12 different column cross sections were designed (A through L). The smallest column cross section with the lowest reinforcement ratio is type A. All the testbed bridges have a continuous prestressed superstructure deck and no expansion joints.

Bridge type 1A (bridge type 1 and column type A) resulted in the highest ductility demands and damage of all the testbed bridges analyzed (Ketchum *et al.* 2004) and was therefore selected for the comparative analysis of three different bridge systems carried out in the present study. The comparison of conventionally-reinforced concrete (RC), fiber-reinforced concrete (FRC) and seismically isolated (BI) bridges was performed in terms of several key structural response parameters, construction costs, as well as post-earthquake repair costs computed for different seismic hazard levels. The type 1A conventionally- reinforced concrete bridge detailed in the present chapter was used as the benchmark fixed-base bridge for the design of the seismic isolated bridge (see section 4.3). The FRC bridge is also based on the geometry, cross sections, and mass properties of the benchmark RC bridge. The reinforcement details, fiber model and

concrete material properties of the FRC column are the only aspects differing from the RC bridge model (see section 4.2).

The seismic performance, repair costs, repair time loss and fragilities of type 1A RC bridge were evaluated in an analytical study (Mackie et. al 2007). The assessment of this type 1A RC bridge, designed for the highest ductility demand levels among all testbed bridges considered (Ketchum *et al.* 2004), served as a baseline for the evaluation of other column, abutment and foundation components, as well as the use of more advanced seismic performance enhancement methods. The analytical model of the RC bridge in OpenSees used for the assessment of the RC bridge (Mackie et. al 2007) was modified to represent the material and component behavior of the FRC and BI bridges, as detailed in sections 4.2 and 4.3. The local linearization repair cost and time methodology (LLRCAT) method used for the assessment of the RC bridge (Mackie et. al 2008) was also applied in the present study to compute the repair costs corresponding to the BI and FRC bridges (see Chapter 6).

4.1.2 Design Procedure

The procedure used to design the testbed reinforced concrete bridges (Ketchum *et al.* 2004) is detailed as follows:

- A basic bridge superstructure design was developed, along with a suite of different column or bent designs that can potentially provide varying levels of seismic performance for that basic bridge design.
- The seismic displacement capacity was evaluated for each column or bent design, using moment-curvature analysis and static pushover analysis.
- The level of ground motion that would push the column to its displacement capacity was evaluated for each column design, by performing response spectrum analyses under various response spectra (ARS curves) that ranged from 0.1g to 1.0g PGA.
- Capacity-protected items such as the foundation, bent cap, superstructure, etc. were designed by carrying out a plastic analysis of the bridge and applying SDC-required over-strength factors.

The final selection of the testbed bridges thoroughly analyzed for the PEER Lifeline project resulted in 7 bridge configurations and 74 column cross sections, among them bridge type 1A.

4.1.3 Bridge Description

The RC bridge consists of a typical reinforced concrete bridge with box-girder superstructure and typical column bent details designed according to AASHTO Standard Specifications for Highway Bridges (AASHTO 1996) and Caltrans SDC (2004). It consists of an Ordinary Nonstandard Bridge according to Caltrans SDC (2004) with simple geometric regularity (symmetry, zero skew, and uniform column height). The geometry of the RC bridge type 1A is presented in Figure 4-1 and Figure 4-2. Additional figures of the abutment details for the RC type 1A bridge are presented in Appendix D.

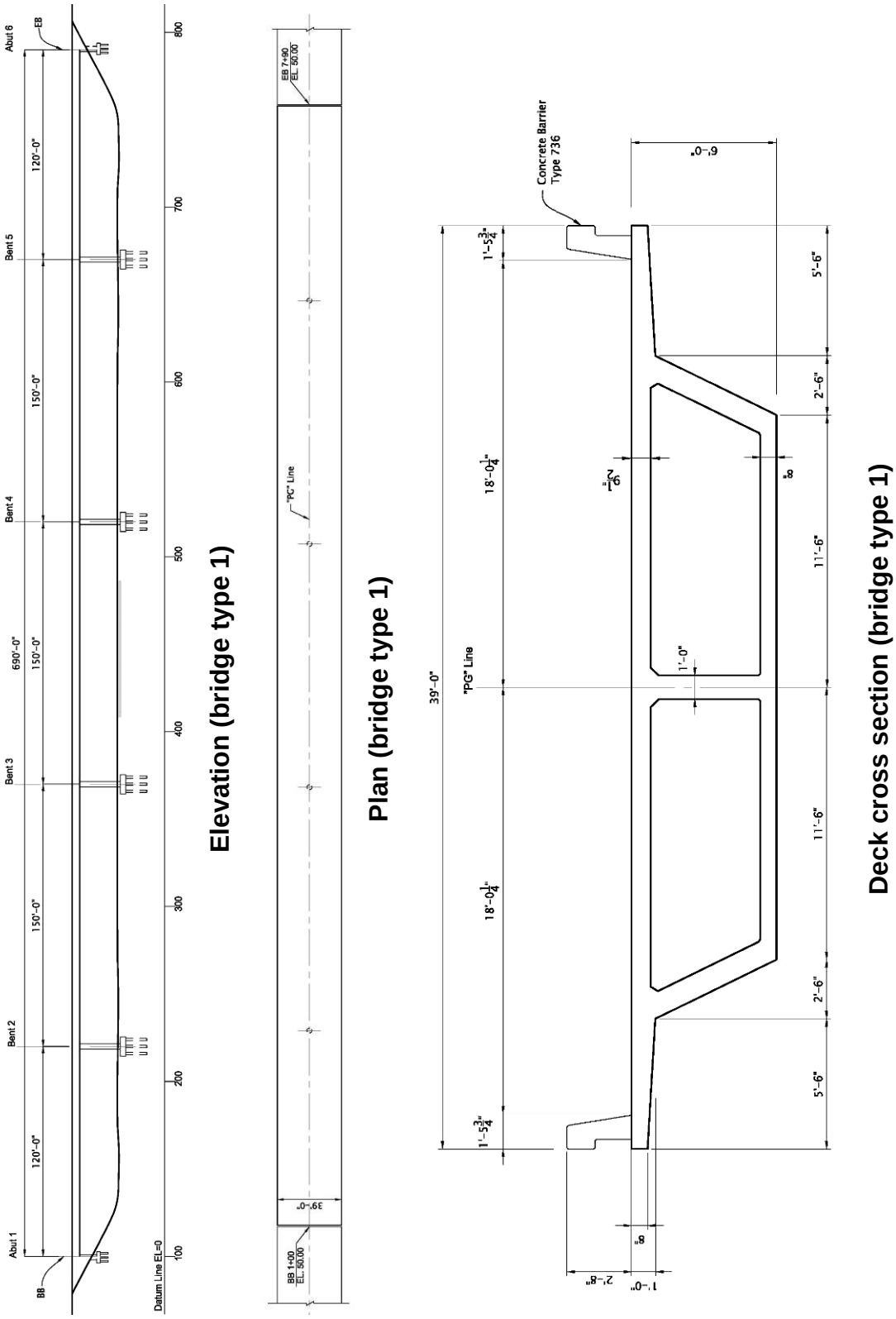

Figure 4-1 Geometry of RC type 1A bridge (Ketchum *et al.* 2004)

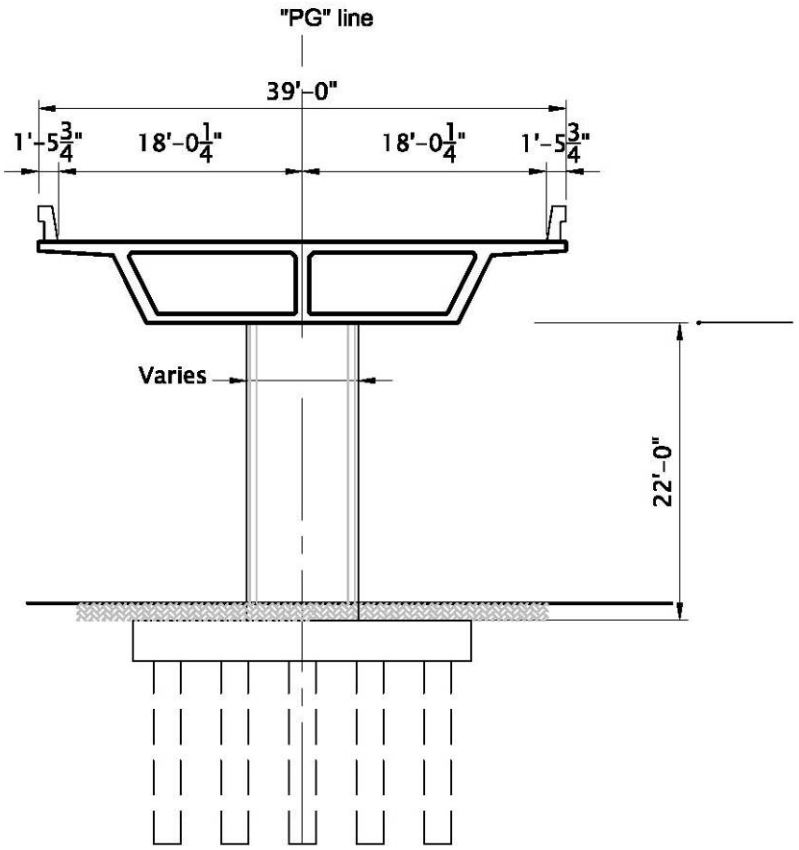

Typical bridge section (type 1)

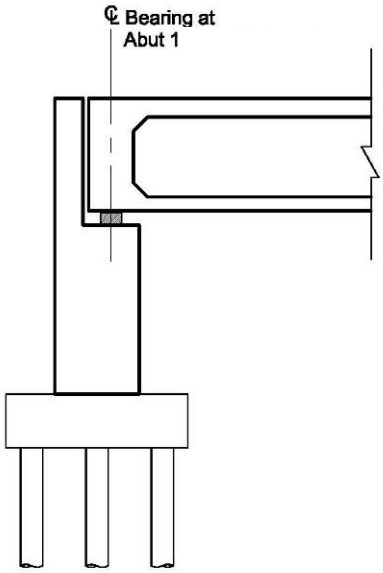

Abutment section (bridge type 1)

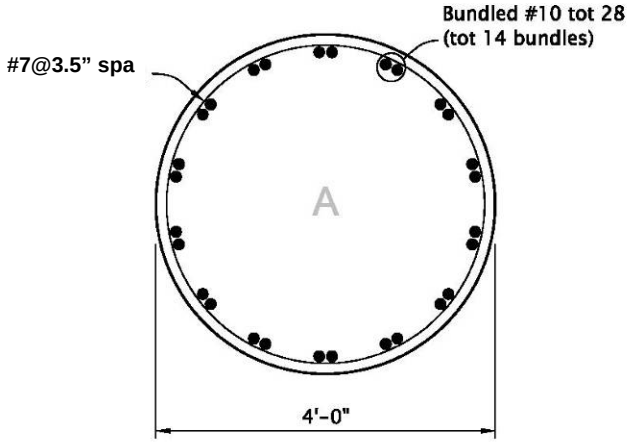

Column section (type A)

Figure 4-2 Details of RC type 1A bridge (Ketchum *et al.* 2004)

The RC bridge is a single column-bent bridge rigidly connected to the superstructure and with fixed column foundations. It has 5 spans of 150 ft and 120 ft for the internal and external spans, respectively, resulting in a total span length of 690 ft. The superstructure of the bridge (type 1) consists of a 39 ft wide and 6 ft deep prestressed cast-in-place concrete box-girder with 2 boxes. The column bents are 22 ft high and have a diameter of 4 ft, longitudinal reinforcement ratio of 0.02 (28#10) and transverse reinforcement ratio of 0.016 (#7@3.5"). Since the aspect ratio of the column is H/D_{col}=22'/4'=5.5, the bridge is classified as short (Ketchum *et al.* 2004).

4.1.4 Seismic Demand

The SDC acceleration response spectra (ARS) and displacement response spectra (DRS) curves for soil profile Type D (firm soil) with magnitudes of 6.5, 7.25 and 8.0 are used as the seismic design criteria for the bridges. The elastic ARS curves used for the design of the bridge (see Figure 4-3) are defined for 5% damping. Soil type D is defined in table B.1 of SDC (2004) as a stiff soil with shear velocity $600<v_s<1200$ ft/sec ($180<v_s<360$ m/sec) or with either standard penetration resistance $15<N<50$ or undrained shear strength $1000<s_u<2000$ psf ($50<s_u<100$ kPa).

The displacement demands for the column were calculated (Ketchum *et al.* 2004) from the displacement of the top of the column relative to the column base. Since the columns were pushed to their capacity, the displacement demand was set equal to the displacement capacity in order to determine the equivalent peak ground acceleration (PGA) and spectral acceleration (S_a) associated with the column displacement capacity. The spectral acceleration was therefore the same for all three magnitude earthquakes while the peak ground acceleration decreased with increasing magnitude of earthquake because of the differing shapes of the spectra. The resulting spectral values corresponding to the transverse and longitudinal modes of bridge type 1A are presented in Table 4-1.

Table 4-1 Spectral acceleration values for the RC bridge type 1A

Parameter	Transverse	Longitudinal
T- Period (sec)	1.30	1.04
S_a- Spectral acceleration (g)	1.07	0.99

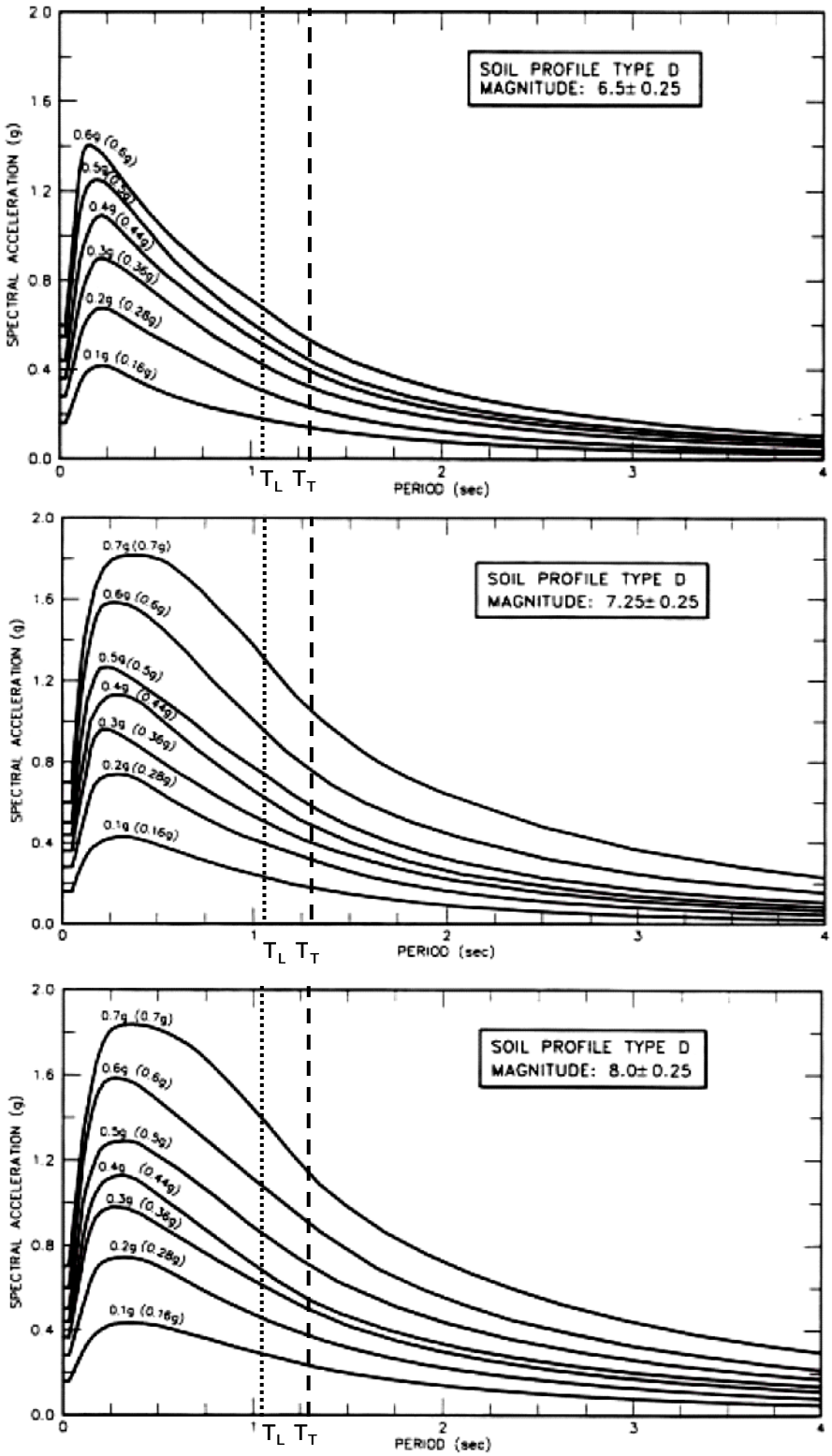

Figure 4-3 SDC 2004 elastic ARS curves for 5% damping defining the seismic demand on the RC bridge type 1A (Caltrans 2004)

4.1.5 Bridge Finite Element Model

The analytical model of the RC bridge type 1A was implemented using OpenSees (Mckenna *et al.*, 2000) structural analysis program. The bridge was modeled using elastic beam-column elements for the superstructure spans and a distributed plasticity fiber model for the column bents. Two segments were used for each span and one segment was defined for each column bent. Effective cross section properties were used for the superstructure elements. Lumped translational and rotational tributary mass were assigned to each node of the substructure and superstructure. The self-weight of the bridge and the P-Delta transformation were used for all static and dynamic analyses.

The column bent was modeled as a distributed-plasticity fiber model with nonlinear force formulation and five integration points. The fiber model included approximately 160 concrete fibers and 28 reinforcing steel fibers corresponding to each reinforcing bar. The discretization of the cross section and the number of concrete fibers represents with sufficient accuracy the column gross section configuration and properties according to the recommendations by Berry and Eberhard (2003).

Expected material strength properties were used for all steel and concrete elements and fibers (Caltrans 2004). In this case, the expected concrete strength used in the analytical OpenSees model was assumed to be equal to the nominal strength defined in the testbed bridge drawings. The concrete constitutive model used in OpenSees was *Concrete02* that has Kent-Scott-Park behavior and includes tensile strength (see Figure 4-4). The steel fibers utilized *Steel02* uniaxial material model that has Giuffre-Menegotto-Pinto behavior with ultimate strains specified according to Caltrans SDC (2004) and softening behavior (see Figure 4-4). Elastic shear deformation was included for all beam and column elements.

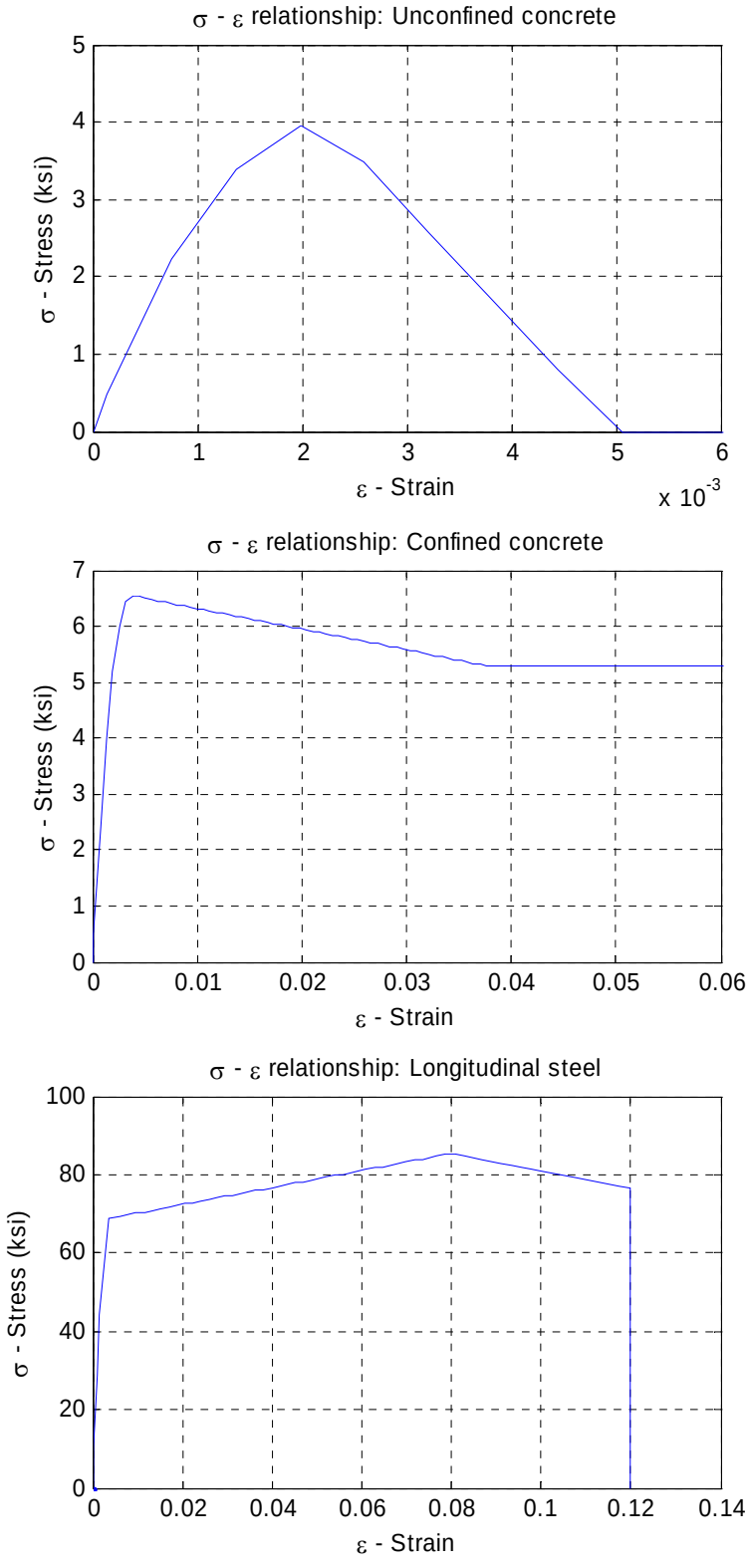

Figure 4-4 Uniaxial stress-stress relationships for column steel and concrete materials

The results of the moment- curvature analysis of column type A carried out in XTRACT (Imbsen 2004) and the moment-curvature relationship obtained from a longitudinal pushover of the of the RC bridge are presented in Figure 4-5. The two moment-curvature relations presented were obtained for an external column of the RC bridge (i.e., closest to the deck ends) for the same level of axial load corresponding to the tributary self weight of the superstructure. The steel model in XTRACT (Imbsen 2004) corresponded to ASTM A706 steel with expected material strength properties as per SDC (Caltrans 2004). Failure was defined in XTRACT (Imbsen 2004) as either rebar fracture in tension or confined concrete crushing in compression. This moment-curvature relation results in a ductility capacity of 6.1 and 4.3 for the longitudinal and transverse direction of the bridge, respectively, according to SDC (Caltrans 2004) and Ketchum (2004) report. The estimation of the ductility capacity and other basic response parameters of the RC bridge are presented in Appendix D.

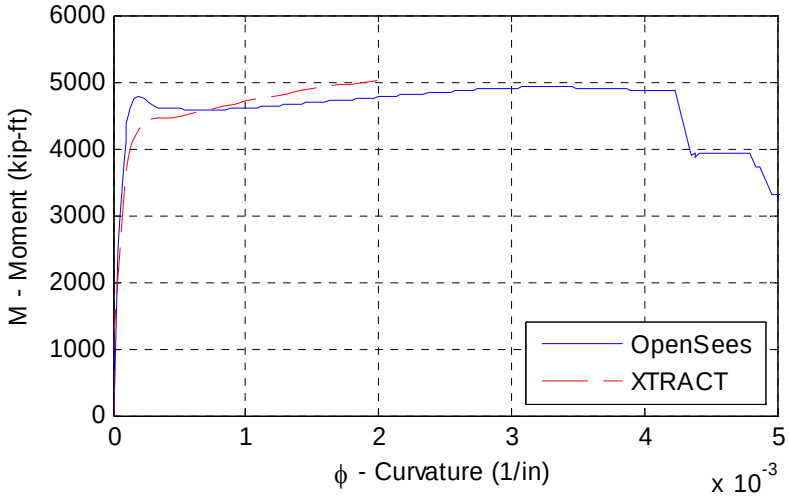

Figure 4-5 Moment-curvature relation for RC type 1A bridge column

The column foundations were modeled as fixed boundary conditions according to the construction details for the single- column bent bridge type 1A (see Figure 4-2). Since nonlinear abutment behavior can contribute significantly to the response of typical Ordinary bridge structures, an elaborate abutment model defined as the Spring Abutment (Aviram *et al.* 2008) was assigned to each superstructure end (see section 4.1.6).

The modeling and analysis assumptions and parameters used in the OpenSees model of the RC type 1A bridge were in agreement with the recommendations developed for typical Ordinary Standard bridge structures in California following an extensive analytical and parametric study (Aviram et. al 2008b). The results of the modal analysis of the RC bridge are presented in section 4.1.7, while the nonlinear static (pushover) and nonlinear dynamic time history analysis results of the bridge are presented in Chapter 5.

4.1.6 Abutment Model

Abutment nonlinear behavior can significantly influence the response of an entire bridge system under moderate to strong intensity ground motions, especially in the case of Ordinary bridge structures with continuous spans and relatively high superstructure stiffness. A realistic abutment

model should therefore incorporate all major resistance mechanisms and components, including an accurate estimation of their mass, stiffness, and nonlinear hysteretic behavior (see Figure 4-6). Different analytical abutment models representing typical seat abutment configurations as the one used in RC type 1A bridge system (see Figure 4-2 and Appendix D) were investigated in a parametric study (Aviram *et al.* 2008a and 2008b).

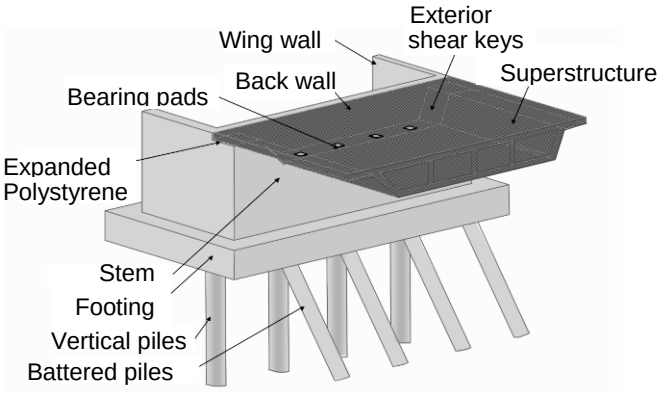

Figure 4-6 Major components of typical seat abutment (Megally et. al 2002)

An elaborate abutment model defined as the Spring Abutment model was developed by Mackie and Stojadinovic (2006), including sophisticated longitudinal, transverse, and vertical nonlinear abutment response, as well as a participating mass corresponding to the concrete abutment and mobilized embankment soil (see Figure 4-7). The Spring Abutment model was found to be superior to the other abutment models investigated (Aviram *et al.* 2008b) since it captures more accurately the nonlinear behavior of major components of the abutment and includes the participating mass of the embankment soil. This abutment model was therefore used and implemented in the OpenSees model of the RC type 1A bridge.

The longitudinal response of the Spring abutment is based on the system response of the elastomeric bearing pads, compression-only gap, abutment back wall, abutment piles, and soil backfill material. Prior to impact or gap closure, the superstructure forces are transmitted through the elastomeric bearing pads to the stem wall, and subsequently to the piles and backfill, in a series system. After gap closure, the superstructure bears directly on the abutment back wall and mobilizes the full passive backfill pressure.

A system of zero-length elements is distributed along two rigid elements oriented in the transverse bridge direction. The discrete zero-length elements represent each component of the abutment that contributes to the combined behavior and allow for differential response in each element as the superstructure rotates about the vertical bridge axis. The bearing pads create a series system between the two transverse rigid elements (Rigid element 1 and 2 in Figure 4-7). Rigid element 1 is connected to the deck end by a rigid joint.

The longitudinal elastomeric bearing pad response and gap closure behavior are illustrated by L_1 in Figure 4-7. The number and distribution of the bearing pads is defined according to the number and location of the girders in the box, with plan and thickness dimensions according to plans or specifications. The yield and ultimate displacement of the bearings are assumed to be at 150% and 300% of the shear strain. A dynamic coefficient of friction of 0.40 for neoprene on concrete is used, guaranteeing that shear failure occurs prior to sliding of the bearing pads. The longitudinal backfill, backwall, and pile system response are

accounted for by the two zero-length elements at the extreme locations of rigid element 2, designated as L_2. The abutment stiffness (K_{abt}) and ultimate strength (P_{bw}) for these elements are obtained from equations 7.43 and 7.44 of the Seismic Design Criteria (Caltrans 2004). The longitudinal response of the Spring Abutment model in the RC type 1A bridge due to a longitudinal pushover analysis is presented in Figure 4-8. The pushover analysis was carried out in the direction of the "right" abutment, away from the "left" abutment.

The transverse response is based on the system response of the elastomeric bearing pads, exterior concrete shear keys, abutment piles, wing walls, and backfill material. The bearing pad model discussed above is used with uncoupled behavior with respect to the longitudinal direction. The constitutive model of the exterior shear keys is derived from experimental tests (Megally *et al.*, 2002). The ultimate shear key strength is assumed to be 30% of the superstructure dead load, according to equation 7.47 of the Seismic Design Criteria (Caltrans 2004). A *Hysteretic* uniaxial material with a tri-linear response backbone curve is used with two hardening and one softening stiffness values. The initial stiffness is a series-system stiffness of the shear and flexural response of a concrete cantilever with shear key dimensions. The hardening and softening branches are assumed to have magnitudes of 2.5% of the initial stiffness. The parallel system of transverse bearing pads and shear keys are labeled T_1 in Figure 4-7.

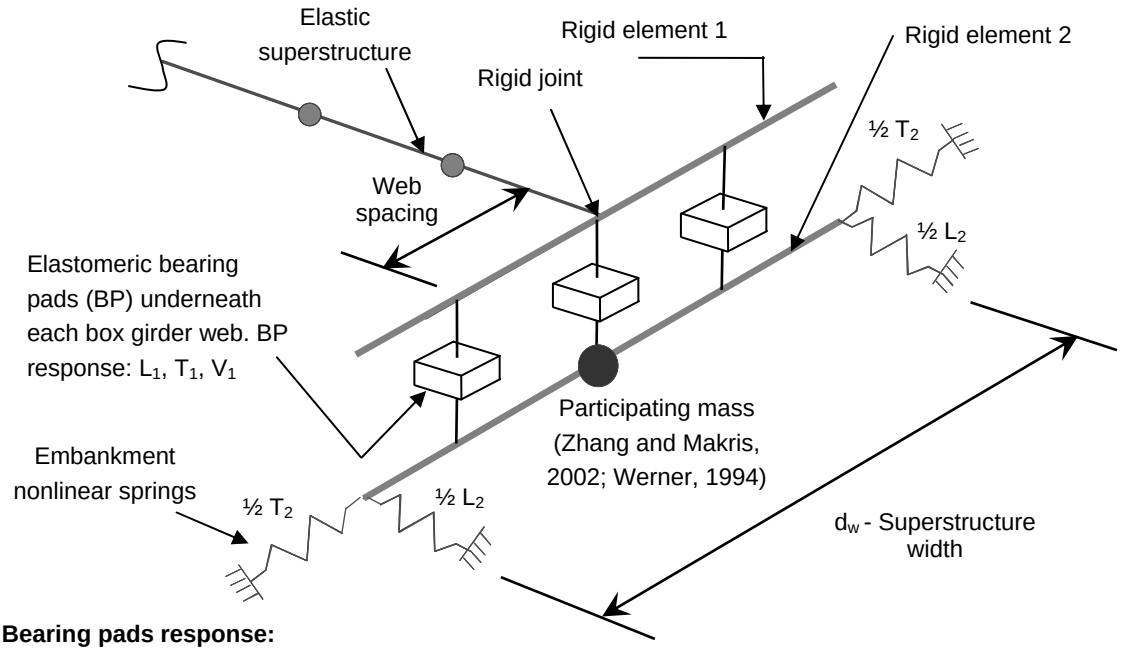

Bearing pads response:

- Longitudinal L_1: BP shear resistance and backwall compression-only gap contact element in parallel.
- Transverse T_1: BP shear resistance and brittle shear keys (extreme BPs only) in parallel.
- Vertical V_1: BP vertical stiffness with bearing crushing in series with embankment vertical stiffness through contact element for stem wall in parallel.

Embankment response:

- Longitudinal L_2: SDC backbone curve.
- Transverse T_2: Modified SDC backbone curve.

Figure 4-7 General scheme of the Spring Abutment model

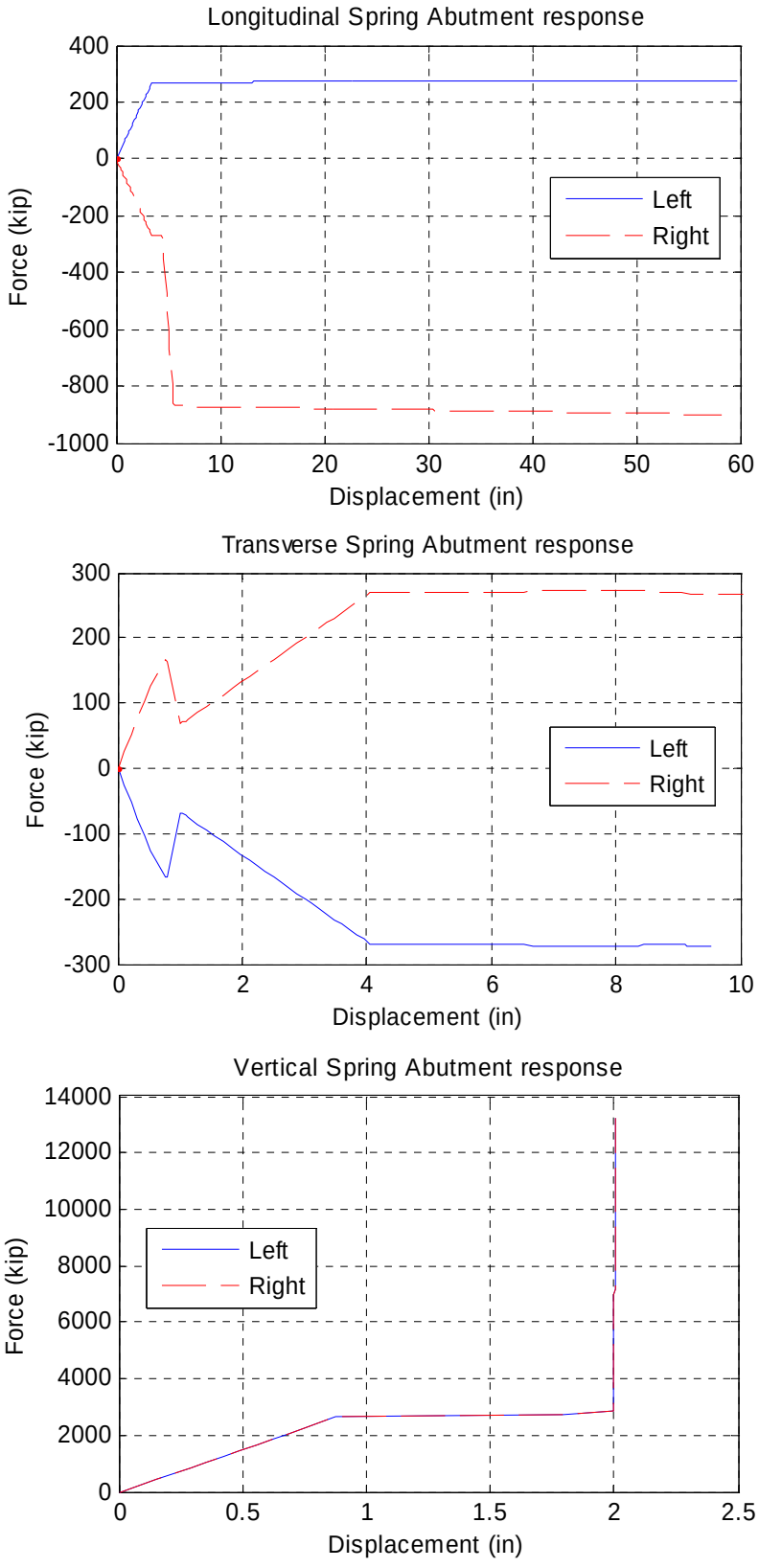

Figure 4-8 Spring abutment response

The transverse stiffness and strength of the backfill, wing wall, and pile system is calculated using the same modification of the SDC procedure for the longitudinal direction as defined for the simplified abutment model. The stiffness and strength are distributed equally to the two extreme zero-length elements (T_2) of rigid element 2. The transverse response of the Spring Abutment model of RC type 1A bridge due to transverse pushover analysis is presented in Figure 4-8 for both left and right abutments.

The vertical response of the abutment model includes the vertical stiffness of the bearing pads (V_1) in series with the vertical stiffness of the trapezoidal embankment (V_2). The embankment stiffness per unit length of embankment was obtained (Zhang and Makris 2001) and modified using the critical length to obtain a lumped stiffness. The abutment is assumed to have a nominal mass proportional to the superstructure dead load at the abutment, including a contribution from structural concrete as well as the participating soil mass. An average of the embankment lengths obtained from Zhang and Makris (2001) and Werner (1994) is included in the calculation of the participating mass due to the embankment of the abutment. The vertical Spring Abutment response of bridge RC type 1A due to a pushunder analysis is presented in Figure 4-8 for both left and right abutments.

4.1.7 Basic Dynamic Properties

A linearized abutment stiffness and an effective stiffness of the column bents (I_{eff}=0.52I_g) were assumed for the SAP2000 bridge models developed by Ketchum *et al.* (2004) for the PEER Center Lifeline project, resulting in the elastic periods presented in Table 4-2. The details of the abutment model are not presented in the mentioned report.

Table 4-2 Modal periods of the RC bridge obtained for different bridge models

Mode	SAP2000		OpenSees model	
	Ketchum 2004-Elastic, cracked col.	Elastic, cracked col.	Nonlinear, uncracked col. (Pre-EQ)	Nonlinear, Post-EQ (B-ICC)
Transverse translation	1.30	1.52	0.95	1.15
Longitudinal translation	1.04	0.72	0.53	0.62
Global torsion	-	0.86	0.56	0.63
Horizontal out-of-plane deck deformation (C-Shape)	-	0.55	0.46	0.47
Vertical in-plane deck deformation (W-shape)	-	0.48	0.40	0.41

Modal analysis of the RC bridge model in OpenSees was repeated using an elastic model of the column with effective cross section properties as well as a nonlinear distributed-plasticity fiber model for the column (see Table 4-2) to verify the previous results obtained from Ketchum (2004). An effective stiffness equal to half the gross cross section stiffness (I_{eff}=0.50I_g) is used for the elastic model of the column in OpenSees, according to Chapter 5 of SDC (Caltrans 2004), for an axial load ratio $P/f'_c A_g$ of 0.25 and a transverse reinforcement ratio, ρ_s of 0.015. The post-earthquake modal periods for the B-ICC ground motions obtained

for the nonlinear RC bridge model in OpenSees is also presented in Table 4-2. The B-ICC record from the LMSR bin (see Appendix E) was defined with a scale factor of 2.0 and a combined peak ground velocity (PGV) of 123.56 cm/sec (48.65 in/sec), representing a relatively high intensity ground motion.

Using the Spring Abutment model in OpenSees, the resulting principal mode shapes and modal periods of the OpenSees bridge model are different from the ones obtained in the Ketchum *et al.* (2004) report. The elastic periods obtained from the SAP2000 and OpenSees model differ primarily due to the boundary conditions at the deck ends. The periods obtained from the nonlinear model of the bridge in OpenSees assume an uncracked column section at the initial stages of the analysis ($I_{eff}=I_g$), thus the pre-earthquake modal periods corresponding to a stiffer bridge are lower than the elastic ones (see Table 4-2). Spalling, cracking and reinforcement yielding develop as the column undergoes into the inelastic range of response due to ground motion excitation.

The mode shapes of the RC bridge structure obtained through an eigenvector analysis in OpenSees are presented in Figure 4-9.

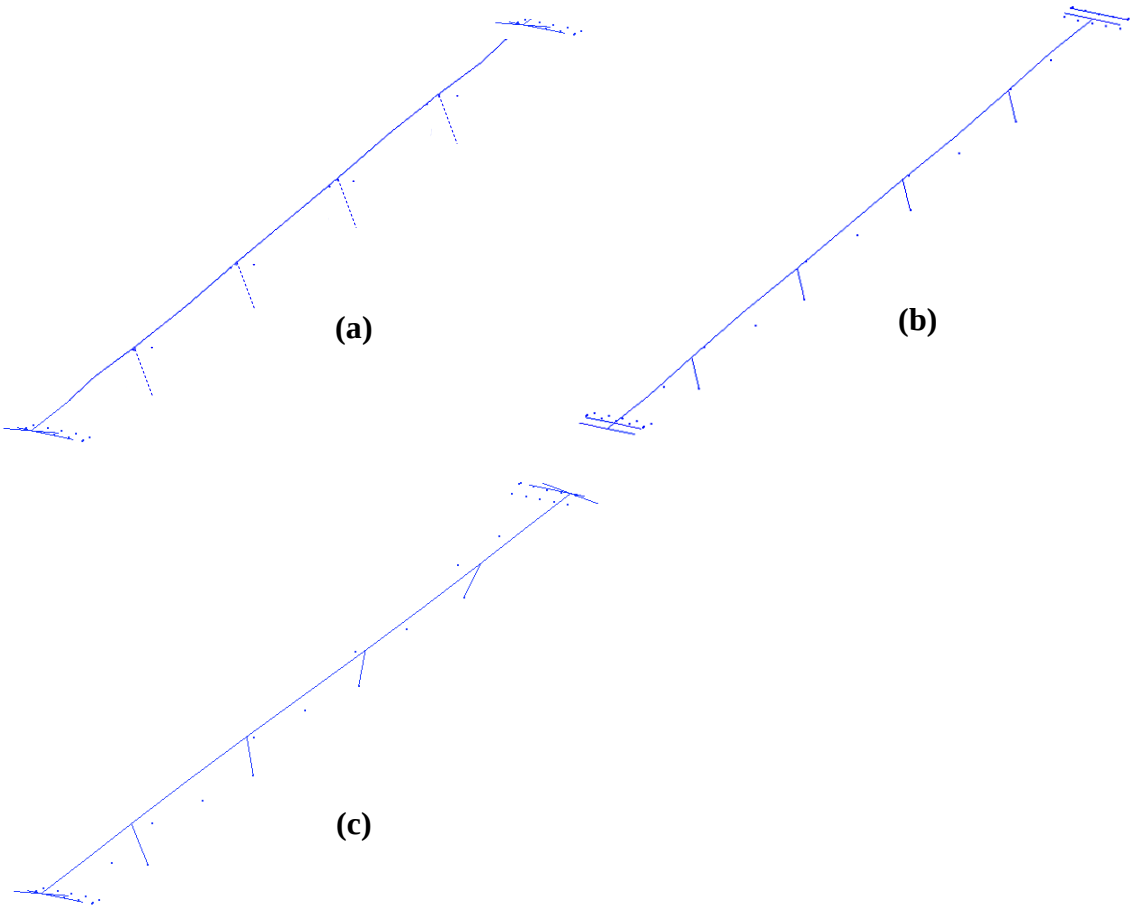

Figure 4-9 Deformation of the RC bridge in the transverse translation (a), longitudinal translation (b), and global torsional (c) modes, recorded in OpenSees

4.2 FIBER-REINFORCED CONCRETE BRIDGE

4.2.1 Introduction

The fiber-reinforced concrete bridge used in this study is a simple re-design of the PEER testbed bridge discussed in Section 4.1. The redesign consists of: 1) replacement of conventional reinforced concrete with HPFRC; 2) introduction of longitudinal reinforcement detail used for Specimen S1, as presented in Chapter 2; and 3) halving the amount of transverse reinforcement by doubling the pitch of the column spiral. There were no changes in column diameter. Furthermore, no other element of the bridge, including the column foundations, the cap beams, the deck and the abutments were modified from the original PEER testbed bridge. The finite element model of the fiber-reinforced concrete bridge was also a modification of the finite element model of the original PEER testbed bridge.

4.2.2 HPFRC Column Model

The FRC bridge model in OpenSees was defined using the same geometry, deck and abutment models as the RC bridge, and a modified column model specified according to the calibrated S1 FRC cantilever column presented in Chapter 3. The S1 FRC column presented improved cyclic behavior in comparison with the BC column and the S2 FRC cantilever column, thus the modeling recommendations obtained for this column were extrapolated for the FRC bridge columns. The total height of the column was divided into three segments, as for the S1 FRC cantilever column, to account for the dowel reinforcement at the column base and the unbounded region in the plastic hinge zone. The geometric properties and reinforcement details defined for the FRC bridge column are presented in Table 4-3. The general modeling scheme of the FRC bridge column defined in OpenSees is shown in **Error! Reference source not found.**.

Table 4-3 Geometric properties and reinforcement details of FRC bridge columns

Mode	RC bridge	FRC bridge		
		Segment 1	Segment 2	Segment 3
D_c- Diameter (in)	48	48	48	48
H- Segment height (in)	307.6	24	24	211.6
Cover (in)	2.0	2.0	2.0	2.0
Longitudinal bar	#10	#10	#10	#10
No. long. Bars	28	46	36	28
ρ_l- Long. reinf. Ratio	0.02	0.032	0.025	0.02
Transverse bar	#7	#7	#7	#7
s- Spacing (in)	3.5	7.0	7.0	7.0
ρ_t- Transv. reinf. Ratio	0.0156	0.0078	0.0078	0.0078

Since the theoretical inflection point of the FRC columns was assumed at mid height, the lengths for the dowel reinforcement and unbounded region were defined with respect to this

measure using the same ratios specified for the S1 FRC cantilever column (see Figure 4-7). Intermediate nodes were created in the OpenSees model with different column cross sections defined at each integration point to account for the additional dowel reinforcement and unbounding details in the plastic hinge zone. A *dispBeamColumn* element was used in OpenSees for the bottom two segments of the columns in the region of the plastic hinge zone with two integration points each, while a *nonlinearBeamColumn* element was employed for the top segment of the columns, defined with five integration points as for the FRC cantilever columns.

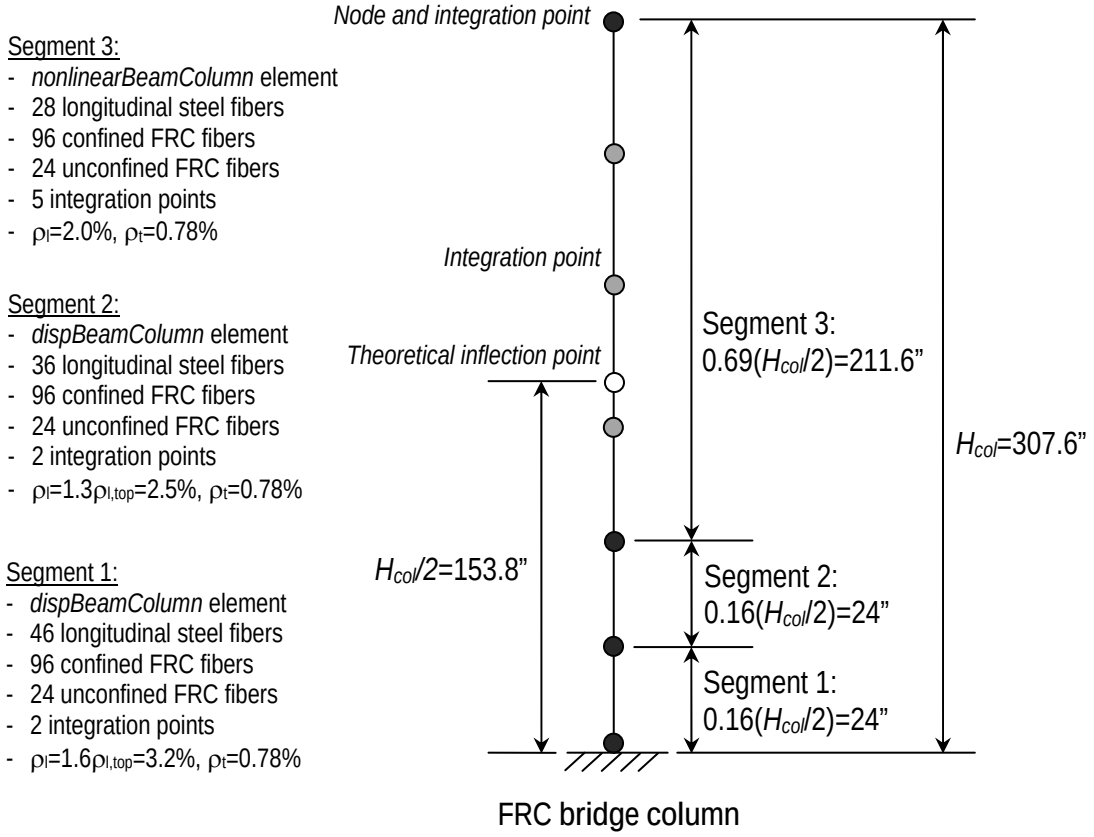

Figure 4-10 General scheme of the FRC bridge column model in OpenSees

The longitudinal reinforcement at the bottom two segments was also defined with the same percent increase with respect to the reinforcement ratio at column top as for the S1 FRC cantilever column. The transverse reinforcement spacing and ratio of the FRC bridge column were defined as twice and half of the RC column transverse reinforcement, respectively. The mass assignment for the FRC bridge column was carried out according to the tributary length of each node. Elastic shear deformation was included for all beam and column elements, similar to the RC bridge. The material properties of confined and unconfined FRC, as well as steel reinforcement were defined in OpenSees according to the calibration of the S1 FRC cantilever model, as discussed in the following sections.

4.2.3 Concrete Material Properties

The concrete cover and core material behaviors of the FRC column were defined using the uniaxial *Concrete02* constitutive model in OpenSees using modified parameters according to material test results in Chapter 2 and the calibrated OpenSees models presented in Chapter 3 of the FRC column specimens subjected to cyclic loading. The column concrete strength was changed from f'_c=4.2ksi to $f'_{c,FRC}$=1.12f'_c=4.7 ksi due to the addition of fiber reinforcement to the concrete mix, according to material test results in Chapter 2.

The resulting FRC cover compressive strength f_{pc} was taken $f'_{c,FRC}$=4.7 ksi, the elastic modulus E_o was taken as $E_{c,FRC}$=4245.5×4.7/6.86=2908.7 ksi, obtained by scaling down the results in Chapter 3 to the design strength f_{pc} used for the FRC bridge model. The strain at peak compressive strength epsc$_0$ was calculated as $2f_{pc}/E_o$=0.0032, equal to the mean results in Chapter 2 and calibrated model in Chapter 3. The residual strength f_{pcU} was defined as $0.1f_{pc}$=0.47 ksi at a strain value eps_U of 0.0325, similar to the calibrated FRC specimens. The tensile strength of concrete f_t was defined with a value of 0.5 ksi, and the tension softening stiffness E_{ts} was defined equal to E_o.

For the FRC core the compressive strength f_{pc} was defined with a value of 6.80 ksi, equal to the compressive strength of confined concrete f'_{cc} by Mander (1988) using the unconfined FRC material properties presented above. The elastic modulus E$_o$ was defined similar to the unconfined FRC material as $E_{c,FRC}$=2908.7 ksi. The corresponding strain at peak compressive stress epsc$_0$= $2f_{pc}/E_o$ was equal to 0.0046. The residual strength f_{pcU} was defined as $0.36f_{pc}$=2.45 ksi, similar to the mean FRC material test results. A minimum ultimate strain of 0.0375 was used for the confined FRC material model, as defined for the confined concrete model of the RC bridge columns, since the addition of fibers to a plain concrete mix have been shown to enhance the ductility of the material. The tensile behavior of the FRC confined concrete was defined similar to the unconfined concrete, with a tensile strength f_t of 0.5 ksi and a tension softening stiffness E_{ts}=E_0.

The resulting stress-strain relationships of confined and unconfined FRC material used in the OpenSees fiber model are presented in Figure 4-11. A total of 96 fibers were used to model the confined concrete core (12 tangential wedges and 8 radial divisions), and 24 fibers were defined for the cover (12 wedges and 2 radial divisions), similar to the FRC cantilever columns.

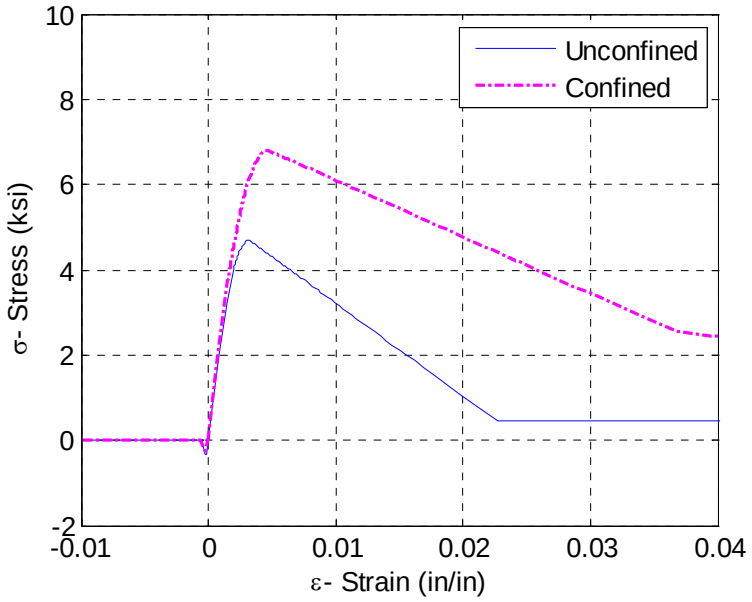

Figure 4-11 Stress-strain relationship for FRC used in OpenSees model of FRC bridge column

4.2.4 Steel Material Properties

The *Hysteretic* constitutive model was used for longitudinal steel of the FRC bridge columns, defined according to the calibrated material parameters presented in Chapter 3 for the FRC cantilever column specimens. The *Hysteretic* material model is defined with a tri-linear hysteretic behavior, pinching of force and deformation, damage due to ductility and energy, and degraded unloading stiffness based on ductility. The first point on the stress-strain envelope (ε_1,σ_1) corresponds to a modified yield point (ε_y,f_y) of the longitudinal steel, where the yield stress f_y was equal to 68 ksi, as in the RC bridge; however, the corresponding strain was defined similar to the FRC cantilever columns as $f_y/0.5E_s$, where E_s=29,000 ksi is the elastic modulus of steel. A reduced initial stiffness was used since the FRC column specimens yielded at a nominal ductility level of 1.5 with respect to the conventionally reinforced concrete column BC yield point. The second and third points of the stress-strain curve of the *Hysteretic* constitutive model for steel were defined similar to the RC bridge as (ε_2,σ_2)=(0.08, f_u=1.25f_y=85 ksi) and (ε_3,σ_3)=($\varepsilon_{failure}$=0.12, $f_{failure}$=75 ksi), corresponding to the steel ultimate and failure points, respectively. This ultimate strain of 0.12 was specified for both tensile and compressive behavior of the steel reinforcement according to the recommendations of Caltrans SDC (2004).

The pinching factors during reloading for strain ($pinch_X$) and stress ($pinch_Y$) were defined similar to the FRC cantilever columns with values of 0.3 and 1.0, respectively. The damage due to ductility and energy using factors $damage_1$ and $damage_2$ was not included in the calibrated *Hysteretic* constitutive model, as for the FRC cantilever columns. A degraded unloading stiffness equal to $\mu^{-\beta}$ was used in the material model based on ductility level of the steel fiber μ, where the parameter β was defined similar to the FRC cantilever columns with a value 0.65. The steel reinforcement monotonic and hysteretic stress-strain relationships defined for the OpenSees FRC bridge column are presented in Figure 4-12 and Figure 4-13, respectively.

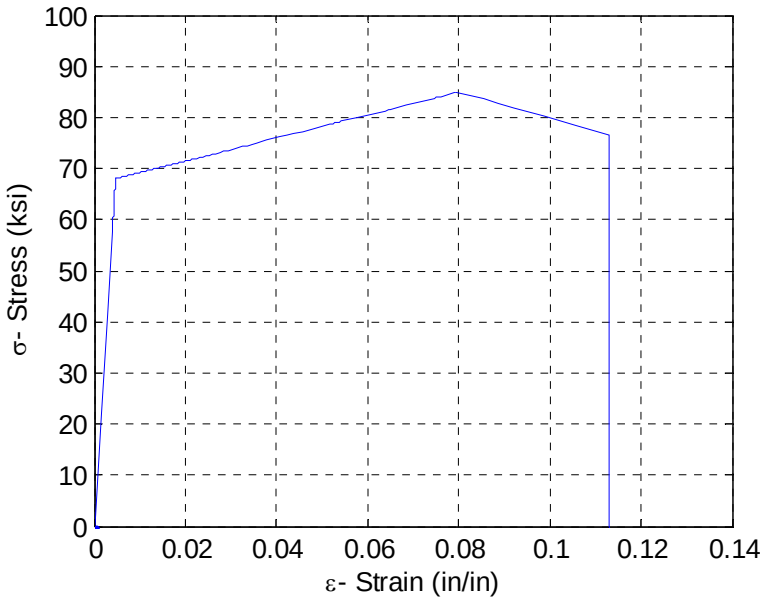

Figure 4-12 Monotonic stress-strain relationship for longitudinal steel reinforcement used in OpenSees fiber model of FRC bridge columns

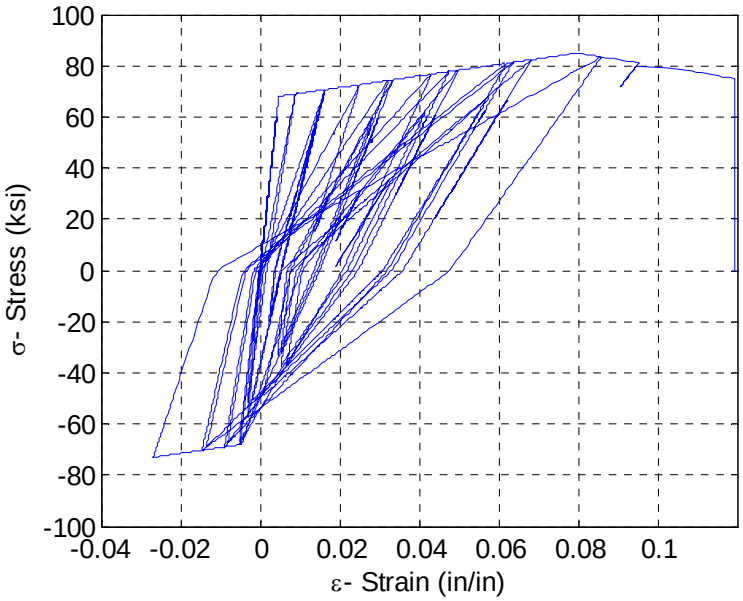

Figure 4-13 Longitudinal steel hysteresis obtained from OpenSees model of FRC bridge columns subjected to bidirectional cyclic loading history

4.2.5 Basic Dynamic Properties

Figure 4-14 presents the general scheme of the complete FRC bridge model obtained from OpenSees structural analysis program. The segmentation of the FRC columns accounting for the additional dowel reinforcement at the column base and the unbounded region in the plastic hinge zone are also shown.

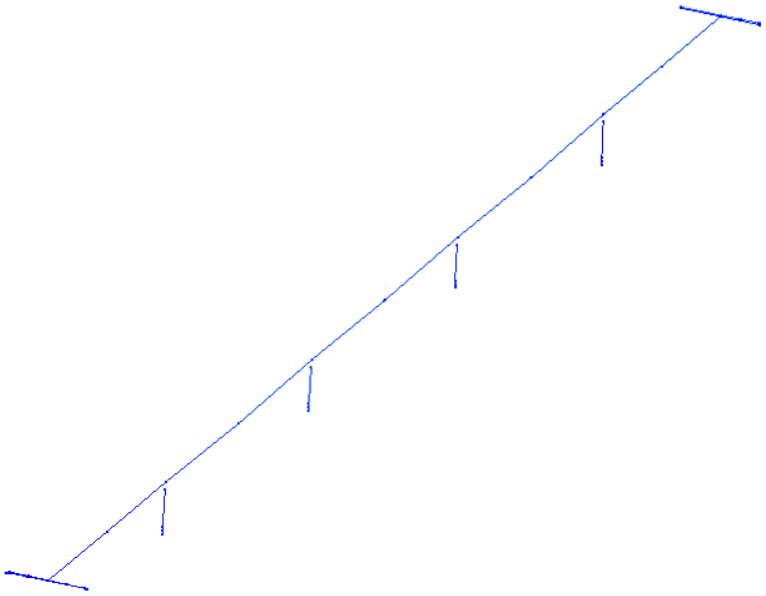

Figure 4-14 Rendering of the FRC bridge model in OpenSees

The modal periods of the nonlinear FRC bridge model in OpenSees are presented in Table 4-4. The modal periods were obtained for the initial state of each nonlinear time history analysis where the column is uncracked (pre-earthquake period) and for the final state of each record where the column is cracked according to the number and intensity of cycles in the nonlinear range of response (post-earthquake period). The post-earthquake modal periods in Table 4-4 were obtained for the B-ICC record from the LMSR ground motion bin (see Appendix E), which represents a relatively high intensity ground motion. The elongated periods of the FRC bridge in comparison to the RC bridge indicate that the FRC columns increase the flexibility of the bridge model, specifically for the transverse and longitudinal translational modes. The pushover curves of the column bents, abutment model and complete bridge system, as well as the nonlinear dynamic time history analysis results for the FRC bridge are presented in Chapter 5.

Table 4-4 Modal periods of the FRC bridge model in OpenSees

Mode	RC bridge		FRC bridge	
	Pre-EQ	Post-EQ (B-ICC)	Pre-EQ	Post-EQ (B-ICC)
Transverse translation	0.95	1.15	1.01	1.35
Longitudinal translation	0.53	0.62	0.60	0.76
Global torsion	0.56	0.63	0.57	0.66
Horizontal out-of-plane deck deformation (C-Shape)	0.46	0.47	0.47	0.48
Vertical in-plane deck deformation (W-shape)	0.40	0.41	0.41	0.46

4.3 ISOLATED BRIDGE

4.3.1 Introduction

Typically, a bridge designed for higher seismic ground motion level or earthquake magnitude results in higher bridge construction cost. Similarly, a bridge designed for better structural performance and minimal damage (lower ductility demand on the substructure elements) results in higher bridge construction cost. Since bridge type 1A has the smallest dimensions and reinforcement ratios, as well as the highest ductility demands under high seismic levels, it is also the most economic. However, consequently it will result in the highest repair costs of all type 1 bridges designed for the testbed bridge project (Ketchum 2004). An alternate bridge design is an isolated bridge, with an isolation system underneath the superstructure limiting the damage and consequently reducing the repair costs of the isolated bridge is presented in this chapter. The fixed-base PEER testbed RC bridge was redesigned for two ductility levels of the column bents, using the same seismic hazard levels defined for the original bridge. The columns of the isolated bridge are made using conventional reinforced concrete.

4.3.2 Design Goals

During seismic excitations characterized primarily by lateral ground motions, the bridge's superstructure mass produces high inertial forces and consequently high seismic base shear demand on the supporting substructure of the bridge. The ductile lateral resistance mechanism of the bridge is provided by the column bents which can suffer significant damage through large excursions in the nonlinear range of response under strong excitations and high displacement demands.

Both the displacement ductility demand and shear force demand on the substructure can be reduced considerably through the installation of isolation devices underneath the bridge's superstructure. Through a specific tuning of the relative stiffness of the flexible isolators and the column bent flexibility working as a series system, the displacement and force demand on each component can be distributed. The isolator devices acting as a fuse are designed to sustain large shear deformations without significant deterioration of the material or degradation of strength, thus stably absorbing the inertial forces developed at the superstructure and limiting the deformations in the substructure.

The isolation of the bridge superstructure and the reduction in the deformations and damage in the column bents do not only reduce the costs associated with the repair of the bridge after a significant earthquake event, but also limit the deterioration of the gravity load-carrying capacity and essential functionality of the bridge after the event. The schematic behavior of a fixed-base and isolated single column-bent bridge is presented in Figure 4-15.

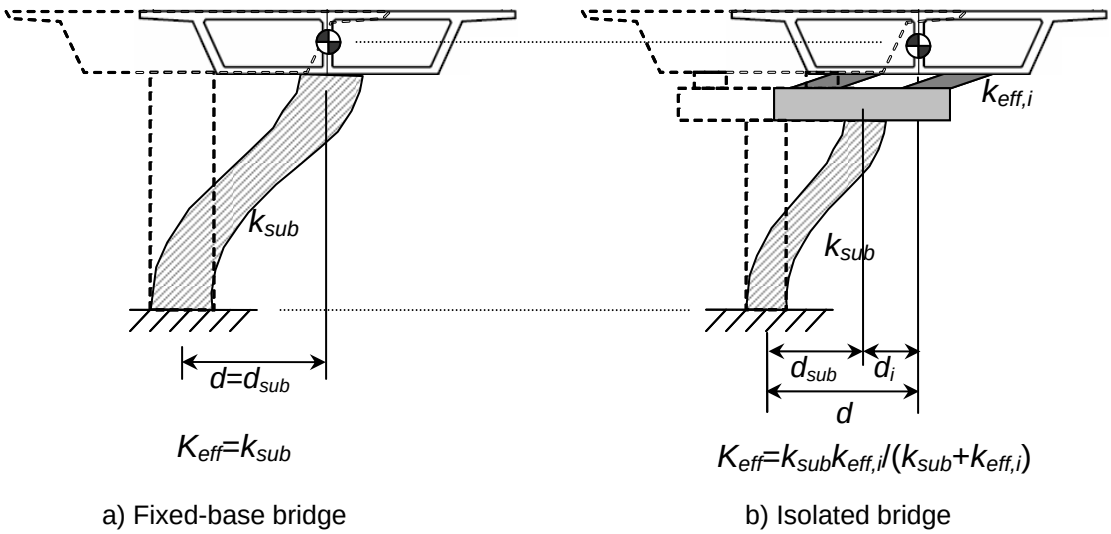

Figure 4-15 Deformation scheme for fixed-base and isolated bridges

In order to limit the force demand on the substructure, the target period of the isolated bridge system is increased, resulting in lower spectral acceleration values used for the preliminary design stage. However, lower spectral acceleration values correspond to higher spectral displacement values for the system. These high displacement demands can be reduced by introducing higher damping into the system provided by the isolation devices undergoing large and stable inelastic excursions under seismic loading. The design goals defined for the redesign of bridge type 1A using isolation devices are presented in Table 4-5.

Table 4-5 Summary of specific design goals for the fixed-based and isolated bridge

Parameter	Fixed-base bridge	Isolated bridge
Dynamic properties		
Damping (β)	5% (column hinging)	20% (column and isolation system)
Period (T)	T_T=1.30 s, T_L=1.04 s	$T_{Target} \approx$ 3.0 s
Seismic demand		
Seismic coefficient ($C_s=S_a/g$)	$S_{a,T}$=1.07g, $S_{a,L}$=0.99g	$S_a \approx$ 0.27g
Displacement (S_d)	$S_{d,T}$=17.7”, $S_{d,L}$=10.5”	$S_d \approx$ 24”
Performance criteria		
Ductility demand (μ_d)	$\mu_{d,T}$=4.3, $\mu_{d,L}$=4.5	$\mu_d \approx$ 1.0 (Elastic); $\mu_d \approx$ 2.0 (Minor yielding)

For the isolated bridge, two design options were used for the column bents. In the first option, the column bent is required to remain elastic (ductility demand $\mu_d \approx 1$), which is intended to result in slightly higher column dimensions and reinforcement ratios but negligible repair costs even for high intensity earthquakes. The second option allows the column to deform

beyond its elastic limit up to displacement ductility of 2 ($\mu_d \approx 2$), but only to induce minor yielding of the reinforcing bars and spalling of the concrete cover. This damage state is expected to be easily reparable, resulting in relatively low post-earthquake repair costs. This alternative inelastic design of the isolated bridge could also limit the deterioration of the gravity load-carrying capacity of the column bents and allow the continuous functionality of the bridge. This latter design of the isolated bridge results in smaller dimensions of the column and isolation bearings.

The seismic demand used for the isolated bridge design corresponds to the same SDC (Caltrans 2004) ARS curves used for the fixed-base RC bridge. The spectral demand and values used for both bridge types are displayed in Figure 4-16.

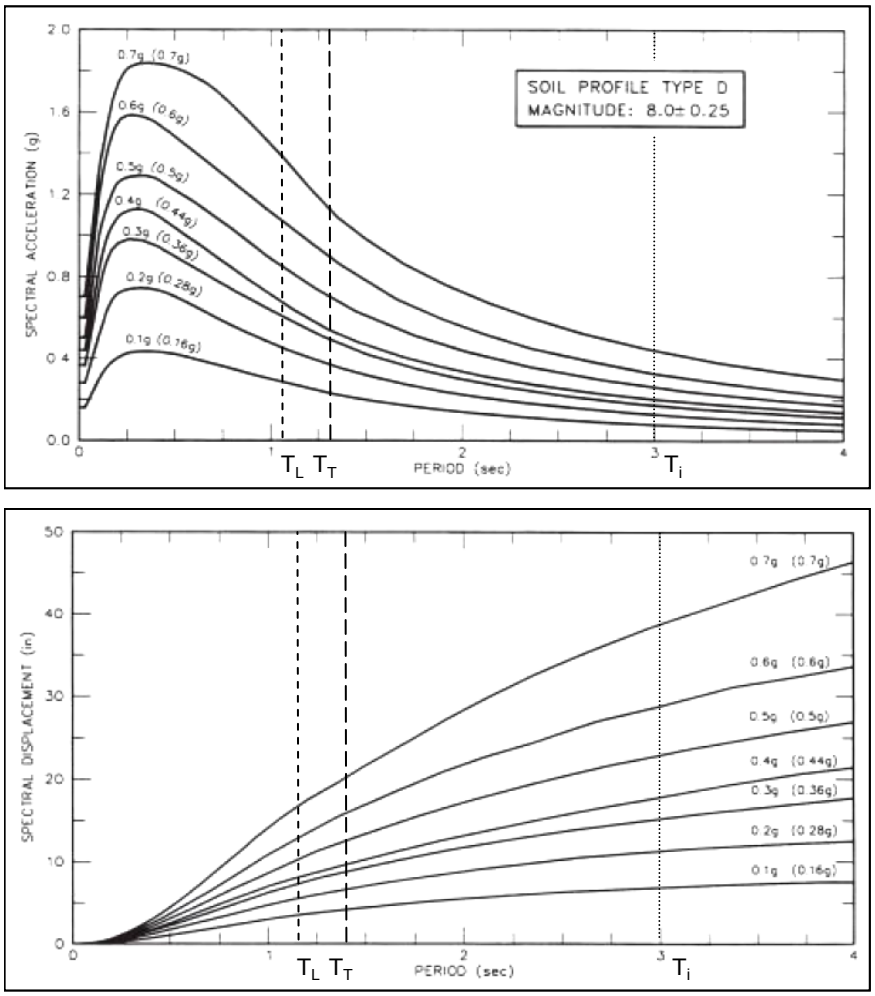

Figure 4-16 SDC (Caltrans 2004) elastic ARS and DRS curves for 5% damping defining the seismic demand on the fixed-base and isolated bridges

4.3.3 Preliminary Design

The design of the isolated bridge was carried out following the AASHTO Guide Specifications for Seismic Isolation Design (AASHTO 1999), the AASHTO Standard Specifications for Highway Bridges: Division IA-Seismic Design (AASHTO 1996) and the Caltrans Seismic Design Criteria V1.3 (Caltrans 2004). The simplified analysis of the isolated bridge was performed using the Uniform Force Method, section 7.1 in the AASHTO (1999) code for the determination of the seismic demand values on the column bents and isolation devices. The SDC (Caltrans 2004) was used for the preliminary design of the column bents. The DIS manuals (Dynamic Isolation Systems 2007) were used for the selection and design of the isolation bearings.

The general design scheme for the preliminary design of the isolated bridges is presented in Figure 4-17. The specific assumptions, values and design equations for the preliminary design of the isolated bridges are presented in Appendix D. The principal considerations used for the design of the column bents and isolation devices are presented in the following paragraphs. The design of the isolated bridge was verified following the nonlinear dynamic time history analysis of the bridge which includes a large representative suite of three component ground motions at different hazard levels (see Chapter 5).

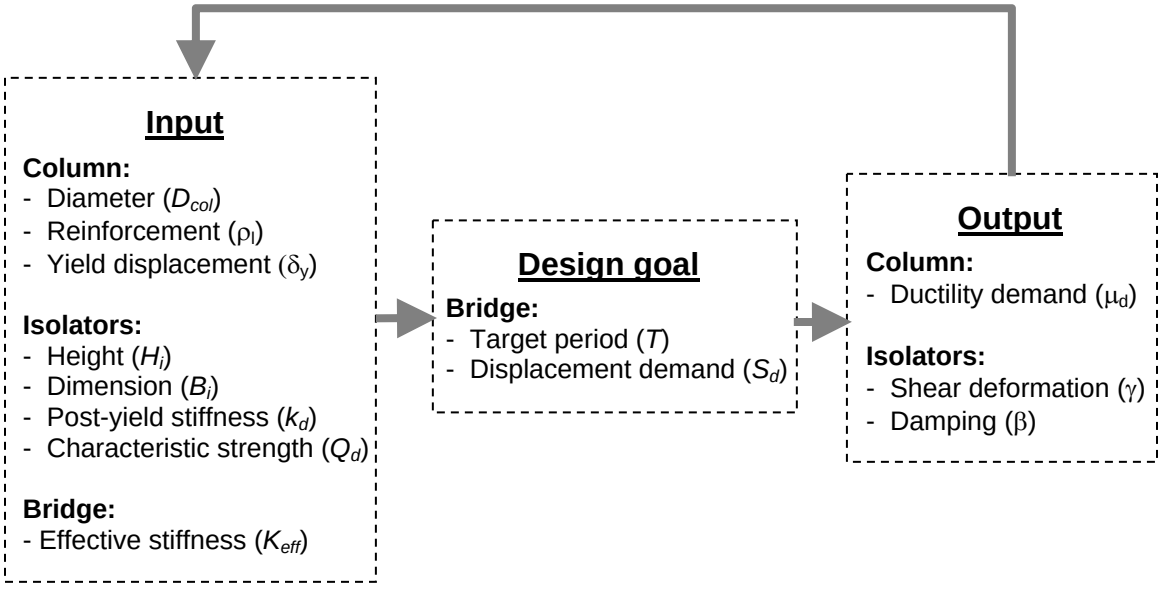

Figure 4-17 Iterative design scheme for isolated bridge

The boundary conditions of the column bent in the isolated bridge were assumed similar to the idealized fixed-base bridge behavior for simplicity in the preliminary design stage. In the longitudinal direction, a fixed-fixed behavior (bending in double curvature) was assumed, provided by the fixity of the column base foundations and the frame action by the superstructure. In the transverse direction, a cantilever behavior of the column was assumed since no significant lateral resistance is provided at the column top due to the presence of a transverse gap at the superstructure ends. Following gap closure, the boundary conditions defined at each of the

superstructure ends were assumed to have negligible effect on the deformed shape of the bents due to the relatively high flexibility of the long-span deck. The actual boundary conditions of the column can only be determined using a three-dimensional nonlinear model of the entire bridge which can accurately capture the relative stiffness of the superstructure, substructure and isolation bearings. The description of the isolated bridge model in OpenSees structural analysis program which incorporates the above requirements is presented in Section 4.3.5.

A moment-curvature analysis was carried out for the column bents according to Chapter 3 of SDC (Caltrans 2004) using XTRACT (Imbsen 2004) (see Figure 4-18). The three moment-curvature relations presented were obtained for a column axial level corresponding to the total tributary dead load and self weight of the superstructure, approximately equal to $0.25P_{max}$, where $P_{max}=f'_cA_g$ is the maximum axial capacity of the original RC column. This axial load ratio was used by Ketchum (2004) for the design of type 1A bridge column. The design equations and procedure according to SDC (Caltrans 2004) and AASHTO (1996, 1999) for the columns of bridges BI1 (isolated bridge with elastic column) and BI2 (isolated bridge with inelastic column) are presented in Appendix D. Table 4-6 summarizes the results for both bridge designs.

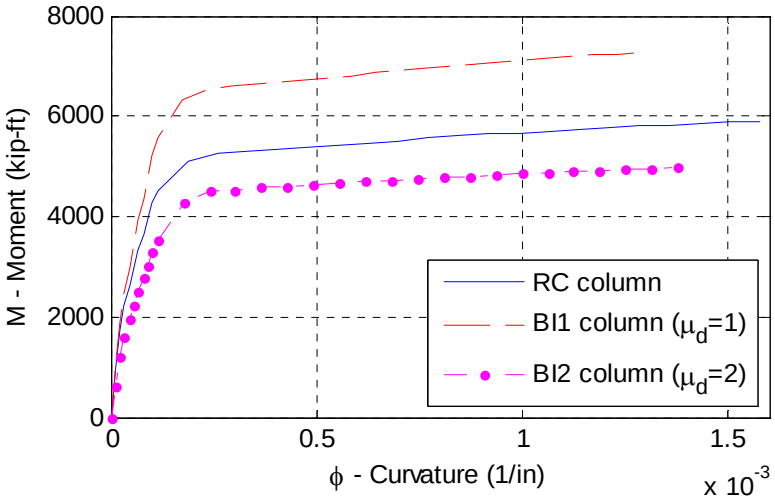

Figure 4-18 Moment-curvature relation for preliminary bridge columns

Table 4-6 Summary of preliminary design results for the isolated bridge columns

Parameter	RC Fixed-base (μ_d=5)	BI1 Isolated (μ_d=1)	BI2 Isolated (μ_d=2)
D_{col} - Column diameter	4’	4’	3.5’
H_{col} – Total column height	22’	20.3’	20.75’
ρ_l - Longitudinal reinforcement	0.02 (28#10)	0.03 (34#11)	0.03 (32#10)
ρ_s - Transverse reinforcement	0.016 (#7@3.5)	0.016 (#7@3.5”)	0.015 (#7@4.0”)

The isolation devices selected for the present bridge consist of lead rubber bearings (LRB) (see Figure 4-19), commonly used for bridge isolation in North America. Only around 25% of isolated bridges in North America are built using other seismic isolation techniques such

as Eradiquake isolators (EQS), friction pendulum systems (FPS), sliding isolators with dissipater-fuse ensemble (FIP), high damping rubber bearings (HDRB) or natural rubber bearings (NRB) (Buckle *et al.* 2006). For bridge construction square isolators are most common, therefore the equivalent square dimension of the bearings can be obtained from design manuals for circular bearings. The behavior of square and circular bearings was assumed similar for the purpose of this study.

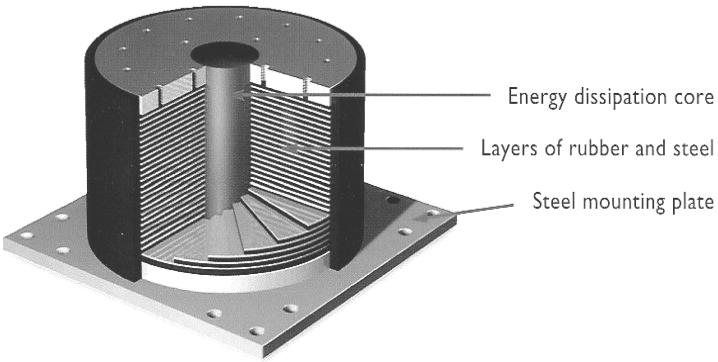

Figure 4-19 Composition of a typical LRB isolator (Dynamic Isolation Systems 2007)

During severe seismic motions, the lead plug is capable of deforming through many low-cycle plastic deformations without a significant loss of strength. Experimental studies indicate that the lead responds essentially with elastic-perfectly plastic loops. Therefore, for practical purposes, the post-yielding isolator stiffness, K_d was equal to the stiffness of the rubber bearing alone. The hysteresis loop of the LRB isolator was represented using a bi-linear behavior with an initial elastic stiffness, K_e=10K_d (see Figure 4-20).

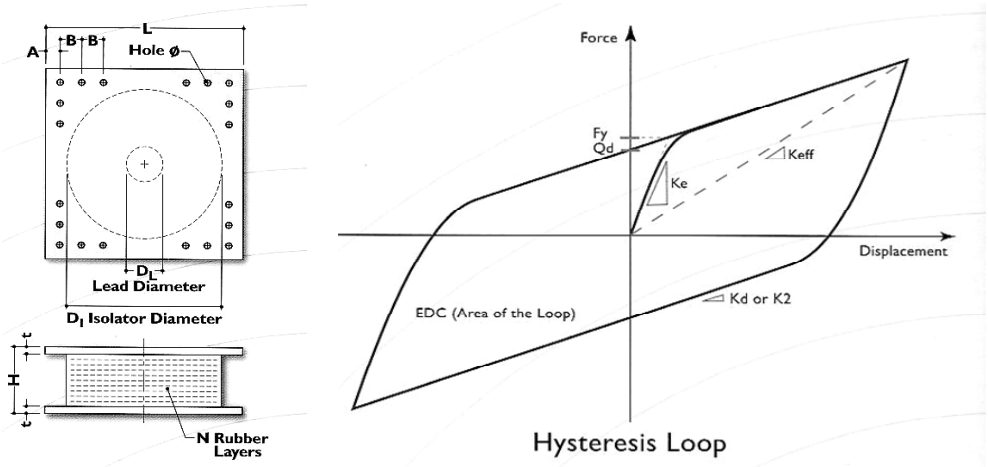

Figure 4-20 Typical dimensions and hysteretic loop of a LRB isolators (Dynamic Isolation Systems 2007)

The design procedure for the isolation bearings of bridges BI1 and BI2 are presented in Appendix D. The results of this design are summarized in Table 4-7.

Table 4-7 Summary of principal design results for the LRB isolators

Parameter	BI1 Isolated (μ_d=1)	BI2 Isolated (μ_d=2)
D_i - Isolator diameter (circular bearing)	39.5”	35.5”
B_i - Equivalent isolator dimension (square)	35”	31.5”
H_i - Total isolator height	20”	15”
t_i - Isolator height (rubber and steel sheets)	16.5”	12”
t_r - Total rubber thickness	14”	10”
K_d - Rubber characteristic stiffness	10 kip/in	10 kip/in
D_{max}- Maximum displacement	26”	22”
τ_y - Shear yield strength	1200 psi	1200 psi
D_L - Lead plug diameter	10”	10”
Q_d - Isolator characteristic strength	100 kip	100 kip
σ_i - Isolator pressure	750 psi	930 psi
σ_{max} - Isolator maximum pressure	1400 psi	1300 psi

The maximum displacement of the bearings D_{max} specified in the design manuals correspond to approximately 250% shear strain of the minimum height bearings available for a specific diameter size. The bearings selected for bridges BI1 and BI2 were defined with a larger height and therefore the specified D_{max} correspond to 160 and 180% shear strain, respectively. For this study, the maximum displacement of the bearings corresponding to failure was defined at 300% shear strain and is equal to 49.5” and 36.0” for BI1 and BI2 bridges, respectively.

Despite having reduced force demand on the column bents with the addition of the isolation system, the column foundations were not redesigned with respect to the RC bridge for simplicity. The design of the bent cap beam included checks for flexure, shear, and torsion.

4.3.4 Final Design

The final dimensions of BI1 and BI2 bridge columns were increased with respect to the preliminary design based on the nonlinear time history analysis results of the bridge to promote elastic behavior in the first case and obtain the desired ductility demand levels in the second case for the high seismic hazard level considered in this study (see Section 4.3.7). The longitudinal and transverse reinforcement ratios were unmodified with respect to the preliminary design. The final design results of BI1 and BI2 bridge columns are presented in Table 4-8. The final design of the LRB isolators required an initial elastic stiffness K_e and post-yield hardening slope K_d of 50 and 5 kip/in, respectively. The remaining dimensions and parameters of the isolation systems used for BI1 and BI2 bridge models were the same as the ones obtained from the preliminary design procedure.

Table 4-8 Summary of final design results for the isolated bridge columns

Parameter	RC Fixed-base (μ_d=5)	BI1 Isolated (μ_d=1)	BI2 Isolated (μ_d=2)
D_{col} - Column diameter	4’	5.0’	4.25’
H_{col} – Total column height	22’	20.3’	20.75
ρ_l - Longitudinal reinforcement	0.02 (28#10)	0.03 (34#14)	0.03 (40#11)
ρ_s – Transverse reinforcement	0.016 (#7@3.5)	0.015 (#8@3.5”)	0.015 (#8@4”)
K_d - Rubber post-yield stiffness	-	5 kip/in	5 kip/in
K_e – Isolator elastic stiffness	-	50 kip/in	50 kip/in

4.3.5 Finite Element Model

The OpenSees model of the isolated bridges included several additional elements, in comparison to the RC bridge, corresponding to the isolation bearings underneath the superstructure as well as top and bottom bent cap beams connecting the superstructure, bearings and column bents, as shown in Figure 4-21. Similar assumptions and modeling scheme were used for both alternatives of the isolated bridge designed for either elastic (BI1 bridge) or inelastic (BI2 bridge) column response.

The column nonlinear model of the BI bridges consisted of a distributed plasticity fiber model with similar fiber discretization as the RC bridge column with cross sectional dimensions and reinforcement details as defined in Table 4-8. The superstructure model was the same to the one used for the RC and FRC bridges, consisting of an elastic beam-column element with effective cross section properties.

The system of rigid links and top and bottom cap beams connecting the superstructure, column bents and elastomeric bearings were defined according to the centerline location of these different elements and the spacing of the LRB isolators. The spacing of the isolators was determined in accordance with their dimension and the superstructure bottom flange width, allowing for clear distance from the deck edges. The rigid links length connecting from the top and bottom cap beams centerline to the bearings included the thickness of the steel end plates of the LRB isolators. The top and bottom cap beams were modeled as elastic beam-column elements with effective cross section properties. The torsional inertia of the top bent cap was significantly increased (J_{eff}=$10^2 J_g$) to account for the monolithic construction of the superstructure and the cap beam system (Aviram *et al.* 2008b). The dimensions of the top cap beam were therefore consistent with the superstructure cross section. The bottom cap beam was checked for shear, flexure, and torsion resistance. No releases were provided in the model for the superstructure-substructure system. Tributary translational and rotational mass was assigned to each node of the bridge system.

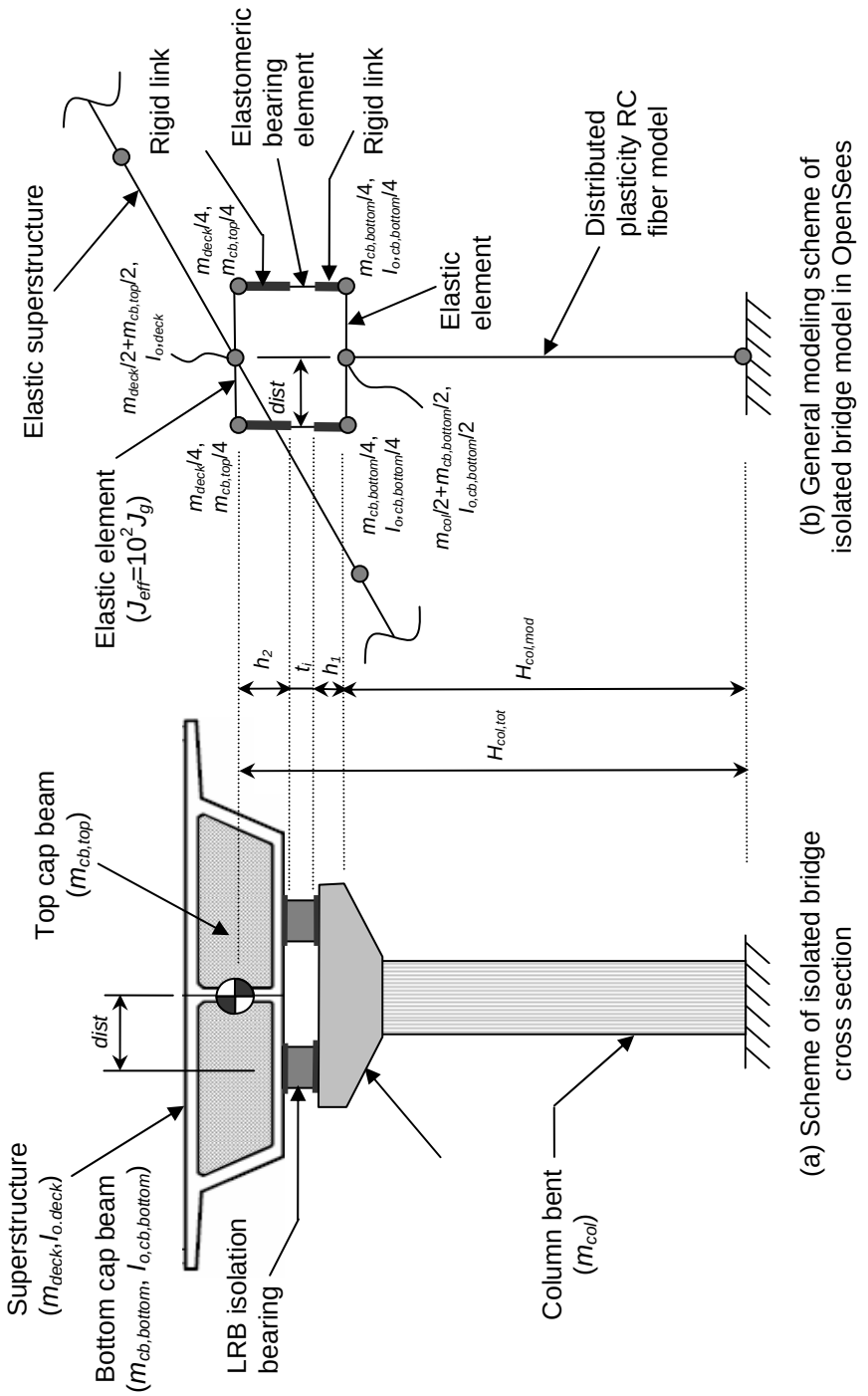

Figure 4-21 Schematic configuration of the isolated bridge models in OpenSees

The LRB isolators were modeled using the e*lastomericBearing* element in OpenSees developed and implemented for this study. The *elastomericBearing* element defines a bilinear response with circular interaction in shear and any uniaxial material behavior for the remaining degrees of freedom. The parameters used to define the bilinear behavior of the bearings correspond to the design values provided by the manufacturer (Dynamic Isolation Systems 1997)

and are presented in Table 4-7. No reduction in the shear resistance was considered for the bearings for low levels of axial loads, i.e., axial load ratio of the isolator with respect to its critical buckling load not exceeding a value of 0.3 (Kelly 1997). The *elastomericBearing* element used for the isolated bridge models was defined with a finite length corresponding to the actual height of the bearing (t_i) including the total rubber and steel sheets thickness and excluding the steel end plates thickness. P-Delta considerations are included for this element if a finite-length segment is used in the model. Linear-elastic material behavior was used to define the axial, torsional and rotational stiffness of the LRB bearings (see Appendix D). The axial stiffness was defined as the compression stiffness of the bearing (K_v) according to the design values provided by the manufacturer (Dynamic Isolation Systems 1997). The rotational stiffness (K_θ) and torsional stiffness (K_T) were approximated following the recommendations by Kelly (1997).

The abutment model implemented for the isolated bridges in OpenSees, denoted as the Isolator Abutment model was similar to the Spring Abutment model used for the RC bridge (see Figure 4-22). The uncoupled elastomeric bearings were replaced by the *elastomericBearing* element in OpenSees which includes circular interaction in shear. In this case, a zero-length *elastomericBearing* element was used to define the isolator behavior. A total of three isolators were specified for the abutment model underneath each web of the box-girder superstructure. Despite having a lower axial load at the superstructure ends due to shorter tributary length, the isolator devices defined for the abutment model were similar to the ones used for the piers, assuming uniform displacement demand at all these locations. The shear capacity of the isolators at the abutments was defined as 2/3 of the capacity of the isolators at the piers (since three isolators are used instead of two, respectively) to obtain similar shear strength at all these locations. The bilinear behavior in shear and the stiffness values for the remaining degrees of freedom were defined similarly as for the peer isolators (see Table 4-7).

To allow lateral displacement of the deck, the size of the longitudinal gap was increased and an additional compression-only gap was provided in the transverse direction. The size of the gap was equal in both directions and was defined according to the maximum lateral displacement specified for the isolators (D_{max}) and the minimum clearances recommended by Buckle *et al.* (2006). The final gap size of bridges BI1 and BI2 abutment models was defined at 26” and 22” corresponding to 160% and 180% shear strain, respectively. The failure of the bearings was not defined in the model since it would only occur at very high displacement demands of 49.5” and 36.0” for bridges BI1 and BI2, respectively, following the failure of the shear keys and the embankment soil.

The gap in the longitudinal direction was modeled in OpenSees using the *ElasticPPGap* uniaxial material with compression-only properties. The shear keys and embankment mobilization in the transverse direction interacts with the superstructure and contributes to the shear resistance only following gap closure. The gap-shear key system was modeled in OpenSees using the *Hysteretic* uniaxial material. The tri-linear *Hysteretic* material was defined with an initial gap (i.e., zero initial stiffness up to gap closure), followed by the shear key stiffness up to ultimate shear key strength, and a final vertical degrading slope corresponding to the failure of the shear keys. The shear key behavior was similar to the one defined for the Spring Abutment model.

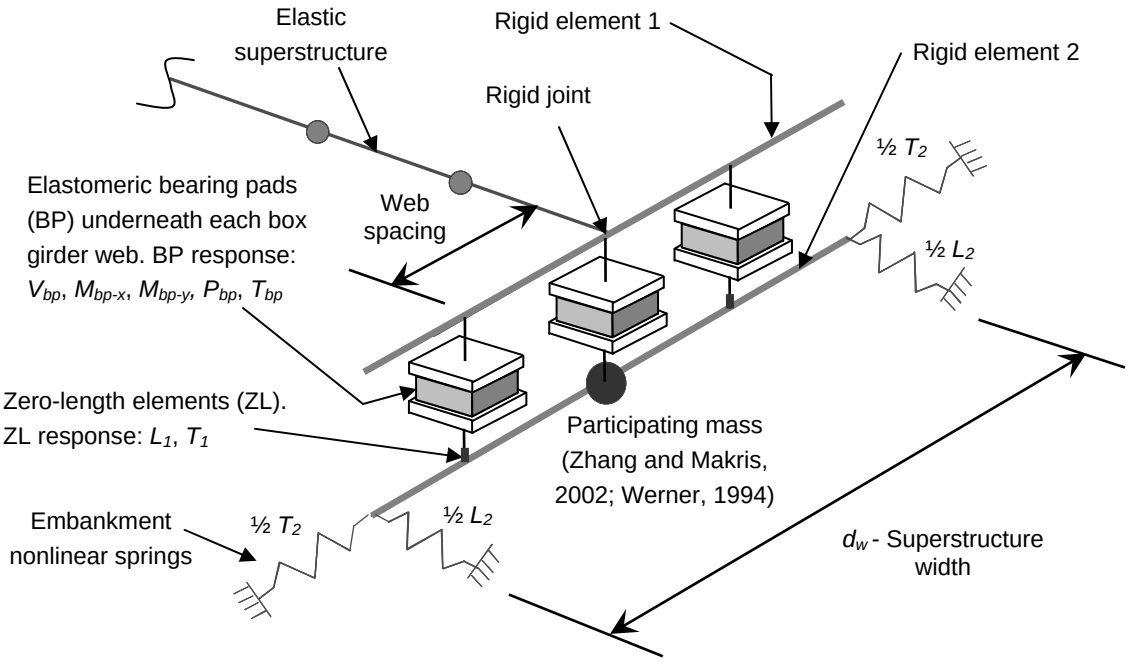

Bearing pads response:

- Shear V_{bp}: BP shear resistance with bilinear behavior and circular interaction.
- Axial P_{bp}: BP elastic vertical stiffness and embankment vertical stiffness in series.
- Moment M_{bp}: BP elastic uncoupled biaxial bending resistance.
- Torsion T_{bp}: BP elastic torsional stiffness.

Zero-length element response:

- Longitudinal L_1: Backwall compression-only gap element.
- Transverse T_1: Brittle shear keys (extreme ZLs only) in series with compression-only gap modeled using a tri-linear behavior.

Embankment response:

- Longitudinal L_2: SDC backbone curve.
- Transverse T_2: Modified SDC backbone curve.

Figure 4-22 General scheme of the Isolator Abutment model

The pushover curves for longitudinal and transverse Isolator Abutment response, as well as the pushunder response, are presented in Chapter 5. A comparison of the Isolator Abutment model used for the isolated bridges and the Spring Abutment model used for the RC and FRC bridges is presented in Chapter 5.

4.3.6 Basic Dynamic Properties

The modal periods of the nonlinear isolated bridge models in OpenSees are presented in Table 4-9 and Table 4-10 for bridges BI1 and BI2, respectively. The modal periods were obtained for the initial state of each nonlinear time history analysis where the column is uncracked (pre-earthquake period) and for the final state of each record where the column is cracked according to the number and intensity of cycles in the nonlinear range of response (post-earthquake period).

As observed in Table 4-2, Table 4-9, and Table 4-10, due to the relatively high initial stiffness of the LRB isolation bearings before yield point, the elongation in the period of the isolated bridges was not very pronounced compared to the fixed-base RC bridge. The pre-

earthquake transverse and longitudinal translational modal periods were increased by 60 and 120% for the isolated bridges, compared to the fixed-base bridge. However, during the dynamic analysis, the yielding of the bearings at early stages of each seismic excitation produced a significant reduction in the overall stiffness of the bridge and correspondingly an even greater shift in the translational modal periods of the bridge.

The effectiveness of the isolation system was evident given the similarity between the pre-earthquake and post-earthquake periods obtained for the bridge systems, indicating that no significant degradation in the stiffness or strength of the nonlinear column model has occurred during the dynamic excitation, even for a high intensity ground motion. The ground motion selected for this comparison is the B-ICC record from the LMSR bin (see Appendix E) with a scale factor of 2.0 and a combined peak ground velocity (PGV) of 123.56 cm/sec (48.65 in/sec), representing a relatively high intensity ground motion. This behavior was observed for the complete ground motion set used for the nonlinear dynamic analysis of the bridges.

Table 4-9 Modal periods (sec) of BI1 bridge obtained from OpenSees

Mode	RC bridge		BI1 bridge	
	Pre-EQ	Post-EQ (B-ICC)	Pre-EQ	Post-EQ (B-ICC)
Transverse translation	0.95	1.15	1.42	1.66
Longitudinal translation	0.53	0.62	1.04	1.06
Global torsion	0.56	0.63	1.02	1.04
Horizontal out-of-plane deck deformation (C-Shape)	0.46	0.47	0.73	0.74
Vertical in-plane deck deformation (W-shape)	0.40	0.41	0.52	0.52

Table 4-10 Modal periods of BI2 bridge obtained from OpenSees

Mode	RC bridge		BI2 bridge	
	Pre-EQ	Post-EQ (B-ICC)	Pre-EQ	Post-EQ (B-ICC)
Transverse translation	0.95	1.15	1.51	1.55
Longitudinal translation	0.53	0.62	1.16	1.17
Global torsion	0.56	0.63	1.03	1.03
Horizontal out-of-plane deck deformation (C-Shape)	0.46	0.47	0.73	0.73
Vertical in-plane deck deformation (W-shape)	0.40	0.41	0.52	0.53

Figure 4-23 presents the global torsion mode shape of isolated bridge BI1 obtained from OpenSees structural analysis program. The pushover curves of the column bents, abutment model and complete bridge system, as well as the nonlinear dynamic time history analysis results for bridges BI1 and BI2 are presented in Chapter 5.

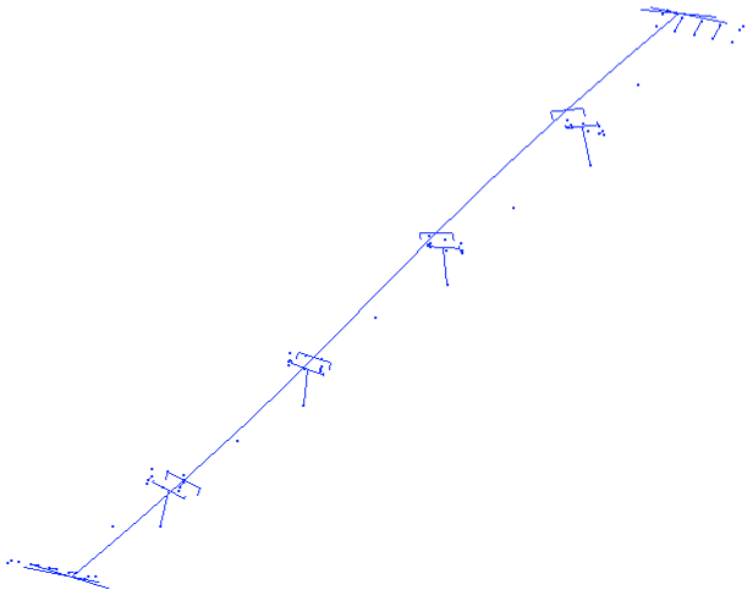

Figure 4-23 Global torsion mode shape of BI1 bridge recorded in OpenSees

4.3.7 Effectiveness of Isolation System

The effectiveness of the isolation system selected for this study in uncoupling the superstructure from the horizontal components of earthquake ground motions and reducing the force and displacement demand on the substructure is demonstrated through the following plots (see Figure 4-25 through Figure 4-29). Selected results obtained from a nonlinear time history analysis of the external column bent and isolation system of BI1 bridge are presented. The B-ICC record of the LMSR ground motion bin with a PGV of 123.56 cm/sec (48.65 in/sec) was used for this illustration due to its relatively high seismic intensity.

The displacement and drift time history analysis of the external column top of both the fixed-base RC bridge and isolated bridge BI1 are presented in Figure 4-24 and Figure 4-25, respectively. In the fixed-base RC bridge model the column top coincides with the centroid of the superstructure while in the isolated bridges the superstructure and column top are separated through the isolation system and cap bents. Therefore, the difference between the superstructure and column top displacement in the isolated bridges corresponds to the shear deformation of the isolation bearings connecting these elements. The peak displacement demand on the superstructure of BI1 bridge for the selected ground motion was over 2.9 and 1.3 times higher than the RC bridge peak displacements for the longitudinal and transverse directions, respectively, due to the increased flexibility of the bridge and the shift in the translational modal periods. However, the peak displacement demand and residual displacement of the column top of BI1 bridge were reduced by over 85% and 90%, respectively, compared to the fixed-base RC bridge. For this strong ground motion the RC column yielded, resulting in ductility demands of 2.7 and 4.0 for the longitudinal and transverse directions, respectively, while the BI1 column remained elastic for the entire time history. The comparison of the displacement time history of the RC and BI1 columns illustrates the high efficiency of the isolation bearings in reducing column lateral deformations and damage.

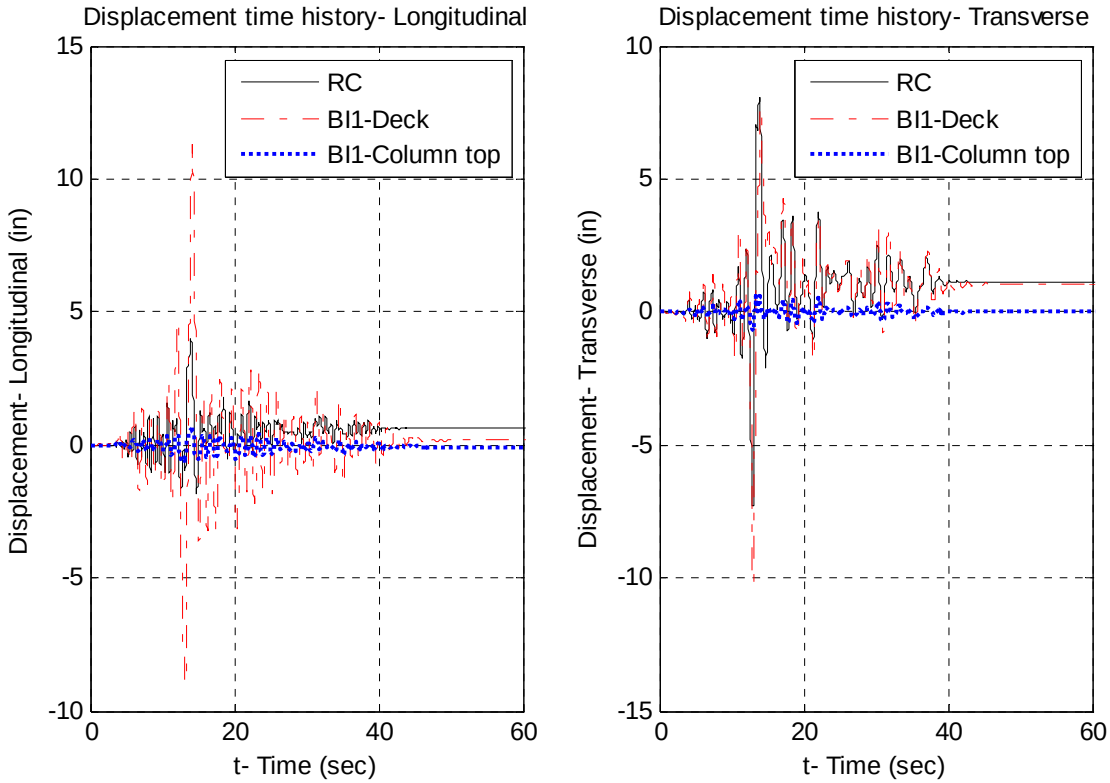

Figure 4-24 Displacement time history of BI1 and RC bridges, B-ICC record

Since the isolated bridge design must accommodate the isolation devices underneath the superstructure while maintaining the same total height of the bridge, the resulting column height of these bridges is shorter than the RC bridge. Due to this shorter column height, the drift demand on the columns was not reduced with respect to the fixed-base RC bridge at the same measure as the displacement demand (see Figure 4-24 and Figure 4-25). Nonetheless, the column drifts predicted for the isolated bridge model were still significantly lower than the RC bridge and do not exceed the yield point of the column.

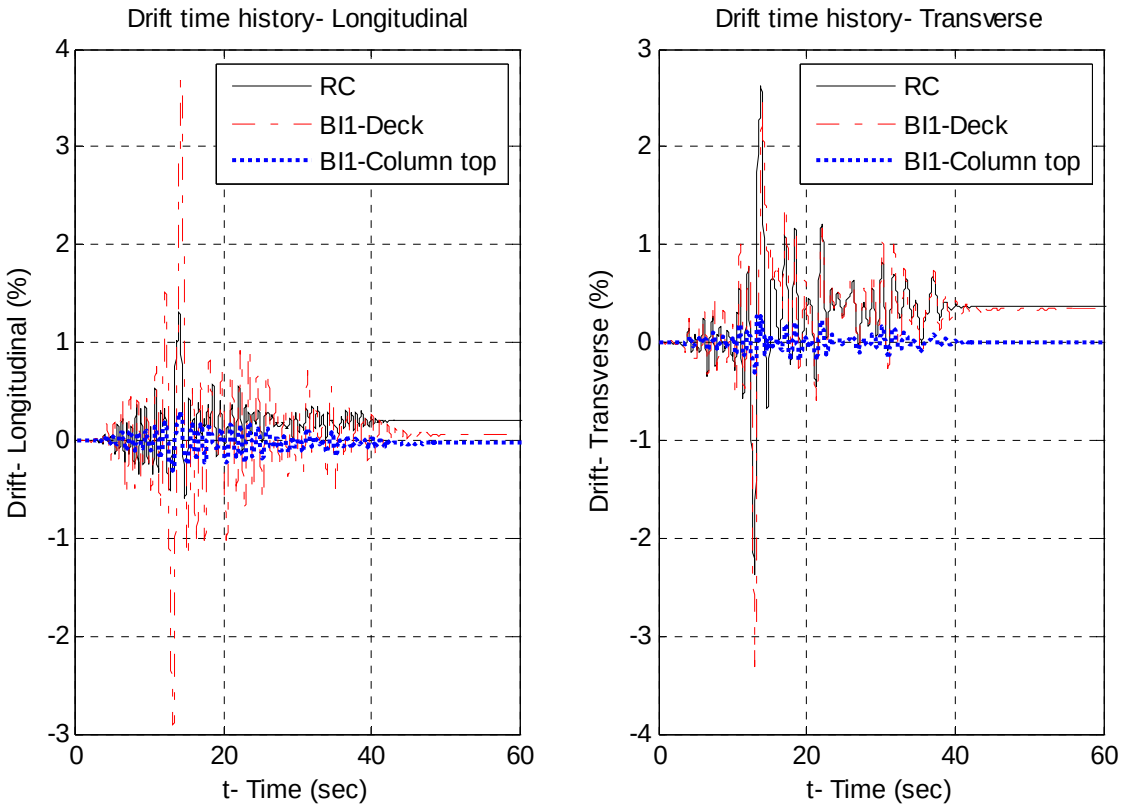

Figure 4-25 Drift time history of BI1 and RC bridges, B-ICC record

The column shear time histories for RC and BI1 bridges are presented in Figure 4-26. Clearly, the isolation system acting as a response modification technique was not as efficient in reducing column shear demands as it was reducing column displacement demands. For this particular ground motion, the column shear of BI1 bridge was merely reduced by around 30% for both the longitudinal and transverse directions, with the isolation and uncoupling of the massive superstructure. This outcome is primarily due to the shape and spectral values of the ground motion acceleration response spectra in the range of the RC and BI1 fundamental periods. For a particular ground motion, the response spectrum does not have a smooth but highly irregular shape with numerous peaks and valleys, which in this particular case resulted in similar pseudo-spectral acceleration values for both the RC and BI1 bridges. The mass of both bridges structures can be considered equal due to the high contribution of the superstructure mass. Despite having a significantly lower lateral stiffness relative to the columns, the isolators can still impart a considerable shear force to the columns.

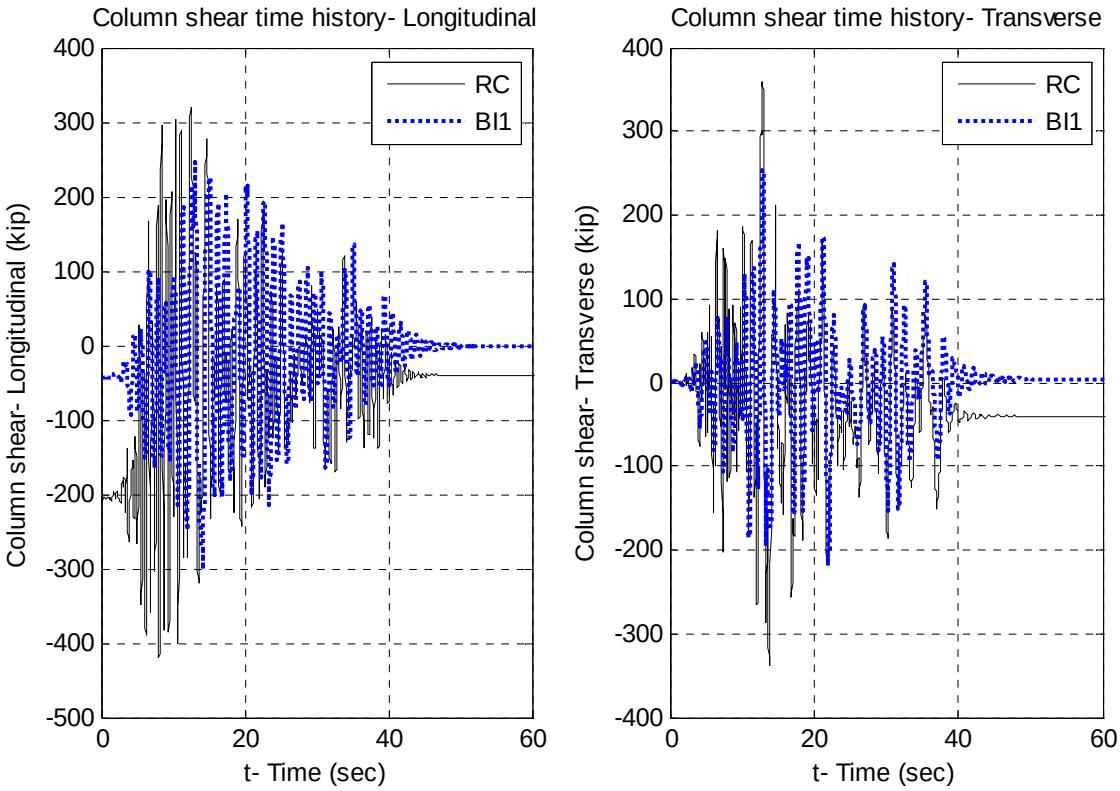

Figure 4-26 Column shear time history of BI1 and RC bridges, B-ICC record

The hysteretic loops of the bearings presented in Figure 4-27 show a stable hysteresis with hardening behavior beyond their yield point. The significant shear flexibility and deformation of the bearing allows for the uncoupling of the bridge massive superstructure from the horizontal components of the ground motion thus reducing the force and deformation demand of the vulnerable substructure. The shape of the hysteretic loops clearly illustrates the elastic and post-yield hardening slopes as well as the circular interaction in shear defined between the orthogonal directions of the bearings.

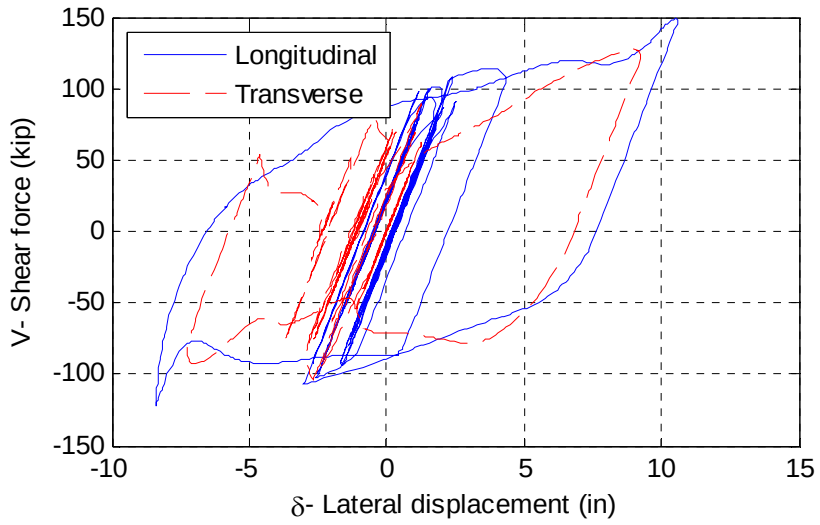

Figure 4-27 Hysteretic loops of BI1 external column bearings, B-ICC record

The circular interaction defined for the horizontal shear resistance of the bearings is observed through Figure 4-28. The interaction surface of the bearing does not resemble a perfect circle due to the post-yield hardening properties defined for the bilinear behavior of the bearings in shear.

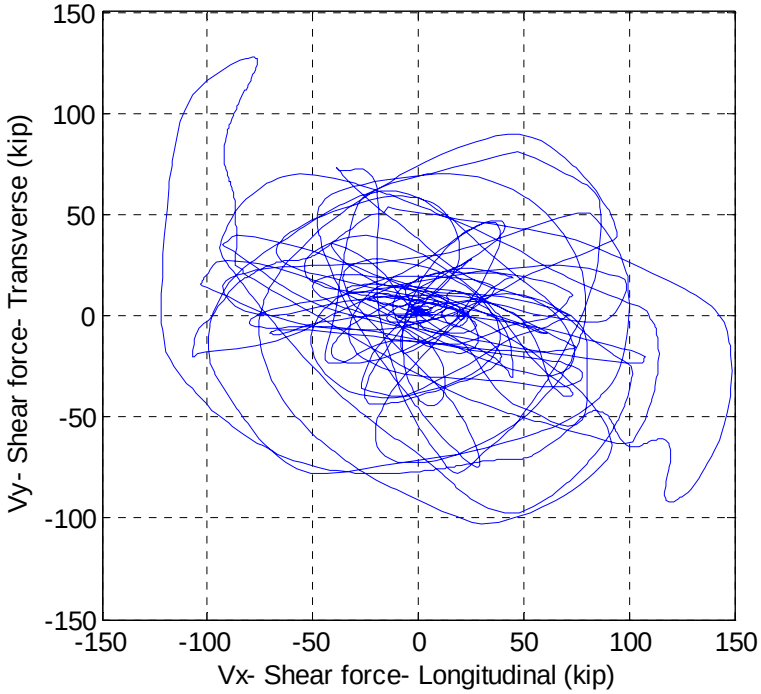

Figure 4-28 Interaction surface of BI1 external column bearings, B-ICC record

The variation of the axial in the isolation bearings of the external column of BI1 bridges is presented in Figure 4-29. Clearly, the bearings remained in compression throughout the entire time history analysis and did not experience uplift forces which could affect their shear

resistance. Also, since the axial compression load ratio of the bearing with respect to its buckling load did not exceed a value of 0.3 for all the ground motions considered, the reduction in the shear resistance of the bearings was negligible (Kelly 1997). The bearing axial load ranged for the B-ICC record from $0.07P_n$ to $0.12P_n$, where P_n is the maximum axial compressive capacity of the fixed-base RC bridge column. This corresponds to a variation in the column axial load between $0.15P_n$ and $0.25P_n$ for the selected ground motion. The axial load on the bearing was monitored in the BI1 and BI2 bridges for all the ground motions used in this study, ensuring bearing uplift forces and tension failure did not occur.

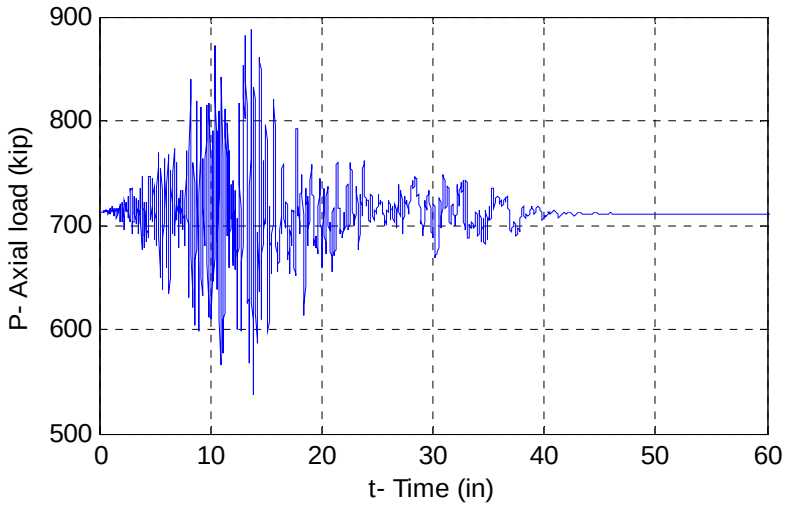

Figure 4-29 Axial load time history of BI1 external column bearings, B-ICC record

5 Bridge Seismic Response

The following section presents the main results obtained from nonlinear static and dynamic analyses carried out in OpenSees for the different bridge systems considered in this study. Pushover curves displaying individual column, abutment, and global bridge response in the longitudinal, transverse, and vertical directions of the bridges are compared. Regressions on major engineering demand parameters obtained from nonlinear time history analyses of the bridges are carried out to provide guidelines for design engineers for the selection of specific and improved design goals and seismic response estimates.

5.1 PUSHOVER ANALYSIS

A pushover analysis was carried out for the RC, FRC, BI1, and BI2 bridge systems considered in this study to evaluate their stiffness and strength at different displacement demand levels, and assess their ductility capacity for each principal direction of loading. The displacement demand used in the longitudinal, transverse and vertical directions was determined iteratively to capture the degrading behavior of each bridge system, and a uniform force pattern was applied on all deck nodes. The longitudinal and transverse pushover, as well as the vertical pushunder response of the individual columns, abutments, and complete bridge systems is discussed separately in the following paragraphs to offer a thorough breakdown of the differences between the selected bridge systems.

5.1.1 Column Response

The longitudinal and transverse pushover curves of an individual external column in the different bridge systems are presented in Figure 5-1 and Figure 5-2, respectively. The principal results of these analyses are summarized in Table 5-1.

Table 5-1 Summary of longitudinal and transverse pushover analysis results for external column response

Parameter	RC	FRC	BI1	BI2
$\delta_{y,L}$- Longitudinal yield displacement (in)	1.5	3.0	1.9	2.1
$\delta_{y,T}$- Transverse yield displacement (in)	2.0	5.0	1.8	2.1
$V_{col,L}$- Longitudinal column shear (kip)	395.0	485.8	487.2	305.6
$V_{col,T}$- Longitudinal column shear (kip)	387.0	478.2	655.6	615.4
$\mu_{d,L}$- Longitudinal displacement ductility	10.3	5.1	4.6	5.2
$\mu_{d,T}$- Transverse displacement ductility	8.5	3.6	4.5	5.9

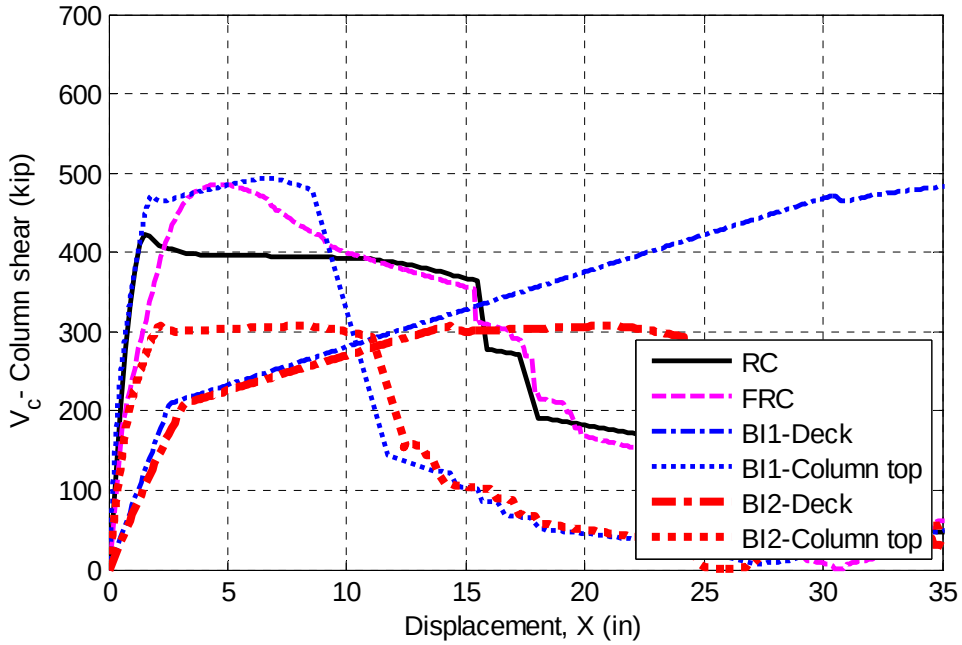

Figure 5-1 Longitudinal pushover curve of individual external column for different bridge types

The initial stiffness of the column in the longitudinal direction representing the uncracked concrete behavior at low displacement demand levels is similar for all bridge systems, despite important differences in the boundary conditions at the column top and the effective column height for the isolated bridge systems, and enhanced concrete material properties for the FRC bridge. The steel reinforcement properties used in the analytical fiber models of the isolated bridge columns are the same as for the RC bridge system. The yield displacements of the different bridge types are therefore relatively comparable. A lower elastic stiffness of the steel reinforcement was defined for the FRC bridge according to experimental results (see Chapters 2 and 3), thus resulting in a significantly higher yield displacement in both longitudinal and transverse directions of the bridge.

The boundary conditions in the longitudinal direction of the column bent top and bottom are similar to fixed-fixed conditions for the RC and FRC bridges due to the relatively high flexural stiffness provided by the superstructure and the frame action. The resulting column bent shears corresponds to the formation of plastic hinges at the top and bottom of the column bents

deforming in double curvature ($V_{col}=2M_{p,col}/H_{eff}$). The pushover curves in Figure 5-1 representing column response present a single yield point for each bridge type due to the simultaneous formation of the top and bottom plastic hinges followed by a yielding plateau and degrading behavior once the corresponding ductility capacity is reached. Conversely, the boundary conditions at the top and bottom of the isolated bridges do not represent fixed-fixed conditions due to the flexibility of the LRB isolators - bent cap beam system in the longitudinal direction of the bridge. The column deforms as a cantilever without any significant rotational resistance at the column top. The column shear of the isolated bridges corresponds to the formation of a single plastic hinge at the column base ($V_{col}=M_{p,col}/H_{eff}$).

The FRC column which presents higher concrete strength results in approximately 25% higher peak strength compared to the RC column, in both the longitudinal and transverse directions. However, according to the calibrated FRC bridge model results, the ductility capacity of the FRC column is reduced from approximately 10.3 to 5.1 in the longitudinal direction and from 8.5 to 3.6 in the transverse, compared to the RC column, due to the fiber-reinforced concrete ductility and material characteristics. Nonetheless, the ultimate displacement capacity of the FRC column is maintained compared to the RC bridge column while the elastic limit is extended. Thus, the initiation of permanent damage is delayed in the FRC bridge and its ultimate displacement capacity is preserved.

The BI1 and BI2 columns with a diameter of 5’ and 4.25’, respectively, present a higher cross-sectional area than the RC column with 4’ diameter. The longitudinal reinforcement ratio of the isolated bridge columns of 3.0% is also higher than the RC reinforcement ratio of 2.0%. The concrete material properties used for the column fiber models are the same for the RC, BI1, and BI2 bridges. Despite the increased gross cross-sectional area and longitudinal reinforcement ratio and distribution, the ductility capacity of BI1 and BI2 bridge columns present a reduced ductility capacity of 4.6 and 5.2, respectively, compared to the displacement ductility capacity of 10.3 of the RC column, due to the reduced height of these column bents. However, due to the effectiveness of the isolation system, the displacement demand on the column bents in these bridge structures and the corresponding structural damage of these elements is expected to be minimal, therefore their reduced ductility capacity is insignificant. The resulting maximum strength of the BI1 and BI2 bridge columns is approximately 25% higher and lower than the RC column strength, respectively.

The pushover curves monitoring the displacement at the superstructure or deck level of the bridges illustrate the behavior of the LRB isolators located between the deck and column bents. For both isolated bridges, the estimated elastic stiffness, yield strength, and post-yield hardening slope were defined with the same values. As seen in Figure 5-1, the idealized initial stiffness of the LRB isolators is lower than the corresponding column bent stiffness and at the initial stages of the pushover analysis, the displacement monitored at the deck level is approximately 3 times higher than the displacement of the column top. Once the LRB isolators reach their yield strength at a combined force of approximately 200 kip (see Chapter 4), the posterior post-yield response is significantly more flexible than the column bents response. The shear deformation of the isolators corresponds to the difference between the superstructure and column top displacements. This increased flexibility of the bridge superstructure with respect to the column base results in reduced displacement and force demands on the column bents and increased demand on the LRB isolators, for a given level of seismic intensity. Since the LRB isolators are designed for such high deformation and force demands, the resulting response of the

isolated bridges will therefore be ductile and stable, and present considerable energy dissipation capabilities.

Clearly, since the BI1 bridge column was designed to remain elastic throughout the entire range of seismic intensity, the moment and shear capacity of the column is higher than the RC and BI2 bridge columns. The capacity of BI2 bridge column in the longitudinal direction of the bridge is approximately 40% lower than BI1 column strength and will therefore result in higher ductility demands (up to 1.5-2.0 for high seismic intensities). Once the isolated bridge columns reach their peak strength, additional shear force cannot be applied to the deck node above the corresponding column top, and instead both the LRB isolators beneath the superstructure and column top deform according to the column post-yield behavior until degradation of strength occurs in the concrete column.

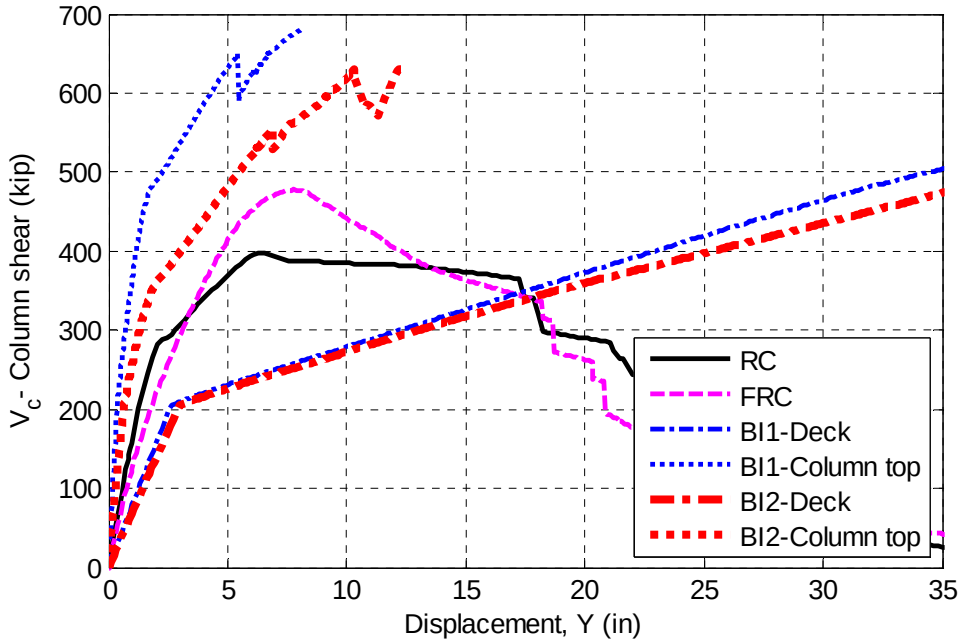

Figure 5-2 Transverse pushover curve of individual external column for different bridge types

The transverse pushover curves of the external column of the different bridge types analyzed are presented in Figure 5-2. The boundary condition at the column top for the RC and FRC bridge systems consists of a semi-rigid rotational spring provided by the out-of-plane stiffness of the superstructure and abutment system. A similar partial fixity is also provided by the LRB isolators-bent cap beam system in the transverse direction for both BI1 and BI2 bridges. The column base presents fixed rotational stiffness for all bridge systems, as in the longitudinal direction. The semi-rigid and fixed boundary conditions of the column top and bottom, respectively, result in two branches of the pushover curve up to peak strength for all the different bridge systems considered. The initial branch of the pushover curve representing the initial stiffness of the column with a behavior similar to cantilever response is followed by a second branch with lower stiffness due to the formation of a plastic hinge at the column base.

The resulting yield displacements in the transverse direction of the RC and FRC bridges are therefore considerably higher than in the longitudinal direction due to the reduced rotational stiffness at the column top (see Table 5-1). In the case of the isolated bridges, the yield

displacement in the transverse direction representing the formation of the first plastic hinge is obtained at similar yield displacement values obtained for the longitudinal direction since both cases represent similar initial boundary conditions and cantilever behavior (see Table 5-1).

The column pushover force-displacement demand continues with the second slope until a second plastic hinge forms at the column top, followed by column degrading behavior once the ductility capacity of the corresponding column is reached. The peak column shear values of the RC and FRC bridge systems in the transverse direction are therefore similar to the longitudinal results due to the formation of plastic hinges at both column top and bottom. The FRC column shear is nearly 25% higher than the RC column.

The peak shear values of the initial slope of the column response of 482.5 and 364.7 kip for bridges BI1 and BI2, respectively, correspond to the formation of the first plastic hinge at the column base and are similar to the corresponding peak shear values obtained for the longitudinal pushover analysis. The overall maximum column shear values of the isolated bridges in the transverse direction are higher than the ones produced in the longitudinal direction due to the formation of a second plastic hinge at the column top. The maximum shear strength of BI1 and BI2 columns in the transverse direction are approximately 70 and 60% higher than the RC column shear, respectively.

The boundary conditions at the column top of the isolated bridges and the reduced column height results in increased stiffness of the column bents in both BI1 and BI2 bridges, in comparison to the RC bridge column. The initial elastic slope of FRC bridge model is also lower than the RC bridge due to calibrated steel material behavior defined according to experimental results. The displacement ductility capacity of the column bent is reduced from 8.5 for the RC bridge to 3.6, 4.5, and 5.9 for the FRC, BI1, and BI2 bridge columns, respectively. Since the column response in the isolated bridge models is designed to have minor ductility demands even for high seismic intensity, the reduction in the ductility capacity in the transverse direction is irrelevant. For the FRC bridge, the initiation of damage is delayed due to a higher elastic limit, while the ultimate displacement capacity of the bridge is preserved; thus, the reduction in the ductility capacity of the FRC bridge column in comparison to the RC bridge is also of no negative consequence to bridge performance.

As in the longitudinal direction, the LRB isolators in parallel reach their yield point at a combined force of approximately 200 kip and provide a significant flexibility to the bridge system through stable shear deformations beyond that point. The idealized elastic and post-yield behavior of the isolation bearings in both BI1 and BI2 bridges are defined with equal values and therefore the pushover curves monitoring the deck or superstructure node result in similar shapes for both isolated bridges. The shear deformation of the bearings at a given force demand level corresponds to the difference between the superstructure and column top displacements which are hugely increasing with increased force or displacement demand on the bridge system.

Despite higher force demands on the FRC bridge column due to increased material strength, the enhanced damage tolerance of the fiber-reinforced concrete material discussed in Chapter 3 results in reduced structural damage and repair efforts, as shown in Chapter 6.

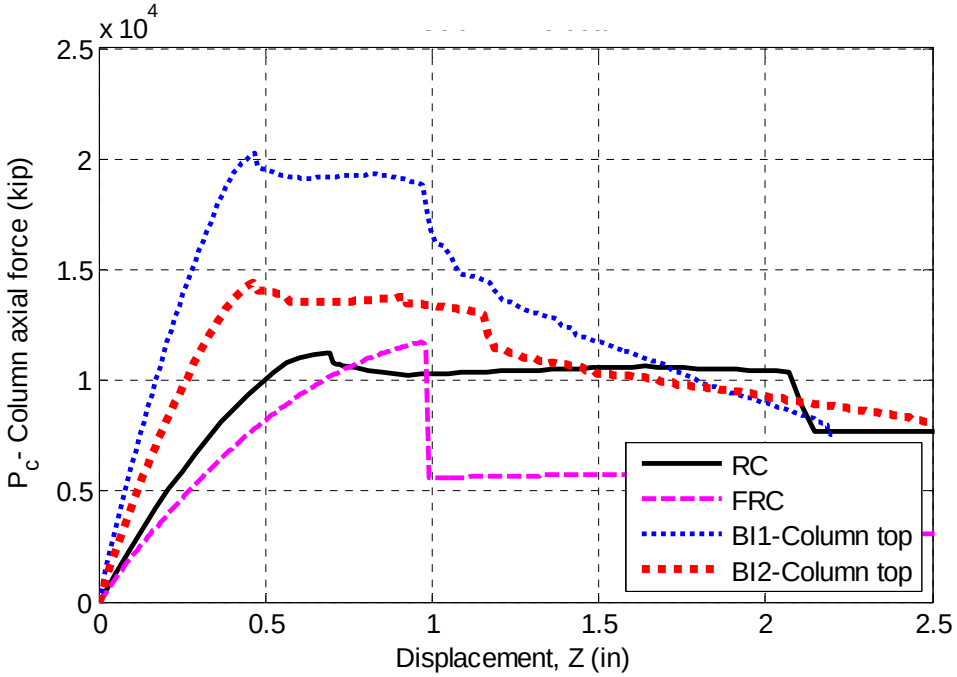

Figure 5-3 Vertical pushunder curve of individual external column for different bridge types

The vertical pushunder response of the column bents is presented in Figure 5-3 for the different bridge systems considered in this study. The pushunder analysis was carried out using a uniform force distribution between the superstructure ends and the column top nodes, for all bridge systems. In the case of the isolated bridges the relative vertical response of the deck with respect to the column top was not considered, assuming the LRB isolators provide adequate stiffness and strength to transfer all vertical motion to the column bents and foundations. For a comparable assessment of the vertical stiffness and strength of the column bent, the monitored point for all the different bridge models corresponds to the column top.

The peak column axial force for each bridge type corresponds approximately to the expected compressive strength of the confined concrete or fiber-reinforced concrete material multiplied by the gross section area of the column. The initial elastic stiffness corresponds to the axial stiffness of the column ($k_v=EA/L$). The RC and FRC bridge columns have the same column height and diameter; however, the elastic stiffness of the steel reinforcement is defined differently in the analytical FRC bridge model thus resulting in different elastic axial stiffness. The column height of BI1 and BI2 bridges is 20.3' and 20.75', respectively, compared to 22' for the RC column. The diameters of BI1 and BI2 bridges were defined with a value of 5' and 4.25', respectively, compared to 4' for the RC bridge. Due to the reduced height and increased diameter of the isolated bridge columns, the resulting axial stiffness of these columns is higher than the RC column stiffness.

5.1.2 Abutment Response

The Spring Abutment model described in Chapter 4 is used for RC and FRC bridge models. The combined longitudinal pushover response of this abutment model assigned to both deck ends is

displayed in Figure 5-4. At the initial stages of the pushover analysis, the lateral resistance of these bridge systems is provided by the shear resistance of the elastomeric bearings with bilinear behavior. Following gap closure on one side of the deck ends defined at 2", the lateral resistance of the abutment backwall and piles are engaged to resist the lateral push. Finally, after the failure of the backwall, the embankment backfill soil with Elastic-Perfectly-Plastic behavior according to Caltrans SDC in series with the previous resistance mechanisms provides the lateral resistance of these bridges in the longitudinal direction.

The combined transverse pushover response of the Spring Abutment model assigned to both deck ends in the RC and FRC bridges is displayed in Figure 5-5. Since no gap is defined in the transverse direction, the lateral resistance of these bridges is initially provided through the shear keys on one side of the push and the shear resistance of the elastomeric bearing pads. After the brittle failure of the shear keys resisting the push, the embankment soil transverse resistance defined with modified Elastic-Perfectly-Plastic behavior according to Caltrans SDC is also engages to resist the lateral pushover.

The total vertical pushunder response of the Spring Abutment model assigned to both deck ends in the RC and FRC bridges is displayed in Figure 5-6. Following the crushing of the 2" thick elastomeric bearings with bilinear behavior in the vertical direction, the high vertical stiffness of the embankment soil is engaged to resist the vertical pushunder.

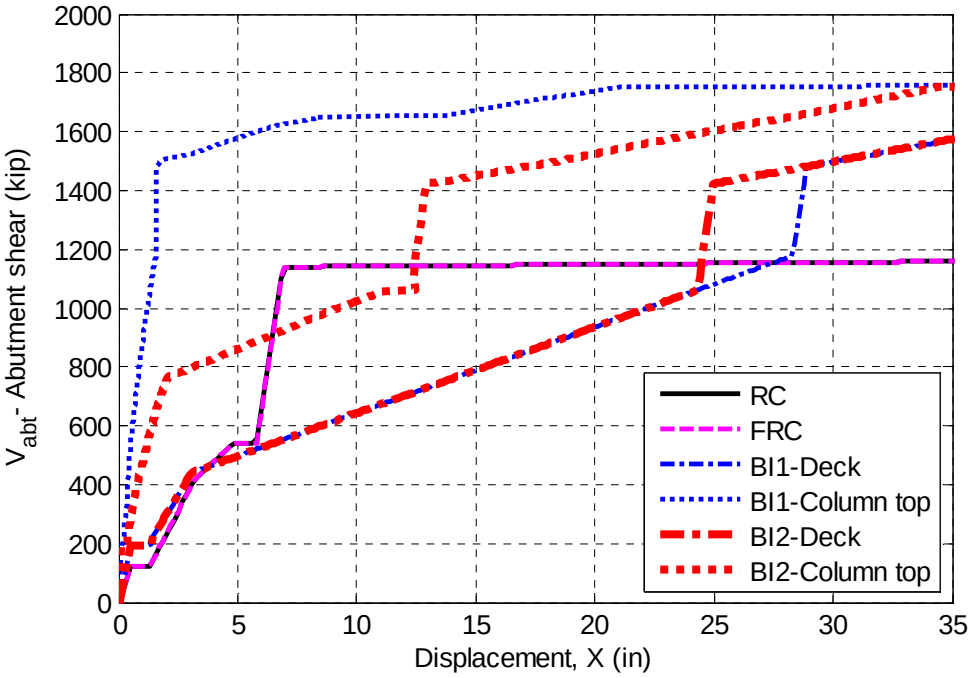

Figure 5-4 Longitudinal abutments response for different bridge types

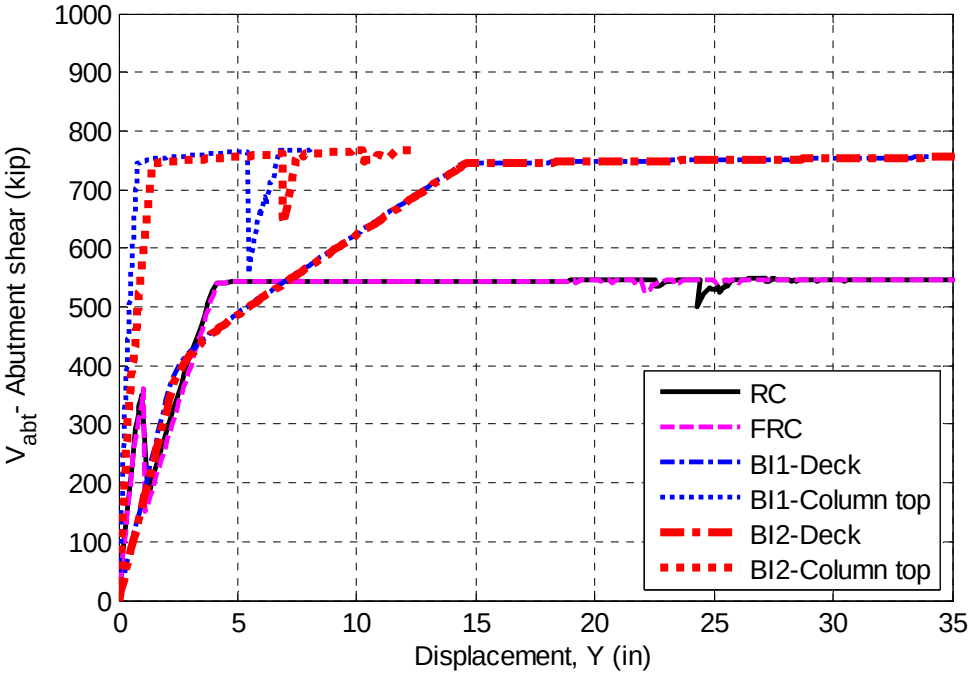

Figure 5-5 Transverse abutments response for different bridge types

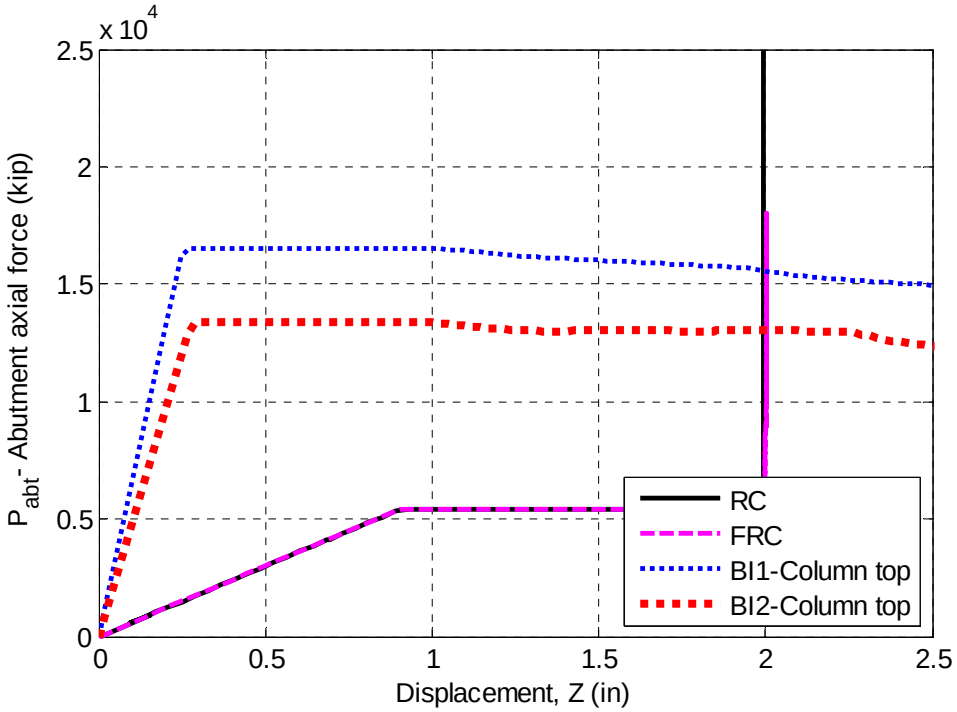

Figure 5-6 Vertical abutments response for different bridge types

The Isolator Abutment model described in Chapter 4 is used for BI1 and BI2 bridge models. Two points in the bridge were monitored to illustrate the lateral pushover response of this abutment model: the deck end node and the external column top node. Three LRB isolators are specified for the abutment model at each deck end under each superstructure web and two

LRB isolators are specified under the superstructure at each column top. Due to this different number of bearings, the shear capacity of each LRB isolator at the abutments is defined as 2/3 the capacity of the LRB isolators at the piers.

The longitudinal and transverse pushover response of the combined Isolator Abutment response at each deck end is observed in Figure 5-4 and Figure 5-5, respectively, through the deck end nodes displacement. The initial lateral stiffness of the bridges is provided by the shear resistance of the LRB bearings in parallel. The bearings at both deck ends yield at a combined force of approximately 400 kip and continue deforming with a post-yield hardening slope K_d of 5 kip/in. The shear interaction of the bearings is displayed in the pushover curves in the transition point between the idealized elastic and inelastic behavior. An initial slip of approximately 2" occurs in the longitudinal direction for all bridge types due to the loss of prestress along the length of the superstructure. Prestress is used in typical reinforced concrete bridge structures to reduce the deflection of the superstructure due to gravity loads. The gap in the longitudinal and transverse directions of BI1 and BI2 bridges is defined at 26" and 22", respectively. However, due to the initial slip of the deck, the bearings must be pushed 28" and 24" for bridges BI1 and BI2, respectively, to close the longitudinal gap.

Following gap closure in the longitudinal direction, the superstructure end is in direct contact with the backwall and embankment soil which resist with increased stiffness the lateral push. After the yielding of the backwall, the bearings continue to resist the lateral load according to the post-yield hardening slope until the plastification of the soil is reached at high displacement demands. The corresponding longitudinal deformation of the column top of bridges BI1 and BI2 is also presented in Figure 5-4. Clearly, the displacement demand of BI1 bridge column designed for elastic response is limited to small values until very high displacement or force demand on the deck end nodes. BI2 bridge column presents a more flexible behavior; however, the displacement demand on the column top is still significantly lower than on the deck ends, preserving the efficiency of the isolation system.

In the transverse direction (see Figure 5-5), the shear keys and embankment stiffness are modeled to resist in series the lateral pushover demand following gap closure. If a smaller gap is defined, the shear keys would present a brittle failure after reaching their maximum capacity, and the bearings would continue to resist through the post-yield hardening shear behavior the lateral push until the ultimate soil capacity is reached and the soil plastifies. However, for this particular bridge response, the soil plastification occurs before gap closure and the shear keys don't fail. This response is presented since the capacity of the embankment soil in the transverse direction is defined as a small fraction of the soil capacity in the longitudinal direction, and the gap size defined for the transverse direction is relatively high.

The specification of a large gap and shear-flexible isolators at the deck ends in both lateral directions of the isolated bridges allows for the free translation of the superstructure and the significant reduction in the displacement demand on the column bents. The efficiency of the isolation system in reducing the force and displacement demand on the substructure in both BI1 and BI2 bridges is evident through the pushover curves in Figure 5-1 and Figure 5-4 for the response longitudinal direction, and in Figure 5-2 and Figure 5-5 for the transverse response.

The total vertical pushunder response of the Isolator Abutment model of bridges BI1 and BI2 is presented in Figure 5-6. The vertical response of the Isolator Abutment model and the Spring Abutment model is similar. The bearings are modeled with bilinear behavior, where the elastic stiffness of 11,000 and 8,000 kip/in for BI1 and BI2 bridges is is defined according to the

DIS design manual. After the crushing of the bearings of 16.5” and 12.0” in rubber height for BI1 and BI2 bridges, respectively, the high vertical soil stiffness is engaged.

5.1.3 Total Bridge Response

The total pushover response of the different bridge systems obtained by summing the shear resistance of all column bents and abutments is presented in Figure 5-7, Figure 5-8, and Figure 5-9 for the longitudinal, transverse and vertical directions, respectively.

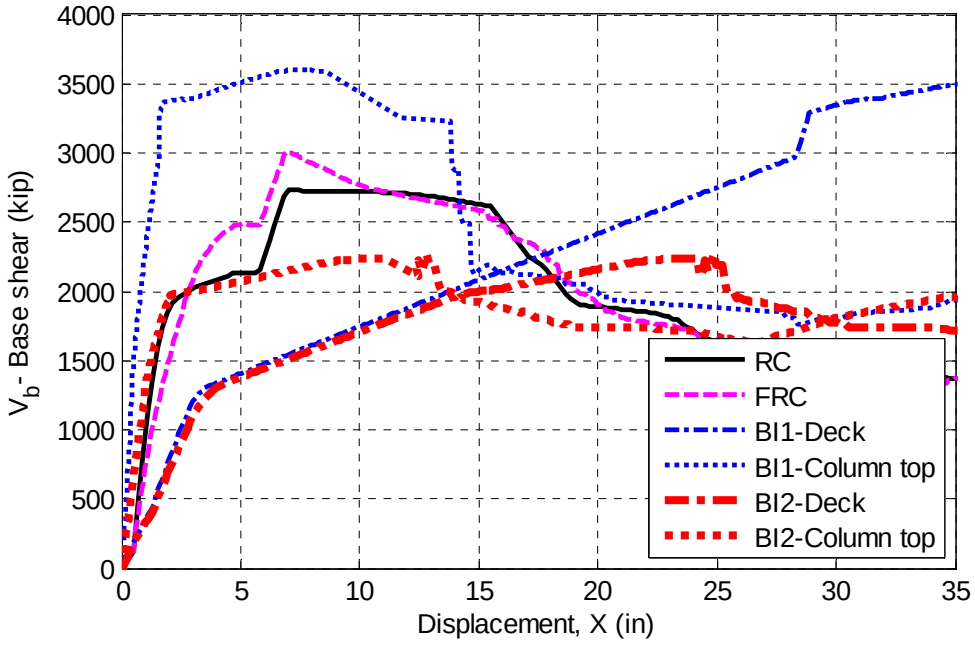

Figure 5-7 Total longitudinal pushover bridge response for different bridge types

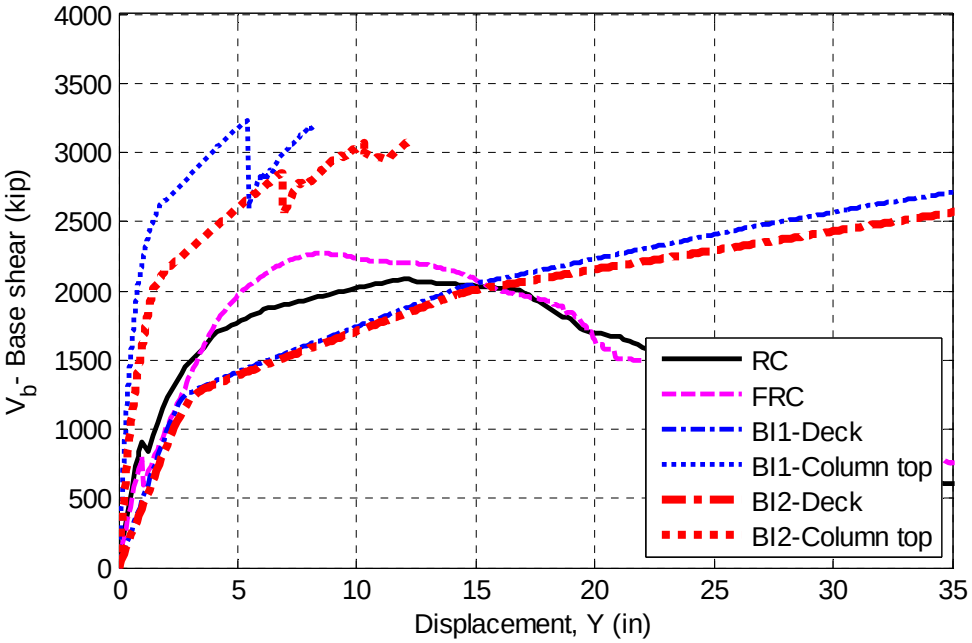

Figure 5-8 Total transverse pushover bridge response for different bridge types

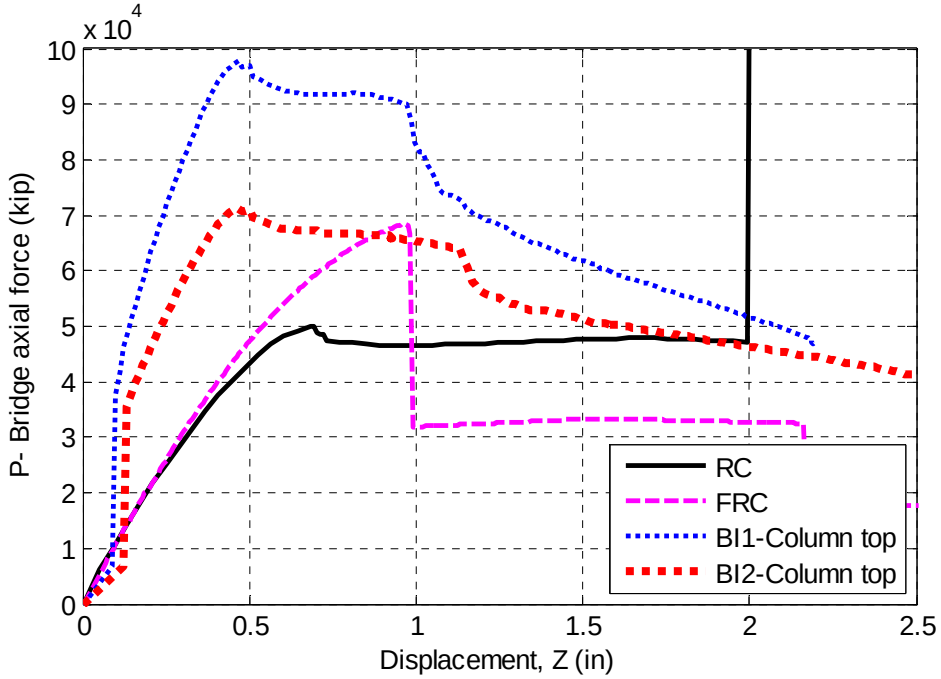

Figure 5-9 Total vertical pushunder bridge response for different bridge types

The overall shape of the pushover curves of the RC and FRC bridges is similar; however, the FRC bridge model results in lower initial stiffness, higher ultimate base shear capacity, and lower ductility capacity in comparison to the RC bridge due to calibrated material properties of the fiber-reinforced concrete columns. The increase in base shear capacity of the FRC bridge compared to the RC bridge is approximately 10% for both the longitudinal and transverse directions, while a substantial increase in the yield displacement is obtained in the order of 100%

and 150% in the longitudinal and transverse directions, respectively. In the vertical direction, the FRC bridge presents approximately 40% higher initial axial capacity than the RC bridge up to the crushing of the bearings. The vertical response of the two bridges beyond this crushing point is similar, with extremely stiff soil behavior.

The overall shape of the pushover curves of the isolated bridges is significantly altered compared to the benchmark RC bridge due to the introduction of the isolation system underneath the superstructure and the corresponding modifications to the abutment model. Observing the longitudinal response of the deck nodes above the column top in the isolated bridges, the increased flexibility of the deck results in a displacement demand over 5 times greater than the RC bridge, for a base shear of up to 2000 kip. The response of the superstructure in both isolated bridges is similar up to this load demand which approximately represent the elastic limit of the RC bridge in the longitudinal direction.

The response of the BI2 bridge columns is similar to the RC bridge column response, up to a load demand of 2000 kip or displacement demand of approximately 6". Beyond this point, in the case of the RC bridge, the backwall and embankment soil resistance is engaged, while in the BI2 bridge, the column plastic hinges are formed at the column base and the shear demand is only increased according to the hardening properties of the reinforced concrete columns. The lateral load degradation initiates when the column top nodes reach a displacement demand of over 10.5", equivalent to the ductility capacity limit of 5.2 estimated for the BI2 column bents. The resulting peak base shear demand of the BI2 bridge is around 20% lower than the RC bridge. Since the BI1 bridge column was designed with a 5' diameter and high reinforcement ratio to remain elastic under severe seismic demand, the response of the bridge observed by monitoring the column top displacement displays a high initial stiffness and high base shear capacity. The superstructure displacement increases significantly compared to the column top through the stable and ductile post-yield shear deformation of the bilinear isolators. Gap closure occurs at a displacement demand of 28" and an increase in the lateral stiffness of the bridge occurs due to the contribution of the concrete backwall and backfill soil resistance. Since the BI1 column reaches its elastic limit at extremely high load and displacement demand, the efficiency of this isolation system design in reducing the demand on the bridge is evident.

In the transverse direction of the bridge, the response of the isolated bridges is significantly different than the RC response. The initial stiffness of the isolated bridge columns is higher than the RC column due to their reduced height and increased cross-sectional dimensions and reinforcement ratios. The transverse response of the isolated bridges is therefore superior to the RC bridge even for low seismic intensity. The displacement of the isolated bridges superstructure is over 30% higher than the RC bridge superstructure response until the elastic limit of the latter bridge. However, this increased flexibility and excessive deformation of the isolated bridges is due to the stable and ductile deformation of the bearings, not the substructure or superstructure deformation. The transverse pushover response of the isolated bridges is similar up to a base shear of approximately 2000 kip corresponding to the yield capacity of BI2 bridge. Beyond that point, the yielding of BI2 column results in a more flexible bridge response than BI1 bridge. The different response of the isolated bridges beyond the yield point of BI2 bridge is not as pronounced in the transverse direction as in the longitudinal, since the reduction in BI1 column height and corresponding yield point is more pronounced in the transverse direction. The limiting base shear value in the transverse direction is reached in the isolated bridges following the plastification of the soil and the brittle failure of the shear keys, not due to the strength degradation of the concrete columns.

The total vertical pushunder response of the isolated bridges is presented in Figure 5-9. Since the seismic demand on bridge systems in the vertical direction is typically not critical, the increased stiffness of the FRC and isolated bridges compared to the RC bridge will not result in a significant reduction of structural or non-structural damage.

5.2 TIME HISTORY ANALYSIS

5.2.1 Seismic Demand and Hazard

5.2.1.1 Ground Motions

Nonlinear time history analysis was carried out for the three-dimensional OpenSees models of the RC, FRC, and isolated bridges BI1 and BI2 using an extended suite of representative ground motions applied uniformly at the base of the bridge structures (see Table 5-2). The general characteristics of the ground motions in each set are presented in Appendix E. The ground motion bins containing 20 records each were selected to cover a wide range of earthquake magnitude and distance to fault, as well as different fault mechanisms. Each record contains three components: two horizontal and one vertical.

Table 5-2 Ground motion sets used in OpenSees bridge models

Bin	Abbrev.	Reference/ source	Mechanisms	SF[5]
Large Moment-Small Distance	LMSR	Medina *et al.*, 2001	RO[1], RS[2], SS[3]	2.0
Large Moment-Large Distance	LMLR	Medina *et al.*, 2001	RO, RS, SS	2.0
Small Moment-Small Distance	SMSR	Medina *et al.*, 2001	R[4], RS, SS	2.0
Small Moment-Large Distance	SMLR	Medina *et al.*, 2001	RO, R, SS	2.0
Highway I-880 Normal to fault	I880n	Sommerville and Collins, 2002a	RO, SS	1.5
Highway I-880 Parallel to fault	I880p	Sommerville and Collins, 2002a	RO, SS	1.5
Van Nuys	VN	Sommerville and Collins, 2002b	RO, R	1.5

[1]RO = Reverse-oblique; [2]RS = Reverse-slip; [3]SS = Strike-slip; [4]R = Reverse; [5]SF = Scale factor

The first four bins in Table 5-2 were obtained from the PEER Strong Motion Database and are characteristic of non-near-field motions (R>15 km) recorded in California. The records in all four bins were separated according to earthquake magnitude: small magnitude (SM) where M<6.5 and large magnitude (LM), where M>6.5. Ground motions with distance to epicenter R between 0 and 30 km were grouped into the small distance (SR) bin, while ground motions with R>30 km were grouped in the large distance (LR) bin. These records are similar to those used by Krawinkler (Medina *et al.*, 2001) in a companion PEER research project related to building

structures. These four sets contain ground motions corresponding to reverse-oblique, reverse-slip, reverse and strike-slip faulting mechanism.

The I880n and I880p record sets were used for the dynamic analysis assuming that the orientation of the transverse axis of the bridge is normal (perpendicular) and parallel to the fault, respectively. Equivalently, the high-intensity fault-normal component is oriented and causes greater shaking in the transverse and longitudinal directions of the bridge for record bins I880n and I880p, respectively. The I880 set obtained from the PEER Strong Motion Database was used for the analysis of the I-880 highway bridge in Oakland, California (Somerville and Collins, 2002a), which suffered a partial collapse during the 1989 Loma Prieta earthquake and was later heavily retrofitted. The set contains ground motions corresponding to strike-slip faulting with near-fault directivity effects.

The Van Nuys record bin containing ground motions corresponding to reverse and reverse-oblique faulting is representative of the Los Angeles area seismicity. This record set was used for the PEER Center VN testbed project (Sommerville and Collins, 2002b), to represent diverse directivity effects and faulting types. The Van Nuys motions were identified as longitudinal and transverse and were therefore applied without modifying their horizontal orientation.

The magnitude-distance combination of all seven ground motion bins used in the dynamic analysis is presented in Figure 5-10. Using this extended ground motions bin the response of the different bridge systems was captured for a wide range of possible seismic scenarios and hazards.

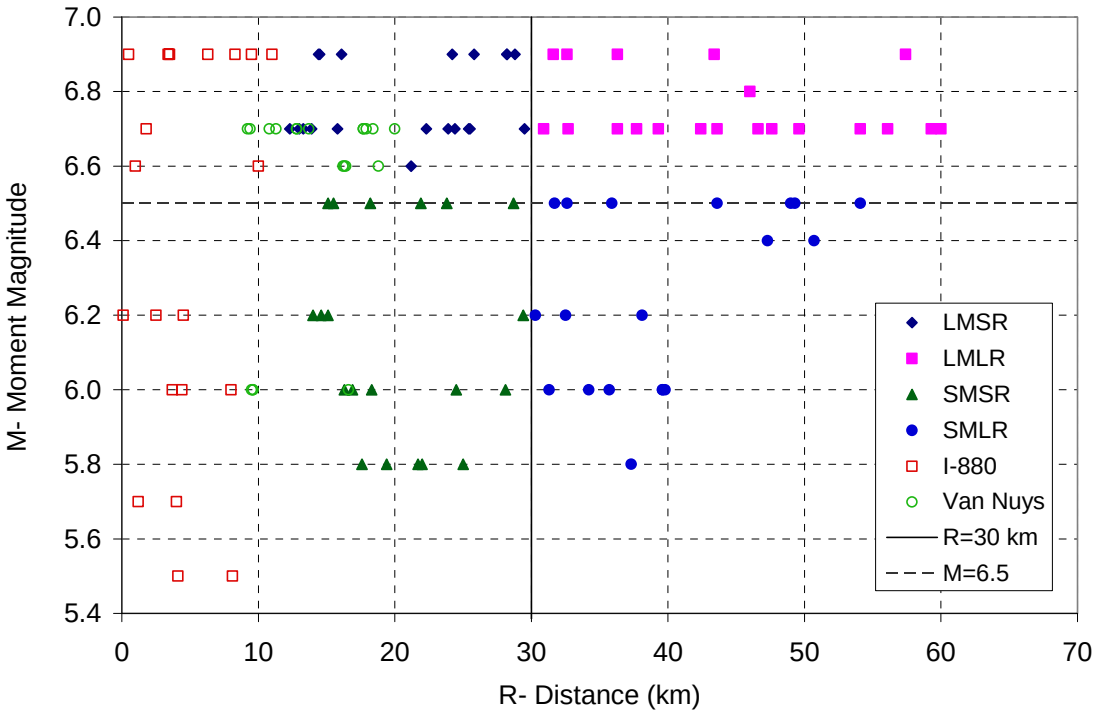

Figure 5-10 Ground motion M-R bins

A uniforms scale factor greater than 1.0 was used for each bin according to Table 5-2 to increase the intensity of the records and guarantee that nonlinear action occurs in the bridge

models. The unscaled records do not correspond to any given hazard level. Since all bridge systems present significantly different fundamental periods, the use of a ground motion scaling method to a specific period-dependent intensity measure would not result in a consistent comparison between the different bridge systems' dynamic results. The use of a period-dependent measure in a three-dimensional bridge analysis using three component ground motions can also be considered incoherent. Additionally, this spectral scaling method was developed for the dynamic analysis of building structures with well-spaced periods and similar failure modes corresponding to the same structural system. The bridge structures analyzed in this study present very distinct failure modes: the nonlinear response in the seismically isolated bridges is primarily controlled by the inelastic shear deformation of the isolation devices, while in the RC and FRC bridges the nonlinear response is developed through plastic hinging of bridge columns. The use of a spectral scaling method to a structure-independent intensity measure characteristic of each ground motion is suitable; however, due to the large number of ground motions, this method is not applied in this study for simplicity.

5.2.1.2 Seismic Hazard Model

To obtain site-specific probabilistic seismic hazard data for a high seismicity zone such as Berkeley, California, the USGS hazard maps are used. The 2%-, 10%-, and 50%-probabilities of exceeding a certain peak ground acceleration (PGA) value in 50 years were determined from these hazard maps and then converted to PGV values using the firm ground conversion of 48 in/sec/g (Newmark and Hall, 1982). The resulting PGV values were 149, 89, 51, and 38 cm/s, for the 2%-, 10%-, 50%-, and 86%-in 50 year probability of exceedance (PE), respectively. The median hazard curve assumed to have a power-law form (see Eq. 5-1) with two unknown parameters was obtained using a least-square fit.

$$H(im) = k_0 (im)^{-k} \qquad \text{[Eq. 5-1]}$$

The resulting nonlinear hazard curve approximation is shown in the logarithmic space in Figure 5-11. Additional median seismic hazard or intensity measure values can be interpolated or extrapolated using the fitted hazard curve.

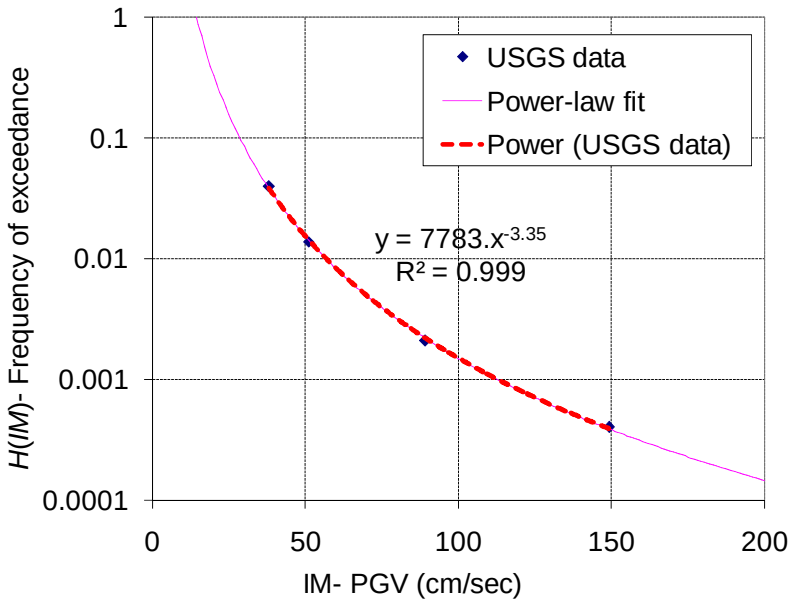

Figure 5-11 Fitted hazard curve to median USGS data for a site in Berkeley, California

5.2.2 Methodology for Comparison of Dynamic Response

The intensity measure selected for the analysis of the response of the different bridge systems is the peak ground velocity (PGV), which is a period-independent measure adequate for structures with fundamental first-mode period in the constant velocity range of the response spectra. The PGV value for each three-component ground motion is obtained as the SRSS combination of the PGV values of the two orthogonal horizontal components of the record. The unscaled PGV values of the motions in the seven record bins are presented in Appendix E.

The engineering demand parameters (EDPs) selected for the analysis of the structural response of the different bridge systems include column, elastomeric bearings, and superstructure response quantities. These include: column peak and residual drift ratio, column ductility demand, maximum column shear, minimum and maximum column axial load ratio, column and abutment elastomeric bearing peak shear strain, and superstructure vertical curvatures and accelerations.

Since the superstructure of the RC bridge was designed to remain elastic under severe ground shaking through the use of high safety factors, the EDPs recorded for this study related to superstructure response of all bridge systems can be used to verify its linear-elastic response and be used as a reference for future design. Additional EDPs related to the total displacements of the superstructure ends could be recorded for a similar bridge structure if a more sophisticated abutment model which accounts for the contribution of the backwall, wingwall and shear keys were to be used.

The comparison of the seismic response of the different bridge systems was carried out relating selected EDPs obtained from nonlinear time history analysis (THA) to an established intensity measure (*IM*) for each record. A natural log fit was used to relate the EDPs of the different bridge systems to the period-independent *IM* of each record defined as the scaled SRSS PGV. The parameters β_1 and β_2 of the natural logarithmic regression

$\ln(EDP) = \beta_1 + \beta_2 \ln(IM)$ or equivalently $EDP = e^{\beta_1} IM^{\beta_2}$ were obtained for the corresponding EDP dispersion of each bridge using the least sum of square of the error. The general scheme for the comparison of major EDPs of the different bridge structures is presented in Figure 5-12.

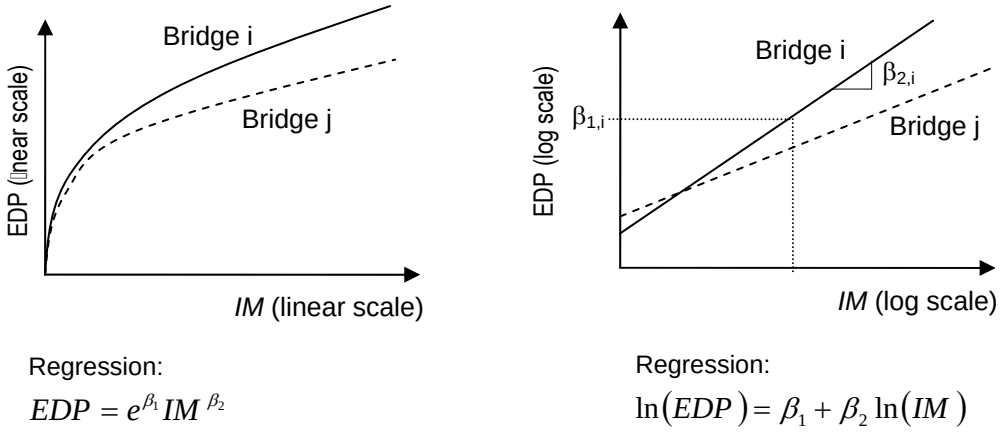

Figure 5-12 General scheme for the comparison of THA results of the different bridge systems in terms of major EDPs

The natural logarithmic regressions were carried out for a range of *IM*=PGV between 0 and 200 cm/sec (78.7 in/sec). The upper limit of the *IM* corresponds approximately to a hazard level of 1%-in-50 year probability of exceedance which represents an extreme demand limit that can be expected during the lifetime of a Standard Ordinary bridge structure. An example of the natural log fit and data dispersion for residual column drift results of the different bridge system analyzed is presented in Figure 5-13.

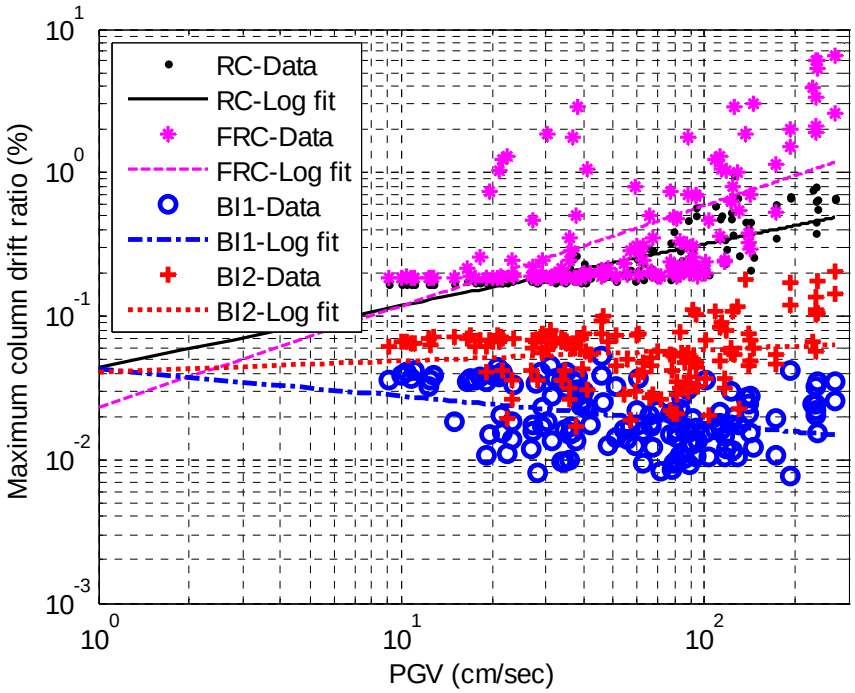

Figure 5-13 Example of natural log fit of residual column drift for different bridges

5.2.3 Results

The natural-log regressions on important EDPs of the different bridge systems are presented in Figure 5-14 through Figure 5-20. The regression analysis displays the general tendency relating the EDPs and the earthquake intensity for the different bridge systems analyzed in this study, and is not considered to provide exact relations between these parameters due to the high data dispersion of the nonlinear dynamic results (as shown in Figure 5-13). In order to compute reliable bias factors of the response EDPs between the different bridge systems at different seismic hazard levels, a comprehensive dynamic analysis is required with different bridge configurations and reinforcement details, as well as an extended ground motion set. Particularly for the FRC bridge, where the available experimental data is currently scarce, the regression analysis results derived using a calibrated bridge model is not considered highly reliable. Nonetheless, the regressions below provide an important insight on the effect of using different seismic performance enhancement techniques on the overall behavior of the bridge response parameters as a function of earthquake intensity.

5.2.3.1 Column Response

The deformation and force demand on the column bents as a function of earthquake intensity is presented in Figure 5-14 through Figure 5-17 for the different bridge systems analyzed. The deformation demand on the column bents is disaggregated in terms of peak drift ratio, displacement ductility, and residual drift ratio. The force demand on the column bents is described in terms of column shear, as well as maximum and minimum axial load ratio (ALR) demands.

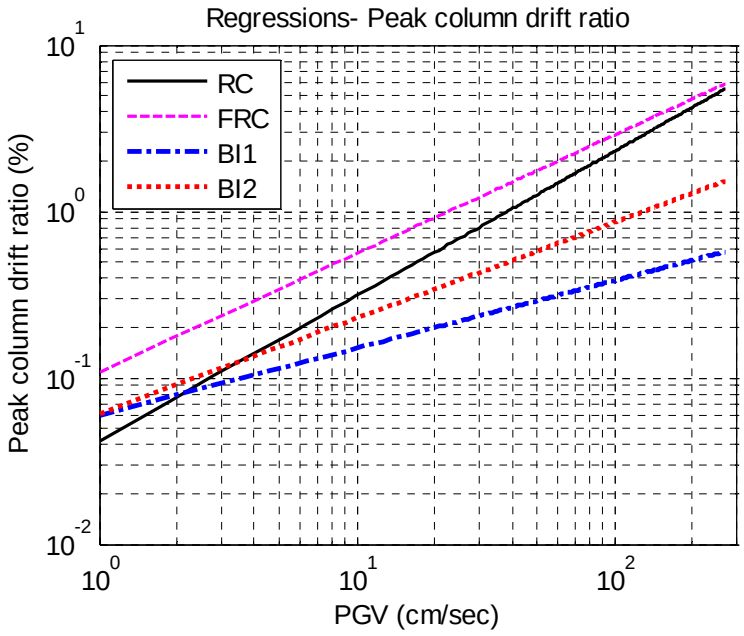

(a)

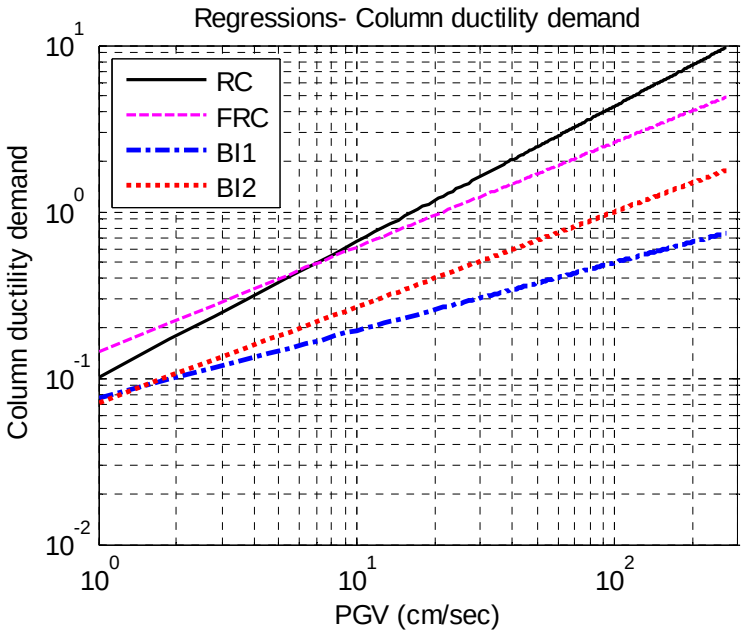

(b)

Figure 5-14 Natural-log regressions for column deformation demand: (a) Peak drift ratio; (b) Displacement ductility.

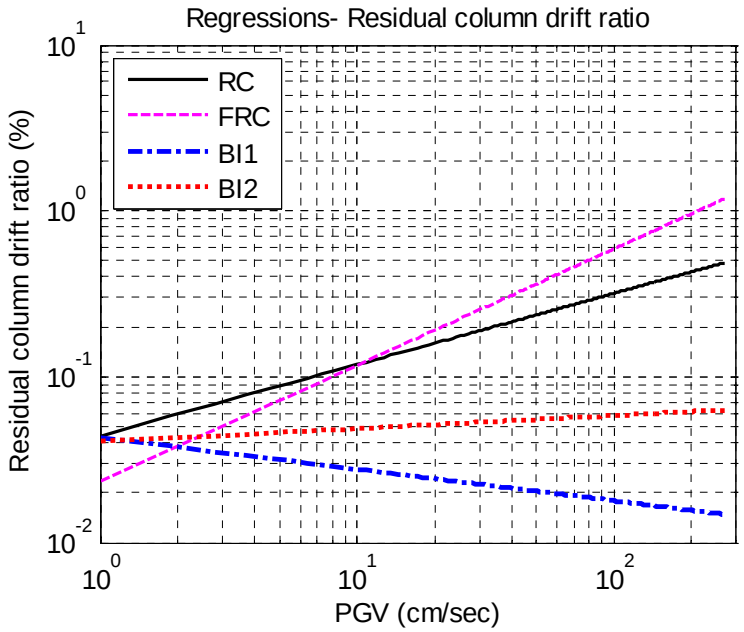

Figure 5-15 Natural-log regressions for column residual drift ratio

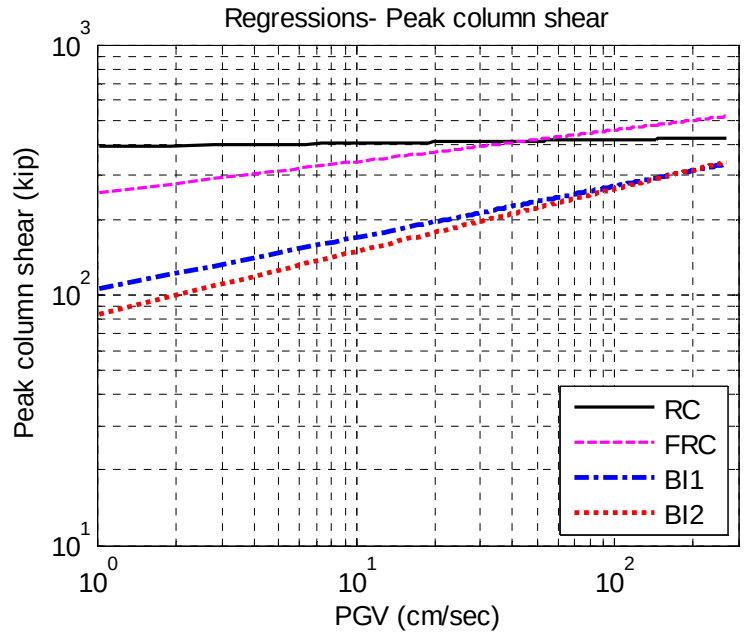

Figure 5-16 Natural-log regressions for column shear

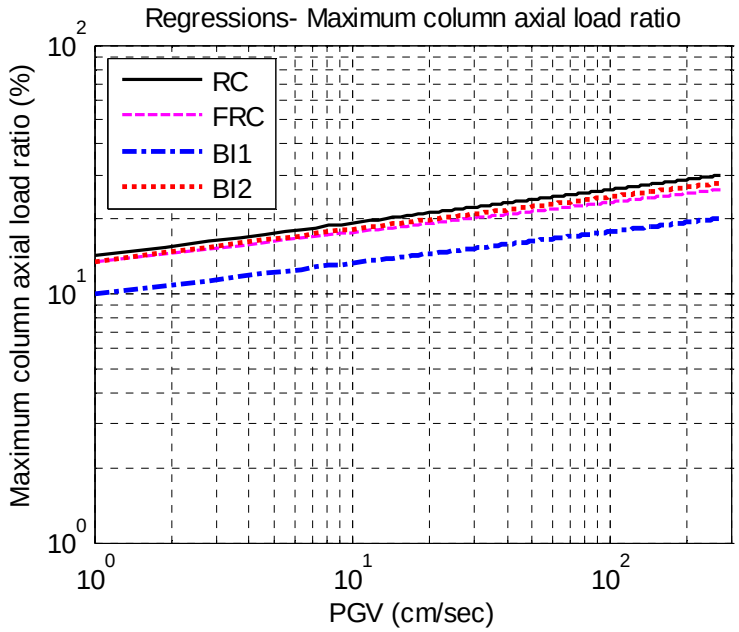

(a)

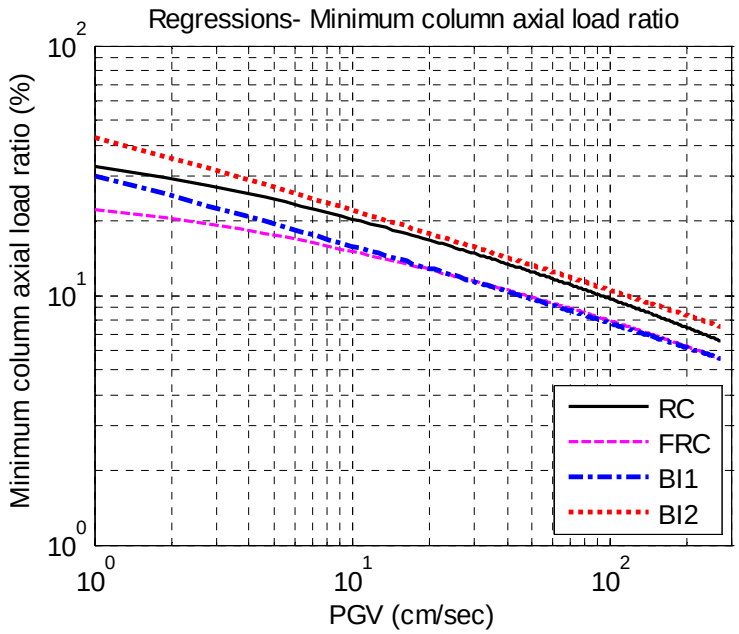

(b)

Figure 5-17 Natural-log regressions for column response: (a) Maximum axial load ratio; (b) Minimum axial load ratio.

The isolation of the superstructure results in a significant reduction in both the peak drift ratio demand and displacement ductility demand, in comparison to the RC bridge. According to the design objectives, the reduction in deformation demand is more pronounced for the BI1 bridge column, which remains in the elastic range of response for the entire range of earthquake intensity considered, while the displacement ductility demand of the BI2 bridge column is between 1 and 2 for high earthquake intensity (PGV greater than 100 cm/sec). Due to the

characteristic capabilities of the isolation system of restoring the bridge superstructure and column bents from their deformed position at the end of a ground motion excitation, the residual drift ratio of the column bents in both isolated bridge is drastically reduced, in comparison to the RC bridge. A significant reduction is also produced in the column shear demand with the use of the isolation devices, similar for both isolated bridges.

According to the analytical bridge results, the drift demands on the FRC present a sizeable increase, in comparison to the RC bridge, for the entire range of earthquake intensity considered. However, due to an increase in the transverse and longitudinal yield displacements of the FRC columns, the resulting displacement demands on the FRC bridge column bents are in fact reduced for the medium to high earthquake intensity range. The residual drift ratio is highly sensitive to the dynamic properties of a bridge system, and in the case of the FRC bridge column, a reduction and increase in this EDP is produced for the low and high hazard levels, respectively, in comparison to the RC bridge.

The maximum axial load ratio presented similar slopes for all bridge types, with an increasing maximum ALR with increasing intensity. Only the BI1 bridge presented a constant 30% reduction in the maximum ALR with respect to the RC bridge for the entire range of seismic intensity considered. Similar regressions were also obtained for the minimum ALR for all bridge types, with increasingly lower values for increasing earthquake intensity. Despite having slightly lower minimum ALR values for the FRC and BI1 bridges, uplift forces were not produced at the column bents for any seismic intensity level.

5.2.3.2 Superstructure and Cap Beam Response

The regressions for the superstructure and cap beam response are presented in Figure 5-18 and Figure 5-19, respectively. The isolated bridges do not produce a significant effect on the peak vertical curvatures and accelerations of the superstructure, in comparison to the RC bridge. Conversely, the analytical model of the FRC bridge results in a significant reduction in superstructure curvature for all seismic intensities, as well as increased and reduced peak superstructure acceleration for low and high seismic intensities, respectively. The pushover response and dynamic properties of the calibrated FRC bridge model differ sufficiently from the RC bridge model results, displaying reduced initial stiffness of the bents, increased yield displacement, higher base shear capacity, and similar ultimate force and displacement capacities. These characteristics result in the altered behavior of the superstructure.

The response of the additional cap beam connecting the isolation devices to the superstructure in the isolated bridges displays an increase in torque demand with increasing seismic intensity. The design of the BI1 bridge aimed to have higher stiffness of the column bents, which consequently results in higher torque demand for this bridge design, with respect to the more flexible BI2 bridge, designed for higher ductility demands.

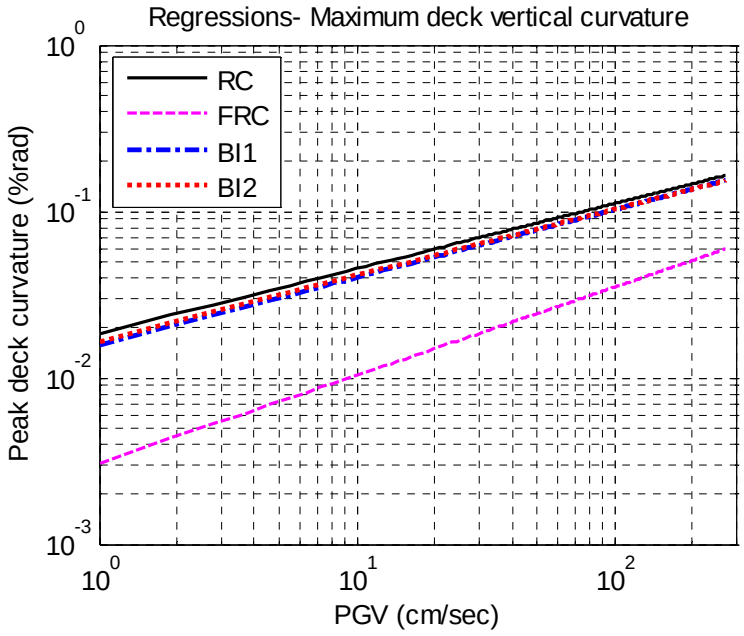

(a)

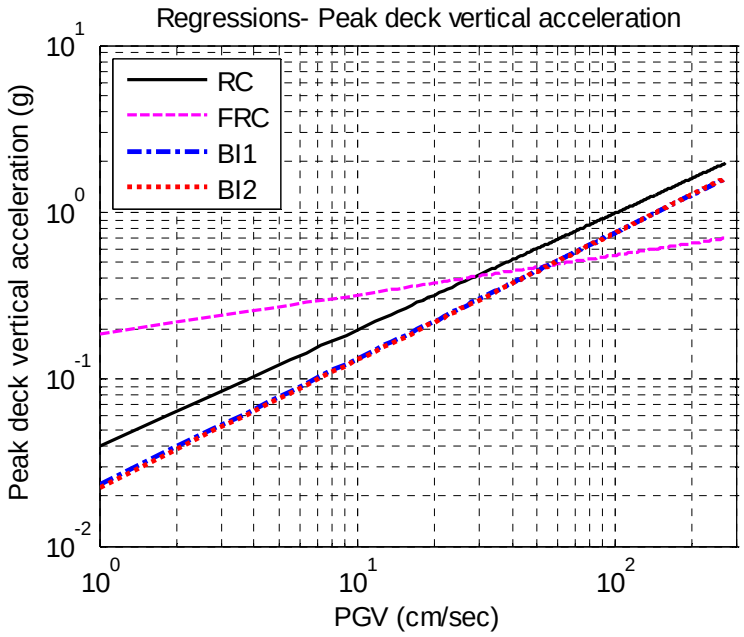

(b)

Figure 5-18 Natural-log regressions for superstructure response: (a) Vertical curvature; (b) Vertical acceleration.

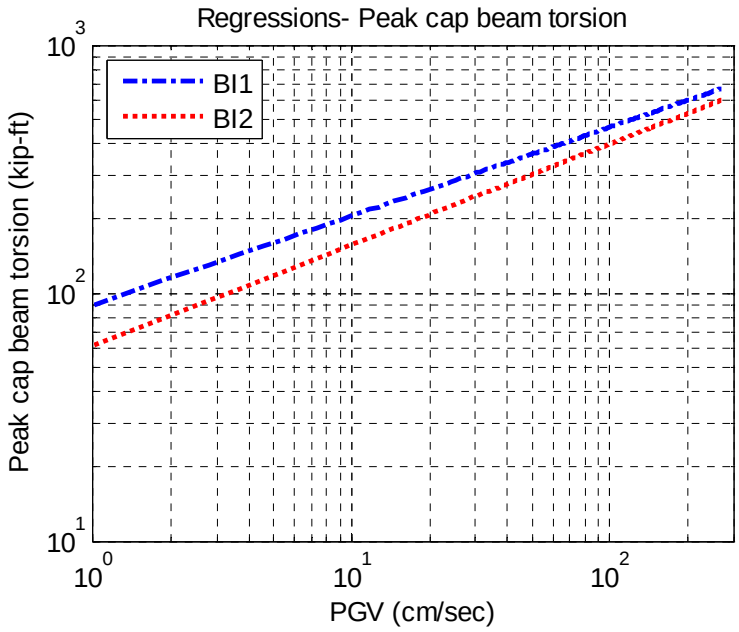

Figure 5-19 Natural-log regressions for cap beam torsion in isolated bridges

5.2.3.3 Bearing Response

The response of the elastomeric bearings of the RC and FRC bridges, as well as the LRB isolator response of BI1 and BI2 bridges, as a function of earthquake intensity, are presented in Figure 5-20. The design of the isolated bridges is deliberately intended to result in higher bearing displacement demands, in comparison to the RC bridge. Since large LRB bearings are provided, the shear strain demands on these bearings are not increased compared to the RC bridge, and the bearings provide stable hysteretic response and high energy dissipating capacity. According to the analytical bridge model of the FRC bridge, due to the increased flexibility of the column bents, the displacement and shear strain demand on the elastomeric bearings is considerably increased, in comparison to the RC bridge response, particularly for the low and moderate seismic intensities.

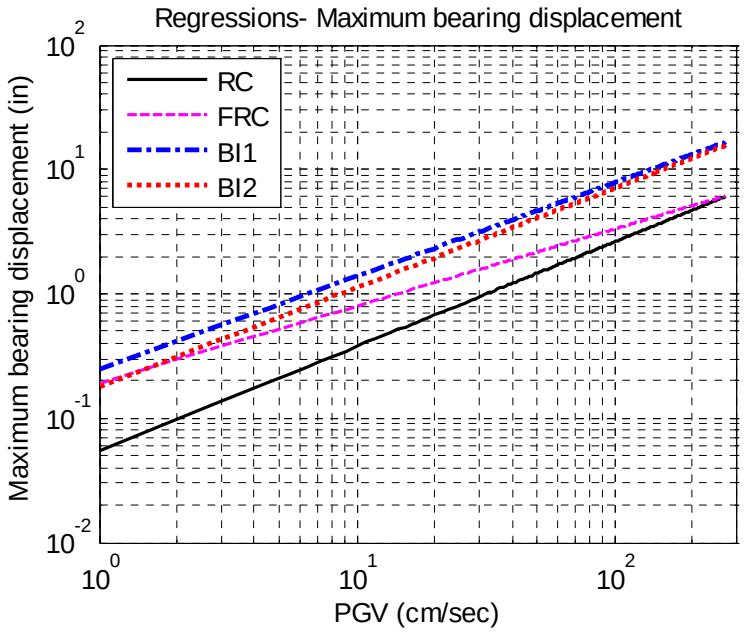

(a)

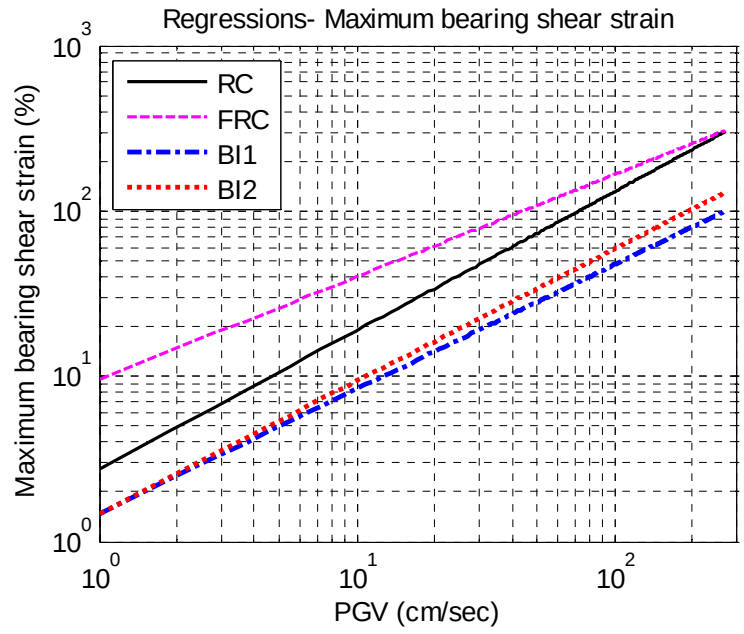

(b)

Figure 5-20 Natural-log regressions for bearing response: (a) Bearing displacement; (b) Bearing shear strain.

6 Bridge Cost Analysis

A comparison of the construction costs and post-earthquake repair costs as a function of earthquake intensity of the RC, FRC, BI1, and BI2 bridges is presented in the following chapter. The new construction costs of the bridges are based on the Ketchum *et al.* (2004) estimates for Type 1A testbed bridge, while the computation of their repair costs and time is based on the local linearization repair cost and time methodology (LLRCAT) developed by Mackie *et al.* (2007). The total cost-effectiveness of the bridges throughout their life span as well as their repair cost ratio (RCR) with respect to the cost of new construction is also derived in this assessment.

6.1 CONSTRUCTION COSTS

The cost of new construction of the different bridge models considered in this study are obtained based on the Ketchum *et al.* (2004) estimates for the Type 1A bridge. The computation of bridge construction costs is carried out by applying unit cost from Caltrans estimates (see Table 6-1) to total material quantities calculated based on specifications and construction drawings (see Table 6-2).

Table 6-1 Unit costs for typical bridge construction

Item	Unit	Unit cost	
		2003Q4	2008Q3
Structure excavation (bridge)	CY	$120	$175
Structure backfill (bridge)	CY	$160	$233
Furnish piling (Caltrans average foundation cost)	EA	$1	$1.46
Drive piling (Caltrans average foundation cost)	EA	$1	$1.46
Prestressed cast-in-place concrete	LB	$2.50	$3.65
Structural concrete, bridge footing	CY	$395	$576
Structural concrete, bridge	CY	$600	$875
Joint seal (type B-MR 2”)	FT	$50	$73
Bar reinforcing steel	LB	$0.70	$1.02
Concrete barrier (type 732)	FT	$60	$88
Steel fibers	LB	$1.20	$1.75
Lead rubber bearing isolators	CI	$1.1	$1.6

The unit costs reported in the Ketchum *et. al* (2004) based on 2003 cost estimates are adjusted according to the price index corresponding to the current 2008 cost data. The quarterly cost index four-quarter moving average is used for comparison (see

http://www.dot.ca.gov/hq/esc/estimates/). The unit costs in Ketchum *et al.* (2004) are corrected to 2008 dollars according to the following equation:

$$Cost_{2008-Q3} = Cost_{2003-Q4} \frac{Index_{2008-Q3}}{Index_{2003-Q4}} = Cost_{2003-Q4} \cdot \frac{388}{266} \qquad \text{[Eq. 6.1]}$$

The cost of the isolation bearings is obtained based on DIS (Dynamic Isolation Systems, Inc.) and EPS (Earthquake Protection Systems, Inc.) estimates for 2008Q3, while the unit cost per pound of steel fibers is obtained from Bekaert Corporation - Dramix steel fibers manufacturer. No additional plasticizers or additives are required for the concrete mix in order to achieve acceptable workability for a low volume fraction of fibers (V_f<2.0%) (Parra-Montesinos *et al.* 2006). Therefore the unit cost of structural concrete casting of the FRC bridge is the same as the RC bridge cost. The resulting increase in the unit cost of fiber-reinforced concrete is less than 5%, in comparison to regular concrete.

The material quantities for the main construction items of the different bridges considered in this study are presented in Table 6-2. The material quantities adjusted for BI1 and BI2 bridges compared to the RC bridge are the structural concrete volume (due to the addition of the bottom bent cap and the adjustment in column dimensions), the reinforcing steel weight (due to the change in longitudinal reinforcing steel ratio) and the volume of rubber for the LRB isolators for the bridge piers and abutments. The material quantities adjusted for the FRC bridge compared to the original RC bridge are the reinforcing steel weight (due to the relaxation in transverse reinforcement and the special reinforcement detail of the plastic hinge of the column bents) and the weight of steel fibers added to the column concrete mix.

Table 6-2 Material quantities of RC, FRC BI1, and BI2 bridges

Item	Unit	Material quantities			
		RC	**FRC**	**BI1**	**BI2**
Structure excavation (bridge)	CY	690	690	690	690
Structure backfill (bridge)	CY	385	385	385	385
Furnish piling (Caltrans ave. foundation cost)	EA	71352	71352	71352	71352
Drive piling (Caltrans ave. foundation cost)	EA	74208	74208	74208	74208
Prestressed cast-in-place concrete	LB	80730	80730	80730	80730
Structural concrete, bridge footing	CY	81	81	81	81
Structural concrete, bridge	CY	1887	1887	**1965**	**1949**
Joint seal (type B-MR 2")	FT	136	136	136	136
Bar reinforcing steel	LB	444282	**441155**	**482525**	**475632**
Concrete barrier (type 732)	FT	920	920	920	920
Steel fibers	LB	0	**9754**	0	0
Lead rubber bearing isolators	CI	0	0	**282975**	**166698**

The resulting costs of new construction of the RC, FRC, BI1, and BI2 bridges are presented in Table 6-3. The additional cost of steel fibers added to the column concrete mix and longitudinal dowels for the special plastic hinge zone detail is compensated by the reduction in the total weight of reinforcing steel bars due to the relaxation in the transverse reinforcement details. Therefore, the resulting cost of new construction of the FRC bridge is only 0.5% higher than the RC bridge.

Table 6-3 New construction costs of RC, FRC, BI1, and BI2 bridges

Item	Total construction cost 2008Q3			
	RC	**FRC**	**BI1**	**BI2**
Structure excavation (bridge)	$120,769	$120,769	$120,769	$120,769
Structure backfill (bridge)	$89,765	$89,765	$89,765	$89,765
Furnish piling (Caltrans ave. fdn. cost)	$104,077	$104,077	$104,077	$104,077
Drive piling (Caltrans ave. fdn. cost)	$108,243	$108,243	$108,243	$108,243
Prestressed cast-in-place concrete	$294,647	$294,647	$294,647	$294,647
Structural concrete, bridge footing	$46,677	$46,677	$46,677	$46,677
Structural concrete, bridge	$1,651,188	$1,651,188	$1,719,376	$1,705,788
Joint seal (type B-MR 2")	$9,919	$9,919	$9,919	$9,919
Bar reinforcing steel	$453,639	$450,446	$492,687	$485,649
Concrete barrier (type 732)	$80,517	$80,517	$80,517	$80,517
Steel fibers	$0	$17,069	$0	$0
Lead rubber bearing isolators	$0	$0	$449,056	$264,535
Subtotal	**$2,959,441**	**$2,973,316**	**$3,515,733**	**$3,310,586**
Percent increase wrt' RC bridge (%)	**0**	**0.5**	**18.8**	**11.9**

Due to the redesign of the isolated bridges with a higher volume of concrete, additional reinforcing steel weight and high cost of the isolation bearings, the total construction cost of BI1 and BI2 bridges are 18.8 and 11.9% higher than the cost of the fixed-base RC bridge, respectively. The additional cost required for the installation of bridge isolation system is tolerable, considering the expected reduction in post-earthquake repair costs and repair time. This outcome is primarily due to the fact that in a long span bridge high quantities of materials are required for the construction of the superstructure, foundations and abutments, which were not modified for the design of the isolated bridges. The contribution of the column bents and bent caps materials (and masses) is minor compared to the remaining bridge components. The bearing devices are the main factor contributing to the increased costs of the isolated bridges. Despite having a reduced force demand on the column bents with the addition of the isolation system, the column foundations of the isolated bridges were not redesigned for this project for simplicity. Therefore, a reduction in the reported construction costs of the isolated bridges in Figure 6-3 can be expected due to reduced foundation size and corresponding material quantities, which is not quantified in this project.

As discussed in Section 6.2, despite slightly higher costs of new construction, the isolated bridges produce minimal post-earthquake repair costs and therefore result in high cost-effectiveness of the system, compared to the fixed-base bridge. According to the repair cost analysis presented in the following section, the FRC bridge can also be considered more cost-effective than the RC. The mobilization and contingency costs are not considered in this study for the computation of the new construction or post-earthquake repair costs, allowing a comparison of costs without local site considerations.

6.2 POST-EARTHQUAKE REPAIR COSTS AND REPAIR TIME

6.2.1 Methodology

A new vector-based probabilistic approach of applying the PEER PBEE framework (see Chapter 1) to compute post-earthquake highway bridge loss models was developed based on the local linearization of the damage model (relationship between damage measure DM and repair quantity Q) at varying degrees of damage (Mackie *et al.* 2006, 2007, 2008). In this methodology for computing bridge fragilities, the thresholds or limit-state values of decision variables (DVs) in the PEER framework are limited to direct losses such as post-earthquake repair cost and repair time for bridge components. This local linearization repair cost and time methodology (LLRCAT) requires a data structure to organize bridge-specific repair actions, quantities, and costs (see Section 6.2.2).

The LRRCAT methodology overcomes many of the challenges of the previous approaches for quantifying loss such as the Fourway method (Mackie and Stojadinovic 2006), piecewise power-law approach, and Monte Carlo simulation (Yang *et al.* 2006), and retains the simplicity of an automated, general closed-form solution of the PEER PBEE framework total probability integral. The LLRCAT can be easily implemented and is compatible with the previous closed-form methods mentioned, allowing the automated computation of performance groups and repairing quantities combinations, regardless of the form of the repair data. Mackie *et al.* (2007, 2008) presents extended details of the LLRCAT methodology.

Mackie *et. al* (2007) computed fragility curves for the repair cost and time of the fixed-base bridge type 1A based on the LLRCAT methodology, AASHTO Standard Specifications for Highway Bridges (1996) and Caltrans Seismic Design Criteria (SDC) (2004). These curves relate the repair cost of the bridge as a percentage of the total construction cost to an intensity measure of a single earthquake event such as the peak ground velocity (PGV). Due to its numerous advantages and simplicity, the LLRCAT methodology is selected in the present study to assess the cost-effectiveness of the fiber-reinforced concrete and seismically isolated bridges, compared to the fixed-base conventionally-reinforced concrete bridge. The repair cost ratio (RCR) obtained by normalizing the post-earthquake repair costs presented in Section 6.2.3 by the cost of original construction computed in Section 6.1 is used to compare the performance and cost-effectiveness of the different bridge design options considered in this study for new construction.

6.2.2 Data Structure

The LLRCAT methodology involves three main pieces: local linearization of the damage to repair quantities (Q-DM) model, extension from repair quantities Q to repair cost and repair time, and a data structure that requires bridge-specific data. This vector approach sums over the bridge performance groups (PGs) or components over all of the discrete damage states (DSs) applicable to each component, and all of the repair quantities (Qs) necessary to repair each DS of each component PG. Each repair quantity Q is therefore treated as a random variable with a given distribution and uncertainty according to the seismic intensity measure. A constant unit

repair cost obtained from Caltrans estimates is finally multiplied by total repair quantities for each repair item or component, thus obtaining total post-earthquake repair costs of the bridge components. The repair cost of all components are added to obtain the total repair cost of the bridge system as a function of earthquake intensity. The loss model for each bridge system is integrated over the entire range of IM, according to the slope of the hazard curve at each IM, to obtain the mean annual frequency (MAF) of exceeding repair cost thresholds of the bridge systems (Der Kiureghian, 2005). The schematic procedure for the LLRCAT methodology for computing the MAF of exceeding a repair cost threshold for a single component is presented in Figure 6-1.

$$\text{Repair cost: } \lambda(RC > rc) = \int_{im}\int_{dm}\int_{edp} G(uc \cdot q \,|\, dm)\, dG(dm \,|\, edp)\, dG(edp \,|\, im) \left| d\lambda(im) \right|$$

$$\text{Repair time: } \lambda(RT > rt) = \int_{im}\int_{dm}\int_{edp} G(lpr \,|\, dm)\, dG(dm \,|\, edp)\, dG(edp \,|\, im) \left| d\lambda(im) \right|$$

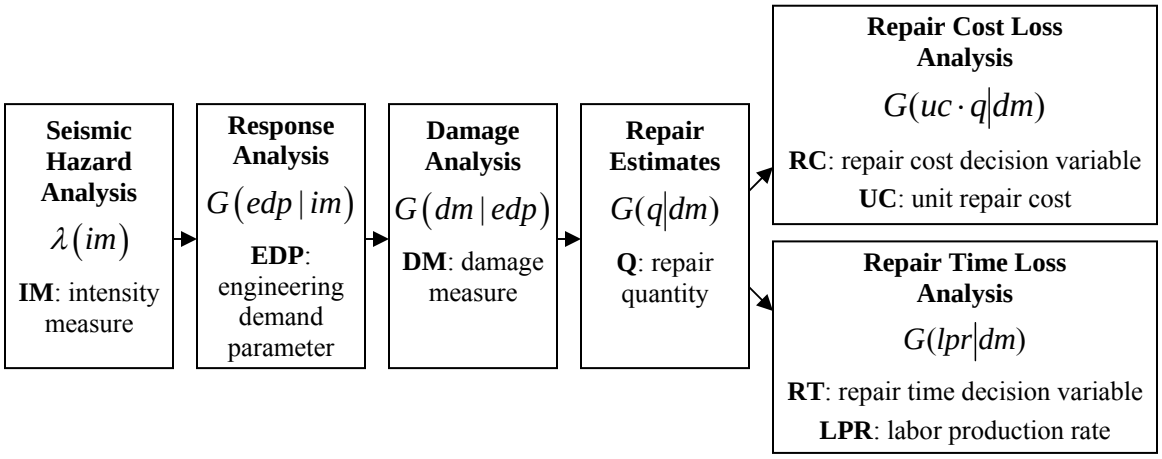

Figure 6-1 Schematic procedure of the LLRCAT methodology for single bridge component

The methodology therefore requires a large bridge-specific data base which includes: Engineering demand parameter (EDPs) results from nonlinear dynamic structural analysis at various intensity measures (IMs) for each PG, damage limit states (DSs) for each PG, repair methods and production rates for each repair quantity Q resulting in total repair quantities Q for each DS and PG, unit costs for each Q to compute estimated repair costs, labor production rates for each Q to compute repair times, and general bridge information and dimensions to compute material quantities. The computational procedure of bridge repair cost and time using the LRRCAT method is further detailed in Mackie *et al.* (2007, 2008).

A method for collecting the data corresponding to different bridge damage scenarios and the appropriate repair methods, items, costs, and time from experts working within state departments of transportation who have experience with real bridge repairs and estimating methods is documented in Mackie *et al.* (2008).

6.2.2.1 Performance Groups

The bridge system is disaggregated into individual structural or non-structural components or subassemblies defined as performance groups that are damaged, assessed and repaired together using a specific combination of different repair methods. The PG repairs are therefore independent of each other.

Among the performance groups considered in this study are the maximum and residual tangential drift ratios of all four columns (obtained as the SRSS of the longitudinal and transverse directions at each time step), maximum relative longitudinal deck- abutment displacement, maximum absolute bearing displacement at the abutments and piers (in the case of the seismically isolated bridges), maximum abutment shear key force and residual vertical displacement of the abutments. Since the superstructure is designed to remain elastic under severe ground shaking through the use of high safety factors during the design process, it is not expected to develop any damage and contribute to the repair costs of the bridge. Therefore, the strain at the roadway surface of each bridge span is set to zero and no additional EDPs are considered for the deck. The residual pile cap displacement at the column and abutment foundations are also assumed negligible and set to zero for all bridge types analyzed in this study. The EDPs for each structural PG selected for this study is computed for different IMs from the nonlinear time history analysis results using 7 ground motion bins with a total of 140 records (see Chapter 5).

The different non-structural components of the bridge systems such as barrier rails, lighting poles, and utility conduits were not incorporated into performance groups and included in the repair cost methodology carried out in this study due to the lack of performance and cost data for these elements.

6.2.2.2 Damage States

The LLRCAT method provides a lower threshold or zero damage state (DS_0) corresponding to the onset of damage when repair costs begin to accumulate and below which the repair cost of the bridge is considered to be \$0, and an upper limit defined as an infinite damage state ($DS\infty$) corresponding to the most severe possible DS for a PG, usually complete failure and replacement of all the elements in the entire PG. The definition of the DS_0 and $DS\infty$ thresholds allows the elimination of an unrealistic, immediate increase in expected repair costs for extremely small earthquake intensities and an overestimated extrapolation of the repair quantities beyond the failure of a particular PG. The LLRCAT computation method assumes that a continuous range of damage exists between the discrete damage states, allowing for a closed-form solution of the PEER PBEE triple integral.

Discrete damage states are defined for each PG for BI1, BI2 and FRC bridges, similarly to the RC bridge DSs and EDPs threshold in Mackie *et al.* (2007). The λ and β parameters defined for each damage state correspond to the median and standard deviation parameters of the lognormal distribution used to define the cumulative distribution function or fragility curve for the DS based on the corresponding EDP.

The DSs for the LRB isolation bearings in the BI1 and BI2 bridges are defined according to the actual bearing properties in each case. The DS_0 threshold of the bearings is defined as the yield displacement estimated at 150% shear strain equivalent to 24.75" and 18.0" for bridges BI1 and BI2 bridges, respectively, while the $DS\infty$ damage state is defined at 300% shear strain equivalent to 49.5" and 36.0" for BI1 and BI2 bridges, respectively. The DSs corresponding to peak tangential drift ratios PGs of the isolated bridges were modified according to their modified reinforcement details and cross-sectional dimensions. According to Mackie *et al.* (2007), the DS corresponding to initial cracking (DS_0) was computed according to the column cracking moment M_{cr}, the concrete cover spalling (DS_1) and longitudinal reinforcing bar buckling according to Berry and Eberhard (2003), and the column failure according to Mackie and Stojadinovic (2007).

Table 6-5 summarizes the resulting median λ and corresponding standard deviations β defining the different DSs fragility curves of the isolated bridges columns associated with the peak tangential drift ratio PGs. Only the $DS_3=DS\infty$ corresponding to concrete failure associated with the residual tangential drift PGs was modified for the isolated bridges, according to the results in Table 6-5.

Table 6-4 Damage states for BI1 and BI2 bridge performance groups corresponding to peak column drift ratio (%)

Damage state	Description	Parameter	BI1 bridge	BI2 bridge
DS_0	Concrete cracking	λ- Median	0.14	0.18
		β- St.dev.	0.30	0.30
DS_1	Spalling	λ- Median	1.68	1.65
		β- St.dev.	0.33	0.33
DS_2	Bar buckling	λ- Median	6.36	6.07
		β- St.dev.	0.25	0.25
DS_∞	Column failure	λ- Median	8.67	8.36
		β- St.dev.	0.35	0.35

The median DS thresholds for the peak tangential drift ratios PGs of the fiber-reinforced concrete columns are adjusted from their original values corresponding to conventionally-reinforced concrete according to the experimental results presented in Chapters 2 and 3. For the PG corresponding to column maximum tangential drift ratio, the cracking damage state DS_0 associated with the cracking moment M_{cr} was increased by a factor of 1.5 from 0.23% to 0.34%. The spalling damage state DS_1 was modified to a concrete crushing damage state DS_1 which occurs only concurrently with the bar buckling damage state DS_2. According to the experimental results of the FRC cantilever columns, spalling was not observed at any stage of the cyclic loading history. Concrete crushing occurred at high levels of rotation of the column and was enhanced due to bar buckling which pushed out the concrete cover. The bar buckling damage state DS_2, estimated according to Berry and Eberhard (2003) was changed from 6.09% to 5.28% due to the relaxation in the transverse reinforcement in the FRC columns. This estimation, nonetheless, accounts for some additional confinement provided by the steel fibers in the concrete matrix. The failure of the column corresponding to $DS_3=DS\infty$ is defined at 6.72% for both RC and FRC columns according to the pushover analysis results, which display similar failure points for both bridges. These DSs results are summarized in Figure 6-2 and Table 6-5. The β value corresponding to the standard deviation of the lognormal distributions defining the

damage states fragility curves for the BI1, BI2 and FRC bridges are defined using the same values as for the RC bridge.

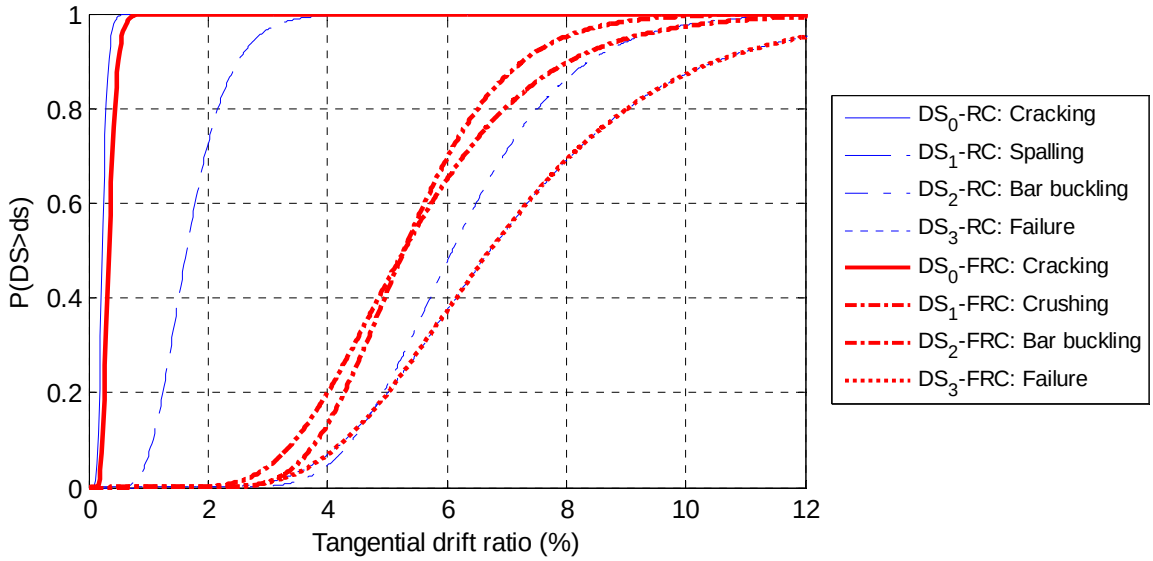

Figure 6-2 Fragility curves for maximum tangential drift ratio damage states for RC and FRC bridges

Table 6-5 Damage states for RC and FRC bridge performance groups corresponding to maximum column drift ratio (%)

DS	Description	Parameter	RC bridge	FRC bridge
DS_0	Concrete cracking	λ- Median	0.23	0.34
		β- St.dev.	0.30	0.30
DS_1	Spalling (RC) or crushing (FRC)	λ- Median	1.64	5.28
		β- St.dev.	0.33	0.33
DS_2	Bar buckling	λ- Median	6.09	5.28
		β- St.dev.	0.25	0.25
DS_∞	Column failure	λ- Median	6.72	6.72
		β- St.dev.	0.35	0.35

For the PGs corresponding to residual tangential drift ratios of the FRC columns, DS_0-DS_2 were not modified with respect to the RC bridge, since these damage states are defined according to aesthetic and functionality criteria, not hazard instability. The DS_3=$DS\infty$ corresponding to column failure is defined similarly for both peak and residual tangential drift ratios PGs, and therefore this DS parameters were not modified with respect to the RC bridge.

6.2.2.3 Repair Methods Costs and Labor Production Rates

Different repair methods are used by Caltrans for the various damage states of each PG or bridge component. The repair methods for each PG require a combination of several repair items, listed in Table 6-6.

Table 6-6 Repair methods unit costs and labor production rates

Repair item	Unit repair cost ($)		Labor production rate		
	Unit	mean	Unit	μ-mean	σ-st.dev.
Structure excavation	CY	128.55	CWD*	1.2	0.2
Structure backfill	CY	171.41	CWD	2.2	0.5
Temporary support (superstructure)	SF	29.61	CWD	34.2	3.8
Temporary support (abutment)	SF	29.61	CWD	33.2	3.8
Structural concrete (bridge)	CY	1733.53	CWD	10.0	0.7
Structural concrete (footing)	CY	405.14	CWD	10.0	0.7
Structural concrete (approach slab)	CY	1266.06	CWD	2.0	0.3
Aggregate base (approach slab)	CY	253.21	CWD	1.2	0.2
Bar reinforcing steel (bridge)	LB	1.05	CWD	1.8	0.2
Bar reinforcing steel (footing, ret. wall)	LB	0.93	CWD	1.8	0.2
Epoxy inject cracks	LF	167.51	CWD	2.0	0.3
Repair minor spalls	EA	233.73	CWD	2.0	0.3
Column steel casing	LF	7.79	CWD	70.0	7.7
Joint seal assembly	LF	214.26	CWD	2.0	0.3
Elastomeric bearings	EA	Per bridge**	CWD	1.2	0.2
Drill and bond dowel	LF	42.85	CWD	1.2	0.2
Furnish steel pipe pile	LF	42.85	CWD	35.0	1.7
Drive steel pipe pile	EA	1597.19	CWD	2.0	0.3
Drive abutment pipe pile	EA	7012.05	CWD	3.0	0.3
Asphalt concrete	TON	206.47	CWD	2.0	0.3
Mud jacking	CY	296.06	CWD	2.0	0.3
Bridge removal (column)	CY	2652.89	CWD	16.2	1.8
Bridge removal (portion)	CY	1834.82	CWD	2.0	0.3
Approach slab removal	CY	779.12	CWD	4.0	0.7
Clean deck for methacrylate	SF	0.31	CWD	1.2	0.2
Furnish methacrylate	GAL	66.22	CWD	20.0	3.3
Treat bridge deck	SF	0.43	CWD	1.2	0.2
Barrier rail	LF	1.56	CWD	1.8	0.2
Re-center column	EA	77.91	CWD	2.0	0.3

*CWD- Crew working days
**Per bridge: See Table 6-7

The repair quantities Q necessary for each repair item depend on the dimensions, reinforcement and construction details of all bridge constituents. The repair costs of each PG are obtained by multiplying the repair quantities Q of each repair item by their corresponding unit cost (UC) obtained from Caltrans estimates for the 2008Q3 semester (see Table 6-6), and

summing the costs of all the corresponding repair items. The unit cost of the elastomeric bearings specified for the RC, FRC, BI1, BI2 bridges is summarized in Table 6-7. A constant value is used for the mean UC of each repair item, estimated based on an average range of material quantities projected by Caltrans for the repair. The UC is not treated as a random variable in the current implementation of the LLRCAT methodology, thus the standard deviation for all unit repair costs is not considered in the computation. The total repair cost loss model of each bridge type is finally obtained by summing the repair costs of all the performance groups or components of the bridge structure computed for the specified range of earthquake intensity.

Table 6-7 Cost of elastomeric bearings for different bridge types

Repair item	Bridge type			
	RC	FRC	BI1	BI2
Elastomeric bearings or LRB isolators	$ 1,169	$1,169	$449,056	$264,535

Contrary to the repair cost estimation, the labor production rate (LPR) of each repair item used in the computation of the repair time of the bridge as a function of earthquake intensity is treated in the LLRCAT methodology as random variables with a defined distribution. The PERT criterion (Harris, 1978; Perry and Grieg, 1975) is used to define the LPR of each repair item. The PERT-beta distribution uses estimates of the minimum, maximum and most likely duration for completing the work for the computation of the mean (μ) and standard deviations (σ) of each repair item LPR (see Table 6-6). Caltrans estimates of the durations in term of CWD (crew working day) representing one working day for a normal sized crew are used to define the LPR distributions. The repair time estimates are based on numerous simplifying assumptions for repair effort instead of repair duration, to avoid complex estimates in the latter that take into account work crew dependencies, furnishing and installation times, and critical paths. The total post-earthquake repair time of all PG and of the different bridge types is obtained by summing the corresponding repair times computed for each repair item and methods as a function of earthquake intensity.

6.2.3 Results

The quantification of direct and indirect economic losses of highway systems due to earthquake damage requires a large probabilistic-based system-level data. However, since Caltrans data for the highway bridge systems analyzed in this study was not available or insufficient for a realistic computation of downtime and other indirect economic losses of the bridges, only direct losses associated with post-earthquake repair cost and time were computed. The assessment of indirect losses and interruption of service of bridge systems can be carried out in future research following the recommendations and procedure described in Werner *et al.* (2000, 2004) and HAZUS (1999). A parametric or sensitivity analysis of different design variables of the bridges can also be addressed in upcoming studies.

The LLRCAT methodology can generate a large array of results related to the repair cost and repair time of the different bridge types considered for this study. The demand results relevant to the characterization of the seismic response and design of the different bridges are presented and discussed in Chapter 5. The intermediate demand and damage analysis and fragilities results required for the computation of the loss analysis are not presented in this report

for simplicity. Some of the intermediate demand and damage results for the RC bridge are presented in Mackie *et al.* (2007).

The vulnerability assessment of the highway bridges analyzed in terms of key repair cost and repair time output is the central focus of this study. The comparison of the different bridge types is carried out in terms of the repair cost fragilities for different cost thresholds, repair cost ratio, total repair cost and repair time loss models as a function of intensity, and repair cost ratio CDFs and disaggregation of repair cost by repair item for different hazard intensity levels. The loss models and fragility curves were obtained considering different possible repair methods used by Caltrans for the various damage states of each performance group or bridge component, resulting in smoothed discontinuous linear piece-wise shapes of repair cost or effort as a function of earthquake intensity for each bridge system. The final assessment of the cost-effectiveness of the different bridge types is achieved by comparing the total cost of the bridges throughout their lifespan, including the costs associated with the construction and post-earthquake repair costs of the structures, as well as their projected duration of post-earthquake repair.

6.2.3.1 Repair Cost Ratio Results

The intensity-dependent variation in repair cost ratios (RCRs) and total repair costs of the different bridge types considered for this study was assessed using LLRCAT methodology and the data presented in Section 6.2.2. The RCR for each bridge type was computed using the corresponding estimated construction cost for each bridge, presented in Table 6-3. The final repair cost loss model computed by summing the costs from all repair items is assumed to follow a normal distribution.

Since the repair cost loss models are intensity-dependent and the fundamental periods of the different bridge types are considerably disparate, as discussed in Chapter 4, a structure-independent intensity measure was used (PGV). The repair cost ratio and total repair cost loss models (see Figure 6-3 and Figure 6-4, respectively) allow for a direct comparison of the repair costs (y-axis) between all bridge types for a specified hazard level or intensity measure (x-axis).

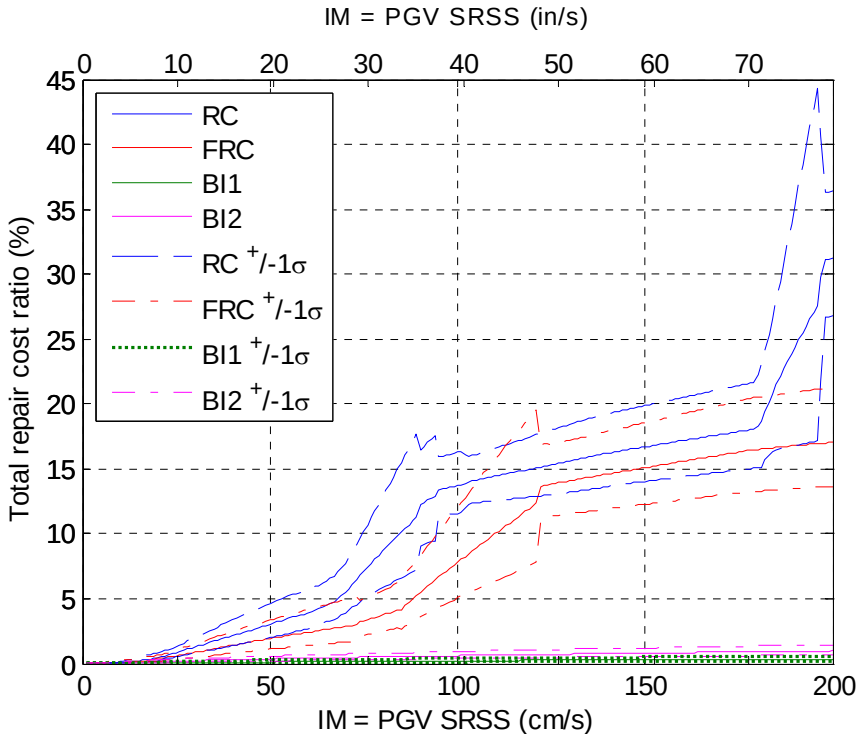

Figure 6-3 Repair cost ratio loss model for different bridge types as a function of earthquake intensity

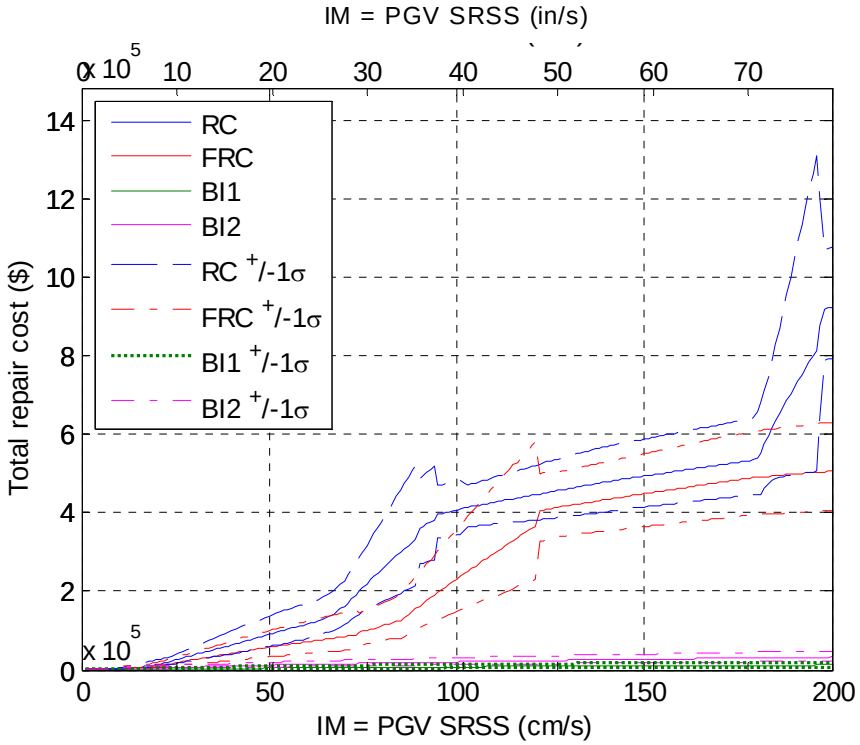

Figure 6-4 Total repair cost loss model for different bridge types as a function of earthquake intensity

The results for all bridge types display an initial branch with zero repair costs for small earthquakes, due to the inclusion of the DS_0 damage states which defines the triggering of damage and need for repair. The linear Q-DM model of the RC bridge model includes several plateaus and branches of rapid damage growth with increasing intensity. The first plateau branch (PGV between 20 and 70 cm/sec) corresponds to the cracking and spalling of the shear keys and pier columns (requiring epoxy injection in cracks and repair of minor spalls). The second branch presenting increased accumulation of repair costs with increasing intensity (PGV between 70 and 90 cm/sec) correspond to the back wall spalling damage state. The second plateau (PGV between 100 and 180 cm/sec) includes the failure of the elastomeric bearing pads at the abutments (requiring temporary support at the abutments and the replacement of the bearings). The final branch with increased repair cost growth (PGV between 180 and 200 cm/sec) is developed due to the failure of both internal columns of the RC bridge, requiring the temporary support of the bridge superstructure and the complete replacement of the columns.

The remaining FRC and isolated bridge models display extended plateaus since no additional damage is triggered beyond the spalling of the shear keys and all column bents, which only require epoxy injection in cracks and repair of minor spalls to bring the bridges to their original undamaged state. The triggering of the different column PGs damage states for the FRC bridge occur at higher EDP levels than the RC and isolated bridges due to the enhanced behavior of the reinforced concrete with the addition of steel fibers. The FRC presents additionally the failure of the bearings at moderate to high intensities (PGV greater than 100 cm/sec) which require the shoring of the abutments and the replacement of the bearing pads for the repair of the bridge. However, this damage state does not result in a significant increase of the repair costs of the FRC bridge. The remaining bridge components damage states, specifically those corresponding to the column bents, are not triggered due to the damage-tolerant fiber-reinforced materials and the effectiveness of the isolation system of the FRC and isolated bridges, respectively.

The RCR of the RC, FRC, BI1, and BI2 bridges at the highest hazard level plotted in Figure 6-3 (PGV of 200 cm/sec) is approximately 32, 17, 0.75 and 1.5%, respectively. For this intensity level (greater than 1% in 50 year PE hazard level), the resulting repair costs of the FRC, BI1, and BI2 bridges are therefore reduced by approximately 2, 40 and 20 times, respectively, compared to the RC bridge costs. The disaggregation of the repair cost loss models by performance group and repair quantity for all bridge types is presented in Appendix F.

The repair cost ratio fragility curves for several discrete hazard levels are presented in Figure 6-5. In this seismic risk assessment for a site in Berkeley, California, the 2%-, 10%-, and 50%- in 50 years PE hazard levels are used, with the corresponding PGV values of 149, 89, and 51 cm/s, respectively, based on USGS hazard data (see Chapter 5). The probabilistic moments in the RCR loss model as a function of intensity in Figure 6-3 were determined for the three discrete hazard scenarios and plotted as complete CDFs ($P[RCR > rcr | IM = im]$) in Figure 6-5. The individual curves are not labeled as RCR fragilities since they do not show the probability of a single loss limit state at different earthquake intensity levels, but rather as normally distributed CDFs obtained from the accumulation at each hazard level considered of several repair costs from different repair items involving one or several PG limit states. Clearly, at any hazard level considered (low, moderate, or high) the CDFs curves in Figure 6-5 display higher probabilities of accumulating repair costs for the RC, FRC, BI2, and BI1 bridge types, in decreasing order. For

example, at the high hazard level (2% in 50 years PE), the median RCR for the RC, FRC, BI2, and BI1 bridges is approximately 17.5, 15, 1, and 0.5%, respectively.

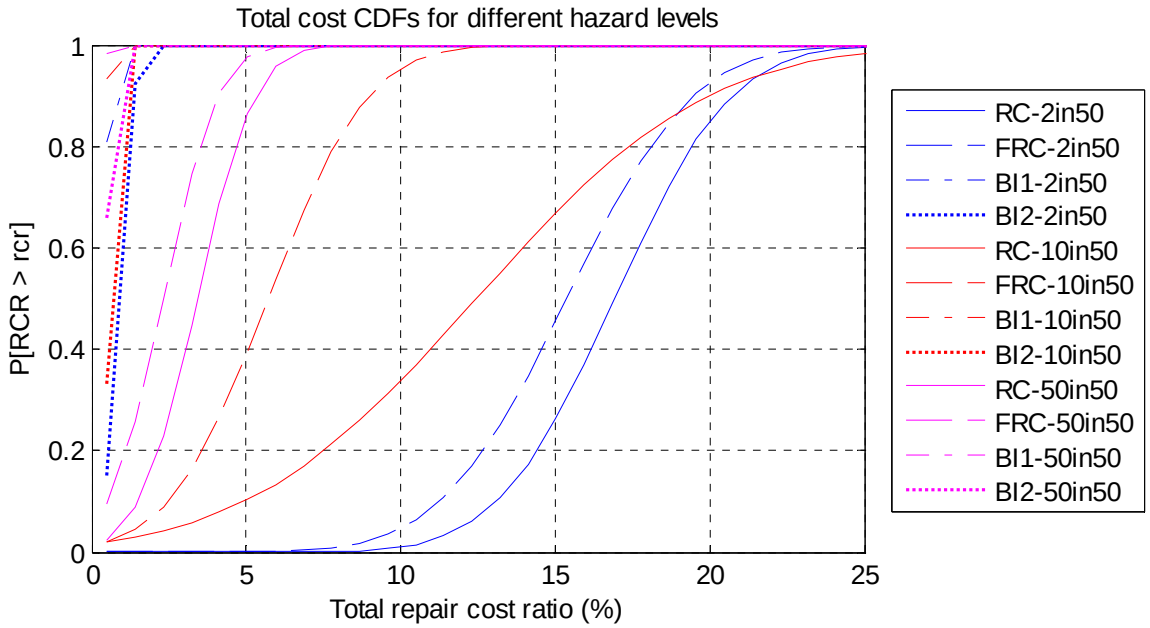

Figure 6-5 Repair cost ratio CDF for different bridge types and different seismic hazard levels

The standard loss fragility curves for all bridge types illustrating the probabilities of exceeding a certain RCR threshold as a function of earthquake intensity are presented in Figure 6-6. The fragility curves are computed for four RCR thresholds (1, 2, 5, and 10%), assuming that the repair cost probability distribution is normal. However, the fragility curves do not necessarily appear like the CDF of a normal distribution since both the mean and standard deviation of each data point on the curve is intensity-dependent. Therefore, for the range of intensities where the repair cost ratios remain essentially constant, so does the probability of exceeding that RCR threshold, thus the resulting curve will present plateau branches. The loss fragility curves are smoothed step-wise CDFs capturing the local behavior of the repair cost estimates in different intensity ranges which are not consistently increasing with earthquake intensity.

Since the RCRs computed for the isolated bridges do not exceed 2%, even for the highest hazard level considered (see Figure 6-3), the fragility curves in Figure 6-6 corresponding to these bridges display zero probability for RCR thresholds of 2% or greater. Similarly, for RCR thresholds greater than 20%, only the RC and FRC bridge fragility curves will present non-zero values in the specified range of seismic intensity, since the RCRs estimated for the FRC bridge do not exceed 17%. Only for extremely low RCR threshold values such as 0.1 and 0.5% in Figure 6-6 the fragility curves for all bridge types is non-zero for the relevant intensity range.

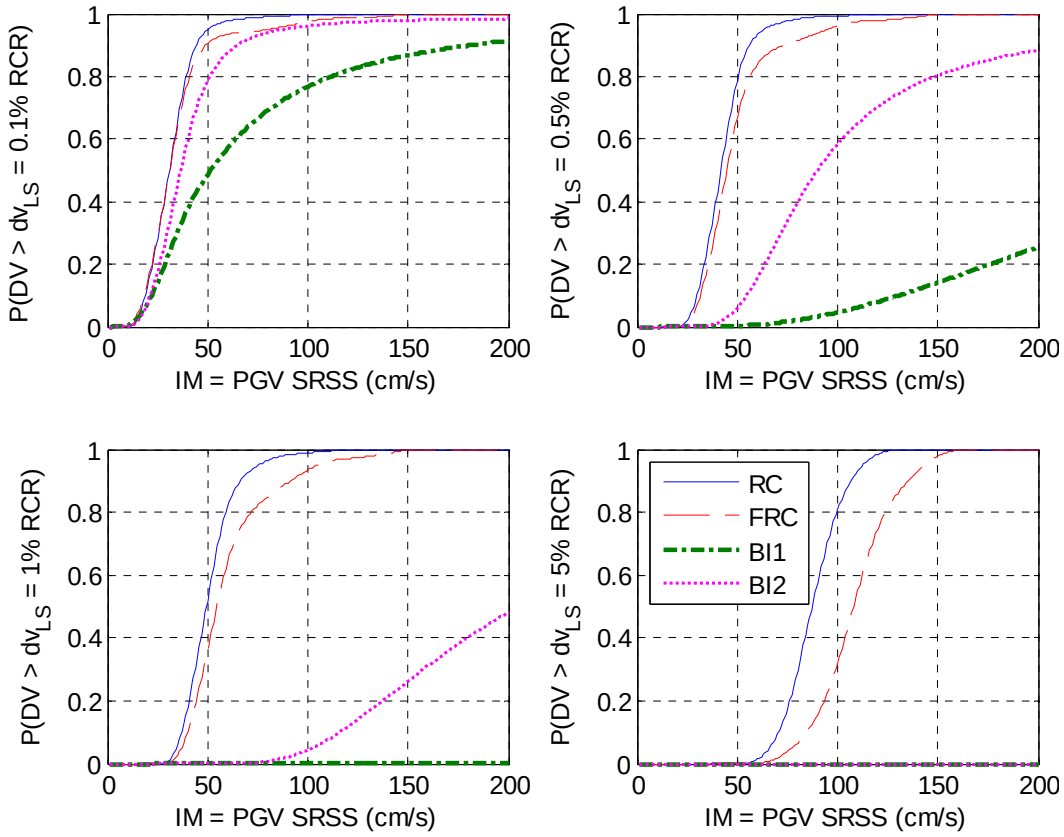

Figure 6-6 Repair cost ratio fragility curves for different bridge types as a function of earthquake intensity

6.2.3.2 Dissaggregation by Repair Quantity and Performance Group

The disaggregation of the final repair costs into individual contributions from each repair quantity or item as a function of earthquake intensity is presented for the different bridge types in Appendix F. A similar presentation of the disaggregation of expected repair cost by repair quantity at discrete hazard levels of interest is presented in the form of a pie chart in Figure 6-7, Figure 6-8, Figure 6-9, and Figure 6-10 for the RC, FRC, BI1, and BI2 bridges, respectively. The hazard levels selected for the disaggregation of expected costs are the 2%-, 10%-, 50%-, and 86% in 50 years PE. The charts have been calibrated such that the main repair quantities or items are labeled and the remaining quantities contributing by less than 10% to the total expected cost are lumped together in a group labeled "Other."

For the RC bridge, the relative contribution of epoxy injecting cracks, minor spalls repair, use of structural concrete and partial bridge removal for cleaning and assembly of blockout volume at the abutments, at the low hazard levels of 86% and 50% in 50 years PE is evident (see Figure 6-7). At the higher hazard levels of 2% and 10% in 50 years PE, the largest contribution to the repair comes from the removal and use of structural concrete for the support slab, abutment temporary support and bridge removal, in addition to the epoxy injecting cracks and minor spalls repair (see Figure 6-7). The peak contribution at the range of intensities between 2%- and 86%- in 50 years PE is from the use of structural concrete at the approach slab.

However, this repair quantity is not the chief contributor at all intensities. For example, for PGV less than 75 cm/s, low-level damage repair items (epoxy inject cracks and minor spalls repair) control, while for PGV of approximately 175 cm/s or higher, serious damage leads to the need to replace a column and hence temporary support of the superstructure begins to rise rapidly as a contributing cost. These results can be observed from the disaggregation plots by repair item presented in Appendix F.

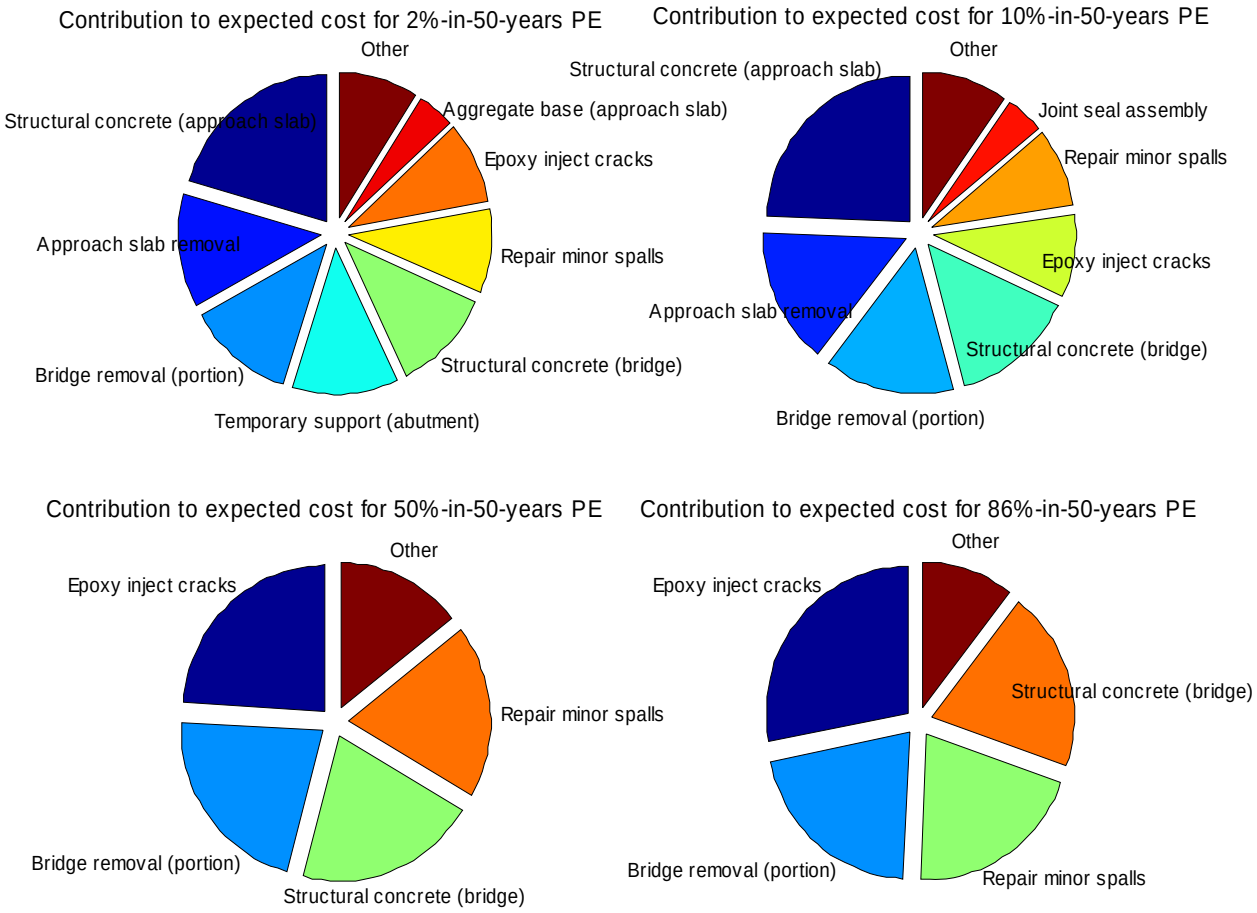

Figure 6-7 Contribution of different repair methods to the total repair cost of RC bridge model at different seismic hazard levels

For the FRC bridge, the relative contribution of epoxy injecting cracks is considerably reduced in comparison to the RC bridge, due to the delay of the concrete cracking damage state for all discrete hazard levels of interest (2%-, 10%-, 50%-, and 86%-in 50 years PE). Similarly, the repair of minor spalls is reduced in comparison to the RC bridge due to the delay of spalling by using FRC material until concrete crushing occurs at high IMs. The main contribution for the repair cost of the bridge is derived from the repair of the abutments due to high values of deck end-abutment relative longitudinal displacement. The repair of the abutment requires temporary support and partial bridge removal for cleaning and assembly of blockout volume at the abutments, repair of joint seal assembly, and structural concrete for the repair of the approach slab. Since serious damage leading to the need of column re-centering or replacement does not

occur in the FRC bridge, even for the highest earthquake intensities considered, temporary support of the superstructure is not required. Therefore, there is no sudden increase in the repair costs at the high hazard levels, as for the RC bridge, due to this superstructure temporary support repair item. The disaggregation plots by repair item and PG for the FRC bridge are presented in Appendix F.

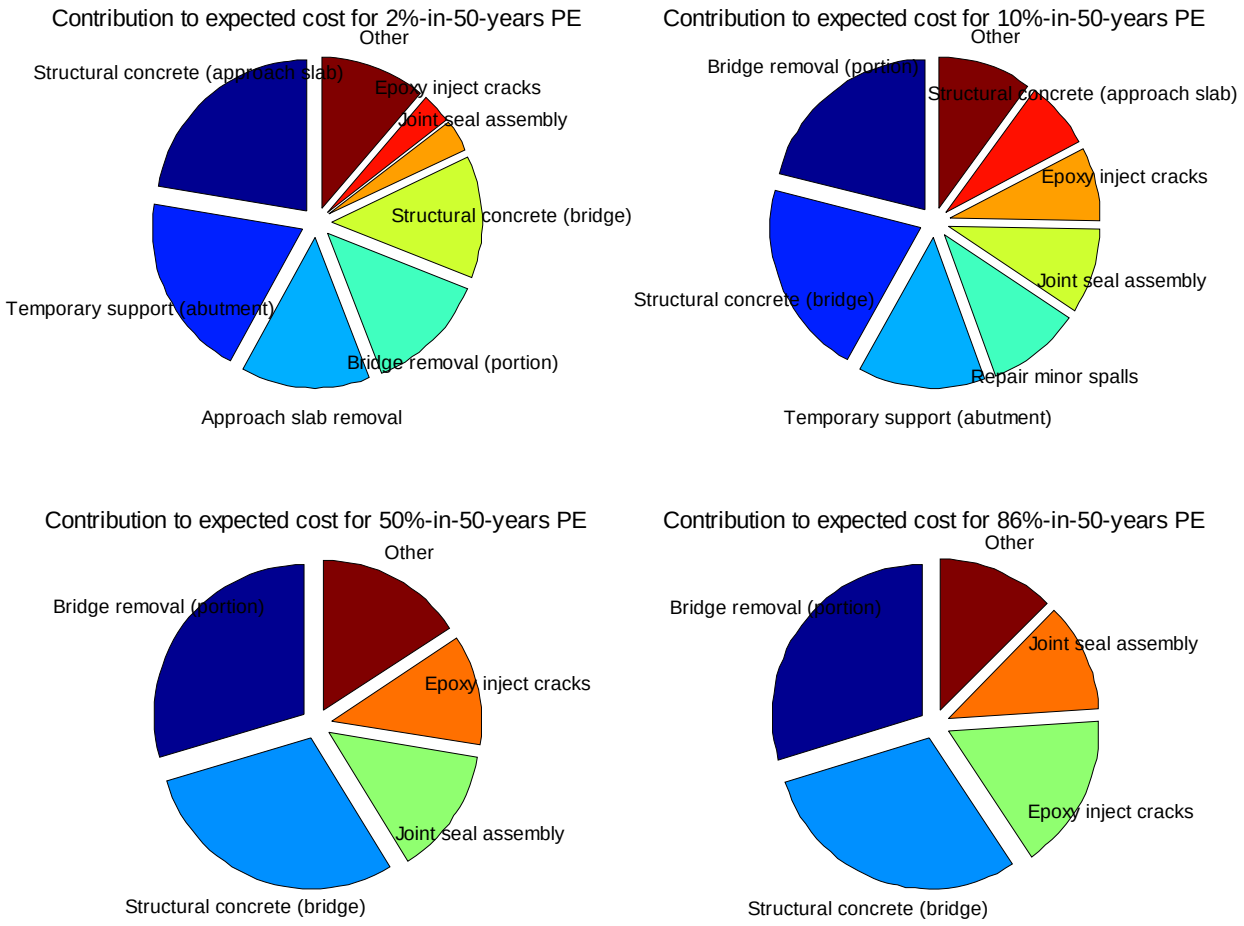

Figure 6-8 Contribution of different repair methods to the total repair cost of FRC bridge model at different seismic hazard levels

Due to the effectiveness of the isolation system specified for BI1 and BI2 bridges in reducing the displacement and force demand in the column bents, the over-conservative design of the superstructure to guarantee elastic behavior for severe seismic intensity, and the specification of a wide gap for the seat abutments, only minor damage occurs in the isolated bridges for the entire earthquake intensity range considered. The resulting repair items related to column cracking and spalling (epoxy injecting cracks, minor spalls repair) are therefore similar for all the discrete hazard levels considered, as can be seen in Figure 6-9 and Figure 6-10 for BI1 and BI2 bridges, respectively. For BI1 bridge, the relative contribution of the repair item related to the use of aggregate base for the approach slab is also evident for the low hazard level of 86%-in 50 years PE. The disaaggregation per PG and repair item for these bridges is also presented in Appendix F.

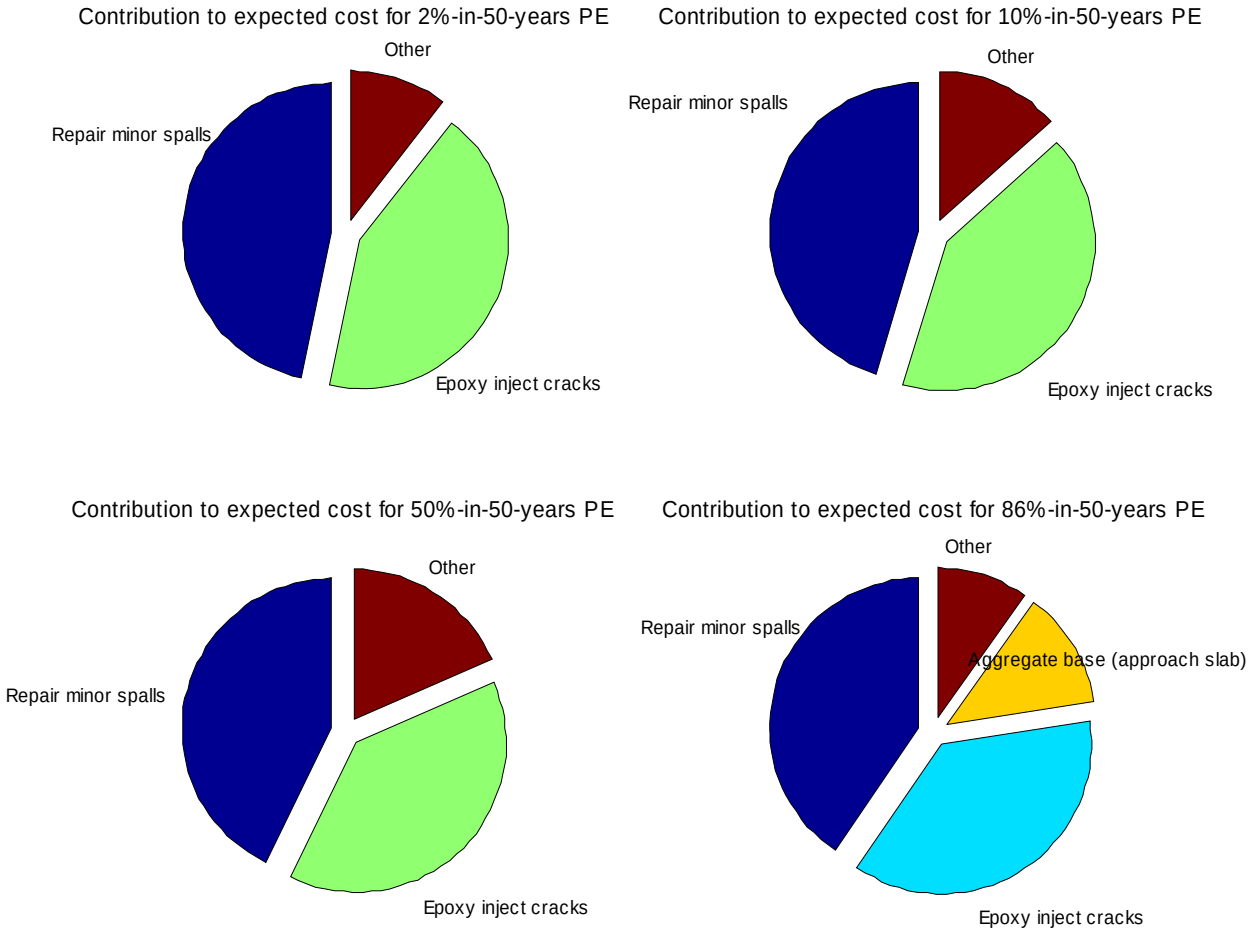

Figure 6-9 Contribution of different repair methods to the total repair cost of BI1 bridge model at different seismic hazard levels

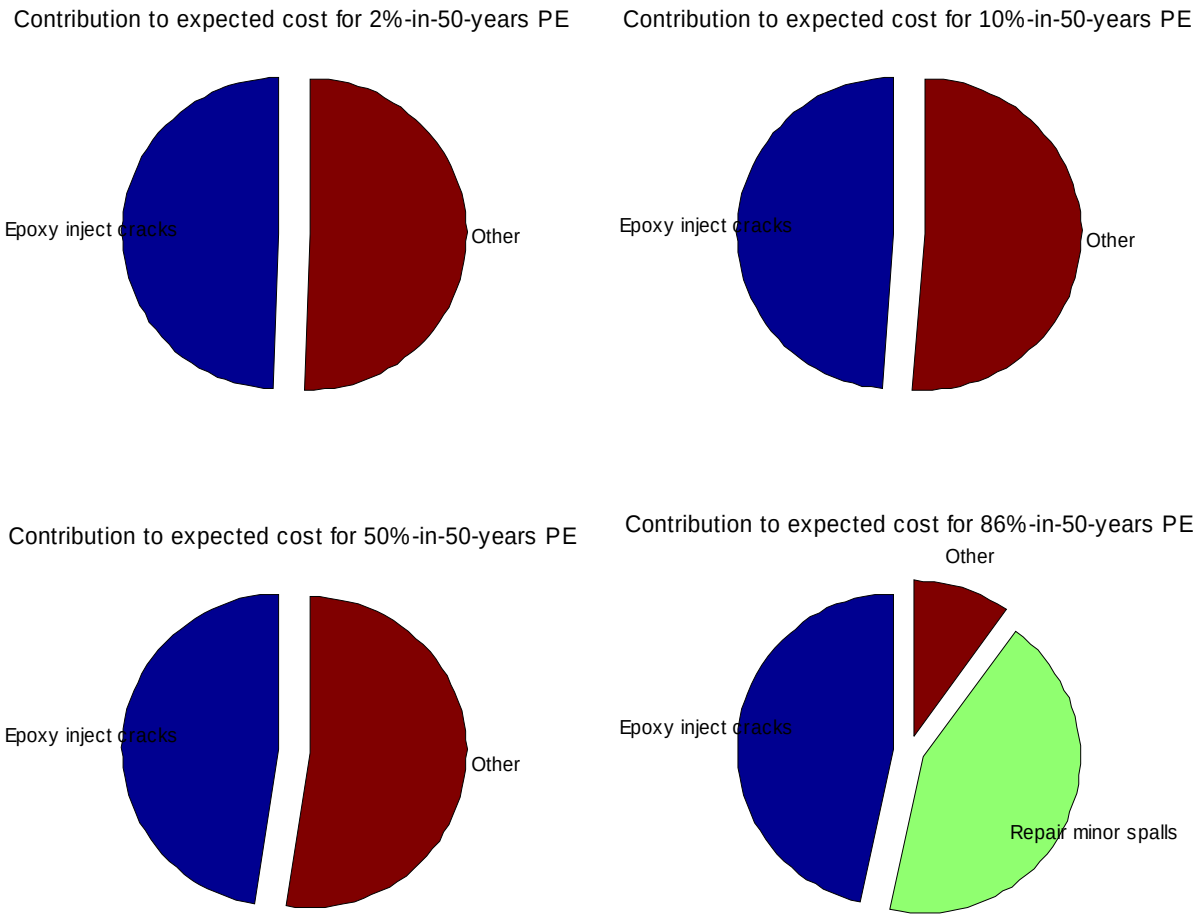

Figure 6-10 Contribution of different repair methods to the total repair cost of BI2 bridge model at different seismic hazard levels

The disaggregation by bridge component or performance group contributing to the ultimate repair cost for the range of earthquake intensity considered is presented in Appendix F. Since the triggering of certain PG damage states leads to a combination of repair methods and items, the disaggregation by PG can provide more insight into why a certain repair quantity employed in several PG repair methods features in the expected repair cost estimate.

For the RC bridge, the shear key force and external columns tangential drift control the repair cost for the low hazard levels, the maximum longitudinal deck-abutment displacement control at the moderate hazard levels, while for the high hazard levels the internal columns tangential drift is excessive and triggers high repair costs due to the need for the re-centering and replacement of the columns. For the FRC, the shear keys force and maximum tangential drift at the four columns contributed to a significant portion of the overall expected repair costs at all seismic intensities considered. At moderate intensities, the maximum longitudinal deck-abutment displacement also contributes to the repair costs of the bridge. For the isolated bridges, only the PGs corresponding to the maximum tangential drift at the columns have an important contribution to the repair costs. The damage states of the remaining PGs are not triggered for the entire earthquake intensity range considered. Since the maximum tangential drift demand at the internal columns is approximately twice the demand at the external columns, their corresponding contribution to the repair costs maintains a similar relation.

6.2.3.3 Repair Time Results

The LLRCAT methodology was used to compute the intensity-dependent total repair time loss model (in terms of CWD) for all bridge types considered in this study (see Figure 6-11). The variability in these plots does not arise from the uncertainty in the repair quantities but rather from the PERT criteria for each of the repair quantities. The repair time estimates are based on numerous simplifying assumptions for repair effort (not repair duration), as discussed in Section 6.2.2. The disaggregation by repair quantity of the repair effort loss model as a function of earthquake intensity for all bridge types is presented in Appendix F.

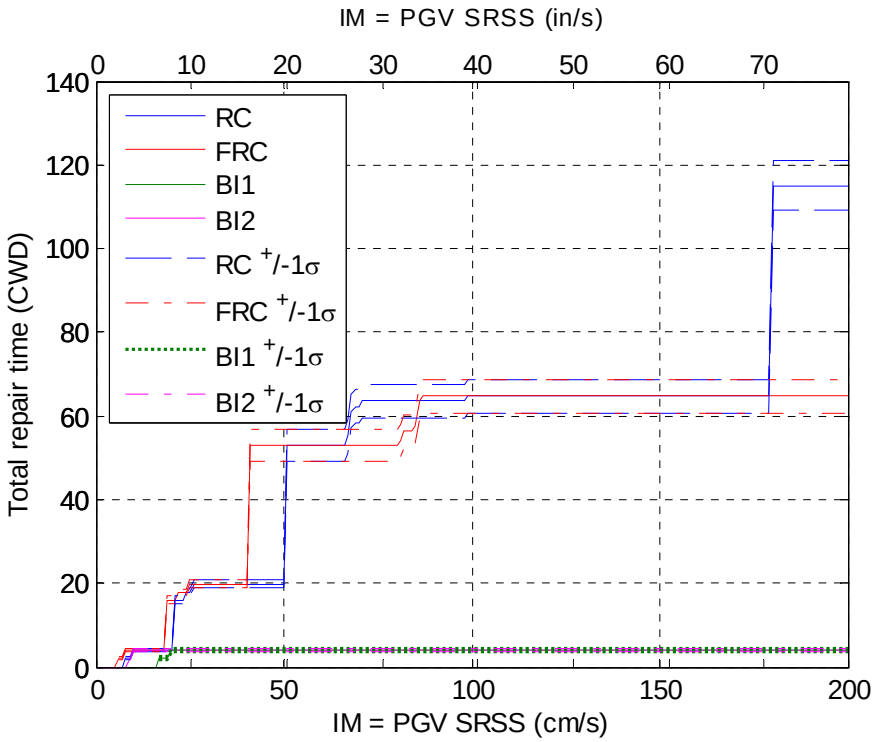

Figure 6-11 Total repair time loss model for different bridge types as a function of earthquake intensity

As can be observed from Figure 6-11, bridges RC and FRC present an accumulation of required repair efforts (in terms of CWD) with increasing earthquake intensity. Bridges BI1 and BI2 only present a low constant value for the repair efforts, triggered at low PGV values of 16 and 8 cm/sec, respectively. Due to the design of bridge BI1 for lower ductility demands of the columns than BI2 bridge, this bridge is more efficient in postponing the need for repair, compared to BI2 bridge. Since the epoxy injecting cracks and minor spalls repair items each take 2 days to complete, the total repair effort for the isolated bridges resulting in only cracking and spalling of the columns is 4 days at any earthquake intensity.

For the RC bridge, the use of structural concrete and temporary support needed to repair the abutments and approach slab triggered at low intensities (PGV<50 cm/sec) require 10 and 33 days to complete, respectively. The remaining repair items triggered such as approach slab

removal, minor spalls repair, joint seal assembly, bar reinforcing steel, aggregate base for approach slab, removal of bridge portion at the abutments, replacement of elastomeric bearings, and structure excavation take less than 5 days to complete and are added to the repair efforts. As with the repair cost plots, at high intensities (PGV greater than 175 cm/sec), the column replacement repair is triggered and both the required repair effort and report cost increase substantially, due to the need of temporary support of the superstructure and column removal. The maximum repair effort at high intensities estimated for the RC bridge is almost 120 days, as seen in Figure 6-11.

For the FRC bridge, similar repair methods are used for the low and moderate IMs. The repair of the abutments and approach slab is triggered earlier than the RC bridge, at a PGV value of 40 cm/sec, due to increased relative longitudinal displacement between the deck ends and the abutments. Since severe damage to the column bents does not occur for the range of intensities considered, the re-centering or replacement of the columns is not needed. The remaining main repair items needed to carry out the retrofit of the bridge are minor spalls repair, partial bridge removal at the abutments, bar reinforcing steel, and joint seal assembly, requiring each less than 5 days to complete. The maximum repair effort at high intensities estimated for the FRC bridge is around 60 days, as seen in Figure 6-11, half of the repair effort for the RC bridge.

The disaggregation by repair quantity plots in Appendix F show only when each repair item triggers a contribution to the total repair effort, which is independent of the actual value of the repair quantity. Therefore, the total repair time values of the different bridge types in Figure 6-11 are merely the summation of the corresponding mean values of the different repair items obtained from the production data. The disaggregation by PG is therefore not carried out for the expected repair time as was done for the repair costs, since multiple PGs may cause an increase in repair quantity that would trigger the repair effort increase.

6.3 COST-EFFECTIVNESS AND EXPECTED REPAIR TIME

The cost-effectiveness of the different bridge types considered in this study throughout their expected lifespan of 75 years is assessed by integrating the repair cost and time loss models along the entire range of earthquake intensities considered, according to the slope of the hazard curve at each IM. The hazard curves for all bridge types were obtained based on USGS hazard data for a site in Berkeley, California (see Chapter 5). The PGA values at discrete hazard levels, converted to PGV values, were used to fit the annual frequency of exceedance a specific IM level or hazard curve, presented in Figure 6-12.

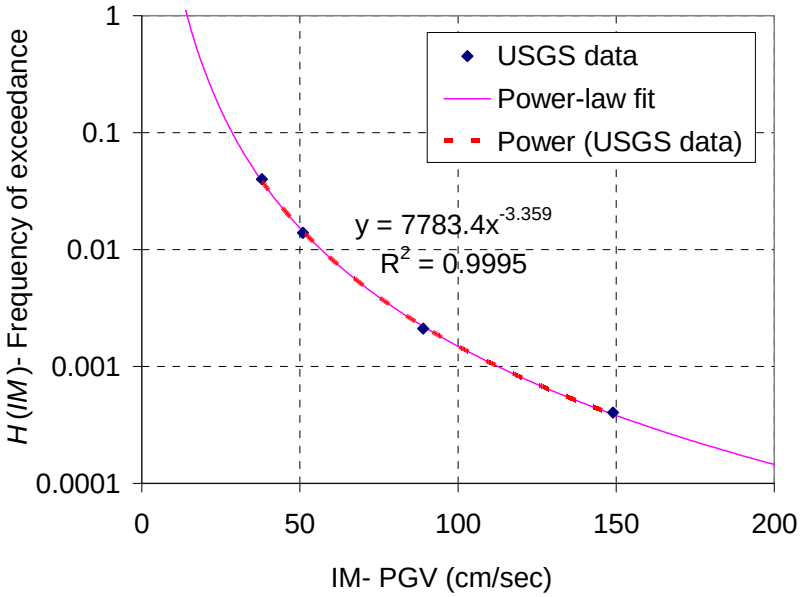

Figure 6-12 Hazard curves for a site in Berkeley, California calculated for 1 year and lifespan of 75 years of the bridges

The loss curves for the RCR and RT of the bridges displaying the MAF of these parameters exceeding specific thresholds were obtained by integrating over the entire range of IM considered the corresponding complementary cumulative distribution functions (ccdf) of RCR and RT curves presented in Figure 6-3 and Figure 6-11, respectively, multiplied by the slope of the hazard curve at each IM (Der Kiureghian, 2005). The resulting MAFs or loss curves for the RCR and RT of the different bridges exceeding different thresholds are presented in Figure 6-13 and Figure 6-14, respectively.

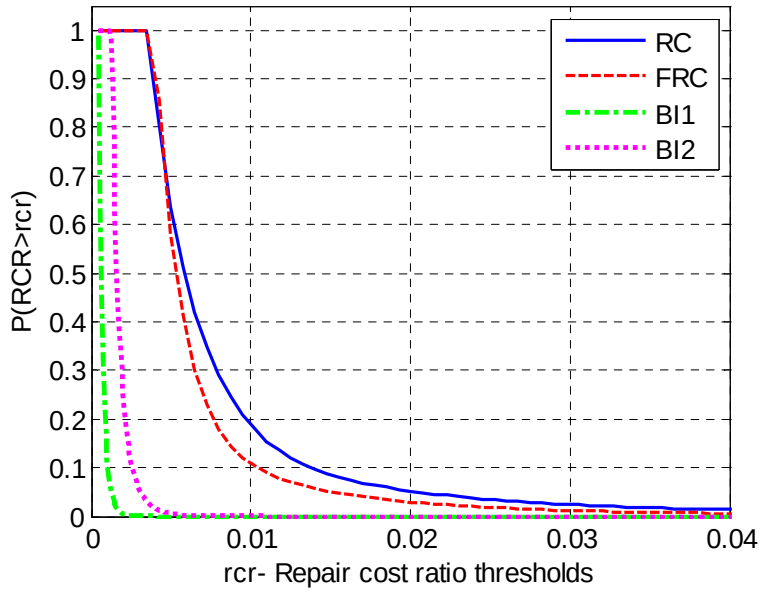

Figure 6-13 RCR MAF or RT loss curve for different bridge types

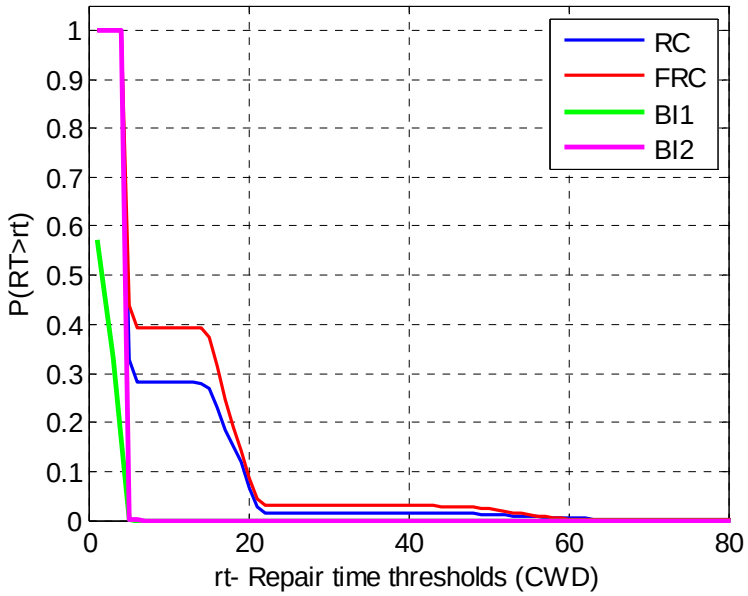

Figure 6-14 RT MAF or RT loss curve for different bridge types

The expected mean annual RCR and RT (A_{RCR}, A_{RT}) were computed by integrating the corresponding MAF curves over the entire range of RCR and RT thresholds considered (Der Kiureghian, 2005). The results for the repair cost and time for all bridge types analyzed, as well as the initial construction costs of these systems are summarized in Table 6-8.

Table 6-8 Construction costs, post-earthquake repair costs, and repair time for different bridge types

Parameter	RC bridge	FRC bridge	BI1 bridge	BI2 bridge
NC- Cost of new construction	$2,959,441	$2,973,316	$3,515,733	$3,310,586
A_{RCR}- Mean annual RCR	0.80%	0.65%	0.02%	0.13%
A- Mean annual repair cost	$23,530	$19,433	$989	$4,388
A_{RT}- Mean annual repair time	8	10	1	4

The results for the FRC, BI1, and BI2 bridges display an important reduction in the mean annual repair costs, in comparison to the baseline RC bridge. BI1 bridge is the most efficient in eradicating structural damage and results in the highest reduction in the annual repair costs, in comparison to the RC bridge, in the order of 97%. BI2 bridge is slightly less efficient, with a reduction of approximately 84% in the mean annual repair cost, compared to the baseline RC bridge. The FRC bridge also presented an 18% reduction in the mean annual repair cost of the bridge system. The repair effort for the isolated bridges was also reduced significantly, requiring of only 1 to 4 days for the repair of minor spalling and cracking of the column bents. Furthermore, since these repair procedures do not interrupt the serviceability of the isolated bridges, in the case of any seismic event, these highway systems will be in continuous operation with zero downtime and therefore zero indirect economic losses. The mean annual repair effort for the FRC bridge is increased, in comparison to the RC bridge, from 8 to 10 crew working days, primarily due to an increase in the shear key force demands and corresponding damage at the abutments for low seismic intensity levels. The increased repair time of the FRC bridge

might possibly result in an increased downtime and some indirect economic losses of this highway system.

The Net Present Value (NPV) of the bridges, which includes the initial construction costs, as well as the total post-earthquake repair costs calculated for a lifespan of 75 years, is presented in Table 6-9 for a wide range of discount rates, i of 2-10%, and different coefficient of variations estimated for the mean annual repair cost, A of each bridge. The present value of the total repair costs accounts for an annual growth rate, g of 3% due primarily to inflation. The variations in the estimation of the mean annual repair cost were established in this financial model to include the effects of epistemic (modeling) uncertainty in the computation of the response estimates of the bridges, as well as other external factors which could result in a considerable reduction or increase in the repair cost. Thus, the NPV of each bridge system is computed for the lower and upper bounds of the annual repair cost A, assuming different values of coefficients of variation (c.o.v.) in this normal distribution.

The color-coded scheme in Table 6-9 displays the order of total cost-effectiveness of the bridges by comparing the NPV of each bridge to the NPV of the remaining bridges for the same discount rate and coefficient of variation applied to the mean annual repair cost. The red color cells represent the highest NPVs or the most expensive bridge under certain discount rate and c.o.v. values. The orange and green color cells represent the second and third most expensive bridge types, respectively, while the blue color cells display the cheapest bridge system, considering both construction and total repair costs over the lifespan of the structures of 75 years.

The selection of an appropriate discount rate, i is an important and complicated task in a financial analysis which, as seen from the dispersion of the NPVs in Table 6-9, can significantly influence the final cost-effectiveness output and the selection of the structural system used for the construction of a highway structure. For low interest rates, the savings in future cash flows derived from post-earthquake repair costs have greater weight in the financial model than the initial capital expenditure corresponding to the cost of new construction of each bridge system.

Therefore, according to the financial analysis results in Table 6-9, despite their high initial construction costs, the isolated bridges result in lower total costs or NPVs, compared to the RC bridge, for low interest rates and high estimates of repair cost annuity. According to this financial model, BI2 bridge, which construction is only 12% more expensive than the cheapest RC bridge, is the most cost-effective of all bridge systems considered and displays the lowest NPVs for most combinations of interest rates and repair cost annuity c.o.v. The BI2 does not present the highest NPV values (red color cells) for any i-c.o.v. combination considered. Due to higher initial construction costs, the BI1 bridge can be considered the most cost-efficient only for extremely low interest rates. This bridge is the most expensive for high interest rates and low estimations of repair cost annuity. Therefore, the initial increase in construction costs of the isolated bridges in the order of 19 and 12% for bridges BI1 and BI2, respectively, can be considered negligible and acceptable for the majority of financial scenarios and epistemic uncertainties considered, due to the substantial elimination of structural damage and the need for repair in all bridge components at any seismic intensity level.

Contrary to the isolated bridges, the cheap RC bridge results in the highest NPVs for low and intermediate interest rate values and high estimates of repair cost annuity. Due to high repair costs in the order of 0.80% annually, the RC bridge does not result in the lowest NPV values for any combination of i-c.o.v. Since the FRC bridge is only slightly more expensive than the RC bridge and results in a reduction of 18% in the mean repair cost annuity, this bridge system presents the lowest NPV values for intermediate and high interest rates and low estimates of

repair cost annuity. Similar to the BI2 bridge, the FRC bridge does not present the highest NPV values for any *i*-c.o.v. combination.

Table 6-9 Net Present Value (NPV) for different bridge types with varying discount rate, *i* and mean annual repair cost, *A* confidence intervals.

RC bridge- NPV ($)		Discount rate, *i* (%)									
C.I.	*A* ($)	2	3	4	5	6	7	8	9	10
μ-σ, c.o.v.=0.4	14,118	4,482,288	3,983,684	3,687,240	3,498,495	3,375,409	3,292,133	3,233,737	3,191,376	3,159,674
μ-σ, c.o.v.=0.3	16,471	4,736,096	4,154,391	3,808,539	3,588,338	3,444,737	3,347,581	3,279,453	3,230,032	3,193,047
μ-σ, c.o.v.=0.2	18,824	4,989,903	4,325,099	3,929,839	3,678,180	3,514,065	3,403,030	3,325,168	3,268,688	3,226,419
μ-σ, c.o.v.=0.1	21,177	5,243,711	4,495,806	4,051,139	3,768,023	3,583,392	3,458,478	3,370,884	3,307,344	3,259,791
μ- Mean	23,530	**5,497,519**	**4,666,513**	**4,172,439**	**3,857,865**	**3,652,720**	**3,513,927**	**3,416,600**	**3,346,000**	**3,293,163**
μ+σ, c.o.v.=0.1	25,883	5,751,327	4,837,220	4,293,738	3,947,707	3,722,048	3,569,376	3,462,316	3,384,656	3,326,536
μ+σ, c.o.v.=0.2	28,236	6,005,134	5,007,927	4,415,038	4,037,550	3,791,376	3,624,824	3,508,032	3,423,312	3,359,908
μ+σ, c.o.v.=0.3	30,589	6,258,942	5,178,635	4,536,338	4,127,392	3,860,704	3,680,273	3,553,748	3,461,968	3,393,280
μ+σ, c.o.v.=0.4	32,943	6,512,750	5,349,342	4,657,638	4,217,235	3,930,032	3,735,721	3,599,464	3,500,624	3,426,652

FRC bridge- NPV ($)		Discount rate, *i* (%)									
C.I.	*A* ($)	2	3	4	5	6	7	8	9	10
μ-σ, c.o.v.=0.4	11,660	4,230,997	3,819,213	3,574,387	3,418,508	3,316,853	3,248,078	3,199,850	3,164,866	3,138,684
μ-σ, c.o.v.=0.3	13,603	4,440,611	3,960,196	3,674,565	3,492,706	3,374,110	3,293,871	3,237,606	3,196,791	3,166,245
μ-σ, c.o.v.=0.2	15,547	4,650,224	4,101,179	3,774,744	3,566,905	3,431,366	3,339,665	3,275,361	3,228,716	3,193,806
μ-σ, c.o.v.=0.1	17,490	4,859,838	4,242,162	3,874,922	3,641,103	3,488,622	3,385,459	3,313,117	3,260,640	3,221,368
μ- Mean	19,433	**5,069,451**	**4,383,144**	**3,975,101**	**3,715,302**	**3,545,878**	**3,431,252**	**3,350,873**	**3,292,565**	**3,248,929**
μ+σ, c.o.v.=0.1	21,376	5,279,065	4,524,127	4,075,279	3,789,501	3,603,134	3,477,046	3,388,628	3,324,490	3,276,490
μ+σ, c.o.v.=0.2	23,320	5,488,679	4,665,110	4,175,457	3,863,699	3,660,391	3,522,839	3,426,384	3,356,415	3,304,052
μ+σ, c.o.v.=0.3	25,263	5,698,292	4,806,093	4,275,636	3,937,898	3,717,647	3,568,633	3,464,139	3,388,340	3,331,613
μ+σ, c.o.v.=0.4	27,206	5,907,906	4,947,076	4,375,814	4,012,097	3,774,903	3,614,427	3,501,895	3,420,265	3,359,174

…Continuation: Table 6-9 Net Present Value (NPV) for different bridge types with varying discount rate, *i* and mean annual repair cost, *A* confidence intervals.

BI1 bridge- NPV ($)		Discount rate, *i* (%)									
C.I.	***A* ($)**	**2**	**3**	**4**	**5**	**6**	**7**	**8**	**9**	**10**
μ-σ, c.o.v.=0.4	490	3,568,620	3,551,304	3,541,009	3,534,454	3,530,179	3,527,287	3,525,259	3,523,788	3,522,687
μ-σ, c.o.v.=0.3	572	3,577,434	3,557,232	3,545,221	3,537,574	3,532,587	3,529,213	3,526,847	3,525,130	3,523,846
μ-σ, c.o.v.=0.2	654	3,586,249	3,563,161	3,549,434	3,540,694	3,534,995	3,531,138	3,528,434	3,526,473	3,525,005
μ-σ, c.o.v.=0.1	735	3,595,063	3,569,089	3,553,647	3,543,814	3,537,402	3,533,064	3,530,022	3,527,815	3,526,164
μ- Mean	817	**3,603,878**	**3,575,018**	**3,557,859**	**3,546,934**	**3,539,810**	**3,534,990**	**3,531,610**	**3,529,158**	**3,527,323**
μ+σ, c.o.v.=0.1	899	3,612,692	3,580,946	3,562,072	3,550,055	3,542,218	3,536,915	3,533,197	3,530,500	3,528,482
μ+σ, c.o.v.=0.2	981	3,621,507	3,586,875	3,566,284	3,553,175	3,544,625	3,538,841	3,534,785	3,531,843	3,529,641
μ+σ, c.o.v.=0.3	1,062	3,630,321	3,592,803	3,570,497	3,556,295	3,547,033	3,540,767	3,536,373	3,533,185	3,530,800
μ+σ, c.o.v.=0.4	1,144	3,639,136	3,598,732	3,574,710	3,559,415	3,549,441	3,542,692	3,537,960	3,534,528	3,531,959

BI2 bridge- NPV ($)		Discount rate, *i* (%)									
C.I.	***A* ($)**	**2**	**3**	**4**	**5**	**6**	**7**	**8**	**9**	**10**
μ-σ, c.o.v.=0.4	2,627	3,593,951	3,501,173	3,446,012	3,410,891	3,387,988	3,372,492	3,361,626	3,353,744	3,347,845
μ-σ, c.o.v.=0.3	3,065	3,641,179	3,532,938	3,468,583	3,427,609	3,400,888	3,382,810	3,370,132	3,360,937	3,354,054
μ-σ, c.o.v.=0.2	3,503	3,688,406	3,564,702	3,491,154	3,444,326	3,413,788	3,393,127	3,378,639	3,368,129	3,360,264
μ-σ, c.o.v.=0.1	3,941	3,735,634	3,596,467	3,513,725	3,461,044	3,426,688	3,403,445	3,387,146	3,375,322	3,366,474
μ- Mean	4,378	**3,782,862**	**3,628,231**	**3,536,296**	**3,477,761**	**3,439,589**	**3,413,763**	**3,395,652**	**3,382,515**	**3,372,684**
μ+σ, c.o.v.=0.1	4,816	3,830,089	3,659,996	3,558,867	3,494,479	3,452,489	3,424,080	3,404,159	3,389,708	3,378,894
μ+σ, c.o.v.=0.2	5,254	3,877,317	3,691,760	3,581,438	3,511,196	3,465,389	3,434,398	3,412,666	3,396,901	3,385,103
μ+σ, c.o.v.=0.3	5,692	3,924,544	3,723,525	3,604,009	3,527,914	3,478,290	3,444,716	3,421,172	3,404,094	3,391,313
μ+σ, c.o.v.=0.4	6,130	3,971,772	3,755,289	3,626,580	3,544,631	3,491,190	3,455,033	3,429,679	3,411,287	3,397,523

For each combination of interest rate and confidence interval of the repair cost annuity, a break-even analysis can be carried out, which computes the variation in the NPV of the different bridge systems over time. From the break-even analysis, the point in time (in years), at which the FRC and isolated bridges result in higher cost-effectiveness (lower NPVs) than the benchmark RC bridge, can be obtained. Figure 6-15 presents the break-even analysis carried out for a discount rate, *i* of 5% and the mean annual repair cost (c.o.v.=0). For this i-c.o.v. combination, the FRC, BI2, and BI1 bridges become more cost effective than the cheapest RC bridge after 5, 23, and 35 years, respectively. Therefore, for this average financial environment, the isolated bridges result in the most cost-effective system (lowest NPVs) for the majority of the lifetime of the bridge structures, specified as 75 years.

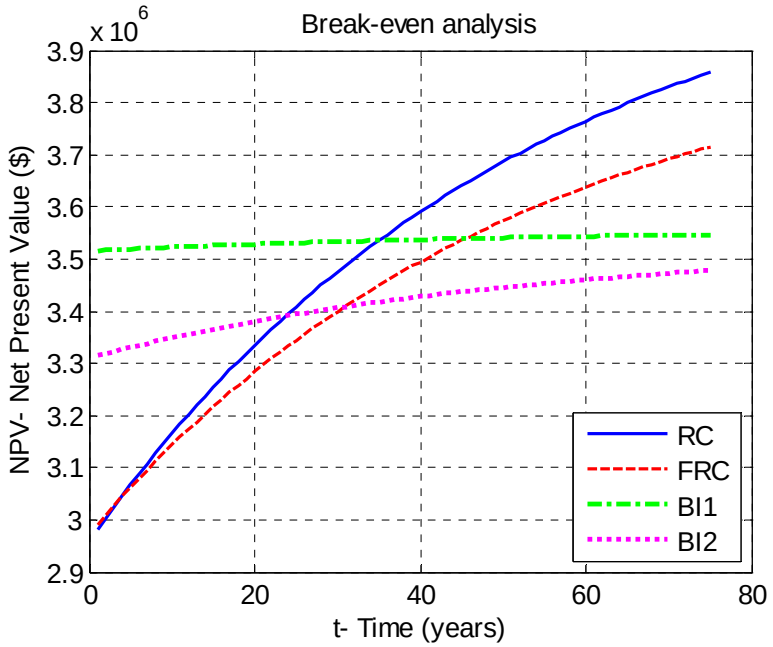

Figure 6-15 Break-even analysis for 5% discount rate and mean annual repair cost of the different bridge systems

7 Conclusions and Future Work

Numerous bridge structures, including cast-in-lace and precast reinforced concrete bridge systems, suffered significant damage or collapse during recent earthquakes around the world (1964 Alaska, USA; 1964 Niigata, Japan; 1971 San Fernando, USA; 1976 Guatemala; 1989 Loma Prieta, USA; 1994 Northridge, USA; 1995 Kobe, Japan; 1999 Kocaeli, Turkey; 1999 Chi-Chi, Taiwan; 2001 Gujarat, India; 2005 Kashmir, Pakistan; etc.). To guarantee post-earthquake serviceability and reduce the repair costs of highway bridge systems, research efforts in recent years have been directed to the development and implementation of innovative designs and materials for new and existing structures to enhance their seismic performance. Since bridge columns provide both the gravity and the lateral load-resisting capacity of bridge structural systems, they can be considered as the most seismically vulnerable components of the structure. During moderate and large earthquake events certain regions of bridge column bents may experience large and repeated cycles in the inelastic range of response. The extent of damage in these plastic hinge regions depends on ground motion characteristics as well as column details. Damage in bridge columns directly affects the overall performance of a bridge during a seismic event and the feasibility of restoring it to its original condition. The seismic performance enhancement methods developed in recent years focus on limiting the load and displacement demand in the column bents as well as improving their damage-tolerance characteristics.

The primary objective of this study was to demonstrate how PEER Performance-Based Earthquake Engineering (PBEE) methodology can be used to evaluate the effectiveness of different methods to improve seismic performance of reinforced concrete bridge structures typical for California. Two methods for enhancing performance of new bridges are investigated: use of fiber reinforced concrete for bridge columns, and the use of lead-rubber base isolation devices to seismically isolate the bridge superstructure. These two performance enhancement methods are use to redesign the PEER PBEE testbed bridge. Then, the seismic performance of the new bridges is compared to the performance of the original, conventional reinforced concrete, PEER testbed bridge in the same seismic hazard environment. This is done by computing the repair cost fragilities for the three bridge systems.

The second objective of this study was to extend the PEER PBEE methodology toward computing the life-cycle cost of a bridge in a seismic hazard environment. The information obtained from computing the repair cost fragilities is combined with estimates of the cost to build the conventional and the enhanced-performance bridges in different financial environments characterized by interest and discount rates. While the cost to maintain the bridges is not considered in this study, the accomplished extension of the PEER PBEE methodology is the essential step toward the goal of a complete probabilistic characterization the expected costs over a lifetime of a bridge in a highly seismic environment.

The third objective of the study was to conduct first-of-a-kind large-scale tests of HRFRC bridge column specimens under bi-directional loading. Such tests provide the missing information about flexure-dominated HPFRC column response up to very high deformation demand levels, enable comparison of different HPFRC plastic hinge details, and serve as the basis to develop design equations for HPFRC bridge columns.

The work on these three objectives is reviewed below.

7.1 REVIEW OF WORK

7.1.1 Seismic Performance of HPFRC Columns

A bidirectional cyclic test was carried out on two approximately ¼-scale circular column specimens built with high-performance fiber-reinforced concrete (HPFRC) and the behavior compared with that of a geometrically "identical" conventionally-reinforced concrete (BC) column tested by Terzic *et al.* (2008). The HPFRC specimens were constructed with a 1.5% volume fraction of commercially available high-strength hooked steel fibers. The columns were detailed with modified longitudinal reinforcement for the plastic hinge zone and relaxed transverse reinforcement compared to the Caltrans Seismic Design Criteria (SDC) (2004) for regular concrete bridge columns. The column base was connected to a massive conventionally-reinforced regular concrete anchor block, simulating fixed boundary conditions. Dowel reinforcement was added at the column base of the HPFRC specimens to prevent concentration of rotations and force inelastic deformations to occur slightly above the column base. Two reinforcement details in the plastic hinge region were evaluated for the HPFRC specimens. In Specimen S1, long dowels were used and the upper portion of the dowels was debonded through the use of plastic tubes in order to avoid premature damage localization that could occur because of the termination of the bars within the plastic hinge zone. In Specimen S2, shorter dowels were provided, terminating within the plastic hinge region and the main longitudinal bars were debonded over a short length in order to prevent strain concentration and premature rebar fracture in the section were the dowels are terminated.

A circular load pattern with increasingly larger radius was defined for the bidirectional quasi-static cyclic test of all column specimens. The highly demanding displacement history on the column, defined by two circular cycles at each displacement level (one clock-wise and the other counter-clock-wise), was selected to minimize the bias in column damage in any particular direction. The loading pattern was defined to exclusively induce lateral displacement and no torsion in the column, accounting for second-order specimen geometry effects and actuator elongations. The ductility demand was computed with respect to the BC column yield point, estimated at 0.55", to enable a direct comparison between the BC and HPFRC specimens by applying the same drift demands. In the post-yield displacement history, each main cycle or displacement level was followed by a small displacement cycle equal to one-third of the primary cycle (maximum drift applied up to that point) to evaluate the column stiffness degradation throughout the loading history. The maximum ductility level attained during the test of the reference column BC was 4.5 (3.9% drift ratio), while the maximum ductility level attained during the test of the S1 and S2 columns without substantial loss of gravity load carrying capacity was 12.5 and 6.25, respectively (10.7 and 5.4% drift ratios). A gravity load equivalent to 10% of the BC column axial capacity was applied to the column top. A finite element model

of a cantilever column was also implemented and analyzed using OpenSees (Mckenna *et al.* 2000) to simulate the cyclic response of the HPFRC columns.

7.1.2 Enhanced-Performance Bridge Design, Modeling and Analysis

A typical Ordinary Nonstandard reinforced concrete (RC) bridge, designed by Ketchum *et al.* (2004) according to AASHTO Standard Specifications for Highway Bridges (AASHTO 1996) and Caltrans Seismic Design Provisions (Caltrans 2004), was redesigned using two seismic-performance enhancement techniques: isolation system underneath the superstructure and fiber-reinforced concrete for the construction of bridge piers. The RC bridge consists of a single column-bent, five-span bridge with prestressed box-girder superstructure, typical column bent details, and simple geometric regularity (symmetry, zero skew, and uniform column height). Highly detailed nonlinear three-dimensional models of the conventionally-reinforced concrete (RC), fiber-reinforced concrete (FRC), and isolated (BI) bridges were implemented in OpenSees.

The fiber-reinforced concrete (FRC) bridge model in OpenSees was defined using the same geometry, superstructure, and abutment models as the RC bridge, and a modified column model specified according to the experimental results and analytical validation of the S1 HPFRC cantilever column tested, which resulted in enhanced cyclic behavior.

The design of the isolated bridges using lead rubber bearings (LRBs) was carried out for two target performance criteria: one with elastic column behavior (BI1) and the other with minor inelastic column behavior (maximum displacement ductility demand of 2) (BI2). The OpenSees model of the isolated bridges included additional elements representing the isolation bearings, top and bottom bent cap beams connecting the superstructure, bearings and column bents, and a system of rigid links. The column nonlinear and superstructure linear-elastic behaviors were defined using similar modeling parameters as in the RC bridge. The abutment models including LRB isolators were modified with respect to the RC abutment model. To allow lateral displacement of the superstructure, the size of the longitudinal gap was increased and an additional compression-only gap was provided in the transverse direction, defined according to the maximum lateral displacement specified for the isolators.

The assessment of the force and displacement demand vs. capacity, as well as dynamic behavior of the RC, FRC, and isolated bridges was carried out by comparing modal, pushover, and nonlinear time history analyses results of the bridges models in OpenSees. For the pushover analysis, a uniform force pattern was applied on all deck nodes for comparative purposes and the displacement of the bridges was monitored at the external column top. Nonlinear time history analysis was carried out by applying a uniform ground motion excitation at the base of the bridges using 140 three-component records covering a wide range of earthquake magnitudes and fault distances, as well as different faulting mechanisms. The comparison of the seismic response of the different bridge systems was carried out by relating selected EDPs obtained from nonlinear time history analysis to an intensity measure for each record. A natural log fit was used to relate the EDPs of the different bridges to the period-independent *IM* of each record, defined as the scaled peak ground velocity (PGV). The modeling and analysis of the different bridge models was carried out in accordance to the recommendations by Aviram *et al.* (2008a, 2008b).

7.1.3 Performance Enhancement Cost-Effectiveness Analysis

The total cost-effectiveness of the isolated and fiber-reinforced concrete bridges, in comparison to the fixed-base conventionally-reinforced concrete bridge, included considerations of the cost of new construction, post-earthquake repair costs required for a 75 year design life of the structures, as well as the repair time of the bridges affecting the downtime of the highway system and producing indirect economic losses. A new vector-based probabilistic approach of applying the PEER Performance-Based Earthquake Engineering framework to compute post-earthquake repair cost and time of highway bridges (Mackie *et al.* 2007) was used in this study. Using this methodology, denominated LLRCAT, loss models relating the repair time and repair cost of each bridge as a percentage of the corresponding total construction cost to an earthquake intensity measure were developed. Fragility curves displaying the probability of exceeding a specific repair cost and time thresholds were also developed, considering the seismic hazard in the region throughout the lifespan of the bridges. A financial analysis accounting for a wide range of discount rates and confidence intervals in the estimation of the mean annual post-earthquake repair cost was performed to evaluate the total cost-effectiveness of the bridges. In the LLRCAT methodology the intensity-dependent repair time or effort loss model of the different bridges was computed using the PERT criterion (Perry and Grieg, 1975).

7.2 FINDINGS AND CONCLUSIONS

The PEER PBEE methodology was successfully utilized to evaluate the effectiveness of two fundamentally different seismic performance enhancement methods to improve the seismic performance of reinforced concrete overpass bridges in California. The first method, based on using a high-performance fiber reinforced concrete material to build bridge columns, relies on the high-performance material and detailing to increase the deformation capacity and shear strength of bridge columns and, thereby, improve the overall seismic performance of the bridge. The second method, based on using seismic isolation devices, relies on changing the dynamics of the bridge structure by introducing a flexible and deformable structural element between the column and the bridge deck in order to reduce the seismic forces and accommodate for the increased displacements.

As seen from the significant differences in the modal, pushover, and nonlinear time history analysis results of the bridge models, the seismic performance enhancement techniques used to redesign the baseline RC bridge system, particularly seismic isolation, resulted in major modification to its resistance mechanisms, relative stiffness and force distribution among the different bridge components, fundamental dynamic properties, as well as total displacement and force demand on the bridge. The overall shape of the pushover curves of the RC and FRC bridges was relatively similar and pre- and post-earthquake periods at different seismic intensities of the FRC bridge were slightly elongated. The FRC bridge presented a higher elastic limit and base shear than the benchmark RC bridge, resulting in reduced displacement ductility demands, as well as increased bearing displacement and shear strain demands which are easily compensated for by the enhanced shear and flexural strength, as well as improved damage tolerance of the fiber-reinforced concrete material. Despite higher displacement demands on the FRC bridge columns obtained from nonlinear time history analysis, due to higher elastic limit observed from the experimental results, the resulting ductility demands on the column bents were

in fact reduced for the medium to high earthquake intensity range. Overall, the FRC bridge behaved better than the reference RC bridge.

The effectiveness of the isolation system in preventing stiffness and strength degradation of all major bridge components was evident given the similarity between the pre-earthquake and post-earthquake periods obtained for all seismic intensities. The overall shape of the pushover curves of the isolated bridges was significantly altered, compared to the RC bridge, due to the increased flexibility of the bearings in shear, connected in series to the flared column top and the modified boundary conditions in both transverse and longitudinal directions. The installation of the bearings at the column top reduced the column heights of the isolated bridge columns, subsequently requiring larger cross sections and higher reinforcement ratios which resulted in an increased stiffness and reduced ductility capacity of the column bents. However, this effect was not relevant since the isolated columns only undergo minor ductility demands, even at high seismic intensities. The isolation system design was highly effective in reducing displacement demands (maximum drift, displacement ductility, and residual drift), as well as force demands on the substructure and other structural components, particularly in the case of the BI1 bridge with elastic column behavior. The inelastic response and energy dissipation in both isolated bridges was developed exclusively through the stable and ductile post-yield shear deformation of the isolator devices.

The effectiveness of these two methods was quantified by computing the cost of construction and the likely cost of bridge repair in a 75-year life span of the bridge considering the variability of the financial conditions by accounting for the changes in the inflation rate and the construction bond interest rate over the life span of the bridge. This important extension of the PEER PBEE methodology was, also, successfully implemented and used to compare the overall life-cycle cost to build and repair the conventional and the enhanced-performance bridges.

The cost of new construction of the FRC bridge was only 0.5% higher than the RC bridge since the additional cost of steel fibers added to the column concrete mix and longitudinal dowels for the special plastic hinge zone detail was compensated by the relaxation in the transverse reinforcement and reduction in the steel weight. The FRC bridges resulted in an approximate reduction in the mean annual repair cost of 18% and an increase in the mean annual repair effort from 8 to 10 CWD, in comparison to the RC bridge. For the RC and FRC bridges, the damage to the abutments controlled the repair cost for low and moderate hazard levels. For the high hazard levels, the internal columns tangential drifts in the RC bridge were excessive and triggered high repair costs due to the need for the re-centering or replacement of the columns. By comparing the net present value of the bridges, the FRC bridge was the most cost-effective for a financial environment with high interest rates and low estimates of repair cost annuity.

The new construction costs of the BI1 and BI2 bridges were nearly 20% and 12% higher than the RC bridge cost, respectively, due to the higher volume of concrete and the additional reinforcing steel weight of the bridge piers, as well as the elevated cost of the isolation bearings. This outcome was primarily due to the fact that in a long span bridge high quantities of materials are required for the construction of the superstructure, foundations and abutments, which were not modified in this study in the design of the isolated bridges. The isolated bridges were extremely efficient in reducing structural damage in all bridge components, resulting in a total reduction in the mean annual repair costs with respect to the RC bridge of 97 and 84% for BI1 and BI2 bridges, respectively. The repair effort for the isolated bridges was also reduced significantly, requiring of only 1 to 4 CWD for the repair of minor spalling and cracking of the

column bents, in comparison to 8 CWD for the RC bridge. Despite their high initial construction costs, the isolated bridges proved to be the most cost-effective for low and intermediate interest rates and for different epistemic uncertainties. Furthermore, since the repair procedures on these bridges are not expected to interrupt bridge traffic, such bridges are expected to remain in continuous operation with zero downtime and zero indirect economic losses. The break-even time required for the isolated bridges to surpass the RC bridge costs, considering average discount rates was estimated at only 20-40 years. Thus, seismic isolation proves to be the most cost-effective system overall when the entire 75-year lifetime of the structures is considered.

The first-of-a-kind large-scale tests of HRFRC bridge column specimens under bi-directional loading, conducted in this project, provide the missing information about flexure-dominated HPFRC column response up to very high deformation demand levels. Two plastic hinge details, consisting of added dowels and selective debonding on longitudinal reinforcement, were evaluated. Both S1 and S2 HPFRC column specimens displayed more ductile behavior and higher damage tolerance in comparison to the geometrically "identical" plain concrete specimen BC. Both HPFRC columns remained elastic up to a nominal ductility of 1.5 of the BC column (1.3% drift). At a ductility demand of 4.5 (3.9% drift), while large portions of the BC column cover spalled off, the HPFRC columns had sustained relatively minor damage, and spalling had not occurred despite relatively large flexural cracks. The S1 and S2 specimens were cycled up to nominal ductility levels of 12.5 and 6.25 (10.7% and 5.4% drift ratios), respectively, while sustaining the applied gravity load.

The plastic hinge length in Specimen S1 was approximately 18" at the end of the test, greater than one column diameter. The propagation of the plastic hinge zone with multiple cracking in the S1 column occurred from the center of the plastic hinge zone at the middle of the debonded region, upwards as well as towards the base of the column. The extension of the BC column plastic hinge zone was estimated at 12", equivalent to ¾ of the column diameter. The S2 column, nonetheless, presented a primary crack at a height of 10" above the foundation at the cut-off point of the dowel bars, resulting in a concentration of rotation and damage around that region and limited spreading of the plastic hinge zone towards the base of the column.

A comparison of HPFRC and BC specimen force-deformation response demonstrates the benefits of using HPFRC: even though the shear demand on the HPFRC specimens increased significantly and the amount of transverse reinforcement was reduced by half compared to the BC specimen, the HPFRC specimens maintained a stable hysteretic behavior governed by flexure throughout the entire cyclic loading history. The addition of steel fibers to the concrete mix helped maintain high levels of shear strength at very large displacement ductility demands. Furthermore, the HPFRC columns presented a post-yield strain-hardening cyclic behavior, while the BC column presented a plateau-like response, maintaining a constant post-yield column shear up to a nominal ductility of 4.5 (3.9% drift).

The degradation of shear force with the progression of damage in the HPFRC specimens that initiated at a nominal displacement ductility of 6.25 (5.4% drift) was solely governed by the loss of flexural capacity (concrete crushing, bar buckling, and finally rebar fracture), not due to shear-related damage. Sliding or significant shear distortions were not evident in the HPFRC specimens, and no pinching (gap-like response) was visible in the hysteretic loops.

Based on an idealized curvature profile and a plastic hinge deformation model, a modified plastic hinge curvature ductility was estimated for the HPFRC specimens, different than the conventional displacement ductility. The estimated ductility demand on Specimen S1 was reduced by an approximately 0.5, in comparison to the demand on the BC specimen, while

for the S2 column the ductility demand was increased due to formation of a primary crack at the cut-off level of the dowels, which resulted in high concentration of rotations and damage at that region. Using the calibrated analytical model of the HPFRC columns implemented in OpenSees, the peak strength and general shape of the hysteretic loops of S1 column were successfully approximated up to a nominal ductility level of 8 (6.9% drift), after which significant damage with unpredictable behavior occurred in the column. The calibrated analytical model of the S1 column was used to approximate its residual gravity load carrying capacity following cyclic loading histories to different ductility demand levels, presenting overall a similar pattern as the experimental results of the BC column.

7.3 FUTURE WORK

Advances in application of the PEER PBEE methodology to evaluate different performance enhancement methods and its extension to include the financial environment risk exposure and an experimental evaluation of seismic performance of high-performance fiber reinforced concrete bridge columns presented in this dissertation open a number of new opportunities for reasearch. They are outlined below.

7.3.1 FRC Materials and Bridge Column Design

The significant difference in the length and location of the plastic hinge mechanism among the three specimens tested demonstrates that it is possible to achieve a highly desirable spreading of plastic deformation. Additional research is therefore needed for the design and detailing of the longitudinal reinforcement and debonding sleeves in the plastic hinge region to best utilize the properties of HPFRC to achieve improved cyclic behavior and enhanced deformation capacity of full-scale bridge columns. The design recommendations should aim at preventing damage concentration in localized regions such as the column-base interface or at the cut-off level of the longitudinal dowels to allow for enough clearance for the stable propagation of inelasticity and offset the fracture of longitudinal rebar.

While the additional shear strength obtained by the use of steel fibers is helpful in developing a very deformable flexural plastic hinge, the adverse consequences of relaxed transverse reinforcement ratio and increased hoop spacing resulting in the reduction of buckling resistance of longitudinal rebar, should be investigated. More specifically, the efficiency of the HPFRC cover in providing confinement and support to the longitudinal bars should also be assessed numerically. Design recommendations for the maximum possible reduction in transverse reinforcement in bridge columns could consequently be determined. Furthermore, since the use of HPFRC is expected to simplify the construction of many critical regions in bridges, which currently require extensive reinforcement detailing resulting in rebar congestion and high construction difficulty, additional material developments and corresponding assessment of its mechanical properties is needed.

Material developments are also needed to achieve improved workability of the HPFRC mix. Additional tests verifying the degradation in the lateral stiffness and strength, as well as the residual gravity load carrying capacity of HPFRC bridge columns, in comparison to regular concrete specimens, are required as well. These tests should verify the observed offset in the

elastic limit in the HPFRC specimens and assess their actual ductility capacity. The analytical model of the HPFRC cantilever columns could be improved using the additional experimental data for its implementation in three-dimensional bridge models. The test on the successful detail of the plastic hinge region in the S1 HPFRC column could also be repeated using other fiber-reinforced cementitious materials to determine their efficiency.

7.3.2 Enhanced-Performance Bridge Design

Different strategies have been developed and implemented over the years for the dissipation of energy and the localization of damage in bridge systems, among them are different shearing mechanisms, sliding bearings, plastic hinge rotations, and rocking. The dissipation of energy in a typical bridge structure in California through the formation of plastic hinges in regular and fiber-reinforced concrete bridge piers, as well as the shearing of elastomeric bearings installed underneath the superstructure, have been thoroughly evaluated in this study. The assessment of the seismic response and cost-effectiveness carried out herein could be extended to additional performance-enhancement strategies for bridge construction to provide design engineers sufficient tools for the selection of the most efficient structural system, given a specific economic state. This assessment should account for the seismic hazard and ground motion variability, the epistemic uncertainty inherent in bridge response estimates, as well as the unpredictability and fluctuations in the financial environment over the lifespan of the structures.

The cost analysis performed accounted for the initial capital expenditure required for the construction of the bridges, as well as the estimated annualized post-earthquake repair cost over time. However, additional cash flows in the financial model related to maintenance, inspection, and indirect losses, were not considered due to lack of available data and should be included in future investigations of bridge fragilities.

The regressions on selected engineering demand parameters of the different bridge structures provide an important insight on the effect of using different seismic performance enhancement techniques on the overall behavior of the bridges response parameters as a function of earthquake intensity. However, due to the high data dispersion of the nonlinear dynamic analysis results, the regressions do not provide exact relations between these parameters and earthquake intensity. A comprehensive dynamic analysis with different bridge configurations and reinforcement details, as well as an extended ground motion set, is required to compute reliable bias factors between the different bridge systems at different hazard levels.

The computation of the new construction cost of the isolated bridges did not include a redesign of the foundations according to the actual column shear demand. For a more precise evaluation of the total cost-effectiveness of these bridges, the reduction in the foundation size and corresponding costs should be accounted for in the financial analysis. In the isolated bridges additional components bridging the gap between the deck end and the abutments were also excluded in the computation of the repair costs due to lack of data on their design and damage states. However, further research is needed on these bridging components since a slight increase in the repair cost and effort of the isolated bridge could occur due to the large lateral displacements of the unrestrained deck ends.

The main contribution to the repair cost and effort for the RC and FRC bridges was damage to the shear keys, the abutments and the approach slab, as well as the different damage states of the column bents. Additional research focused on these bridge components is needed to

better understand their behavior and to develop new designs that are more damage resistant, easier to repair, and more cost-effective to maintain over the expected life of a bridge.

Bibliography

AASHTO (1998). *LRFD Specification for Highway Bridge Design*. American Association of State Highway and Transportation Officials, Washington, D.C.

AASHTO (1996). *Standard Specifications for Highway Bridges*. 16th Edition. American Association of State Highway and Transportation Officials, Washington, D.C.

AASHTO (1999). *Guide Specifications for Seismic Isolation Design*, 2nd Edition, American Association of State Highway and Transportation Officials, Washington, D.C.

Aboutaha, R.S., Engelhardt, M.D., Jirsa, J.O., and Kreger, M.E. (1999). Experimental Investigation of Seismic Repair of Lap Splice Failures in Damaged Concrete Columns, *ACI Structural Journal*, 96(2): 297-307.

Agrawal, R., Singh, A.K., and Singhal, D. (1996). Effect of Fiber Reinforcing Index on Compressive Strength and Bond Strength of Steel Fiber Reinforced Concrete. *Institute of Engineers (India)*, 77(1): 37-40.

Aoude, H., Cook, W.D., and Mitchell, D. (2009). Behavior of Columns Constructed with Fibers and Self-Consolidating Concrete. *ACI Structural Journal*, 106(3): 349-357.

Aviram, A., Mackie, K., and Stojadinovic, B. (2008). Effect of Abutment Modeling on the Seismic Response of Bridge Structures. In *Proceedings of the 6th National Seismic Conference on Bridges and Highways*. Charleston, South Carolina.

Aviram, A., Mackie, K. and Stojadinovic, B., (2008). Guidelines for Nonlinear Analysis of Bridge Structures in California. *Technical Report 2008/03, Pacific Earthquake Engineering Research Center*, University of California, Berkeley.

Banthia, N., and Gupta, R. (2004). Hybrid Fiber Reinforced Concrete (HyFRC): Fiber Synergy in High Strength Matrices. *Materials and Structures*, 37: 707-716.

Banthia, N., and Soleimani, S.M. (2005). Flexural Response of Hybrid Fiber-Reinforced Cementitious Composites. *ACI Materials Journal*, 102(6): 382-389.

Berry, M., and Eberhard, M. (2003). *Performance Models for Flexural Damage in Reinforced Concrete Columns*. Report No. 2003/18. Pacific Earthquake Engineering Research Center, University of California, Berkeley.

Billington, S.L. and Yoon, J.K. (2004). Cyclic Response of Precast Bridge Columns with Ductile Fiber-reinforced Concrete. *ASCE Journal of Bridge Engineering*. 9(4): 353-363.

Buckle, I.G., Constantinou, M.C., Dicleli, M., and Ghasemi, H. (2006). Seismic Isolation of Highway Bridges. *Special Publication MCEER-06-SP07*, Multidisciplinary Center for Extreme Events Research, Buffalo, NY.

Caltrans (2004). *Seismic Design Criteria 1.3*. California Department of Transportation, Sacramento, CA.

Campione, G. (2002). The Effects of Fibers on the Confinement Models for Concrete Columns. *Canadian Journal of Civil Engineering*, 29: 742-750.

Canbolat, B.A., Parra-Montesinos, G.J., and Wight, J.K. (2005). Experimental Study on Seismic Behavior of High-Performance Fiber-Reinforced Cement Composite Coupling Beams. *ACI Structural Journal*, 102(1): 159-166.

Chai, Y., Priestly, M.J., and Seible, F. (1991). Seismic Retrofit of Circular Bridge Columns for Enhanced Flexural Performance. *ACI Structural Journal*, 88(5): 572-584.

Chao, S., Liao, W., Wongtanakitcharoen, T., and Naaman, A. (2007). Large scale tensile tests of high performance fiber reinforced cement composites. In *Proceedings of the 5th Int. RILEM Workshop on High Performance Fiber Reinforced Cement Composites (HPFRCC5)*, Mainz, Germany.

CHBDC (2000). *Canadian Highway Bridge Design Code*. Canadian Standards Association International, Toronto, Ontario.

Cheng, M.Y., and Parra-Montesinos, G.J. (2007). Punching Shear Resistance and Deformation Capacity of HPFRC Connections in Slab-Column Frames Subjected to Earthquake-Induced Displacement. *Proceedings of High Performance Fiber Reinforced Cement Composite 5 (HPFRCC5)*, edited by H.W. Reinhardt and A.E. Naaman, Mainz, Germany.

Choi, E., DesRoches, R., and Nielson, B.G. (2004). Seismic Fragility of Typical Bridges in Moderate Seismic Zones. *Engineering Structures*, 26(2): 187-199.

Chung, Y.S., Park, C.K., and Meyer, C. (2008). Residual Seismic Performance of Reinforced Bridge Piers after Moderate Earthquakes. *ACI Structural Journal*, 105(1): 87-95.

Cornell, C.A., and Krawinkler, H. (2000). Progress and Challenges in Seismic Performance Assessment. *PEER Center News* 3(2):1-2.

Der Kiureghian, A. (2005). Non-ergodicity and PEER's Framework Formula. *Earthquake Engineering and Structural Dynamics* 34:1643-1652.

DesRoches, R., Nielson, B., and Padgett, J. (2006). Fragility Curves for Mid-America Bridges. In *Proceedings of the 8th National Conference on Earthquake Engineering* (8NCEE), San Francisco, CA.

Dicleli, M. (2008). Performance of Seismic-Isolated Bridges with and without Elastic-Gap Devices in Near-Fault Zones. *Earthquake Engineering and Structural Dynamics*, 37(6):935-954.

Dynamic Isolation Systems (2007). *Seismic Isolation for Buildings and Bridges*. Design Manual, Dynamic Isolation Systems, Inc., Sparks, Nevada.

Eligehausen, R., Popov, E.P., and Bertero, V.V. (1983). Local Bond Stress-Slip Relationships of Deformed Bars under Generalized Excitations. *Report No. UCB/EERC-83/23, Earthquake Engineering Research Center*, University of California, Berkeley.

Elwood, K.J. (2002). *Shake Table Tests and Analytical Studies on the Gravity Load Collapse of Reinforced Concrete Frames*. Ph.D. Dissertation, University of California, Berkeley.

Elwood, K.J. and Moehle, J.P. (2005). Axial Capacity Model for Shear-Damaged Columns. *ACI Structural Journal*, 102(4): 578-587.

Fanella, D.A., and Naaman, A.E. (1983). Stress-Strain Properties of Fiber Reinforced Mortar in Compression. *ACI Journal Proceedings*, 82(4): 475-483.

Filiatrault, A., Pineau, S., and Houde, J. (1995). Seismic Behavior of Steel-Fiber Reinforced Concrete Interior Beam-Column Joints. *ACI Structural Journal*, 92(5): 1-10.

Gao, J., Sun, W., and Morino, K. (1997). Mechanical Properties of Steel Fiber Reinforced High Strength Light Weight Concrete. *Cementitious Concrete Composites*, 19: 307-313.

Ghosh, S., Battacharya, C., and Ray, S.P. (1989). Tensile Strength of Steel Fiber Reinforced Concrete. *Institute of Engineers* (India), 69(1): 222-227.

Grant, D., Fenves, G.L., and Auricchio, F. (2004). Bridge isolation with high-damping rubber bearings- analytical modelling and system response. In *Proceedings of the 13th World Conference on Earthquake Engineering*, Vancouver, B.C.

Graybeal, B.A. (2006). Material Property Characterization of Ultra-High Performance Concrete. *Report No. FHWA-HRT-06-103*. Federal Highway Administration, Washington D.C.

Graybeal, B.A. (2007). Compressive Behavior of Ultra-High-Performance Fiber-Reinforced Concrete. *ACI Materials Journal*, 104(2): 146-152.

Habel, K., Denarié, E., and Brühwiler, E. (2007). Experimental Investigation of Composite Ultra-High-Performance Fiber-Reinforced Concrete and Conventional Concrete Members. *ACI Structural Journal*, 104(1): 93-101.

Hachem, M.M., Mahin, S.A., and Moehle, J.P. (2003). Performance of Circular Reinforced Concrete Bridge Columns under Bidirectional Earthquake Loading. *PEER Report 2003-06*. Pacific Earthquake Engineering Research Center. Berkeley, California.

Han, T.S., Feenstra, P.H., and Billington, S.L., (2003). Simulation of Highly Ductile Cement-Based Composites. *ACI Structural Journal*, 100(6): 749-757.

Harajili, M.H., Maalouf, D., and Khatib, H. (1995). Effect of Fibers on the Punching Shear Strength of Slab-Column Connections. Cement *& Concrete Composites*, 17(2): 161-170.

Harajli, M.H., and Rteil, A.M. (2004). Effect of Confinement Using Fiber-Reinforced Polymer or Fiber-Reinforced Concrete on Seismic Performance of Gravity Load-Designed Columns. *ACI Structural Journal*, 101(1): 47-56.

Harris, R.B. (1978). *Precedence and Arrow Networking Techniques for Construction*. Wiley, New York, NY, 326-329 pp.

HAZUS (1999). *Earthquake Loss Estimation Methodology HAZUS™ User's Manual*. SR2 Edition. National Institute of Building Sciences for Federal Emergency Management Agency, Washington, D.C.

Henager, C.H. (1977). Steel Fibrous, Ductile Concrete Joints for Seismic-Resistance Structures. *Reinforced Concrete Structures in Seismic Zones*: 371-386. American Concrete Institute, Detroit.

Hsu, L.S., and Hsu, C.T. (1994). Stress-Strain Behavior of Steel-Fiber High-Strength Concrete under Compression. *ACI Structural Journal*, 91(4): 448-457.

Imbsen Software Systems (2004). *XTRACT, Cross Section Analysis Program*. Imbsen & Associates, Inc., Sacramento, California.

Ito, T., Yamaguchi, T., and Ikeda, S. (1997). The seismic performance of concrete piers prestressed in vertical direction. *Japan Concrete Institute*, 19(2): 1197-1202.

Jiuru, T., Chaobin, H., Kijian, Y., and Yongcheng, Y. (1992). Seismic Behavior and Shear Strength of Framed Joints Using Steel-Fiber Reinforced Concrete. *Journal of Structural Engineering*, ASCE 118(2): 341-358.

JRA (2002). *Design Specifications of Highway Bridges*, *Part V Seismic Design*. Japan Road Association (in Japanese).

Karim, K R., and Yamazaki, F. (2007). Effect of isolation on fragility curves of highway bridges based on simplified approach. *Soil Dynamics and Earthquake Engineering*, 27 (5): 414-426.

Kato, D., and Ohnishi, K. (2002). Axial Load Carrying Capacity of Reinforced Concrete Columns under Lateral Load Reversals. *Technical report PEER 2002/02*: 247-255, Pacific Earthquake Engineering Research Center, University of California, Berkeley.

Kelly, J. (1997). *Earthquake Resistant Design with Rubber*. Earthquake Engineering Research Center, National Information Service for Earthquake Engineering, Springer-Verlag London Limited, 2nd Edition. Richmond, California.

Kesner, K.E., Billington, S.L., and Douglas, K.S. (2003). Cyclic Response of Highly Ductile Cement-Based Composites. *ACI Materials Journal*, 100(5): 381-390.

Ketchum, M., Chang, V., and Shantz, T. (2004). *Influence of Design Ground Motion Level on Highway Bridge Costs*. Report No. Lifelines 6D01, University of California, Pacific Earthquake Engineering Research Center, Berkeley CA.

Khuntia, M., Stojadinovic, B., and Goel, S.C. (1999). Shear Strength of Normal and High-Strength Fiber Reinforced Concrete Beams without Stirrups. *ACI Structural Journal*, 96(2): 282-289.

Kim, K., and Parra-Montesinos, G. (2003). Behavior of HPFRCC Low-Rise Walls Subjected to Displacement Reversals. *High Performance Fiber Reinforced Cement Composites (HPFRCC4)*. Proceedings of the Fourth International RILEM Workshop, A.E. Naaman and H.W. Reinhardt, eds., RILEM Publications s.a.r.l., Cachan Cedex, France.

Koh, H.M., Song, J., and Ha, D.H. (2000). Cost Effectiveness of Base Isolation for Bridges in Low and Moderate Seismic Region. In *Proceedings of the 12th World Conference on Earthquake Engineering* (12WCEE), Auckland, New Zealand.

Kumar, R., Gardoni, P., and Sanchez-Silva, M. (2009). Effect of Cumulative Seismic Damage and Corrosion on the Life-Cycle Cost of Reinforced Concrete Bridges. *Earthquake Engineering and Structural Dynamics*, 38:887-905.

Laplace, P.N., Sanders, D.H., Saiidi, M.S., Douglas, B.M., and El-Azazy, S. (2005). Retrofitted Concrete Bridge Columns Under Shaketable Excitation. *ACI Structural Journal*, 102(4): 622-628.

Lawler, J., Zampini, D., and Shah, S. (2002). Permeability of Cracked Hybrid Fiber-Reinforced Mortar Under Load. *ACI Materials Journal*, 99(4): 379-385.

Lawler, J., Zampini, D., and Shah, S. (2005). Microfiber and Macrofiber Hybrid Fiber-Reinforced Concrete. *Journal of Materials in Civil Engineering*, 17(5): 595-604.

Lee, W., Jeong, H., Billington, S., Mahin, S.A., and Sakai, J. (2007). Post-Tensioned Structural Concrete Bridge Piers with Self-Centering Characteristics. In *Proceedings of the 2007 Structures Congress*, Long Beach, California, USA.

Lehman, D.E., Gookin, S.E., Nacamuli, A.M., and Moehle, J.P. (2001). Repair of Earthquake-Damaged Bridge Columns, *ACI Structural Journal,* 98(2): 233-242.

Li, V.C. (1993). From Micromechanics to Structural Engineering - The Design of Cementitious Composites for Civil Engineering Applications. *Journal of Structural Mechanics and Earthquake Engineering*, JSCE, 10(2): 37-48.

Mackie, K., and Stojadinovic, B. (2006a). Fragilities of PEER Center Testbed Bridges. In *Proceedings of the 1st European Conference on Earthquake Engineering and Seismology*, Geneva, Switzerland.

Mackie, K. R. and Stojadinovic, B. (2006b). Fourway: a Graphical Tool for Performance-Based Earthquake Engineering. *Journal of Structural Engineering* 132(8): 1274-1283.

Mackie, K.R., Wong, J.M., and Stojadinovic, B. (2007). Integrated Probabilistic Performance-Based Evaluation of Benchmark Reinforced Concrete Bridges. *Technical Report PEER 2007/09*. Pacific Earthquake Engineering Research Center, University of California, Berkeley California.

Mackie, K.R., Wong, J.M., and Stojadinovic, B. (2008). Probabilistic Methodologies for Prediction of Post-Earthquake Repair Costs and Repair Times. In *Proceedings of the 14th World Conference on Earthquake Engineering*. Beijing, China.

Mander, J.B., and Basoz, N. (1999). Seismic Fragility Curve Theory for Highway Bridges. *Technical Council on Lifeline Earthquake Engineering Monograph* 16: 31-40. ASCE, New York, N.Y.

Mander, J.B., and Cheng, C.T. (1997). Seismic design of bridge piers based on damage avoidance design. *Technical Report NCEER-97-0014*. National Center for Earthquake Engineering, Buffalo, N.Y.

Marti, P., Pfyl, T., Sigrist, V., and Ulaga, T. (1999). Harmonized Test Procedures for Steel Fiber-Reinforced Concrete. *ACI Materials Journal,* 96(6): 676-685.

Mckenna, F., Fenves, G.L., Scott, M.H., and Jeremic, B., (2000). *Open system for earthquake engineering simulation*. http://opensees.berkeley.edu.

Medina, R., Krawinkler, H., and Alavi, B. (2001). Seismic drift and ductility demands and their dependence on ground motions. In *Proceedings of the US-Japan Seminar on Advanced Stability and Seismicity Concepts for Performance-Based Design of Steel and Composite Structures*, July 23-27, 2001, Kyoto, Japan.

Megally, S.H., Silva, P.F., and Seible, F. (2002). Seismic Response of Sacrificial Shear Keys in Bridge Abutments. *Report No. 2001/23, Structural Systems Research Project*. University of California, San Diego.

Mosqueda, G., Whittaker, A., Fenves, G.L., and Mahin, S.A. (2004). Experimental and analytical studies of the friction pendulum system for the seismic protection of simple bridges. *Report UCB/EERC-2004/01*, Earthquake Engineering Research Center, University of California, Berkeley.

Naaman, A.E. (1987). High Performance Fiber-Reinforced Cement Composites. *Concrete Structures for the Future*, IABSE Symposium, Zurich, Switzerland.

Naaman, A.E., and Reinhardt, H.W. (1996). Characterization of High Performance Fiber Reinforced Cement Composites – HPFRCC. *High Performance Fiber Reinforced Cement Composites 2 (HPFRCC2).* Proceedings of the Second International RILEM Workshop, A. E. Naaman and H. W. Reinhardt, eds., RILEM Publications, s.a.r.l., Cachan Cedex, France.

Naaman, A.E. (1999). Fibers with Slip Hardening Bond. *High Performance Fiber Reinforced Cement Composites 3 (HPFRCC 3).* Proceedings of the Third International RILEM Worshop, H.W. Reinhardt and A.E. Naaman eds., RILEM Publications, s.a.r.l., Cachan Cedex, France.

Naaman, A.E., Likhitruangslip, V., and Parra-Montesinos, G. (2007). Punching Shear Response of High-Performance Fiber-Reinforced Cementitious Composite Slab. *ACI Structural Journal*, 140(2): 170-179.

Nataraja, M.C., Dhang, N., and Gupta, A.P. (1999). Stress-Strain Curves for Steel-Fiber Reinforced Concrete under Compression. *Cement and Concrete Composites*, 21: 383-390.

Newmark, N.M., and Hall, W.J. (1982). *Earthquake Spectra and Design.* Earthquake Engineering Research Institute, Berkeley, California.

Olesen, J.F. (2001). Fictitious Crack Propagation in Fiber-Reinforced Concrete Beams. *Journal of Engineering Mechanics*, 127(3): 272-280.

Padmarajaiah, S.K. (1999). *Influence of Fibers on the Behavior of High Strength Concrete in Fully/Partially Prestressed Beams: An Experimental and Analytical Study*. Ph.D. Thesis, Indian Institute of Science, Bangalore, India.

Parra-Montesinos, G., and Wight, J.K. (2000). Seismic Response of Exterior RC Column-to-Steel Beam Connections. *Journal of Structural Engineering*, ASCE, 126(10): 1113-1121.

Parra-Montesinos, G.J. (2005). High-Performance Fiber-Reinforced Cement Composites: An Alternative for Seismic Design of Structures. *ACI Structural Journal*, 102(5): 668-675.

Parra-Montesinos, G.J., Canbolat, B.A., and Jeyaraman, G.R. (2006). Relaxation of Confinement Reinforcement Requirements in Structural Walls Through the Use of Fiber Reinforced Cement Composites. In *Proceedings of the 8th National Conference on Earthquake Engineering*, San Francisco, California.

Parra-Montesinos, G. J., and Chompreda, P. (2006). Use of High-Performance Fiber Reinforced Cement Composites for Increasing Shear Strength and Displacement Capacity in Reinforced Concrete Flexural Members. In *Proceedings of the 8th National Conference on Earthquake Engineering*. San Francisco, California.

Parra-Montesinos, G. J., and Chompreda, P. (2007). Deformation Capacity and Shear Strength of Fiber-Reinforced Cement Composite Flexural Members Subjected to Displacement Reversals. *Journal of Structural Engineering*, 133(3): 421-431.

Parra-Montesinos, G.J., Peterfreund, S.W., and Chao, S.H. (2007). Highly Damage-Tolerant Beam-Column Joints Through Use of High-Performance Fiber-Reinforced Cement Composites. *ACI Structural Journal*, 102(3): 487-495.

Pereira, E.N.B., Barros, J.A.O., and Camões, A. (2008). Steel Fiber-Reinforced Self-Compacting Concrete: Experimental Research and Analytical Simulation. *Journal of Structural Engineering* 134(8): 1310-1321.

Perry, C., and Grieg, I.D. (1975). Estimating the Mean and Variance of Subjective Distributions in PERT and decision analysis. *Management Science* 21(12): 1477-1480.

Qian, C., and Stroeven, P. (2000). Fracture Properties of Concrete Reinforced with Steel-Polyproylene Hybrid Fibers. *Cement and Concrete Composites*, 22: 343-351.

Ramey, M.R. (1984). Fiber Reinforced Concrete for Seismic Joints. In *Proceedings of the 8th World Conference on Earthquake Engineering (8WCEE)*, San Francisco.

Rossi, P., Acker, P., and Malier, Y. (1987). Effect of Steel Fibers at Two Different Stages: the Material and the Structure. *Materials and Structures*, 20: 436-439.

Saadatmanesh, H., Ehsani, M.R., and Jin, L. (1996). Seismic Strengthening of Circular Bridge Pier Models with Fiber Composites. *ACI Structural Journal*, 93(6): 639-647.

Saiidi, S.M., O'Brien, M., and Sadrossadat-Zadeh, M. (2009). Cyclic Response of Concrete Bridge Columns Using Superelastic Nitinol and Bendable Concrete. *ACI Structural Journal*, 106(1): 69-77.

Shinozuka, M. (1998). Development of Bridge Fragility Curves. In *Proceedings of the U.S.-Italy Workshop on Seismic Protective Systems for Bridges*.

Solberg, K., Mashiko, N., Mander, J.B., and Dhakal, R.P. (2009). Performance of a Damage-Protected Highway Bridge Pier Subjected to Bidirectional Earthquake Attack. ASCE Journal of Structural Engineering, 135(5): 469-478.

Sommerville, P., and Collins, N. (2002). *Ground Motion Time Histories for the I880 bridge, Oakland*. PEER Methodology Testbeds Project. Pacific Earthquake Engineering Research Center, University of California, Berkeley and URS Corporation, Pasadena, CA.

Sommerville, P., and Collins, N. (2002). *Ground Motion Time Histories for Van Nuys Building*. PEER Methodology Testbeds Project. Pacific Earthquake Engineering Research Center, University of California, Berkeley and URS Corporation, Pasadena, CA.

Song, H.W., and Hwang, S. (2004). Mechanical Properties of High Strength Reinforced Concrete. *Construction and Building Materials*, 18: 669-673.

Sritharan, S., Priestly, M.J.N., and Seible, F. (1996). Seismic response of column/cap beam connections with cap beam prestressing. *Report No. SSRP-96/09*, University of California, San Diego.

Taerwe, L.R. (1992). Influence of Steel Fibers on Strain Softening of High Strength Concrete. *ACI Materials Journal*, 89(1): 54-60.

Tasai, A. (1999). Residual Axial Capacity and Restorability of Reinforced Concrete Columns Damaged due to Earthquake. *Technical Report PEER 1999/10*: 191-202, Pacific Earthquake Engineering Research Center, University of California, Berkeley.

Tasai, A. (2000). Residual Axial Capacity of Reinforced Concrete Columns during Shear Degradation. *Technical Report PEER 2000/10*: 257-267, Pacific Earthquake Engineering Research Center, University of California, Berkeley.

Terzic, V., Mackie, K., Stojadinovic, B. (2006). Validation of Finite Element Model Ability to Evaluate Residual Live Load Capacity of Bridge Columns. In *Proceedings of the 5th National Seismic Conference on Bridges and Highways*, San Mateo, USA.

Terzic. V, Mackie, K., and Stojadinovic, B. (2008). Experimental Evaluation of the Residual Axial Load Capacity of Circular Bridge Columns. In *Proceedings of the 14th World Conference on Earthquake Engineering*, Beijing, China.

Thomas, J., and Ramaswamy, A. (2007). Mechanical Properties of Steel Fiber-Reinforced Concrete. *Journal of Materials in Civil Engineering*, ASCE, 19(5): 385-392.

Vasconez, R.M., Naaman, A.E., and Wight, J.K. (1998). Behavior of HPFRC Connections for Precast Concrete Frames Under Reversed Cyclic Loading. *PCI Journal*, 43(6): 58-71.

Warn, G.P., and Whittaker, A.S. (2004). Performance Estimates in Seismically Isolated Bridge Structures. *Engineering Structures*, 26(9): 1261-1278.

Warn, G.P., and Whittaker, A.S. (2006). Property Modification Factors for Seismically Isolated Bridges. *Journal of Bridge Engineering*, 11(3): 371-377.

Werner, S.D. (1994). Study of Caltrans' Seismic Evaluation Procedures for Short Bridges. In *Proceedings of the 3rd Annual Seismic Research Workshop*. Sacramento, California.

Werner, S.D., Taylor, C.E., Cho, S., Lavoie, J.-P., Eitzel, C., Eguchi, R., and Moore, J.E. (2004). New Developments in Seismic Risk Analysis of Highway Systems. In *Proceedings of the 13th World Conference on Earthquake Engineering*. Vancouver, Canada.

Werner, S.D., Taylor, C.E., Moore, J.E., and Walton, J.S. (2000). A Risk-Based Methodology for Assessing the Seismic Performance of Highway Systems. *Report No. MCEER-00-0014*, University at Buffalo, Multidisciplinary Center for Earthquake Engineering Research, Buffalo, N.Y.

Wight, J.K., Parra-Montesinos, G.J., and Lequesne, R. (2007). High-Performance Fiber Reinforced Concrete for Earthquake-Resistant Coupled Wall Systems. *High-Performance Fiber Reinforced Cement Composites 5 (HPFRCC 5)*, edited by H.W. Reinhardt and A.E. Naaman, Mainz, Germany.

Xia, Z., and Naaman, A.E. (2002). Behavior and Modeling of Infill Fiber-Reinforced Concrete Damper Element for Steel-Concrete Shear Wall. *ACI Structural Journal*, 99(6): 727-739.

Yang, T.Y., Moehle, J., Stojadinovic, B., and Der Kiureghian, A. (2006). An Application of the PEER Performance-Based Earthquake Engineering Methodology. In *Proceedings of the 8th National Conference on Earthquake Engineering*. San Francisco.

Yoshimura, M., and Nakamura, T. (2002). Axial Collapse of Reinforced Concrete Short Columns. *Technical Report PEER 2002/21*: 187-198, Pacific Earthquake Engineering Research Center, University of California, Berkeley.

Yoon, J.K., Billington, S.L., and Rouse, J.M. (2002). Precast Segmental Bridge Piers with Unbonded Post-tensioning and Ductile, Fiber Reinforced Concrete for Seismic Applications. In *Proceedings of the 7th National Conference of Earthquake Engineering (NCEE)*, Boston.

Zhang, J., and Makris, N. (2001). Seismic Response Analysis of Highway Overcrossings Including Soil-Structure Interaction. *Technical Report PEER 2001/02*. Pacific Earthquake Engineering Research Center. University of California, Berkeley.

Appendix A: Extended Literature Review

This appendix presents an extended literature review carried out for the present study related to the behavior of fiber-reinforced concrete and its seismic applications, as well as the testing of the flexural and axial capacity concrete bridge piers.

A.1 GENERAL BEHAVIOR OF FIBER-REINFORCED CONCRETE (FRC)

The effect of fibers on the mechanical performance of concrete is typically evaluated with tensile or flexural testing. Fibers have been shown to have a major influence in delaying the failure process of unreinforced concrete in tension (Rossi *et al.* 1987; Naaman and Reinhardt 1996; Campione 2002; Banthia and Gupta 2004; Lawler *et al.* 2005). According to these studies, during the first stage of behavior, the propagation of randomly distributed microcracks in the fiber-reinforced concrete is restricted due the presence of microfibers (short fibers) stitching the cracks. The result of this behavior is reflected in a higher peak stress in the tensile stress-strain relationship of the material (see Figure A-1a). The delay of crack propagation in FRC has additional implications for increased durability of the element due to a reduction in water permeability (Lawler *et al.* 2002).

The second phase of behavior consists of the propagation and opening of microcracks in the directions of the principal strains as fibers pullout, thus delaying the formation of macrocracks. The third and final stage of behavior is characterized by macrocrack opening (fiber pullout) along the direction of the principal tensile strain. Macrocrak growth is delayed due to macrofibers (long fibers) in tension bridging the gaps. The resulting tensile stress-strain relationship presents increased post-peak ductility of the material (see Figure A-1a). Although ductile fibers may yield locally (at the location of the hooks), they generally remain elastic throughout the different stages of FRC behavior.

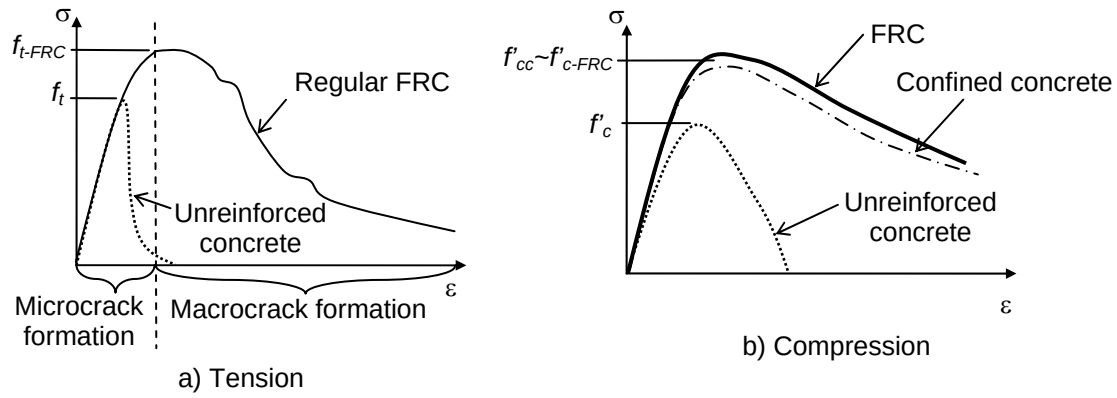

Figure A-1 Stress-strain behavior of regular FRC

The ultimate failure of the FRC element occurs with either fracture or pull-out of the fibers. Fiber pull-out takes place if the tensile strength of the fiber is not exceeded by the bond stresses around the fiber. This failure mode is typically more desirable for maximizing composite performance since it consumes more energy than fiber fracture and leads to higher ductility. Frictional forces over the full length of the fiber must be overcome to pull the fiber out of the composite, compared to the brittle fracture of the fiber in one critical point along its length. High-performance fiber-reinforced concrete (HPFRC) discussed in detail in section 1A.2A.2.1 presents strain-hardening tensile behavior with multiple cracking instead of strain-softening tensile behavior exhibited by regular FRC materials.

In compression tests, fiber-reinforced concrete and mortar with a minimum fiber volume fraction of 1% have been shown to have similar behavior to that of well-confined concrete characterized by a shallow post-peak response with large strain capacity. Only small variations in the maximum compressive strength were observed in FRC with different fiber types and volume fractions used in the mixtures (Fanella and Naaman 1983; Hsu and Hsu 1994; Nataraja *et al.* 1999; Campione 2002). Figure A-1b) shows the compressive stress-strain relationship of regular FRC, compared to the inferior behavior of plain concrete. It was also established (Campione 2002), that the addition of macrofibers (most commonly hooked steel fibers) in volume percentages up to 2-3%, produces significant increases in maximum compressive (as well as tensile) strain capacities of the concrete material.

The enhancement of concrete behavior provided by fibers is similar to the role played by steel bars in reinforced concrete. The brittleness properties and poor resistance to crack growth of plain concrete are replaced, with the inclusion of fibers, by increased peak-strength, ductility and flexural toughness in both tension and compression. Fibers can therefore be considered a viable replacement to transverse or shear reinforcement (Parra-Montesinos *et al.* 2006), and in some measure to longitudinal or flexural reinforcement.

The main parameters investigated to date, affecting the performance of FRC, are the fiber type (steel, carbon, polyolefin, polyethylene, etc.), the fiber shape (crimped, hooked, flat, straight, twisted), the volume percentage of fibers (V_f), the aspect ratio of the fibers (i.e., the ratio of fiber length L_f to fiber diameter ϕ_f), the composition of the cementitous matrix, average bond strength at the fiber-matrix interface, the shape and dimensions of the specimens, the presence of longitudinal and transverse steel reinforcement and their arrangements, and the type and rate of loading (Campione 2002; Banthia and Soleimani 2005; Thomas and Ramaswamy 2007). Proper material selection is therefore critical to achieve the desired behavior of the composite.

A.2.1 High-Performance Fiber Reinforced Concrete (HPFRC)

The typical tensile performance obtained with traditional FRC mixes, displayed in Figure A-1a), is characterized by a softened response after first cracking (tensile-softening). Strain-hardening or high-performance tensile behavior with multiple cracking, where the post-cracking strength is larger than the first cracking strength (see Figure A-2), was observed for selected types and contents of fibers (Naaman 1987). This enhanced behavior in FRC materials was previously achieved through the use of large fiber volume fractions (V_f>4%), making these materials difficult to apply in typical building and bridge construction. Previous material developments (Li 1993; Naaman 1999) led to achievements of high-performance tensile behavior with relatively low fiber volume fractions (V_f=1.5-2.0%) of hooked steel macrofibers with an aspect ratio of 50-100 and either regular or high-strength properties (Naaman and Reinhardt 1996). This new class of FRC, referred to as high-performance FRC (HPFRC), is a viable alternative for use in large-scale structural applications.

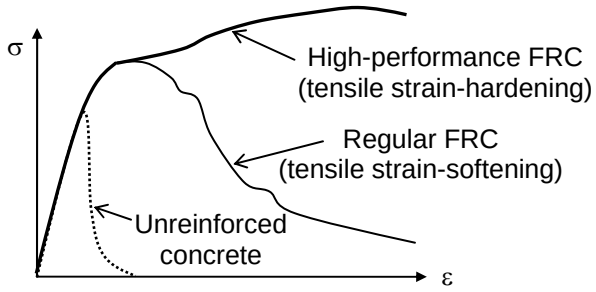

Figure A-2 Tensile stress-strain response of regular and high-performance FRC

Localization of damage in HPFRC is typically observed after crack saturation occurs and at tensile strains ranging between 1.0 and 5.0%, depending on the type and amount of fibers used, matrix composition, and matrix-fiber interface (Naaman and Reinhardt 1996). The compression behavior is found to resemble that of well-confined concrete, better than regular FRC (Parra-Montesinos *et al.* 2007). HPFRC are considered to be tougher and are thought to be more durable than concretes containing conventional fiber sizes and contents. The use of HPFRC leads to better cracking pattern with a denser array of cracks of smaller width compared to the conventionally reinforced concrete elements. Besides providing high ductility capacity both in compression and tension, HPFRC materials also provide high values of residual strength and energy-absorption capacity. These properties are favorable in structural members that require extensive reinforcement detailing to prevent brittle failures.

In previous studies on the behavior of HPFRC members under reversed cyclic loading, it has been reported that the use of these materials leads to significantly higher shear deformation capacity with superior damage tolerance compared to conventionally reinforced members (Parra-Montesinos and Wight 2000; Yoon *et al.* 2002; Kim and Parra-Montesinos 2003).

A.2.2 Hybrid Fiber Reinforced Concrete (HyFRC)

Hybrid fiber reinforced concrete (HyFRC) can be obtained through a combination of different fiber types. One type of HyFRC mix consists of the combination of different fiber sizes, i.e., microfibers and macrofibers. Microfibers or short fibers are stiffer, producing increased first crack strength and ultimate strength. Macrofibers or long fibers are more flexible, leading to increased fracture toughness and strain capacity in the post-crack zone. Another type of HyFRC mix combines different fiber material properties. In this mix, a stronger fiber adds to the material strength, while a more ductile fiber enhances its ductility. A third type of HyFRC mix consists of a combination of fiber action over the lifecycle of concrete. In this hybrid material, one type of fiber improves matrix performance, allowing for the remaining fiber types to perform more effectively afterward. The desired performance of a HyFRC mix can be achieved by combining several of the approaches discussed above (Lawler *et al.* 2005).

Achieving positive synergy of a HyFRC material is the main design goal of the mix. Positive synergy can be defined as a positive interaction between different fiber types, where the resulting fiber performance exceeds the sum of individual fiber performances (Lawler *et al.* 2002). Several studies of HyFRC mixes summarized in Banthia and Soleimani (2005) resulted in positive synergy and enhanced performance of the concrete material. These blends required several trials to achieve optimum mix and the use of superplasticizes to improve their workability. Nonetheless, additional studies of HyFRC blends resulted in negative or partial synergy (Qian and Stroeven 2000; Banthia and Gupta 2004; Banthia and Soleimani 2005). In the experimental study by Banthia and Soleimani (2005) 32 different concrete mixtures were investigated using seven different types of fibers including steel, carbon and polypreopylene, in different volume fractions, sizes and shapes. Many of these and other hybridization attempts mentioned resulted in negative synergy with poorer performance of the hybrid mix compared to its control, or partial synergy, where the improved concrete behavior disappeared in the small or large displacements range. Further research is therefore required to develop adequate criteria for the optimization of hybrid mixtures (Banthia and Gupta 2004).

Despite the benefits in the material behavior obtained through the addition of microfibers, their use in the concrete mix is generally difficult. It was found (Lawler *et al.* 2005) that an extremely large volume of paste is required to coat the high surface area of microfibers and simultaneously obtain acceptable flow and resistance to bleeding and segregation. Proper workability and fiber dispersion in HyFRC mixtures is critical for achieving a reliable compressive strength. If improperly produced, HyFRC may entrap excessive air, possess lower and more variable density, and consequently result in reduced mechanical properties (Banthia and Soleimani 2005). The addition of superplasticyzers to the concrete mix is usually required to obtain tolerable workability conditions, resulting in increased construction costs. Another setback in the use of microfiber is related to the failure process of HyFRC mixes consisting of different fiber sizes. Since microfibers reinforce the concrete matrix and strengthen its hold on the macrofibers, the increased bond stresses in the composite delay the pull-out failure of the fibers, causing them to break instead. The fracture failure mode of the fibers is less efficient in dissipating energy. Additionally, concrete reinforced with only microfibers is not expected to demonstrate anywhere near the post-peak strength and toughening that can be achieved with macrofibers (Lawler *et al.* 2005). Due to the workability issues and the undesirable failure mode promoted by the addition of microfibers in the concrete mix, FRC mixtures with only

macrofibers are more commonly used in experimental studies and engineering practice to achieve enhanced material behavior.

In an experimental study by Lawler *et al.* (2005) several HyFRC mixes were compared to HPFRC and unreinforced concrete. The hybrid blends were obtained combining steel macrofibers with either polyvynil alcohol (PVA) or steel microfibers. The HPFRC mix used only steel macrofibers in a volume fraction of around 1% and presented flexural strain-hardening behavior. According to the study, the hybrid blends outperformed the HPFRC steel marcofiber reinforcement under bending at small deflections, achieving a higher peak response at the end of the elastic range. The ultimate nominal flexural strength of the optimum hybrid mix was also slightly higher than the steel macrofiber mix. However, when the full range of response is considered, the ability of macrofibers to bridge macrocracks became apparent and the superior improvement produced by these fibers in toughness and energy dissipation was undoubtedly observed. The strain-hardening properties of the steel macrofiber mix resulted in increased ductility and displacement capacity of the specimen, compared to the hybrid mix. The results of this study regarding the behavior of HyFRC and HPFRC are summarized in Figure A-3.

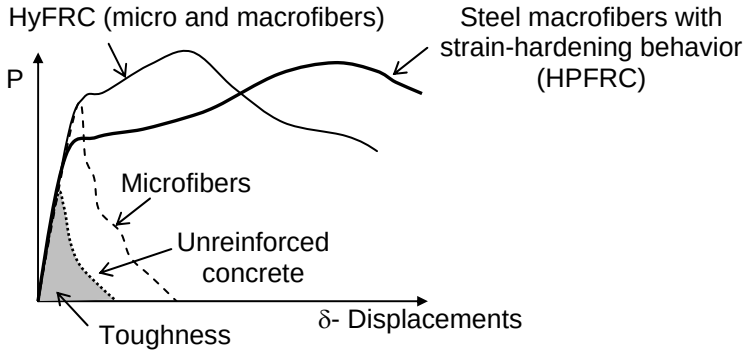

Figure A-3 Flexural response of FRC

A.2.3 Advantages of HPFRC in Seismic Applications and Bridge Construction

The base shear and force demand on the main structural components of a bridge system is primarily controlled by the flexural and shear strength of the bridge piers and combined capacity of the soil-abutment system at the superstructure's ends. The stability and gravity load-carrying capacity of a bridge system are also predominantly dependent on the bridge column bents. Due to enhanced material properties of FRC mixes, their use for the construction of bridge piers is therefore considered highly beneficial, if designed correctly.

Since an increase in flexural strength of the FRC mix in the column bent plastic hinge region will result in an increase in the force demand on all structural components of the bridge, this material behavior is not desirable for seismic application. Thus, the use of microfibers which produces increased cracking and ultimate strength will not enhance the seismic response of the bridge structure and is not recommended. Conversely, a ductile material with strain-hardening behavior is a desirable seismic performance goal. The use of flexible ductile fibers, such as steel macrofibers with a high aspect ratio and relatively low volume fraction resulting in HPFRC is therefore expected to be more effective in achieving the optimum response of the bridge.

Excellent seismic performance was found to be obtained in shear-critical members constructed with HPFRC materials, such as beam-column joints, squat walls, slab-column connections, and coupling beams, as well as in flexural members subjected to high shear stress reversals (Parra-Montesinos 2005).

In end regions of bridge piers and lateral load-resistant frame structures, a large number of closely spaced hoops are required to provide concrete confinement, shear resistance, and lateral support to longitudinal bars to avoid bar buckling under high flexural and compressive loads. Because of the degradation of shear-resistance mechanisms in flexural members under displacement reversals, bridge and building design codes require the use of closely spaced transverse steel reinforcement for the stable behavior of plastic hinges at the ends of the structural elements. It was shown (Parra-Montesinos *et al.* 2006) that substantial reductions or even elimination of transverse reinforcement used to provide confinement and shear strength of critical beam and column regions in frame systems can be achieved through the use of HPFRC. Using HPFRC, plastic hinge rotations were equal to or higher than conventionally reinforced members with seismic detailing according to the ACI Code.

The use of HPFRC is expected to simplify the construction of critical regions in bridge structures designed for earthquake ground motions and displacement reversals, compared to those designed according to current seismic codes, which required significant reinforcement that results in rebar congestion and high construction difficulty. Since the use of HPFRC leads to an increase in displacement capacity, shear strength, energy dissipation and damage tolerance in members subjected to gravity loads and reversed cyclic loading, these composites are also desirable for reducing post-earthquake repair costs of bridge structures. Due to the significant seismic performance enhancement described above, acceptable workability and cost-effectiveness of HPFRC using steel macrofibers, the use of this material is highly attractive for use in bridge construction in high seismic hazard zones. A research program was initiated to characterize many of the behaviors relevant to the use of HPFRC in the highway bridge industry (Graybeal 2006). However, further experimental and analytical research involving the testing of large-scale bridge piers and connections is required to develop design guidelines for the safe and optimum use of these materials for bridge applications.

A.2.4 Analytical Models for Mechanical Properties of FRC

Several research studies have been carried out to date for the prediction of the tensile, compressive and flexural strength and deformation capacity of regular FRC, high-performance FRC, ultra-high-performance FRC, and ductile FRC. Crack propagation models using multi-linear stress-crack opening relationships have also been developed by researchers to predict tensile or compressive strength of FRC, generally ignoring the closure or unloading of an open crack (Olesen 2001; Campione 2002).

Analytical models predicting the mechanical properties of steel FRC were developed (Thomas and Ramaswamy 2007) based on the regression analysis of 60 test data. The various properties studied include compressive strength, split tensile strength, modulus of rupture, Poisson's ratio, modulus of elasticity and strain at peak compressive stress. The results presented excellent correlation with strength models proposed in previous studies (Agrawal et at. 1996; Padmarajaiah 1999; Song and Hwang 2004; Ghosh *et al.* 1989; Gao *et al.* 1997; Taerwe 1992). An approximate constant bond shear stress formula have also been proposed for steel FRC

mixes, where this value has been successfully applied to various problems of structural members (Marti *et al.* 1999).

Based on an extensive literature review and analytical study carried out by Khuntia *et al.* (1999), a design equation for steel fiber reinforced concrete beams without stirrups was proposed, similar to the ACI code approach for conventionally reinforced concrete beams. The predictive formula, accounting for concrete strength, fiber factor, beam span-to depth ratio, and longitudinal steel ratio, was found to be conservative with the experimental results obtained from numerous previous investigations considered in the study.

An empirical formula for the contribution of the steel fibers to the joint shear strength was developed based on the experimental results of joints under reversed cyclic loading (Jiuru *et al.* 1992). This formula accounts for the length of fibers, diameter of fibers, volume fraction of fibers in the concrete mix, and the cross-sectional area of the joint in the direction of the shear force. This formula matched reasonably well the experimental results of a test carried out by Filiatrault *et al.* (1995).

Ultra-high-performance FRC (UHPFRC) was found to exhibit superior properties in terms of compressive behaviors, tensile behaviors, stiffness, and durability, compared to high-performance concrete (HPC) and regular FRC. The typical composition of this material consists of Portland cement, fine sand, silica fume, ground quartz, high-range water-reducing admixture, accelerator, steel fibers and water. Approximate equations predicting the compressive behavior of this material were proposed (Graybeal 2007). An analytical model predicting the composite UHPFRC beam response was also developed (Habel *et al.* 2007). This approach, based on bending beam theory, is an extension of the commonly employed cross-sectional model where plane sections are assumed to remain plane, typical material laws describe the stress-strain behavior of reinforcing bars, RC and FRC, and equilibrium of forces and moments is enforced. The analytical model for flexural strength matched reasonably the experimental results of the composite beam tested (Habel *et al.* 2007).

A constitutive model has been developed for finite-element modeling of highly ductile FRC (DFRC) composites, consisting of a low volume fraction of high modulus, high aspect ratio polymeric fibers (Han *et al.* 2003). Due to significant differences in the uniaxial tensile response of specimens with different geometries and scale, further experimental and analytical research is required for this material type (Kesner *et al.* 2003).

The material properties of self-compacting steel FRC developed by Pereira *et al.* (2008) were assessed by inverse analysis of the constitutive material model calibrated to the fracture parameters obtained though three-point notched beam bending tests. The contribution of steel fibers to concrete punching shear resistance was the main focus of that assessment.

A.2 PREVIOUS RESEARCH ON LARGE-SCALE STRUCTURAL MEMBERS WITH FRC

In addition to fiber material development, many research studies involving large-scale structural applications of different fiber types and combinations have been carried out to date. These studies have focused on shear-critical members such as shear walls, coupling beams, beam-column joints, slabs and slab-column connections, as well as flexural-critical elements such as slender walls, beams in frame systems, and bridge piers. The main aspects and findings of some

of these research studies are discussed in the following paragraphs. The research studies related to the use of FRC in bridge applications are mentioned in Chapter 1.

A.2.1 Walls

The use of FRC in critical regions of slender structural walls was experimentally evaluated (Parra-Montesinos *et al.* 2006; Xia and Naaman 2002; Kim and Parra-Montesinos 2003). In the study by Parra-Montesinos *et al.* (2006) three full-scale wall specimens with an aspect ratio of 3.7 using twisted or hooked steel fibers in volume fractions of either 1.5 or 2.0% were tested under large displacement reversals and compared to a control specimen with regular concrete and seismic detailing according to the ACI Building Code. The FRC specimens exhibited stable behavior with drift capacities of 3.5%, superior to the ACI-detailed wall which exhibited severe shear-related damage at this drift level. The results indicated that the use of FRC in wall boundary regions can eliminate the need for special confinement reinforcement while maintaining adequate displacement capacity of the members.

A.2.2 Coupling Beams

The use of HPFRC with a simplified reinforcement detailing for coupling beams subjected to load-reversals was experimentally investigated (Canbolat *et al.* 2005; Wight *et al.* 2007). In the experimental study by Canbolat *et al.* (2005), four full-scale coupling beam specimens were tested using 2% volume fraction of polyethylene fibers or 1.5% volume fraction of steel fibers. The results demonstrated the superior damage tolerance and stiffness retention capacity of HPFRC materials. It was also observed that diagonal reinforcement is necessary to achieve large displacement capacity but transverse reinforcement around the diagonal bars can be eliminated due to the confinement provided by the fibers. The HPFRC beams with supplemental diagonal bars achieved drift levels greater than 4% while maintaining approximately 80% of their shear-carrying capacity. The two types of fiber reinforcement producing tensile-hardening behavior displayed similar results. In the ongoing experimental study by Wight *et al.* (2007) the focus is to evaluate possible embedment strategies that provide sufficient development of the precast section into the structural wall without interfering with wall reinforcement. In this study, a HPFRC mix with a 1.5% volume fraction of high-strength hooked steel fibers was proposed for the full-scale specimens, displaying stable hysteretic behavior and energy dissipation characteristics.

A.2.3 Slab Systems

An experimental study was carried out concerning the use of FRC as a means to increase punching shear resistance in slabs and slab-column connections subjected to combined gravity loads and displacement reversals simulating earthquake-induced loads (Harajili *et al.* 1995; Cheng and Parra-Montesinos 2007; Naaman *et al.* 2007). In the study by Cheng and Parra-Montesinos (2007), full-scale specimens of slab-column connections for building structures using a 1.5% volume-fraction of regular and high strength hooked and twisted steel fibers (aspect

ratio of 55-80) were subjected to combined gravity loads and displacement reversals. The FRC with high-strength hooked fibers displayed strain-hardening behavior. Test specimens with either regular or high-strength hooked fibers displayed optimum results in terms of punching shear strength and ductility under gravity loads, as well as drift capacities under cyclic loading exceeding 4%. In the test by Naaman *et al.* (2007), simply supported square slab panels with conventional distributed steel reinforcement simulating a bridge deck designed according to AASHTO LRFD specifications were concentrically loaded to determine their punching shear strength. Three fiber types were tested, including polyvinyl alcohol, polyethylene, and twisted steel fibers. Test results suggested that HPFRC slabs displayed twice the strength recommended for design by ACI codes.

A.2.4 Beam-Column Joints

The use of FRC to improve the behavior of beam-column joints under earthquake excitation and the reduction of confinement (transverse) reinforcement for was investigated (Henager 1977; Ramey 1984; Filiatrault *et al.* 1995; Vasconez *et al.* 1998; Parra-Montesinos *et al.* 2007). In the experimental study by Filiatrault *et al.* (1995), three full-scale interior beam-column joints with 1.6% steel fiber volume fraction or seismic detailing according to the Canadian building codes were tested using a quasi-static test protocol. Up to ductility levels of 2.5, the hysteretic loops of the FRC specimen were large and had higher peak loads than the specimen with the required conventional reinforcement details for seismic zone. For higher ductility demands, the repetitive stretching and buckling of the fibers in the joint region caused degradation in the joint shear strength and pinching in the hysteretic loops as more fibers pulled out. The shear strength of the FRC specimen obtained during the test was about 95% of the predicted strength from the empirical formula developed by Jiuru *et al.* (1992). At the end of the test, the shear strength of the SFRC specimen was still higher than the specimen with seismic detailing. Therefore, despite the degrading behavior of the SFRC, it has an extremely high shear strength, ductility and energy dissipation capacities. The results also indicated that by producing a ductile behavior and increased joint shear strength in the steel FRC specimen, this material provide an excellent alternative for reducing requirements for closely spaced ties.

In the experimental study by Parra-Montesinos *et al.* (2007), a volume fraction of 1.5% of polyethylene fibers was used in two large-scale subassemblies of beam-column connections designed according to ACI Building Code and subjected to combined shear and displacement reversals. The use of HPFRC materials in the beam plastic hinge regions allowed an increase in transverse reinforcement spacing to half the effective beam depth. In these test specimens, a crushing strain of 0.01 was estimated for the HPFRCC material, which translated into a plastic hinge rotation capacity of approximately 0.04 rad and 5% drift. The maximum beam shear stress was $1.2\sqrt{f'_c}$ (MPa), achieving the required ACI criteria.

A.2.5 Flexural Members

The use of HPFRC to develop highly damage-tolerant flexural members under earthquake-induced displacements was investigated (Parra-Montesinos and Chompreda 2006; Parra-Montesinos and Chompreda 2007). A total of seven full-scale specimens, each featuring two

cantilever flexural members with an aspect ratio of 2.75 and using volume fractions between 1.0 and 2.0% of polyethylene or steel fibers with no transverse reinforcement, were compared to a specimen constructed with regular concrete with seismic detailing according to the ACI Building Code. All strain-hardening FRC test specimens with or without transverse reinforcement exhibited a stable behavior with drift capacities equal or greater than 4% with superior damage tolerance and multiple flexural and diagonal cracking, compared to the ACI-designed specimen. Maximum drifts of 5% and 7% were achieved for the specimens with 2.0% volume fraction of polyethylene and steel fibers, respectively, while the conventionally reinforced specimen achieved only 4.0% maximum drift. The minimum shear stress presented in all strain-hardening members was $0.3\sqrt{f'_c}$ (MPa). Tensile and compressive strain capacities exceeding 5% and 1% were recorded for the FRC materials. This large strain capacity makes these materials excellent candidates for enhancing the displacement capacity, shear resistance and damage tolerance of concrete members subjected to inelastic displacement reversals. The increase in concrete ductility due to the addition of fibers, both in tension and compression, also allows a relaxation in the transverse reinforcement detailing in critical regions of reinforced concrete flexural members while ensuring a stable behavior under displacement reversals. Buckling of longitudinal bars occurred only after a 4.0% plastic hinge rotation, indicating that HPFRC materials are effective in providing lateral support to longitudinal reinforcement.

In the literature review conducted by Khuntia *et al.* (1999), a list of 10 previous experimental studies evaluating the shear capacity of steel fiber reinforced concrete beams is presented. The volume fraction of the steel reinforcement in these investigations ranged from 0.25 to 1.5% and the concrete strength ranged from normal to high-strength values.

In a study by Harajli and Rteil (2004) of rectangular concrete columns designed for gravity loads for building structures, external carbon fiber-reinforced polymers sheets and internal steel fiber reinforced concrete specimens (with volume fractions of 1% and 2%) were compared to conventionally reinforcement columns using transverse steel hoops, designed for moderate seismic hazard. The specimens using fiber polymers or concrete had a similar behavior, increasing the bond strength and strength capacity of the columns, significantly reducing concrete spalling and bond deterioration in the column end zone, and resulting in considerable improvement in the seismic performance of the columns, compared to the conventionally reinforced specimen. The enhanced behavior of the specimens was found to be independent of the total reinforcement ratio of the columns, depending only on the level of improvement of the bond behavior of the outermost column longitudinal reinforcement.

Composite ultra-high-performance FRC (UHPFRC) and conventional reinforced concrete members were also investigated to assess the rehabilitation potential for existing concrete structures (Habel *et al.* 2007). Twelve full-scale composite beams with a UHPFRC layer in tension were tested monotonically, displaying improved ultimate force, stiffness and cracking behavior.

A.3 RELATED STUDIES: AXIAL AND LATERAL LOAD CAPACITY OF BRIDGE PIERS

The gravity and lateral-load carrying capacity of bridge structures is conveyed primarily by the column bents. The design goal in current seismic codes for bridge construction has therefore been directed to preventing brittle failure modes of bridge piers which can lead to the complete

collapse of the entire structure. If a ductile and stable failure mode occurs in the column bents under seismic excitation, some residual strength remains in the member. Hachem *et al.* (2003) experimentally tested the performance of four circular reinforced concrete bridge columns under bidirectional earthquake ground motions. This investigation determined that the use of fiber-based elements for the analytical models of the columns provided the most accurate predictions of local and global forces and deformations.

Solberg *et al.* (2009) experimentally tested 1/3-scale bridge pier specimen constructed with damage avoidance design details with armored joints (eliminating plastic hinge formation), steel-steel armored rocking interfaces, and supplemental tension-only energy dissipation devices to increase tie down forces and further reduce dynamic response. The results of the bidirectional quasi-static and pseudodynamic tests showed with a 90% confidence interval that the pier constructed with damage avoidance design details will survive a design basis earthquake without sustaining any damage, while the conventional ductile column design will result in substantial damage.

Several research studies have assessed the axial failure of columns, focusing primarily on members in reinforced concrete building frames. Axial failure or gravity load collapse is defined in these studies as the inability of the column to support the imposed axial load corresponding to the tributary dead load under lateral excitation. The axial failure of columns in a RC frame has been studied through analytical and experimental shake-table tests (Elwood 2002; Elwood and Moehle 2005). An experimental test on RC columns in building frames tested through a monotonically applied lateral load and either constant or varying axial load has been conducted (Kato and Ohnishi, 2002). In this study, empirical equations for the evaluation of the maximum deflection of the column under a given axial load were proposed. The axial collapse of short and normal length reinforced concrete columns was experimentally assessed through monotonic and cyclic lateral loading using constant axial load (Yoshimura and Nakamura 2002).

However, the level of post-earthquake residual axial capacity of reinforced concrete columns using an explicit uniaxial force-deformation relation has been largely has scarcely been assessed in current research studies. The deterioration of the axial strength of flexural columns was analyzed by inelastic moment-curvature analysis of the section and experimental testing using cyclic loading (Tasai 1999). The degradation in the axial capacity of the columns was found to be critical for large long long-term axial loads or large compressive varying axial load. In this study, the comparison between experimental and analytical results was based on only two half-scale column specimens, showing little or no deterioration in the axial load capacity of the columns under low levels of axial load during the lateral testing.

An experimental and analytical research study of typical circular reinforced concrete bridge piers was carried out to determine their residual post-earthquake axial strength (Terzic *et al.* 2006, 2008). In this study, axial load tests were conducted on the columns, predamaged due to lateral cyclic excitation to different levels of lateral displacement ductility. Hybrid simulation of a complete bridge structure using real column specimens was conducted to verify the results of the axial tests. Empirical relations for the axial load capacity vs. ductility demand were developed for the columns.

Appendix B: Experimental Test Setup

This appendix presents the details of the construction process and experimental setup used for the two fiber-reinforced cantilever column specimens tested under bidirectional cyclic loading.

B.1 CONSTRUCTION PROCESS

The construction of the two FRC column test specimens was carried out by a local contractor in the structural laboratory of the Civil and Environmental Engineering Department of the University of California at Berkeley, located on the 2nd floor of Davis Hall. The construction process presented several principal stages, including the construction of the anchor block forms and the assembly of the reinforcement cages, the preparation of the column forms and bracing of the steel jackets at the column top, the casting of the anchor blocks, and finally the casting of the fiber-reinforced concrete columns.

All the reinforcing steel was cut and bent off-site according to the specified geometry and delivered to the job site. The anchor block forms were built using plywood and rectangular wood bracing. The top and bottom portions of the anchor block cages, as well as the column cages with spiral reinforcement were assembled separately and then placed inside the forms (see Figure B-1).

Figure B-1 (a) Anchor block formwork and unfinished cage; (b) Column cage

Concrete spacers 1.5” thick were placed at the bottom of the anchor block cages to allow proper rebar cover on all sides of the anchor block. Horizontal and aluminum tubes were placed inside the anchor block formwork to allow the translation of the specimens to their assigned position in the lab using a crane. Vertical tubes were similarly used to anchor the specimen anchor blocks to the strong floor of the lab (see Figure B-2). Once the column cages with pre-installed strain gages on the longitudinal rebar were placed in the desired position, the remaining rebar of the top portion of the anchor blocks crossing the column were placed and secured (see Figure B-2). Additional strain gages were then installed on the spiral reinforcement at three points around its circumference and at the elevations corresponding to the strain gages of the longitudinal rebar.

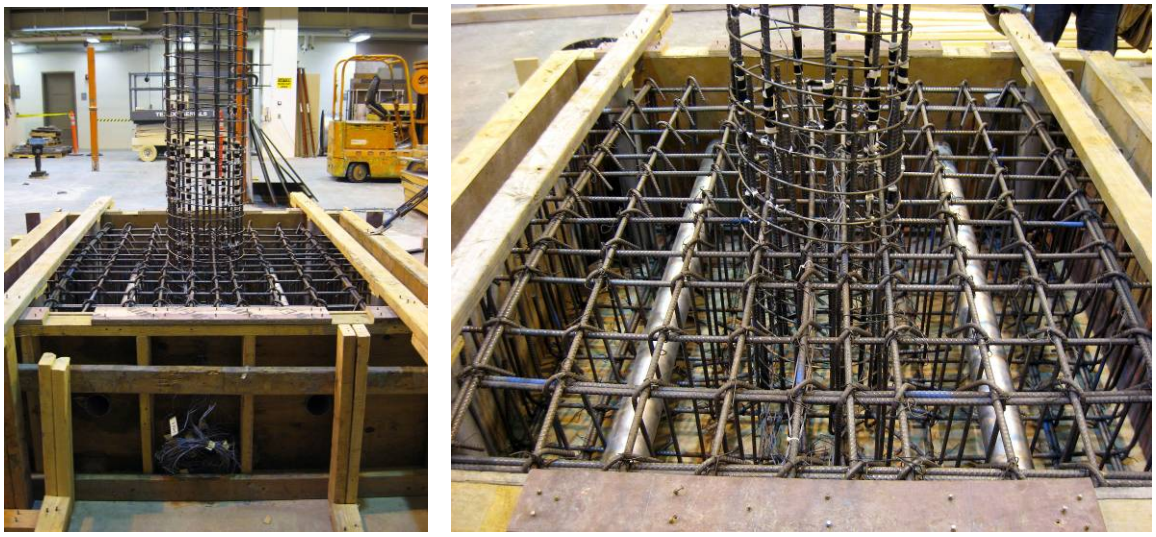

Figure B-2 (a) Completed anchor block and column cage, specimen S1; (b) Horizontal and vertical cylinders in anchor block, specimen S1

PVC tubes with an internal diameter of 0.55” (corresponding to the external diameter of a #4 bar) of 4” and 10” length for specimens S1 and S2, respectively, were placed around the corresponding dowels and continuous longitudinal rebar of to unbond the steel rebar from the concrete mix in the area of the plastic hinge zone of each specimen, according to the desired detail (see Figure B-3 and Figure B-4).

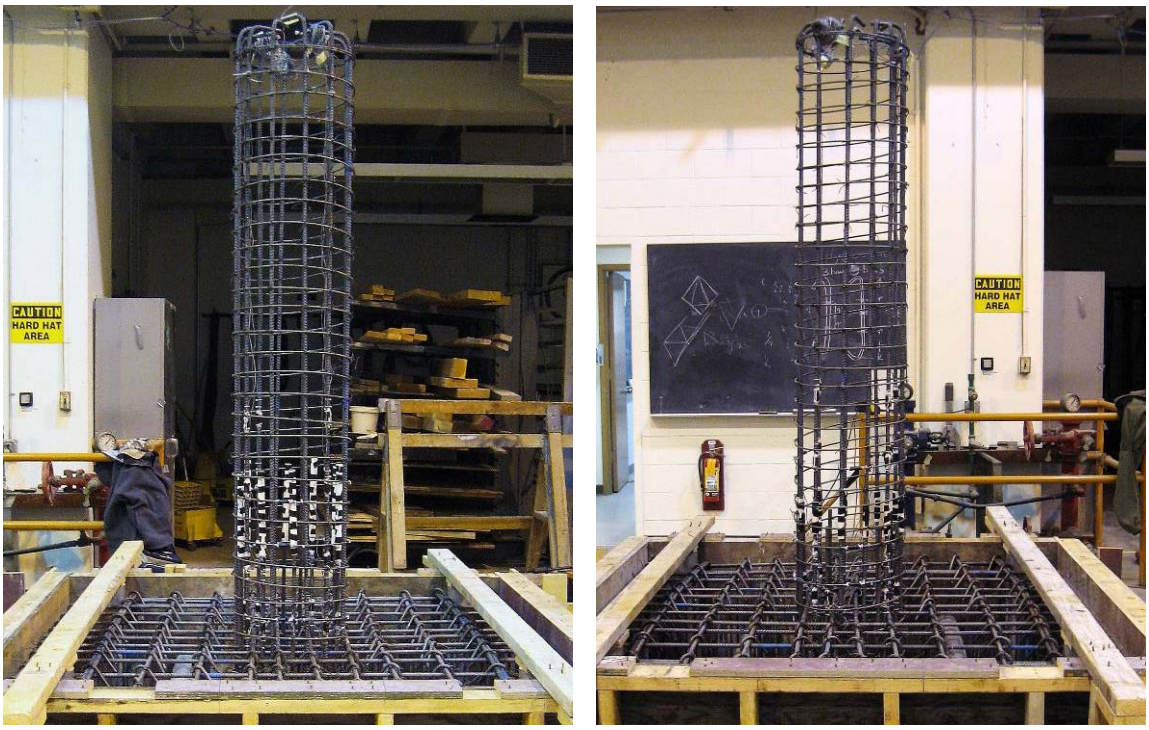

Figure B-3 Column cages with strain gages on longitudinal and transverse reinforcement and unbonded PVC tubes: (a) specimen S1; (b) specimen S2

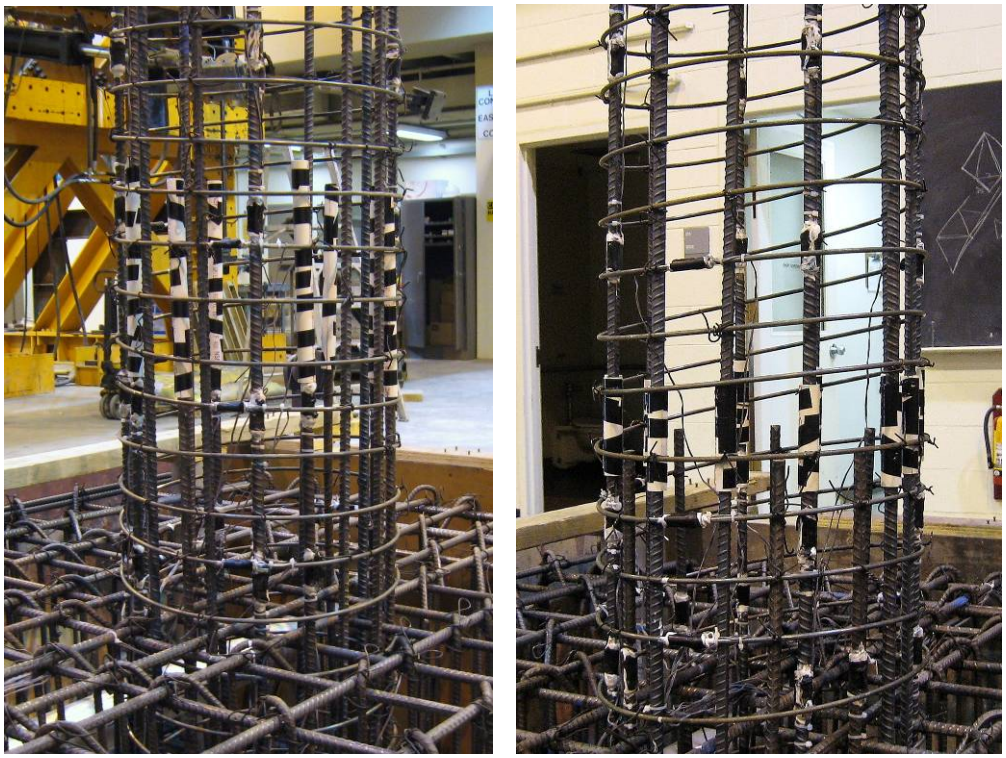

Figure B-4 Detail of plastic hinge zone: (a) specimen S1; (b) specimen S2

A heavy-wall 1/4” thick Sonotube was placed over each column cage to serve as formwork. The plumbed column forms were secured to the anchor blocks through several horizontal, vertical, and lateral wooden bracing (see Figure B-5). Plastic spacers were used between the column cages and the form to ensure the columns are adequately plumbed and have a uniform concrete cover after their pour (see Figure B-6). The strain gage wires of each specimen were pulled out from the anchor block formwork on one of its sides and from the column top. The threaded rods serving as instrumentation rods were placed through holes in the column formwork at the specified location.

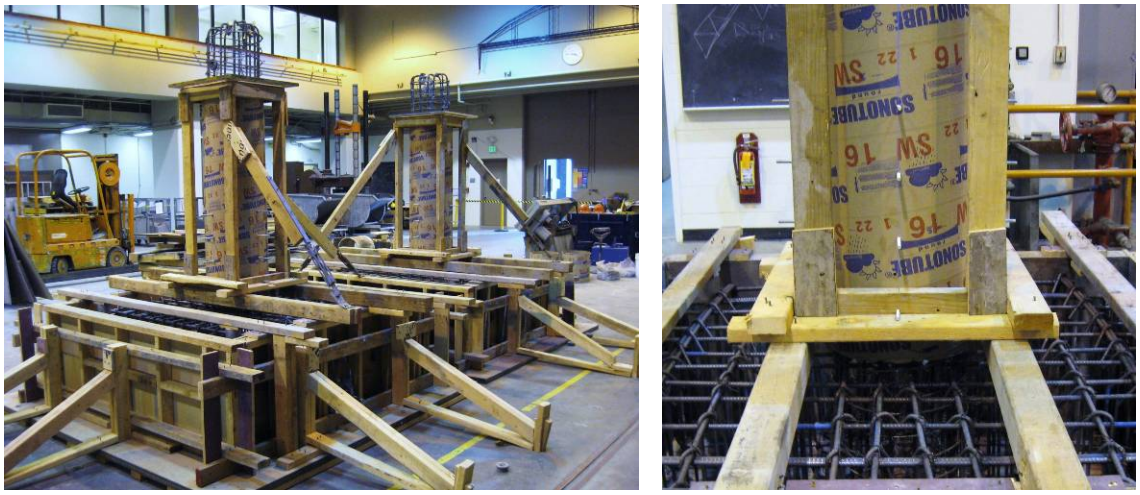

Figure B-5 (a) Laterally-braced column formwork; (b) Detail of instrumentation rods in column base

A modified steel jacket connecting the column top to the test actuators was placed on top of the braced column formwork of each specimen, serving as a form for the top 16” of the column (see Figure B-6). The bracing wooden structure of the column was designed to hold the heavy steel jackets in place. The anchor block forms were braced thorough additional kickers secured to the laboratory floor, thus completing the reinforcement cage construction and formwork (see Figure B-5).

Figure B-6 (a) Installed steel jacket connecting the column top to the actuators; (b) Spacers used between column cage and formwork or steel jackets

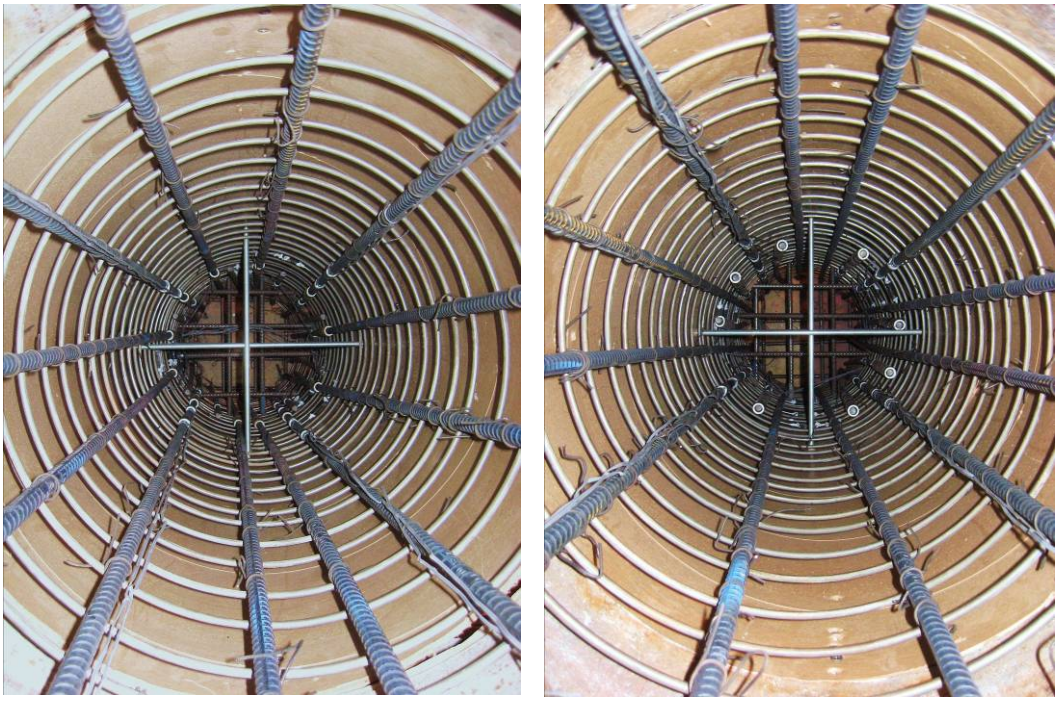

Figure B-7 Interior view of column cages: (a) specimen S1; (b) specimen S2

The casting of the anchor blocks of the two test specimens was carried out in accordance with the Caltrans Standard Procedures used in typical reinforced-concrete bridge construction in California. Concrete from the shoot of a concrete truck was placed into the anchor block formwork and vibrated (see Figure B-8). The exposed surface was finished (see Figure B-9).

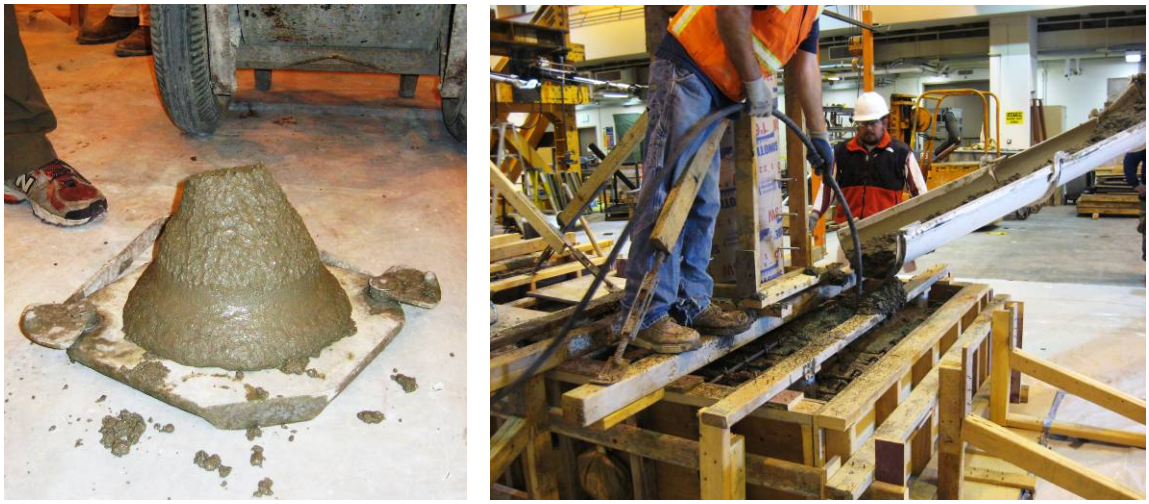

Figure B-8 (a) Slump test of plain concrete mix; (b) Casting of anchor blocks

Figure B-9 (a) Finished surface of anchor block; (b) Fibers added to concrete mix inside truck

The casting of the columns was carried out following the construction of the anchor blocks using a similar plain concrete mix delivered from a second truck. Modifications were made for the casting of the fiber-reinforced concrete columns, since no established criteria or guidelines are currently available for this novel mix. A concrete bucket with a funnel shape, controlled mechanic opening at its bottom, and 1/3 cubic yard capacity was used for the casting of the columns. After fibers were added and mixed inside the concrete truck, the resulting mix was poured into the bucket (see Figure B-10). The closed bucket was then raised through a crane in the structural lab of Davis Hall and placed on top of the column specimens. The concrete mix in the bucket was vibrated from above using a scissors lift to increase its workability and allow its pour through the bottom of the funnel (see Figure B-10). The columns with fiber-reinforced concrete were also vibrated to guarantee proper and uniform cover of the rebar throughout the height of the column and eliminate air pockets. A wooden form was used to secure in place the threaded anchor rods connecting the spreader beam to the column top.

Figure B-10 (a) Fiber-reinforced concrete mix poured to concrete bucket; (b) Casting of fiber-reinforced concrete columns

Following the construction of the specimens, the top surface of the anchor blocks was wet cured using Dunlop and covered with thick nylon sheets for a period of 7 days (see Figure B-11). The forms were stripped 11 days after the casting of the specimens following a set of concrete cylinders testing of both plain and fiber-reinforced concrete to guarantee that the specimens had gained sufficient strength required for such operation (see Figure B-12).

Figure B-11 (a) Curing of column specimens; (b) Curing of plain concrete and fiber-reinforced concrete cylinders and beams

Figure B-12 Specimens after the removal of the forms (a) S1 column; (b) S2 column

Since the casting of specimen S1 resulted in minor holes due to the formation of air pockets around the perimeter of the column during the casting of the column, non-shrink high-strength grout (f'_c=10 ksi) was used to repair the required area (see Figure B-13). The grout was cured for a period of 3 days to avoid the formation of cracks in a high cement content mix. The holes were formed at an approximate elevation of 2' above the foundation level and the plastic hinge zone. The shear capacity of S1 column specimen and its ability to properly transfer shear loads to the column base was numerically verified prior to the cyclic testing.

Figure B-13 Detail of S1 column after repair of cover using high-strength grout

The use of a superplasticizer and a slightly higher water-cement ratio is recommended to increase the workability conditions of the fiber-reinforced concrete mix and avoid the formation of air pockets or the excessive use of vibration resulting in segregation. Following a period of 28 days, the specimens were translated to their assigned position in the lab for testing, painted with white wash paint, connected according to the experimental setup in section B.2, and externally instrumented according to the instrumentation scheme in Chapter 2 (see Figure B-14).

Figure B-14 Final setup of S1 and S2 FRC column specimens

B.2 TEST SETUP

The bidirectional quasi-static cyclic test of the two FRC column specimens was carried out in the Structural Laboratory in Davis Hall at the University of California, Berkeley. This experimental test was performed in order to comprehensively characterize the cyclic response of circular FRC bridge columns subjected to bidirectional lateral loading and compare their response to conventionally reinforced concrete columns tested by Terzic *et al.* (2008). The plan and elevation views of the specimen and test setup in Davis Hall are shown in Figure B-15 through Figure B-17.

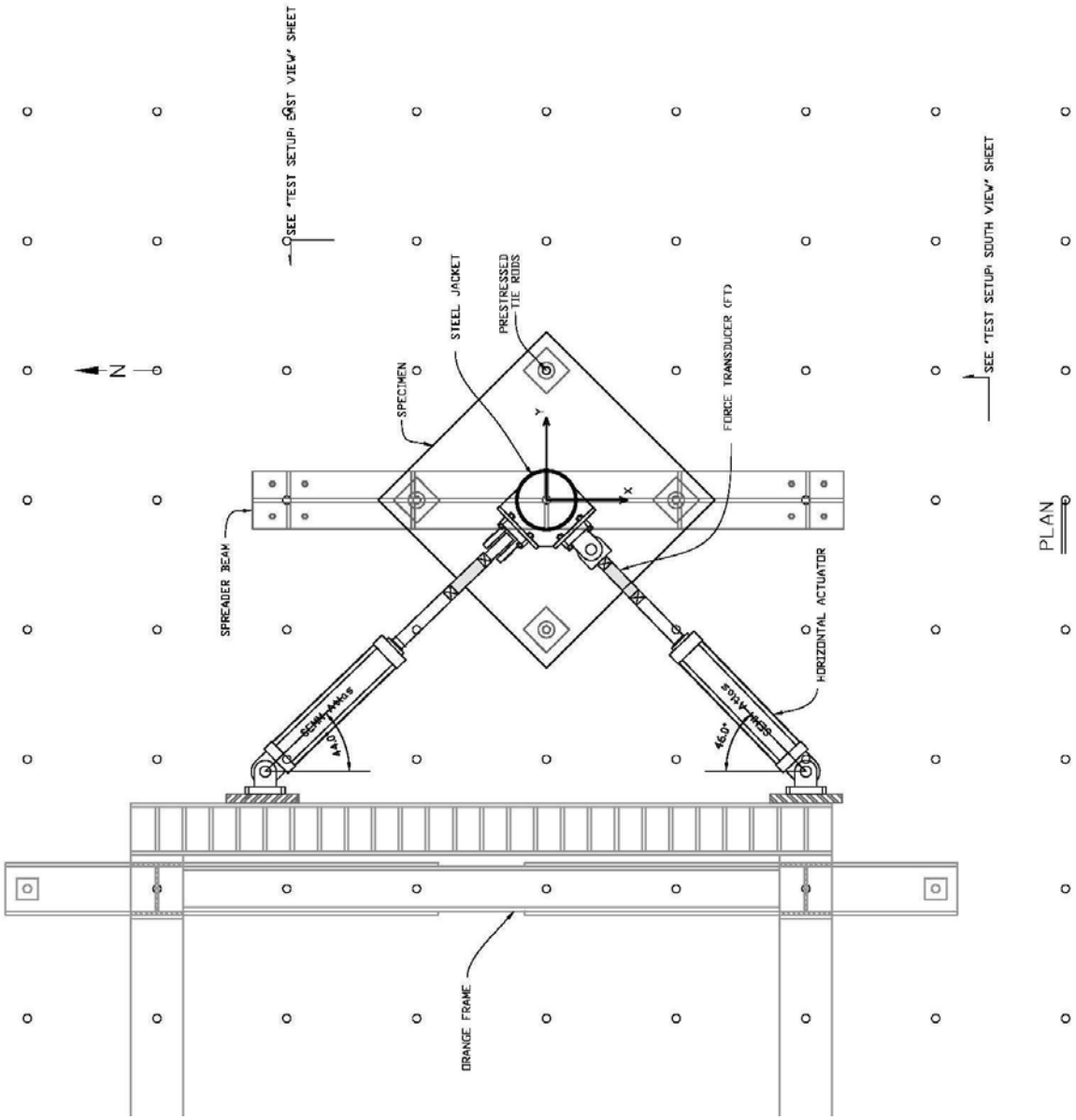

Figure B-15 Plan view of experimental setup of FRC column specimen subjected to bidirectional cyclic loading

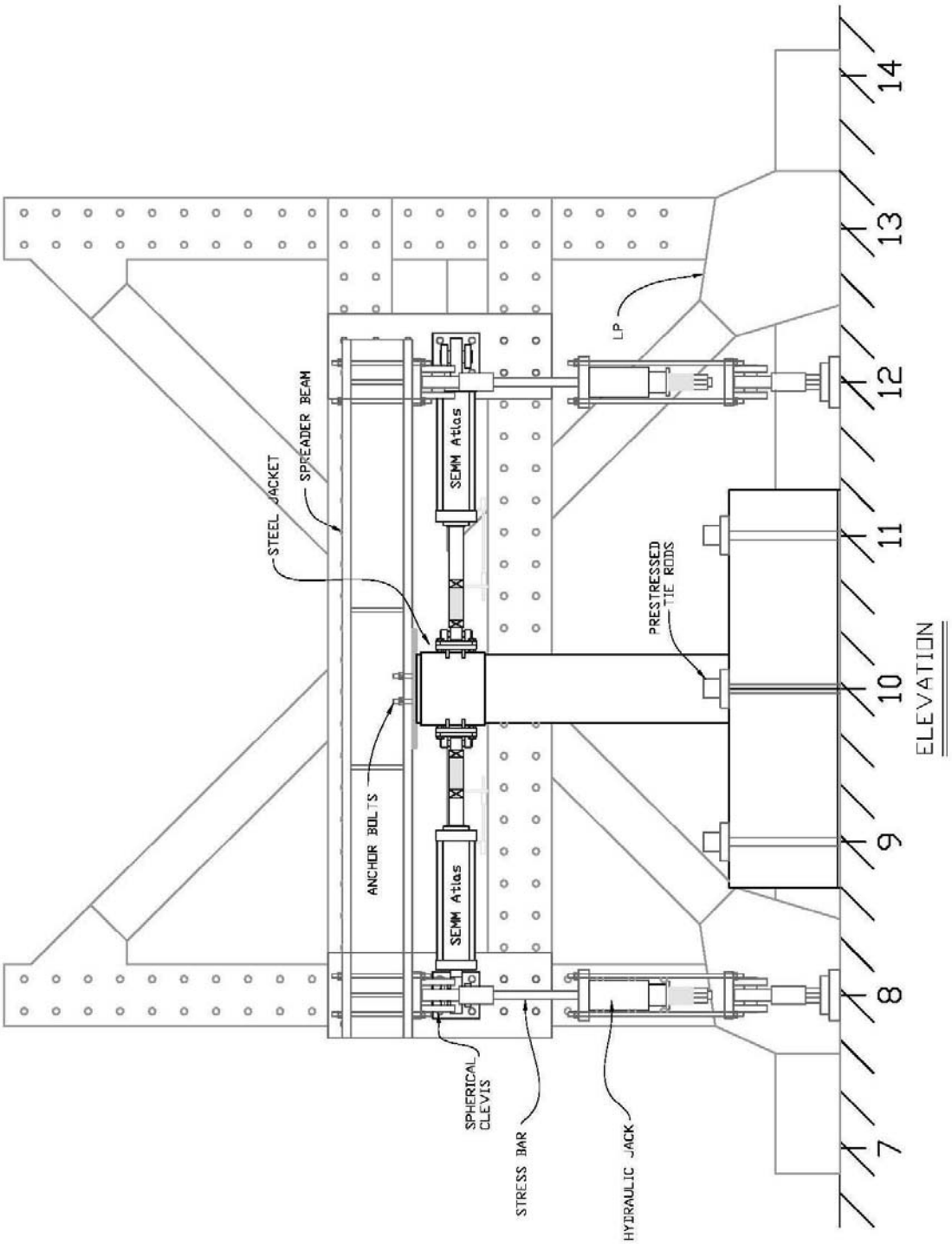

Figure B-16 East view of experimental setup of FRC column specimen subjected to bidirectional cyclic loading

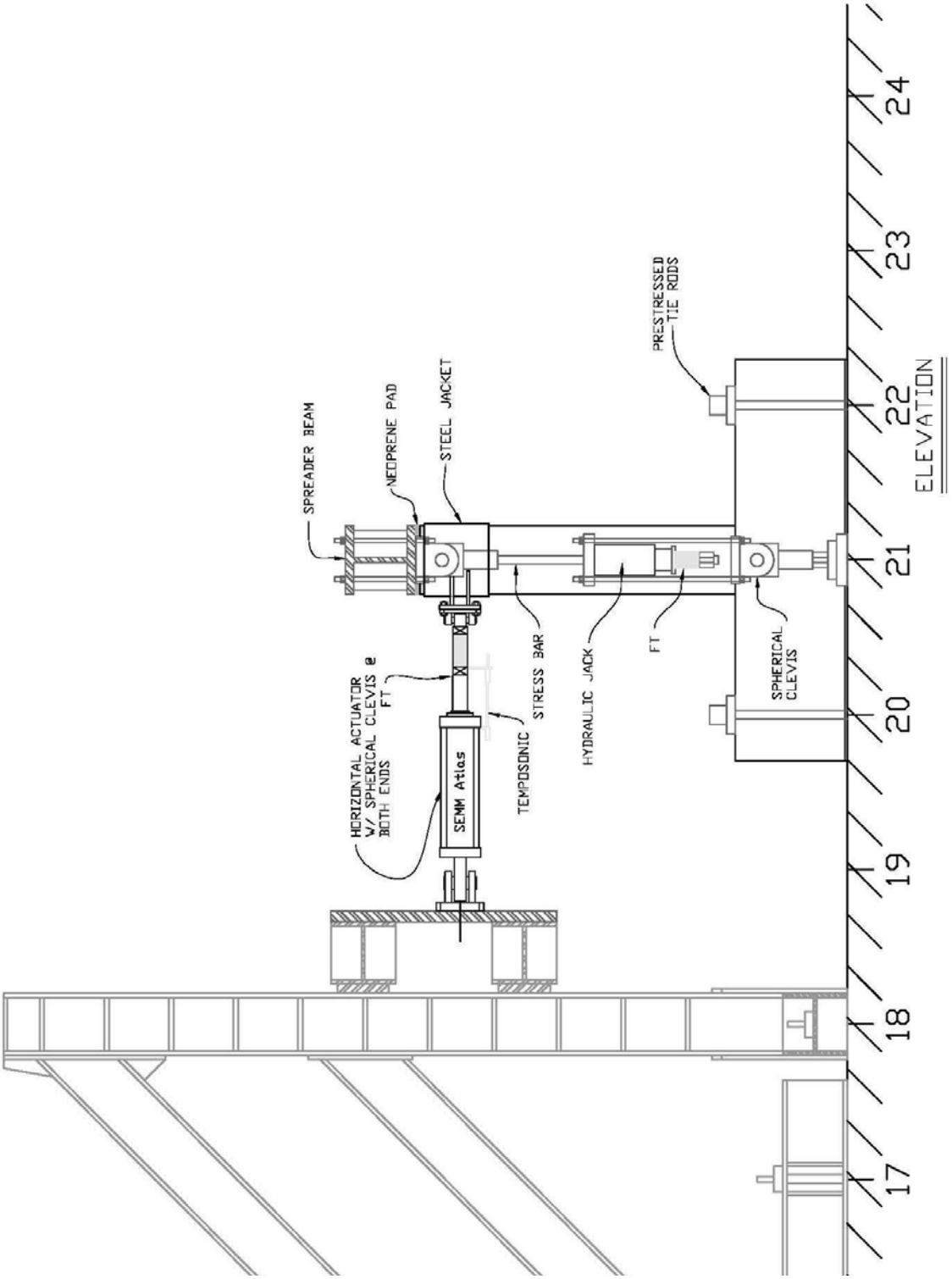

Figure B-17 South view of experimental setup of FRC column specimen subjected to bidirectional cyclic loading

The cyclic test of the FRC columns was carried out by applying lateral and axial loads at the top of the column specimen at a height of 64” above the anchor block corresponding to the mid-height or inflection point of the idealized bridge column. The lateral cyclic load with a

circular displacement pattern as described in Chapter 2 was applied using two horizontal servo-controlled hydraulic actuators which reacted against a rigid orange frame. The estimated shear capacity of the FRC specimens was approximately 35 kip, while the two actuators used in tests had a load capacity of 125 kips each and a stroke of ±18". The two actuators were attached with an approximate 45^{o} angle with respect to the principal axes of column specimen, as seen in Figure B-15. The selected position of the two actuators was intended to be as symmetrical as possible with respect to the Y-axis of the setup, and pin-pin boundary conditions were provided on either end of each actuator to avoid significant torsion of the column top. The attachment of the two actuators to the column top was done through a steel jacket with two thick vertical steel plates welded to its sides, as seen in Figure B-18.

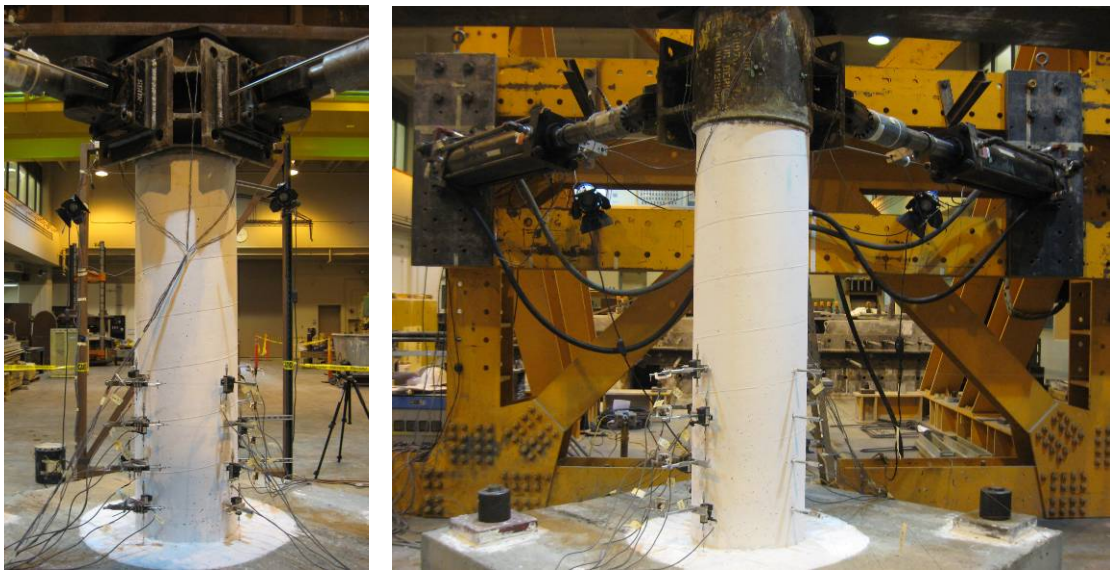

Figure B-18 (a) West view of actuators attachment to steel jacket at the column top; (b) East view of test setup

The anchor block of each column specimen was hydrostoned and prestressed to the laboratory strong floor using four post-tensioning rods passing through holes constructed as described in section B.1 (see Figure B-15 through Figure B-17). This was done to restrict the rotation and sliding of the foundation during the application of the lateral load on the column top. The movement of the foundation was monitored using displacement potentiometers, as described in Chapter 2.

The axial load equal to 100.5 kip corresponding to approximately 10% of the axial capacity of the benchmark BC column specimen tested by Terzic *et al.* (2008) was applied by two post-tensioning rods, one on each side of the specimen, using manually controlled jacks. The axial load was transferred from the rods to the column top through a spreader beam, as shown in Figure B-16. The spreader beam was attached to the column top through six ¾" diameter steel anchor rods to ensure no sliding occurred between these two elements during the large cycles of lateral displacements of the column top. A 1" thick neoprene rubber was used between the spreader beam and the column top to uniformly distribute the axial load over the column cross section and prevent concrete crushing of the column top produced due to minor relative rotation between the two components during the lateral displacements of the column (see Figure B-18).

The jacks used to apply the gravity load on the column were designed for 300 kips each and a 5" stroke. However, due to limitations of the hydraulic pressure in the pumps used, the load cells have a maximum capacity of 200 kips, while the clevises have a 150 kips limit. Therefore, the maximum vertical load that can be applied on the column top is approximately 300 kips (150 kips on each jack). The vertical load specified for this experimental test of 100.5 kip was below the specified limit of the gravity load assembly available in Davis Hall.

Spherical clevises (swivels) were provided at both ends of the rods to prevent the bending and buckling of the rods during the bidirectional displacements of the spreader beam attached to the column top. The lower clevises were hydrostoned and prestressed to the laboratory strong floor while the top clevises were connected to the pressure jacks and the spreader beam by short threaded rods, as seen in Figure B-19.

Figure B-19 Vertical load setup including spreader beam, top and bottom spherical clevises, prestressed rods, and hydraulic jacks: (a) Detail; (b) Global view

Appendix C: Additional Experimental Results

This appendix presents additional experimental results obtained from the bidirectional quasi-static cyclic test of the two FRC columns such as longitudinal and transverse reinforcement strain profiles, shear deformations, and progression of damage with increasingly larger displacement cycles.

C.1 DAMAGE PROGRESSION

The results of the displacement history corresponding to the main cycles are presented in this short report. The progression of damage throughout the loading history is displayed in Figure C-1 through Figure C-8 for S1 specimen and in Figure C-9 through Figure C-14 for S2 specimen. The damage state of the FRC column specimens corresponding to ductility levels of 1.5, 3, and 4.5 can be compared to the ones sustained by the BC and SSC specimens presented in Figure C-15 through Figure C-18.

The S1 specimen presented multiple initial cracking at a region located approximately 7 to 12 inches above the column foundation at a ductility level (with respect to BC column yield point) of 1.5. An additional crack had also formed at the ductility level of 1.5 at the bottom of the column. Previous to this ductility level there was no apparent damage at any level of the S1 column. The initial cracks formed above the foundations only became more visibly apparent at ductility levels of 3 and 4.5, while the bottom crack did not continue to propagate at these higher demand levels. As the ductility demand increased, the damage zone spreaded primarily downwards towards the column base. The S1 column displayed minor damage up to a ductility level of 4.5 and spalling of the concrete cover was not produced at any ductility demand level.

At a ductility level of 6.25 the spiral reinforcement in the S1 column fractured at an approximate height of 6”. At the following cycles corresponding to ductility levels of 6.25 or higher the spiral fractured resulted in longitudinal bar buckling and concrete crushing. At the end of the cycle corresponding to a ductility level of 12.5, all longitudinal bars had fractured. The dowels did not fracture nor buckled, even at the higher demand levels imposed on the column. The total plastic hinge length observed was approximately 12-16” (3/4-1 of the column diameter). Starting at a ductility demand level of 6.25 additional damage zones began to form at discrete locations around the perimeter of the column at an approximate height of 20” above the foundations. This elevation corresponds to the termination of the longitudinal dowels and the location of the discrete damage zones corresponded in all cases to the end of a dowel.

In the S2 specimen an initial primary flexural crack formed at a ductility level (with respect to BC column yield point) of 1, while additional flexural cracks formed at a ductility level of 2 and were below the primary crack. As the ductility demand increased, the damage zone

spreaded downwards towards the column base. The S2 column displayed negligible damage up to a ductility level of 3, and damage became more evident only at a ductility level of 4.5. Spalling of the concrete cover was not produced at any ductility demand level. At a ductility demand level of 6.25 the S2 column specimen underwent longitudinal bar buckling and spiral fracture at two levels, followed by fracture of two longitudinal reinforcement bars. Similar damage states were produced for the S1 column at this ductility level. Since the S2 column presented a considerable loss of gravity load carrying capacity at the end of the cycle corresponding to a ductility level of 6.25, additional cycles with higher ductility demand levels were not imposed on the column due to safety hazards and the test was interrupted following a smaller cycle corresponding to a ductility demand of 2.

The fracture of the spiral and the buckling of the main longitudinal rebar damage states were produced in the FRC specimens since the spiral reinforcement spacing in the S1 and S2 column was twice that provided in the conventional concrete BC specimen, specified according to Caltrans SDC requirements. The ductility levels discussed in this section are reported with reference to the BC specimen. However, the actual displacement ductility demand on S1 and S2 specimens is different than 6.25 estimated for the BC specimen due to the following reasons: 1- The effective length of S1 and S2 column specimens was shorter than the effective length of the BC column specimen equal to 64” because the center of rotation in the damage zone is 6-12” above the foundation level; 2- Due to enhanced behavior and damage tolerance of the ductile FRC material, inelastic behavior in the plastic hinge zone is postponed. Compared to the S2 FRC column test, improved detailing used in the S1 FRC specimen enabled better spreading of the plastic hinge zone and therefore, improved response.

The damage sustained by the BC specimen displayed in Figure C-15 through Figure C-17 at ductility levels of 1.5, 3 and 4.5 corresponded primarily to concrete cracking and spalling of the cover. The damage of the SSC column at the end of the cycle corresponding to a ductility level of 4.5 produced due to cracking, spalling, longitudinal bar buckling, and concrete crushing, is presented in Figure C-18. At the maximum ductility demand level of 4.5 imposed on the BC and SSC specimens, the damage observed in both S1 and S2 FRC columns was significantly smaller to the conventional concrete specimens. S1 and S2 columns had only sustained minor damage at a ductility demand of 4.5, and spalling did not occur at any stage of the loading history.

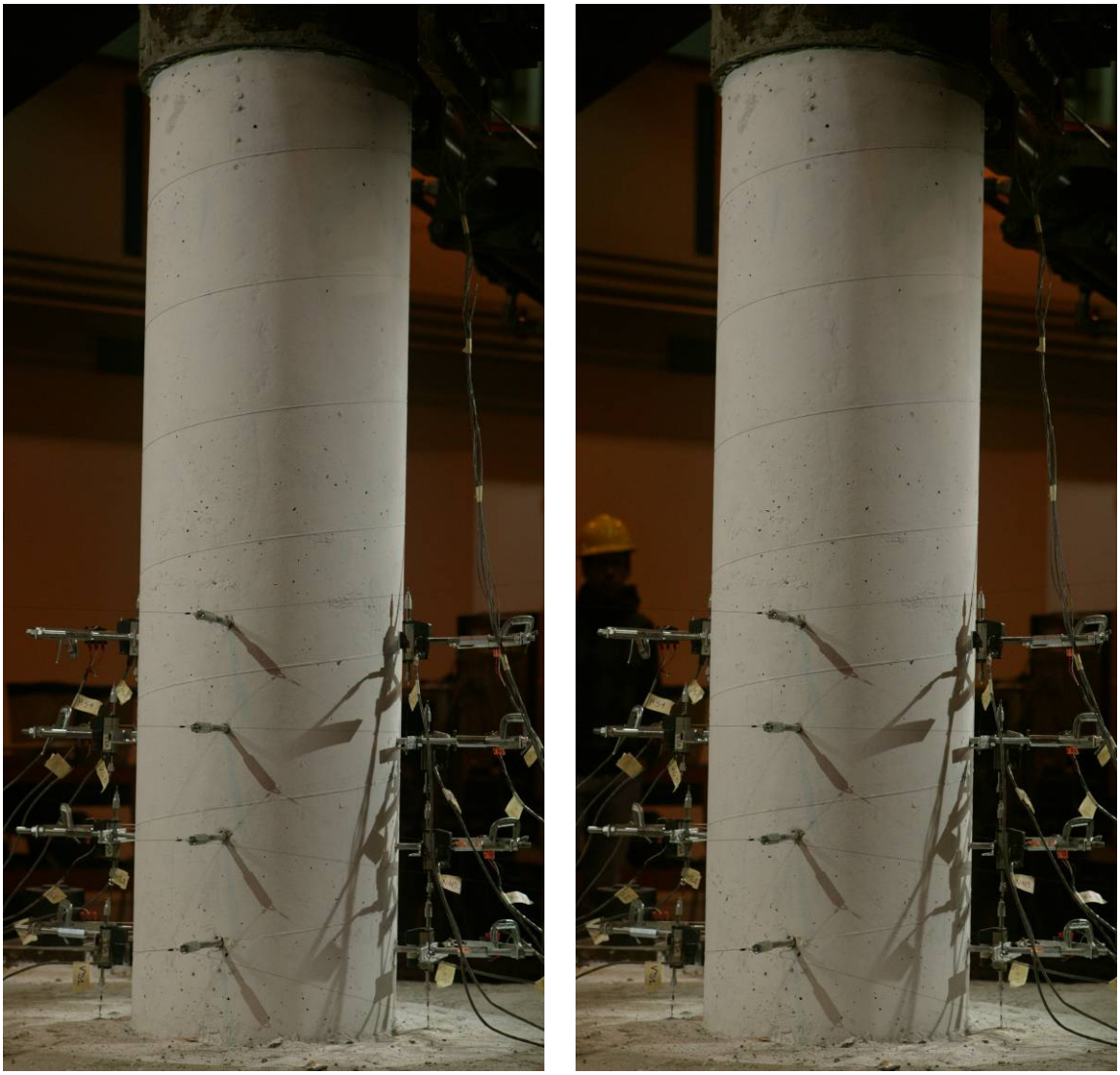

(a) (b)

Figure C-1 State of specimen S1 at the end of the cycle corresponding to a ductility demand of (a) 1 and (b) 1.5 of BC specimen (Northeast view)

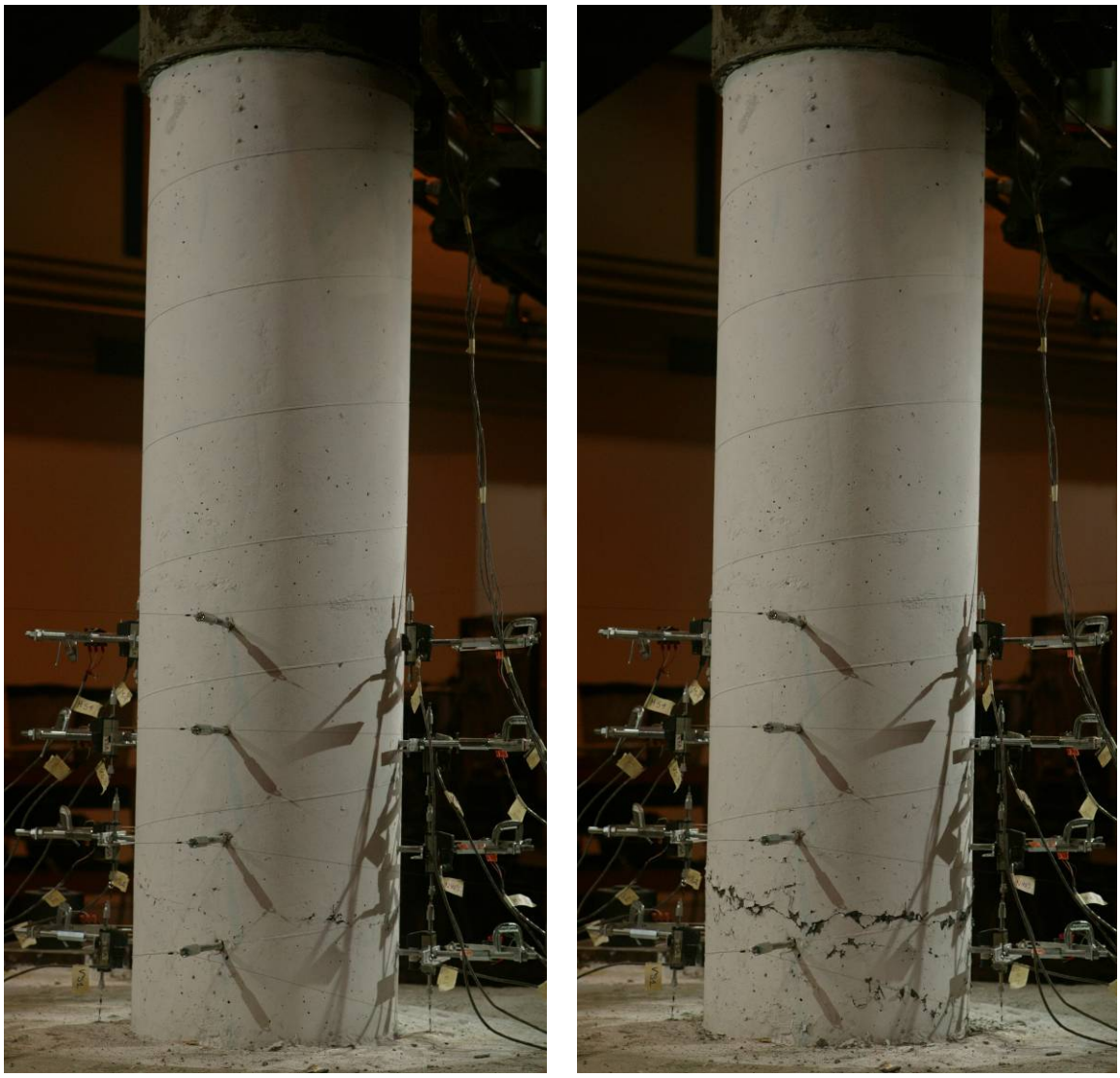

(a) (b)

Figure C-2 State of specimen S1 at the end of the cycle corresponding to a ductility demand of (a) 2 and (b) 3 of BC specimen (Northeast view)

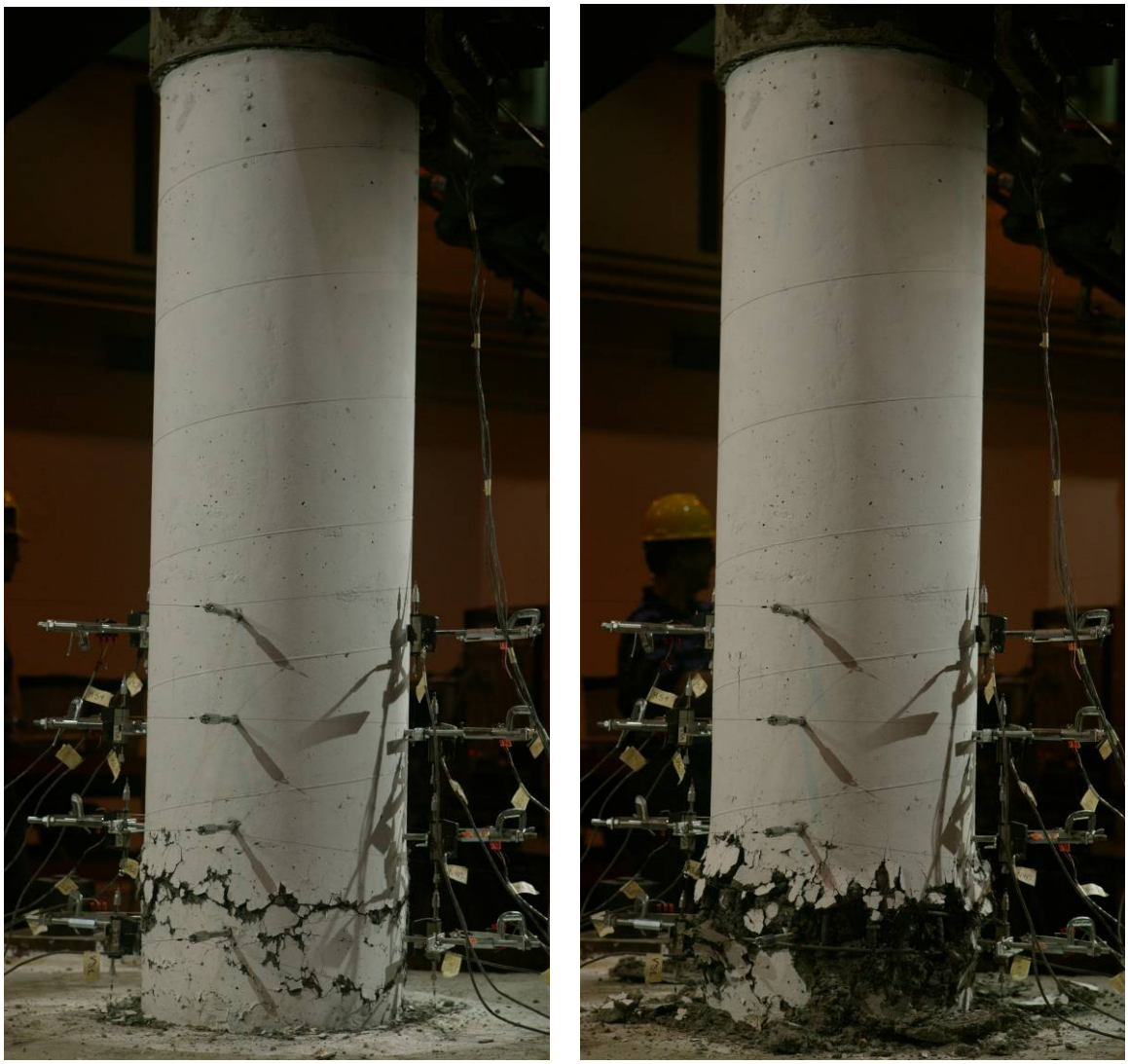

(a) (b)

Figure C-3 State of specimen S1 at the end of the cycle corresponding to a ductility demand of (a) 4.5 and (b) 6.25 of BC specimen (Northeast view)

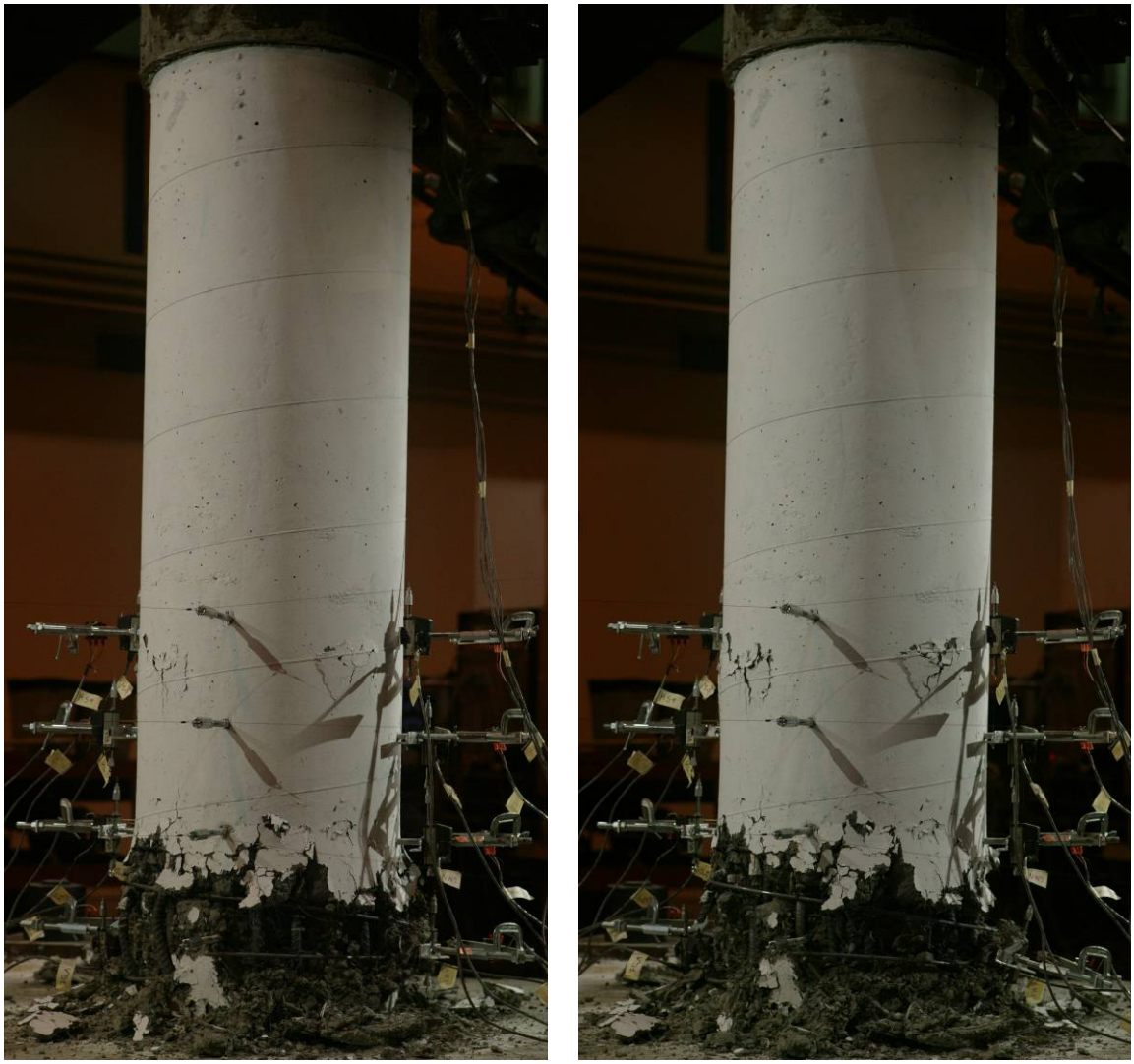

(a) (b)

Figure C-4 State of specimen S1 at the end of the cycle corresponding to a ductility demand of (a) 8 and (b) 12.5 of BC specimen (Northeast view)

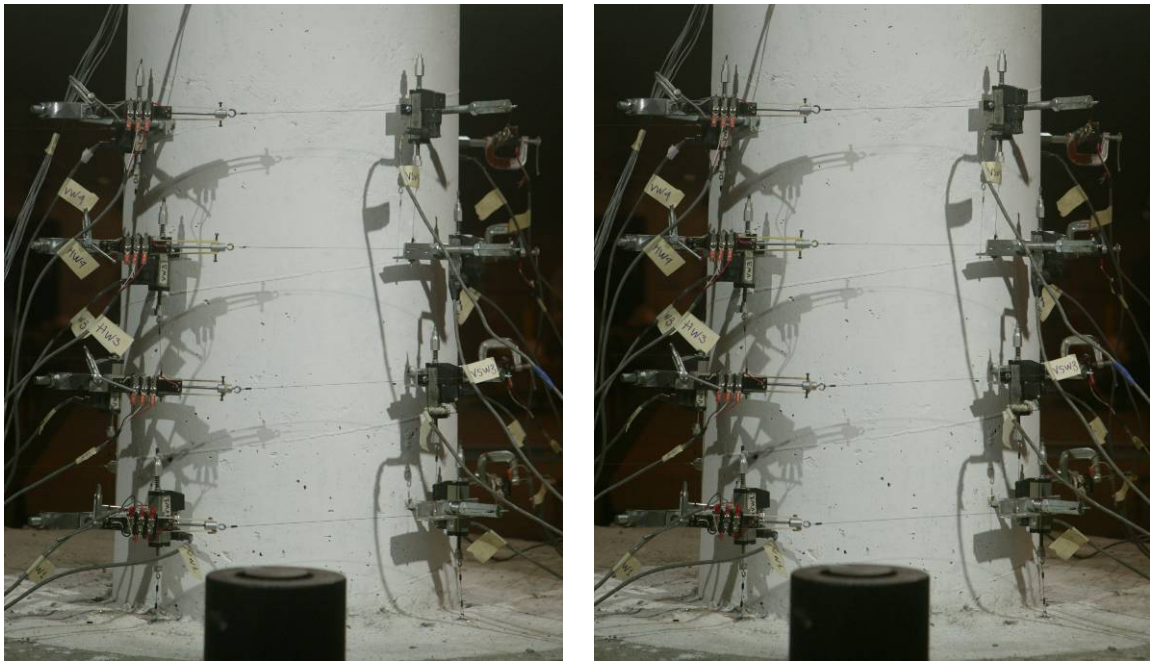

(a) (b)

Figure C-5 State of specimen S1 at the end of the cycle corresponding to a ductility demand of (a) 1 and (b) 1.5 of BC specimen (West view)

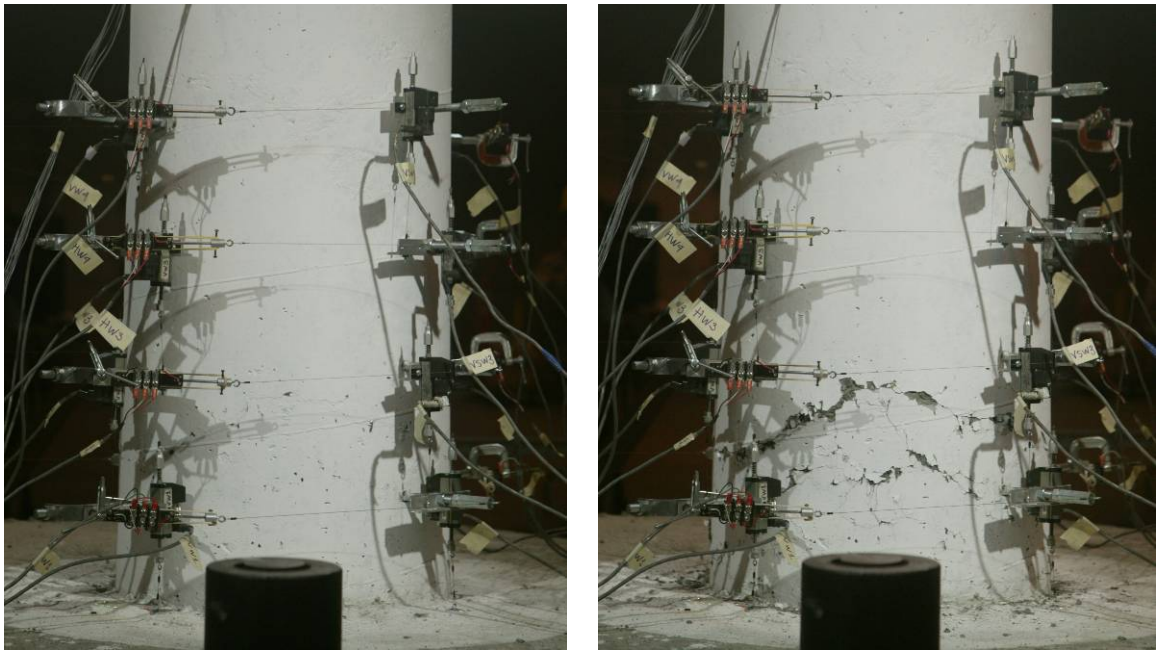

(a) (b)

Figure C-6 State of specimen S1 at the end of the cycle corresponding to a ductility demand of (a) 2 and (b) 3 of BC specimen (West view)

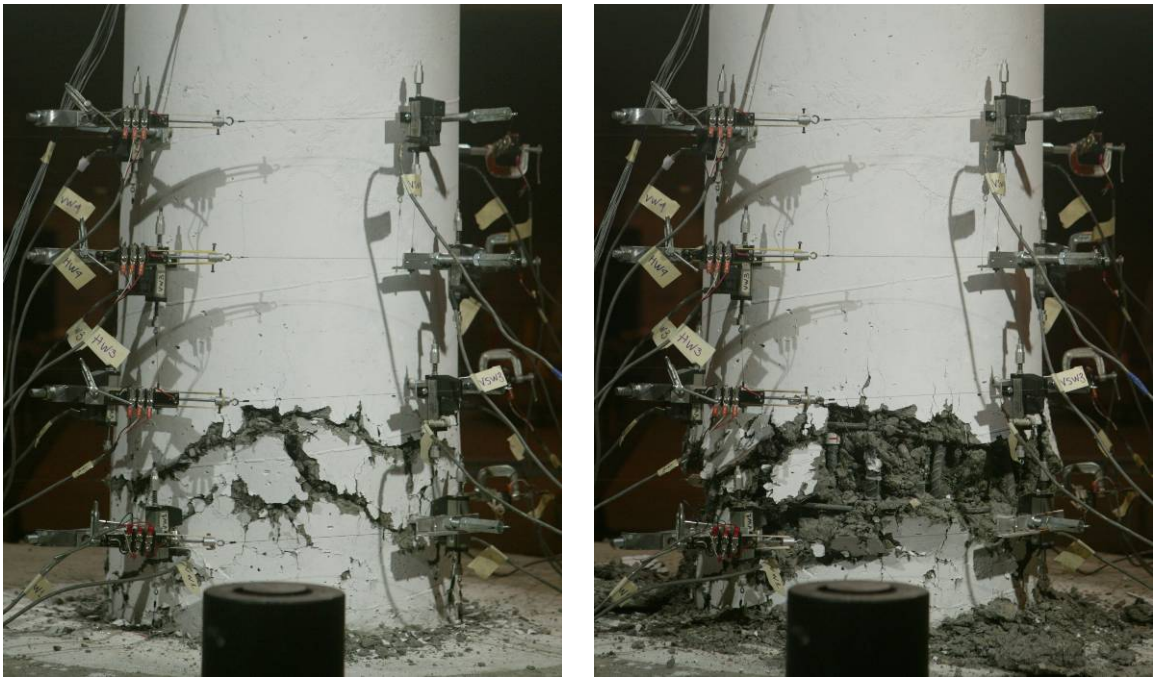

(a) (b)

Figure C-7 State of specimen S1 at the end of the cycle corresponding to a ductility demand of (a) 4.5 and (b) 6.25 of BC specimen (West view)

(a) (b)

Figure C-8 State of specimen S1 at the end of the cycle corresponding to a ductility demand of (a) 8 and (b) 12.5 of BC specimen (West view)

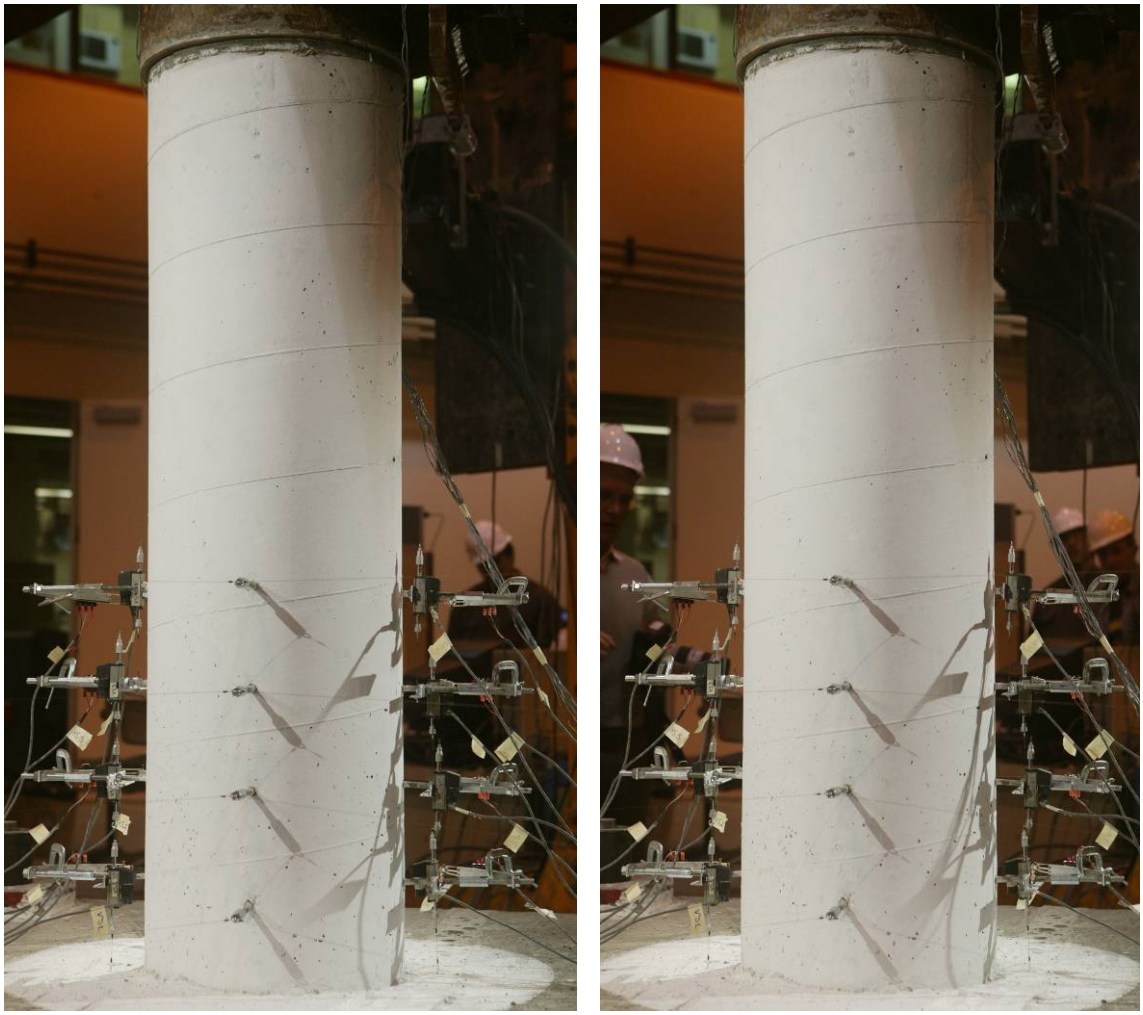

(a) (b)

Figure C-9 State of specimen S2 at the end of the cycle corresponding to a ductility demand of (a) 1 and (b) 1.5 of BC specimen (Northeast view)

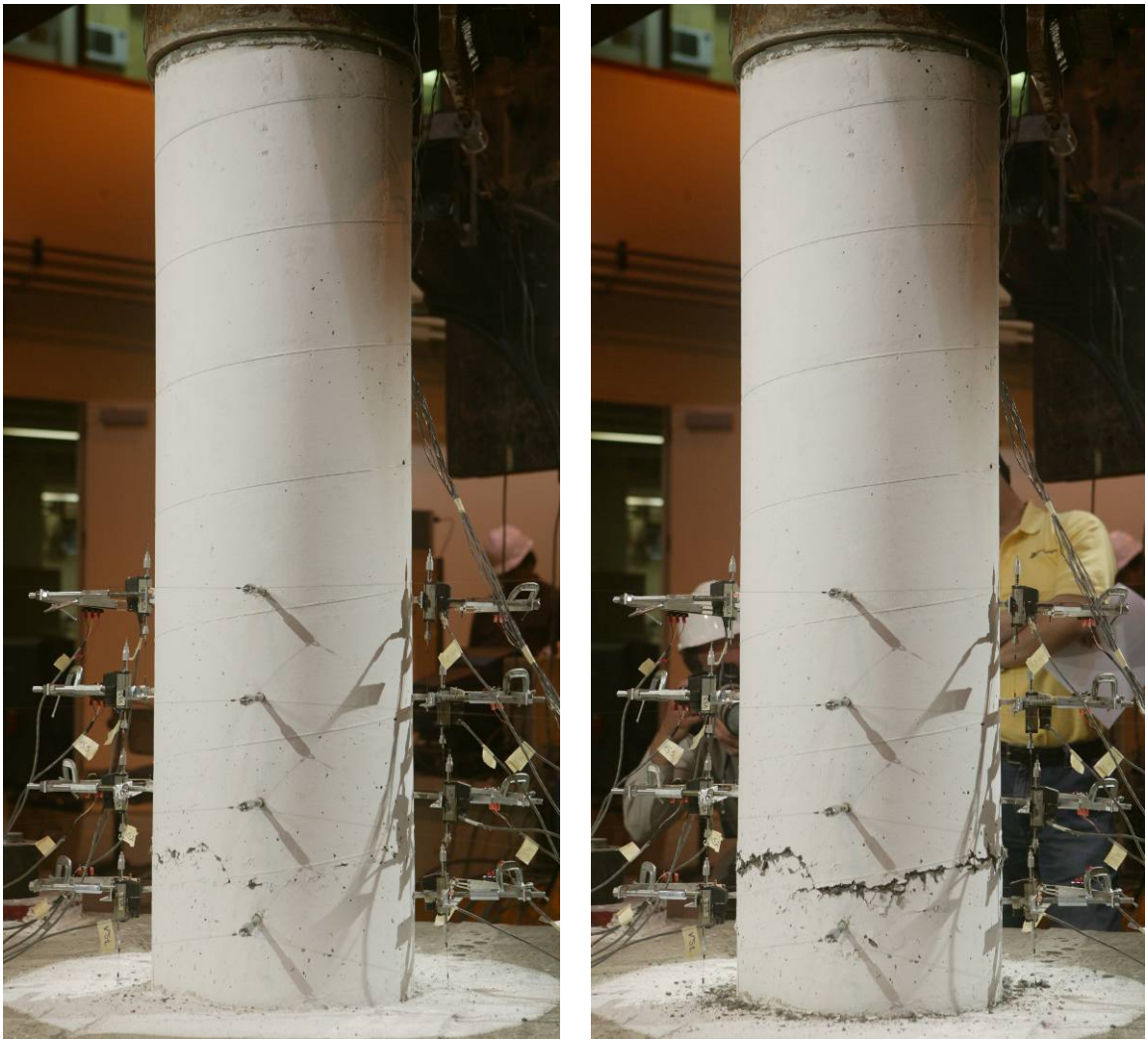

(a) (b)

Figure C-10 State of specimen S2 at the end of the cycle corresponding to a ductility demand of (a) 2 and (b) 3 of BC specimen (Northeast view)

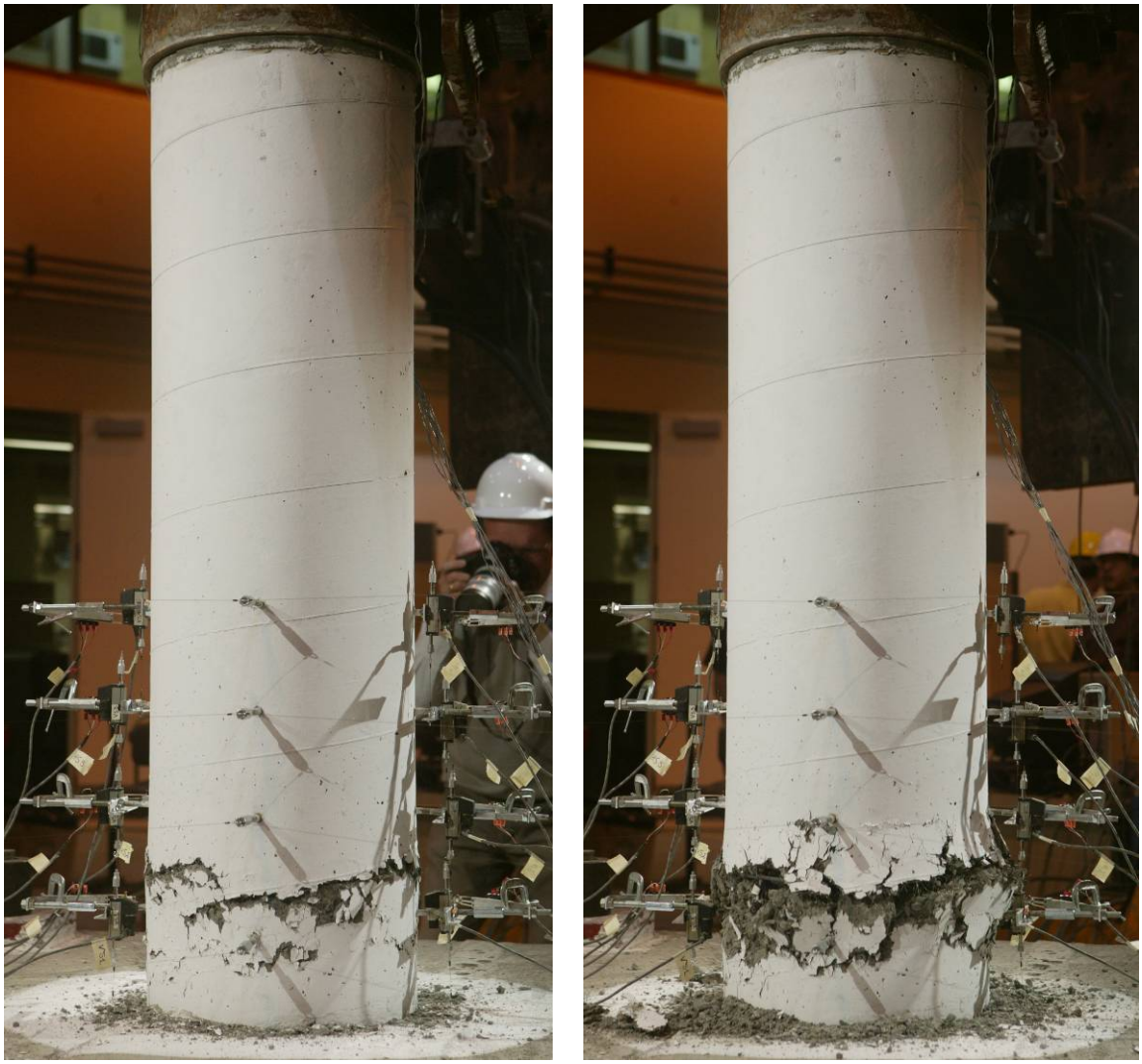

(a) (b)

Figure C-11 State of specimen S2 at the end of the cycle corresponding to a ductility demand of (a) 4.5 and (b) 6.25 of BC specimen (Northeast view)

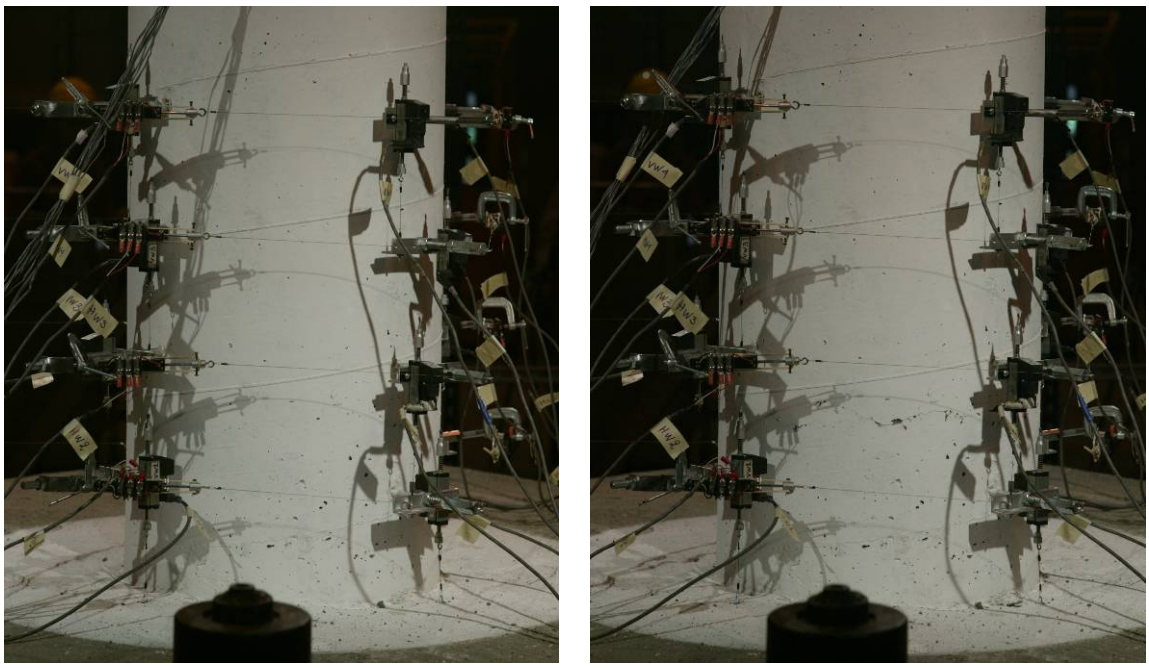

(a) (b)

Figure C-12 State of specimen S2 at the end of the cycle corresponding to a ductility demand of (a) 1 and (b) 1.5 of BC specimen (West view)

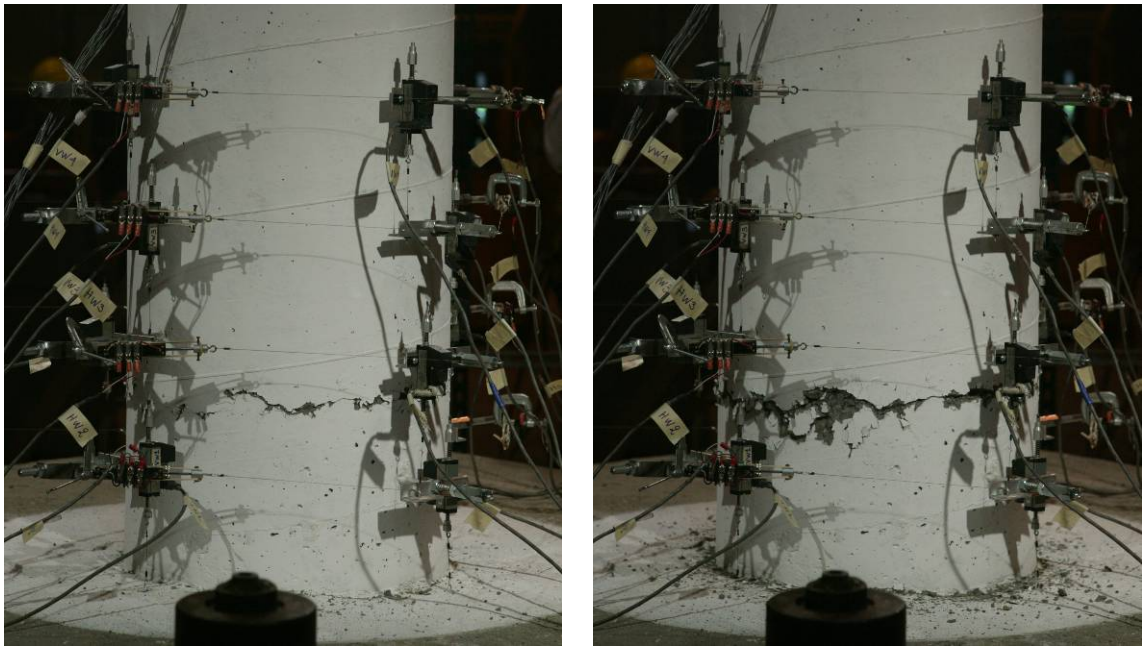

(a) (b)

Figure C-13 State of specimen S2 at the end of the cycle corresponding to a ductility demand of (a) 2 and (b) 3 of BC specimen (West view)

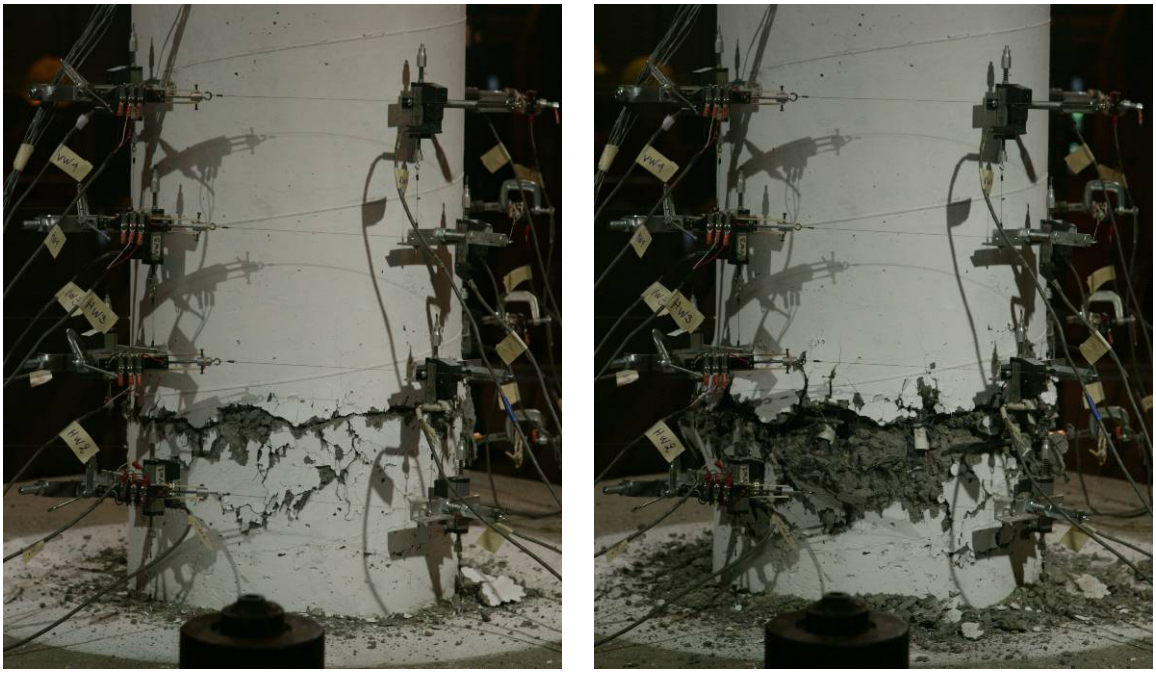

(a) (b)

Figure C-14 State of specimen S2 at the end of the cycle corresponding to a ductility demand of (a) 4.5 and (b) 6.25 of BC specimen (West view)

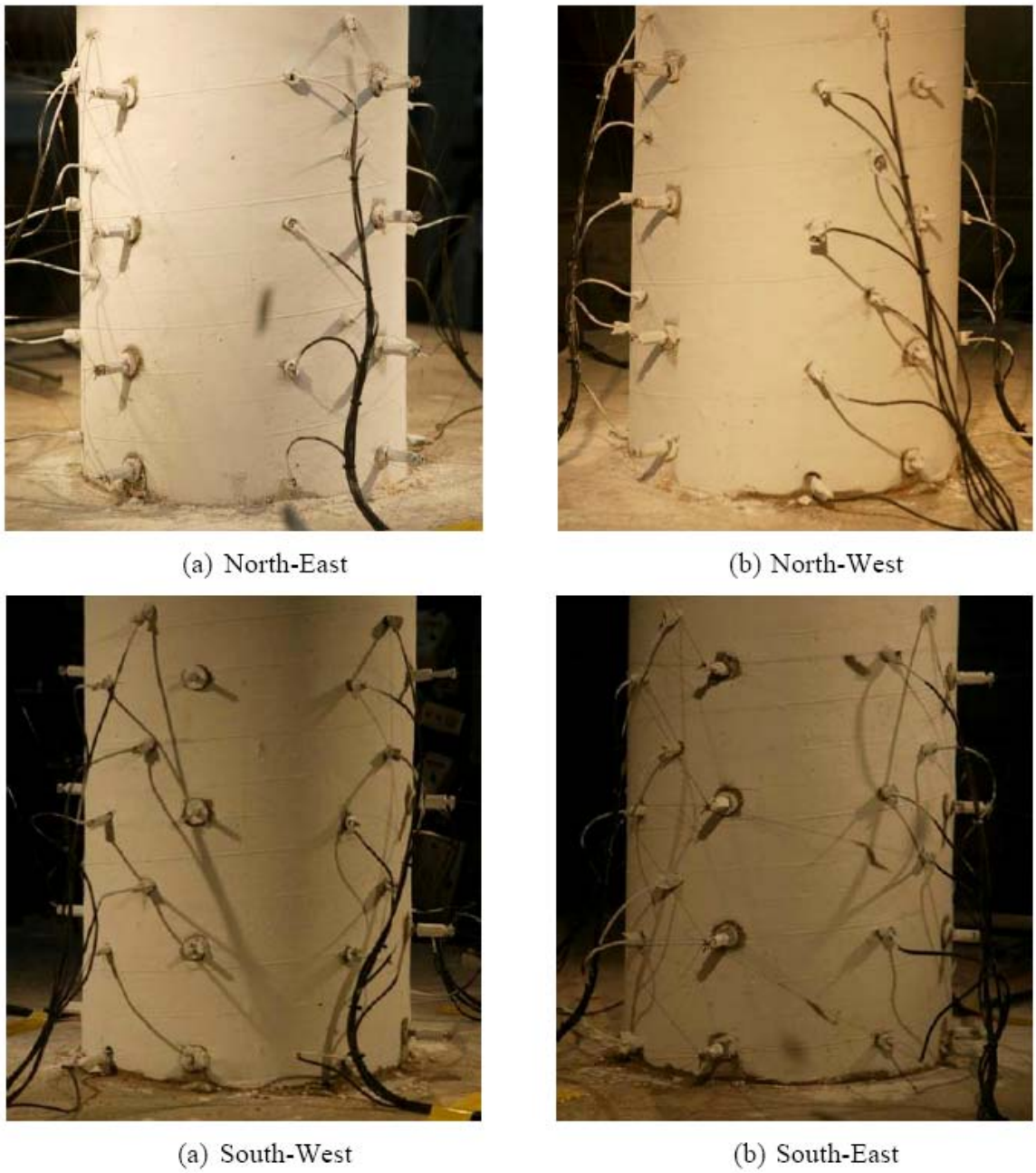

(a) North-East (b) North-West

(a) South-West (b) South-East

Figure C-15 State of specimen BC at the end of the cycle corresponding to a ductility demand of 1.5

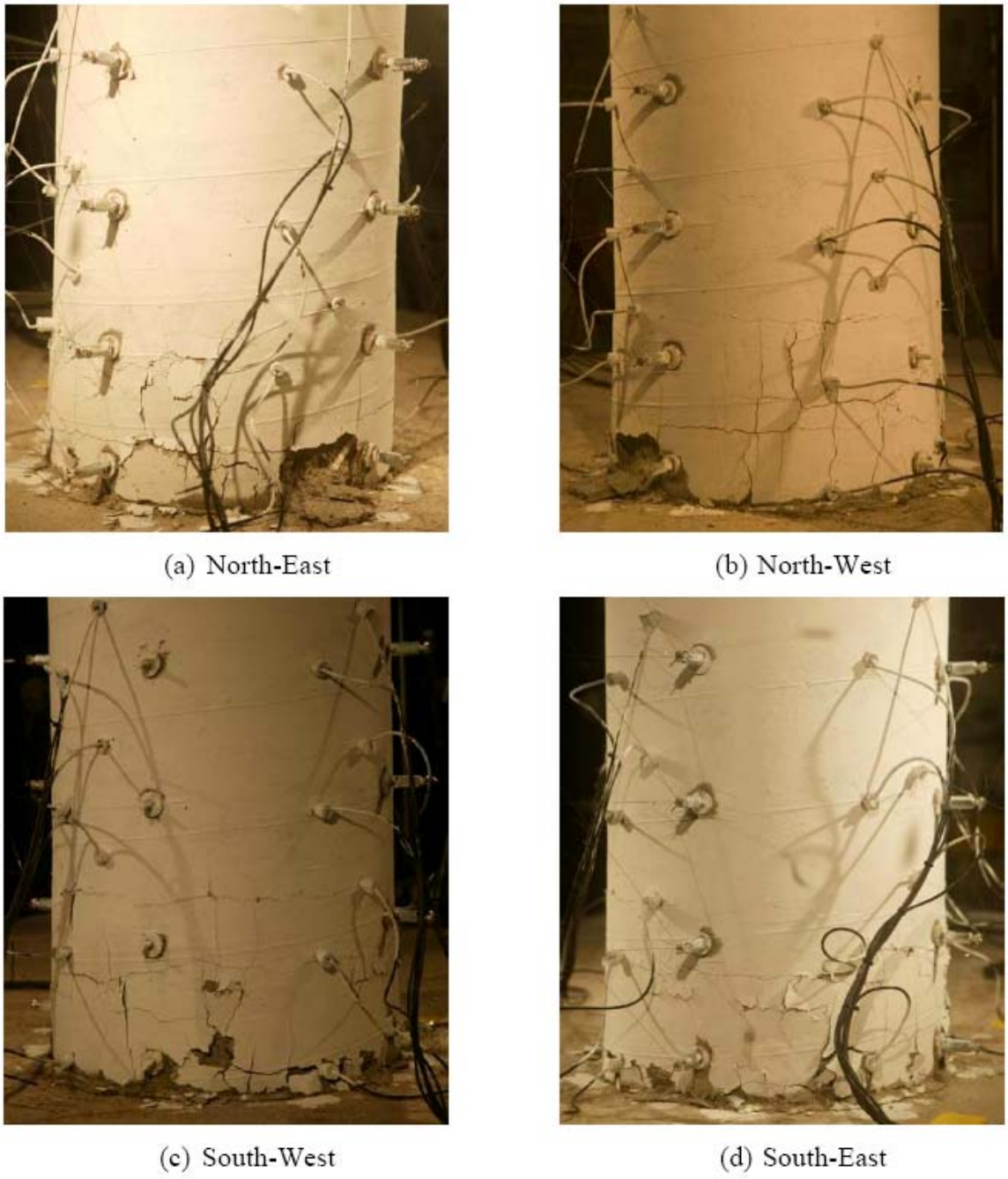

(a) North-East (b) North-West

(c) South-West (d) South-East

Figure C-16 State of specimen BC at the end of the cycle corresponding to a ductility demand of 3

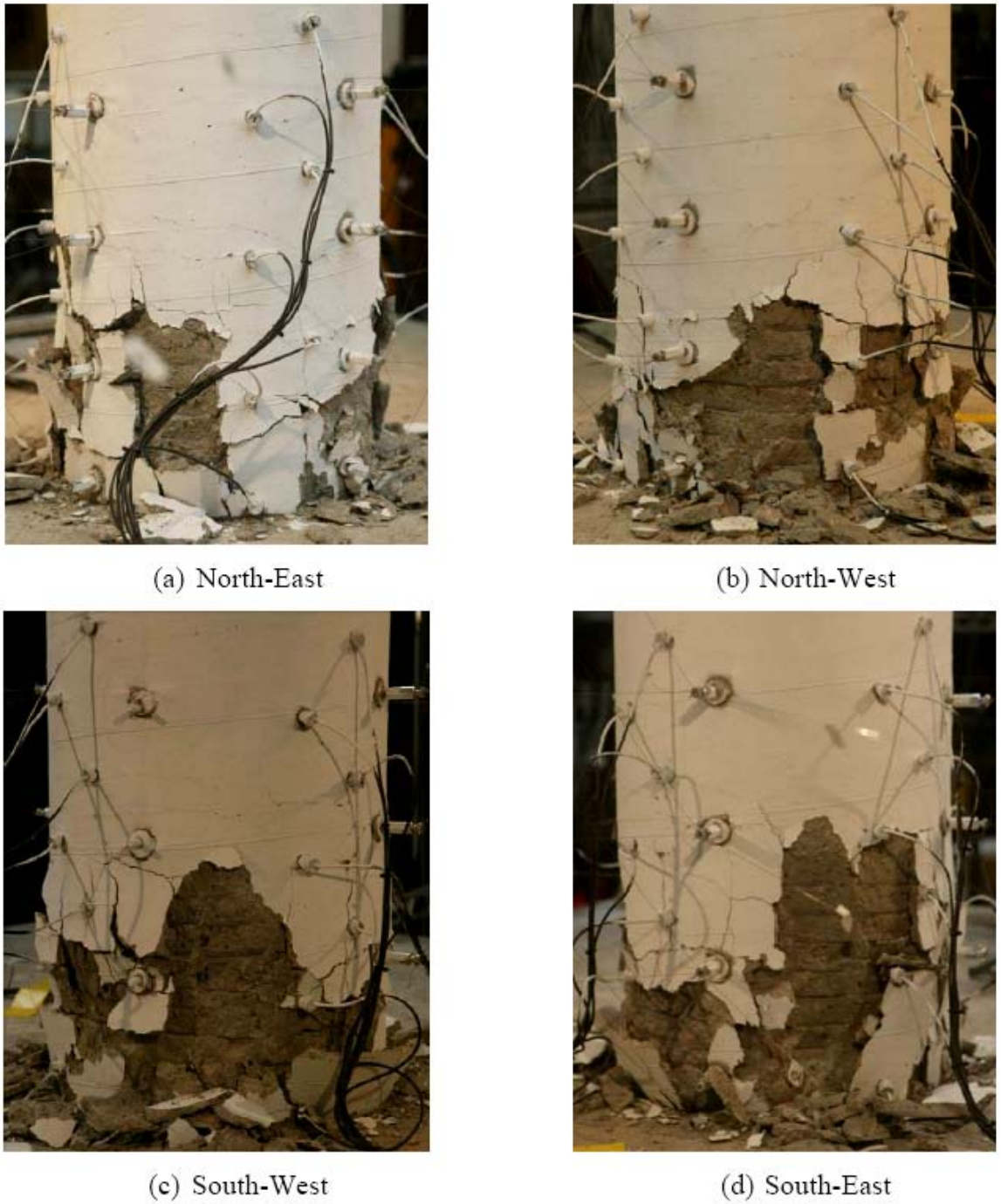

(a) North-East (b) North-West

(c) South-West (d) South-East

Figure C-17 State of specimen BC at the end of the cycle corresponding to a ductility demand of 4.5

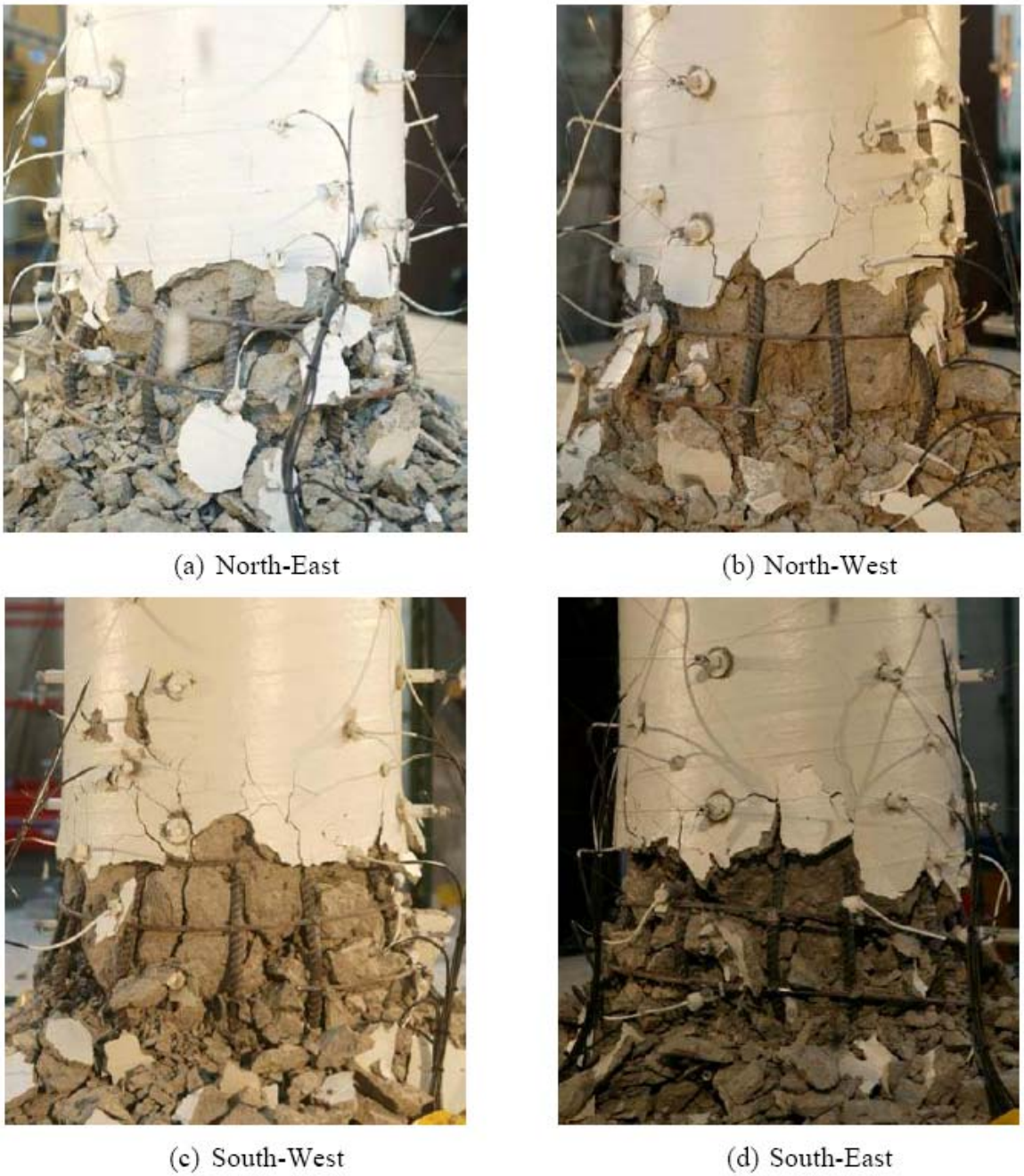

(a) North-East (b) North-West

(c) South-West (d) South-East

Figure C-18 State of specimen SSC at the end of the cycle corresponding to a ductility demand of 4.5

C.2 STRAIN PROFILES

The results of the strain gage measurements of S1 and S2 bidirectional cyclic tests are presented in Figure C-19 through Figure C-25. The strain results obtained for the continuous longitudinal steel, dowels, and spiral were normalized with respect to the corresponding yield strain values

obtained from coupon tension tests. The yield strain values were estimated as the yield stress divided by the corresponding elastic modulus of measured for each steel type. For the continuous longitudinal rebar the estimated yield strain was 2.36×10^{-3} (65 ksi / 27,600 ksi), for the dowels it was 2.86×10^{-3} (70 ksi / 24,500 ksi), while for the spiral it was 3.19×10^{-3} (92.5 ksi / 29,000 ksi).

The peak strains experienced during each cycle corresponding to a specific ductility demand level are summarized in Figure C-20 through Figure C-25. The maximum or minimum normalized strains measured are plotted along the x-axis, while the y-axis denotes the location of the gage along the height of the column (the footing base corresponds to zero height). Positive and negative strain values correspond to tension and compression, respectively. Data adjustment was done for missing strain data at high ductility levels where strain gages have failed, specifically at the center of the plastic hinge zone. At those locations (indicated with a diamond marker), missing strain values were taken from previous cycles at lower ductility levels where data was available. Despite these irregularities, the results are still useful in showing strain profile experienced for low and high ductility levels, and the progression of peak strain values with increasing loading demands.

C.2.1 Normalized Strain History

Figure C-19 presents the normalized strain time history of specimen S1 test recorded for cycles corresponding to ductility levels 1 and 3 at the southern corner of the specimen (positive X-axis) at Elevation 1-S.

The results for the continuous longitudinal rebar, dowel, and spiral at that location display a fairly symmetrical linear response at a ductility level of 1 and an asymmetrical nonlinear response at a higher level of ductility demand of 3. The strain values corresponding to a ductility level of 1 (Figure C-19a) do not exceed the estimated yield strain values for the different reinforcement types, while for a ductility level of 3 (Figure C-19b), the recorded strain values at the base of the column significantly exceed the estimated yield values of the longitudinal reinforcement. At these two ductility levels the peak spiral strain does not exceed the estimated yield strain.

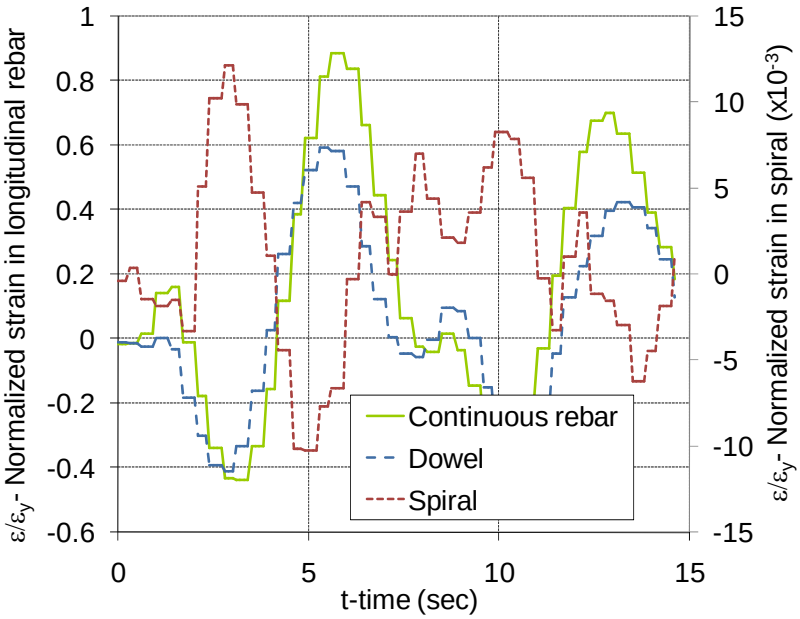

(a) Displacement ductility of 1 (with respect to BC yield point)

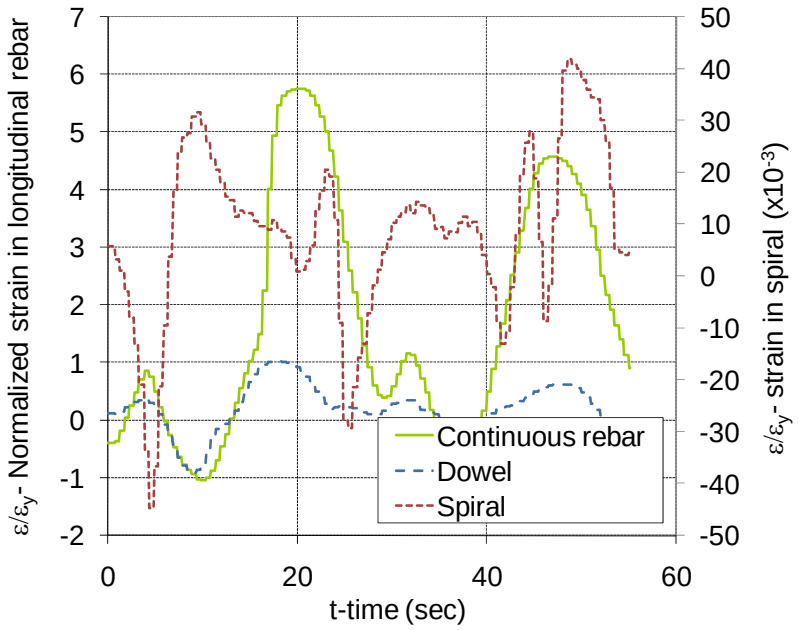

(b) Displacement ductility of 3 (with respect to BC yield point)

Figure C-19 Normalized strain time history of S1 specimen at Elevation 1-S, South corner at two ductility levels

C.2.2 Normalized Strain Profile in Continuous Longitudinal Rebar

The strain profiles of the continuous longitudinal steel of specimens S1 and S2 are presented in Figure C-20 and Figure C-21, respectively. The distribution of strain along the length of the four

instrumented continuous longitudinal rebar allows identifying the limit of elastic behavior of the column and the location of the plastic hinge zone at high ductility levels. For both specimens S1 and S2, the strain profiles of the continuous longitudinal rebar displayed a linear distribution only for cycles with a nominal ductility level of 1 or smaller. For higher ductility levels, linear strain distribution was only maintained from the column top up to an approximate height of 22” and 18” above the foundations, for specimens S1 and S2, respectively. The top portion of the column remained in the elastic range of response even for the higher ductility demand levels since the strain values recorded at these locations do not exceed the estimated yield strains and damage was not observed. Nonlinear distribution of strains was recorded in the base of the column.

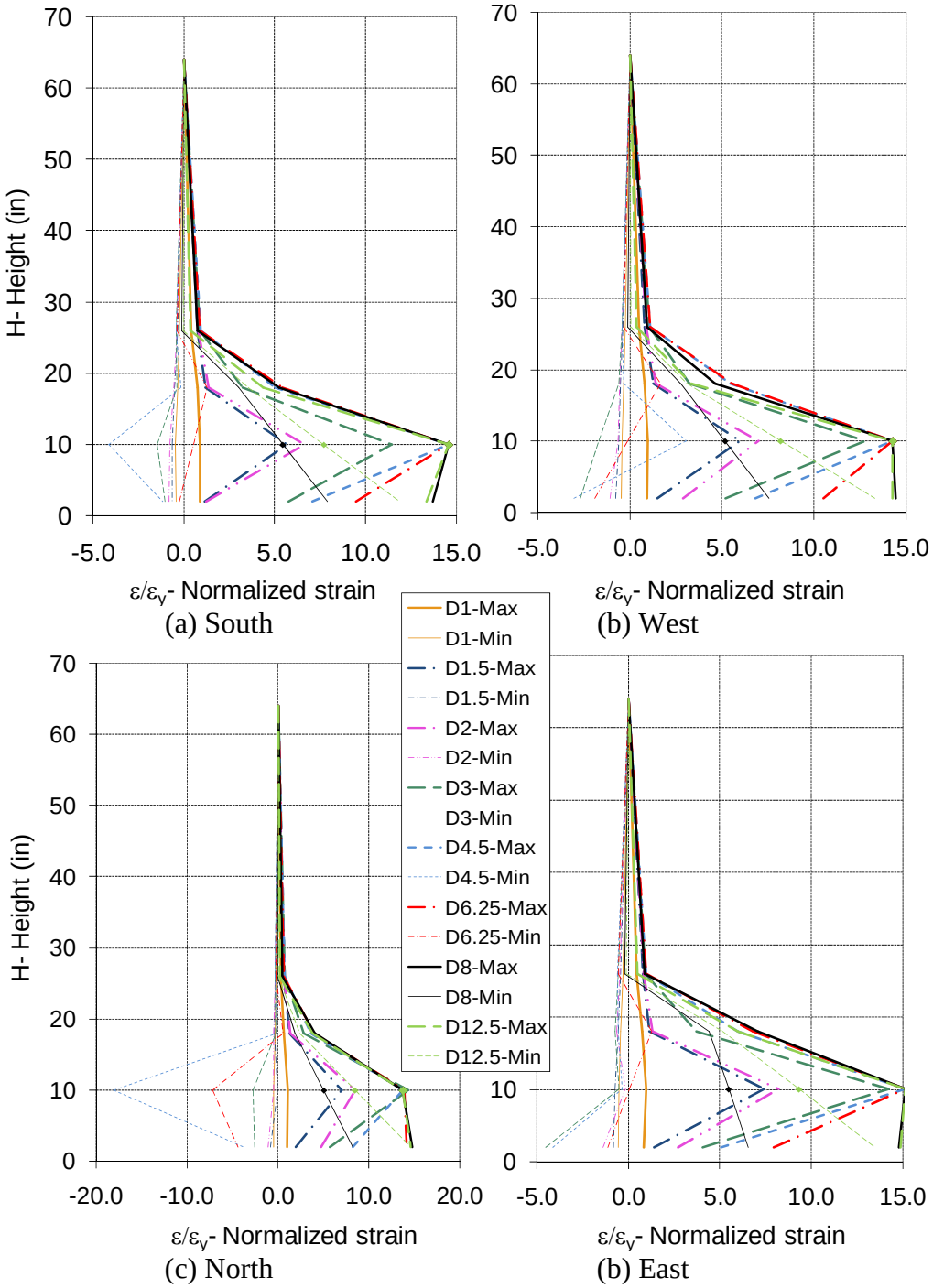

Figure C-20 Normalized strain profile of continuous longitudinal rebar in S1 specimen

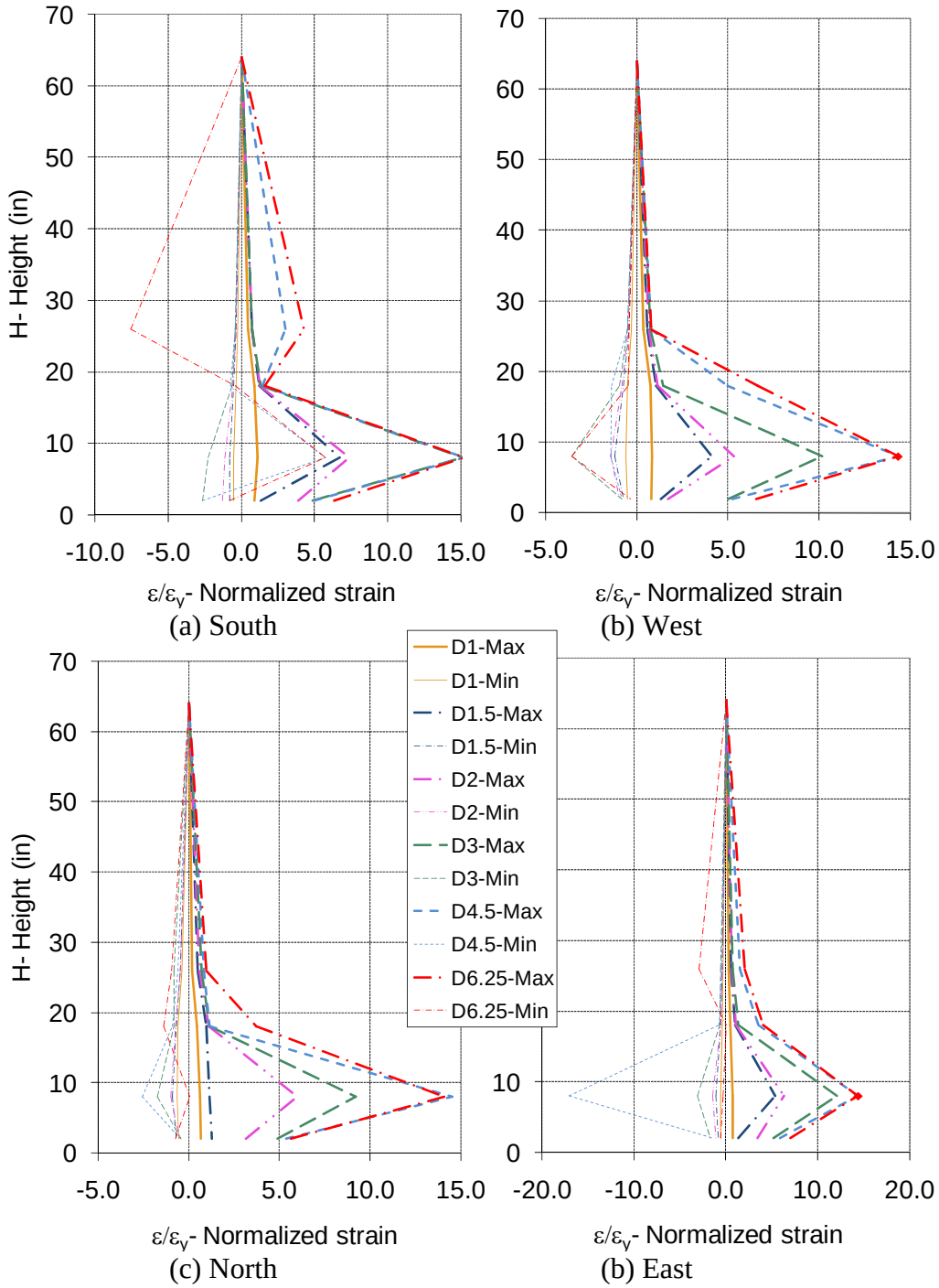

Figure C-21 Normalized strain profile of continuous longitudinal rebar in S2 specimen

For specimen S1, strains along longitudinal rebar exceeding the yield strain value extended from the base of the column up to an approximate height of 22". However, peak strains were concentrated from a height of approximately 2" to a height of 18", a total length of 16" which is equivalent to the diameter of the column (d_{col}), indicating the approximate length of the plastic hinge zone. The maximum strains in S1 column were obtained at an approximate height of 10" above the foundations, coinciding with the location of observed bar fracture.

In S2 specimen, peak strains extended from approximately 4” to 14” above the foundations, with a total plastic hinge length of roughly 10”. Maximum strains were recorded at 8” from the top of the footing, which also coincided with the location of rebar fracture of the continuous longitudinal rebar.

Bar buckling was identified in the column specimens mainly from the minimum strain values recorded in longitudinal bars and dowels. For S1 specimens, bar buckling was observed for the North and South longitudinal bars, as well as the West and North dowels at a reference ductility level of 4.5. The buckling of the East dowel in S1 specimen only occurred at a higher ductility level of 8. For this specimen, due to the crushing of the concrete cover and loss of confinement in the plastic hinge at a ductility level of 4.5, bar buckling occurred approximately at the center of the plastic hinge zone, as verified by the strain gage profile in Figure C-20 and Figure C-22.

For S2 specimen, the East longitudinal rebar buckled approximately at the center of the plastic hinge zone, while the South rebar buckled at an approximate height of 24”, both at a ductility level of 4.5. The short dowels in the S2 specimen did not present any bar buckling.

C.2.3 Dowel Normalized Strain Profile

The strain profile recorded for the dowels in S1 and S2 specimens are presented in Figure C-22 and Figure C-23, respectively. The strain distribution in tension and compression in the dowels can be easily observed for the South dowel in specimen S1, where bar buckling did not occur even for high ductility demands of the column. The maximum strain distribution of the dowel in tension displayed the effectiveness of the unbounded region located at the top 10” of the bar. The development length or positive strain values corresponding to tension in the dowel was primarily initiated at a height of 10” above the footing or at the bottom of the unbounded region, not at the end of the dowel. In compression, the strain distribution along the length of the dowel was close to linear, indicating that the unbounded region was mostly effective in tension.

Maximum tension and compression strain values at the bottom of the column were in the same order of magnitude for all ductility levels; however, for a particular cycle they were not completely comparable, possibly due to slip, crushing or de-bonding of the rebar. Similar observations were obtained for the remaining dowels in specimen S1, where bar buckling occurred in the West, East and North dowels at high ductility demands in an arbitrary direction and therefore strain values in either tension or compression are of a higher order of magnitude.

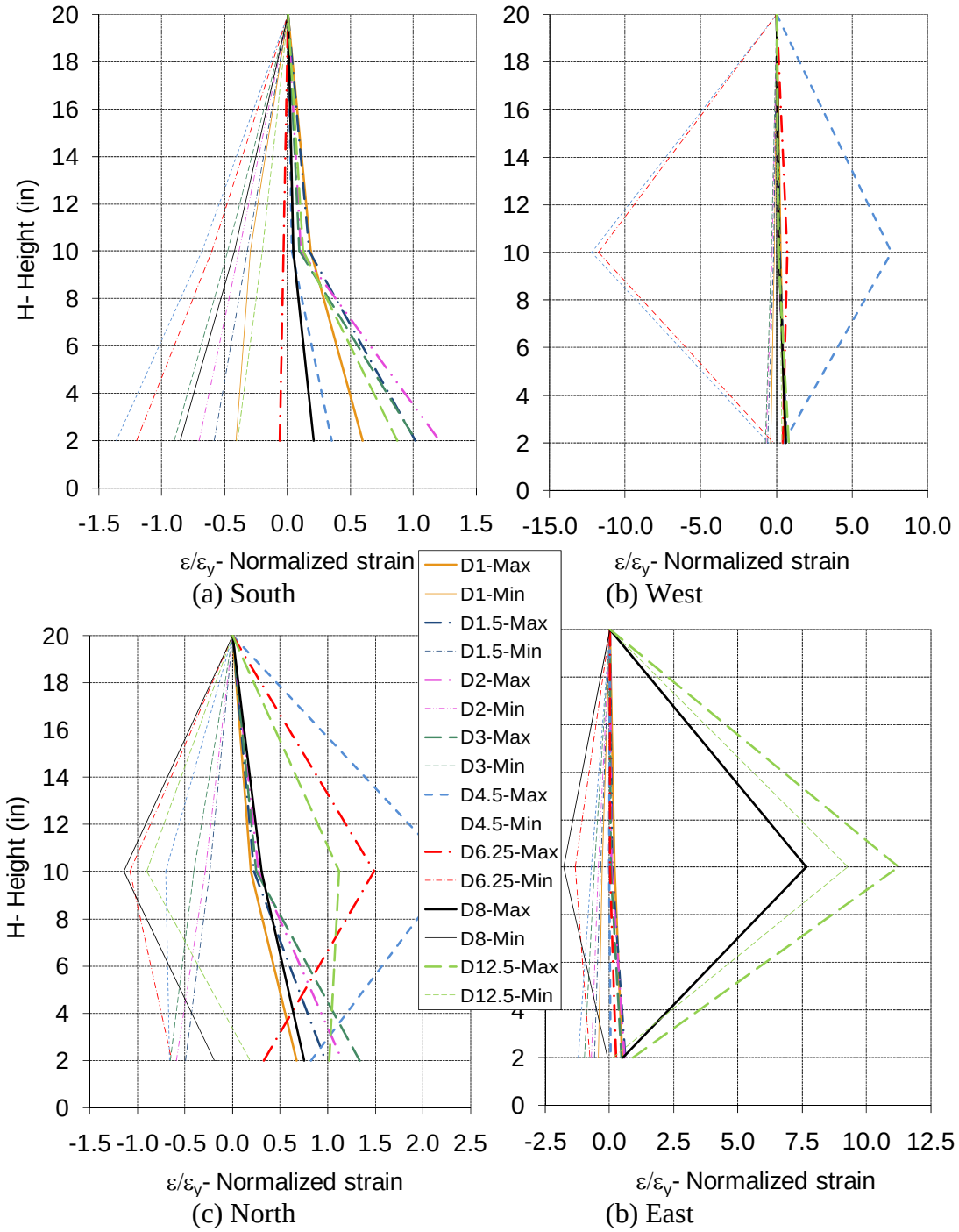

Figure C-22 Normalized strain profile of dowels in S1 specimen

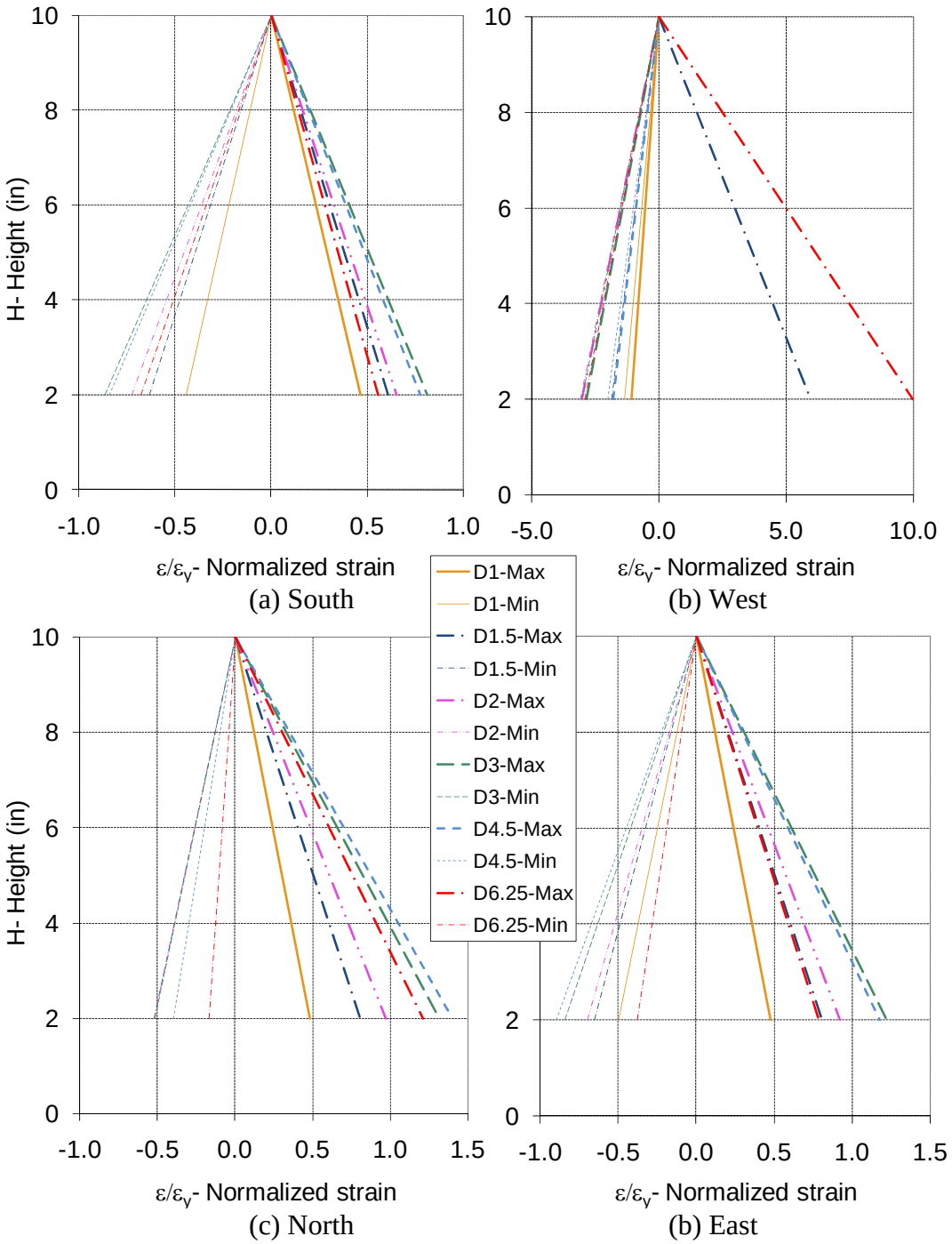

Figure C-23 Normalized strain profile for dowels in S2 specimen

In S2 specimen, the unbounded region in the plastic hinge zone was specified on the continuous longitudinal rebar, not the dowels. A linear distribution of strains was observed in both tension and compression, indicating no interruption in the development length of the dowel. The minimum and maximum strain values for a specific cycle or ductility level were of the same order of magnitude but not directly comparable, as in S1 specimen. Since the length of the

dowels above the footing in S2 specimen was only 10” long, the dowels in this column did not present any bar buckling in compression nor fracture in tension.

C.2.4 Spiral Normalized Strain Profile

The distribution of peak spiral strains along the height for the main cycles of each test is shown in Figure C-24 and Figure C-25 for specimens S1 and S2, respectively. The plots follow the same convention as for the longitudinal rebar. In these plots the average peak strain at each elevation was obtained using two methods: peak strain value of the average strain computed at each time step (Ave,Max) and the average of the peak strains computed along the entire time history (Max,Ave). The peak strain values in tension obtained from these two methods were comparable, displaying a similar strain distribution along the height of the column.

The peak spiral strains computed for the different ductility levels were not constant along the height of the plastic hinge zone for almost all cases in both column specimens, with higher peak strains computed at an elevation of 10” and 8” for specimens S1 and S2, respectively. For both specimens, peak strain values did not exceed the estimated spiral yield strains for ductility levels equal or smaller than 3. For higher ductility levels, strains exceeding yield values were computed, specifically at the center of the plastic hinge zone, with increasingly larger peak values at higher intensities. Spiral fracture occurred in one location in specimen S1 at a ductility level of 6.25, while for specimen S2 the spiral fractured during the cycle corresponding to a ductility level of 4.5 at two points in the column, one above and one below the end of the short 10”-dowel.

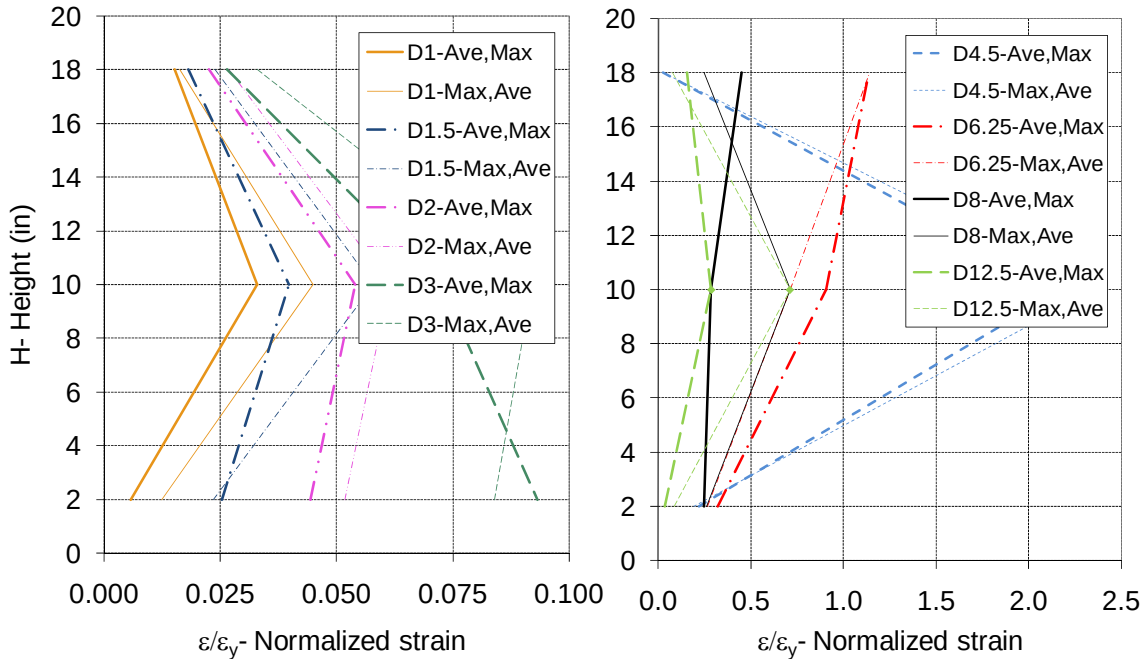

Figure C-24 Average spiral strain profile in S1 specimen

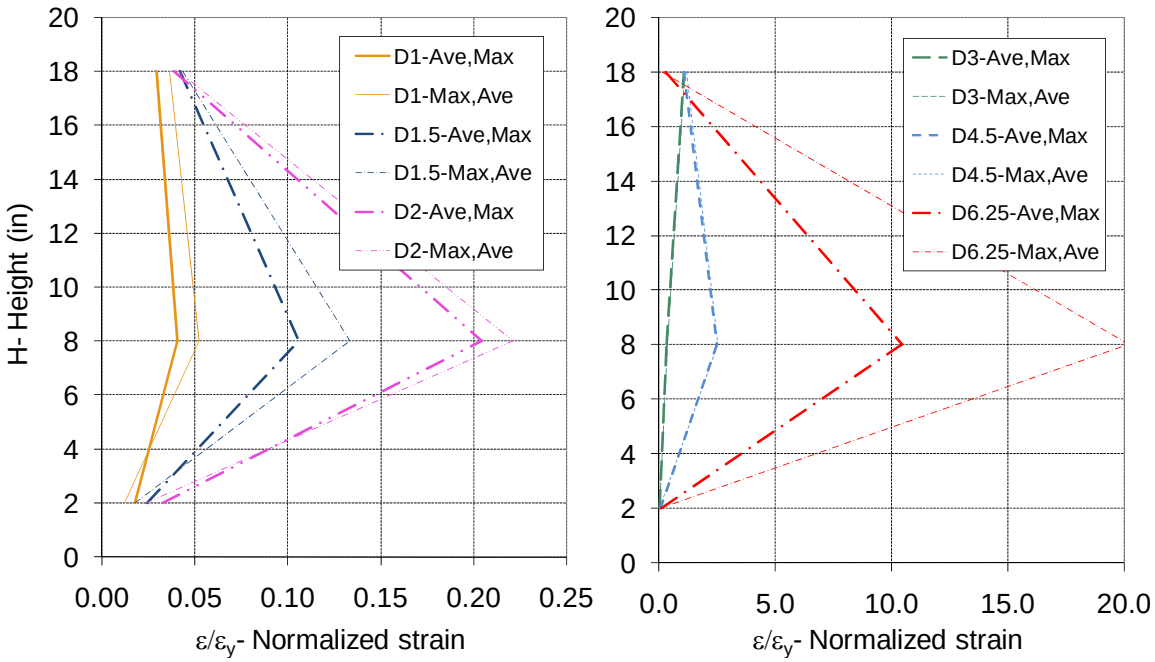

Figure C-25 Average spiral strain profile in S2 specimen

C.2.5 Correlation of Strain Measurements with Observed Damage

The conclusions derived from the strain profiles of the different steel reinforcement types were concurrent with the observed damage in the column presented in Figure C-26 and section C.1. In specimen S1 at least 8 continuous longitudinal bars buckled and all 12 fractured, while only 3 dowels fractured at an approximate height of 8-12" above the foundation. At the end of the dowels, at an approximate height of 20" above the footing, additional damage was observed starting at high ductility demands of 6.25, where a second plastic hinge zone began to develop. Spiral fracture only occurred in one location (as seen in Figure C-26) at an approximate height of 10". In specimen S2 all 12 longitudinal bars buckled and only 2 bars fractured. The short dowels suffered no buckling or fracture. The spiral fractured on the West side of the specimen at two different elevations: 8.5 and 11" above the foundations- one below and one above the end of the dowel.

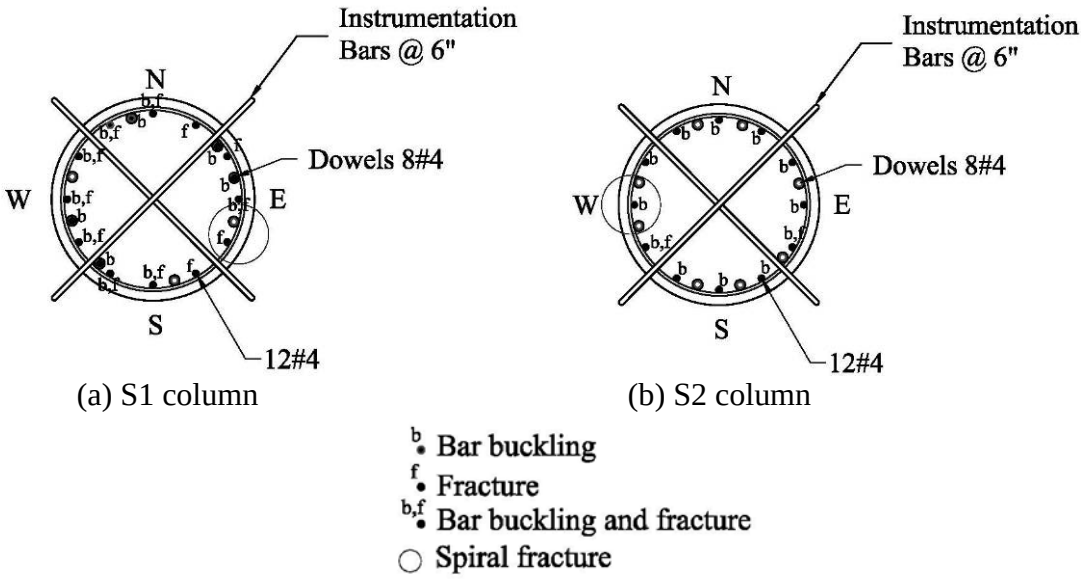

Figure C-26 Observed damage in specimens S1 and S2

C.3 ADDITIONAL RESPONSE MEASURES

C.3.1 Vertical Deformations

The vertical deformation of the column was estimated over several regions extending between the different locations of displacement potentiometers attached to the face of the column measuring relative displacements, as seen in the external instrumentation scheme in Chapter 2. The displacement potentiometers measuring vertical deformations were placed on three sides of the face of the column (Northwest, Southwest, and Southeast) at four elevations (Elevation D-1 through D-4). At each time step of the cyclic loading, a plane was fitted through the three displaced points instrumented at each level of the column. The vertical deformation on the Northeast side of the column at each elevation was then extrapolated for each time step using the fitted plane. The axial strains (ε_i) over the different regions were calculated as the average of the readings on all four sides divided by the height of the region equal to 6", as defined in Eq. C-1.

$$\varepsilon_i = \frac{(v_{NE} + v_{NW} + v_{SE} + v_{SW})_i}{4h_i} \qquad \text{[Eq. C-1]}$$

The total axial deformation of the column (v) was obtained by summing over the height of the column the average vertical deformation of each region (v_i, i=1,…,4), as defined in Eq. C-2.

$$v = \sum_{i=1}^{4} v_i = \sum_{i=1}^{4} (v_{NE} + v_{NW} + v_{SE} + v_{SW})_i / 4 \qquad \text{[Eq. C-2]}$$

Figure C-27 displays the vertical deformation time history of the four bottom sections of S1 column recorded for a ductility level of 1 (with respect to the BC yield point). For example, the vertical section deformation at Elevation 4-D represents the average vertical deformation readings on all four sides of the column obtained between Elevation 3-D and 4-D. Negative deformations correspond to the contraction of the column compared to its original position while positive readings indicate elongation of the column section.

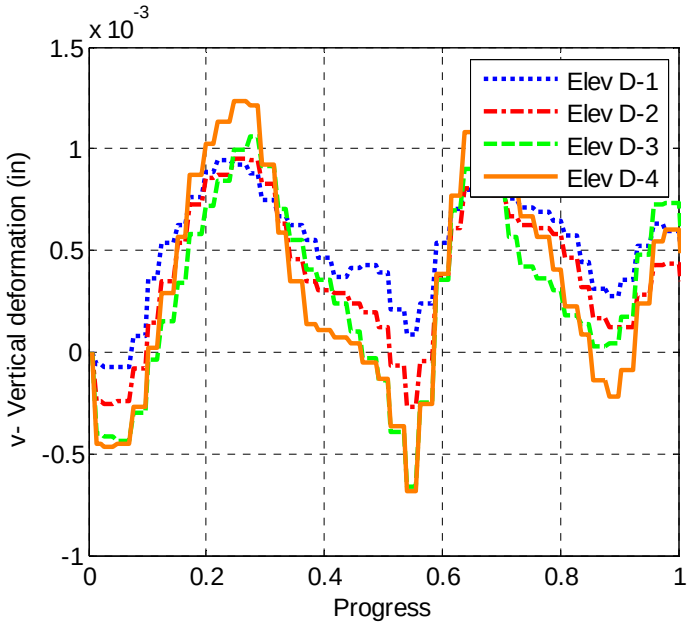

Figure C-27 Vertical section deformation time history of S1 column for ductility level of 1 (with respect to BC yield point)

The total vertical deformation time history of the FRC column presented in Figure C-28 was obtained by summing the four section deformations at each time step for each ductility level considered. The total vertical deformation at the column top was assumed to be equal to the one obtained at Elevation D-4.

During the first main cycles (up to a ductility level of 4.5) both FRC specimens experience minor elongation (positive vertical deformation) of the column due to the lengthening of the longitudinal steel in tension produced during the biaxial bending. It can be observed that during the second circular cycle of the S1 specimen at a ductility level of 6.25 where spiral fracture and buckling of the longitudinal reinforcing steel occurred, a significant shortening of the column was produced. During the following cycles at ductility levels of 8 and 12.5, the crushing of the concrete around the perimeter of the column produced during the repeated cyclic loading and the inability of the longitudinal steel to sustain compression, further shortening (negative vertical deformation) of the column was produced. At the end of the cyclic history the S1 column had contracted approximately 0.26” with respect to its original position. Specimen S2 did not experience such a severe shortening of the column since only two longitudinal bars had buckled and crushing of the perimeter concrete was not severe at a ductility level of 6.25. The resulting negative vertical deformation of S2 column at the end of the cyclic test was approximately 0.1”.

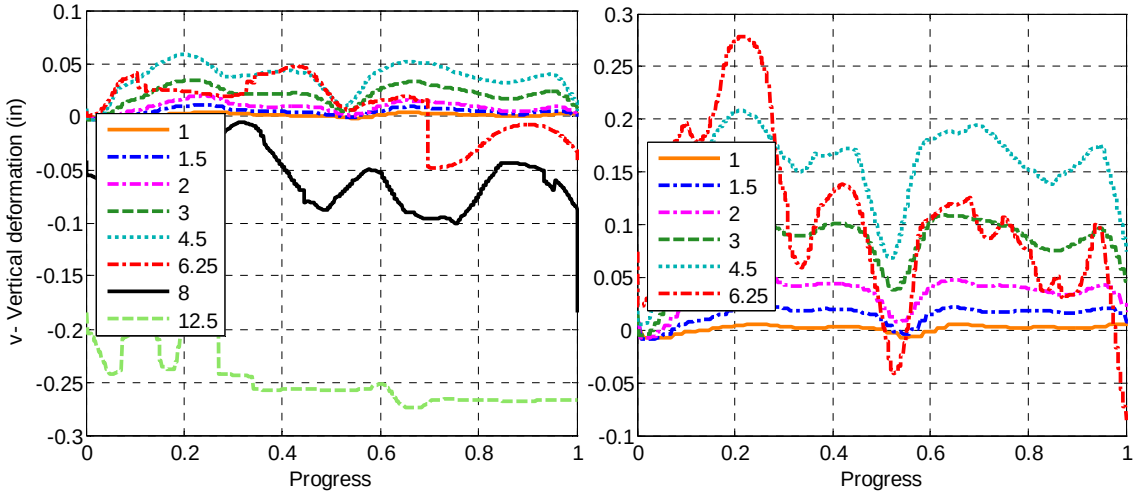

(a) S1 columns (b) S2 column

Figure C-28 Total vertical deformation time history of FRC columns for different ductility levels

Figure C-29 presents the axial strain time history of the two FRC columns obtained as the total vertical deformation at the column top divided by the column height of 64". According to the analysis of the gravity-load carrying capacity of the FRC columns presented in Chapter 3, the maximum axial compression strain of 11e-3 and 4e-3 measured for S1 and S2 columns, respectively, correspond to approximately 100% and a residual capacity of 50% of the maximum axial capacity of the columns.

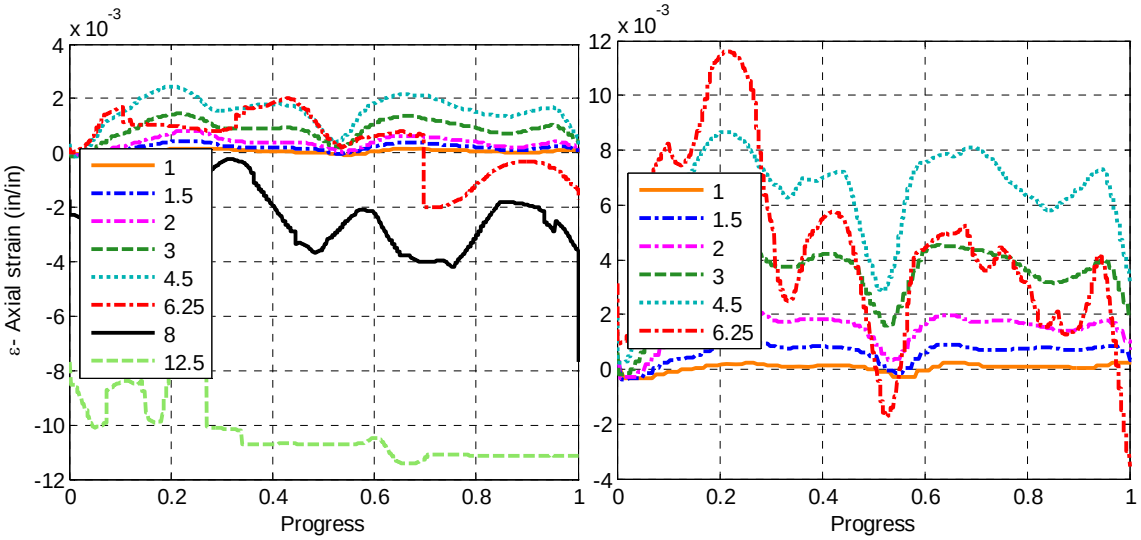

(a) S1 columns (b) S2 column

Figure C-29 Axial strain time history of FRC columns for different ductility levels

C.3.2 Shear Deformations

Shear deformations were estimated for the FRC columns using absolute and relative displacement measurements at the face of the column according to the external instrumentation scheme in Chapter 2. The total displacement profiles measured included the effects of shear, flexure, slip, and twist of the column specimens. The relative vertical deformation measurements allowed to obtain curvature and rotation readings. The shear distortion angles for each segment of the FRC were calculated by subtracting the estimates of flexural deformations obtained through curvature or rotation integration from the total measured displacement and dividing by the height of the corresponding segment. Since the twist of the column was controlled through the test setup but not monitored or instrumented directly during the cyclic test, the shear deformation profiles of the FRC columns presented in Figure C-30 also include the twist contribution to the measured lateral deformation. Additionally, the vertical deformation of the column at the location of external lateral displacement measurements were not monitored directly but extrapolated using the readings on the opposite sides of the column.

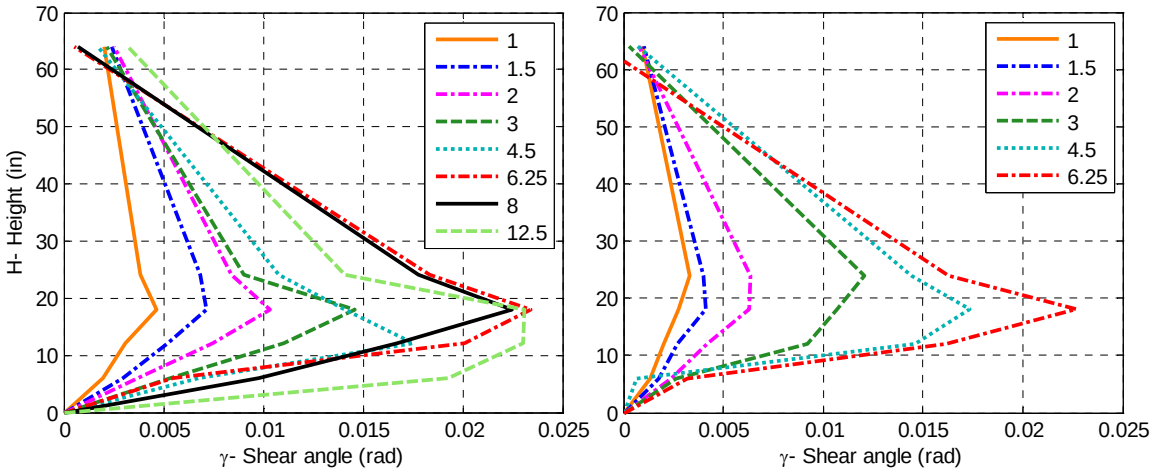

Figure C-30 Approximate shear deformation profile of FRC columns

The shear deformation profile obtained for the BC column by Terzic *et al.* (2008) is presented in Figure C-31. Clearly, the BC specimen, as well as the FRC columns presented negligible shear deformations and no sign of sliding failure.

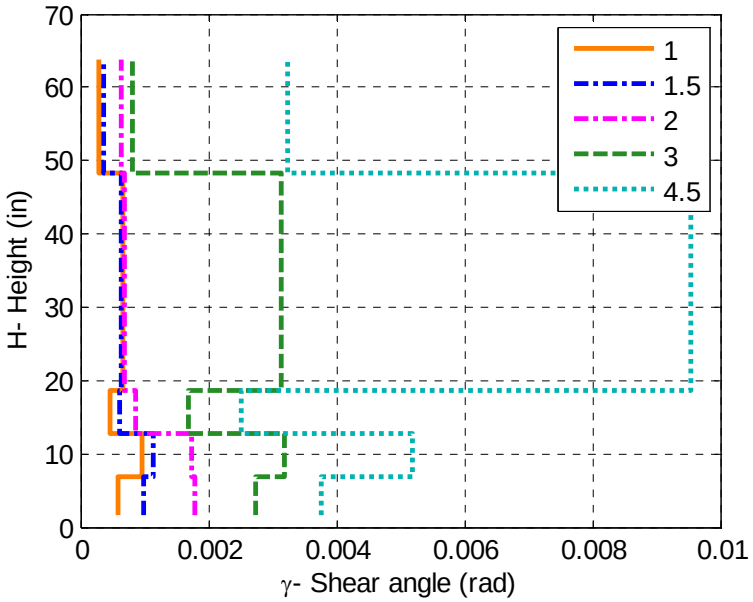

Figure C-31 Shear deformation profile of BC specimen

The degradation in shear resisting mechanisms of different FRC elements was evaluated in previous studies by comparing the shear stress versus plastic hinge shear distortion response, as well as analyzing the variations in the ratio between shear distortion and rotation in the plastic hinge region. These comparisons were found useful in the identification of safe shear stress and drift limits to control shear-related damage during earthquake-induced displacements (Parra and Chompreda, 2006). However, in the present study, the shear deformation measurements can be considered rough approximations since they include the contribution of column twist and were obtained indirectly using extrapolation of vertical deformations at the locations where lateral displacements were instrumented. Therefore, additional analysis using this data was not carried out.

Appendix D: Bridge Modeling Details

This appendix presents additional figures of the abutment details for the RC type 1A bridge representing a typical seat abutment configuration. The estimation of the ductility capacity and other basic response parameters of the RC bridge are also presented in this section.

The specific assumptions, values and design equations for the preliminary design of the isolated bridges according to SDC (Caltrans 2004) and AASHTO (1996, 1999) are presented in detail in this appendix. Bilinear behavior was defined for the lateral shear resistance of the lead rubber bearings, linear-elastic material behavior was used to define their axial, torsional and rotational stiffness, while the rotational and torsional stiffnesses were approximated following the recommendations by Kelly (1997).

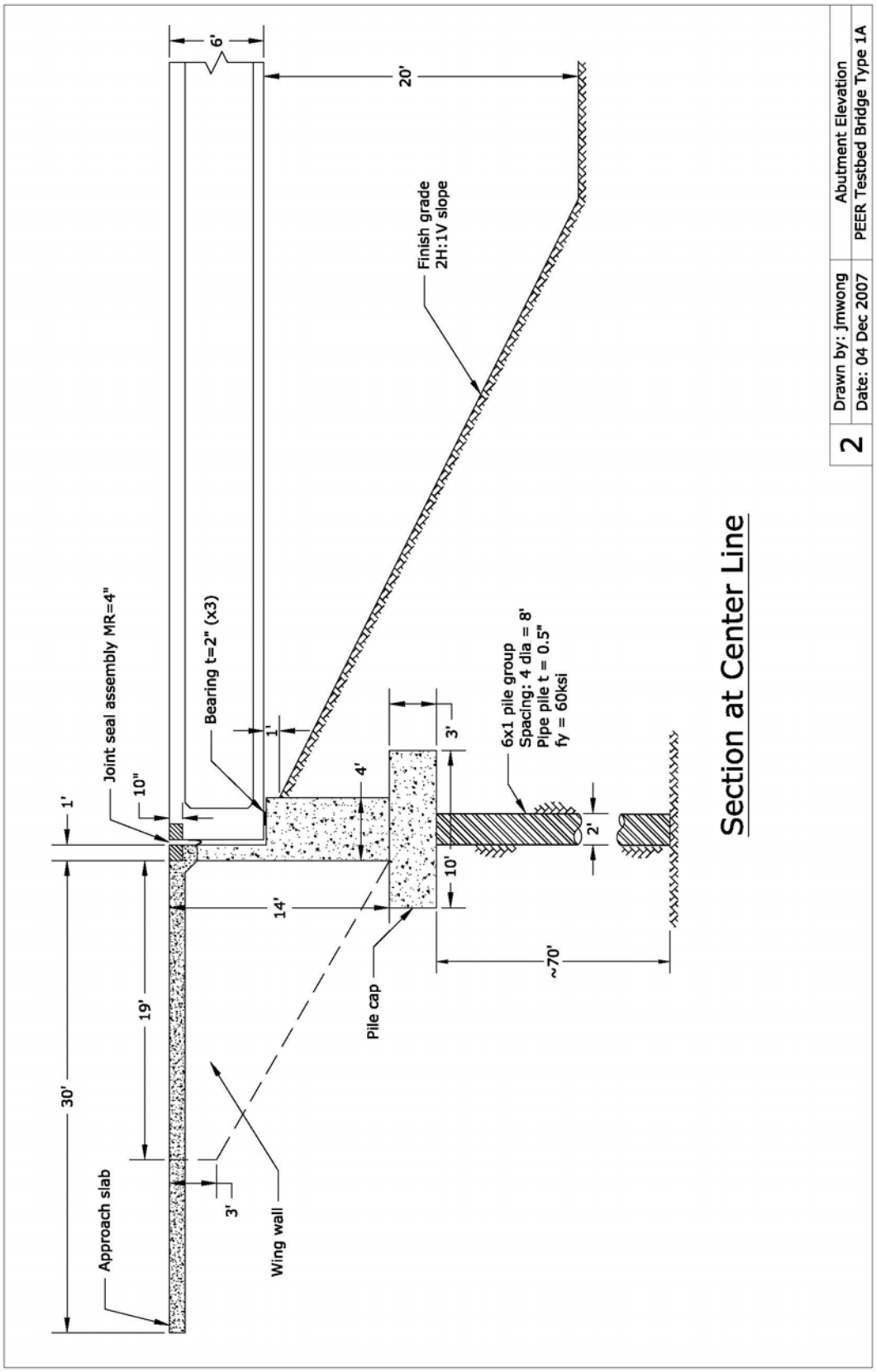

Figure D-1 Abutment section/elevation (Mackie *et al.* 2007)

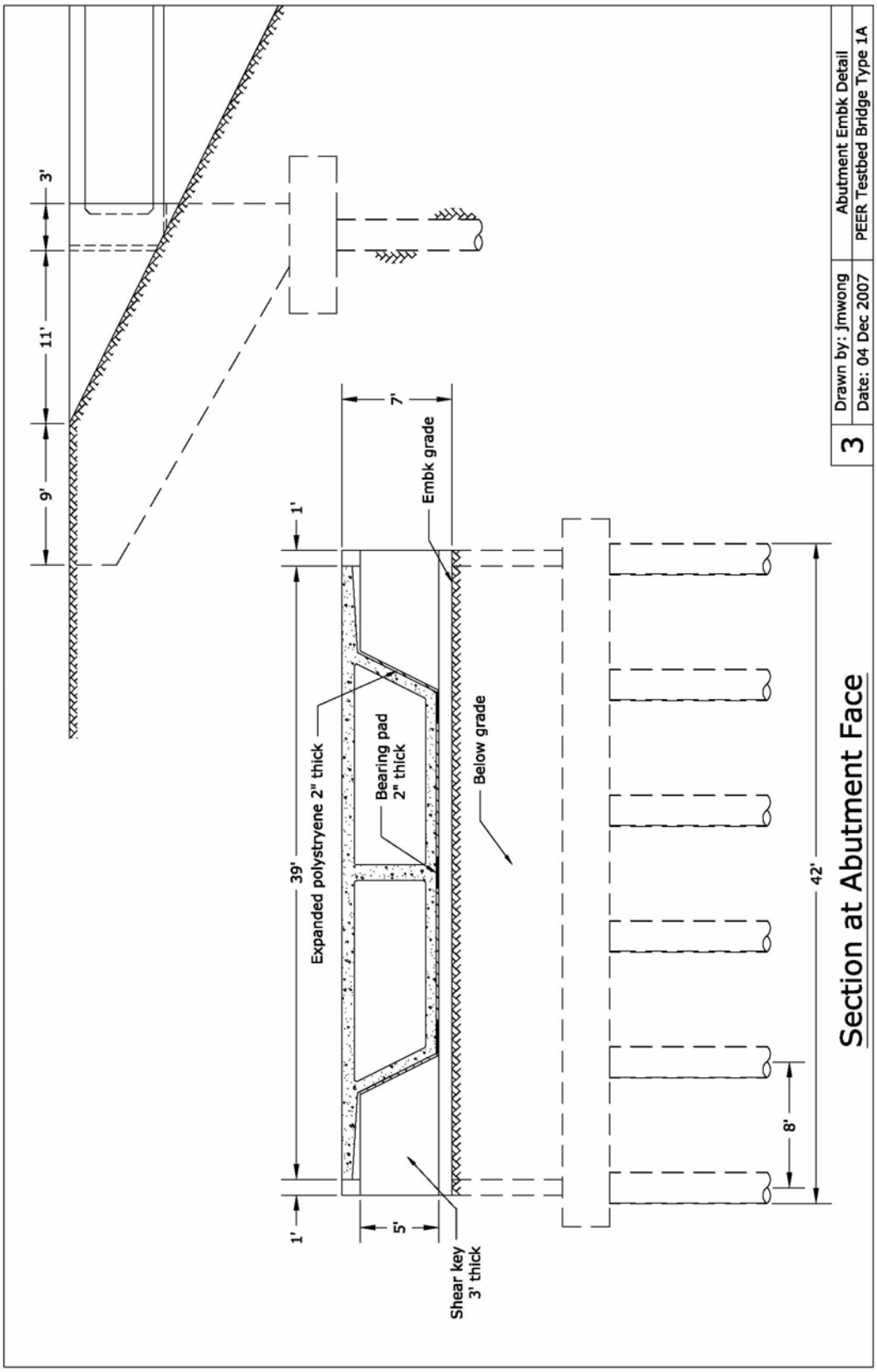

Figure D-2 Abutment embankment detail (Mackie *et al.* 2007)

Original RC bridge design – Page 1

1. ORIGINAL BRIDGE DESIGN

1.1 Gravity loads:

The relevent characteristics of the superstructure are as follows:

$A\_deck := 8869.0\ in2$ Superstructure (deck) area

$sw\_deck := 276\ in$ Width of superstructure bottom flange

$d\_deck := 72\ in$ Deck height

$Yb := 43.6\ in$ Height of superstructure's center of mass above column

$\rho\_RC := 150\ pcf$ Density of concrete deck

$L\_trib := 150\ ft$ Tributary length to each column

$WDL\_trib := 450\ kip$ Dead load on the deck, tributary to column

$$W\_trib := \left(\frac{\rho\_RC}{1000}\right)\cdot\left(\frac{A\_deck}{12^2}\right)\cdot L\_trib + WDL\_trib$$

$W\_trib = 1.836 \times 10^3\ kip$ Tributary weight to each column

1.2 Ductility capacity of column:

$Dcol\_orig := 4.0\cdot 12\ in$ $Acol\_orig := \frac{\pi\cdot Dcol\_orig^2}{4}$ $Hcol\_orig := 22\cdot 12 + Yb$ $Hcol\_orig = 307.6\ in$

Longitudinal reinforcement:

$\rho l\_orig := 0.02$ Longitudinal reinforcement between 0.01 and 0.03

$Nbars\_orig := 28$

$Abar\_l\_orig := 1.27\ in2$ $dbl\_orig := 1.27\ in$ Bars #10

$As\_orig := Nbars\_orig\cdot Abar\_l\_orig$

$$\rho l\_spec\_orig := \frac{As\_orig}{Acol\_orig} \qquad \rho l\_spec\_orig = 0.02$$

Transverse reinforcement:

$Ag\_orig := Acol\_orig$ $cover := 1.5\ in$ $fc := 4\ ksi$ $fy := 60\ ksi$ $fye := 68\ ksi$

$Dconf\_orig := Dcol\_orig - 2\cdot cover$ $Ac\_orig := \frac{\pi Dconf\_orig^2}{4}$ $Pe := W\_trib$

Minimum reinforcement:

$$\rho s1\_orig := 0.45\cdot\left[\left(\frac{Ag\_orig}{Ac\_orig}\right) - 1\right]\cdot\left(\frac{fc}{fy}\right)$$ BDS eq. 8-62

$$\rho s2\_orig := 0.12\cdot\left(\frac{fc}{fy}\right)\cdot\left(0.5 + \frac{1.25\cdot Pe}{fc\cdot Ag\_orig}\right)$$ BDS eq. 8-62B for columns with Dcol>3'

$\rho s\_orig := \max(\rho s1\_orig, \rho s2\_orig)$ $\rho s\_orig = 6.536 \times 10^{-3}$

$smin := 3.5\ in$ $s\_spec\_orig := 3.5\ in$ $Abar\_v\_orig := 0.6\ in2$ Bars #7

$$\rho s\_spec\_orig := \frac{\pi\cdot Dconf\_orig\cdot Abar\_v\_orig}{Ac\_orig\cdot s\_spec\_orig} \qquad \rho s\_spec\_orig = 0.015$$

Original RC bridge design – Page 2

Moment - curvature analysis results:

$\phi y\_orig := 1.3 \times 10^{-4}$ $\phi u\_orig := 0.001375$ $\phi p\_orig := \phi u\_orig - \phi y\_orig$ $\phi p\_orig = 1.245 \times 10^{-3}$

Cantilever behavior (transverse direction):

$Lp\_orig\_T := \max(0.08 \cdot Hcol\_orig + 0.15 \cdot fye \cdot dbl\_orig, 0.3 \cdot fye \cdot dbl\_orig)$ $Lp\_orig\_T = 37.562$ in

$\Delta y\_orig\_T := \phi y\_orig \cdot \frac{Hcol\_orig^2}{3}$ $\Delta y\_orig\_T = 4.1$ in $\Delta p\_orig\_T := \phi p\_orig \cdot Lp\_orig\_T \cdot \left(Hcol\_orig - \frac{Lp\_orig\_T}{2}\right)$

$\Delta p\_orig\_T = 13.507$ in $\Delta u\_orig\_T := \Delta y\_orig\_T + \Delta p\_orig\_T$ $\Delta u\_orig\_T = 17.607$ in

$\mu c\_orig\_T := \frac{\Delta u\_orig\_T}{\Delta y\_orig\_T}$ $\mu c\_orig\_T = 4.294$

Column behavior in double curvature (fixed-fixed) (longitudinal direction):

$Lp\_orig\_L := \max\left(0.08 \cdot \frac{Hcol\_orig - Yb}{2} + 0.15 \cdot fye \cdot dbl\_orig, 0.3 \cdot fye \cdot dbl\_orig\right)$ $Lp\_orig\_L = 25.908$ in

$\Delta y\_orig\_L := 2 \cdot \phi y\_orig \cdot \frac{\left(\frac{Hcol\_orig - Yb}{2}\right)^2}{3}$ $\Delta y\_orig\_L = 1.51$ in

$\Delta p\_orig\_L := 2 \cdot \phi p\_orig \cdot Lp\_orig\_L \cdot \left(\frac{Hcol\_orig - Yb}{2} - \frac{Lp\_orig\_L}{2}\right)$ $\Delta p\_orig\_L = 7.68$ in

$\Delta u\_orig\_L := \Delta y\_orig\_L + \Delta p\_orig\_L$ $\Delta u\_orig\_L = 9.19$ in

$\mu c\_orig\_L := \frac{\Delta u\_orig\_L}{\Delta y\_orig\_L}$ $\mu c\_orig\_L = 6.086$

1.3 Seismic Demand:

Transverse direction:

$Sa\_original\_T := 0.99$

$T\_T := 1.30$ sec

$PGA\_Mw65\_T := 1.0$

$PGA\_Mw725\_T := 0.70$

$PGA\_Mw8\_T := 0.67$

Longitudinal direction:

$Sa\_original\_L := 1.07$

$T\_L := 1.04$ sec

$PGA\_Mw65\_L := 0.93$

$PGA\_Mw725\_L := 0.60$

$PGA\_Mw8\_L := 0.56$

BI1 bridge design (isolated bridge with elastic column response) – Page 1

2. ISOLATED BRIDGE DESIGN- ELASTIC COLUMN

2.1 Preliminary design of RC column:

$Dcol := 4 \cdot 12$ in $\quad Acol := \frac{\pi \cdot Dcol^2}{4}$

$H\_est := 20$ in — Estimated height of isolators

$Hcol\_mod := Hcol\_orig - Yb - H\_est$ — $Hcol\_mod = 244$ in

Longitudinal reinforcement:

$\rho l := 0.03$ — Longitudinal reinforcement between 0.01 and 0.03

$Nbars := 34$

$Abar\_l := 1.56$ in2 $\quad dbl := 1.41$ in — Bars #11

$As := Nbars \cdot Abar\_l$

$\rho l\_spec := \frac{As}{Acol}$ $\quad \rho l\_spec = 0.029$

Transverse reinforcement:

$Ag := Acol$ $\quad cover = 1.5$ in $\quad fc = 4$ ksi $\quad fy = 60$ ksi $\quad fye = 68$ ksi

$Dconf := Dcol - 2 \cdot cover$ $\quad Ac := \frac{\pi Dconf^2}{4}$ $\quad Pe = 1.836 \times 10^3$

Minimum reinforcement:

$\rho s1 := 0.45 \cdot \left[\left(\frac{Ag}{Ac}\right) - 1\right] \cdot \left(\frac{fc}{fy}\right)$ — BDS eq. 8-62

$\rho s2 := 0.12 \cdot \left(\frac{fc}{fy}\right) \cdot \left(0.5 + \frac{1.25 \cdot Pe}{fc \cdot Ag}\right)$ — BDS eq. 8-62B for columns with Dcol>3'

$\rho s := \max(\rho s1, \rho s2)$ $\quad \rho s = 6.536 \times 10^{-3}$

$smin = 3.5$ in $\quad s\_spec := 3.5$ in $\quad Abar\_v := 0.6$ in2 — Bars #7

$\rho s\_spec := \frac{\pi \cdot Dconf \cdot Abar\_v}{Ac \cdot s\_spec}$ $\quad \rho s\_spec = 0.015$

BI1 bridge design (isolated bridge with elastic column response) – Page 2

Moment-curvature analysis:

$\phi y := 1.72 \times 10^{-4}$ $\phi u := 0.00129$

$\phi p := \phi u - \phi y$ $\phi p = 1.118 \times 10^{-3}$

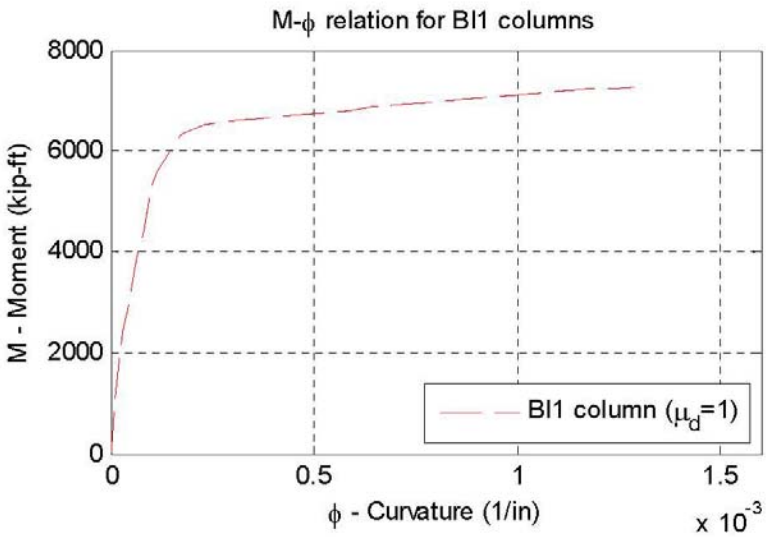

Cantilever behavior (transverse direction):

$Lp\_T := \max(0.08 \cdot Hcol\_mod + 0.15 \cdot fye \cdot dbl, 0.3 \cdot fye \cdot dbl)$ $Lp\_T = 33.902$ in

$\Delta y\_T := \phi y \cdot \frac{Hcol\_mod^2}{3}$ $\Delta y\_T = 3.413$ in $\Delta p\_T := \phi p \cdot Lp\_T \cdot \left(Hcol\_mod - \frac{Lp\_T}{2}\right)$ $\Delta p\_T = 8.606$ in

$\Delta u\_T := \Delta y\_T + \Delta p\_T$ $\Delta u\_T = 12.019$ in $\mu c\_T := \frac{\Delta u\_T}{\Delta y\_T}$ $\mu c\_T = 3.521$ Displacement ductility capacity

$\mu d\_des := 1$ Design goal: ductility demand on column limited to 2.0

$\Delta u\_des\_T := \mu d\_des \cdot \Delta y\_T$

$\Delta u\_des\_T = 3.413$ in Maximum desired displacement demand on column

Column behavior in double curvature (fixed-fixed) (longitudinal direction):

$dcap\_est := 3 \cdot 12$ in Estimated height of cap bent supporting the bearings

$Lp\_L := \max\left(0.08 \cdot \frac{Hcol\_mod - dcap\_est}{2} + 0.15 \cdot fye \cdot dbl, 0.3 \cdot fye \cdot dbl\right)$ $Lp\_L = 28.764$ in

$\Delta y\_L := 2 \cdot \phi y \cdot \frac{\left(\frac{Hcol\_mod - dcap\_est}{2}\right)^2}{3}$ $\Delta y\_L = 1.24$ in

$\Delta p\_L := 2 \cdot \phi p \cdot Lp\_L \cdot \left[\left(\frac{Hcol\_mod - dcap\_est}{2}\right) - \frac{Lp\_L}{2}\right]$ $\Delta p\_L = 5.764$ in

$\Delta u\_L := \Delta y\_L + \Delta p\_L$ $\Delta u\_L = 7.004$ $\mu c\_L := \frac{\Delta u\_L}{\Delta y\_L}$ $\mu c\_L = 5.647$ Displacement ductility capacity

$\mu d\_des = 1$ Design goal: ductility demand on column limited to 2.0

$\Delta u\_des\_L := \mu d\_des \cdot \Delta y\_L$

$\Delta u\_des\_L = 1.24$ in Maximum desired displacement demand on column

BI1 bridge design (isolated bridge with elastic column response) – Page 3

2.2 Seismic demand on isolated bridge:

$T\_target := 3.0\ sec$ Target period of the isolated bridge

$\omega\_target := \frac{2\cdot(\pi)}{T\_target}$ $g := 386.4\ in/sec^2$

From the SDC 1.3 (2004) ARS curves for Soil type D we obtain the spectral values corresponding to the target period for each earthquake magnitude (Mw=6.5,7.25,8.0):

Transverse direction:

$Sa\_65\_T := 0.30$

$Sa\_725\_T := 0.35$

$Sa\_8\_T := 0.40$

$Sd\_65\_T := \frac{Sa\_65\_T\cdot g}{\omega\_target^2}$ $Sd\_65\_T = 26.427$

$Sd\_725\_T := \frac{Sa\_725\_T\cdot g}{\omega\_target^2}$ $Sd\_725\_T = 30.831$

$Sd\_8\_T := \frac{Sa\_8\_T\cdot g}{\omega\_target^2}$ $Sd\_8\_T = 35.235$

$Sd\_target\_T := \max(Sd\_65\_T, Sd\_725\_T, Sd\_8\_T)$

$Sd\_target\_T = 35.235$

Longitudinal direction:

$Sa\_65\_L := 0.25$

$Sa\_725\_L := 0.225$

$Sa\_8\_L := 0.30$

$Sd\_65\_L := \frac{Sa\_65\_L\cdot g}{\omega\_target^2}$ $Sd\_65\_L = 22.022$

$Sd\_725\_L := \frac{Sa\_725\_L\cdot g}{\omega\_target^2}$ $Sd\_725\_L = 19.82$

$Sd\_8\_L := \frac{Sa\_8\_L\cdot g}{\omega\_target^2}$ $Sd\_8\_L = 26.427$

$Sd\_target\_L := \max(Sd\_65\_L, Sd\_725\_L, Sd\_8\_L)$

$Sd\_target\_L = 26.427$

$\beta\_target := 0.20$ Target damping in the isolated bridge (bearings and substructure)

$H\_\beta := \left(\frac{1.5}{40\cdot\beta\_target + 1}\right) + 0.5$ $H\_\beta = 0.667$ Reduction factor in spectral values obtained using a 5% damping elastic spectrum.

The total estimated displacement demand on isolated bridge in the transverse and longitudinal directions are:

$Sd\_est\_T := H\_\beta\cdot Sd\_target\_T$ $Sd\_est\_T = 23.49$ in

$Sd\_est\_L := H\_\beta\cdot Sd\_target\_L$ $Sd\_est\_L = 17.618$ in

Estimated displacement demand on isolation bearings

$di\_T := Sd\_est\_T - \Delta u\_des\_T$ $di\_T = 20.077$ in $\Gamma i\_T := \frac{di\_T}{Sd\_est\_T}$ $\Gamma i\_T = 0.855$

$di\_L := Sd\_est\_L - \Delta u\_des\_L$ $di\_L = 16.377$ in $\Gamma i\_L := \frac{di\_L}{Sd\_est\_L}$ $\Gamma i\_L = 0.93$

BI1 bridge design (isolated bridge with elastic column response) – Page 4

2.3 Preliminary design of isolation bearings:

We select lead rubber bearings (LRB) for the isolation of the superstructure. From the DIS (Dynamic Isolation Systems) manual we select a LRB with the following properties (the criteria for the selection of the bearing is: di<Di/2):

$Dmax := 26\ in$	Maximum displacement (DIS)
$Di := 39.5\ in$	Isolator diameter (DIS)
$Ai := \frac{\pi \cdot Di^2}{4}$ $Ai = 1.225 \times 10^3\ in2$	Isolator bearing area
$Bi := \sqrt{Ai}$ $Bi = 35.006\ in$	Equivalent dimension of square isolator
$kd := 10$ kip / in	Yielded stiffness (DIS) affected primarily by rubber properties
$Kv := 11000$ kip / in	Compression stiffness (DIS)
$Pmax := 1700\ kip$	Axial load capacity (DIS)
$\sigma max := \frac{Pmax \cdot 1000}{Ai}$ $\sigma max = 1.387 \times 10^3\ ksi$	Maximum allowable bearing stress
$H := 20\ in$	Isolator total height (DIS)
$t := 1.75\ in$	End plates thickness (DIS)
$L := 41.5$	Isolator total length (DIS)
$tr := (H - 2 \cdot t) \cdot 0.85$ $tr = 14.025\ in$	Approximated total rubber thickness

Plug design:

$DL := 10\ in$ $AL := \pi \cdot \frac{DL^2}{4}$	Lead diameter and area
$\tau y := 1.20\ ksi$	Shear yield stress of lead
$Qd := AL \cdot \tau y$ $Qd = 94.248\ kip$	Characteristic strength influenced primarily by lead core
$ke := 10 \cdot kd$	Elastic stiffness for analytical bilinear model of bearing
$dy := \frac{Qd}{ke - kd}$ $dy = 1.047\ in$	Yield displacement for analytical bilinear model of bearing
$Fy := ke \cdot dy$ $Fy = 104.72\ kip$	Yield strength for analytical bilinear model of bearing

The number of isolation bearings is determined according to superstructure dead load. The maximum bearing capacity (Pmax) and compressive stress (σmax) of the isolators is checked.

$ni := 2$	Number of isolators for each column
$Wi := \frac{W\_trib}{ni}$ $Wi = 917.891\ kip$	Axial load on each bearing
$\sigma i := \frac{Wi \cdot (1000)}{Ai}$ $\sigma i = 749.043\ psi$	Compressive stress on each bearing

Since Wi<Pmax and σi<σmax, the selected type and number of isolation bearings is acceptable.

BI1 bridge design (isolated bridge with elastic column response) – Page 5

Buckling load (circular ~ square bearing pad):

$G := 75 \quad psi$ — Typical value for rubber shear modulus (available from 55-100 psi from DSI)

$Sc := \frac{\frac{Di}{2}}{2tr}$ — Shape factor for circular bearing pad

$Pcrit := \sqrt{2}\cdot\pi\cdot G\cdot Ai\cdot Sc\cdot\left(\frac{\frac{Di}{2}}{tr}\right) \qquad Pcrit = 4.049\times 10^{}\,kip$ — Critical buckling load

$p := \frac{Wi}{Pcrit} \qquad p = 2.267\times 10^{-3}$ — Ratio of axial load. If p>0.3 then horizontal stiffness changes: Kh~Kho(1-p2)

Rotational stiffness:

$S := \sqrt{\frac{\left(\frac{Bi}{2}\right)^2}{tr^2}}$ — Shape factor for strip or rectangular bearing pad

$Ec := 4\cdot G\cdot S^2 \qquad Ec = 467.24\ psi$ — Compression modulus

$I := \frac{Bi\cdot Bi^3}{12} \quad (in4)$ — Moment of inertia of square bearing pad

$EIeff := \frac{Ec\cdot I}{5\cdot 1000} \quad (kip - in2)$ — Effective EI for strip or rectangular bearing pad

$k\theta := \frac{EIeff}{tr} \quad k\theta = 833.784$ (kip - in)/rad — Rotational stiffness of bearing pad

Torsional stiffness:

$Ji := \left(\frac{Bi^4}{6}\right)$ — Polar moment of inertia of square isolation bearing

$GJ := Ji\cdot\frac{G}{1000} \quad GJ = 1.877\times 10^4$ kip-in2/rad — Torsional stiffness

BI1 bridge design (isolated bridge with elastic column response) – Page 6

3. UNIFORM LOAD METHOD (AASHTO Section 7.1):

Weights of column and cap bent:

$D\_col\_T := 4 \cdot 12 \quad in \quad Ig\_col\_T := \frac{\pi \cdot D\_col\_T^4}{64} \quad Ieff\_col\_T := 0.7 Ig\_col\_T$

$D\_col\_L := 4 \cdot 12 \quad in \quad Ig\_col\_L := \frac{\pi \cdot D\_col\_L^4}{64} \quad Ieff\_col\_L := 0.7 Ig\_col\_L$

$A\_col := \frac{\pi \cdot D\_col\_T \cdot D\_col\_L}{4} \qquad Wcol\_mod := \frac{\rho\_RC}{1000} \cdot \frac{A\_col}{12^2} \cdot \left(\frac{Hcol\_mod}{12} \right) \qquad Wcol\_mod = 38.327 \quad kip$

Bent cap: original and isolated bridges

$Acap\_orig := (6 \cdot 5) \cdot 12^2 \quad in2 \qquad Lcap\_orig := sw\_deck \qquad Lcap\_orig = 276 \quad in$

$Wcap\_orig := \left(\frac{\rho\_RC}{1000} \right) \cdot \left(\frac{Acap\_orig}{12^2} \right) \cdot \left(\frac{Lcap\_orig}{12} \right)$

$Wcap\_orig = 103.5 \quad kip$

$Acap\_mod := (3 \cdot 4) \cdot 12^2 \quad in2 \qquad Lcap\_mod := Dcol + 3 \cdot L \qquad Lcap\_mod = 172.5 \, in$

$Wcap\_mod := \left(\frac{\rho\_RC}{1000} \right) \cdot \left(\frac{Acap\_mod}{12^2} \right) \cdot \left(\frac{Lcap\_mod}{12} \right)$

$Wcap\_mod = 25.875 \quad kip$

Stiffness of isolated structure:

Stiffness of new substructure, assuming cantilever and fixed-fixed behavior for the transverse and longitudinal directions of the bridge, respectively.

$fc = 4 \quad ksi \qquad Ec := 33 \cdot \rho\_RC^{1.5} \cdot \frac{\sqrt{fc \cdot 1000}}{1000}$

$k\_sub\_T := 3 \cdot Ec \cdot \frac{Ieff\_col\_T}{Hcol\_mod^3} \qquad f\_sub\_T := k\_sub\_T^{-1}$

$k\_sub\_L := 12 \cdot Ec \cdot \frac{Ieff\_col\_L}{(Hcol\_mod - dcap\_est)^3} \qquad f\_sub\_L := k\_sub\_L^{-1}$

Isolator stiffness:

$di\_T = 20.077 \quad in \qquad Qi\_T := Qd + di\_T \cdot kd \qquad keffi\_T := \frac{Qi\_T}{di\_T} \qquad keff\_T := ni \cdot keffi\_T \qquad feff\_T := keff\_T^{-1}$

$di\_L = 16.377 \quad in \qquad Qi\_L := Qd + di\_L \cdot kd \qquad keffi\_L := \frac{Qi\_L}{di\_L} \qquad keff\_L := ni \cdot keffi\_L \qquad feff\_L := keff\_L^{-1}$

Effective stiffness of the substructure-isolators series system, calculated for the entire bridge:

$Keff\_T := \frac{k\_sub\_T \cdot keff\_T}{k\_sub\_T + keff\_T} \qquad Feff\_T := Keff\_T^{-1} \qquad Keff\_L := \frac{k\_sub\_L \cdot keff\_L}{k\_sub\_L + keff\_L} \qquad Feff\_L := Keff\_L^{-1}$

$Keff\_T\_tot := 4 \cdot Keff\_T \qquad Keff\_L\_tot := 4 \cdot Keff\_L$

BI1 bridge design (isolated bridge with elastic column response) – Page 7

Weight of bridge:

$Ltot := 3 \cdot 150 + 2 \cdot 120 \quad ft$

$WDL\_tot := WDL\_trib \cdot \frac{Ltot}{L\_trib}$

$Wtot := \left(\frac{\rho\_RC}{1000}\right) \cdot \left(\frac{A\_deck}{12^2}\right) \cdot Ltot + WDL\_tot + 4 \cdot Wcol\_mod + 4 \cdot Wcap\_mod \qquad Wtot = 8.701 \times 10^3 \quad kip$

$Teff\_T := 2 \cdot \pi \cdot \sqrt{\frac{Wtot}{Keff\_T\_tot \cdot g}} \quad Teff\_T = 3.017 \quad sec$

$Teff\_L := 2 \cdot \pi \cdot \sqrt{\frac{Wtot}{Keff\_L\_tot \cdot g}} \quad Teff\_L = 2.7 \quad sec$

Verification of seismic demand:

$Si := 1.5$ Site coefficient for soil Type II

$B := 1.5$ Damping coefficient B assuming β=0.20

$Sa\_T := \frac{\omega\_target^2 \cdot Sd\_est\_T}{g}$ $Sa\_L := \frac{\omega\_target^2 \cdot Sd\_est\_T}{g}$

$A\_T := Sa\_T \cdot Teff\_T \cdot \frac{B}{Si} \quad A\_T = 0.804$ $A\_L := Sa\_L \cdot Teff\_L \cdot \frac{B}{Si} \quad A\_L = 0.72$

$d\_T := \frac{10 \cdot A\_T \cdot Si \cdot Teff\_T}{B} \quad d\_T = 24.27$ $d\_L := \frac{10 \cdot A\_L \cdot Si \cdot Teff\_T}{B} \quad d\_L = 21.724$

Transverse	Stiffness	Flexibility	Contribution
Substructure	$k\_sub\_T = 144.433$	$f\_sub\_T = 6.924 \times 10^{-3}$	$\Gamma\_sub\_T := \frac{f\_sub\_T}{Feff\_T} \quad \Gamma\_sub\_T = 0.169$
Isolators	$keff\_T = 29.389$	$feff\_T = 0.034$	$\Gamma i\_T\_calc := \frac{feff\_T}{Feff\_T} \quad \Gamma i\_T\_calc = 0.831$
System	$Keff\_T = 24.42$	$Feff\_T = 0.041$	$\Gamma tot\_T := \Gamma\_sub\_T + \Gamma i\_T\_calc \quad \Gamma tot\_T = 1$

Longitudinal	Stiffness	Flexibility	Contribution
Substructure	$k\_sub\_L = 932.62$	$f\_sub\_L = 1.072 \times 10^{-3}$	$\Gamma\_sub\_L := \frac{f\_sub\_L}{Feff\_L} \quad \Gamma\_sub\_L = 0.033$
Isolators	$keff\_L = 31.509$	$feff\_L = 0.032$	$\Gamma i\_L\_calc := \frac{feff\_L}{Feff\_L} \quad \Gamma i\_L\_calc = 0.967$
System	$Keff\_L = 30.48$	$Feff\_L = 0.033$	$\Gamma tot\_L := \Gamma\_sub\_L + \Gamma i\_L\_calc \quad \Gamma tot\_T = 1$

BI1 bridge design (isolated bridge with elastic column response) – Page 8

Isolators check:

$di\_T\_calc := \Gamma i\_T\_calc \cdot d\_T$ $\quad di\_T\_calc = 20.167$ in $\quad \gamma s\_T := \frac{di\_T\_calc}{tr}$ $\quad \gamma s\_T = 1.438$

$Qi\_T\_calc := Qd + di\_T\_calc \cdot kd$ $\quad keffi\_T\_calc := \frac{Qi\_T\_calc}{di\_T\_calc}$ $\quad keff\_T\_calc := ni \cdot keffi\_T\_calc$

$di\_L\_calc := \Gamma i\_L\_calc \cdot d\_L$ $\quad di\_L\_calc = 21.014$ in $\quad \gamma s\_L := \frac{di\_L\_calc}{tr}$ $\quad \gamma s\_L = 1.498$

$Qi\_L\_calc := Qd + di\_L\_calc \cdot kd$ $\quad keffi\_L\_calc := \frac{Qi\_L\_calc}{di\_L\_calc}$ $\quad keff\_L\_calc := ni \cdot keffi\_L\_calc$

Damping:

$EDC\_T := ni \cdot 4 \cdot Qd \cdot (di\_T\_calc - dy)$ $\quad EDC\_L := ni \cdot 4 \cdot Qd \cdot (di\_L\_calc - dy)$

$\beta\_T := \frac{EDC\_T}{2 \cdot \pi \cdot keff\_T\_calc \cdot di\_T\_calc^2}$ $\quad \beta\_T = 0.192$ Damping in the isolators produced in the transverse direction

$\beta\_L := \frac{EDC\_L}{2 \cdot \pi \cdot keff\_L\_calc \cdot di\_L\_calc^2}$ $\quad \beta\_L = 0.187$ Damping in the isolators produced in the longitudinal direction

$\beta tot\_T := 0.03 + \beta\_T$ $\quad \beta tot\_T = 0.222$

Total damping in the system, assuming damping in the substructure is around 3%

$\beta tot\_L := 0.03 + \beta\_L$ $\quad \beta tot\_L = 0.217$

Substructure check:

$dsub\_T\_calc := \Gamma\_sub\_T \cdot d\_T$ $\quad dsub\_T\_calc = 4.104$ in $\quad \mu d\_T\_calc := \frac{dsub\_T\_calc}{\Delta y\_T}$ $\quad \mu d\_T\_calc = 1.202$

$dsub\_L\_calc := \Gamma\_sub\_L \cdot d\_L$ $\quad dsub\_L\_calc = 0.71$ in $\quad \mu d\_L\_calc := \frac{dsub\_L\_calc}{\Delta y\_L}$ $\quad \mu d\_L\_calc = 0.572$

Seismic Coefficient:

$Cs1\_T := \frac{Keff\_T \cdot d\_T}{Wtot}$ $\quad Cs1\_T = 0.068$ $\quad Cs2\_T := \min\left(2.5 \cdot A\_T, \frac{A\_T \cdot Si}{Teff\_T \cdot B}\right)$ $\quad Cs2\_T = 0.267$

$Cs1\_L := \frac{Keff\_L \cdot d\_L}{Wtot}$ $\quad Cs1\_L = 0.076$ $\quad Cs2\_L := \min\left(2.5 \cdot A\_L, \frac{A\_L \cdot Si}{Teff\_L \cdot B}\right)$ $\quad Cs2\_L = 0.267$

$Cs := \max(Cs1\_T, Cs2\_T, Cs1\_L, Cs2\_L)$ $\quad Cs = 0.267$

$Vb := Cs \cdot Wtot$ $\quad Vb = 2.32 \times 10^3$ kip

$Vs\_col := \frac{Vb}{4}$ $\quad Vs\_col = 580.094$ kip

BI2 bridge design (isolated bridge with nonlinear column response) – Page 1

2. ISOLATED BRIDGE DESIGN- NONLINEAR

2.1 Preliminary design of RC column:

$Dcol := 3.5 \cdot 12$ in $\quad Acol := \frac{\pi \cdot Dcol^2}{4}$

$H\_est := 15$ in — Estimated height of isolators

$Hcol\_mod := Hcol\_orig - Yb - H\_est$ $\quad Hcol\_mod = 249$ in

Longitudinal reinforcement:

$\rho l := 0.03$ — Longitudinal reinforcement between 0.01 and 0.03

$Nbars := 32$

$Abar\_l := 1.27$ in2 $\quad dbl := 1.27$ in — Bars #10

$As := Nbars \cdot Abar\_l$

$\rho l\_spec := \frac{As}{Acol}$ $\quad \rho l\_spec = 0.029$

Transverse reinforcement:

$Ag := Acol$ $\quad cover = 1.5$ in $\quad fc = 4$ ksi $\quad fy = 60$ ksi $\quad fye = 68$ ksi

$Dconf := Dcol - 2 \cdot cover$ $\quad Ac := \frac{\pi Dconf^2}{4}$ $\quad Pe = 1.836 \times 10^3$

Minimum reinforcement:

$\rho s1 := 0.45 \cdot \left[\left(\frac{Ag}{Ac}\right) - 1\right] \cdot \left(\frac{fc}{fy}\right)$ — BDS eq. 8-62

$\rho s2 := 0.12 \cdot \left(\frac{fc}{fy}\right) \cdot \left(0.5 + \frac{1.25 \cdot Pe}{fc \cdot Ag}\right)$ — BDS eq. 8-62B for columns with Dcol>3'

$\rho s := \max(\rho s1, \rho s2)$ $\quad \rho s = 7.313 \times 10^{-3}$

$smin = 3.5$ in $\quad s\_spec := 4$ in $\quad Abar\_v := 0.6$ in2 — Bars #7

$\rho s\_spec := \frac{\pi \cdot Dconf \cdot Abar\_v}{Ac \cdot s\_spec}$ $\quad \rho s\_spec = 0.015$

BI2 bridge design (isolated bridge with nonlinear column response) – Page 2

Moment-curvature analysis:

$\phi y := 1.8 \times 10^{-4}$ $\phi u := 0.00144$

$\phi p := \phi u - \phi y$ $\phi p = 1.26 \times 10^{-3}$

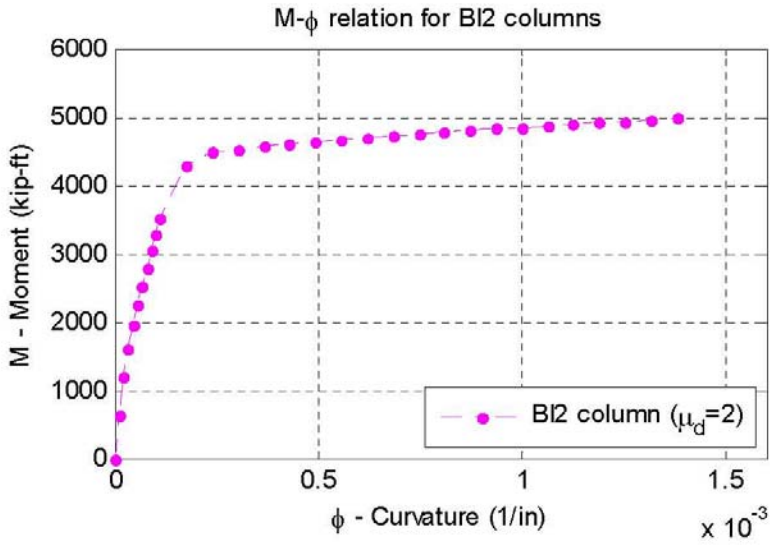

Cantilever behavior (transverse direction):

$Lp\_T := \max(0.08 \cdot Hcol\_mod + 0.15 \cdot fye \cdot dbl, 0.3 \cdot fye \cdot dbl)$ $Lp\_T = 32.874$ in

$\Delta y\_T := \phi y \cdot \frac{Hcol\_mod^2}{3}$ $\Delta y\_T = 3.72$ in $\Delta p\_T := \phi p \cdot Lp\_T \cdot \left(Hcol\_mod - \frac{Lp\_T}{2}\right)$ $\Delta p\_T = 9.633$ in

$\Delta u\_T := \Delta y\_T + \Delta p\_T$ $\Delta u\_T = 13.353$ in $\mu c\_T := \frac{\Delta u\_T}{\Delta y\_T}$ $\mu c\_T = 3.589$ Displacement ductility capacity

$\mu d\_des := 2$ Design goal: ductility demand on column limited to 2.0

$\Delta u\_des\_T := \mu d\_des \cdot \Delta y\_T$

$\Delta u\_des\_T = 7.44$ in Maximum desired displacement demand on column

Column behavior in double curvature (fixed-fixed) (longitudinal direction):

$dcap\_est := 3 \cdot 12$ in Estimated height of cap bent supporting the bearings

$Lp\_L := \max\left(0.08 \cdot \frac{Hcol\_mod - dcap\_est}{2} + 0.15 \cdot fye \cdot dbl, 0.3 \cdot fye \cdot dbl\right)$ $Lp\_L = 25.908$ in

$\Delta y\_L := 2 \cdot \phi y \cdot \frac{\left(\frac{Hcol\_mod - dcap\_est}{2}\right)^2}{3}$ $\Delta y\_L = 1.361$ in

$\Delta p\_L := 2 \cdot \phi p \cdot Lp\_L \cdot \left[\left(\frac{Hcol\_mod - dcap\_est}{2}\right) - \frac{Lp\_L}{2}\right]$ $\Delta p\_L = 6.107$ in

$\Delta u\_L := \Delta y\_L + \Delta p\_L$ $\Delta u\_L = 7.469$ $\mu c\_L := \frac{\Delta u\_L}{\Delta y\_L}$ $\mu c\_L = 5.487$ Displacement ductility capacity

$\mu d\_des = 2$ Design goal: ductility demand on column limited to 2.0

$\Delta u\_des\_L := \mu d\_des \cdot \Delta y\_L$

$\Delta u\_des\_L = 2.722$ in Maximum desired displacement demand on column

BI2 bridge design (isolated bridge with nonlinear column response) – Page 3

2.2 Seismic demand on isolated bridge:

$T\_target := 3.0\ sec$ Target period of the isolated bridge

$\omega\_target := \frac{2\cdot(\pi)}{T\_target}$ $g := 386.4\ in/sec^2$

From the SDC 1.3 (2004) ARS curves for Soil type D we obtain the spectral values corresponding to the target period for each earthquake magnitude (Mw=6.5,7.25,8.0):

Transverse direction:

$Sa\_65\_T := 0.30$

$Sa\_725\_T := 0.35$

$Sa\_8\_T := 0.40$

$Sd\_65\_T := \frac{Sa\_65\_T\cdot g}{\omega\_target^2}$ $Sd\_65\_T = 26.427$

$Sd\_725\_T := \frac{Sa\_725\_T\cdot g}{\omega\_target^2}$ $Sd\_725\_T = 30.831$

$Sd\_8\_T := \frac{Sa\_8\_T\cdot g}{\omega\_target^2}$ $Sd\_8\_T = 35.235$

$Sd\_target\_T := \max(Sd\_65\_T, Sd\_725\_T, Sd\_8\_T)$

$Sd\_target\_T = 35.235$

Longitudinal direction:

$Sa\_65\_L := 0.25$

$Sa\_725\_L := 0.225$

$Sa\_8\_L := 0.30$

$Sd\_65\_L := \frac{Sa\_65\_L\cdot g}{\omega\_target^2}$ $Sd\_65\_L = 22.022$

$Sd\_725\_L := \frac{Sa\_725\_L\cdot g}{\omega\_target^2}$ $Sd\_725\_L = 19.82$

$Sd\_8\_L := \frac{Sa\_8\_L\cdot g}{\omega\_target^2}$ $Sd\_8\_L = 26.427$

$Sd\_target\_L := \max(Sd\_65\_L, Sd\_725\_L, Sd\_8\_L)$

$Sd\_target\_L = 26.427$

$\beta\_target := 0.20$ Target damping in the isolated bridge (bearings and substructure)

$H\_\beta := \left(\frac{1.5}{40\cdot\beta\_target + 1}\right) + 0.5$ $H\_\beta = 0.667$ Reduction factor in spectral values obtained using a 5% damping elastic spectrum.

The total estimated displacement demand on isolated bridge in the transverse and longitudinal directions are:

$Sd\_est\_T := H\_\beta\cdot Sd\_target\_T$ $Sd\_est\_T = 23.49$ in

$Sd\_est\_L := H\_\beta\cdot Sd\_target\_L$ $Sd\_est\_L = 17.618$ in

Estimated displacement demand on isolation bearings

$di\_T := Sd\_est\_T - \Delta u\_des\_T$ $di\_T = 16.05$ in $\Gamma i\_T := \frac{di\_T}{Sd\_est\_T}$ $\Gamma i\_T = 0.683$

$di\_L := Sd\_est\_L - \Delta u\_des\_L$ $di\_L = 14.896$ in $\Gamma i\_L := \frac{di\_L}{Sd\_est\_L}$ $\Gamma i\_L = 0.845$

BI2 bridge design (isolated bridge with nonlinear column response) – Page 4

2.3 Preliminary design of isolation bearings:

We select lead rubber bearings (LRB) for the isolation of the superstructure. From the DIS (Dynamic Isolation Systems) manual we select a LRB with the following properties (the criteria for the selection of the bearing is: di<Di/2):

$Dmax := 22\ in$	Maximum displacement (DIS)
$Di := 35.5\ in$	Isolator diameter (DIS)
$Ai := \frac{\pi \cdot Di^2}{4}$ $Ai = 989.798\ in2$	Isolator bearing area
$Bi := \sqrt{Ai}$ $Bi = 31.461\ in$	Equivalent dimension of square isolator
$kd := 10$ kip / in	Yielded stiffness (DIS) affected primarily by rubber properties
$Kv := 8000$ kip / in	Compression stiffness (DIS)
$Pmax := 1300\ kip$	Axial load capacity (DIS)
$\sigma max := \frac{Pmax \cdot 1000}{Ai}$ $\sigma max = 1.313 \times 10^3\ ksi$	Maximum allowable bearing stress
$H := 15\ in$	Isolator total height (DIS)
$t := 1.5\ in$	End plates thickness (DIS)
$L := 37.5$	Isolator total length (DIS)
$tr := (H - 2 \cdot t) \cdot 0.85$ $tr = 10.2\ in$	Approximated total rubber thickness

Plug design:

$DL := 10\ in$ $AL := \pi \cdot \frac{DL^2}{4}$	Lead diameter and area
$\tau y := 1.20\ ksi$	Shear yield stress of lead
$Qd := AL \cdot \tau y$ $Qd = 94.248\ kip$	Characteristic strength influenced primarily by lead core
$ke := 10 \cdot kd$	Elastic stiffness for analytical bilinear model of bearing
$dy := \frac{Qd}{ke - kd}$ $dy = 1.047\ in$	Yield displacement for analytical bilinear model of bearing
$Fy := ke \cdot dy$ $Fy = 104.72\ kip$	Yield strength for analytical bilinear model of bearing

The number of isolation bearings is determined according to superstructure dead load. The maximum bearing capacity (Pmax) and compressive stress (σmax) of the isolators is checked.

$ni := 2$	Number of isolators for each column
$Wi := \frac{W\_trib}{ni}$ $Wi = 917.891\ kip$	Axial load on each bearing
$\sigma i := \frac{Wi \cdot (1000)}{Ai}$ $\sigma i = 927.351\ psi$	Compressive stress on each bearing

Since Wi<Pmax and σi<σmax, the selected type and number of isolation bearings is acceptable.

BI2 bridge design (isolated bridge with nonlinear column response) – Page 5

Buckling load (circular ~ square bearing pad):

$G := 75 \quad psi$ — Typical value for rubber shear modulus (available from 55-100 psi from DSI)

$Sc := \frac{\frac{Di}{2}}{2tr}$ — Shape factor for circular bearing pad

$Pcrit := \sqrt{2} \cdot \pi \cdot G \cdot Ai \cdot Sc \cdot \left(\frac{\frac{Di}{2}}{tr} \right)$ $Pcrit = 4.994 \times 10^{3}\ kip$ — Critical buckling load

$p := \frac{Wi}{Pcrit}$ $p = 1.838 \times 10^{-3}$ — Ratio of axial load. If p>0.3 then horizontal stiffness changes: Kh~Kho(1-p2)

Rotational stiffness:

$S := \sqrt{\frac{\left(\frac{Bi}{2}\right)^2}{tr^2}}$ — Shape factor for strip or rectangular bearing pad

$Ec := 4 \cdot G \cdot S^2$ $Ec = 713.522\ psi$ — Compression modulus

$I := \frac{Bi \cdot Bi^3}{12} \quad (in4)$ — Moment of inertia of square bearing pad

$EIeff := \frac{Ec \cdot I}{5 \cdot 1000} \quad (kip - in2)$ — Effective EI for strip or rectangular bearing pad

$k\theta := \frac{EIeff}{tr}$ $k\theta = 1.142 \times 10^{3}$ (kip - in)/rad — Rotational stiffness of bearing pad

Torsional stiffness:

$Ji := \left(\frac{Bi^4}{6} \right)$ — Polar moment of inertia of square isolation bearing

$GJ := Ji \cdot \frac{G}{1000}$ $GJ = 1.225 \times 10^{4}$ kip-in2/rad — Torsional stiffness

BI2 bridge design (isolated bridge with nonlinear column response) – Page 6

3. UNIFORM LOAD METHOD (AASHTO Section 7.1):

Weights of column and cap bent:

$D\_col\_T := 3.5 \cdot 12 \quad in \qquad Ig\_col\_T := \frac{\pi \cdot D\_col\_T^4}{64} \qquad Ieff\_col\_T := 0.65 Ig\_col\_T$

$D\_col\_L := 3.5 \cdot 12 \ in \qquad Ig\_col\_L := \frac{\pi \cdot D\_col\_L^4}{64} \qquad Ieff\_col\_L := 0.65 Ig\_col\_L$

$A\_col := \frac{\pi \cdot D\_col\_T \cdot D\_col\_L}{4} \qquad Wcol\_mod := \frac{\rho\_RC}{1000} \cdot \frac{A\_col}{12^2} \cdot \left(\frac{Hcol\_mod}{12} \right) \qquad Wcol\_mod = 29.946 \quad kip$

Bent cap: original and isolated bridges

$Acap\_orig := (6 \cdot 5) \cdot 12^2 \quad in2 \qquad Lcap\_orig := sw\_deck \qquad Wcap\_orig := \left(\frac{\rho\_RC}{1000} \right) \cdot \left(\frac{Acap\_orig}{12^2} \right) \cdot \left(\frac{Lcap\_orig}{12} \right)$

$Lcap\_orig = 276 \quad in$

$Wcap\_orig = 103.5 \quad kip$

$Acap\_mod := (3 \cdot 4) \cdot 12^2 \quad in2 \qquad Lcap\_mod := Dcol + 3 \cdot L \qquad Wcap\_mod := \left(\frac{\rho\_RC}{1000} \right) \cdot \left(\frac{Acap\_mod}{12^2} \right) \cdot \left(\frac{Lcap\_mod}{12} \right)$

$Lcap\_mod = 154.5 \ in$

$Wcap\_mod = 23.175 \quad kip$

Stiffness of isolated structure:

Stiffness of new substructure, assuming cantilever and fixed-fixed behavior for the transverse and longitudinal directions of the bridge, respectively.

$fc = 4 \quad ksi \qquad Ec := 33 \cdot \rho\_RC^{1.5} \cdot \frac{\sqrt{fc \cdot 1000}}{1000}$

$k\_sub\_T := 3 \cdot Ec \cdot \frac{Ieff\_col\_T}{Hcol\_mod^3} \qquad f\_sub\_T := k\_sub\_T^{-1}$

$k\_sub\_L := 12 \cdot Ec \cdot \frac{Ieff\_col\_L}{(Hcol\_mod - dcap\_est)^3} \qquad f\_sub\_L := k\_sub\_L^{-1}$

Isolator stiffness:

$di\_T = 16.05 \quad in \qquad Qi\_T := Qd + di\_T \cdot kd \qquad keffi\_T := \frac{Qi\_T}{di\_T} \qquad keff\_T := ni \cdot keffi\_T \qquad feff\_T := keff\_T^{-1}$

$di\_L = 14.896 \quad in \qquad Qi\_L := Qd + di\_L \cdot kd \qquad keffi\_L := \frac{Qi\_L}{di\_L} \qquad keff\_L := ni \cdot keffi\_L \qquad feff\_L := keff\_L^{-1}$

Effective stiffness of the substructure-isolators series system, calculated for the entire bridge:

$Keff\_T := \frac{k\_sub\_T \cdot keff\_T}{k\_sub\_T + keff\_T} \qquad Feff\_T := Keff\_T^{-1} \qquad Keff\_L := \frac{k\_sub\_L \cdot keff\_L}{k\_sub\_L + keff\_L} \qquad Feff\_L := Keff\_L^{-1}$

$Keff\_T\_tot := 4 \cdot Keff\_T \qquad Keff\_L\_tot := 4 \cdot Keff\_L$

BI2 bridge design (isolated bridge with nonlinear column response) – Page 7

Weight of bridge:

$Ltot := 3 \cdot 150 + 2 \cdot 120 \quad ft$

$WDL\_tot := WDL\_trib \cdot \frac{Ltot}{L\_trib}$

$Wtot := \left(\frac{\rho\_RC}{1000}\right) \cdot \left(\frac{A\_deck}{12^2}\right) \cdot Ltot + WDL\_tot + 4 \cdot Wcol\_mod + 4 \cdot Wcap\_mod \qquad Wtot = 8.657 \times 10^3 \quad kip$

$Teff\_T := 2 \cdot \pi \cdot \sqrt{\frac{Wtot}{Keff\_T\_tot \cdot g}} \quad Teff\_T = 3.155 \quad sec$

$Teff\_L := 2 \cdot \pi \cdot \sqrt{\frac{Wtot}{Keff\_L\_tot \cdot g}} \quad Teff\_L = 2.691 \quad sec$

Verification of seismic demand:

$Si := 1.5$ Site coefficient for soil Type II

$B := 1.5$ Damping coefficient B assuming β=0.20

$Sa\_T := \frac{\omega\_target^2 \cdot Sd\_est\_T}{g}$ $Sa\_L := \frac{\omega\_target^2 \cdot Sd\_est\_T}{g}$

$A\_T := Sa\_T \cdot Teff\_T \cdot \frac{B}{Si} \quad A\_T = 0.841$ $A\_L := Sa\_L \cdot Teff\_L \cdot \frac{B}{Si} \quad A\_L = 0.717$

$d\_T := \frac{10 \cdot A\_T \cdot Si \cdot Teff\_T}{B} \quad d\_T = 26.547$ $d\_L := \frac{10 \cdot A\_L \cdot Si \cdot Teff\_T}{B} \quad d\_L = 22.638$

Transverse	Stiffness	Flexibility	Contribution
Substructure	$k\_sub\_T = 73.975$	$f\_sub\_T = 0.014$	$\Gamma\_sub\_T := \frac{f\_sub\_T}{Feff\_T} \quad \Gamma\_sub\_T = 0.3$
Isolators	$keff\_T = 31.744$	$feff\_T = 0.032$	$\Gamma i\_T\_calc := \frac{feff\_T}{Feff\_T} \quad \Gamma i\_T\_calc = 0.7$
System	$Keff\_T = 22.212$	$Feff\_T = 0.045$	$\Gamma tot\_T := \Gamma\_sub\_T + \Gamma i\_T\_calc \quad \Gamma tot\_T = 1$

Longitudinal	Stiffness	Flexibility	Contribution
Substructure	$k\_sub\_L = 472.72$	$f\_sub\_L = 2.115 \times 10^{-3}$	$\Gamma\_sub\_L := \frac{f\_sub\_L}{Feff\_L} \quad \Gamma\_sub\_L = 0.065$
Isolators	$keff\_L = 32.654$	$feff\_L = 0.031$	$\Gamma i\_L\_calc := \frac{feff\_L}{Feff\_L} \quad \Gamma i\_L\_calc = 0.935$
System	$Keff\_L = 30.545$	$Feff\_L = 0.033$	$\Gamma tot\_L := \Gamma\_sub\_L + \Gamma i\_L\_calc \quad \Gamma tot\_T = 1$

BI2 bridge design (isolated bridge with nonlinear column response) – Page 8

Isolators check:

$di\_T\_calc := \Gamma i\_T\_calc \cdot d\_T$ $\quad di\_T\_calc = 18.575$ in $\quad \gamma s\_T := \frac{di\_T\_calc}{tr}$ $\quad \gamma s\_T = 1.821$

$Qi\_T\_calc := Qd + di\_T\_calc \cdot kd$ $\quad keffi\_T\_calc := \frac{Qi\_T\_calc}{di\_T\_calc}$ $\quad keff\_T\_calc := ni \cdot keffi\_T\_calc$

$di\_L\_calc := \Gamma i\_L\_calc \cdot d\_L$ $\quad di\_L\_calc = 21.175$ in $\quad \gamma s\_L := \frac{di\_L\_calc}{tr}$ $\quad \gamma s\_L = 2.076$

$Qi\_L\_calc := Qd + di\_L\_calc \cdot kd$ $\quad keffi\_L\_calc := \frac{Qi\_L\_calc}{di\_L\_calc}$ $\quad keff\_L\_calc := ni \cdot keffi\_L\_calc$

Damping:

$EDC\_T := ni \cdot 4 \cdot Qd \cdot (di\_T\_calc - dy)$ $\quad EDC\_L := ni \cdot 4 \cdot Qd \cdot (di\_L\_calc - dy)$

$\beta\_T := \frac{EDC\_T}{2 \cdot \pi \cdot keff\_T\_calc \cdot di\_T\_calc^2}$ $\quad \beta\_T = 0.202$ Damping in the isolators produced in the transverse direction

$\beta\_L := \frac{EDC\_L}{2 \cdot \pi \cdot keff\_L\_calc \cdot di\_L\_calc^2}$ $\quad \beta\_L = 0.186$ Damping in the isolators produced in the longitudinal direction

$\beta tot\_T := 0.03 + \beta\_T$ $\quad \beta tot\_T = 0.232$

Total damping in the system, assuming damping in the substructure is around 3%

$\beta tot\_L := 0.03 + \beta\_L$ $\quad \beta tot\_L = 0.216$

Substructure check:

$dsub\_T\_calc := \Gamma\_sub\_T \cdot d\_T$ $\quad dsub\_T\_calc = 7.971$ in $\quad \mu d\_T\_calc := \frac{dsub\_T\_calc}{\Delta y\_T}$ $\quad \mu d\_T\_calc = 2.143$

$dsub\_L\_calc := \Gamma\_sub\_L \cdot d\_L$ $\quad dsub\_L\_calc = 1.463$ in $\quad \mu d\_L\_calc := \frac{dsub\_L\_calc}{\Delta y\_L}$ $\quad \mu d\_L\_calc = 1.075$

Seismic Coefficient:

$Cs1\_T := \frac{Keff\_T \cdot d\_T}{Wtot}$ $\quad Cs1\_T = 0.068$ $\quad Cs2\_T := \min\left(2.5 \cdot A\_T, \frac{A\_T \cdot Si}{Teff\_T \cdot B}\right)$ $\quad Cs2\_T = 0.267$

$Cs1\_L := \frac{Keff\_L \cdot d\_L}{Wtot}$ $\quad Cs1\_L = 0.08$ $\quad Cs2\_L := \min\left(2.5 \cdot A\_L, \frac{A\_L \cdot Si}{Teff\_L \cdot B}\right)$ $\quad Cs2\_L = 0.267$

$Cs := \max(Cs1\_T, Cs2\_T, Cs1\_L, Cs2\_L)$ $\quad Cs = 0.267$

$Vb := Cs \cdot Wtot$ $\quad Vb = 2.309 \times 10^3$ kip

$Vs\_col := \frac{Vb}{4}$ $\quad Vs\_col = 577.138$ kip

Appendix E: Ground Motion Characteristics

The general ground motion characteristics of seven record bins used for the nonlinear time history analysis of the different bridge systems considered in this study are presented in this appendix. The characterization includes the magnitude, epicentral distance, soil type, fault mechanism, and station of the different earthquake records in each ground motion bin.

Table E-1 LMSR ground motion bin data (source: Medina *et al.*, 2001)

Record ID	Event	Year	*M*	*R* (km)	Station	Soil	Mechanism
AGW	Loma Prieta	1989	6.9	28.2	Agnews State Hospital	D	reverse-oblique
CAP	Loma Prieta	1989	6.9	14.5	Capitola	D	reverse-oblique
G03	Loma Prieta	1989	6.9	14.4	Gilroy Array #3	D	reverse-oblique
G04	Loma Prieta	1989	6.9	16.1	Gilroy Array #4	D	reverse-oblique
GMR	Loma Prieta	1989	6.9	24.2	Gilroy Array #7	D	reverse-oblique
HCH	Loma Prieta	1989	6.9	28.2	Hollister City Hall	D	reverse-oblique
HDA	Loma Prieta	1989	6.9	25.8	Hollister Differential Array	D	reverse-oblique
SVL	Loma Prieta	1989	6.9	28.8	Sunnyvale - Colton Ave.	D	reverse-oblique
CNP	Northridge	1994	6.7	15.8	Canoga Park - Topanga Can.	D	reverse-slip
FAR	Northridge	1994	6.7	23.9	LA - N Faring Rd.	D	reverse-slip
FLE	Northridge	1994	6.7	29.5	LA - Fletcher Dr.	D	reverse-slip
GLP	Northridge	1994	6.7	25.4	Glendale - Las Palmas	D	reverse-slip
HOL	Northridge	1994	6.7	25.5	LA - Holywood Stor FF	D	reverse-slip
NYA	Northridge	1994	6.7	22.3	La Crescenta-New York	D	reverse-slip
LOS	Northridge	1994	6.7	13.0	Canyon Country - W Lost Cany	D	reverse-slip
RO3	Northridge	1994	6.7	12.3	Sun Valley - Roscoe Blvd	D	reverse-slip
PEL	San Fernando	1971	6.6	21.2	LA - Hollywood Stor Lot	D	reverse-slip
B-ICC	Superstition Hills	1987	6.7	13.9	El Centro Imp. Co. Cent	D	strike-slip
B-IVW	Superstition Hills	1987	6.7	24.4	Wildlife Liquef. Array	D	strike-slip
B-WSM	Superstition Hills	1987	6.7	13.3	Westmorland Fire Station	D	strike-slip

Table E-2 LMLR ground motion bin data (source: Medina *et al.*, 2001)

Record ID	Event	Year	*M*	*R* (km)	Station	Soil	Mechanism
A-ELC	Borrego Mountain	1968	6.8	46.0	El Centro Array #9	D	strike-slip
A2E	Loma Prieta	1989	6.9	57.4	APEEL 2E Hayward Muir Sch.	D	reverse-oblique
FMS	Loma Prieta	1989	6.9	43.4	Fremont - Emerson Court	D	reverse-oblique
HVR	Loma Prieta	1989	6.9	31.6	Halls Valley	D	reverse-oblique
SJW	Loma Prieta	1989	6.9	32.6	Salinas - John & Work	D	reverse-oblique
SLC	Loma Prieta	1989	6.9	36.3	Palo Alto - SLAC Lab.	D	reverse-oblique
BAD	Northridge	1994	6.7	56.1	Covina - W. Badillo	D	reverse-slip
CAS	Northridge	1994	6.7	49.6	Compton - Castlegate St.	D	reverse-slip
CEN	Northridge	1994	6.7	30.9	LA - Centinela St.	D	reverse-slip
DEL	Northridge	1994	6.7	59.3	Lakewood - Del Amo Blvd.	D	reverse-slip
DWN	Northridge	1994	6.7	47.6	Downey - Co. Maint. Bldg.	D	reverse-slip
JAB	Northridge	1994	6.7	46.6	Bell Gardens - Jaboneria	D	reverse-slip
LH1	Northridge	1994	6.7	36.3	Lake Hughes #1	D	reverse-slip
LOA	Northridge	1994	6.7	42.4	Lawndale - Osage Ave.	D	reverse-slip
LV2	Northridge	1994	6.7	37.7	Leona Valley #2	D	reverse-slip
PHP	Northridge	1994	6.7	43.6	Palmdale - Hwy 14 & Palmdale	D	reverse-slip
PIC	Northridge	1994	6.7	32.7	LA - Pico & Sentous	D	reverse-slip
SOR	Northridge	1994	6.7	54.1	West Covina - S. Orange Ave.	D	reverse-slip
SSE	Northridge	1994	6.7	60.0	Terminal Island - S. Seaside	D	reverse-slip
VER	Northridge	1994	6.7	39.3	LA - E Vernon Ave.	D	reverse-slip

Table E-3 SMSR ground motion bin data (source: Medina *et al.*, 2001)

Record ID	Event	Year	*M*	*R* (km)	Station	Soil	Mechanism
H-CAL	Imperial Valley	1979	6.5	23.8	Calipatria Fire Station	D	strike-slip
H-CHI	Imperial Valley	1979	6.5	28.7	Chihuahua	D	strike-slip
H-E01	Imperial Valley	1979	6.5	15.5	El Centro Array #1	D	strike-slip
H-E12	Imperial Valley	1979	6.5	18.2	El Centro Array #12	D	strike-slip
H-E13	Imperial Valley	1979	6.5	21.9	El Centro Array #13	D	strike-slip
H-WSM	Imperial Valley	1979	6.5	15.1	Westmorland Fire Station	D	strike-slip
A-SRM	Livermore	1980	5.8	21.7	San Ramon Fire Station	D	strike-slip
A-KOD	Livermore	1980	5.8	17.6	San Ramon - Eastman Kodak	D	strike-slip
M-AGW	Morgan Hill	1984	6.2	29.4	Agnews State Hospital	D	strike-slip
M-G02	Morgan Hill	1984	6.2	15.1	Gilroy Array #2	D	strike-slip
M-G03	Morgan Hill	1984	6.2	14.6	Gilroy Array #3	D	strike-slip
M-GMR	Morgan Hill	1984	6.2	14.0	Gilroy Array #7	D	strike-slip
PHN	Point Mugu	1973	5.8	25.0	Port Hueneme	D	reverse-slip
BRA	Westmorland	1981	5.8	22.0	5060 Brawley Airport	D	strike-slip
NIL	Westmorland	1981	5.8	19.4	724 Niland Fire Station	D	strike-slip
A-CAS	Whittier Narrows	1987	6.0	16.9	Compton - Castlegate St.	D	reverse
A-CAT	Whittier Narrows	1987	6.0	28.1	Carson - Catskill Ave.	D	reverse
A-DWN	Whittier Narrows	1987	6.0	18.3	14368 Downey - Co Maint Bldg	D	reverse
A-W70	Whittier Narrows	1987	6.0	16.3	LA - W 70th St.	D	reverse
A-WAT	Whittier Narrows	1987	6.0	24.5	Carson - Water St.	D	reverse

Table E-4 SMLR ground motion bin data (source: Medina *et al.*, 2001)

Record ID	Event	Year	*M*	*R* (km)	Station	Soil	Mechanism
B-ELC	Borrego	1942	6.5	49.0	El Centro Array #9	D	unknown
H-C05	Coalinga	1983	6.4	47.3	Parkfield - Cholame 5W	D	reverse-oblique
H-C08	Coalinga	1983	6.4	50.7	Parkfield - Cholame 8W	D	reverse-oblique
H-CC4	Imperial Valley	1979	6.5	49.3	Coachella Canal #4	D	strike-slip
H-CMP	Imperial Valley	1979	6.5	32.6	Compuertas	D	strike-slip
H-DLT	Imperial Valley	1979	6.5	43.6	Delta	D	strike-slip
H-NIL	Imperial Valley	1979	6.5	35.9	Niland Fire Station	D	strike-slip
H-PLS	Imperial Valley	1979	6.5	31.7	Plaster City	D	strike-slip
H-VCT	Imperial Valley	1979	6.5	54.1	Victoria	D	strike-slip
A-STP	Livermore	1980	5.8	37.3	Tracy - Sewage Treatment Plant	D	strike-slip
M-CAP	Morgan Hill	1984	6.2	38.1	Capitola	D	strike-slip
M-HCH	Morgan Hill	1984	6.2	32.5	Hollister City Hall	D	strike-slip
M-SJB	Morgan Hill	1984	6.2	30.3	San Juan Bautista	C	strike-slip
H06	N. Palm Springs	1986	6.0	39.6	San Jacinto Valley Cemetery	D	strike-slip
INO	N. Palm Springs	1986	6.0	39.6	Indio	D	strike-slip
A-BIR	Whittier Narrows	1987	6.0	56.8	Downey - Birchdale	D	reverse
A-CTS	Whittier Narrows	1987	6.0	31.3	LA - Century City CC South	D	reverse
A-HAR	Whittier Narrows	1987	6.0	34.2	LB - Harbor Admin FF	D	reverse
A-SSE	Whittier Narrows	1987	6.0	35.7	Terminal Island - S. Seaside	D	reverse
A-STC	Whittier Narrows	1987	6.0	39.8	Northridge - Saticoy St.	D	reverse

Table E-5 I-880 ground motion bin data (source: Sommerville and Collins, 2002a)

Record ID	Event	Year	*M*	*R* (km)	Station	Soil	Mechanism
cclyd	Coyote Lake	1979	5.7	4.0	Coyote Lake Dam abutment	C	strike-slip
gil6	Coyote Lake	1979	5.7	1.2	Gilroy #6	C	strike-slip
temb	Parkfield	1966	6.0	4.4	Temblor	C	strike-slip
cs05	Parkfield	1966	6.0	3.7	Array #5	D	strike-slip
cs08	Parkfield	1966	6.0	8.0	Array #8	D	strike-slip
fgnr	Livermore	1980	5.5	4.1	Fagundes Ranch	D	strike-slip
mgnp	Livermore	1980	5.5	8.1	Morgan Territory Park	C	strike-slip
clyd	Morgan Hill	1984	6.2	0.1	Coyote Lake Dam abutment	C	strike-slip
andd	Morgan Hill	1984	6.2	4.5	Anderson Dam Downstream	C	strike-slip
hall	Morgan Hill	1984	6.2	2.5	Halls Valley	C	strike-slip
lgpc	Loma Prieta	1989	6.9	3.5	Los Gatos Presentation Center	C	reverse-oblique
srtg	Loma Prieta	1989	6.9	8.3	Saratoga Aloha Ave	C	reverse-oblique
cor	Loma Prieta	1989	6.9	3.4	Corralitos	C	reverse-oblique
gav	Loma Prieta	1989	6.9	9.5	Gavilan College	C	reverse-oblique
gilb	Loma Prieta	1989	6.9	11.0	Gilroy historic	C	reverse-oblique
lex1	Loma Prieta	1989	6.9	6.3	Lexington Dam abutment	C	reverse-oblique
kobj	Kobe, Japan	1995	6.9	0.5	Kobe JMA	C	strike-slip
ttr007	Tottori, Japan	2000	6.6	10.0	Kofu	C	strike-slip
ttrh02	Tottori, Japan	2000	6.6	1.0	Hino	C	strike-slip
erzi	Erzincan, Turkey	1992	6.7	1.8	Erzincan	C	strike-slip

Table E-6 VN ground motion bin data (source: Sommerville and Collins, 2002b)

Record ID	Event	Year	*M*	*R* (km)	Station	Soil	Mechanism
plma	North Palm Springs	1986	6.0	9.6	Palm Springs Airport	D	reverse-oblique
plmb	North Palm Springs	1986	6.0	9.6	Palm Springs Airport, reversed components	D	reverse-oblique
env1	Northridge	1994	6.7	17.7	Encino, Ventura Blvd. #1	D	reverse
env9	Northridge	1994	6.7	17.9	Encino, Ventura Blvd. #9	D	reverse
nhl2	Northridge	1994	6.7	18.4	North Hollywood, Lankershim Blvd. #1	D	reverse
vns1	Northridge	1994	6.7	12.8	Van Nuys, Sherman Way #1	D	reverse
vnsc	Northridge	1994	6.7	12.8	Van Nuys - Sherman Circle #1	D	reverse
whox	Northridge	1994	6.7	20.0	Woodland Hills, Oxnard Street #4	D	reverse
cnpk	Northridge	1994	6.7	17.7	Canoga Park, Topanga Canyon Blvd.	D	reverse
spva	Northridge	1994	6.7	9.2	Sepulveda VA Hospital - ground	D	reverse
vnuy	Northridge	1994	6.7	11.3	Van Nuys - 7-Story Hotel	D	reverse
nord	Northridge	1994	6.7	9.4	Arleta, Nordhoff Fire Station	D	reverse
nrr1	Northridge	1994	6.7	13.7	Northridge, Roscoe #1	D	reverse
rosc	Northridge	1994	6.7	10.8	Sun Valley, 13248 Roscoe Blvd.	D	reverse
sf253	San Fernando	1971	6.6	16.3	Los Angeles, 14724 Ventura Blvd.	D	reverse
sf461	San Fernando	1971	6.6	16.2	Los Angeles, 15910 Ventura Blvd.	D	reverse
sf466	San Fernando	1971	6.6	16.4	Los Angeles, 15250 Ventura Blvd.	D	reverse
glen	San Fernando	1971	6.6	18.8	Glendale, Muni. Bldg., 633 E. Broadway	D	reverse
vnuy	Whittier Narrows	1987	6.0	9.5	Van Nuys - 7-Story Hotel	D	reverse
athl	Whittier Narrows	1987	6.0	16.6	Cal Tech, Brown Athletic Building	D	reverse

Table E-7 Ground motion unscaled peak ground velocity (SRSS)

LMSR		LMLR		SMSR		SMLR		I880		VN	
Record ID	PGV, SRSS (cm/s)	Record ID	PGV, SRSS (cm/s)	Record ID	PGV, SRSS (cm/s)	Record ID	PGV, SRSS (cm/s)	Record ID	PGV, SRSS (cm/s)	Record ID	PGV, SRSS (cm/s)
AGW	31.33	A-ELC	17.91	H-CAL	30.37	B-ELC	40.41	cclyd	85.77	plma	17.29
CAP	61.78	A2E	29.44	H-CHI	4.54	H-C05	6.37	gil6	117.72	plmb	17.29
G03	45.67	FMS	9.05	H-E01	31.61	H-C08	8.40	temb	61.65	env1	71.07
G04	38.88	HVR	9.82	H-E12	19.72	H-CC4	5.03	cs05	40.71	env9	64.77
GMR	45.59	SJW	30.00	H-E13	5.19	H-CMP	10.00	cs08	44.56	nhl2	46.88
HCH	68.40	SLC	15.21	H-WSM	21.17	H-DLT	10.67	fgnr	117.53	vns1	56.49
HDA	33.84	BAD	17.91	A-SRM	14.60	H-NIL	5.53	mgnp	117.22	vnsc	46.94
SVL	28.42	CAS	18.12	A-KOD	13.91	H-PLS	5.38	clyd	70.47	whox	73.05
CNP	57.29	CEN	20.48	M-AGW	20.35	H-VCT	14.65	andd	50.64	cnpk	44.22
FAR	54.07	DEL	10.74	M-G02	39.01	A-STP	11.69	hall	134.63	spva	114.22
FLE	14.43	DWN	13.36	M-G03	19.05	M-CAP	19.97	lgpc	22.80	vnuy	47.21
GLP	23.28	JAB	11.62	M-GMR	27.98	M-HCH	16.97	srtg	58.27	nord	43.13
HOL	59.20	LH1	10.46	PHN	19.64	M-SJB	41.86	cor	18.58	nrr1	65.15
NYA	56.46	LOA	11.24	BRA	30.40	H06	10.79	gav	17.60	rosc	71.34
LOS	33.04	LV2	18.80	NIL	7.49	INO	6.25	gilb	39.56	sf253	35.19
RO3	62.59	PHP	19.00	A-CAS	13.65	A-BIR	10.44	lex1	96.18	sf461	27.07
PEL	16.89	PIC	47.53	A-CAT	16.92	A-CTS	14.00	kobj	41.38	sf466	35.94
B-ICC	24.07	SOR	8.29	A-DWN	9.49	A-HAR	9.52	ttr007	33.27	glen	43.40
B-IVW	44.24	SSE	18.37	A-W70	8.75	A-SSE	11.65	ttrh02	15.62	vnuy	38.66
B-WSM	51.77	VER	13.65	A-WAT	15.53	A-STC	6.16	erzi	25.68	athl	16.06

Appendix F: Bridge Repair Cost and Time

This appendix presents additional figures of the LLRCAT methodology (Mackie *et al.* 2007) used for the computation of the repair cost and time of the different bridge systems. Among these figures are the disaggregation plots of the repair costs loss models by PG and repair item, as well as the disaggregation of the repair efforts loss models by repair item, as a function of earthquake intensity.

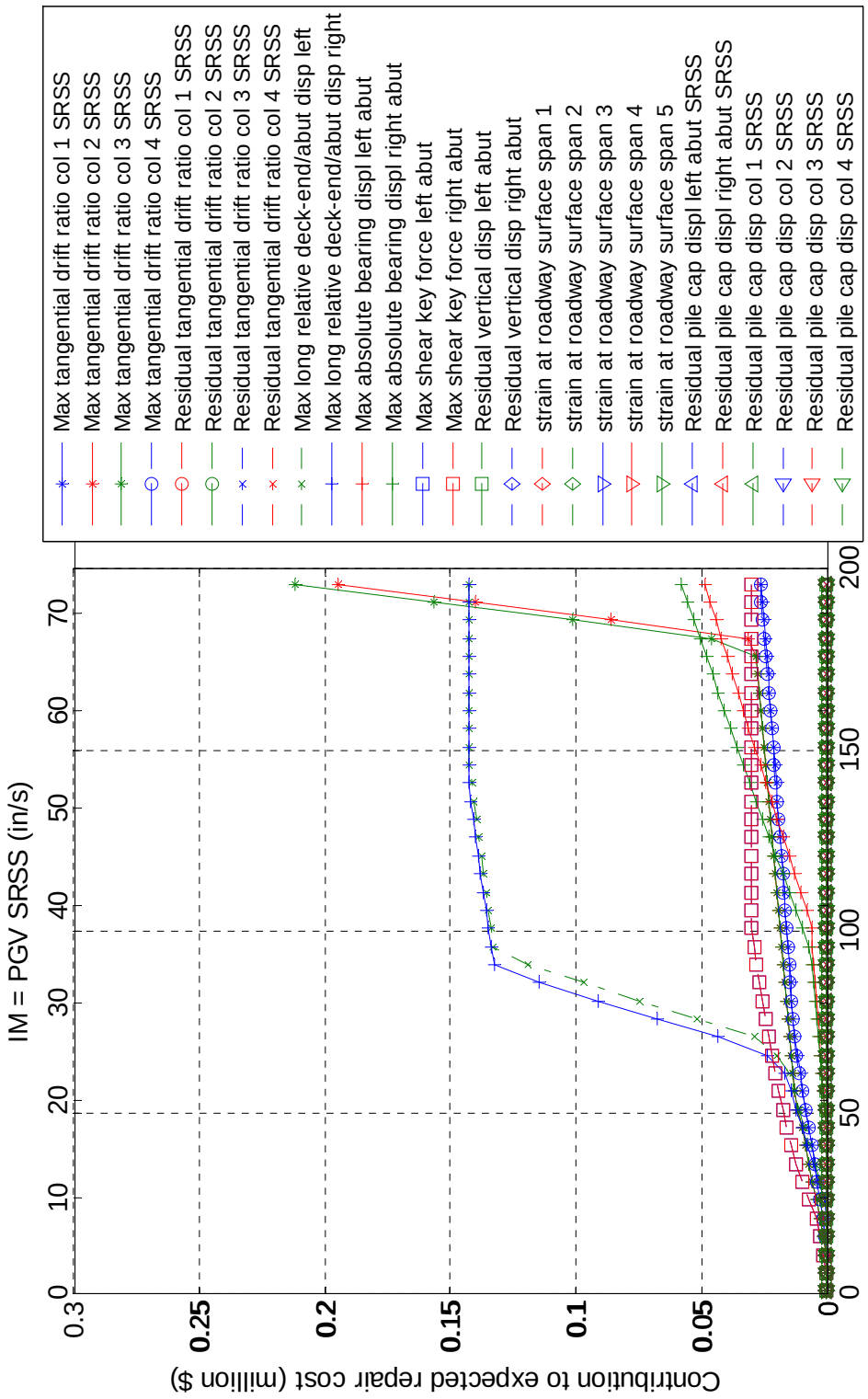

Figure F-1 Disaggregation of repair costs by PG for RC bridge

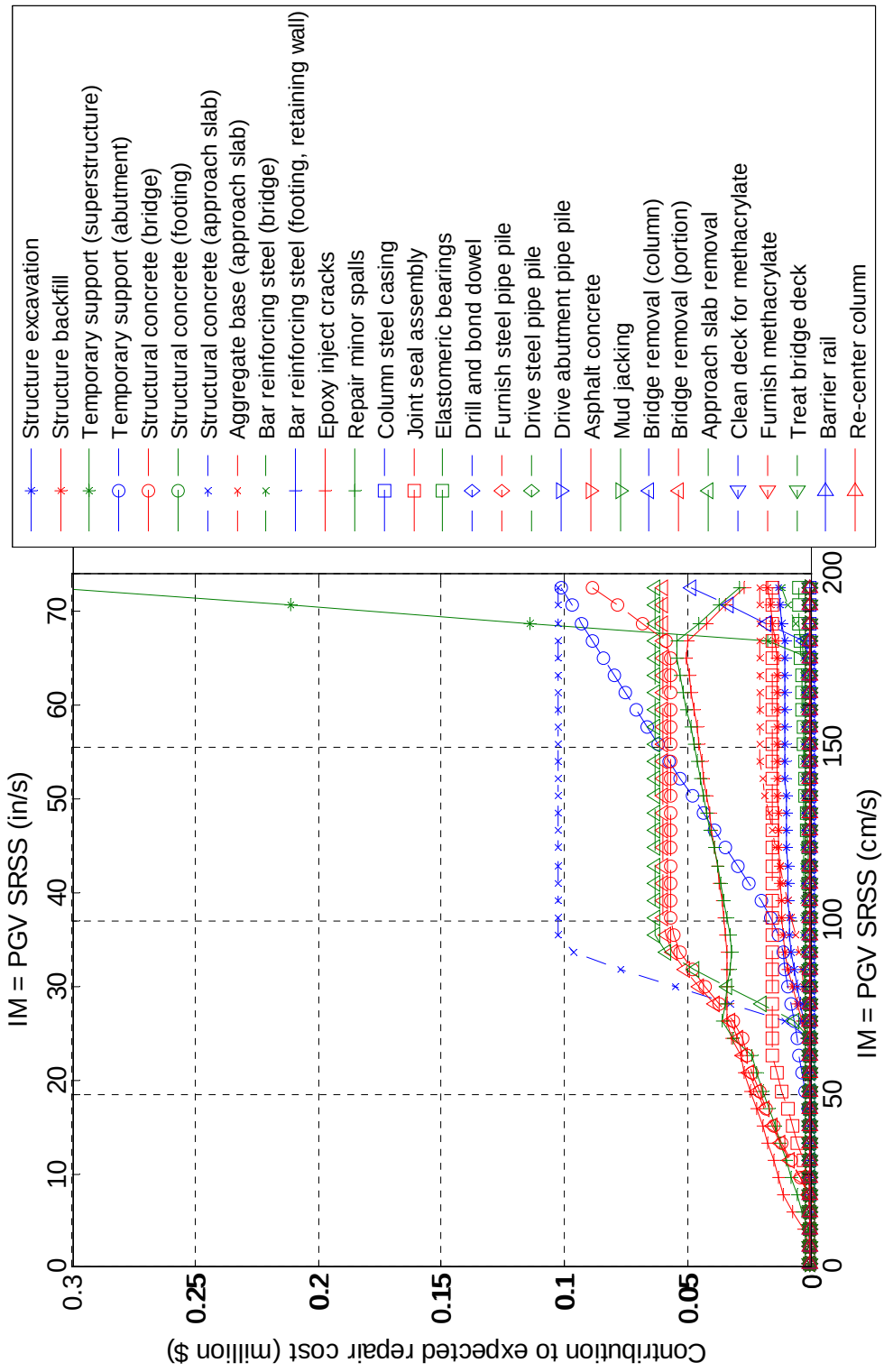

Figure F-2 Disaggregation of repair costs by repair item for RC bridge

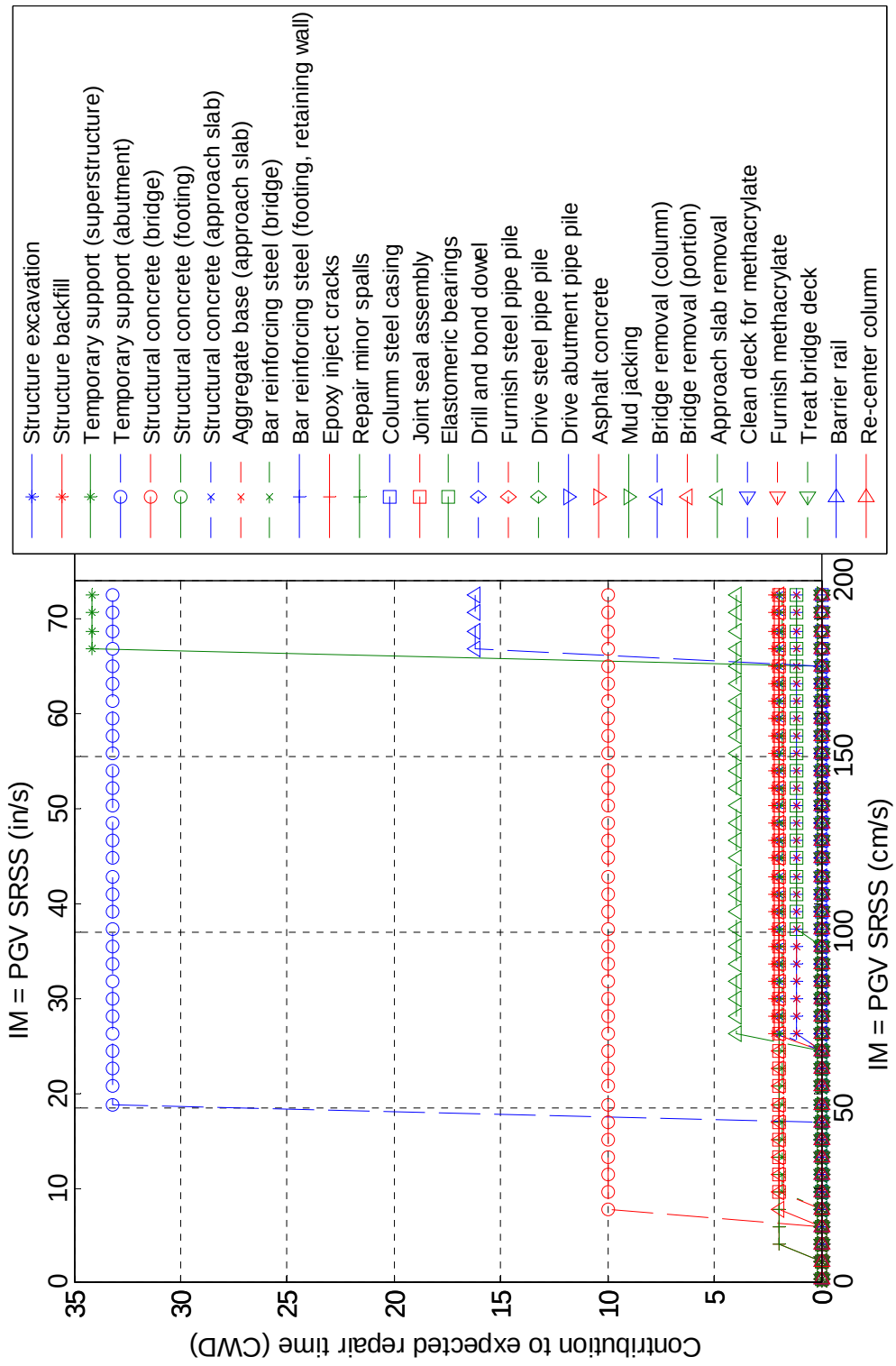

Figure F-3 Disaggregation of repair efforts by repair item for RC bridge

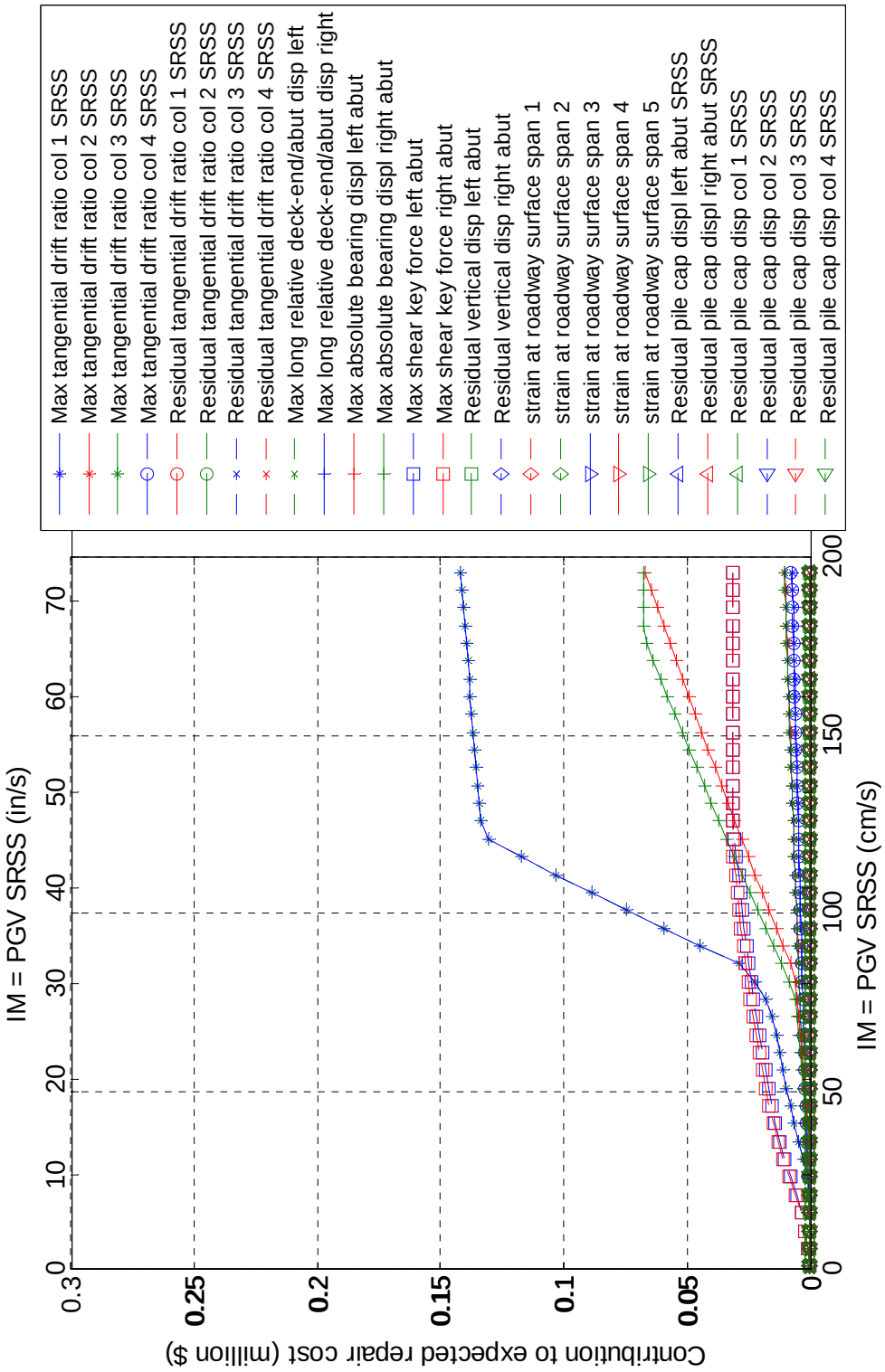

Figure F-4 Disaggregation of repair costs by PG for FRC bridge

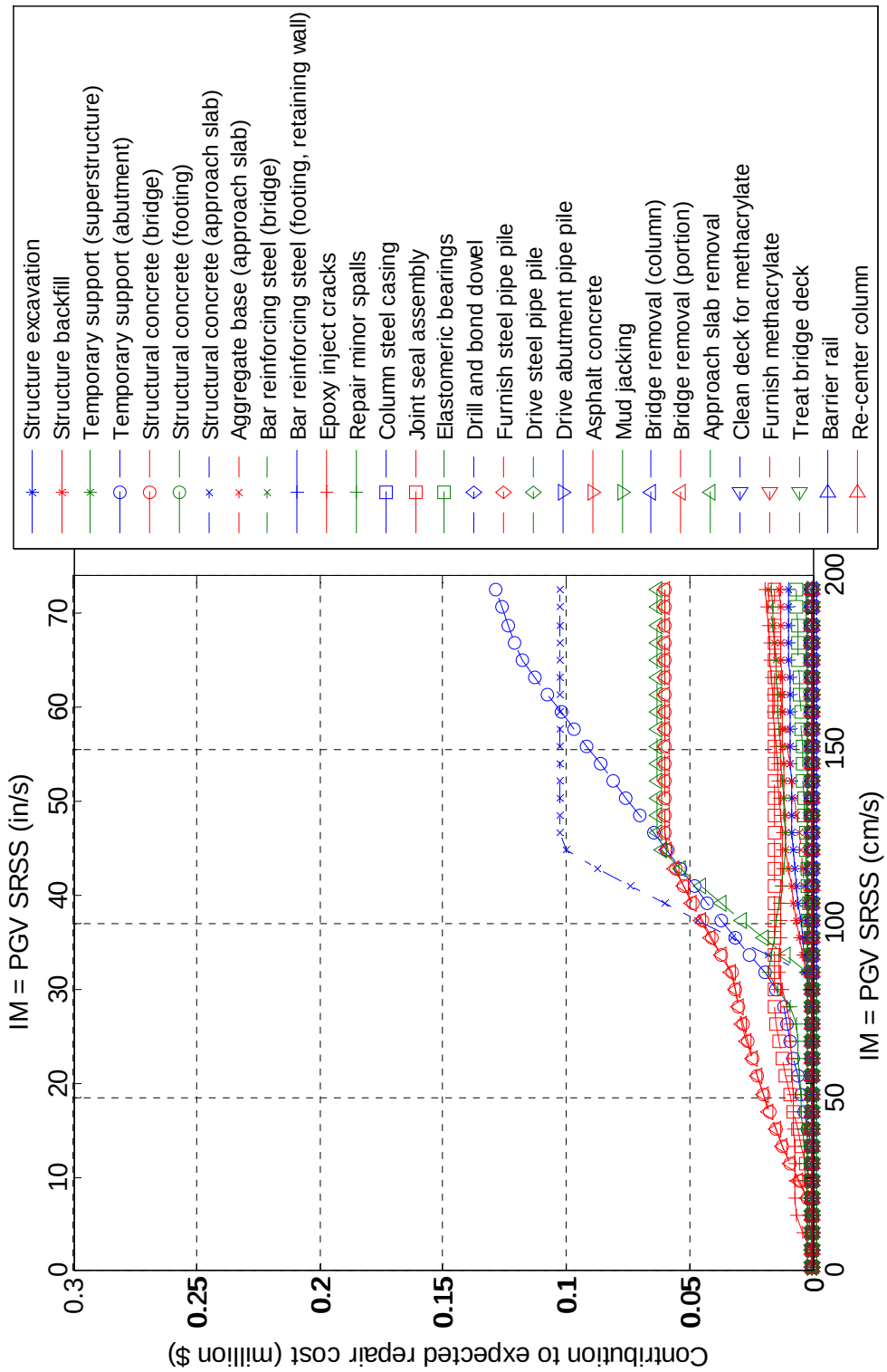

Figure F-5 Disaggregation of repair costs by repair item for FRC bridge

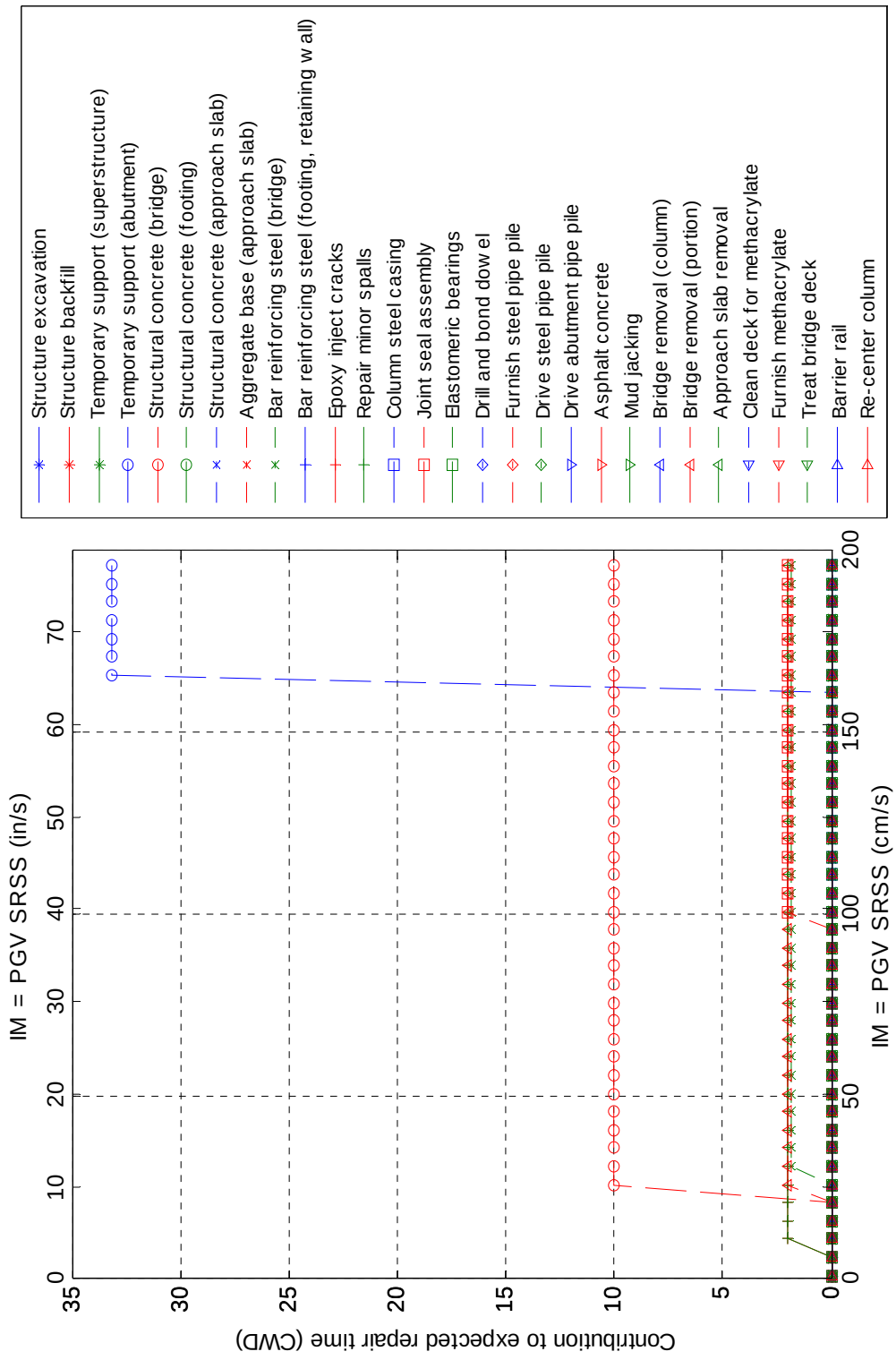

Figure F-6 Disaggregation of repair efforts by repair item for FRC bridge

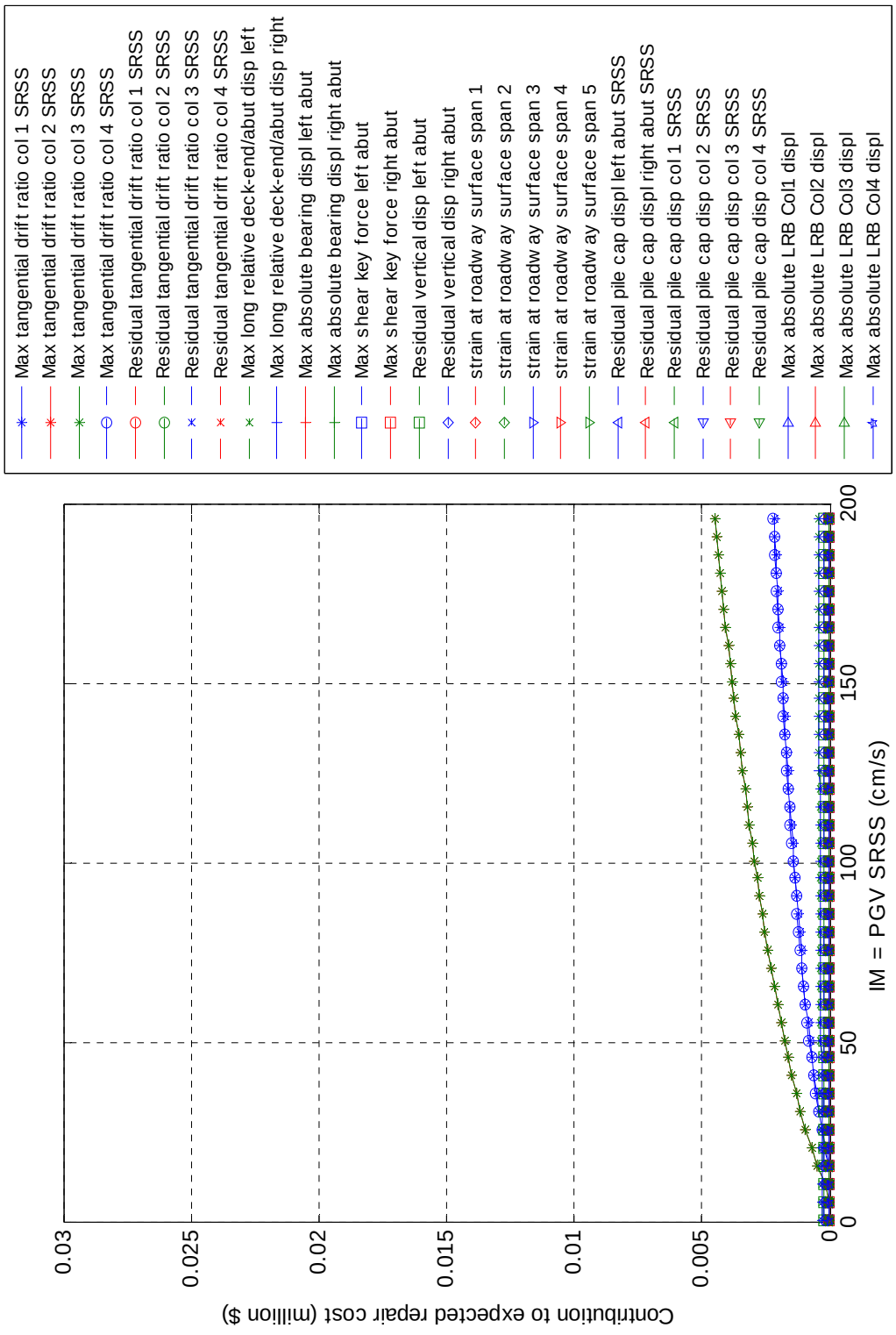

Figure F-7 Disaggregation of repair costs by PG for BI1 bridge

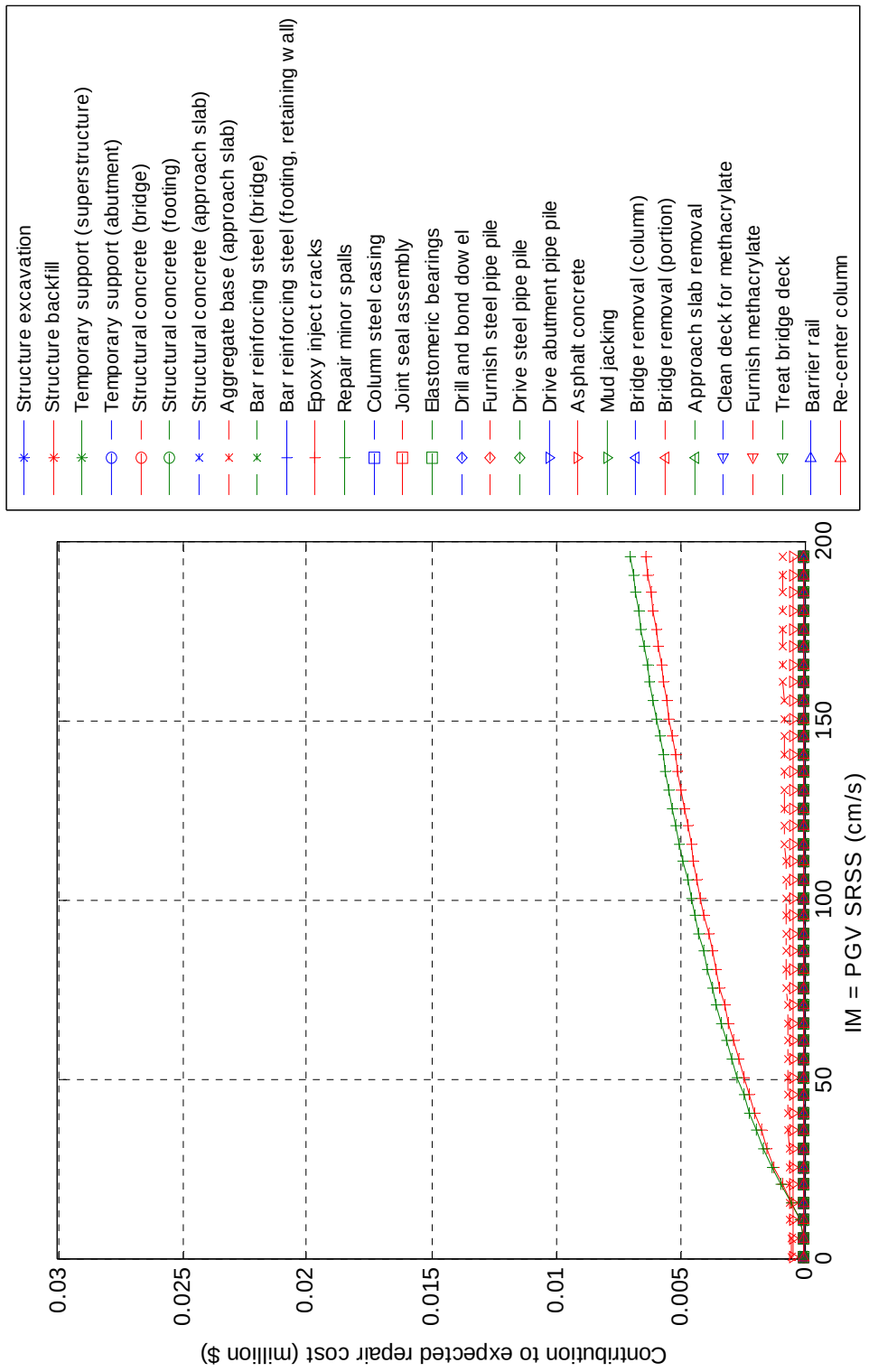

Figure F-8 Disaggregation of repair costs by repair item for BI1 bridge

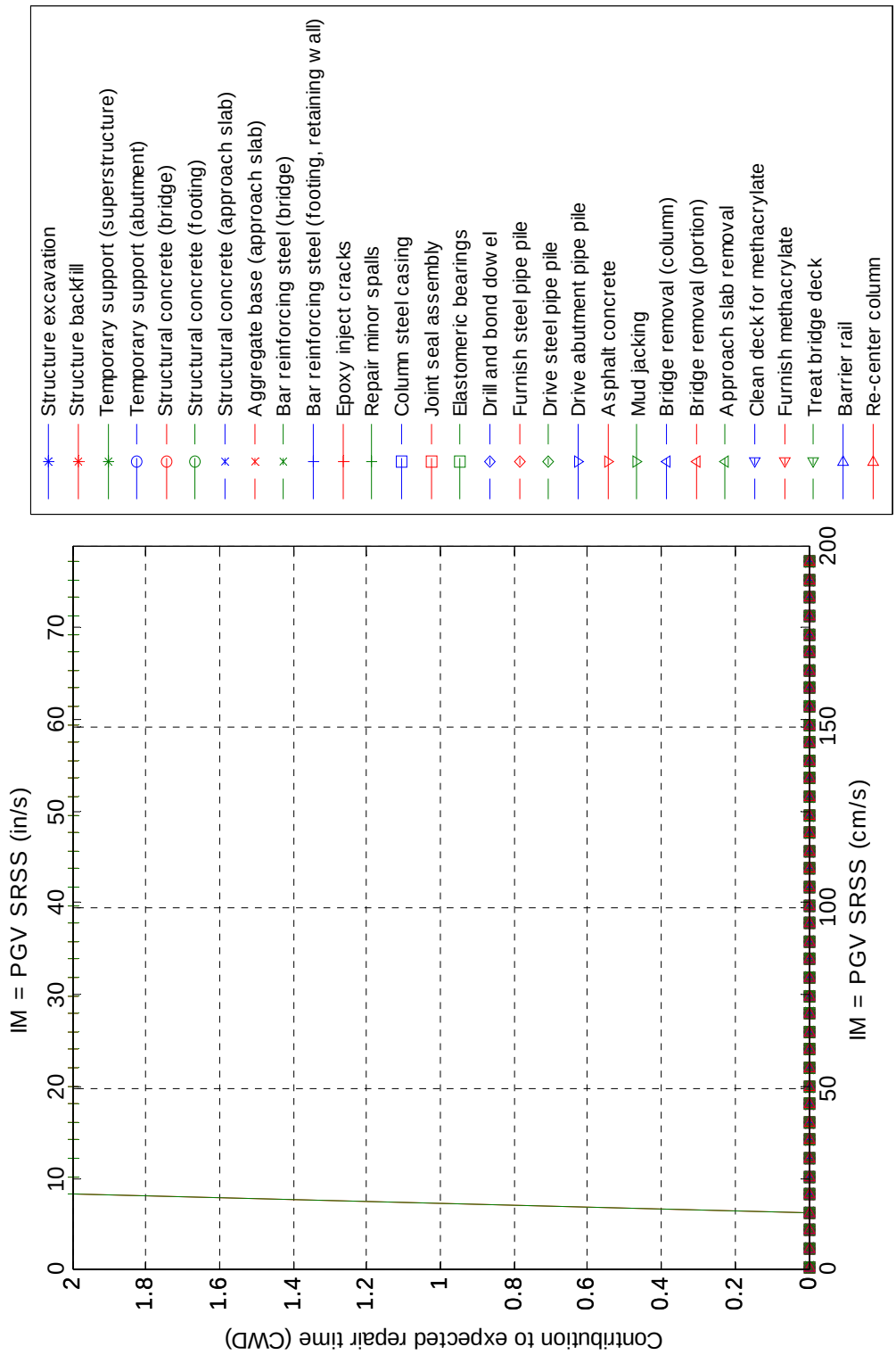

Figure F-9 Disaggregation of repair efforts by repair item for BI1 bridge

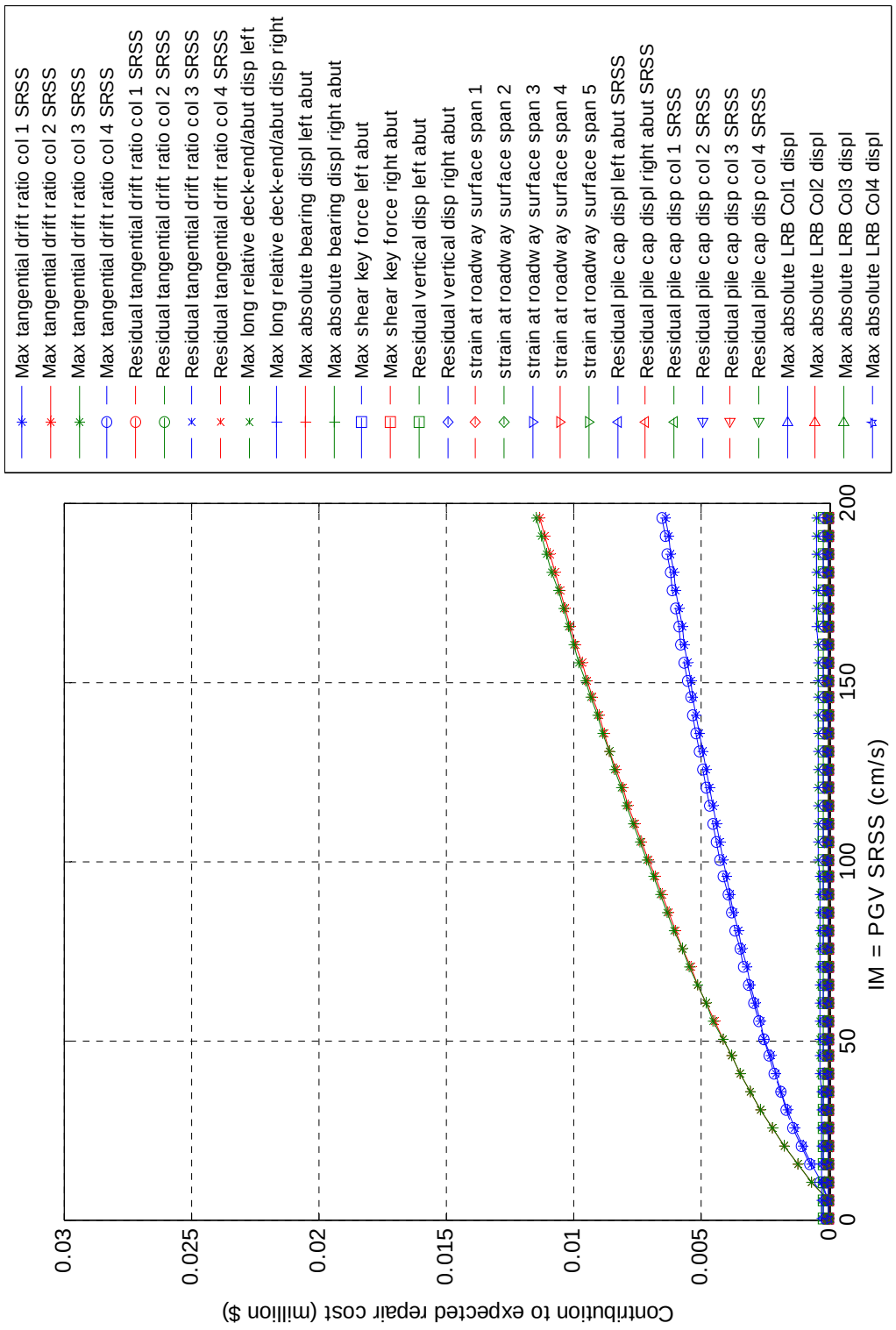

Figure F-10 Disaggregation of repair costs by PG for BI2 bridge

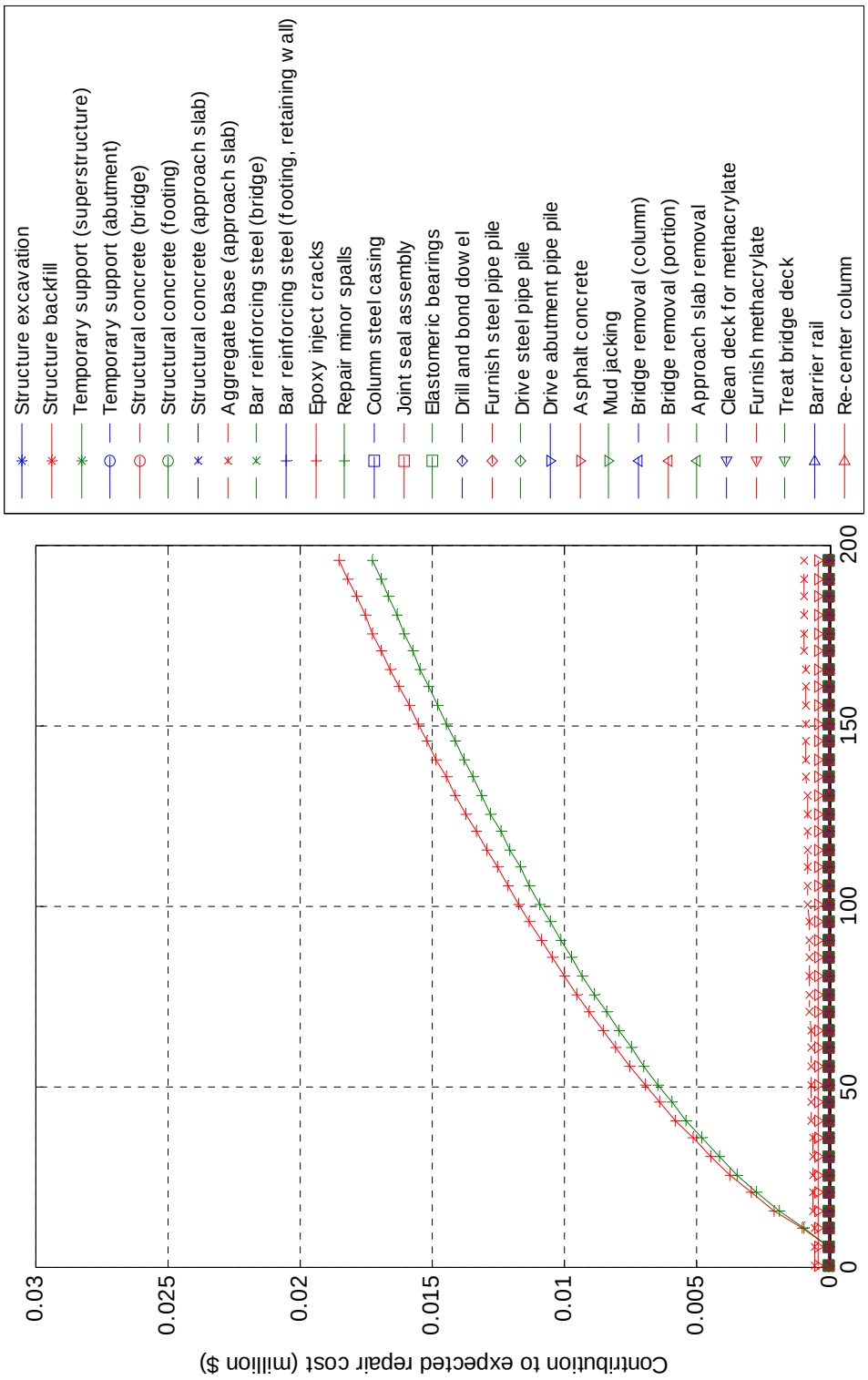

Figure F-11 Disaggregation of repair costs by repair item for BI2 bridge

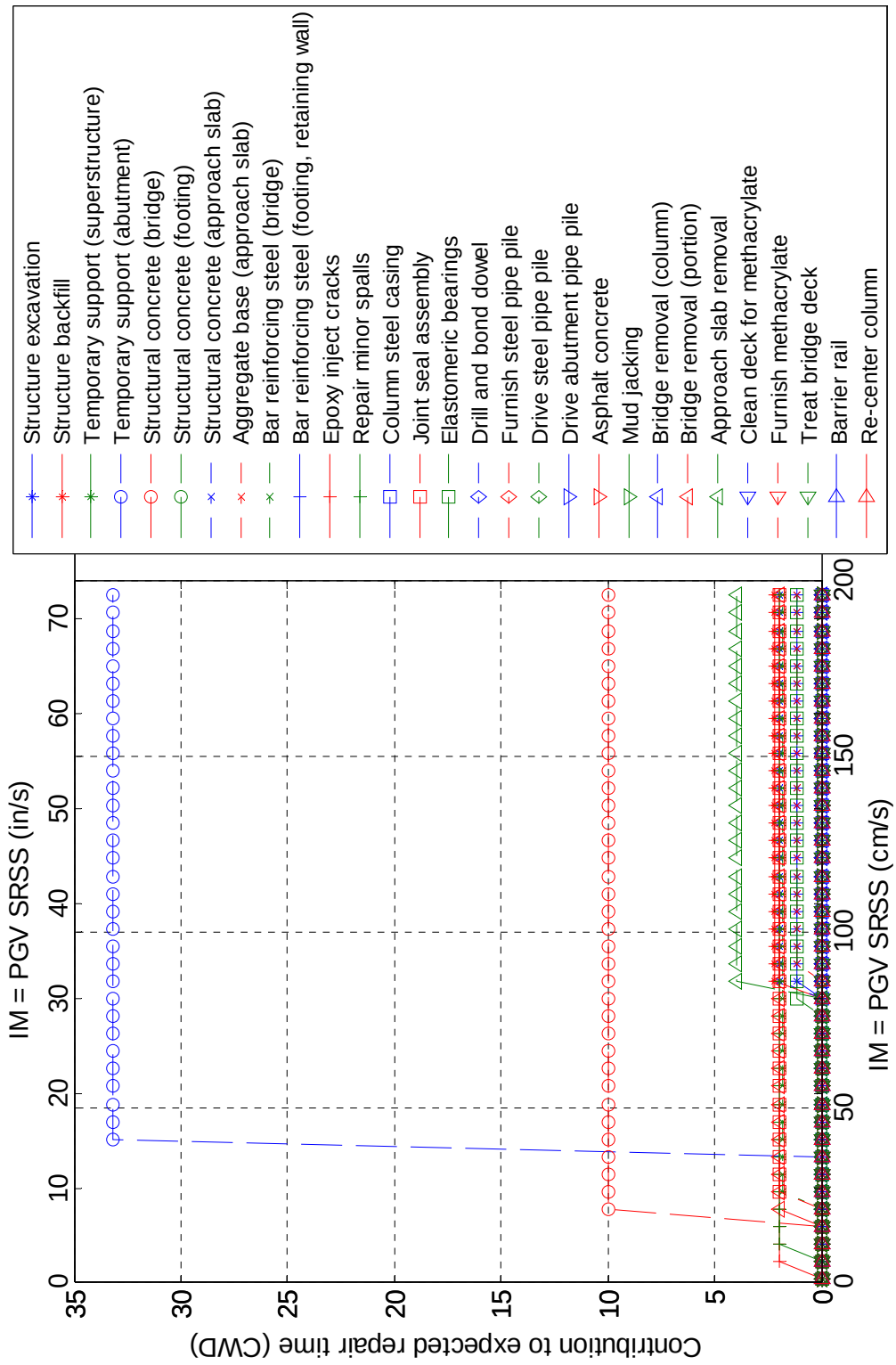

Figure F-12 Disaggregation of repair efforts by repair item for BI2 bridge